

# Quantum and Topological Phase Transitions in Multi-QuDit Systems and 2D Materials

Presented by

Alberto Mayorgas Reyes

A thesis presented for the degree of  
Doctor of Philosophy

Supervised by  
Manuel Calixto Molina  
Julio Guerrero García (UJA)

Departamento de Matemática Aplicada  
Universidad de Granada, Spain  
Granada, Marzo 2024



Universidad  
de Granada



Programa de Doctorado  
en Física y Matemáticas

Editor: Universidad de Granada. Tesis Doctorales  
Autor: Alberto Mayorgas Reyes  
ISBN: 978-84-1195-342-9  
URI: <https://hdl.handle.net/10481/92572>



*If I were not a physicist,  
I would probably be a musician.  
I often think in music.  
I live my daydreams in music.  
I see my life in terms of music.*

— Albert Einstein

## Agradecimientos

En primer lugar, me gustaría agradecer a mis directores de tesis, Manuel y Julio, su dedicación durante estos cuatro años. Gracias Manuel por recibirme con los brazos abiertos desde el primer día que llegué a Granada en 2019 para realizar el Máster FisyMat. Tu dedicación e infinita paciencia conmigo han hecho posible que aprenda todo lo que está plasmado en esta tesis. Gracias Julio por estar dispuesto a trabajar conmigo de forma remota desde Jaén, siempre con ganas de investigar nuevas temáticas y de hacer todos los cálculos que ello implicaba codo con codo, por muy tediosos que fueran. Tu perspectiva hacia la física matemática me ha abierto a la visión hacia nuevos campos que jamás pensaba que podría entender. Gracias a ambos por involucrarme desde el principio en toda vuestra investigación y publicaciones, por todo el material que me habéis facilitado, por los congresos y las visitas a Jaén. Sin vosotros no sería la misma persona.

Durante este último año de tesis, estoy muy agradecido de haber conocido personalmente a Octavio Castaños. Su experiencia y dedicación a la física son inspiradoras para mí. Siempre llega el primero y está dispuesto a ayudar en cualquier cálculo o problema que surja. Gracias por el buen ambiente que has creado con Manuel y conmigo en el Despacho 53. Gracias de corazón por haberme ofrecido investigar en México. También quería agradecer a mis coautores Elvira Romera y Nicolás Cordero por haberme abierto las puertas al campo de los materiales 2D. Gracias Antonio Sojo por haber compartido parte de tu tiempo a la investigación con nosotros.

Del Departamento de Matemática Aplicada quería agradecer a Juan Calvo y Pedro González su cercanía e interés por mis proyectos musicales, todavía tengo pendiente el concierto en Granada. También quiero mencionar a José Antonio Galán y Juan Soler por su ayuda con todos los trámites burocráticos que me han surgido durante la tesis. Del Departamento de Matemática Aplicada también me gustaría agradecer a mis compañeros de docencia René Fabregas, Clotilde Martínez, Abdelouahed Kouibia, Antonio López, Joaquín Sánchez, Pedro Torres, Lidia Fernández. Sin vosotros las clases no hubieran sido lo mismo, ni hubiera tenido al alcance todo el material y las facilidades que me habéis proporcionado.

Dentro del Departamento hay una habitación que para mí ha sido muy especial durante este tiempo, el Despacho 60. En ese despacho hemos compartido los mejores y los peores momentos que la formación predoctoral implica, pero siempre manteniendo una sonrisa y el buen rollo entre compañeros. Gracias Carlos por tu bondad con todos nosotros, tu actitud positiva y por ser nuestro maestro repostero, te debemos la alegría que nos transmites cada día. Gracias Alexis por estar siempre

dispuesto a escucharme y a ayudarme en cualquier momento por muy ocupado que estuvieses, tu compostura es una de tus mayores virtudes y que más valoro. Gracias Elena por el frescor que le has aportado al despacho desde que llegaste, sin ti las quedadas no serían igual de divertidas. Gracias Manuel por integrarme desde el primer día en el Departamento y en la ciudad, tu actitud hacia los problemas me ha enseñado a ser paciente y a relativizar todo lo que me ocurría. Sin ti Granada no hubiese sido lo mismo. Gracias Víctor por enseñarme el buen comer y las calles de Granada, todo un maestro inspirador, investigador y músico. Gracias también a David Poyato y a Claudia García por ayudarme en los momentos difíciles con las ayudas y contratos posdoctorales y aportarme una visión más amplia del mundo de la investigación. Ganivet y Pedro Antonio nos esperan chicos, es cuestión de tiempo que volvamos a coincidir.

Dentro del mundo de la investigación, quería mencionar a Jean Pierre Gazeau y A. Vourdas por sus inspiradores trabajos sobre estados coherentes y su calidez como persona durante el congreso de Strasbourg 2022. Gracias a Edu, Maricarmen, Gerardo y Salvio por haberme acompañado en las calles de Praga y por ayudarme tanto con ponencias en congresos en México como con ofertas de trabajo en Madrid. Gracias a Martin Plenio y Julen Pedernales por haber hecho posible mi estancia en Ulm, fue una experiencia única. Gracias también a todos mis compañeros de Ulm, José, Marwa, Marcos, Kirill, Trini, Benjamin, Albert, Moi, Clara, Julia, Mauro, Marit, Dario, Felix, Nicola, Matthias. Gracias a Antonio Prados por tutorizarme durante la carrera y estar dispuesto a investigar conmigo, aunque el destino hiciera que finalmente abandonara Sevilla. Gracias también a todos los profesores y profesoras que me habéis formado como físico y matemático en la Universidad de Sevilla y en la de Granada, sin vosotros y vosotras no tendría la bella percepción de la naturaleza que te dan ambas ciencias.

Este párrafo va dedicado a todos mis amigos de Sevilla. Desde el instituto me habéis acompañado hasta día de hoy. Gracias Emilio, Adri, Jesús, Pedro, Eva, Álvaro, Quini, Samu, Dani, Pablo, Álvaro, Edu, Laura, Angy, Luismi, Gonzalo. Gracias Isra y Andrés por haberme acompañado desde el Campus 2014, la trifuerza siempre estará presente. Gracias a mis compañeros de Lemniscata por compartir la música durante todos estos años, David, Luis, Yeyo, Edu, Javi, Pedro, María, Ismael, Samuel. Gracias a mis compañeros de carrera por todos esos momentos divertidos, Pablo, Lucas, María, Dani, Fernando, Pilar, Clara, Luis, Pedro, Toni, Anto, Miguel, Enrique, Edu; siempre nos quedará la Alameda. Gracias a todos los amigos de mis padres, Sergio, Miguel, Dani, Gala, Seba, J. Ramón, M. José, Lola, Fermín, Ana, Búho, Cristóbal; nos espera el hotel de Seba en Portugal.

La familia siempre ha ocupado un lugar muy importante para mí. Gracias a mi hermano Pablo por haber estado siempre conmigo y compartir toda una infancia juntos llena de risas, travesuras y juegos. Gracias a todos mis primos y primas, Carlos, Cristina, Javier, María, Marta y Pepe, por todos los momentos únicos que hemos vivido y que nos quedan. Gracias a mis tíos y tías, José, Cecilia, M. José, Alfonso, Lola y Lucas, por esos buenos momentos ensayando, esas comidas familiares en casa de los abuelos, esas noches de verano en Rota, esas tardes en

Castilleja, y por ser tan generosos conmigo. Gracias a mis abuelos y abuelas, José M., Dolores, Manolo y Carmen, por vuestro cariño y por haber sacrificado todo siempre por los nietos. Me gustaría también dar gracias a María José, Raúl, Javier, Castle, Alaska, Eva y Luzma, para mi sois ya parte de mi familia.

Por último, me gustaría dedicar estos renglones a los tres pilares de mi vida, tres mujeres que me ayudan en el día, tres generaciones de personas que me aportan una visión más completa de la vida. Gracias abuela por escuchar mis problemas, eterna confidente; por esos viernes almorzando en tu piso; por esas tardes de café, té y conversación; por esos momentos tan bonitos en los que me contabas la infancia de mi padre. Gracias mama por regalarme la vida y darme siempre la mejor educación; por estar siempre para todos mis problemas; por tu infinita bondad y hacer siempre que todo lo tuyo fuera nuestro también; por tu enseñarme la actitud positiva hacia la vida y los problemas; por tu fortaleza, resiliencia y ganas de luchar; por enseñarnos medio mundo a Pablo y a mí y despertarnos la pasión por viajar; por enseñarme a sentirme libre; sin ti nunca hubiera evolucionado desde que era pequeño. Gracias Julia por ser mi caminante. Apareciste en mi vida en uno de los momentos más difíciles, como una estrella fugaz que brilla en el cielo pero de repente el tiempo se congela y te acompaña eternamente. Gracias por tu amor sin límites; por la alegría que me transmites todos los días y tu poder para reflexionar y relativizar los problemas; por acompañarme siempre pese a las adversidades; por estar dispuesta a sacrificarte por la relación; por esperarme y por tu paciencia; por enseñarme a amar las cosas, la vida y las personas; por convertirme en una mejor persona; por tus besos, sonrisas y abrazos. Os quiero mucho. Papa, allá donde estés, te echamos de menos. Me gustaría mucho compartir este momento contigo, espero que estés orgulloso de mi.



# Abstract

This thesis is mainly focused on the study of quantum phase transitions of multi-quDit systems ( $D$ -level many-body systems, extending standard 2-level qubit systems) and topological phase transitions in 2D materials. For this purpose, we have extended the concept of spin coherent states and its adaptation to parity symmetry from 2-level to  $D$ -level systems, using the representation theory of the unitary group  $U(D)$ . Entanglement measures and phase space methods are also defined for the specific case of symmetric multi-quDits (bosons). The extension of quantum phase transitions from 2-level (qubits) to  $D$ -level (quDits) systems entails an enlarged variety of phases, which could be potentially exploited for quantum technological prospects. Parallely, we have devoted our efforts to implement the topological phase transitions formalism in new 2D anisotropic materials such as phosphorene, which are a hot topic in material sciences and constitute the building blocks for future photonic and optoelectronic devices.

This thesis is a compilation work of 7 publications [1–7] in scientific journals, which are indexed in the Journal Citation Report of the Science Citation Index, and are ranked in relevant positions, mostly in the first quartile (Q1) of the corresponding category. I have also published 4 international conference proceedings [8–11] derived from the main articles. The organization of this work begins with Chapter 1, an introduction to the state-of-the-art of quantum and topological phase transitions in the new quantum technological world, followed by the objectives and methodology. We find Chapter 5 at the end, a collection of the main results and conclusions derived from the publications, which compose the body of this thesis in Chapters 2, 3 and 4. A summary of these central chapters is as follows:

In Chapter 2, we include 5 articles [1–5] arranged in 3 sections. In general, we study quantum phase transitions (QPT) in multi-quDit systems, using the 3-level Lipkin-Meshkov-Glick (LMG) model as paradigmatic example. The QPTs are characterized by the control parameter  $\lambda$ , measuring the interaction strength of the LMG model. The  $D$ -level or multi-quDit systems of  $N$  particles, will be modeled by collective spin operators generating a  $U(D)$  symmetry. Therefore, we have made a review of the construction of  $U(D)$  unitary irreducible representations and how to define coherent states (CS) with this symmetry, which will work as variational states modeling the lowest-energy eigenstates of our Hamiltonian in the thermodynamic limit  $N \rightarrow \infty$ .

In Section 2.1, the article [1] is presented. We extend the concept of quantum phase transitions, from totally symmetric to different  $U(3)$  permutation symmetry sectors of a system of identical particles, defining the so called mixed symmetry

quantum phase transitions (MSQPT). In them, the representation parameter plays the role of a new control parameter, so that the phase space will have 4 phases and a "quadruple" point where all 4 phases coexist. In Section 2.2, the articles [2, 3] are presented. We compute entanglement and information measures for "symmetric" indistinguishable particles (bosons) in multi-quDit systems, restricting ourselves to the fully symmetric representations of  $U(D)$ . In Section 2.3, the articles [4, 5] are presented. We define a generalized parity adaptation of  $U(D)$ -spin CS and make a phase space analysis of them and the LMG model eigenstates.

In Chapter 3, the article [6] is presented. The Lieb-Mattis theorem is applied to  $U(N)$  quantum Hall ferromagnets at filling factor  $M$  for  $L$  Landau/lattice sites. The Hilbert space of the low energy sector in this model is identified with the carrier space of irreducible representations of  $U(N)$ , described by rectangular Young tableaux of  $M$  rows and  $L$  columns, and associated with Grassmannian phase spaces  $\mathbb{G}_M^N = U(N)/[U(M) \times U(N - M)]$ . This chapter shed light on the many-body problems with mixed symmetry sectors, ranging from the LMG model in the previous chapter to the 2D materials in the next one.

In Chapter 4, the article [7] is presented. We study how the transmittance and the Faraday angle are universal markers of topological phase transitions in a collection of 2D materials, including graphene and other Dirac materials, and HgTe quantum wells. We also show how these magnitudes become critical even for non-topological anisotropic materials such as phosphorene. For this purpose, we show how external electromagnetic fields affect these materials, and derive the current operators and the magneto-optical conductivities from the Kubo-Greenwood formula.

# Resumen en español

Esta tesis se centra principalmente en el estudio de transiciones de fase cuánticas en sistemas multi-quDit (sistemas de muchas partículas de  $D$  niveles, generalizando los sistemas de dos niveles) y de las transiciones de fase topológicas en materiales bidimensionales (2D). Para ello, hemos extendido el concepto de estados coherentes de espín y su adaptación a la simetría de paridad de sistemas de 2 niveles a sistemas de  $D$  niveles, utilizando la teoría de representaciones del grupo unitario  $U(D)$ . También se definen medidas de entrelazamiento y métodos de espacio de fases para el caso específico de multi-quDits simétricos (bosones). La extensión de las transiciones de fase cuánticas a multi-quDits conlleva una mayor variedad de fases, que podrían explotarse potencialmente con perspectivas en las tecnológicas cuánticas. Paralelamente, hemos dedicado nuestros esfuerzos a implementar el formalismo de las transiciones de fase topológicas en nuevos materiales 2D anisótropos como el fosforeno, que son un tema candente en las ciencias de los materiales y constituyen los bloques fundamentales para la construcción de futuros dispositivos fotónicos y optoelectrónicos.

La tesis se presenta por compendio de 7 publicaciones [1–7] en revistas científicas, que están indexadas en el Journal Citation Report del Science Citation Index, y están clasificadas en posiciones relevantes, mayormente en el primer cuartil Q1 del JIF en la categoría correspondiente. También he publicado 4 actas de congresos internacionales [8–11] derivados de los artículos principales. La organización de este trabajo comienza con el Capítulo 1, una introducción al estado del arte de las transiciones de fase cuánticas y topológicas en el contexto de las tecnologías cuánticas, seguido de los objetivos y la metodología. Encontramos al final el Capítulo 5, una recopilación de los principales resultados y conclusiones derivados de las publicaciones, que componen el cuerpo de esta tesis en los Capítulos 2, 3 y 4. A continuación se presenta un resumen de estos capítulos centrales:

En el capítulo 2, incluimos 5 artículos [1–5] ordenados en 3 secciones. En general, estudiamos las transiciones de fase cuánticas (QPT) en sistemas multi-quDit, utilizando el modelo de Lipkin-Meshkov-Glick (LMG) con 3 niveles como ejemplo paradigmático. Las QPT se caracterizan por el parámetro de control  $\lambda$ , que mide la fuerza de interacción del modelo LMG. Los sistemas de  $D$  niveles ó multi-quDits de  $N$  partículas, serán modelados por operadores colectivos de espín generando una simetría  $U(D)$ . Por ello, hemos hecho una revisión de la construcción de representaciones irreducibles unitarias de  $U(D)$  y de cómo definir estados coherentes (CS) con esta simetría, que funcionarán como estados variacionales modelando los autoestados de más baja energía de nuestro Hamiltoniano en el

límite termodinámico  $N \rightarrow \infty$ .

En la sección 2.1, se presenta el artículo [1]. Extendemos el concepto de transiciones de fase cuánticas, de sectores de simetría totalmente simétricos a diferentes sectores de simetría de permutación de  $U(3)$  en un sistema de partículas idénticas, definiendo las llamadas transiciones cuánticas de fase de simetría mixta (MSQPT). En ellas el parámetro de la representación juega el papel de un nuevo parámetro de control, dando lugar a un espacio de fases con 4 fases y un punto "cuádruple" donde coexisten las 4 fases. En la sección 2.2, se presentan los artículos [2, 3]. Calculamos medidas de entrelazamiento e información para partículas "simétricas" indistinguibles (bosones) en sistemas multi-quDit, restringiéndonos a las representaciones completamente simétricas de  $U(D)$ . En la sección 2.3, se presentan los artículos [4, 5]. Definimos una adaptación de paridad generalizada de  $U(D)$ -spin CS y hacemos un análisis de espacio de fases de ellos y de los autoestados del modelo LMG.

En el capítulo 3, se presenta el artículo [6]. Se aplica el teorema de Lieb-Mattis a los llamados  $U(N)$  quantum Hall ferromagnets con factor de llenado  $M$  para  $L$  sitios Landau. El espacio de Hilbert del sector de baja energía en este modelo se identifica con el espacio soporte de representaciones irreducibles de  $U(N)$ , descrito por tableros de Young rectangulares de  $M$  filas y  $L$  columnas, y asociado con los espacios de fase Grassmannianos  $\mathbb{G}_M^N = U(N)/[U(M) \times U(N - M)]$ . Este capítulo arroja luz sobre los problemas de muchos cuerpos con sectores de simetría mixta, que van desde el modelo LMG del capítulo anterior hasta los materiales 2D del siguiente.

En el capítulo 4, se presenta el artículo [7]. Estudiamos cómo la transmitancia y el ángulo de Faraday son marcadores universales de transiciones de fase topológicas en una colección de materiales 2D, incluyendo grafeno y otros materiales de Dirac, y pozos cuánticos de HgTe. También mostramos cómo estas magnitudes se vuelven críticas incluso para materiales anisótropos y no topológicos como el fosforeno. Para ello, mostramos cómo afectan los campos electromagnéticos externos a estos materiales, y derivamos los operadores de corriente y las conductividades magneto-ópticas a partir de la fórmula de Kubo-Greenwood.

# Contents

<b>Abstract</b>	<b>ix</b>
<b>Resumen en español</b>	<b>xi</b>
<b>Contents</b>	<b>xi</b>
<b>List of Abbreviations</b>	<b>xiii</b>
<b>List of Articles</b>	<b>xv</b>
<b>1 Introduction</b>	<b>1</b>
1.1 Objectives . . . . .	3
1.2 Methodology . . . . .	4
<b>2 Quantum phase transitions in multi-quDit systems</b>	<b>5</b>
2.1 Mixed symmetry quantum phase transitions . . . . .	5
2.2 Entanglement measures in symmetric multi-quDit systems . . . . .	21
2.2.1 Information measures in the study of entanglement . . . . .	40
2.3 Phase space and parity adapted DSCS in symmetric multi-quDit systems . . . . .	56
2.3.1 Schmidt decomposition of parity adapted coherent states . . . . .	78
<b>3 Hilbert space structure of the low energy sector of U(D) quantum Hall ferromagnets</b>	<b>101</b>
<b>4 Topological phase transitions in 2D materials</b>	<b>127</b>
<b>5 Conclusions</b>	<b>151</b>
<b>References</b>	<b>153</b>



# List of Abbreviations

<b>2CAT</b>	. . . . .	Parity adapted SU(2)-spin coherent states
<b>3CAT</b>	. . . . .	Parity adapted SU(3)-spin coherent states
<b>CS</b>	. . . . .	Coherent state
<b>DCAT</b>	. . . . .	Parity adapted SU( $D$ )-spin coherent states, a generalization of the "Schrödinger cats"
<b>DSCS</b>	. . . . .	SU( $D$ )-spin coherent states, a generalization of the SU(2)-spin coherent states
<b>ESQPT</b>	. . . . .	Excited states quantum phase transition
<b>EV</b>	. . . . .	Expected values
<b>GS</b>	. . . . .	Ground state
<b>GT</b>	. . . . .	Gelfand-Tsetlin
<b>HW</b>	. . . . .	Highest weight
<b>IBM</b>	. . . . .	Interacting boson model
<b>irrep</b>	. . . . .	Irreducible representation of a Lie group
<b>MSQPT</b>	. . . . .	Mixed symmetry quantum phase transition
<b>LMG</b>	. . . . .	Lipkin-Meshkov-Glick model
<b>LW</b>	. . . . .	Lowest weight
<b>QPT</b>	. . . . .	Quantum phase transition
<b>RDM</b>	. . . . .	Reduced density matrix
<b>TPT</b>	. . . . .	Topological phase transition
<b>unirrep</b>	. . . . .	Unitary irreducible representation of a Lie group



# List of Articles

- <sup>1</sup> M. Calixto, A. Mayorgas, and J. Guerrero, “Role of mixed permutation symmetry sectors in the thermodynamic limit of critical three-level Lipkin–Meshkov–Glick atom models”, *Phys. Rev. E* 103, 012116 (2021).
- <sup>2</sup> M. Calixto, A. Mayorgas, and J. Guerrero, “Entanglement and  $U(D)$ -spin squeezing in symmetric multi-qudit systems and applications to quantum phase transitions in Lipkin–Meshkov–Glick  $D$ -level atom models”, *Quantum Information Processing* 20, 304 (2021).
- <sup>3</sup> J. Guerrero, A. Mayorgas, and M. Calixto, “Information diagrams in the study of entanglement in symmetric multi-qudit systems and applications to quantum phase transitions in Lipkin–Meshkov–Glick  $D$ -level atom models”, *Quant. Inf. Process.* 21, 223 (2022).
- <sup>4</sup> A. Mayorgas, J. Guerrero, and M. Calixto, “Localization measures of parity adapted  $U(D)$ -spin coherent states applied to the phase space analysis of the  $D$ -level lipkin-meshkov-glick model”, *Phys. Rev. E* 108, 024107 (2023).
- <sup>5</sup> J. Guerrero, A. Sojo, A. Mayorgas, and M. Calixto, “Schmidt decomposition of parity adapted coherent states for symmetric multi-qudits”, *Journal of Physics A: Mathematical and Theoretical* 56, 355304 (2023).
- <sup>6</sup> M. Calixto, A. Mayorgas, and J. Guerrero, “Hilbert space structure of the low energy sector of  $U(N)$  quantum Hall ferromagnets and their classical limit”, *Symmetry* 14 (2022).
- <sup>7</sup> M. Calixto, A. Mayorgas, N. A. Cordero, E. Romera, and O. Castaños, “Faraday rotation and transmittance as markers of topological phase transitions in 2D materials”, *SciPost Phys.* 16, 077 (2024).



*Nothing in life is to be feared,  
it is only to be understood.  
Now is the time to understand more,  
so that we may fear less.*

— Marie Curie

# 1

## Introduction

It is common to define quantum phase transitions (QPTs) as singularities in the ground state (GS) of some quantum systems at zero temperature, when some parameter of its Hamiltonian is varied [12, 13]. More explicitly, we shall work with a many-body system Hamiltonian in the form  $H = H_0 + \lambda H_1$ , where  $H_0$  and  $H_1$  are the free and interaction terms respectively, and  $\lambda$  is a control parameter measuring the interaction strength, so that the QPT will occur when  $\lambda$  is modified until reaching certain critical value  $\lambda = \lambda_c$ . At this point, the GS energy becomes a non-analytic function of  $\lambda$ , and the energy difference between the GS and the first excited state vanishes [14]. Actually, these singularities only take place when the number of particles of the many-body system tends to infinity  $N \rightarrow \infty$ , which is also known as thermodynamic or classical limit. Nevertheless, we can observe precursors of the QPT for a finite number of particles by defining some scaling behavior of relevant quantities, such as the fidelity  $F_\psi(\lambda, \delta\lambda) = |\langle \psi(\lambda) | \psi(\lambda + \delta\lambda) \rangle|^2$  and the level population density [15–17].

In the last fifty years, QPTs have been studied in different fields of physics, ranging from the Lipkin and interacting boson models in nuclear physics [18–24], to the Dicke model (radiation-matter) in quantum optics [25–31], and the Bose-Einstein condensate and quantum Hall effects in condensed matter [32–35]. Despite QPTs occur at the unfeasible zero temperature, they have become essential in the experimental and theoretical treatment of quantum systems such as rare-earth magnetic insulators [36], superconductors [37–39], 2D electron gases [40], and heavy-fermion compounds [41]. Among all these examples, we have chosen the Lipkin-Meshkov-Glick model (LMG) as a paradigmatic case to study, aiming to extend the study of QPTs from 2-level systems (qubits) to  $D$ -level (multi-quDit) systems.

It is well-known how to describe two-level systems via the symmetry group  $SU(2)$  (special unitary Lie group in two dimensions) and the spin in many-body physics [13, 26, 42, 43]. However, when we have  $N$  particles distributed among  $D$  energy levels (multi-quDits), we are forced to study the  $SU(D)$  group and its representations

[44–46], in order to transform the second quantized Hamiltonian of the quantum many-body problem into a simpler version in terms of collective  $U(D)$ -spin operators  $S_{ij}$  [47–50]. This is possible when the interactions are of long range, i.e. when the coupling parameters do not depend on the particle indexes. They are elements of the Lie algebra of  $SU(D)$ , and can be represented in many different ways depending on our preferences, including matrix forms [51, 52] and diagrammatic patterns such as Young diagrams and GT patterns [49, 53, 54]. These tools allow us, among many other applications, to decompose the  $D^N$  dimensional (tensor product) Hilbert space of the  $N$  multi-quDit system into a direct sum of unitary irreducible representations (unirreps) [44, 52, 53]. The representation theory will also be fundamental in the Lieb–Mattis ordering theorem of electronic energy levels, which identifies the symmetry sector (representation) containing the ground state [55]. In addition, along this thesis we will frequently use the generalization of spin coherent states to the different  $SU(D)$  representations [56–58]. They are good variational states that model the ground state in multi-quDit problems, so they make it possible to study QPT from an analytical approach, using energy surface methods [59].

In the QPT framework, it is crucial to perform measurements that detect and quantify quantum correlations. We shall focus on interparticle and interlevel entanglement [60, 61], so we will use the reduced density matrix (RDM) formalism [62–64], and the linear  $\mathcal{L}$  and von Neumann  $\mathcal{S}$  entropies as entanglement measures [65, 66]. Both entropies are also regarded as information measures of a given RDM  $\rho$ , and can be related via information diagrams of the form  $(\mathcal{L}(\rho), \mathcal{S}(\rho))$ , which provide qualitative information about the rank of the RDM [65, 67, 68].

Parallely, phase space methods have proved to be effective in the description and characterization of QPT [69–71], connecting quantum mechanics with the classical statistical mechanics formalism [72, 73]. The concept of probability distributions in statistical mechanics is transformed into quasiprobability distribution functions in quantum mechanics. For the multi-quDit problem, they are defined using the coherent states of  $SU(D)$ , whose specific form depends on the phase space associated with the chosen representation. For instance, for the totally symmetric representation (bosons, identical and indistinguishable particles) the phase space is the complex projective space  $\mathbb{C}P^{D-1} = U(D)/[U(1) \times U(D-1)]$ ; for rectangular Young diagram representation (fermions) is the Grassmann phase space  $\mathbb{G}_M^D = U(D)/[U(M) \times U(D-M)]$ ; and for other particle mixtures is the flag manifold  $U(D)/U(1)^D$  [56, 74]. The most popular quasiprobability functions are Wigner  $W$ , Husimi  $Q$ , and Glauber-Sudarshan  $P$  functions, related to the symmetric, antinormal and normal ordering of the creation and annihilation operator respectively in the quantum harmonic oscillator phase space (Heisenberg-Weyl group) [75–77]. They admit a generalization to other symmetry groups and phase spaces [75, 78].

Complex many-body quantum systems also require algebraic and topological mathematical tools for their study, such as Chern and Pontryagin numbers. Specifically, new and exotic topological quantum phases of matter are emerging and being exploited for technological application in the last years [79–81]. This includes high-temperature semiconductors [82, 83] and two-dimensional (2D) materials [84].

Topological phase transitions are usually defined in two-dimensional graphene at low temperature, where the spin-orbit interactions alter the low energy electronic structure, converting the 2D semimetallic graphene into a quantum spin Hall insulator [79, 85–87]. They have been also studied in the theory and experiment in other 2D materials such as in mercury cadmium telluride (HgTe/CdTe) semiconductor quantum wells [88, 89]. It is interesting to adapt this knowledge to other promising 2D materials like phosphorene [90–93], in order to give an insight into new and exotic phases of matter. In general, 2D materials have remarkable electronic and magneto-optical properties [94–100], making them candidates for next generation optoelectronic devices. Therefore, we give special attention to the magneto-optical conductivity, obtained from the Kubo-Greenwood formula when applying a perpendicular magnetic field and an oscillating electric field to the material [101–103].

## 1.1 Objectives

We focus on the understanding and exploitation of the quantum properties and critical phenomena (phase transitions) occurring in quantum systems, including atomic and molecular models, and nanomaterials, with real and potential applications in the emerging and rapidly developing field of Quantum Technologies. For example, in the design and fabrication of innovative nanodevices with exotic physical properties, in the development of next generation electronics and spintronics, as well as applications in quantum computing, quantum information theory and quantum sensors.

The development of Quantum Technologies requires a deep understanding of quantum systems in order to properly model them, which is our main goal. The rapid experimental progress in this field requires a good theoretical understanding to efficiently analyze and deal with the enormous amount of information available. The specific objectives of this thesis are:

- Extending Lipkin- Meshkov-Glick model (used in nuclear physics, quantum optics, condensed matter, etc) from two-level systems (described by  $SU(2)$  symmetry) to  $D$  levels (described by  $SU(D)$  symmetry). In particular, we will often deal with the  $D = 3$  case for simplicity. The consideration of more levels for the atom introduces much more richness in the model and in its phase diagram, and the LMG model works perfectly as initial toy model before dealing with more complex quantum systems.
- Extending the concept of parity adaptation, entanglement measures, phase space and Schmidt decomposition to symmetric multi-quDit states. This will build a mathematical framework that could be applied to any Hamiltonian model with  $SU(D)$  symmetry, not only to the LMG model.
- Study how can we apply the Lieb-Mattis theorem to any quantum system invariant under  $SU(D)$ , in order to classify the energy levels according to the different permutation symmetry sectors of the Hamiltonian. This could provide

a powerful algebraic method for the Hamiltonian spectrum classification, saving computational resources for the simulation of large systems. We propose the  $U(N)$  quantum Hall ferromagnets as paradigmatic example.

- Characterize the topological phase transitions in emergent two-dimensional materials such as HgTe quantum wells, phosphorene, and other Dirac materials. Study how thickness, the presence of electric, magnetic and external laser fields affect their spectrum and conductivity.

## 1.2 Methodology

The project of the thesis is theoretical and computational, where all the calculations have been performed in personal computers and in servers located at the University of Granada (Departamento de Matemática Aplicada) and the University of Jaén (Departamento de Matemáticas). The methodology includes the following activities:

- Study books and research articles related with the different topic of the thesis.
- Periodic meetings in Granada and Jaén with the thesis supervisors to perform brainstorming, present results and new ideas, and create software together.
- Periodic video calls with the research collaborators contributing in the different articles.
- Attending courses, seminars and conferences of the Doctoral Program (Programa de Doctorado en Física y Matemáticas) and of the Escuela Internacional de Posgrado.
- Attending international conferences to share ideas and do networking.
- Complete a predoctoral stay in another country to encourage the internationalization of the student formation (University of Ulm, Germany).

*Alles Gescheite ist schon gedacht worden.  
Man muss nur versuchen, es noch einmal zu denken.*

*All intelligent thoughts have already been thought;  
what is necessary is only to try to think them again.*

— Johann Wolfgang von Goethe [104]

# 2

## Quantum phase transitions in multi-quDit systems

### 2.1 Mixed symmetry quantum phase transitions

<sup>1</sup> M. Calixto, A. Mayorgas, and J. Guerrero, “Role of mixed permutation symmetry sectors in the thermodynamic limit of critical three-level Lipkin-Meshkov-Glick atom models”, *Phys. Rev. E* 103, 012116 (2021).

#### Quality metrics JCR

- Year: 2022
- Category: PHYSICS, MATHEMATICAL
- Journal Impact Factor (JIF): 2.4
- JIF Rank: 11/56 (Q1)

Publication citations in Google Scholar (March 2024): 13

# Role of mixed permutation symmetry sectors in the thermodynamic limit of critical three-level Lipkin-Meshkov-Glick atom models

Manuel Calixto\* and Alberto Mayorgas†

*Department of Applied Mathematics and Institute Carlos I of Theoretical and Computational Physics,  
University of Granada, Fuentenueva s/n, 18071 Granada, Spain*

Julio Guerrero‡

*Department of Mathematics, University of Jaen, Campus Las Lagunillas s/n, 23071 Jaen, Spain*

We introduce the notion of Mixed Symmetry Quantum Phase Transition (MSQPT) as singularities in the transformation of the lowest-energy state properties of a system of identical particles inside each permutation symmetry sector  $\mu$ , when some Hamiltonian control parameters  $\lambda$  are varied. We use a three-level Lipkin-Meshkov-Glick (LMG) model, with  $U(3)$  dynamical symmetry, to exemplify our construction. After reviewing the construction of  $U(3)$  unirreps using Young tableaux and Gelfand basis, we firstly study the case of a finite number  $N$  of three-level atoms, showing that some precursors (fidelity-susceptibility, level population, etc.) of MSQPTs appear in all permutation symmetry sectors. Using coherent (quasi-classical) states of  $U(3)$  as variational states, we compute the lowest-energy density for each sector  $\mu$  in the thermodynamic  $N \rightarrow \infty$  limit. Extending the control parameter space by  $\mu$ , the phase diagram exhibits four distinct quantum phases in the  $\lambda$ - $\mu$  plane that coexist at a quadruple point. The ground state of the whole system belongs to the fully symmetric sector  $\mu = 1$  and shows a four-fold degeneracy, due to the spontaneous breakdown of the parity symmetry of the Hamiltonian. The restoration of this discrete symmetry leads to the formation of four-component Schrödinger cat states.

Keywords: Quantum phase transitions, many-body systems, tensor-products and direct-sum Clebsch-Gordan decompositions, mixed permutation symmetries, coherent states.

## I. INTRODUCTION

The role of permutation symmetry is crucial in the study of the evolution of quantum systems of identical particles (the simplest example is the classification of indistinguishable particles as bosons or fermions attending to their permutation properties) and should be taken into consideration, not only to simplify the problem and classify their solutions, but also at a deeper level. A non-trivial example, which is in the realm of many important physical models, is that of a number of identical particles distributed in a set of levels and a second quantized Hamiltonian describing pair correlations. In this case, the tensor product Hilbert space corresponding to  $N$  particles/atoms distributed among  $L$   $N$ -fold degenerate levels is  $L^N$  dimensional (the number of ways to put  $N$  particles in  $L$  levels). Particular interesting cases are systems of qubits ( $L = 2$ ) and qutrits ( $L = 3$ ), to use the quantum information jargon. When atoms are identical, permutation symmetry  $S_N$  allows to decompose this tensor product into a “Clebsch-Gordan” direct sum of unitary irreducible representations (unirreps) of the unitary group  $U(L)$ , whose generators define the dynamical algebra of the Hamiltonian in terms of collective operators. Young tableaux turn out to be a useful graphical method to represent these kind of decompositions into different

symmetry sectors and we shall make use of them in the next Sections.

When dealing with critical and chaotic quantum systems in the thermodynamic (classical) limit  $N \rightarrow \infty$ , like in quantum phase transitions (QPTs), only the totally symmetric sector is considered in the literature (see e.g. [1–5]), which reduces the size of the original Hilbert space from  $L^N$  to  $N + 1$  for  $L = 2$  (symmetric spins, qubits) or to  $(N + 1)(N + 2)/2$  for  $L = 3$  (symmetric qutrits) and so on, that is, the number of ways of exciting  $N$  atoms with  $L$  levels when order does not matter. This means to make the atoms/particles indistinguishable. This is a common procedure in the literature which is mostly assumed without a clear physical justification (usually for computational convenience). It is true that there are particular situations where restricting to the totally symmetric sector can be physically justified. Namely, for the Dicke model of superradiance, the assumption that the  $N$  two-level atoms are indistinguishable is admissible when the emitters are confined to a cavity volume  $V \ll \ell^3$  much smaller than the scale of the wavelength  $\ell$  of the optical transition. Also, in the analysis of the phase diagram and critical points of a QPT, the restriction to the fully symmetric sector is justified under the assumption that the ground state always belongs to this sector. However, as far as we know, there is not a general proof of this fact. One can find arguments in the literature (see e.g. [3] for the study of quantum chaos in a three-level LMG shell model) precluding the consideration of other permutation symmetry sectors than the totally symmetric under the argument that mixed symmetry sectors correspond to systems with more degrees of freedom that do

---

\* calixto@ugr.es

† albmayer97@gmail.com

‡ jguerrer@ujaen.es

not approach the classical  $N \rightarrow \infty$  limit as “rapidly” as the totally symmetric sector does. However, no notion of “speed/order” of convergence to  $N \rightarrow \infty$  appears in these studies.

In this work, we want to explore the role of mixed permutation symmetry sectors usually disregarded in the study of the thermodynamic limit of many-body critical quantum systems. For this purpose, we shall consider the paradigmatic and ubiquitous LMG Hamiltonian used in several fields (nuclear, quantum optics, condensed matter, etc.) of physics to model many-body  $L$ -level (usually  $L = 2$ ) systems (see e.g. [6] and references therein). We shall consider  $L = 3$ , since for  $L = 2$  all sectors can be reduced to the symmetric one (standard Clebsch-Gordan decomposition), although we shall give a brief of the  $L = 2$  case for pedagogical reasons. We shall classify the Hamiltonian spectrum according to different permutation symmetry sectors and we shall analyze the lowest-energy state inside each of these sectors, leading to the new notion of *Mixed Symmetry Quantum Phase Transition* (MSQPT) in the  $N \rightarrow \infty$  limit. Mixed symmetry sectors correspond in general with larger phase spaces than the fully symmetric sector (except for its conjugated representation), which contains the ground state of the system, defining the standard QPT. This notion of MSQPT is consistent since temporal evolution does not mix different symmetry sectors. If the initial state lays in one of these sectors, it remains trapped there. Phase diagrams and critical points depend on the particular symmetry sector and we give the explicit dependence for the three-level LMG model. Firstly we make a numerical treatment for large (but finite)  $N$ , computing some “precursors” of the MSQPT (level populations and information-theoretic measures). Then we analyze the thermodynamic  $N \rightarrow \infty$  limit by using mixed-symmetry coherent states as variational states for the lowest-energy state inside each sector. The variational approach provides the phase diagram for each MSQPT.

This notion of MSQPT overlaps with the existing notion of Excited State Quantum Phase Transition (ESQPT) already present in the literature [7, 8]. ESQPT is a continuation of the concept of QPT for singularities of the ground state to singularities of the excited states and singular level densities. From this point of view, our lowest-energy states inside each mixed symmetry sector are in fact excited energy states of the whole system, although ESQPT generally make reference to excited states inside the fully symmetric representation (other mixed symmetry sectors are disregarded). Therefore, our concept of MSQPT differs from the ESQPT notion, although there are some formal similarities.

The organization of the article is as follows. In Sec. II the general LMG model with  $L$  levels is introduced, giving its main properties and particular expressions for the case  $L = 2$  and  $L = 3$ . In Sec. III the unirreps of  $U(L)$  are discussed using the diagrammatic approach of Young tableaux, Weyl patterns, and Gelfand-Tsetlin (GT) basis to classify and label the states in each unirrep. In Sec. IV

the case of a finite number  $N$  of three-level atoms is thoroughly discussed for the LMG Hamiltonian, and the fidelity susceptibility and level population are used to detect precursors of phase transitions (that, properly speaking, take place in the thermodynamic limit  $N \rightarrow \infty$ ) as the interaction/control parameter  $\lambda$  is varied. Sec. V is devoted to the definition of coherent (quasi-classical) states for each unirrep of  $U(3)$  and the computation of expectation values of  $U(3)$  generators on coherent states (the so called “symbols”). In Sec. VI, the thermodynamic limit is performed in the expectation value of the LMG Hamiltonian on coherent states, thus defining a energy surface which is minimized to obtain the minimum energy inside each symmetry sector  $\mu$  as a function of the control parameter  $\lambda$ . This defines a phase diagram in the extended  $\lambda$ - $\mu$  plane with four distinct phases that coexist at a quadruple point. We pay special attention to the totally symmetric sector  $\mu = 1$ , where the (degenerated) ground state lives, calculating level population densities and studying the spontaneous breakdown of parity symmetry. After a conclusion section, Appendix A contains the details of the derivation of the differential realization of the generators of  $U(3)$  and their symbols, and in Appendix B we explicitly calculate the exponential action of  $U(3)$  Cartan generators, that leads to parity transformations when acting on coherent states.

## II. THE $L$ -LEVEL LMG MODEL

Many models describing pairing correlations in condensed matter and nuclear physics are defined by a second quantized Hamiltonian of the form

$$H_L = \sum_{i=1}^L \sum_{\mu=1}^N \varepsilon_i c_{i\mu}^\dagger c_{i\mu} - \sum_{i,j,k,l=1}^L \sum_{\mu,\nu=1}^N \lambda_{ij}^{kl} c_{i\mu}^\dagger c_{j\mu} c_{k\nu}^\dagger c_{l\nu} \quad (1)$$

where  $c_{i\mu}^\dagger$  ( $c_{i\mu}$ ) creates (destroys) a fermion in the  $\mu$  state of a  $L$ -level,  $i = 1, \dots, L$ , system (namely,  $L$  energy levels) with level energies  $\varepsilon_i$ . That is, the model has  $N$  identical particles distributed among  $L$  energy levels, each of which is  $N$ -fold degenerate. The two-body residual interactions (with strength  $\lambda$ ) scatter pairs of particles between the  $L$  levels without changing the total number of particles. For hermitian  $H_L$  we have  $\bar{\lambda}_{ij}^{kl} = \lambda_{lk}^{ji}$ . Defining the  $U(L)$  “quasispin” collective operators

$$S_{ij} = \sum_{\mu=1}^N c_{i\mu}^\dagger c_{j\mu} \quad (2)$$

the Hamiltonian (1) can be written as

$$H_L = \sum_{i=1}^L \varepsilon_i S_{ii} - \sum_{i,j,k,l=1}^L \lambda_{ij}^{kl} S_{ij} S_{kl}. \quad (3)$$

In this article we shall adopt a  $L$ -level atom picture and denote by  $E_{ij} = |i\rangle\langle j|$  the (Hubbard) operator describing a transition from the single-atom level  $|j\rangle$  to the level

$|i\rangle$ , with  $i, j = 1, \dots, L$ . The expectation values of  $E_{ij}$  account for complex polarizations or coherences for  $i \neq j$  and occupation probability of the level  $i$  for  $i = j$ . The  $E_{ij}$  represent the  $L^2$  generators (step operators) of  $U(L)$  (or  $GL(L; \mathbb{C})$  to be more precise) in the fundamental  $L \times L$  representation, whose (Cartan-Weyl) matrices are  $\langle l|E_{ij}|k\rangle = \delta_{il}\delta_{jk}$  (entry 1 in row  $i$ , column  $j$  and zero elsewhere) with commutation relations

$$[E_{ij}, E_{kl}] = \delta_{jk}E_{il} - \delta_{il}E_{kj}. \quad (4)$$

Denoting by  $E_{ij}^\mu$ ,  $\mu = 1, \dots, N$  the embedding of the single  $\mu$ -th atom  $E_{ij}$  operator into the  $N$ -atom Hilbert space (namely,  $E_{ij}^3 = \mathbb{1}_L \otimes \mathbb{1}_L \otimes E_{ij} \otimes \mathbb{1}_L$  for  $N = 4$ , with  $\mathbb{1}_L$  the  $L \times L$  identity), the collective quasispin operators are

$$S_{ij} = \sum_{\mu=1}^N E_{ij}^\mu. \quad (5)$$

They constitute the  $U(L)$  dynamical algebra of our system, with the same commutation relations as those of  $E_{ij}$  in (4).

We shall eventually particularize to  $L = 3$ -level atoms (qutrits) for concrete calculations. The best known case is the original  $L = 2$  levels LMG schematic shell model [9–11] to describe the quantum phase transition from spherical to deformed shapes in nuclei. This model assumes that the nucleus is a system of fermions which can occupy two levels  $i = 1, 2$  with the same degeneracy  $N$ , separated by an energy  $\varepsilon = 2\varepsilon_2 = -2\varepsilon_1$ . It can also describe a system of  $N$  interacting two-level identical atoms (“qubits”), or an anisotropic XY Ising model

$$H_{XY} = \varepsilon \sum_{\mu=1}^N \sigma_\mu^z + \sum_{\mu < \nu} \lambda_x \sigma_\mu^x \sigma_\nu^x + \sum_{\mu < \nu} \lambda_y \sigma_\mu^y \sigma_\nu^y, \quad (6)$$

in an external transverse magnetic field  $\varepsilon$  with infinite-range constant interactions. In terms of the  $U(2)$  angular momentum  $\vec{J}$  collective operators  $J_+ = S_{21}, J_- = S_{12}$  and  $J_z = \frac{1}{2}(S_{22} - S_{11})$ , the two-level LMG schematic shell model Hamiltonian reads [9, 10]:

$$H_2 = \varepsilon J_z + \frac{\lambda_1}{2}(J_+^2 + J_-^2) + \frac{\lambda_2}{2}(J_+ J_- + J_- J_+). \quad (7)$$

The  $\lambda_1$  interaction term annihilates pairs of particles in one level and creates pairs in the other level, and the  $\lambda_2$  term scatters one particle up while another is scattered down. The total number of particles  $N$  and the squared angular momentum  $\vec{J}^2 = j(j+1)$  are conserved. Since the Hamiltonian is symmetric under permutation of particle labels, it does not couple different angular momentum sectors  $j = N/2, N/2 - 1, \dots, 1/2$  or  $0$  (for odd or even  $N$ , respectively), with dimensions  $2j+1$ . Therefore, permutation symmetry reduces the size of the largest matrix to be diagonalized from  $2^N$  to  $N+1$ . As already said, quantum calculations are usually restricted to this

$(N+1)$ -dimensional totally symmetric subspace under the assumption that the  $N$  two-level particles are indistinguishable. Therefore, the Hilbert space is spanned by Dicke states  $|j, m\rangle, m = -j, \dots, j$ , where the eigenvalue  $m$  of  $J_z$  gives the number  $n = m + j$  of excited particle-hole pairs or atoms. The Hamiltonian  $H_2$  also commutes with the parity operator  $\Pi = e^{i\pi(J_z + j)}$ , so that temporal evolution does not connect states with different parity. This parity symmetry  $\mathbb{Z}_2$  is spontaneously broken in the thermodynamic  $N \rightarrow \infty$  limit, giving rise to a degenerate ground state.

In this article we shall tackle the less familiar case of  $L = 3$  level LMG model, of which there are some studies in the literature (see e.g. [1–5]). As in Ref. [3], we shall choose for simplicity vanishing interactions for particles in the same level and equal interactions for particles in different levels [similar to setting  $\lambda_2 = 0$  in (7)]. More explicitly, we take

$$\lambda_{ij}^{kl} = \frac{\lambda}{N(N-1)} \delta_{ik} \delta_{jl} (1 - \delta_{ij}) \quad (8)$$

in (3), where we are dividing two-body interactions by the number of particle pairs  $N(N-1)$  to make the Hamiltonian an intensive quantity (energy density) since we are interested in the thermodynamical limit  $N \rightarrow \infty$ . We shall also place the levels symmetrically about the level  $i = 2$  and write the intensive energy splitting per particle  $\varepsilon_3 = -\varepsilon_1 = \varepsilon/N$  and  $\varepsilon_2 = 0$ . Therefore, our Hamiltonian density will be:

$$H = H_3 = \frac{\varepsilon}{N}(S_{33} - S_{11}) - \frac{\lambda}{N(N-1)} \sum_{i \neq j=1}^3 S_{ij}^2. \quad (9)$$

This Hamiltonian density is invariant under the combined interchange of levels  $1 \leftrightarrow 3$  and  $\varepsilon \rightarrow -\varepsilon$ . We shall take  $\varepsilon > 0$ , for simplicity, measure energy in  $\varepsilon$  units, and discuss the energy spectrum and the phase diagram in terms of the control parameter  $\lambda$ . The existence of an interesting parity symmetry (like in the two-level case) also deserves attention. Indeed, this symmetry of the Hamiltonian has to do with the fact that the interaction only scatters pairs of particles, thus conserving the parity  $\Pi_i = \exp(i\pi S_{ii})$ , even (+) or odd (−), of the population  $S_{ii}$  in each level  $i = 1, \dots, L$ . For concreteness, we shall restrict to the case  $L = 3$  (see also [3]). Therefore, there are four different Hamiltonian matrices identified by  $(\Pi_1, \Pi_2, \Pi_3)$

$$(+, +, +), (+, -, -), (-, -, +), (-, +, -)$$

for even  $N$  and

$$(-, -, -), (-, +, +), (+, +, -), (+, -, +)$$

for odd  $N$ . This discrete symmetry corresponds to the finite group  $\mathbb{Z}_2 \times \mathbb{Z}_2 \times \mathbb{Z}_2$  with the constraint  $\Pi_1 \Pi_2 \Pi_3 = e^{i\pi N}$ . It is spontaneously broken in the thermodynamic limit and gives rise to a highly degenerated ground state,

as compared to the  $L = 2$  case (see Section VI and Appendix B for more details).

As for the two-level case of  $H_2$ , with regard the rotation group  $U(2)$  and Dicke states, the Hamiltonian matrix of  $H_3$  is block diagonal when the basis vectors are adapted to irreducible representations of the Lie group  $U(3)$ . Let us make a brief summary the general decomposition of the Hilbert space of  $N$   $L$ -level atoms into  $U(L)$  irreducibles. We shall restrict ourselves to  $L = 2$  (qubits) and  $L = 3$  (qutrits) for the sake of simplicity, although the procedure can be easily extrapolated to general  $L$ . Those readers acquainted with this language can skip to the next section.

### III. $U(L)$ UNIRREPS: YOUNG TABLEAUX, GELFAND BASIS AND MATRIX ELEMENTS

Let us symbolize the fundamental  $L \times L$  representation of  $U(L)$  by the Young box  $\square$ . The single atom states are represented by Weyl patterns/tableaux by filling in the boxes with integers  $i = 1, \dots, L$  (the number of levels). For example, for  $L = 2$

$$\boxed{1} = |1\rangle, \quad \boxed{2} = |2\rangle,$$

symbolize the (spin) doublet, and for  $L = 3$

$$\boxed{1} = |1\rangle, \quad \boxed{2} = |2\rangle, \quad \boxed{3} = |3\rangle,$$

symbolize the triplet. The unitary group  $U(L)$  is represented in this space by the fundamental ( $L$ -dimensional) representation. For  $L = 2$ , unitary matrices  $V \in U(2)$  can be obtained by applying Gram-Schmidt orthonormalization procedure to the columns of the triangular matrix  $T$  as

$$T = \begin{pmatrix} 1 & 0 \\ \alpha & 1 \end{pmatrix} \xrightarrow{\text{G-S}} V = \begin{pmatrix} \frac{1}{\sqrt{\ell}} & \frac{-\bar{\alpha}}{\sqrt{\ell}} \\ \frac{\alpha}{\sqrt{\ell}} & \frac{1}{\sqrt{\ell}} \end{pmatrix} \quad (10)$$

where  $\alpha$  is a complex number and  $\ell = |T^\dagger T|_1 = 1 + \alpha\bar{\alpha}$  is the leading principal minor of  $T^\dagger T$ . The addition of two phases (complex numbers  $u_1$  and  $u_2$  of modulus 1), as  $U = V \cdot \text{diag}(u_1, u_2)$ , completes the parametrization of  $U(2)$  by the coordinates:  $\alpha, u_1$  and  $u_2$ . For  $L = 3$  levels, unitary matrices  $U = V \cdot \text{diag}(u_1, u_2, u_3) \in U(3)$  can be constructed following a similar procedure, with

$$T = \begin{pmatrix} 1 & 0 & 0 \\ \alpha & 1 & 0 \\ \beta & \gamma & 1 \end{pmatrix} \xrightarrow{\text{G-S}} V = \begin{pmatrix} \frac{1}{\sqrt{\ell_1}} & \frac{-\bar{\alpha}-\gamma\bar{\beta}}{\sqrt{\ell_1\ell_2}} & \frac{-\bar{\beta}+\bar{\alpha}\bar{\gamma}}{\sqrt{\ell_2}} \\ \frac{\alpha}{\sqrt{\ell_1}} & \frac{1+\beta\bar{\beta}-\alpha\gamma\bar{\beta}}{\sqrt{\ell_1\ell_2}} & \frac{-\bar{\gamma}}{\sqrt{\ell_2}} \\ \frac{\beta}{\sqrt{\ell_1}} & \frac{\gamma-\beta\bar{\alpha}+\gamma\alpha\bar{\alpha}}{\sqrt{\ell_1\ell_2}} & \frac{1}{\sqrt{\ell_2}} \end{pmatrix} \quad (11)$$

where  $\alpha, \beta, \gamma$  are complex numbers and

$$\begin{aligned} \ell_1 &= |T^\dagger T|_1 = 1 + \alpha\bar{\alpha} + \beta\bar{\beta}, \\ \ell_2 &= |T^\dagger T|_2 = 1 + \gamma\bar{\gamma} + (\beta - \alpha\gamma)(\bar{\beta} - \bar{\alpha}\bar{\gamma}), \end{aligned} \quad (12)$$

are the leading principal minors of order 1 and 2 of  $T^\dagger T$  (or the squared inverse leading principal minors of order 1 and 2 of  $V$ ), which play an important role in computing coherent state expectation values (see later on Section V).

For  $N$  identical  $L$ -level atoms, the  $L^N$ -dimensional Hilbert space is the  $N$ -fold tensor product

$$\square \otimes \dots \otimes \square.$$

The tensor product representation of  $U(L)$  is now reducible and the invariant subspaces are graphically represented by Young frames of  $N$  boxes

$$\begin{array}{c} \overbrace{\square \dots \square}^{h_1} \\ \vdots \\ \square \end{array} \quad (13)$$

of shape  $h = [h_1, \dots, h_L]$ , with  $h_1 \geq \dots \geq h_L$ ,  $h_i$  the number of boxes in row  $i = 1, \dots, L$  and  $h_1 + \dots + h_L = N$ . For example, let us consider the case of  $N = 3$  two-level identical atoms (three qubits in the quantum information jargon). The Hilbert space is the  $2^3 = 8$ -dimensional 3-fold tensor product of the 2-dimensional Hilbert space of a single atom. In Young diagram notation, the Clebsch-Gordan direct sum decomposition of this 3-fold tensor product gives (dimensions are displayed on the top)

$$\square^2 \otimes \square^2 \otimes \square^2 = \square^4 \oplus 2 \square^2$$

which is the analogous of the usual coupling of three spin-1/2 yielding a spin 3/2 and two spins 1/2. Note that the representations  $\square^2$  and  $\square$  are equivalent from the point of view of  $SU(2)$ . This procedure can be iterated combining  $N$  doublets (spin-1/2) to obtain the Clebsch-Gordan decomposition series (Catalan's triangle)

$$2^{\otimes N} = \bigoplus_{k=0}^{\lfloor N/2 \rfloor} M_k(N+1-2k), \quad M_k = \frac{N+1-2k}{N+1} \binom{N+1}{k}, \quad (14)$$

where  $\lfloor N/2 \rfloor$  is the integer floor function. That is, the angular momentum  $j_k = \frac{N}{2} - k$  appears with multiplicity  $M_k$ . Note that the fully symmetric representation  $k = 0$  always appears with multiplicity  $M_0 = 1$ . For the case of  $N = 4$  qutrits, the direct-sum decomposition of the  $3^4 = 81$ -dimensional 4-fold tensor product into  $U(3)$  irreducibles gives

$$\square^3 \otimes \square^3 \otimes \square^3 \otimes \square^3 = \square^{15} \oplus 3 \square^{15} \oplus 2 \square^6 \oplus 3 \square^3. \quad (15)$$

The last Young frame in the previous decomposition is equivalent to  $\square$  from the point of view of  $SU(3)$ . In general,  $h = [h_1, h_2, h_3]$  is equivalent to  $h' = [h_1 - h_3, h_2 - h_3, 0]$  from the point of view of  $SU(3)$ .

A Weyl pattern (a Young frame filled up with level labels  $i = 1, \dots, L$ ) is said to be in the semistandard form (or column strict) if the sequence of labels is non-decreasing from the left to the right, and strictly increasing from the top to the bottom. For example, for a Young frame of shape  $h = [3, 2, 1]$  ( $N = 6$  atoms), the following Weyl pattern

$$\begin{array}{|c|c|c|} \hline 1 & 1 & 2 \\ \hline 2 & 3 & \\ \hline 3 & & \\ \hline \end{array} \quad (16)$$

is in the semistandard form. The dimension of the representation  $h$  coincides with the number of Weyl patterns in the semistandard form that one can construct. The weight or content of a Weyl pattern is a vector  $w = (w_1, \dots, w_L)$  whose components  $w_k$  are the population of level  $k$  [the eigenvalues of the quasispin operators  $S_{kk}$  in (5)], with  $w_1 + \dots + w_L = N$ . For example, the weight of (16) is  $w = (2, 2, 2)$ .

Gelfand-Tsetlin (GT) patterns (see e.g. [12]) are a convenient way to label Weyl patterns in semistandard form (i.e., quantum states of an irreducible representation of  $U(L)$  with label  $h$ ). For example, for  $L = 2$ , each irreducible subspace of  $U(2)$  is spanned by the GT basis vectors

$$|\mathfrak{m}\rangle = \left| \begin{array}{cc} m_{12} = h_1 & m_{22} = h_2 \\ & m_{11} \end{array} \right\rangle, \quad h_2 \leq m_{11} \leq h_1. \quad (17)$$

The equivalence with more standard  $SU(2)$  angular momentum  $j$  or Dicke states  $\{|j, m\rangle, -j \leq m \leq j\}$  is

$$|j = \frac{h_1 - h_2}{2}, m = m_{11} - \frac{h_1 + h_2}{2}\rangle, \quad (18)$$

with  $h_1 + h_2 = N$  the linear Casimir eigenvalue of  $U(2)$ . Note that two  $U(2)$  irreps,  $h = [h_1, h_2]$  and  $h' = [h'_1, h'_2]$ , with the same angular momentum  $j = \frac{h_1 - h_2}{2} = \frac{h'_1 - h'_2}{2}$  are equivalent under the point of view of  $SU(2)$ . In particular  $h = [h_1, h_2]$  is equivalent to  $h' = [h_1 - h_2, 0]$  under  $SU(2)$  (same angular momentum). The totally symmetric irrep  $h = [N, 0]$  (depicted by a Young frame with a single row of  $N$  boxes) has the higher angular momentum  $j = N/2$  in the Clebsch-Gordan sum decomposition of the  $N$ -fold tensor product (14). For  $L = 3$ -level atoms, unirreps of  $U(3)$  of shape/label  $h = [h_1, h_2, h_3]$  are spanned by GT basis vectors

$$|\mathfrak{m}\rangle = \left| \begin{array}{ccc} m_{13} = h_1 & m_{23} = h_2 & m_{33} = h_3 \\ & m_{12} & m_{22} \\ & & m_{11} \end{array} \right\rangle, \quad (19)$$

which are subject to the betweenness conditions:

$$\begin{aligned} h_1 &\geq m_{12} \geq h_2, & h_2 &\geq m_{22} \geq h_3, \\ & & m_{12} &\geq m_{11} \geq m_{22}. \end{aligned} \quad (20)$$

The dimension of the carrier Hilbert space  $\mathcal{H}_h$  of an irrep of  $U(3)$  of shape  $h$  is then

$$\begin{aligned} \dim(\mathcal{H}_h) &= \sum_{m_{12}=h_2}^{h_1} \sum_{m_{22}=h_3}^{h_2} \sum_{m_{11}=m_{22}}^{m_{12}} 1 \\ &= \frac{1}{2}(1 + h_1 - h_2)(2 + h_1 - h_3)(1 + h_2 - h_3). \end{aligned} \quad (21)$$

The connection between Weyl and GT patterns is the following. Denoting by  $n_{ki}$  the number of times that the level  $i$  appears in the row  $k$  (counting downwards) of a Weyl pattern (that is, the population of level  $i$  in the row  $k$ ), the corresponding GT labels are  $m_{kj} = \sum_{i=1}^j n_{ki}$ . If we denote the GT pattern (19) by its rows:  $\mathfrak{m} = \{m_3, m_2, m_1\}$  with  $m_3 = [m_{13}, m_{23}, m_{33}]$ ,  $m_2 = [m_{12}, m_{22}]$  and  $m_1 = [m_{11}]$ , then  $m_3$  is directly read off the shape of the Weyl pattern,  $m_2$  is read off the shape that remains after all boxes containing label 3 are removed and, finally,  $m_1$  is read off the shape that remains after all remaining boxes containing label 2 are removed. In the example (16) we have the correspondence

$$\begin{array}{|c|c|c|} \hline 1 & 1 & 2 \\ \hline 2 & 3 & \\ \hline 3 & & \\ \hline \end{array} = \left| \begin{array}{ccc} 3 & 2 & 1 \\ & 3 & 1 \\ & & 2 \end{array} \right\rangle. \quad (22)$$

The population of level  $k$  (the weight component  $w_k$ ) is then directly computed from a GT pattern  $|\mathfrak{m}\rangle$  as  $w_k = \bar{m}_k - \bar{m}_{k-1}$ , where we denote by  $\bar{m}_k = \sum_{i=1}^k m_{ik}$ , the average of row  $k$  of the pattern  $\mathfrak{m}$  (one sets  $\bar{m}_0 \equiv 0$  by convention). Therefore, the action of diagonal operators  $S_{kk}$  on an arbitrary GT vector  $|\mathfrak{m}\rangle$  is

$$S_{kk}|\mathfrak{m}\rangle = w_k|\mathfrak{m}\rangle = (\bar{m}_k - \bar{m}_{k-1})|\mathfrak{m}\rangle. \quad (23)$$

For example, the weight of the GT vector (17) is  $(w_1, w_2) = (m_{11}, N - m_{11})$  or  $(\frac{N}{2} + m, \frac{N}{2} - m)$  in terms of the angular momentum third component  $m$  in (18).

A state  $|\mathfrak{m}'\rangle$  is said to be of lower weight  $w'$  than  $|\mathfrak{m}\rangle$  if the first non-vanishing coefficient of  $w - w'$  is positive. This is called the lexicographical rule. In more physical but less precise terms, populating lower levels  $k$  increases the weight  $w$ . It is clear that the highest weight (HW) vector  $|\mathfrak{m}_{\text{hw}}\rangle$  has weight  $w = (h_1, h_2, h_3)$ . In GT notation, the HW vector of an irrep  $h$  of  $U(3)$  corresponds to

$$|\mathfrak{m}_{\text{hw}}\rangle = \left| \begin{array}{ccc} h_1 & h_2 & h_3 \\ & h_1 & h_2 \\ & & h_1 \end{array} \right\rangle = \begin{array}{|c|c|c|} \hline 1 & \dots & 1 \\ \hline 2 & \dots & 2 \\ \hline 3 & \dots & 3 \\ \hline \end{array} \quad (24)$$

Analogously, the lowest weight (LW) vector has weight  $w = (h_3, h_2, h_1)$  and is given by

$$|\mathfrak{m}_{\text{lw}}\rangle = \left| \begin{array}{ccc} h_1 & h_2 & h_3 \\ & h_2 & h_3 \\ & & h_3 \end{array} \right\rangle = \begin{array}{|c|c|c|} \hline 1 & \dots & 1 & 2 & \dots & 2 & 3 & \dots & 3 \\ \hline 2 & \dots & 2 & 3 & \dots & 3 \\ \hline 3 & \dots & 3 \\ \hline \end{array} \quad (25)$$

In general, all states of the representation  $h = [h_1, \dots, h_L]$  of  $U(L)$  can be obtained from a HW vector  $|\mathfrak{m}_{\text{hw}}\rangle$  by applying lowering operators  $S_{jk}, j > k$ , or from a LW vector  $|\mathfrak{m}_{\text{lw}}\rangle$  by applying rising operators  $S_{jk}, j < k$ . Indeed, let us denote by  $\mathfrak{e}_{jk}$  the pattern with 1 at place  $(j, k)$  and zeros elsewhere. The action of step 1 lowering  $S_{-k} \equiv S_{k, k-1}$  and rising operators  $S_{+k} \equiv S_{k-1, k}$  is given

by (see e.g. [12])

$$S_{\pm k}|\mathfrak{m}\rangle = \sum_{j=1}^{k-1} c_{j, k-1}^{\pm}(\mathfrak{m})|\mathfrak{m} \pm \mathfrak{e}_{j, k-1}\rangle, \quad (26)$$

with coefficients

$$c_{j, k-1}^{\pm}(\mathfrak{m}) = \left( -\frac{\prod_{i=1}^N (m'_{ik} - m'_{j, k-1} + \frac{1 \mp 1}{2}) \prod_{i=1}^{k-2} (m'_{i, k-2} - m'_{j, k-1} - \frac{1 \pm 1}{2})}{\prod_{i \neq j} (m'_{i, k-1} - m'_{j, k-1}) (m'_{i, k-1} - m'_{j, k-1} \mp 1)} \right)^{1/2}, \quad (27)$$

where  $m'_{ik} = m_{ik} - i$  and  $c_{j, k-1}^{\pm}(\mathfrak{m}) \equiv 0$  whenever any indeterminacy arises. In fact, from the commutation relations

$$\begin{aligned} [S_{ii}, S_{jk}] &= \delta_{ij} S_{ik} - \delta_{ik} S_{ji} \\ \Rightarrow S_{ii} S_{jk} |\mathfrak{m}_{\text{hw}}\rangle &= (m_{iN} + \delta_{ij} - \delta_{ik}) S_{jk} |\mathfrak{m}_{\text{hw}}\rangle, \end{aligned} \quad (28)$$

the weight  $w'$  of  $S_{-k}|\mathfrak{m}\rangle$  is given by

$$S_{ii} S_{-k} |\mathfrak{m}\rangle = (w_i + \delta_{i, k} - \delta_{i, k-1}) S_{-k} |\mathfrak{m}\rangle = w'_i S_{-k} |\mathfrak{m}\rangle, \quad (29)$$

and therefore,  $S_{-k}|\mathfrak{m}\rangle$  becomes of lower weight than  $|\mathfrak{m}\rangle$  since the first non-vanishing coefficient of  $w - w'$  is  $(w - w')_{k-1} = 1 > 0$ . Applying recursion formulas

$$\begin{aligned} S_{i, i-l} &= [S_{i, i-1}, S_{i-1, i-l}], \\ S_{i-l, i} &= [S_{i-l, i-1}, S_{i-1, i}] \quad l > 0, \end{aligned} \quad (30)$$

one can obtain any non diagonal operator  $S_{ij}$  matrix element from (26). In particular, the HW vector verifies

$$S_{ij} |\mathfrak{m}_{\text{hw}}\rangle = h_i \delta_{ij} |\mathfrak{m}_{\text{hw}}\rangle \quad \forall i \leq j, \quad (31)$$

whereas the action of lowering operators  $S_{ij}, i > j$ , is given by (26, 27, 30). From the definition (27) one can prove that

$$c_{j, k-1}^{\pm}(\mathfrak{m}) = c_{j, k-1}^{\mp}(\mathfrak{m} \pm \mathfrak{e}_{j, k-1}), \quad (32)$$

which means that  $S_{+k}^{\dagger} = S_{-k}$ . Also, applying induction and the recurrence formulas (30), one obtains  $S_{k, k-h}^{\dagger} = S_{k-h, k}$ . As a particular case, using the equivalence (18) between GT and Dicke vectors for  $U(2)$ , one can recover the usual angular momentum,  $J_z = (S_{22} - S_{11})/2$ ,  $J_+ = S_{21}$  and  $J_- = S_{12}$ , matrix elements

$$\begin{aligned} \langle j, m' | J_z | j, m \rangle &= m \delta_{m', m}, \\ \langle j, m' | J_{\pm} | j, m \rangle &= \sqrt{(j \mp m)(j \pm m + 1)} \delta_{m', m \pm 1}. \end{aligned} \quad (33)$$

from the general expressions (23, 26, 27).

With all this whole mathematical arsenal, we are now ready to tackle the analysis of the Hamiltonian (9) spectrum according to permutation symmetry, and the structure of the low-energy states inside each symmetry sector.

#### IV. SYMMETRY CLASSIFICATION OF HAMILTONIAN EIGENSTATES FOR A FINITE NUMBER OF 3-LEVEL ATOMS AND QPT PRECURSORS

Let us firstly analyze the spectrum of the noninteracting free Hamiltonian part  $H^{(0)} = \frac{\epsilon}{N}(S_{33} - S_{11})$  of the LMG Hamiltonian (9). For level splitting  $\epsilon > 0$ , the lowest-energy (ground) state coincides with the highest-weight state

$$|\psi_0\rangle = |\mathfrak{m}_{\text{hw}}\rangle = \left| \begin{array}{ccc} N & 0 & 0 \\ & N & 0 \\ & & N \end{array} \right\rangle = \overbrace{\boxed{1 \cdots 1}}^N \quad (34)$$

of the fully symmetric representation  $h = [N, 0, 0]$ . That is, all  $N$  atoms are placed at the level  $i = 1$ . The energy density is then  $E_0 = -\epsilon$ . The excited states correspond to energy densities  $E_n = (n - N)\epsilon/N, n = 1, \dots, 2N$ . The highest-energy  $E_{2N}$  state corresponds to the lowest-weight vector

$$|\psi_{2N}\rangle = |\mathfrak{m}_{\text{lw}}\rangle = \left| \begin{array}{ccc} N & 0 & 0 \\ & 0 & 0 \\ & & 0 \end{array} \right\rangle = \overbrace{\boxed{3 \cdots 3}}^N \quad (35)$$

of the fully symmetric representation  $h = [N, 0, 0]$ . That is, all  $N$  atoms are placed at the level  $i = 3$ . These free Hamiltonian eigenvalues  $E_n$  are highly degenerated, except for  $E_0$  and  $E_{2N}$ . For example, the states

$$\boxed{1 \cdots 1 \ 1 \ 2} \quad \text{and} \quad \begin{array}{c} \boxed{1 \cdots 1} \\ \boxed{2} \end{array},$$

which belong to different symmetry sectors, have the same energy  $E_1$  (first excited energy level). The eigenvector composition and degeneracy of higher excited states is a bit more involved. Note that all GT vectors  $|\mathfrak{m}\rangle$  in (19) are eigenvectors of the free Hamiltonian density  $H^{(0)}$  and their eigenvalues can be easily calculated as

$$E_{\mathfrak{m}} = \frac{\epsilon}{N}(w_3 - w_1) = \frac{\epsilon}{N}(N - m_{11} - m_{12} - m_{22}). \quad (36)$$

Therefore, the degeneracy of each energy level coincides with the total number of GT patterns  $\mathfrak{m}$  with a common

value of  $m_{11} + m_{12} + m_{22}$ . The highest- and the lowest-energy levels correspond to  $m_{11} + m_{12} + m_{22} = 0$  and  $m_{11} + m_{12} + m_{22} = 2N$ , respectively, and they have degeneracy 1, coinciding with the lowest- and the highest-weight vectors in (35) and (34), respectively.

This degeneracy is partially lifted when the two-body interaction [with coupling constant  $\lambda$ , like in (9)] is introduced. This interaction affects each permutation symmetry sector in a different manner, so that energy bands emerge in the interacting Hamiltonian spectrum, as we can perceive in Figure 1 for  $N = 4$  identical 3-level atoms. Excited states belong not only to the fully symmetric representation but all symmetry sectors are involved. Therefore, if we are in a physical situation where our identical atoms are not necessarily indistinguishable, we should not disregard symmetry sectors other than the fully symmetric, since they play an important role in the analysis of excited states.

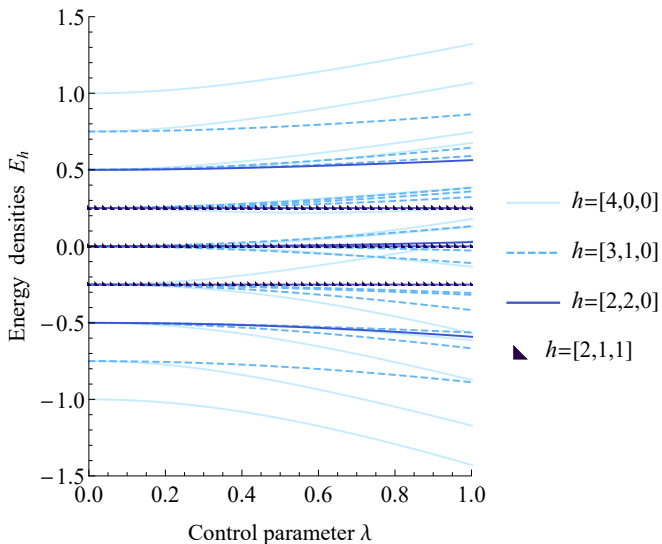


FIG. 1. LMG Hamiltonian energy density spectrum, for  $N = 4$  identical  $L = 3$  level atoms, as a function of the interacting control parameter  $\lambda$  (both in  $\epsilon$  units). Energy curves associated to the four different symmetry sectors  $h$ , depicted in (15), are plotted with different color. The free Hamiltonian ( $\lambda = 0$ ) eigenvalues are highly degenerated, the corresponding eigenspaces containing vectors belonging to different symmetry sectors  $h$ . This degeneracy is partially lifted when the two-body interaction ( $\lambda \neq 0$ ) is introduced, giving rise to the appearance of energy bands.

Since Hamiltonian evolution does not mix different symmetry sectors  $h$ , we are interested in the analysis of critical phenomena occurring inside each Hilbert subspace  $\mathcal{H}_h$  corresponding to the carrier space of an irrep  $h$  of  $U(3)$ . Therefore, we shall select the lowest-energy vector  $|\psi_0^h\rangle$  inside each  $\mathcal{H}_h$  and look for drastic changes in its structure when varying  $\lambda$  for  $N \rightarrow \infty$  (thermodynamic limit). With this analysis we will introduce the concept of MSQPT in the next sections. Before, for finite  $N$ , there still are some QPT precursors which can anticipate

the approximate location of critical points. The drastic change of the structure of a state  $|\psi(\lambda)\rangle$  in the vicinity of a critical point  $\lambda^{(0)}$  can be quantified with information theoretic measures like the so called fidelity [13–15]

$$F_\psi(\lambda, \delta\lambda) = |\langle \psi(\lambda) | \psi(\lambda + \delta\lambda) \rangle|^2,$$

which measures the overlap between two states in the vicinity ( $\delta\lambda \ll 1$ ) of  $\lambda$ . The fidelity is nearly 1 far from a critical point  $\lambda^{(0)}$  and drastically falls down in the vicinity of  $\lambda^{(0)}$ , the more the higher is  $N$ . Instead of  $F_\psi(\lambda, \delta\lambda)$ , which is quite sensitive to the step  $\delta\lambda$ , we shall use the so called susceptibility

$$\chi_\psi(\lambda, \delta\lambda) = 2 \frac{1 - F_\psi(\lambda, \delta\lambda)}{(\delta\lambda)^2}. \quad (37)$$

See e.g. References [16–18] for the use of information-theoretic concepts like susceptibility and Rényi-Wehrl entropies in the 2-level LMG case and other paradigmatic QPT models. In Figure 2 we represent the susceptibility of the ground (fully symmetric) state of the 3-level LMG Hamiltonian (9) for increasing values of  $N$ . We see that the susceptibility is sharper and sharper as  $N$  increases, divining the existence of a QPT at a critical point around  $\lambda^{(0)} \simeq 0.6\epsilon$ . Actually, the variational/semiclassical  $N \rightarrow \infty$  study, using coherent states à la Gilmore [19], in sections V and VI will reveal the existence of a second order QPT at exactly  $\lambda^{(0)} = 0.5\epsilon$  (see [6] for the variational study of the 2-level LMG case and its phase diagram).

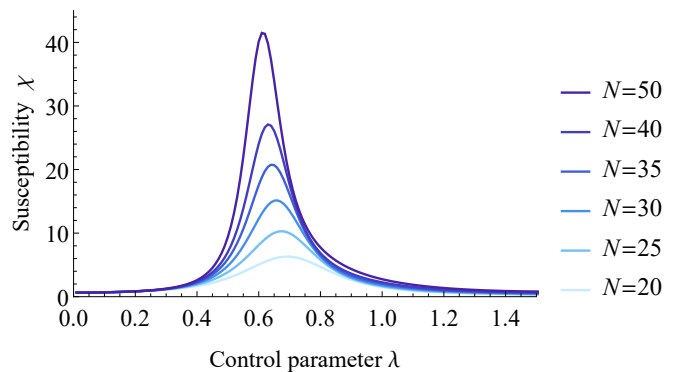


FIG. 2. Susceptibility  $\chi_\psi$  of the ground (fully symmetric) state  $\psi$  of the LMG Hamiltonian (9) as a function of  $\lambda$  for increasing values of the number of atoms  $N$ . A step  $\delta\lambda = 0.01$  has been used. The analysis divines the existence of a QPT at a critical point around  $\lambda^{(0)} \simeq 0.6$ . We use  $\epsilon$  units for  $\lambda$ .

The same critical phenomenon occurs for the lowest-energy state belonging to other mixed symmetry sectors  $h$ . In Figure 3 we represent the susceptibility  $\chi_{\psi_0^h}$  of the lowest-energy vector  $\psi_0^h$  inside some mixed symmetry sectors  $h$  for  $N = 36$  atoms. The analysis of the first maxima of the susceptibility in Figure 3 indicates that the would-be critical points  $\lambda^{(0)}(h)$  are shifted to the right from  $h = [36, 0, 0]$  to  $h = [24, 12, 0]$  and then to

the left from  $h = [24, 12, 0]$  to  $h = [18, 18, 0]$ . In fact, the semiclassical  $N \rightarrow \infty$  analysis that we shall make in Section VI, Figures 5 and 6, indicates that the “hand-gun” sector  $h = [2N/3, N/3, 0]$  (we shall use this terminology for this special case, which coincides with the adjoint “octet” representation in quantum chromodynamics  $N = 3$ ) corresponds to a quadruple point. Therefore, the susceptibility is able to capture this special point. The susceptibility second maxima in Figure 3 correspond to a new QPT that eventually takes place at  $\lambda^{(0)} = 1.5\epsilon$ . We shall not discuss this last QPT until Section VI since it occurs at a different scale and requires much higher values of  $N$ , and more computational requirements, to be properly captured.

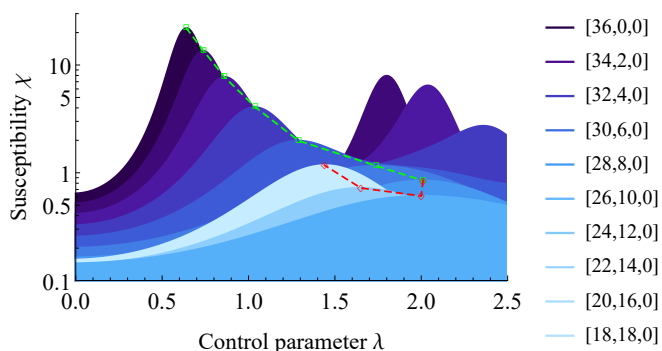


FIG. 3. Susceptibility  $\chi_{\psi_0^h}$  of the lowest-energy vector  $\psi_0^h$  inside some mixed symmetry sectors  $h$  for  $N = 36$  atoms. Logarithmic scale. The dashed line interpolates between maxima of the susceptibility that are precursors of prospective critical points separating phase I from phase II (green squares) and phase I from phase IV (red diamonds); see later on Figures 5 and 6. The “recoil point” corresponds to the “hand-gun” unirrep  $h = [24, 12, 0]$ , where four phases will coexist (see later on Sec. VI). We use  $\epsilon$  units for  $\lambda$ .

Level  $i = 1, 2, 3$  population densities  $\langle \psi_0^h | S_{ii} | \psi_0^h \rangle / N$ , of the ground state  $\psi_0^h$  inside each sector  $h$ , also behave as precursors of order parameters. In fact, Figure 4 represents level population densities for  $N = 48$  three-level atoms and different symmetry sectors  $h$ , which include the symmetric sector  $h = [48, 0, 0]$ , the “hand-gun” sector  $h = [2N/3, N/3, 0] = [32, 16, 0]$  already commented in the previous paragraph, and the rectangular Young tableau  $h = [24, 24, 0]$ . We perceive a population change for the fully symmetric case around  $\lambda^{(0)} = 0.5\epsilon$ , as already pointed out, a displacement of this critical point to the right for  $h = [32, 16, 0]$  (the would-be quadruple point), and a displacement to the left for  $h = [24, 24, 0]$ . Level  $i$  population densities depend both on  $\lambda$  and  $h$ , and suffer changes when approaching a critical point (see Figure 9 later on).

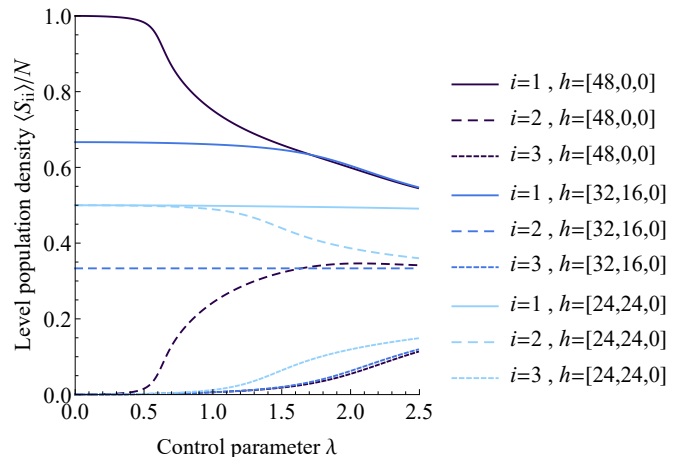


FIG. 4. Level  $i = 1, 2, 3$  population densities  $\langle \psi_0^h | S_{ii} | \psi_0^h \rangle / N$  of the lowest-energy state  $\psi_0^h$  inside each sector  $h$  for  $N = 48$  three-level atoms and three different representative values of  $h$  (the fully symmetric, the “hand-gun” and the rectangular Young tableau), as a function of  $\lambda$ , in  $\epsilon$  units. Appreciable changes in the population densities can be observed at some values of  $\lambda$  depending on the particular sector  $h$  (see main text), anticipating the existence of a MSQPT in the thermodynamic limit.

## V. $U(L)$ COHERENT QUASI-CLASSICAL STATES AND THEIR OPERATOR EXPECTATION VALUES

$U(L)$  Coherent states  $|h, U\rangle$  turn out to be excellent variational states that reproduce the structure and mean energy of lowest-energy states inside each symmetry sector  $h$  (see e.g [6] for for the case of the  $L = 2$  level LMG model and [20, 21] for a system of  $N$  indistinguishable atoms of  $L$  levels interacting dipolarly with  $\ell$  modes of an electromagnetic field). They can be constructed by rotating each single particle state in, namely, the HW vector state  $|\mathfrak{m}_{\text{hw}}\rangle$  by the same unitary matrix  $U$ . For example, for  $L = 3$  level atoms, an using the parametrization (11) of a unitary matrix  $U \in U(3)$ , the  $|h, U\rangle$  can be factorized as

$$|h, U\rangle = K_h(U) |h; \alpha, \beta, \gamma\rangle, \quad (38)$$

where

$$|h; \alpha, \beta, \gamma\rangle = e^{\beta S_{31}} e^{\alpha S_{21}} e^{\gamma S_{32}} |\mathfrak{m}_{\text{hw}}\rangle. \quad (39)$$

is the exponential action of lowering operators  $S_{ij}$ ,  $i > j$  on the HW state  $|\mathfrak{m}_{\text{hw}}\rangle$  and

$$K_h(U) = |U|_1^{h_1-h_2} |U|_2^{h_2-h_3} |U|_3^{h_3} = \frac{u_1^{h_1} u_2^{h_2} u_3^{h_3}}{\ell_1^{(h_1-h_2)/2} \ell_2^{(h_2-h_3)/2}} \quad (40)$$

is a normalizing factor for  $|h; \alpha, \beta, \gamma\rangle$  which depends on the lengths (12) which appear in the products of first, second and third upper minors  $|U|_i$  of  $U = V \cdot$

$\text{diag}(u_1, u_2, u_3)$  in (11). The overlap

$$\begin{aligned} B_h(\bar{\alpha}', \bar{\beta}', \bar{\gamma}'; \alpha, \beta, \gamma) &\equiv \{h; \alpha', \beta', \gamma' | h; \alpha, \beta, \gamma\} \\ &= (1 + \alpha\bar{\alpha}' + \beta\bar{\beta}')^{h_1 - h_2} \\ &\quad \cdot (1 + \gamma\bar{\gamma}' + (\beta - \alpha\gamma)(\bar{\beta}' - \bar{\alpha}'\bar{\gamma}'))^{h_2 - h_3} \end{aligned} \quad (41)$$

defines the so called reproducing Bergman kernel  $B_h$ . Note that

$$B_h(\bar{\alpha}, \bar{\beta}, \bar{\gamma}; \alpha, \beta, \gamma) = |K_h(U)|^{-2}. \quad (42)$$

Coherent state expectation values  $s_{ij}$  of the basic symmetry operators  $S_{ij}$  can be easily computed through derivatives of the Bergman kernel as

$$s_{ij} = \langle h, U | S_{ij} | h, U \rangle = \frac{\mathcal{S}_{ij} B_h(\bar{\alpha}, \bar{\beta}, \bar{\gamma}; \alpha, \beta, \gamma)}{B_h(\bar{\alpha}, \bar{\beta}, \bar{\gamma}; \alpha, \beta, \gamma)}. \quad (43)$$

where  $\mathcal{S}_{ij}$  is the differential representation (A3) of  $S_{ij}$  on anti-holomorphic functions  $\psi(\bar{\alpha}, \bar{\beta}, \bar{\gamma}) = \{h; \alpha, \beta, \gamma | \psi\}$  (see Appendices A and B for a more detailed explanation). The explicit expression of the coherent state expectation values  $s_{ij}$  can be seen in the equation (A4) of Appendix A. They will be very useful to compute the energy surface for each symmetry sector of the system in the next section. In Appendix B we study the interesting transformation properties of  $U(3)$  coherent states under parity symmetry operations. These properties are strongly related to the degenerate structure of the ground state in the thermodynamic limit, as we shall see in the next section.

## VI. ENERGY SURFACE, PHASE DIAGRAM AND SPONTANEOUSLY BROKEN PARITY SYMMETRY

Let us consider a general  $U(3)$  unirrep of shape  $h = [h_1, h_2, h_3]$  given by the following proportions  $\mu, \nu$

$$\begin{aligned} h_3 = \nu N, \quad h_2 = (1 - \mu)(1 - \nu)N, \quad h_1 = \mu(1 - \nu)N, \\ \forall \nu \in [0, \frac{1}{3}], \quad \mu \in [\frac{1}{2}, \frac{1-2\nu}{1-\nu}]. \end{aligned} \quad (44)$$

Note that the set of  $U(3)$  unirreps labeled by  $(\mu, \nu)$  is dense in the corresponding intervals as  $N \rightarrow \infty$ . The energy surface associated to a Hamiltonian density  $H$  inside the Hilbert space sector  $(\mu, \nu)$  is defined as the coherent state expectation value of the Hamiltonian density in the thermodynamic limit

$$E_{\mu, \nu}^U(\epsilon, \lambda) = \lim_{N \rightarrow \infty} \langle h, U | H | h, U \rangle. \quad (45)$$

For the Hamiltonian density (9), the energy surface becomes

$$E_{\mu, \nu}^U(\epsilon, \lambda) = \lim_{N \rightarrow \infty} \left( \frac{\epsilon(s_{33} - s_{11})}{N} - \frac{\lambda \sum_{i \neq j=1}^3 s_{ij}^2}{N(N-1)} \right), \quad (46)$$

with  $s_{ij}$  defined in (43) and calculated in (A4). Note that we have used the result (A6) which states that there are no fluctuations in the classical limit. This energy surface depends on the kind of unirrep  $(\mu, \nu)$  (which become continuous parameters in the thermodynamic limit), on the complex (phase space) coordinates of  $U$  (namely,  $\alpha, \beta$  and  $\gamma$ ) and on the control parameters  $\epsilon$  and  $\lambda$  related to the strength of interactions. Note that

$$E_{\mu, \nu}^U(\epsilon, \lambda) = \epsilon E_{\mu, \nu}^U(1, \lambda/\epsilon), \quad (47)$$

which allows us to discuss the phase diagram in terms of the renormalized two-body interaction strength  $\tilde{\lambda} = \lambda/\epsilon$  for  $\epsilon \neq 0$ . That is, we shall fix  $\epsilon$  and measure energy and  $\lambda$  in  $\epsilon$  units.

Moreover, the fact that the unirreps  $h = [h_1, h_2, h_3]$  and  $h' = [h_1 - h_3, h_2 - h_3, 0]$  are equivalent, under the point of view of  $SU(3)$ , introduces the following relation between energy surfaces

$$E_{\mu, \nu}^U(\epsilon, \lambda) = (1 - 3\nu) E_{\tilde{\mu}, 0}^U(\epsilon, (1 - 3\nu)\lambda), \quad \tilde{\mu} = \frac{\mu(1 - \nu) - \nu}{1 - 3\nu}, \quad (48)$$

and therefore we can restrict ourselves to the analysis of the parent case  $\nu = 0, \mu \in [\frac{1}{2}, 1]$ . The right end point  $\mu = 1$  corresponds to totally symmetric representations, associated to Young tableaux of a single row and four-dimensional phase spaces whose points are labeled by  $\alpha, \beta \in \mathbb{C}$ . Inserting the coherent state expectation values  $s_{ij}$  of Eq. (A4) into (46) for the fully symmetric representation  $[h_1, h_2, h_3] = [N, 0, 0]$ , the corresponding energy surface turns out to be

$$\begin{aligned} E_{1,0}^{(\alpha, \beta)}(\epsilon, \lambda) &= \epsilon \frac{\beta\bar{\beta} - 1}{\alpha\bar{\alpha} + \beta\bar{\beta} + 1} \\ &\quad - \lambda \frac{\alpha^2(\bar{\beta}^2 + 1) + (\beta^2 + 1)\bar{\alpha}^2 + \bar{\beta}^2 + \beta^2}{(\alpha\bar{\alpha} + \beta\bar{\beta} + 1)^2}. \end{aligned} \quad (49)$$

Note that this energy surface is invariant under  $\alpha \rightarrow -\alpha, \beta \rightarrow -\beta$ , a symmetry which is inherited from the discrete parity symmetry of the Hamiltonian (9) already discussed at the end of Section II and in Appendix B.

All representations with  $h_1 > h_2 = h_3$  (that is,  $\mu = \frac{1-2\nu}{1-\nu}$ ) can be reduced to this totally symmetric case  $E_{1,0}^{(\alpha, \beta)}$ ; more precisely

$$E_{\frac{1-2\nu}{1-\nu}, \nu}^U(\epsilon, \lambda) = (1 - 3\nu) E_{1,0}^U(\epsilon, (1 - 3\nu)\lambda), \quad 0 \leq \nu < 1/3, \quad (50)$$

according to (48). The left end point  $\mu = 1/2$  corresponds to the representations associated to rectangular Young tableaux of two equal rows of  $h_1 = N/2 = h_2$  boxes each and four-dimensional phase spaces whose points are labeled by two complex numbers  $\gamma$  and  $\beta' = \beta - \alpha\gamma$  [see the expression of  $\ell_2$  in (12)]. The energy surface for this case is related to the totally symmetric case (49) through

$$E_{\frac{1}{2}, 0}^U(\epsilon, \lambda) = \frac{1}{2} E_{1,0}^{(\gamma, \beta')}(\epsilon, \frac{\lambda}{2}), \quad \beta' = \beta - \alpha\gamma. \quad (51)$$

For intermediate values  $\mu \in (\frac{1}{2}, 1)$  the associated phase space is six-dimensional (a “flag manifold”) and its points are labeled by three independent complex numbers  $\alpha, \beta, \gamma$ . The explicit expression of the energy surface for this case is more bulky and we will not write it down.

Now we have to find the minimum energy

$$E_\mu^{(0)}(\epsilon, \lambda) = \min_{U \in U(3)} E_{\mu,0}^U(\epsilon, \lambda) \quad (52)$$

$$E_\mu^{(0)}(\epsilon, \lambda) = \begin{cases} \begin{cases} -\epsilon\mu & 0 \leq \lambda \leq \frac{\epsilon}{2(1-\mu)} \\ -\frac{1}{2} \left( \lambda(1-\mu)^2 + \frac{\epsilon^2}{4\lambda} + (3\mu-1)\epsilon \right) & \frac{\epsilon}{2(1-\mu)} \leq \lambda \leq \frac{3\epsilon}{6\mu-2} \\ -\frac{2}{3}\lambda(1-3(1-\mu)\mu) - \frac{\epsilon^2}{2\lambda} & \lambda \geq \frac{3\epsilon}{6\mu-2} \end{cases} & \frac{1}{2} \leq \mu \leq \frac{2}{3}, \\ \begin{cases} -\epsilon\mu & 0 \leq \lambda \leq \frac{\epsilon}{4\mu-2} \\ 2\lambda\mu(1-\mu) - \frac{(2\lambda+\epsilon)^2}{8\lambda} & \frac{\epsilon}{4\mu-2} \leq \lambda \leq \frac{3\epsilon}{2} \\ -\frac{2}{3}\lambda(1-3(1-\mu)\mu) - \frac{\epsilon^2}{2\lambda} & \lambda \geq \frac{3\epsilon}{2} \end{cases} & \frac{2}{3} \leq \mu \leq 1. \end{cases} \quad (53)$$

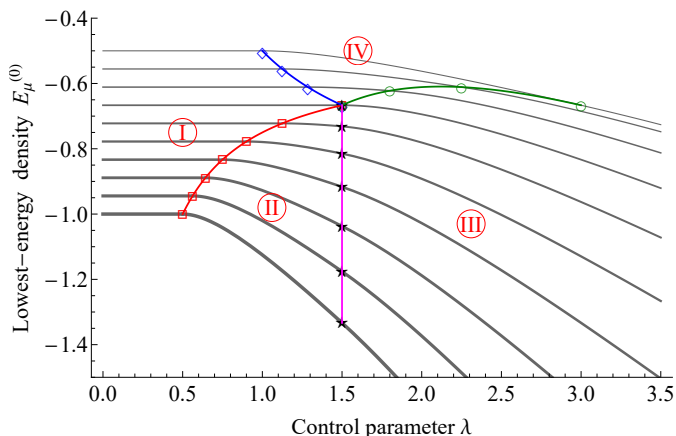


FIG. 5. Lowest-energy density  $E_\mu^{(0)}(\epsilon, \lambda)$  as a function of the control parameter  $\lambda$  (both in  $\epsilon$  units) for ten different values of  $\mu = n/18 + 8/18, n = 1, \dots, 10$ , from  $\mu = 1/2$  (thinnest black curve) to  $\mu = 1$  (thickest black curve). Extending the control parameter space by  $\mu$ , the phase diagram exhibits four distinct quantum phases in the  $\lambda$ - $\mu$  plane that coexist at a quadruple point  $(\lambda, \mu)_q = (3/2, 2/3)$ . Curves of critical points separating two phases are depicted in color red, blue, magenta and green, according to formulas (54)

See Figure 5 for a graphical representation of this energy as a function of  $\lambda$  for several symmetry sectors  $\mu$ . Note that, in this new context of MSQPT, the sector parameter  $\mu$  behaves as an additional control parameter. In fact, we can choose our initial quantum state inside a sector  $\mu$  and Hamiltonian evolution will not take it out of this sector. We can also study quantum properties of arbitrarily close symmetry sectors  $\mu$  and  $\mu + \delta\mu$ . Therefore, in this context, we extend the control param-

eter space  $(\epsilon, \lambda)$  by  $\mu$ . Disregarding  $\epsilon$ , which only sets the scale (units), the phase diagram exhibits four distinct quantum phases (I, II, III and IV) in the  $\lambda$ - $\mu$  plane. These four quantum phases coexist at a quadruple point  $(\lambda, \mu)_q = (3\epsilon/2, 2/3)$ , as it can be appreciated in Figures 5 and 6. We also represent curves of critical points separating two phases

$$\begin{aligned} \lambda_{\text{I} \leftrightarrow \text{II}}^{(0)}(\mu) &= \frac{\epsilon}{4\mu-2}, & \frac{2}{3} \leq \mu \leq 1, & \text{ (red)} \\ \lambda_{\text{II} \leftrightarrow \text{III}}^{(0)}(\mu) &= \frac{3\epsilon}{2}, & \frac{2}{3} \leq \mu \leq 1, & \text{ (magenta)} \\ \lambda_{\text{I} \leftrightarrow \text{IV}}^{(0)}(\mu) &= \frac{\epsilon}{2(1-\mu)}, & \frac{1}{2} \leq \mu \leq \frac{2}{3}, & \text{ (blue)} \\ \lambda_{\text{III} \leftrightarrow \text{IV}}^{(0)}(\mu) &= \frac{3\epsilon}{6\mu-2}, & \frac{1}{2} \leq \mu \leq \frac{2}{3}, & \text{ (green)} \end{aligned} \quad (54)$$

at which a second order QPT takes place in general.

To fully appreciate the nature of the phase-transitions, we show in Figure 6 contour plots of the minimum energy  $E_\mu^{(0)}(\epsilon, \lambda)$  and its first and second derivatives in the extended  $(\lambda, \mu)$  phase diagram (i.e., considering both  $\lambda$  and  $\mu$  as control parameters). It is clear from the graphics that, while the first derivatives are continuous (see also Figure 7), the second derivatives are discontinuous at the critical curves (54) (at the curve  $\lambda_{\text{II} \leftrightarrow \text{III}}^{(0)}$  only  $\partial_{\lambda\lambda} E_\mu^{(0)}$  is discontinuous). An interesting feature is the anomalous behavior at phase IV where  $\partial_{\mu\lambda} E_\mu^{(0)} > 0$ , while it is non-positive in the rest of phases, this sign playing the role of an “order parameter” for the MSQPTs I  $\leftrightarrow$  IV and IV  $\leftrightarrow$  III. This behavior can also be appreciated in Figure 5, where one can see that energy curves of constant  $\mu$  are parallel at region I, move away from each other as  $\lambda$  increases at regions II and III, and get closer at region IV. To better perceive it, we also represent in Figure 7 3D plots of  $\partial_\lambda E_\mu^{(0)}(\epsilon, \lambda)$  and  $\partial_\mu E_\mu^{(0)}(\epsilon, \lambda)$  in the extended phase diagram  $(\lambda, \mu)$ . As already said, we see that both

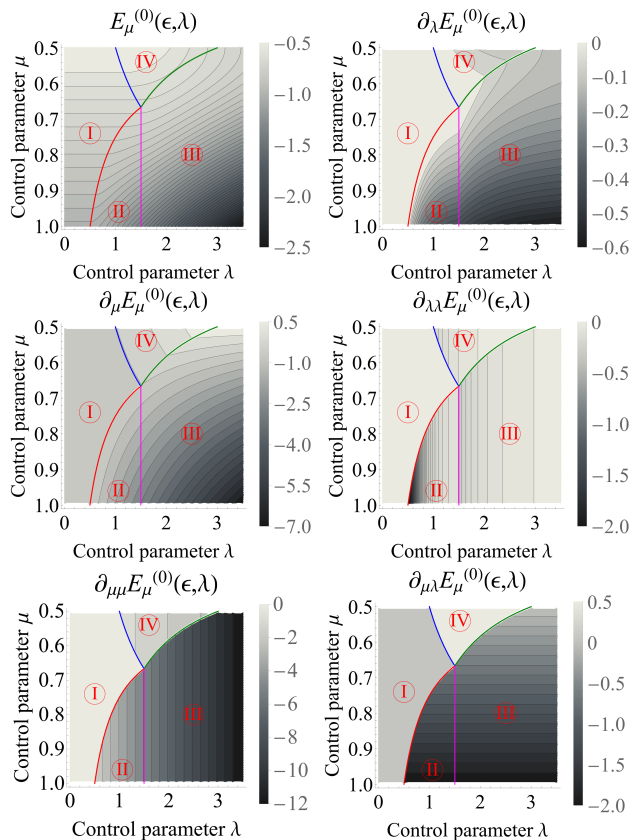


FIG. 6. Contour plots of  $E_\mu^{(0)}(\epsilon, \lambda)$  and its first and second derivatives in the phase diagram  $(\lambda, \mu)$  (We use  $\epsilon$  units for  $E$  and  $\lambda$ ). Critical curves (54) are shown, where the second derivatives are discontinuous.

first derivatives of the energy are continuous. Moreover, taking into account that the derivative  $\partial_\mu E_\mu^{(0)}$  measures the density of  $\mu$ -levels with energy  $E_\mu^{(0)}$ , Figure 7 (bottom panel) shows that the level density grows with  $\lambda$  in phase IV, whereas it is non-increasing in the other phases, attaining its maximum value in phase IV. One can also perceive it in the fact that  $\partial_{\mu\lambda} E_\mu^{(0)} > 0$  in phase IV, as commented before. This discussion somehow connects with the traditional classification of ESQPTs characterized by a divergence in the density of excited states. We do not find any divergence of this kind (although we identify higher density level phases), but we must remind that our “excited energy levels”  $E_\mu^{(0)}$  actually are the lower-energy levels inside each permutation symmetry sector  $\mu$ , the ground state corresponding to the symmetric sector  $\mu = 1$ . This fact allows a variational analysis, both for QPTs and MSQPTs, in terms of coherent states  $|h, U\rangle$  of  $U(3)$ .

Returning to our discussion on the minimization (52), the lowest-energy state for general  $\mu$  turns out to be highly degenerated. There are many phase space critical points  $\alpha_0, \beta_0, \gamma_0$  with the same energy  $E_\mu^{(0)}$  and the expressions are quite bulky. Therefore, we shall restrict

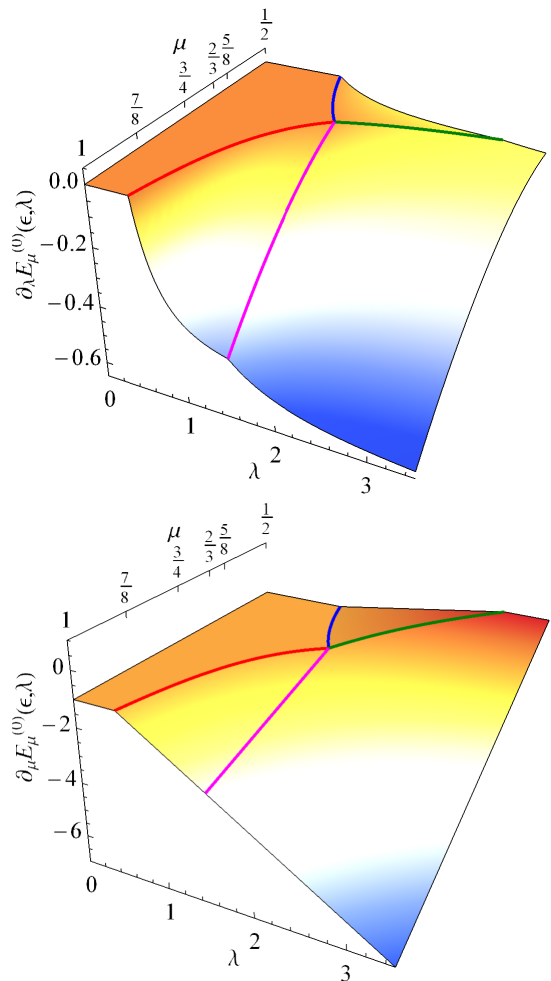


FIG. 7. 3D plots of  $\partial_\lambda E_\mu^{(0)}(\epsilon, \lambda)$  and  $\partial_\mu E_\mu^{(0)}(\epsilon, \lambda)$  in the extended phase diagram  $(\lambda, \mu)$  (We use  $\epsilon$  units for  $E$  and  $\lambda$ ). Critical curves (54) are shown, where a second order MSQPT occurs. 3D plots show that both,  $\partial_\lambda E_\mu^{(0)}$  and  $\partial_\mu E_\mu^{(0)}$ , are continuous. The bottom plot shows that  $\partial_\mu E_\mu^{(0)}$  attains its maximum at phase IV, where the density of  $\mu$ -levels with energy  $E_\mu^{(0)}$  increases with  $\lambda$ .

ourselves from now on to the particular totally symmetric case  $\mu = 1$ , which has a lower-dimensional phase space parameterized by  $\alpha$  and  $\beta$ . The  $\mu$ -dependent lowest-energy (53) simplifies for  $\mu = 1$  to

$$E_1^{(0)}(\epsilon, \lambda) = \begin{cases} -\epsilon, & 0 \leq \lambda \leq \frac{\epsilon}{2}, & \text{(I)} \\ -\frac{(2\lambda+\epsilon)^2}{8\lambda}, & \frac{\epsilon}{2} \leq \lambda \leq \frac{3\epsilon}{2}, & \text{(II)} \\ -\frac{4\lambda^2+3\epsilon^2}{6\lambda}, & \lambda \geq \frac{3\epsilon}{2}. & \text{(III)} \end{cases} \quad (55)$$

Here we clearly distinguish the three different phases: I, II and III, and two second-order QPTs at  $\lambda_{\text{I} \leftrightarrow \text{II}}^{(0)} = \epsilon/2$  and  $\lambda_{\text{II} \leftrightarrow \text{III}}^{(0)} = 3\epsilon/2$ , respectively. The critical values of  $\alpha$  and  $\beta$  which make (49) minimum turn out to be real and

their explicit expression is given by:

$$\alpha_0^\pm(\epsilon, \lambda) = \pm \begin{cases} 0, & 0 \leq \lambda \leq \frac{\epsilon}{2}, \\ \sqrt{\frac{2\lambda - \epsilon}{2\lambda + \epsilon}}, & \frac{\epsilon}{2} \leq \lambda \leq \frac{3\epsilon}{2}, \\ \sqrt{\frac{2\lambda}{2\lambda + 3\epsilon}}, & \lambda \geq \frac{3\epsilon}{2}, \end{cases}$$

$$\beta_0^\pm(\epsilon, \lambda) = \pm \begin{cases} 0, & 0 \leq \lambda \leq \frac{3\epsilon}{2}, \\ \sqrt{\frac{2\lambda - 3\epsilon}{2\lambda + 3\epsilon}}, & \lambda \geq \frac{3\epsilon}{2}. \end{cases} \quad (56)$$

Indeed, inserting (56) into (49) gives (55). The location of these minima for the energy surface (49) can also be perceived by looking at the equipotential curves of Figure 8. Indeed, the real and imaginary parts of the complex phase-space variables  $\alpha = x_\alpha + ip_\alpha$  and  $\beta = x_\beta + ip_\beta$  can be seen as “position”  $x$  and momenta  $p$  (in dimensionless units). Minimum (potential) energy is attained for zero kinetic energy ( $p=0$ ), i.e., real  $\alpha$  and  $\beta$ . Looking at Figure 8, we perceive a single potential energy minimum in phase I,  $0 \leq \lambda/\epsilon \leq 1/2$ , located at  $\alpha = \beta = 0$ . In phase II,  $1/2 \leq \lambda/\epsilon \leq 3/2$ , this single minimum degenerates into a double well potential. In phase III,  $\lambda/\epsilon \geq 3/2$ , we have a more degenerated case with a quadruple well potential, according to the critical values of  $\alpha$  and  $\beta$  in (56).

As already commented, this structure of degenerated minima is directly related with the spontaneous breaking of the discrete parity symmetry of the Hamiltonian (9) discussed at the end of Section II and in Appendix B. Indeed, in the limit  $N \rightarrow \infty$ , the four coherent states  $|\alpha_0^\pm, \beta_0^\pm\rangle$  attain the same minimum energy (55). According to formula (B3), the parity operations  $\hat{\Pi}_i = \Pi_i e^{-i\pi h_i}$  map between these four degenerate ground states; for example  $\hat{\Pi}_1 |\alpha_0^\pm, \beta_0^\pm\rangle = |\alpha_0^\mp, \beta_0^\mp\rangle$ . Parity symmetry can still be restored by projecting any of the four  $|\alpha_0^\pm, \beta_0^\pm\rangle$  degenerated ground states onto the symmetric (unnormalized) superposition

$$|\psi_0\rangle \equiv (1 + \hat{\Pi}_1 + \hat{\Pi}_2 + \hat{\Pi}_3) |\alpha_0^\pm, \beta_0^\pm\rangle, \quad (57)$$

which remains invariant (even) under parity operations. These kind of “parity-adapted coherent states” have been extensively used in the literature and they are sometimes called “Schrödinger cat states”, since they are a superposition of almost orthogonal semiclassical (coherent) states. The restoration of parity is convenient when one wants to compare between variational and (finite  $N$ ) numerical calculations. For example, see [22, 23] for their use in the Dicke model of superradiance (two and three level atoms, respectively, interacting with one-mode radiation), [17, 24] for the 2-level LMG model and [25, 26] for vibron models of molecules. We shall exploit this parity-symmetry restoration in future works.

To finish, let us discuss other interesting order parameters of the QPT like the population density of each level. In Figure 9 we show the level population density of the fully symmetric ground state ( $h = [N, 0, 0]$ ) in the ther-

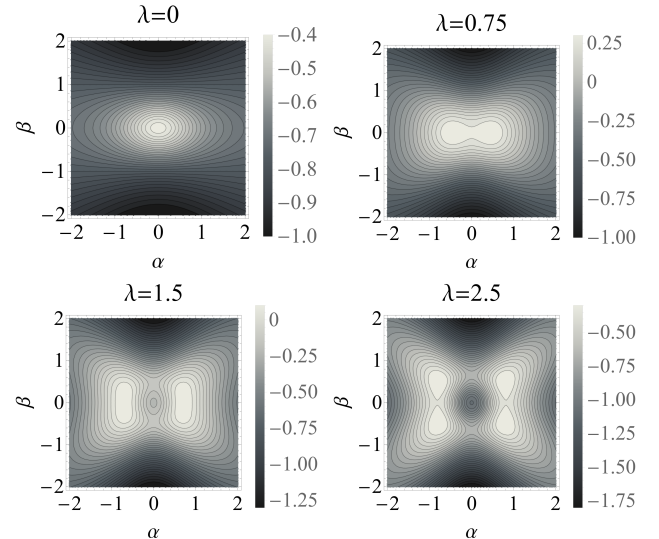


FIG. 8. Contour plot of the energy surface (49) of the fully symmetric case for real  $\alpha$  and  $\beta$ , in the vicinity of the critical points  $\lambda = \epsilon/2$  and  $\lambda = 3\epsilon/2$  (in  $\epsilon$  units). Degenerate minima are perceived in light gray color.

dynamic limit

$$p_{ii}^{(0)}(\epsilon, \lambda) = \lim_{N \rightarrow \infty} \frac{\langle h, U_0 | S_{ii} | h, U_0 \rangle}{N}. \quad (58)$$

It can be explicitly calculated by using the expressions of the average values  $s_{ii}$  of the operators  $S_{ii}$  given in formulas (43) and (A4), and then evaluating them at the critical points (56) as

$$p_{11}^{(0)}(\epsilon, \lambda) = \frac{1}{\ell_1(\alpha_0^\pm, \beta_0^\pm)} = \begin{cases} 1, & 0 \leq \lambda \leq \frac{\epsilon}{2}, \\ \frac{1}{2} + \frac{\epsilon}{4\lambda}, & \frac{\epsilon}{2} \leq \lambda \leq \frac{3\epsilon}{2}, \\ \frac{1}{3} + \frac{\epsilon}{2\lambda}, & \lambda \geq \frac{3\epsilon}{2}, \end{cases}$$

$$p_{22}^{(0)}(\epsilon, \lambda) = \frac{|\alpha_0^\pm|^2}{\ell_1(\alpha_0^\pm, \beta_0^\pm)} = \begin{cases} 0, & 0 \leq \lambda \leq \frac{\epsilon}{2}, \\ \frac{1}{2} - \frac{\epsilon}{4\lambda}, & \frac{\epsilon}{2} \leq \lambda \leq \frac{3\epsilon}{2}, \\ \frac{1}{3}, & \lambda \geq \frac{3\epsilon}{2}, \end{cases}$$

$$p_{33}^{(0)}(\epsilon, \lambda) = \frac{|\beta_0^\pm|^2}{\ell_1(\alpha_0^\pm, \beta_0^\pm)} = \begin{cases} 0, & 0 \leq \lambda \leq \frac{3\epsilon}{2}, \\ \frac{1}{3} - \frac{\epsilon}{2\lambda}, & \lambda \geq \frac{3\epsilon}{2}. \end{cases} \quad (59)$$

Note that both energy-degenerate values  $\pm$  also give the same population density, since  $s_{ii}$  depend on squared modulus. We also compare in Figure 9 with the population densities obtained for finite  $N = 50$ , which already capture the critical behavior. We perceive a different population structure in each phase. In Phase I,  $0 \leq \lambda/\epsilon \leq 1/2$ , all atoms are in level 1. In phase II,  $1/2 \leq \lambda/\epsilon \leq 3/2$ , level 2 starts populating at the expense of level 1. Finally, level 3 begins to populate in phase III,  $\lambda/\epsilon \geq 3/2$ .

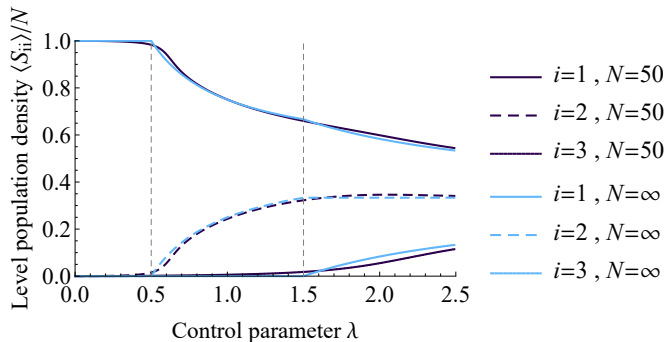


FIG. 9. Level population densities  $p_{ii}^{(0)}$ ,  $i = 1, 2, 3$ , in eq. (59), corresponding to the fully-symmetric ground state in the thermodynamic limit as a function of the control parameter  $\lambda$  (in  $\epsilon$  units). Critical points indicate a change of behavior and are marked with vertical grid lines. We also compare with the finite case  $N = 50$ , which already captures the critical behavior.

## VII. CONCLUSIONS AND OUTLOOK

Quantum Phase Transitions in many-body systems usually presuppose the indistinguishability of the particles that compose the system, thus restricting the study to the fully symmetric representation ( $\mu = 1$  in our parametrization), but this should not be the more general situation. In this article we have analyzed the role played by other mixed symmetry sectors ( $\mu \neq 1$ ) in the thermodynamic limit  $N \rightarrow \infty$  for a 3-level LMG model with  $U(3)$  dynamical symmetry. We have seen that every lowest-energy state belonging to a given symmetry sector  $\mu$  undergoes a QPT and the critical point  $\lambda$  depends on  $\mu$ . This fact motivates the notion of *Mixed Symmetry Quantum Phase Transition* (MSQPT), leading to an extended phase diagram in an enlarged control parameter space including  $\mu$ . Therefore, the system undergoes abrupt changes, not only for some critical values of the control parameters  $\lambda$ , but also for some critical values of the symmetry sector  $\mu$ . We also find that  $\mu = 2/3$  (the “octet” for  $N = 3$  particles/“quarks”) represents a quadruple point where four distinct phases coexist. A numerical treatment for large (but finite) size  $N$  gives some QPT precursors, like information-theoretic measures (fidelity-susceptibility) and level population densities, which anticipate some mean-field calculations using coherent (quasi-classical) states in the limit  $N \rightarrow \infty$ .

It would be interesting to further investigate the possible overlap between the proposed notion of MSQPT and the existing notion of Excited State Quantum Phase Transition (ESQPT) already present in the literature [7, 8], as we also find variability in the energy  $\mu$ -level density  $\partial_\mu E_\mu^{(0)}$ .

Regarding the possibility to exploit permutation symmetry for quantum technological prospects, we could mention for example some recent proposals commenting on thermodynamic advantages of bosonic over fermionic

symmetry [27], or the role of mixed symmetries in the quantum Gibbs paradox [28, 29]. The role of mixed symmetry in quantum computation and information theory also deserves our attention and will be investigated in future work.

Intermediate, fractionary, parastatistics also play a fundamental role in the quasiparticle zoo [30], that provides a deep understanding of complex phenomena in many-body and condensed matter physics. Recently, a proposal to describe composite fermions (in multicomponent fractional quantum Hall systems) in terms rectangular Young tableaux has been put forward [31, 32] and showed to describe the quantum phases of bilayer quantum Hall systems with  $U(4)$  dynamical symmetry [33, 34]. This is also an excellent area to explore the role of permutation symmetry.

## ACKNOWLEDGMENTS

We thank the support of the Spanish MICINN through the project PGC2018-097831-B-I00 and Junta de Andalucía through the projects SOMM17/6105/UGR, UHU-1262561 and FQM-381. JG also thanks MICINN for financial support from FIS2017-84440-C2-2-P. AM thanks the Spanish MIU for the FPU19/06376 predoctoral fellowship. We all thank Octavio Castaños and Emilio Perez-Romero for their valuable collaboration in the early stages of this work.

### Appendix A: Differential realization of $S_{ij}$ and coherent state expectation values

Let us justify the useful formula (43) and provide an explicit expression for the differential realization  $\mathcal{S}_{ij}$  of the operators  $S_{ij}$  on functions  $\psi(\bar{\alpha}, \bar{\beta}, \bar{\gamma})$ . An alternative construction is also given in Appendix B.

A group element  $U' \in U(3)$  can be written as the exponential  $U' = \exp(g'^{ij} S_{ij})$ , with  $g'^{ij}$  canonical coordinates at the identity. Using this, the coherent state expectation value (43) can also be written as

$$\langle h, U | \mathcal{S}_{ij} | h, U \rangle = \left. \frac{\partial \langle h, U | U' | h, U \rangle}{\partial g'^{ij}} \right|_{U'=1}. \quad (\text{A1})$$

Since  $U' | h, U \rangle = | h, U'U \rangle$  and

$$\langle h, U | h, U'U \rangle = \overline{K_h(U)} K_h(U'U) B_h(U^\dagger; U'U),$$

[with  $K_h$  and  $B_h$  in (40,41)], applying the chain rule of differentiation, the relation (42) and the identification

$$(g'^{ij}) = \begin{pmatrix} u_1 & -\bar{\alpha} & -\bar{\beta} \\ \alpha & u_2 & -\bar{\gamma} \\ \beta & \gamma & u_3 \end{pmatrix}, \quad (\text{A2})$$

one finally arrives to the formula (43). In order to apply the chain rule, one has to previously work out the group

law  $U'' = U'U$ , which means to write  $g''^{ij}$  as a function of  $g'^{ij}$  and  $g^{ij}$ . The corresponding group law is quite cumbersome and we shall only write the final expression of the differential operators:

$$\begin{aligned}
S_{21} &= \bar{\alpha}(h_1 - h_2) - (\bar{\beta} - \bar{\alpha}\bar{\gamma})\partial_{\bar{\gamma}} - \bar{\alpha}(\bar{\beta}\partial_{\bar{\beta}} + \bar{\alpha}\partial_{\bar{\alpha}}), \\
S_{12} &= \partial_{\bar{\alpha}}, \\
S_{31} &= (h_1 - h_3)\bar{\beta} + (h_3 - h_2)\bar{\alpha}\bar{\gamma} - \bar{\gamma}(\bar{\beta} - \bar{\alpha}\bar{\gamma})\partial_{\bar{\gamma}} \\
&\quad - \bar{\beta}(\bar{\beta}\partial_{\bar{\beta}} + \bar{\alpha}\partial_{\bar{\alpha}}), \\
S_{13} &= \partial_{\bar{\beta}}, \\
S_{32} &= (h_2 - h_3)\bar{\gamma} - \bar{\gamma}^2\partial_{\bar{\gamma}} + \bar{\beta}\partial_{\bar{\alpha}}, \\
S_{23} &= \partial_{\bar{\gamma}} + \bar{\alpha}\partial_{\bar{\beta}}, \\
S_{11} &= h_1 - \bar{\beta}\partial_{\bar{\beta}} - \bar{\alpha}\partial_{\bar{\alpha}}, \\
S_{22} &= h_2 + \bar{\alpha}\partial_{\bar{\alpha}} - \bar{\gamma}\partial_{\bar{\gamma}}, \\
S_{33} &= h_3 + \bar{\gamma}\partial_{\bar{\gamma}} + \bar{\beta}\partial_{\bar{\beta}}.
\end{aligned} \tag{A3}$$

With this, the corresponding expectation values (43) can be calculated and they are

$$\begin{aligned}
s_{11} &= \frac{h_1}{\ell_1} + \frac{h_2|\alpha + \beta\bar{\gamma}|^2}{\ell_1\ell_2} + \frac{h_3|\beta - \alpha\bar{\gamma}|^2}{\ell_2}, \\
s_{22} &= \frac{h_1|\alpha|^2}{\ell_1} + \frac{h_2|1 - \alpha\bar{\beta}\bar{\gamma} + \beta\bar{\beta}|^2}{\ell_1\ell_2} + \frac{h_3|\bar{\gamma}|^2}{\ell_2}, \\
s_{33} &= \frac{h_1|\beta|^2 + h_2(1 + |\alpha|^2)}{\ell_1} + \frac{h_3 - h_2}{\ell_2}, \\
s_{12} &= \frac{(h_1 - h_2)\alpha}{\ell_1} + \frac{(h_2 - h_3)\bar{\gamma}(\beta - \alpha\bar{\gamma})}{\ell_2}, \\
s_{13} &= \frac{(h_1 - h_2)\beta}{\ell_1} + \frac{(h_2 - h_3)(\beta - \alpha\bar{\gamma})}{\ell_2}, \\
s_{23} &= \frac{(h_1 - h_2)\bar{\alpha}\beta}{\ell_1} + \frac{(h_2 - h_3)\bar{\gamma}}{\ell_2}
\end{aligned} \tag{A4}$$

and  $s_{ij} = \bar{s}_{ji}$  for the reminder.

In the same way, the coherent state expectation value of operator higher powers can also be easily computed by repeated differentiation of the Bergman kernel. For example, for quadratic powers we have

$$\langle h, U | S_{ij} S_{kl} | h, U \rangle = \frac{S_{ij}(S_{kl} B_h(\bar{\alpha}, \bar{\beta}, \bar{\gamma}; \alpha, \beta, \gamma))}{B_h(\bar{\alpha}, \bar{\beta}, \bar{\gamma}; \alpha, \beta, \gamma)}. \tag{A5}$$

However, to compute the energy surface (46) we can restrict ourselves to expectation values (A4) since, in the thermodynamic/classical limit  $N \rightarrow \infty$ , quantum fluctuations disappear and we have

$$\lim_{N \rightarrow \infty} \frac{\langle h, U | S_{ij} S_{kl} | h, U \rangle}{\langle h, U | S_{ij} | h, U \rangle \langle h, U | S_{kl} | h, U \rangle} = 1. \tag{A6}$$

## Appendix B: Parity symmetry operations on coherent states

At the end of Section II, we have seen that the parity operators  $\Pi_i = \exp(i\pi S_{ii})$ ,  $i = 1, 2, 3$ , are a symmetry of the Hamiltonian (9). This discrete symmetry is spontaneously broken in the thermodynamic limit, and degenerate ground states (“vacua”) arise in this limit. Coherent states (38) are excellent variational states reproducing the ground state energy in the limit  $N \rightarrow \infty$ . Ground state degeneracy is perceived, for example, in the structure of multiple minima of the energy surface (46,49) depicted in Figure 8 and calculated in (56). Note that critical values of the coherent state parameters ( $\alpha, \beta, \gamma$ ) appear in degenerate opposite pairs. Let us show that this is intimately related to the intrinsic parity symmetry of the Hamiltonian and discuss its consequences. We want to know the effect of a parity symmetry operation  $\Pi_i$  on a (non normalized) coherent state (39), that is

$$\Pi_i |h; \alpha, \beta, \gamma\rangle = e^{i\pi S_{ii}} e^{\beta S_{31}} e^{\alpha S_{21}} e^{\gamma S_{32}} |m_{hw}\rangle. \tag{B1}$$

All commutators  $[S_{ii}, S_{jk}]$ , with  $j > k$ , are either zero or of the kind  $[A, B] = \pm B$ , for which we know that  $[A, B^n] = \pm n B^{n-1}$  and  $[A, e^{\alpha B}] = \pm \alpha e^{\alpha B}$ , which can be formally written as  $[A, e^{\alpha B}] = \pm \alpha \partial_{\alpha} e^{\alpha B}$ . In the same way, for the repeated commutator (adjoint action), we have

$$\text{ad}_A^k(e^{\alpha B}) \equiv [A, [A, \dots, [A, e^{\alpha B}] \dots]] = (\pm \alpha \partial_{\alpha})^k e^{\alpha B},$$

and therefore

$$\begin{aligned}
e^{i\theta A} e^{\alpha B} e^{-i\theta A} &= \sum_{k=0}^{\infty} \frac{(i\theta)^k}{k!} \text{ad}_A^k(e^{\alpha B}) = e^{\pm i\theta \alpha \partial_{\alpha}} e^{\alpha B} \\
&= e^{e^{\pm i\theta} \alpha B}.
\end{aligned} \tag{B2}$$

Taking into account the particular commutators  $[S_{ii}, S_{jk}]$ ,  $j > k$ , setting  $\theta = \pi$  and noting that  $e^{\pm i\pi} = -1$  and  $S_{ii}|m_{hw}\rangle = h_i|m_{hw}\rangle$ , we finally arrive to

$$\begin{aligned}
\Pi_1 |h; \alpha, \beta, \gamma\rangle &= e^{i\pi h_1} |h; -\alpha, -\beta, \gamma\rangle, \\
\Pi_2 |h; \alpha, \beta, \gamma\rangle &= e^{i\pi h_2} |h; -\alpha, \beta, -\gamma\rangle, \\
\Pi_3 |h; \alpha, \beta, \gamma\rangle &= e^{i\pi h_3} |h; \alpha, -\beta, -\gamma\rangle.
\end{aligned} \tag{B3}$$

From here we recover the fact that  $\Pi_1 \Pi_2 \Pi_3 = e^{i\pi N}$ . We prefer to define the normalized parity operators  $\hat{\Pi}_i = \Pi_i e^{-i\pi h_i}$ , which verify  $\hat{\Pi}_1 \hat{\Pi}_2 \hat{\Pi}_3 = 1$  and  $\hat{\Pi}_i^{-1} = \hat{\Pi}_i$ . Therefore,  $\hat{\Pi}_3 = \hat{\Pi}_1 \hat{\Pi}_2$ .

To finish, let us provide an alternative procedure to obtain the differential realization  $S_{ij}$  of  $S_{ij}$  in (A3). Indeed, the property  $[A, e^{\alpha B}] = \pm \alpha \partial_{\alpha} e^{\alpha B}$  implies that

$$\begin{aligned}
S_{11} |h; \alpha, \beta, \gamma\rangle &= (h_1 - \beta \partial_{\beta} - \alpha \partial_{\alpha}) |h; \alpha, \beta, \gamma\rangle, \\
S_{22} |h; \alpha, \beta, \gamma\rangle &= (h_2 + \alpha \partial_{\alpha} - \gamma \partial_{\gamma}) |h; \alpha, \beta, \gamma\rangle, \\
S_{33} |h; \alpha, \beta, \gamma\rangle &= (h_3 + \gamma \partial_{\gamma} + \beta \partial_{\beta}) |h; \alpha, \beta, \gamma\rangle,
\end{aligned} \tag{B4}$$

which recovers the differential representation (A3) of  $S_{ii}$ , for holomorphic functions this time. The deduction of non-diagonal  $S_{ij}$ ,  $i \neq j$  follows a similar procedure, but it is a bit more involved and we shall not derive it here.

- 
- [1] S. Gnutzmann and M. Kuš, *Journal of Physics A: Mathematical and General* **31**, 9871 (1999).
- [2] S. Gnutzmann, F. Haake, and M. Kuš, *Journal of Physics A: Mathematical and General* **33**, 143 (1999).
- [3] D. C. Meredith, S. E. Koonin, and M. R. Zirnbauer, *Phys. Rev. A* **37**, 3499 (1988).
- [4] W.-G. Wang, F. M. Izrailev, and G. Casati, *Phys. Rev. E* **57**, 323 (1998).
- [5] P. Leboeuf and M. Saraceno, *Journal of Physics A: Mathematical and General* **23**, 1745 (1999).
- [6] O. Castaños, R. López-Peña, J. G. Hirsch, and E. López-Moreno, *Phys. Rev. B* **74**, 104118 (2006).
- [7] M. A. Caprio, P. Cejnar, and F. Iachello, *Annals of Physics* **323**, 1106 (2008).
- [8] P. Pérez-Fernández, A. Relaño, J. M. Arias, P. Cejnar, J. Dukelsky, and J. E. García-Ramos, *Phys. Rev. E* **83**, 046208 (2011).
- [9] H. J. Lipkin, N. Meshkov, and A. J. Glick, *Nuclear Physics* **62**, 188 (1965).
- [10] H. J. Lipkin, N. Meshkov, and A. J. Glick, *Nuclear Physics* **62**, 211 (1965).
- [11] P. Ring and P. Schuch, *The Nuclear Many-Body Problem* (Springer, Berlin, 1980).
- [12] A. Barut and R. Raczka, *Theory of Group Representations and Applications* (Polish Scientific Publishers, Warszawa, 1980).
- [13] P. Zanardi and N. Paunković, *Phys. Rev. E* **74**, 031123 (2006).
- [14] S.-J. Gu, *International Journal of Modern Physics B* **24**, 4371 (2010).
- [15] P. Zanardi, P. Giorda, and M. Cozzini, *Phys. Rev. Lett.* **99**, 100603 (2007).
- [16] J. Ma, L. Xu, H.-N. Xiong, and X. Wang, *Phys. Rev. E* **78**, 051126 (2008).
- [17] E. Romera, M. Calixto, and O. Castaños, *Physica Scripta* **89**, 095103 (2014).
- [18] O. Castaños, M. Calixto, F. Pérez-Bernal, and E. Romera, *Phys. Rev. E* **92**, 052106 (2015).
- [19] R. Gilmore, *Catastrophe Theory for Scientists and Engineers* (Wiley, New York, 1981).
- [20] S. Cordero, E. Nahmad-Achar, R. López-Peña, and O. Castaños, *Phys. Rev. A* **92**, 053843 (2015).
- [21] S. Cordero, O. Castaños, R. López-Peña, and E. Nahmad-Achar, *Phys. Rev. A* **94**, 013802 (2016).
- [22] O. Castaños, E. Nahmad-Achar, R. López-Peña, and J. G. Hirsch, *Phys. Rev. A* **84**, 013819 (2011).
- [23] R. López-Peña, S. Cordero, E. Nahmad-Achar, and O. Castaños, *Physica Scripta* **90**, 068016 (2015).
- [24] M. Calixto, O. Castaños, and E. Romera, *Journal of Statistical Mechanics: Theory and Experiment* **2017**, 103103 (2017).
- [25] M. Calixto, E. Romera, and R. del Real, *Journal of Physics A: Mathematical and Theoretical* **45**, 365301 (2012).
- [26] M. Calixto and F. Pérez-Bernal, *Phys. Rev. A* **89**, 032126 (2014).
- [27] N. M. Myers and S. Deffner, *Phys. Rev. E* **101**, 012110 (2020).
- [28] M. A. M. Versteegh and D. Dieks, *American Journal of Physics* **79**, 741 (2011).
- [29] B. Yadin, B. Morris, and G. Adesso (2020) <https://arxiv.org/abs/2006.12482>.
- [30] L. Venema, B. Verberck, I. Georgescu, G. Prando, E. Couderc, S. Milana, M. Maragkou, L. Persechini, G. Pacchioni, and L. Fleet, *Nature Physics* **12**, 1085 (2016).
- [31] M. Calixto, C. Peón-Nieto, and E. Pérez-Romero, *Annals of Physics* **373**, 52 (2016).
- [32] M. Calixto and E. Pérez-Romero (2019) <https://arxiv.org/abs/1904.06932>.
- [33] M. Calixto, C. Peón-Nieto, and E. Pérez-Romero, *Phys. Rev. B* **95**, 235302 (2017).
- [34] M. Calixto and C. Peón-Nieto, *Journal of Statistical Mechanics: Theory and Experiment* **2018**, 053112 (2018).

## 2.2 Entanglement measures in symmetric multi-quDit systems

- <sup>2</sup> M. Calixto, A. Mayorgas, and J. Guerrero, “Entanglement and  $U(D)$ -spin squeezing in symmetric multi-qudit systems and applications to quantum phase transitions in Lipkin–Meshkov–Glick  $D$ -level atom models”, *Quantum Information Processing* 20, 304 (2021).

### Quality metrics JCR

- Year: 2022
- Category: PHYSICS, MATHEMATICAL
- Journal Impact Factor (JIF): 2.5
- JIF Rank: 10/56 (Q1)

Publication citations in Google Scholar (March 2024): 13

# Entanglement and $U(D)$ -spin squeezing in symmetric multi-quDit systems and applications to quantum phase transitions in Lipkin-Meshkov-Glick $D$ -level atom models

Manuel Calixto\* and Alberto Mayorgas†

*Department of Applied Mathematics and Institute Carlos I of Theoretical and Computational Physics (iC1),  
University of Granada, Fuentenueva s/n, 18071 Granada, Spain*

Julio Guerrero‡

*Department of Mathematics, University of Jaen, Campus Las Lagunillas s/n, 23071 Jaen, Spain*

(Dated: March 19, 2024)

Collective spin operators for symmetric multi-quDit (namely, identical  $D$ -level atom) systems generate a  $U(D)$  symmetry. We explore generalizations to arbitrary  $D$  of  $SU(2)$ -spin coherent states and their adaptation to parity (multicomponent Schrödinger cats), together with multi-mode extensions of NOON states. We write level, one- and two-quDit reduced density matrices of symmetric  $N$ -quDit states, expressed in the last two cases in terms of collective  $U(D)$ -spin operator expectation values. Then we evaluate level and particle entanglement for symmetric multi-quDit states with linear and von Neumann entropies of the corresponding reduced density matrices. In particular, we analyze the numerical and variational ground state of Lipkin-Meshkov-Glick models of 3-level identical atoms. We also propose an extension of the concept of  $SU(2)$  spin squeezing to  $SU(D)$  and relate it to pairwise  $D$ -level atom entanglement. Squeezing parameters and entanglement entropies are good markers that characterize the different quantum phases, and their corresponding critical points, that take place in these interacting  $D$ -level atom models.

## I. INTRODUCTION

The development of quantum technologies partially relies on the efficient preparation of nonclassical atomic states and the exploitation of many-body entanglement [1–3] and spin squeezing [4], specially to enhance the sensitivity of precision measurements like in quantum metrology. Such is the case of many-body entangled (and spin-squeezed) states of cold atoms generated for instance in atom-atom collisions in Bose-Einstein condensates (BECs) [2].

Indistinguishable particles are naturally correlated due to exchange symmetry and there has been a long-standing debate on whether identical particle entanglement is physical or merely a mathematical artifact (see e.g [5] and references therein). Recent work like [6] shows indeed entanglement between identical particles as a consistent quantum resource in some typical optical and cold atomic systems with immediate practical impact. It can also be extracted and used as a resource for standard quantum information tasks [7]. Moreover, multipartite entanglement of symmetric multi-qubit systems can add robustness and stability against the loss of a small number of particles [5].

Understanding the role of the indistinguishability of identical bosons and quantum entanglement has been the subject of many recent work (see e.g. [8, 9] and references therein). We know that, for  $N = 2$  particles, any quantum state is either separable or entangled. However, for  $N > 2$ , one needs further classifications for multipartite entanglement [10]. Many different measurements have been proposed to detect and quantify quantum correlations [3]. We shall restrict ourselves to bipartite entanglement of pure states, where necessary conditions for separability in arbitrary dimensions exist.

In order to quantify entanglement between identical particles we shall follow Wang and Mølmer’s [11] procedure, who wrote the reduced density matrix (RDM) of one- and two- qubits, extracted at random from a symmetric multi-qubit state  $\psi$ , in terms of expectation values  $\langle \vec{S} \rangle_\psi$  of collective spin operators  $\vec{S}$ . For pairwise entanglement, the concurrence  $C$  (an entanglement measure introduced by Wootters [12]) was calculated for spin coherent states (SCSs) [13, 14], Dicke and Kitagawa-Ueda [15] spin squeezed states, together with mixed states of Heisenberg models. Kitagawa-Ueda [15] spin squeezed states are the spin version of traditional parity adapted CSs, sometimes called “Schrödinger cat states” since they are a quantum superposition of weakly-overlapping (macroscopically distinguishable) quasi-classical coherent wave packets. They were first introduced by Dodonov, Malkin and Man’ko [16] and later adapted to more general finite groups than the parity group  $\mathbb{Z}_2 = \{1, -1\}$  [17]. In this article we shall introduce  $U(D)$  SCSs (denoted

---

\* calixto@ugr.es: corresponding author

† albmayer97@gmail.com

‡ jguerrer@ujaen.es

DSCSs for brevity) adapted to the parity symmetry  $\mathbb{Z}_2 \times \mathbb{Z}_2$ , which are a  $D$ -dimensional generalization of U(2) Schrödinger cats, and we shall refer to them as DCATS for short. In general, parity adapted CSs are a special set of “nonclassical” states with interesting statistical properties (see [18–20] for several seminal papers). Parity adapted DSCSs arise as variational states reproducing the energy and structure of ground states in Lipkin-Meshkov-Glick (LMG)  $D$ -level atom models (see [21] and later in Sec. V).

In Ref. [22], the concurrence  $C$  was related to the spin squeezing parameter  $\xi^2 = 4(\Delta S_{\vec{n}_\perp})^2/N$  introduced by [15], which measures spin fluctuations in an orthogonal direction to the mean value  $\vec{n} \propto \langle \vec{S} \rangle$  with minimal variance. Spin squeezing means that  $\xi^2 < 1$ , that is, when the variance  $(\Delta S_{\vec{n}_\perp})^2$  is smaller than the standard quantum limit  $S/2 = N/4$  (with  $S$  the spin) attained by (quasiclassical) SCSs. This study shows that spin squeezing is related to pairwise correlation for even and odd parity multi-qubit states. Squeezing is in general a redistribution of quantum fluctuations between two noncommuting observables  $A$  and  $B$  while preserving the minimum uncertainty product  $\Delta_\psi A \Delta_\psi B \geq \frac{1}{2} |\langle [A, B] \rangle_\psi|$ . Roughly speaking, it means to partly cancel out fluctuations in one direction at the expense of those enhanced in the “conjugated” direction. For the standard radiation field, it implies the variance relation  $(\Delta q)^2 < 1/4$  for quadrature (position  $q$  and momentum  $p$ ) operators. For general U( $D$ ) spin systems of identical  $D$ -level atoms or “quDits”, the situation is more complicated and we shall extend the  $D = 2$  definition of spin squeezing to general  $D$ .

Spin squeezing can be created in atom systems by making them to interact with each other for a relatively short time in Kerr-like medium with “twisting” nonlinear Hamiltonians like  $H = \lambda S_x^2$  [15], generating entanglement between them [23, 24]. This effective Hamiltonian can be realized in ion traps [25] and has produced four-particle entangled states [26]. There are also some proposals for two-component BECs [23]. Likewise, the ground state at zero temperature of Hamiltonian critical many-body systems possessing discrete (parity) symmetries also exhibits a cat-like structure. The parity symmetry is spontaneously broken in the thermodynamic limit  $N \rightarrow \infty$  and degenerated ground states arise. Parity adapted coherent states are then good variational states, reproducing the energy of the ground state of these quantum critical models in the thermodynamic limit  $N \rightarrow \infty$ , namely in matter-field interactions (Dicke model) of two-level [27, 28] and three-level [29, 30] atoms, BEC [31], U(3) vibron models of molecules [32, 33], bilayer quantum Hall systems [34] and (LMG) models for two-level atoms [35–37]. Quantum information (fidelity, entropy, fluctuation, entanglement, etc) measures have proved to be useful in the analysis of the highly correlated ground state structure of these many-body systems and the identification of critical points across the phase diagram. Special attention must be paid to the deep connection between entanglement, squeezing and quantum phase transitions (QPTs); see [1, 4] and references therein.

In this article we want to explore squeezing and interparticle and interlevel quantum correlations in symmetric multi-quDit systems like the ones described by critical LMG models of identical  $D$ -level atoms (see e.g. [21, 38–42] for  $D = 3$  level atom models). The literature mainly concentrates on two-level atoms, displaying a U(2) symmetry, which is justified when we make atoms to interact with an external monochromatic electromagnetic field. However, the possibility of polychromatic radiation requires the activation of more atom levels and increases the complexity and richness of the system (see e.g. [29]). In any case, this also applies to general interacting boson models [43] and multi-mode BECs with two or more boson species. Collective operators generate a U( $D$ ) spin symmetry for the case of  $D$ -level identical atoms or  $D$  boson species (quDits). Recently [21] we have calculated the phase diagram of a three-level LMG atom model. Here we want to explore the connection between entanglement and squeezing with QPTs for this symmetric multi-quDit system. For this purpose, we extend to  $D$  levels the usual definition of Dicke, parity-adapted SCSs and NOON states, and propose linear and von Neumann entropies of certain reduced density matrices as a measure of interlevel and interparticle entanglement. We also introduce a generalization of SU(2) spin squeezing to SU( $D$ ).

The organization of the paper is as follows. In Sec. II we introduce collective U( $D$ ) spin operators  $S_{ij}$ , their boson realization, their matrix elements in Fock subspaces of  $N$  symmetric quDits, DSCSs and their adaptation to parity (“DCATS”), and a generalization of NOON states to  $D$ -level systems (“NODONS”). In Sec. III we give a brief overview on the concepts and measures of interlevel and interparticle entanglement, considering different bipartitions of the whole system, that we put in practice later in Sec. VI. As entanglement measures, we concentrate on linear (unpurity) and von Neumann entropies. We compute entanglement between levels and atoms for DSCSs, DCAT and NODON states. In Sec. IV we extend Kitagawa-Ueda’s definition of SU(2) spin squeezing to SU( $D$ ) and we also connect it with two-quDit entanglement introduced in the previous Section. In Sec. V we introduce  $D$ -level Lipkin-Meshkov-Glick (LMG) atom models (we particularize to  $D = 3$  for simplicity) and study their phase diagram and critical points. In Sec. VI we analyze the ground state structure of the three-level LMG atom model across the phase diagram with the quantum information measures of Sec. III and the SU(3)-spin squeezing parameters of Sec. IV, thus revealing the role of entanglement and squeezing as signatures of quantum phase transitions and detectors of critical points. We only compute linear entropy in Sec. VI, since it is easier to compute than von Neuman entropy and eventually provides similar qualitative information for our purposes; the interested reader can consult Refs. [44, 45] for a more general study on the relation between both entropies. Finally, Sec. VII is devoted to conclusions.

## II. STATE SPACE, SYMMETRIES AND COLLECTIVE OPERATOR MATRIX ELEMENTS

Those readers acquainted with the boson realization of  $U(D)$  spin operators and coherent states can skim read all the way to equation (16), just to introduce essential notation and necessary formulas. We consider a system of  $N$  identical atoms of  $D$  levels ( $N$  quDits in the quantum information jargon). Let us denote by  $E_{ij} = |i\rangle\langle j|$  the Hubbard operator describing a transition from the single-atom level  $|j\rangle$  to the level  $|i\rangle$ , with  $i, j = 1, \dots, D$ . These are a generalization of Pauli matrices for qubits ( $D = 2$ ), namely  $E_{12} = \sigma_+$ ,  $E_{21} = \sigma_-$ ,  $E_{11} - E_{22} = \sigma_3$  and  $E_{11} + E_{22} = \sigma_0$  (the  $2 \times 2$  identity matrix). The expectation values of  $E_{ij}$  account for complex polarizations or coherences between levels for  $i \neq j$  and occupation probability of the level  $i$  for  $i = j$ . The  $E_{ij}$  represent the  $D^2$  step operators of  $U(D)$ , whose (Cartan-Weyl) matrices  $\langle l|E_{ij}|k\rangle = \delta_{il}\delta_{jk}$  fulfill the commutation relations

$$[E_{ij}, E_{kl}] = \delta_{jk}E_{il} - \delta_{il}E_{kj}. \quad (1)$$

Let us denote by  $E_{ij}^\mu$ ,  $\mu = 1, \dots, N$  the embedding of the single  $\mu$ -th atom  $E_{ij}$  operator into the  $N$ -atom Hilbert space; namely,  $E_{ij}^3 = \mathbb{1}_D \otimes \mathbb{1}_D \otimes E_{ij} \otimes \mathbb{1}_D$  for  $N = 4$ , with  $\mathbb{1}_D$  the  $D \times D$  identity matrix. The collective  $U(D)$ -spin ( $D$ -spin for short) operators are

$$S_{ij} = \sum_{\mu=1}^N E_{ij}^\mu, \quad i, j = 1, \dots, D. \quad (2)$$

They are the generators of the underlying  $U(D)$  dynamical symmetry with the same commutation relations as those of  $E_{ij}$  in (1). When focusing on two levels  $i > j$ , we might prefer to use

$$\vec{J}^{(ij)} = (J_x^{(ij)}, J_y^{(ij)}, J_z^{(ij)}), \quad J_x^{(ij)} = \frac{S_{ij} + S_{ji}}{2}, \quad J_y^{(ij)} = i\frac{S_{ij} - S_{ji}}{2}, \quad J_z^{(ij)} = \frac{S_{jj} - S_{ii}}{2}, \quad (3)$$

(roman i denotes the imaginary unit throughout the article) with commutation relations  $[J_x^{(ij)}, J_y^{(ij)}] = iJ_z^{(ij)}$  (and cyclic permutations of  $x, y, z$ ), which is an embedding of  $D(D-1)/2$   $SU(2)$  subalgebras into  $U(D)$ . Although the form (3) for  $D$ -spin operators could be more convenient to extrapolate all the  $D = 2$  level machinery to arbitrary  $D$ , we shall still prefer the form (2) (at least in this paper), which allows for more compact formulas.

The  $D^N$ -dimensional Hilbert space is the  $N$ -fold tensor product  $[\mathbb{C}^D]^{\otimes N}$ . The tensor product representation of  $U(D)$  is reducible and decomposes into a Clebsch-Gordan direct sum of mixed symmetry invariant subspaces. Here we shall restrict ourselves to the  $\binom{N+D-1}{N}$ -dimensional fully symmetric sector (see [21] for the role of other mixed symmetry sectors), which means that our  $N$  atoms are indistinguishable (bosons). Denoting by  $a_i^\dagger$  (resp.  $a_i$ ) the creation (resp. annihilation) operator of an atom in the  $i$ -th level, the collective  $D$ -spin operators (2) can be expressed (in this fully symmetric case) as bilinear products of creation and annihilation operators as (Schwinger representation)

$$S_{ij} = a_i^\dagger a_j, \quad i, j = 1, \dots, D. \quad (4)$$

$S_{ii}$  is the operator number of atoms at level  $i$ , whereas  $S_{ij}$ ,  $i \neq j$  are raising and lowering operators. The fully symmetric representation space of  $U(D)$  is embedded into Fock space, with Bose-Einstein-Fock basis ( $|\vec{0}\rangle$  denotes the Fock vacuum)

$$|\vec{n}\rangle = |n_1, \dots, n_D\rangle = \frac{(a_1^\dagger)^{n_1} \dots (a_D^\dagger)^{n_D}}{\sqrt{n_1! \dots n_D!}} |\vec{0}\rangle, \quad (5)$$

when fixing  $n_1 + \dots + n_D = N$  (the linear Casimir  $C_1 = S_{11} + \dots + S_{DD}$ ) to the total number  $N$  of atoms. There are other realizations of  $D$ -spin operators in terms of more than  $D$  bosonic modes (e.g. when each level  $j$  contains  $M$  degenerate orbitals), which describe mixed symmetries [46–48], but we shall not consider them here.

Collective  $D$ -spin operators (4) matrix elements are given by

$$\langle \vec{m} | S_{ij} | \vec{n} \rangle = \sqrt{(n_i + 1)n_j} \delta_{m_i, n_i + 1} \delta_{m_j, n_j - 1} \prod_{k \neq i, j} \delta_{m_k, n_k}, \quad \forall i \neq j, \quad \langle \vec{m} | S_{ii} | \vec{n} \rangle = n_i \delta_{\vec{m}, \vec{n}}. \quad (6)$$

The expansion of a general symmetric  $N$ -particle state  $\psi$  in the Fock basis will be written as

$$|\psi\rangle = \sum_{\vec{n}} c_{\vec{n}} |\vec{n}\rangle = \sum_{n_1 + \dots + n_D = N} c_{n_1, \dots, n_D} |n_1, \dots, n_D\rangle, \quad (7)$$

where  $\sum'$  is a shorthand for the restricted sum.  $D$ -spin operator expectation values (EVs) can then be easily computed as

$$\langle S_{ij} \rangle_\psi = \langle \psi | S_{ij} | \psi \rangle = \sum_{\vec{n}}' \bar{c}_{\vec{n}_{ij}} c_{\vec{n}} \sqrt{(n_i + 1)n_j}, \quad i \neq j, \quad \langle S_{ii} \rangle_\psi = \sum_{\vec{n}}' n_i |c_{\vec{n}}|^2, \quad (8)$$

where we have used (6) and where by  $\vec{n}_{ij}$  we mean to replace  $n_i \rightarrow n_i + 1$  and  $n_j \rightarrow n_j - 1$  in  $\vec{n}$ .

Among all symmetric multi-quDit states, we shall pay special attention to  $U(D)$  SCSs (DSCSs for short)

$$|\mathbf{z}\rangle = |(z_1, z_2, \dots, z_D)\rangle = \frac{1}{\sqrt{N!}} \left( \frac{z_1 a_1^\dagger + z_2 a_2^\dagger + \dots + z_D a_D^\dagger}{\sqrt{|z_1|^2 + |z_2|^2 + \dots + |z_D|^2}} \right)^N |\vec{0}\rangle, \quad (9)$$

which are labeled by complex points  $\mathbf{z} = (z_1, \dots, z_D) \in \mathbb{C}^D$ . To be more precise, there is an equivalence relation:  $|\mathbf{z}'\rangle \sim |\mathbf{z}\rangle$  if  $\mathbf{z}' = q\mathbf{z}$  for any complex number  $q \neq 0$ , which means that  $|\mathbf{z}\rangle$  is actually labeled by class representatives of complex lines in  $\mathbb{C}^D$ , that is, by points of the complex projective phase space

$$\mathbb{C}P^{D-1} = [\mathbb{C}^D / \sim] = U(D)/[U(1) \times U(D-1)].$$

A class/coset representative can be chosen as  $\tilde{\mathbf{z}} = \mathbf{z}/z_i$  when  $z_i \neq 0$ , which corresponds to a certain patch of the manifold  $\mathbb{C}P^{D-1}$ . This is equivalent to chose  $i$  as a reference level and set  $z_i = 1$ . For the moment, we shall allow redundancy in  $\mathbf{z}$  to write general expressions, although we shall eventually take  $i = 1$  as a reference (lower energy) level and set  $z_1 = 1$  in Section V.

DSCSs (multinomial) can be seen as BECs of  $D$  modes, generalizing the spin  $U(2)$  (binomial) coherent states of two modes introduced by [13] and [14] long ago. For  $\mathbf{z} = \mathbf{e}_i$  (the standard/canonical basis vectors of  $\mathbb{C}^D$ ), the DSCS  $|\mathbf{e}_i\rangle = (a_i^\dagger)^N |\vec{0}\rangle / \sqrt{N!}$  corresponds to a BEC of  $N$  atoms placed at level  $i$ .<sup>1</sup> If we order levels  $i = 1, \dots, D$  from lower to higher energies, the state  $|\mathbf{e}_1\rangle$  would be the ground state, whereas general  $|\mathbf{z}\rangle$  could be seen as coherent excitations. Coherent states are sometimes called ‘‘quasi-classical’’ states and we shall see in Section V that  $|\mathbf{z}\rangle$  turns out to be a good variational state that reproduces the energy and wave function of the ground state of multilevel LMG atom models in the thermodynamic (classical) limit  $N \rightarrow \infty$ .

Expanding the multinomial (9), we identify the coefficients  $c_{\vec{n}}$  of the expansion (7) of the DSCS  $|\mathbf{z}\rangle$  in the Fock basis as

$$c_{\vec{n}}(\mathbf{z}) = \sqrt{\frac{N!}{\prod_{i=1}^D n_i!}} \frac{\prod_{i=1}^D z_i^{n_i}}{|\mathbf{z}|^N}, \quad (10)$$

where we have written  $|\mathbf{z}| = (\mathbf{z} \cdot \mathbf{z})^{1/2} = (\sum_{i=1}^D |z_i|^2)^{1/2}$  for the length of  $\mathbf{z}$ . Note that DSCS are not orthogonal (in general) since

$$\langle \mathbf{z}' | \mathbf{z} \rangle = \frac{(\mathbf{z}' \cdot \mathbf{z})^N}{(\mathbf{z}' \cdot \mathbf{z}')^{N/2} (\mathbf{z} \cdot \mathbf{z})^{N/2}}, \quad \mathbf{z}' \cdot \mathbf{z} = \bar{z}'_1 z_1 + \dots + \bar{z}'_D z_D. \quad (11)$$

However, contrary to the standard CSs, they can be orthogonal when  $\mathbf{z}' \cdot \mathbf{z} = 0$ . EVs of  $D$ -spin operators  $S_{ij}$  (coherences for  $i \neq j$  and mean level populations for  $i = j$ ) in a DSCS are simply written as

$$\langle S_{ij} \rangle_{\mathbf{z}} = \langle \mathbf{z} | S_{ij} | \mathbf{z} \rangle = N \bar{z}_i z_j / |\mathbf{z}|^2. \quad (12)$$

DSCS non-diagonal matrix elements of  $D$ -spin operators can also be compactly written as

$$\langle \mathbf{z}' | S_{ij} | \mathbf{z} \rangle = N \bar{z}'_i z_j \frac{(\mathbf{z}' \cdot \mathbf{z})^{N-1}}{|\mathbf{z}'|^N |\mathbf{z}|^N}. \quad (13)$$

Similarly, EVs of quadratic powers of  $D$ -spin operators in a DSCS state can be concisely written as

$$\langle \mathbf{z} | S_{ij} S_{kl} | \mathbf{z} \rangle = \frac{\bar{z}_i z_l}{|\mathbf{z}|^4} (N \delta_{jk} |\mathbf{z}|^2 + N(N-1) \bar{z}_k z_j), \quad (14)$$

<sup>1</sup> Note the difference between Fock states  $|n_1, \dots, n_D\rangle$  and DSCSs  $|(z_1, \dots, z_D)\rangle$ , which are placed inside parentheses to avoid confusion. For instance,  $|\mathbf{e}_i\rangle = |(0, \dots, 1, \dots, 0)\rangle = (a_i^\dagger)^N |\vec{0}\rangle / \sqrt{N!} = |0, \dots, N, \dots, 0\rangle$ .

and their DSCS matrix elements as

$$\langle \mathbf{z}' | S_{ij} S_{kl} | \mathbf{z} \rangle = \frac{\bar{z}'_i z_l}{|\mathbf{z}'|^N |\mathbf{z}|^N} (N \delta_{jk} (\mathbf{z}' \cdot \mathbf{z})^{N-1} + N(N-1) \bar{z}'_k z_j (\mathbf{z}' \cdot \mathbf{z})^{N-2}). \quad (15)$$

Note that, for large  $N$ , quantum fluctuations are negligible and we have  $\langle \mathbf{z} | S_{ij} S_{kl} | \mathbf{z} \rangle \simeq \langle \mathbf{z} | S_{ij} | \mathbf{z} \rangle \langle \mathbf{z} | S_{kl} | \mathbf{z} \rangle$ . Otherwise stated, in the thermodynamical (classical) limit we have

$$\lim_{N \rightarrow \infty} \frac{\langle \mathbf{z} | S_{ij} S_{kl} | \mathbf{z} \rangle}{\langle \mathbf{z} | S_{ij} | \mathbf{z} \rangle \langle \mathbf{z} | S_{kl} | \mathbf{z} \rangle} = 1. \quad (16)$$

We shall use these ingredients when computing one- and two-quDit RDMs in the next Section.

We shall see that DSCSs are separable and exhibit no atom entanglement (although they do exhibit level entanglement). The situation changes when we deal with parity adapted DSCSs, sometimes called ‘‘Schrödinger cat states’’ (commented at the introduction), since they are a quantum superposition of weakly-overlapping (macroscopically distinguishable) quasi-classical coherent wave packets, as we shall explicitly see below. These kind of cat states arise in several interesting physical situations. As we have already mentioned, they can be generated via amplitude dispersion by evolving CSs in Kerr media, with a strong nonlinear interaction, like the already commented spin-squeezed states of [15]. They exhibit statistical properties similar to squeezed states, with deviations from Poissonian (CS) distributions. Squeezing and multiparticle entanglement are important quantum resources that make Schrödinger cats useful for quantum enhanced metrology [2]. They are also good variational states [14], reproducing the energy of the ground state of quantum critical models in the thermodynamic limit  $N \rightarrow \infty$ . To construct them, we require parity operators defined as

$$\Pi_j = \exp(i\pi S_{jj}), \quad j = 1, \dots, D. \quad (17)$$

They are conserved when the Hamiltonian scatters pairs of particles conserving the parity of the population  $n_j$  in each level  $j = 1, \dots, D$ . It is easy to see that  $\Pi_j (a_j^\dagger)^{n_j} |\vec{0}\rangle = (-a_j^\dagger)^{n_j} |\vec{0}\rangle$ , so that the effect of parity operations on number states (5) is  $\Pi_j |\vec{n}\rangle = (-1)^{n_j} |\vec{n}\rangle$ . Likewise, using the multinomial expansion (9), it is easy to see that the effect of parity operators on symmetric DSCSs  $|\mathbf{z}\rangle$  is then

$$\Pi_i |\mathbf{z}\rangle = \Pi_i |(z_1, \dots, z_i, \dots, z_D)\rangle = |(z_1, \dots, -z_i, \dots, z_D)\rangle \quad (18)$$

Note that  $\Pi_i^{-1} = \Pi_i$  and  $\Pi_1 \dots \Pi_D = (-1)^N$ , a constraint that says that the parity group for symmetric quDits is not  $\mathbb{Z}_2 \times \dots \times \mathbb{Z}_2$  but  $\mathbb{Z}_2 \times \dots \times \mathbb{Z}_2$  instead. In order to define a projector on definite parity (even or odd), we have to chose a reference level, namely  $i = 1$ . Doing so, the projector on even parity becomes

$$\Pi_{\text{even}} = 2^{1-D} \sum_{\mathbb{b} \in \{0,1\}^{D-1}} \Pi_2^{b_2} \Pi_3^{b_3} \dots \Pi_D^{b_D}, \quad (19)$$

where we denote the binary string  $\mathbb{b} = (b_2, \dots, b_D) \in \{0,1\}^{D-1}$ . Likewise, the projection operator on odd parity is  $\Pi_{\text{odd}} = \mathbb{1} - \Pi_{\text{even}}$ . Choosing level  $i = 1$  as a reference level is equivalent to choose a patch on the manifold  $\mathbb{C}P^{D-1}$  where  $z_1 \neq 0$ ; in this way, any coherent state  $|\mathbf{z}\rangle$  is equivalent to the class representative  $|\mathbf{z}/z_1\rangle$ , due to equivalence relation  $|\mathbf{z}'\rangle \sim |\mathbf{z}\rangle$  if  $\mathbf{z}' = q\mathbf{z}$  with  $q \neq 0$ . Let us simply denote by  $\mathbf{z} = (1, z_2, \dots, z_D)$  the class representative in this case. It will be useful, for later use as variational ground states, to define the (unnormalized) generalized Schrödinger even cat state

$$|\text{DCAT}\rangle = \Pi_{\text{even}} |\mathbf{z}\rangle = 2^{1-D} \sum_{\mathbb{b}} |\mathbf{z}^{\mathbb{b}}\rangle, \quad (20)$$

where  $\mathbf{z}^{\mathbb{b}} = (1, (-1)^{b_2} z_2, \dots, (-1)^{b_D} z_D)$  and we are using  $\sum_{\mathbb{b}}$  as a shorthand for  $\sum_{\mathbb{b} \in \{0,1\}^{D-1}}$ . It is just the projection of a DSCS on the even parity subspace. The state (20) is a generalization of the even cat state for  $D = 2$  in the literature [16], given by

$$|2\text{CAT}\rangle = \frac{1}{2} (|(1, \alpha)\rangle + |(1, -\alpha)\rangle) \quad (21)$$

for the class representative  $\mathbf{z} = (z_1, z_2) = (1, \alpha)$ . The shorthand  $|\alpha\rangle = |(1, \alpha)\rangle$  is used in the literature when a class representative (related to highest  $|\mathbf{e}_1\rangle$  or lowest  $|\mathbf{e}_2\rangle$  weight fiducial vectors) is implicitly chosen. The squared norm of  $|2\text{CAT}\rangle$  is simply

$$\mathcal{N}(2\text{CAT})^2 = \langle 2\text{CAT} | 2\text{CAT} \rangle = \frac{1}{2} \left[ 1 + \left( \frac{1 - |\alpha|^2}{1 + |\alpha|^2} \right)^N \right]. \quad (22)$$

Note that the overlap  $\langle 1, \alpha | 1, -\alpha \rangle = ((1 - |\alpha|^2)/(1 + |\alpha|^2))^N \xrightarrow{N \rightarrow \infty} 0$ , which means that  $|1, \alpha\rangle$  and  $|1, -\alpha\rangle$  are macroscopically distinguishable wave packets for any  $\alpha$  (they are orthogonal for  $|\alpha| = 1$ ). Likewise, the unnormalized 3CAT is explicitly given by

$$|3\text{CAT}\rangle = \frac{1}{4}(|1, \alpha, \beta\rangle + |1, -\alpha, \beta\rangle + |1, \alpha, -\beta\rangle + |1, -\alpha, -\beta\rangle) \quad (23)$$

when setting  $\mathbf{z} = (z_1, z_2, z_3) = (1, \alpha, \beta)$  as a class representative. The squared norm is now

$$\mathcal{N}(3\text{CAT})^2 = \frac{1}{4} \left[ 1 + \frac{(1 - |\alpha|^2 + |\beta|^2)^N + (1 + |\alpha|^2 - |\beta|^2)^N + (1 - |\alpha|^2 - |\beta|^2)^N}{(1 + |\alpha|^2 + |\beta|^2)^N} \right]. \quad (24)$$

These expressions can be generalized to arbitrary  $D$  as

$$\mathcal{N}(\text{DCAT})^2 = 2^{1-D} \frac{\sum_{\mathbf{b}} (\mathbf{z}^{\mathbf{b}} \cdot \mathbf{z})^N}{|\mathbf{z}|^{2N}}. \quad (25)$$

We shall use (23) and (24) in Sections V and VI, when discussing a LMG model of atoms with  $D = 3$  levels. These 3CAT states have also been used in U(3) vibron models of molecules [32, 33] and Dicke models of 3-level atoms interacting with a polychromatic radiation field [29, 30].

The  $D$ -spin EVs on a DCAT state (20) can be now computed and the general expression is

$$\langle \text{DCAT} | S_{ij} | \text{DCAT} \rangle = N \delta_{ij} \frac{\sum_{\mathbf{b}} (-1)^{b_i} |z_i|^2 (\mathbf{z}^{\mathbf{b}} \cdot \mathbf{z})^{N-1}}{\sum_{\mathbf{b}} (\mathbf{z}^{\mathbf{b}} \cdot \mathbf{z})^N}, \quad (26)$$

where we set  $(-1)^{b_i} = 1 = |z_i|$  for  $i = 1$  (reference level). Similarly, EVs of quadratic powers of  $D$ -spin operators in a DCAT state can be concisely written as

$$\begin{aligned} \langle \text{DCAT} | S_{ij} S_{kl} | \text{DCAT} \rangle &= N (\delta_{ij} \delta_{kl} + \delta_{ik} \delta_{jl} + \delta_{il} \delta_{jk} - 2 \delta_{ij} \delta_{jk} \delta_{kl} \delta_{li}) \\ &\times \frac{\sum_{\mathbf{b}} (-1)^{b_i} \bar{z}_i z_l [\delta_{jk} (\mathbf{z}^{\mathbf{b}} \cdot \mathbf{z})^{N-1} + (N-1) (-1)^{b_k} \bar{z}_k z_j (\mathbf{z}^{\mathbf{b}} \cdot \mathbf{z})^{N-2}]}{\sum_{\mathbf{b}} (\mathbf{z}^{\mathbf{b}} \cdot \mathbf{z})^N}. \end{aligned} \quad (27)$$

To finish this Section, let us comment on a generalization to arbitrary  $D$  of another prominent example of quantum states that are useful for quantum-enhanced metrology and provide phase sensitivities beyond the standard quantum limit. We refer to Greenberger-Horne-Zeilinger (GHZ) or ‘‘NOON’’ (when considering bosonic particles) states. For  $D = 2$  level systems, NOON states can be written in the Fock state notation (5) as (see e.g. [2])

$$|\text{NOON}\rangle = \frac{1}{\sqrt{2}} (|N, 0\rangle + e^{i\phi} |0, N\rangle) = \frac{1}{\sqrt{2}} \left( \frac{(a_1^\dagger)^N}{\sqrt{N!}} |\vec{0}\rangle + e^{i\phi} \frac{(a_2^\dagger)^N}{\sqrt{N!}} |\vec{0}\rangle \right). \quad (28)$$

Using the canonical basis vectors  $\{\mathbf{e}_1, \mathbf{e}_2\}$  of  $\mathbb{C}^2$ , we can write the NOON state as a linear superposition of U(2) SCSs

$$|\text{NOON}\rangle = \frac{1}{\sqrt{2}} (e^{i\phi_1} |\mathbf{e}_1\rangle + e^{i\phi_2} |\mathbf{e}_2\rangle), \quad (29)$$

with phases  $e^{i\phi_{1,2}}$ , which coincides with (28) (up to an irrelevant global phase  $e^{i\phi_1}$ ) for the relative phase  $\phi = \phi_2 - \phi_1$ . Multi-mode (or multi-level, in our context) generalizations of NOON states have been proposed in the literature (see e.g. [49, 50]). In our scheme, this generalization of NOON states (29) to  $D$  level systems adopts the following form

$$|\text{NODON}\rangle = \frac{1}{\sqrt{D}} \left( \sum_{j=1}^D e^{i\phi_j} |\mathbf{e}_j\rangle \right) = \frac{1}{\sqrt{D}} (e^{i\phi_1} |N, 0, \dots\rangle + e^{i\phi_2} |0, N, 0, \dots\rangle + \dots + e^{i\phi_D} |0, 0, \dots, N\rangle). \quad (30)$$

EVs of linear and quadratic powers of  $D$ -spin operators in NODON states can be easily calculated as

$$\langle \text{NODON} | S_{ij} | \text{NODON} \rangle = \frac{N}{D} \delta_{ij}, \quad \langle \text{NODON} | S_{ij} S_{kl} | \text{NODON} \rangle = \frac{N}{D} \delta_{il} (\delta_{jk} + (N-1) \delta_{ik} \delta_{ij}). \quad (31)$$

The computations in this section will be necessary to discuss entanglement and squeezing properties of all these states in the Sections III and IV.

### III. ENTANGLEMENT MEASURES IN MULTI-QUDIT SYSTEMS

In this Section we define several types of bipartition of the whole system, computing the corresponding RDMs and entanglement measures for different kinds of symmetric multi-quDit states  $\psi$  in terms of linear  $\mathcal{L}$  and von Neumann  $\mathcal{S}$  entropies. We start computing interlevel entanglement in Section III A and then (one- and two-quDit) interparticle entanglement in Section III B.

#### A. Entanglement among levels

For a general symmetric  $N$ -particle state  $\psi$  like (7), the RDM on the level  $i$  is

$$\varrho_i(\psi) = \text{tr}_{j \neq i} \left( \sum'_{\vec{n}, \vec{n}'} c_{\vec{n}'} \bar{c}_{\vec{n}} |n'_1, \dots, n'_D\rangle \langle n_1, \dots, n_D| \right) = \sum'_{\vec{n}} |c_{\vec{n}}|^2 |n_i\rangle \langle n_i|. \quad (32)$$

Thus  $\varrho_i(\psi)$  lies in a single boson Hilbert space of dimension  $N + 1$ . Its purity is then

$$\mathcal{P}_i^\ell(\psi) = \text{tr}(\varrho_i^2(\psi)) = \sum'_{\vec{n}, \vec{m}} |c_{\vec{n}}|^2 |c_{\vec{m}}|^2 \delta_{n_i, m_i}. \quad (33)$$

Here the superscript  $\ell$  makes reference to “level”, to distinguish it from “atom” purity  $\mathcal{P}^a$  in the next section. It can also make reference to entanglement between different boson species  $\ell$ , like rotational-vibrational entanglement [32, 33] in algebraic molecular models [51, 52] such as the vibron model based on a bosonic  $U(3)$  spectrum-generating algebra [53, 54]. For the case of the DSCS  $|\mathbf{z}\rangle$  in (9), taking the coefficients  $c_{\vec{n}}$  in (10), and after a lengthy calculation, the RDM on level  $i$  turns out to be diagonal

$$\varrho_i(\mathbf{z}) = \sum_{n=0}^N \lambda_n(x_i, y_i) |N-n\rangle \langle N-n|, \quad \lambda_n(x_i, y_i) = \binom{N}{n} \frac{x_i^{N-n} y_i^n}{(x_i + y_i)^N}, \quad x_i = |z_i|^2, y_i = |\mathbf{z}|^2 - |z_i|^2. \quad (34)$$

Note that the eigenvalues  $\lambda_n$  can be expressed in terms of only two positive real coordinates  $(x_i, y_i)$ , except for the reference level  $z_i = 1$ , for which  $x_i = 1$  and therefore there is only one independent variable  $y_i = |\mathbf{z}|^2 - 1$ . For example, for  $U(3)$  SCSs, choosing  $i = 1$  as the reference level and using the parametrization  $\mathbf{z} = (1, \alpha, \beta)$  for the phase space  $\mathbb{C}P^2$  in (23), we have  $x_1 = 1, x_2 = |\alpha|^2, x_3 = |\beta|^2$  and  $y_1 = |\alpha|^2 + |\beta|^2, y_2 = 1 + |\beta|^2, y_3 = 1 + |\alpha|^2$ . The purity of  $\varrho_i(\mathbf{z})$  is simply  $\mathcal{P}_i^\ell(x_i, y_i) = \sum_{n=0}^N \lambda_n^2(x_i, y_i)$ . In Figure 1 we represent the Linear and von Neumann

$$\mathcal{L}_i^\ell = \frac{N+1}{N} (1 - \mathcal{P}_i^\ell), \quad \mathcal{S}_i^\ell = - \sum_{n=0}^N \lambda_n \log_{N+1} \lambda_n \quad (35)$$

entanglement entropies for a general level  $i$  as a function of  $(x, y)$  [for the reference level  $i = 1$ , we have to restrict ourselves to the cross section  $x = 1$ ]. We normalize linear and von Neumann entropies so that their interval range is  $[0, 1]$ , the extremal values corresponding to pure and completely mixed RDMs, respectively. We shall see that both entropies,  $\mathcal{L}$  and  $\mathcal{S}$ , provide similar qualitative behavior for the bipartitions studied in this paper. Interlevel isentropic contours correspond to the straight lines  $y = mx$  (see Figure 1), and the maximum is attained for  $y = x$ . The large  $N$  behavior of the interlevel linear entanglement entropy  $\mathcal{L}_i^\ell(\mathbf{z})$  around the maximum  $y = x$  is  $\mathcal{L}_i^\ell = 1 - 1/\sqrt{\pi N} + O(N^{-3/2})$ . In Figure 2 we represent contour plots of  $\mathcal{L}_{1,2}^\ell$  and  $\mathcal{S}_{1,2}^\ell$  for the RDM of a 3CAT of  $N = 20$  qutrits on levels  $i = 1$  and  $i = 2$ . Note that linear and von Neumann entropies display a similar structure. We omit  $\mathcal{L}_3^\ell$  and  $\mathcal{S}_3^\ell$  since they are just the reflection in a diagonal mirror line of  $\mathcal{L}_2^\ell$  and  $\mathcal{S}_2^\ell$ , respectively.  $\mathcal{L}_1^\ell$  attains its maximum at the isentropic circle  $|\alpha|^2 + |\beta|^2 = 1$ , whereas  $\mathcal{L}_2^\ell$  attains its maximum at the isentropic hyperbola  $|\alpha|^2 - |\beta|^2 = 1$ . The large  $N$  behavior of the interlevel linear entanglement entropy for a DCAT around the maximum is  $\mathcal{L}_i^\ell = 1 - 2/\sqrt{\pi N} + O(N^{-3/2})$ . Figure 2 also shows (in magenta color) the parametric curve  $(\alpha(\lambda), \beta(\lambda))$  obtained later in Section V and related to the stationary points (59) of the energy surface (57) in the quantum phase diagram of a LMG 3-level atom model, where  $\lambda$  is the atom-atom interaction coupling constant. For high interactions we have  $(\alpha(\lambda), \beta(\lambda)) \xrightarrow{\lambda \rightarrow \infty} (1, 1)$ , which does not lie inside the maximum isentropic curve, although the difference between both entropies tends to zero in the limit  $N \rightarrow \infty$  (see later in Sections V and VI for more information).

For NODON states (30), the RDM on level  $i$  and its purity are

$$\varrho_i(\text{NODON}) = \frac{D-1}{D} |0\rangle_i \langle 0| + \frac{1}{D} |N\rangle_i \langle N|, \quad \text{tr}(\varrho_i^2(\text{NODON})) = 1 - 2 \left( \frac{D-1}{D^2} \right), \quad (36)$$

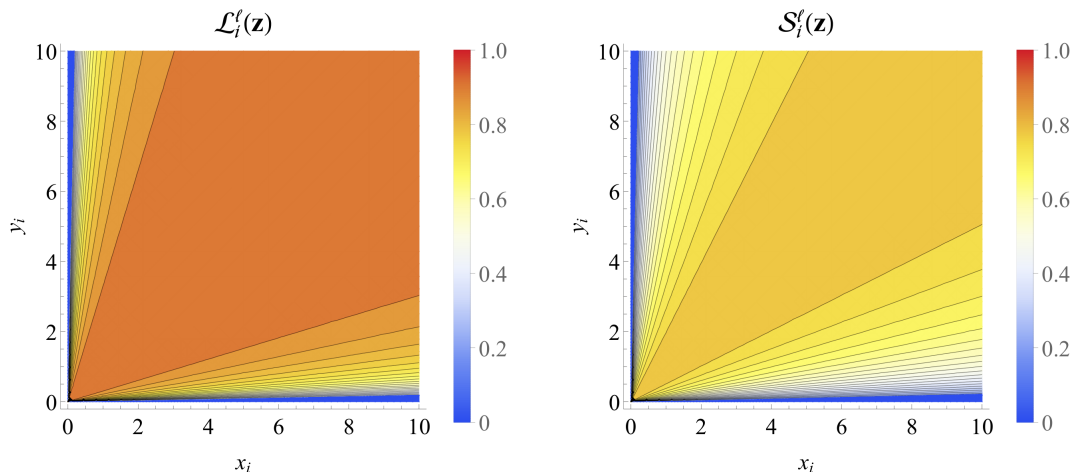


FIG. 1. Contour plots of the linear  $\mathcal{L}_i^\ell$  and von Neumann  $\mathcal{S}_i^\ell$  entanglement entropies, associated to the RDM of a  $U(D)$ -spin coherent state  $|\mathbf{z}\rangle$  of  $N = 10$  quDits on level  $i$  (34), as a function of the phase-space coordinates  $(x, y)$ .

which is independent of the level  $i$ . Therefore, the linear entropy is given by  $\mathcal{L}_i^\ell(\text{NODON}) = 2 \frac{N+1}{N} \frac{D-1}{D^2}$ , which reduces to  $\mathcal{L}_i^\ell(\text{NOON}) = \frac{N+1}{2N}$  for  $D = 2$ .

## B. Entanglement among atoms

We compute the one- and two-particle RDMs for a single and a pair of particles extracted at random from a symmetric  $N$ -quDit state. The corresponding entanglement entropies are expressed in terms of EVs of collective  $D$ -spin operators  $S_{ij}$ .

### 1. One-quDit reduced density matrices

Any density matrix of a single quDit can be written as a combination of Hubbard matrices  $E_{ij}$  with commutation relations (1) as

$$\rho_1 = \sum_{i,j=1}^D r_{ij} E_{ij}, \quad r_{ij} = \text{tr}(\rho_1 E_{ji}) = \langle E_{ji} \rangle \quad (37)$$

with  $r_{ij}$  complex numbers (the generalized Bloch vector) fulfilling  $\bar{r}_{ij} = r_{ji}$  and (the generalized Bloch sphere)

$$\text{tr}[\rho_1] = \sum_{i=1}^D r_{ii} = 1, \quad 0 < \text{tr}[(\rho_1)^2] = \sum_{i,j=1}^D |r_{ij}|^2 \leq 1. \quad (38)$$

We want to construct the one-quDit RDM for one quDit extracted at random from a symmetric  $N$ -quDit state  $\psi$ . The procedure consists of writing the one-quDit RDM entries in terms of expectation values (EVs) of collective  $D$ -spin operators (2). Remember the definition of  $E_{ij}^\mu$ ,  $\mu = 1, \dots, N$  after (1) as the embedding of the single  $\mu$ -th atom  $E_{ij}$  operator into the  $N$ -atom Hilbert space. Atom indistinguishability implies that  $\langle E_{ij}^\mu \rangle = \frac{1}{N} \langle S_{ij} \rangle$ , for any  $\mu = 1, \dots, N$ , and therefore the one-quDit RDM of any normalized symmetric  $N$ -quDit state  $\psi$  like (7) can be expressed as

$$\rho_1(\psi) = \frac{1}{N} \sum_{i,j=1}^D \langle S_{ji} \rangle E_{ij}. \quad (39)$$

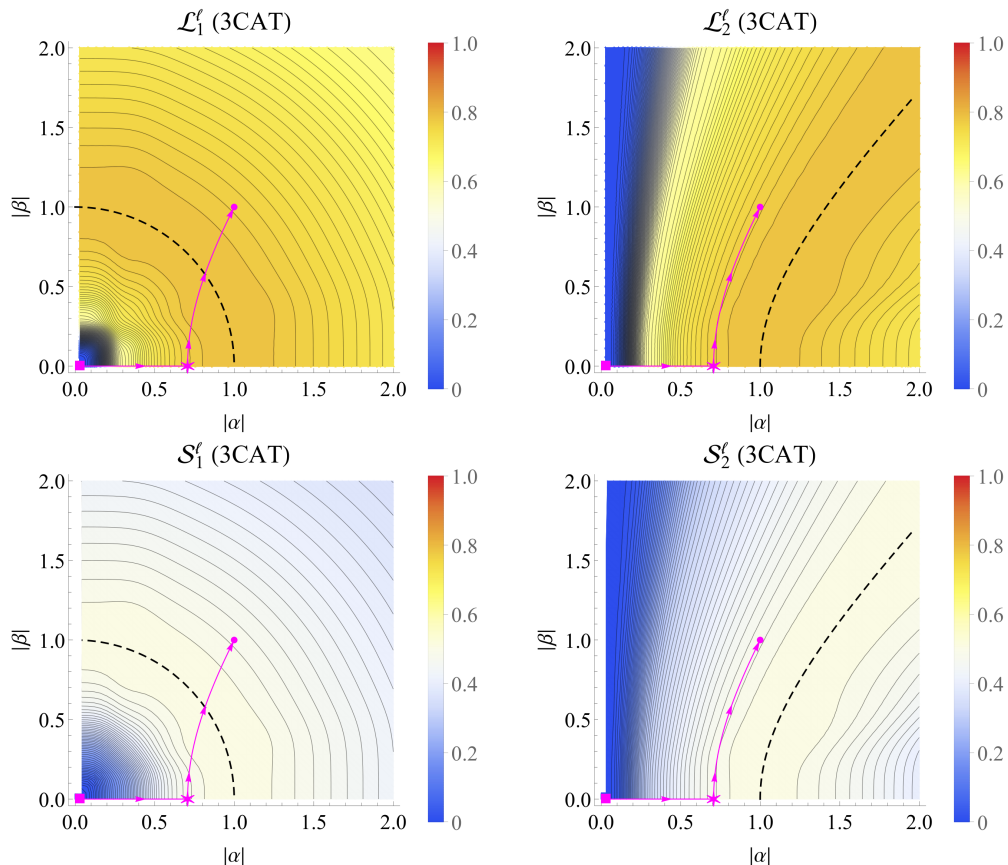


FIG. 2. Contour plots of the linear  $\mathcal{L}_i^l$  and von Neumann  $\mathcal{S}_i^l$  entanglement entropies, associated to the RDM of a 3CAT of  $N = 20$  qutrits on levels  $i = 1$  and  $i = 2$  (the case  $i = 3$  is just the reflection in a diagonal mirror line of  $i = 2$ ), as a function of the phase-space coordinates  $(\alpha, \beta)$  (they just depend on moduli). Dashed contours represent maximum entanglement entropy. The meaning of the magenta curve is explained in the main text.

with  $D$ -spin EVs (8). Note that  $\text{tr}[\rho_1(\psi)] = 1$  since  $\sum_{i=1}^D \langle S_{ii} \rangle = N$  (total population of the  $D$  levels), which is related to the linear Casimir operator  $C_1 = \sum_{i=1}^D S_{ii}$  of  $U(D)$ . From the condition  $\text{tr}(\rho_1(\psi)^2) \leq 1$  we obtain the general relation

$$\sum_{i,j=1}^D |\langle S_{ij} \rangle|^2 \leq N^2, \quad (40)$$

which could be seen as a measure of the fluctuations or departure from the linear  $C_1$  and quadratic  $C_2$  Casimir operators given by  $C_1 = N\mathbb{1}$  and

$$C_2 = \sum_{i,j=1}^D S_{ij}S_{ji} = N(N + D - 1)\mathbb{1}. \quad (41)$$

The quantum limit  $N^2$  in (40) is attained for DSCSs. Indeed, for  $|\psi\rangle = |\mathbf{z}\rangle$  in (9), the DSCS operator EVs were calculated in (12). Therefore, the purity of the corresponding one-quDit/atom RDM is simply [we denote interatom purity by  $\mathcal{P}^a$  to distinguish from the interlevel purity  $\mathcal{P}^l$  discussed in the previous section]

$$\mathcal{P}_1^a(\mathbf{z}) = \text{tr}(\rho_1(\mathbf{z})^2) = \frac{1}{N^2} \sum_{i,j=1}^D |\langle \mathbf{z} | S_{ij} | \mathbf{z} \rangle|^2 = \sum_{i,j=1}^D \frac{|z_i|^2 |z_j|^2}{|\mathbf{z}|^4} = 1, \quad (42)$$

which means that there is not entanglement between atoms in a DSCS. This is because a DSCS is eventually obtained by rotating each atom individually. The situation changes when we deal with parity adapted DSCSs or ‘‘Schrödinger

cat states" (20). Indeed, the one-quDit RDM  $\rho_1(\text{DCAT})$  does not correspond now to a pure state since, using the  $D$ -spin EVs on a DCAT state (26), the purity gives

$$\mathcal{P}_1^{\text{a}}(\text{DCAT}) = \text{tr}(\rho_1(\text{DCAT})^2) = \frac{(\sum_{\mathbf{b}} (\mathbf{z}^{\mathbf{b}} \cdot \mathbf{z})^{N-1})^2 + \sum_{i=2}^D |z_i|^4 (\sum_{\mathbf{b}} (-1)^{b_i} (\mathbf{z}^{\mathbf{b}} \cdot \mathbf{z})^{N-1})^2}{(\sum_{\mathbf{b}} (\mathbf{z}^{\mathbf{b}} \cdot \mathbf{z})^N)^2} \leq 1. \quad (43)$$

That is, unlike  $|\mathbf{z}\rangle$ , the Schrödinger cat  $|\text{DCAT}\rangle$  is not separable in the tensor product Hilbert space  $[\mathbb{C}^D]^{\otimes N}$ . In Figure 3, we represent contour plots of linear and von Neumann

$$\mathcal{L}_1^{\text{a}} = \frac{D}{D-1}(1 - \mathcal{P}_1^{\text{a}}), \quad \mathcal{S}_1^{\text{a}} = -\text{tr}(\rho_1 \log_D \rho_1) \quad (44)$$

entanglement entropies of the one-quDit RDM  $\rho_1(\text{3CAT})$  of a U(3) Schrödinger cat (23) as a function of the phase-space  $\mathbb{C}P^2$  coordinates  $\alpha, \beta$  [actually, they just depend on the moduli]. Both entropies are again normalized to 1. They attain their maximum value of 1 at the phase-space point  $(\alpha, \beta) = (1, 1)$  corresponding to a maximally mixed RDM. Figure 3 also shows (in magenta color) the stationary curve  $(\alpha(\lambda), \beta(\lambda))$  previously mentioned at the end of Sec. III A in relation to the Figure 2. For high interactions we have  $(\alpha(\lambda), \beta(\lambda)) \xrightarrow{\lambda \rightarrow \infty} (1, 1)$ , which means that highly coupled atoms are maximally entangled in a cat-like ground state (see later in Sections V and VI for more information).

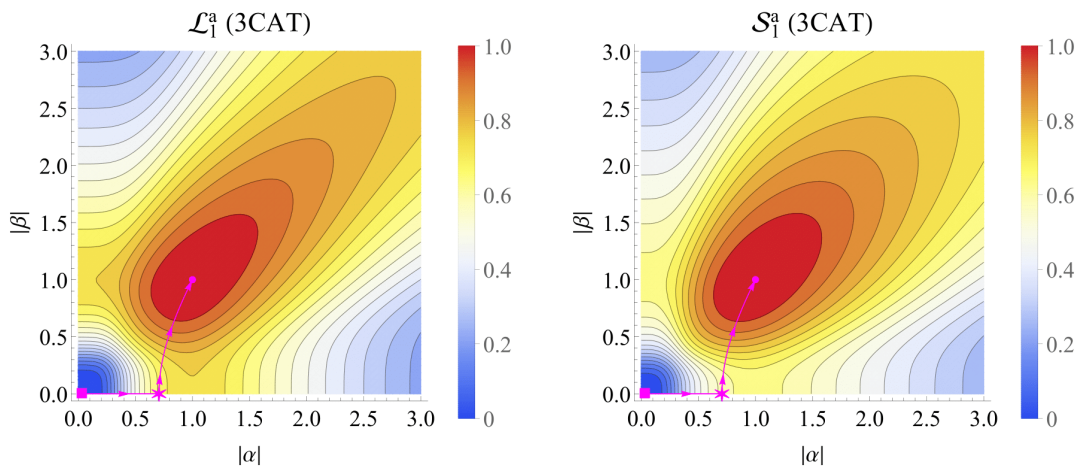


FIG. 3. 3D plots of linear  $\mathcal{L}_1^{\text{a}}$  and von Neumann  $\mathcal{S}_1^{\text{a}}$  entanglement entropies of the one-quDit RDM  $\rho_1(\text{3CAT})$  of a U(3) Schrödinger cat (23) for  $N = 10$  atoms, as a function of the phase-space coordinates  $\alpha, \beta$  (they just depend on moduli). The meaning of the magenta curve is the same as in the Figure 2.

To finish this Section, let us comment on one-quDit entanglement for NODON states (30). Taking into account the  $D$ -spin EV (31), the one-quDit RDM of a NODON is simply  $\rho_1(\text{NODON}) = \frac{1}{D} \mathbb{1}_D$  and its linear entropy  $\mathcal{L}_1^{\text{a}} = 1$ , implying maximally mixed RDM.

## 2. Two-quDit reduced density matrices

Likewise, any density matrix of two quDits can be written as

$$\rho_2 = \sum_{i,j,k,l=1}^D r_{ijkl} E_{ij} \otimes E_{kl}, \quad r_{ijkl} = \text{tr}(\rho_2 E_{ji} \otimes E_{lk}) = \langle E_{ji} \otimes E_{lk} \rangle. \quad (45)$$

with  $\bar{r}_{ijkl} = r_{jilk}$  complex parameters subject to  $\text{tr}[\rho_2] = 1$  and  $0 < \text{tr}[(\rho_2)^2] \leq 1$ . Now we need to express the RDM on a pair of particles, extracted at random from a symmetric state of  $N$   $D$ -level atoms, in terms of EVs of bilinear products of collective  $D$ -spin operators  $S$ . In particular, we have

$$\begin{aligned} \langle S_{ij} S_{kl} \rangle &= \sum_{\mu, \nu=1}^N \langle E_{ij}^{\mu} E_{kl}^{\nu} \rangle = \sum_{\mu=1}^N \delta_{jk} \langle E_{il}^{\mu} \rangle + \sum_{\mu \neq \nu=1}^N \langle E_{ij}^{\mu} E_{kl}^{\nu} \rangle \\ &= \delta_{jk} \langle S_{il} \rangle + N(N-1) \langle E_{ij}^1 E_{kl}^2 \rangle, \end{aligned} \quad (46)$$

due to indistinguishableness. Therefore, the two-particle RDM of a symmetric state  $\psi$  of  $N > 2$  quDits is written as

$$\rho_2(\psi) = \frac{1}{N(N-1)} \sum_{i,j,k,l=1}^D (\langle S_{ji}S_{lk} \rangle - \delta_{il}\langle S_{jk} \rangle) E_{ij} \otimes E_{kl}. \quad (47)$$

Using the Casimir values (41), one can directly prove that  $\text{tr}[\rho_2(\psi)] = 1$  for any normalized symmetric state  $\psi$ . The case  $D = 2$  was considered by Wang and Mølmer in [11]. The procedure is straightforwardly extended to  $\rho_M$  for an arbitrary number  $M \leq N/2$  of quDits. The purity of  $\rho_2(\psi)$  can be compactly written as

$$\mathcal{P}_2^a(\psi) = \text{tr}(\rho_2(\psi)^2) = \frac{1}{N^2(N-1)^2} \left[ \sum_{i,j,k,l=1}^D \langle S_{ji}S_{lk} \rangle \langle S_{ij}S_{kl} \rangle - 2 \sum_{i,j,k=1}^D \langle S_{ji}S_{kj} \rangle \langle S_{ik} \rangle + \sum_{i,j=1}^D \langle S_{ii} \rangle \langle S_{jj} \rangle \right]. \quad (48)$$

In order to construct the two-particle RDM of a DSCS (9), we need the EVs of quadratic powers (14). With these ingredients, we can easily compute the two-particle RDM of a DSCS (9) which, for large  $N$  has the following asymptotic expression

$$\rho_2(\mathbf{z}) = \sum_{i,j,k,l=1}^D (\bar{z}_j z_i \bar{z}_l z_k + O(1/N)) E_{ij} \otimes E_{kl}. \quad (49)$$

The purity of  $\rho_2(\mathbf{z})$  is 1 since  $\mathbf{z}$  is separable in the tensor product Hilbert space  $[\mathbb{C}^D]^{\otimes N}$ , as we have already commented. Moreover, one can see that  $\rho_2(\mathbf{z}) = \rho_1(\mathbf{z}) \otimes \rho_1(\mathbf{z})$ . However, the Schrödinger cat (20) is non-separable and has an intrinsic pairwise entanglement. Taking into account the particular structure of linear (26) and quadratic (27)  $D$ -spin operator EVs, The general formula (48) becomes

$$\mathcal{P}_2^a(\text{DCAT}) = \frac{1}{N^2(N-1)^2} \left[ \sum_{\substack{i,j,k,l=1 \\ j \neq k}}^D \langle S_{ji}S_{lk} \rangle \langle S_{ij}S_{kl} \rangle + \sum_{i,j=1}^D \langle S_{ji}S_{ij} \rangle (\langle S_{ij}S_{ji} \rangle - 2\langle S_{ii} \rangle) + \sum_{i,j=1}^D \langle S_{ii} \rangle \langle S_{jj} \rangle \right]. \quad (50)$$

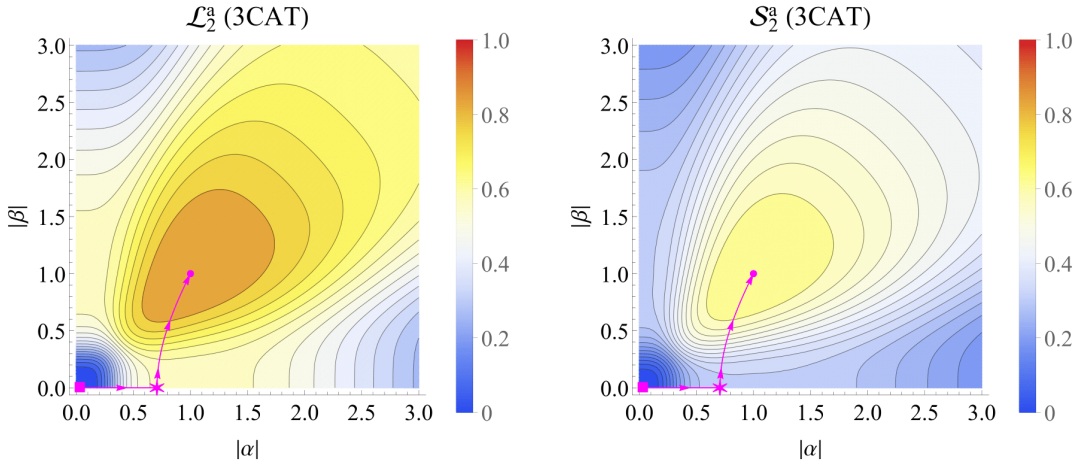


FIG. 4. Contour plots of linear  $\mathcal{L}_2^a$  and von Neumann  $\mathcal{S}_2^a$  entanglement entropies of the two-qutrit RDM  $\rho_{2(3\text{CAT})}$  of a U(3) Schrödinger cat (23) for  $N = 10$  atoms, as a function of the phase-space coordinates  $\alpha, \beta$  (they just depend on moduli). The meaning of the magenta curve is the same as in the Figure 2.

In Figure 4, we represent contour plots of normalized linear and von Neumann

$$\mathcal{L}_2^a = \frac{D^2}{D^2 - 1} (1 - \mathcal{P}_2^a), \quad \mathcal{S}_2^a = -\text{tr}(\rho_2 \log_{D^2} \rho_2) \quad (51)$$

entanglement entropies for the two-qutrit RDM  $\rho_2(\text{3CAT})$  of a  $U(3)$  Schrödinger cat (23) as a function of the phase-space  $\mathbb{C}P^2$  coordinates  $\alpha, \beta$  [they just depend on the moduli]. As for the one-quDit case, they attain their maximum value at the phase-space point  $(\alpha, \beta) = (1, 1)$ ; however, unlike the one-quDit case, pairwise entanglement entropies do not attain the maximum value of 1 at this point, but  $\mathcal{L}_2^a = 5/6$  and  $\mathcal{S}_2^a \simeq 0.623$  for large  $N$ . As already commented, variational (spin coherent) approximations to the ground state of the LMG 3-level atom model [discussed later in Section V] recover this maximum entanglement point  $(\alpha, \beta) = (1, 1)$  at high interactions  $\lambda \rightarrow \infty$  (as can be seen in the magenta curve).

For NODON states (30), the two-quDit RDM is

$$\rho_2(\text{NODON}) = \frac{1}{D} \sum_{k=1}^D E_{kk} \otimes E_{kk}, \quad (52)$$

and therefore  $\rho_2(\text{NODON})^2 = \frac{1}{D} \rho_2(\text{NODON})$ , which means that the linear entropy is  $\mathcal{L}_2^a(\text{NODON}) = D/(D+1)$ , indicating a high level of pairwise entanglement in a NODON state.

#### IV. SU(D) SPIN SQUEEZING: A PROPOSAL

As we have already commented in the introduction, Wang and Sanders [22] showed a direct relation between the concurrence  $C$ , extracted from the two-qubit RDM (47) for  $D = 2$ , and the  $SU(2)$  spin  $\vec{J} = (J_x, J_y, J_z)$  squeezing parameter

$$\xi^2 = \frac{4}{N} \min_{\theta} \langle (\cos(\theta)J_x + \sin(\theta)J_y)^2 \rangle = \frac{2}{N} \left[ \langle J_x^2 + J_y^2 \rangle - \sqrt{\langle J_x^2 - J_y^2 \rangle^2 + \langle J_x J_y + J_y J_x \rangle^2} \right] \quad (53)$$

introduced by [15], which measures spin fluctuations in an orthogonal direction to the mean value  $\langle \vec{J} \rangle$  with minimal variance. Actually, the definition (53) refers to even and odd symmetric multi-qubit states [remember the extension of this concept to multi-quDits after (17)] for which  $\langle \vec{J} \rangle = (0, 0, \langle J_z \rangle)$  and therefore the orthogonal direction lies in the plane  $XY$ . This definition can be extended to even and odd symmetric multi-quDit states for which  $\langle S_{ij} \rangle \propto \delta_{ij}$  [see e.g. (26) for the case of the even DCAT state]. Using the embedding (3) of  $D(D-1)/2$   $SU(2)$  spin subalgebras into  $U(D)$ , and mimicking (53), we can define  $D(D-1)/2$  spin squeezing parameters  $\xi_{ij}, i > j$  for  $D$ -spin systems as:

$$\xi_{ij}^2 = \frac{1}{N(D-1)} [\langle S_{ij} S_{ji} + S_{ji} S_{ij} \rangle - 2|\langle S_{ij}^2 \rangle|], \quad i > j = 1, \dots, D-1. \quad (54)$$

We have chosen the normalization factor  $\frac{1}{N(D-1)}$  so that (54) reduces to (53) for  $D = 2$  and so that the total  $D$ -spin squeezing parameter

$$\xi_D^2 = \sum_{i>j=1}^D \xi_{ij}^2 \quad (55)$$

is one (no squeezing) for the DSCSs  $|\mathbf{z}\rangle$  in (9). Actually, for DSCSs we have that  $\xi_{ij}^2 = (|z_i|^2 + |z_j|^2)/(|\mathbf{z}|^2(D-1))$  is written in terms of average level populations  $\langle \mathbf{z} | S_{ii} | \mathbf{z} \rangle = N|z_i|^2/|\mathbf{z}|^2$  of levels  $i$  and  $j$ , according to (12). Therefore, the presence of  $D$ -spin squeezing means in general that  $\xi_D^2 < 1$ . Using the EVs (31) for NODON states (30), the corresponding spin squeezing parameters are  $\xi_{ij} = 2/[D(D-1)]$ , which gives  $\xi_D^2 = 1$ , thus implying that NODON states do not exhibit spin squeezing.

Note that  $D$ -spin squeezing parameters  $\xi_{ij}$  are constructed in terms of  $D$ -spin quadratic EVs, as the two-quDit RDM (47) and its purity (48) do. Therefore, the deep relation between pairwise entanglement and spin squeezing revealed by Wang-Sanders in [22] for symmetric multi-qubit systems is extensible to symmetric multi-quDits in the sense proposed here. In Figure 5 we show a contour plot of the total  $D$ -spin squeezing parameter  $\xi_D^2$  for the 3CAT. As in previous figures, the magenta curve represents the trajectory in phase space of the stationary points (59) of the energy surface (57) of the three-level LMG Hamiltonian (56) as a function of the control parameter  $\lambda$ . See later around Figure 9 in Section VI for further discussion.

#### V. LMG MODEL FOR THREE-LEVEL ATOMS AND ITS QUANTUM PHASE DIAGRAM

In this section we apply the previous mathematical machinery to the study and characterization of the phase diagram of quantum critical  $D$ -level Lipkin-Meshkov-Glick atom models. The standard case of  $D = 2$  level atoms has

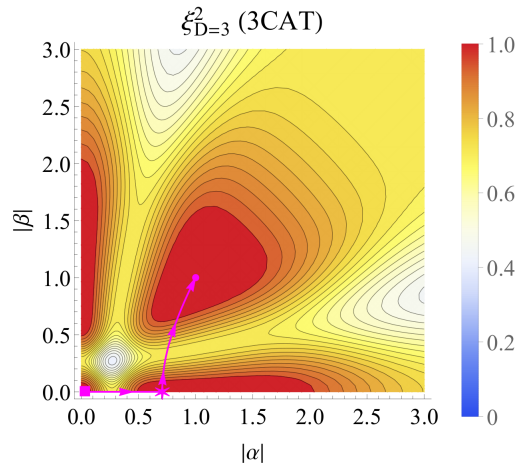


FIG. 5. Contour plots of the squeezing parameter  $\xi_{D=3}^2$  of a U(3) Schrödinger cat for  $N = 10$  atoms, as a function of the phase-space coordinates  $\alpha, \beta$  (it just depends on moduli). The meaning of the magenta curve is the same as in previous Figures.

already been studied in the literature (see e.g. [37]). We shall restrict ourselves to  $D = 3$  level atoms for practical calculations, although the procedure can be easily extended to general  $D$ . In particular, we propose the following LMG-type Hamiltonian

$$H = \frac{\epsilon}{N}(S_{33} - S_{11}) - \frac{\lambda}{N(N-1)} \sum_{i \neq j=1}^3 S_{ij}^2, \quad (56)$$

written in terms of collective U(3)-spin operators  $S_{ij}$ . Hamiltonians of this kind have already been proposed in the literature [38–42] [see also [21] for the role of mixed symmetry sectors in QPTs of multi-quDit LMG systems]. We place levels symmetrically about  $i = 2$ , with intensive energy splitting per particle  $\epsilon/N$ . For simplicity, we consider equal interactions, with coupling constant  $\lambda$ , for atoms in different levels, and vanishing interactions for atoms in the same level (i.e., we discard interactions of the form  $S_{ij}S_{ji}$ ). Therefore,  $H$  is invariant under parity transformations  $\Pi_j$  in (17), since the interaction term scatters pairs of particles conserving the parity of the population  $n_j$  in each level  $j = 1, \dots, D$ . Energy levels have good parity, the ground state being an even state. We divide the two-body interaction in (56) by the number of atom pairs  $N(N-1)$  to make  $H$  an intensive quantity, since we are interested in the thermodynamic limit  $N \rightarrow \infty$ . We shall see that parity symmetry is spontaneously broken in this limit.

As already pointed long ago by Gilmore and coworkers [14, 55], coherent states constitute in general a powerful tool for rigorously studying the ground state and thermodynamic critical properties of some physical systems. The energy surface associated to a Hamiltonian density  $H$  is defined in general as the coherent state expectation value of the Hamiltonian density in the thermodynamic limit. In our case, the energy surface acquires the following form

$$E_{(\alpha,\beta)}(\epsilon, \lambda) = \lim_{N \rightarrow \infty} \langle \mathbf{z} | H | \mathbf{z} \rangle = \epsilon \frac{\beta \bar{\beta} - 1}{\alpha \bar{\alpha} + \beta \bar{\beta} + 1} - \lambda \frac{\alpha^2 (\bar{\beta}^2 + 1) + (\beta^2 + 1) \bar{\alpha}^2 + \bar{\beta}^2 + \beta^2}{(\alpha \bar{\alpha} + \beta \bar{\beta} + 1)^2}, \quad (57)$$

where we have used DSCS EVs of linear (12) and quadratic (14) powers of  $D$ -spin operators  $S_{ij}$  [actually, linear powers are enough due to the lack of quantum spin fluctuations in the thermodynamic limit (16)], and we have used the parametrization  $\mathbf{z} = (1, \alpha, \beta)$ , as in eq. (23), for U(3) SCSs. Note that this energy surface is invariant under  $\alpha \rightarrow -\alpha$  and  $\beta \rightarrow -\beta$ , which is a consequence of the inherent parity symmetry of the Hamiltonian (56). The minimum energy

$$E_0(\epsilon, \lambda) = \min_{\alpha, \beta \in \mathbb{C}} E_{(\alpha,\beta)}(\epsilon, \lambda) \quad (58)$$

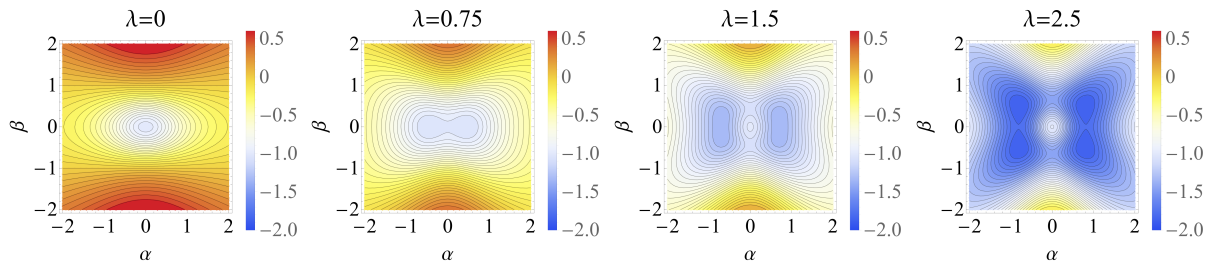


FIG. 6. Contour plot of the energy surface (57) for real  $\alpha$  and  $\beta$ , in the vicinity of the critical points  $\lambda = 1/2$  and  $\lambda = 3/2$  (in  $\epsilon$  units). Degenerate minima are perceived in phases II ( $\frac{1}{2} \leq \lambda \leq \frac{3}{2}$ ) and III ( $\lambda \geq \frac{3}{2}$ ).

is attained at the stationary (real) phase-space values  $\alpha_0^\pm = \pm\alpha_0$  and  $\beta_0^\pm = \pm\beta_0$  with

$$\alpha_0(\epsilon, \lambda) = \begin{cases} 0, & 0 \leq \lambda \leq \frac{\epsilon}{2}, \\ \sqrt{\frac{2\lambda - \epsilon}{2\lambda + \epsilon}}, & \frac{\epsilon}{2} \leq \lambda \leq \frac{3\epsilon}{2}, \\ \sqrt{\frac{2\lambda}{2\lambda + 3\epsilon}}, & \lambda \geq \frac{3\epsilon}{2}, \end{cases}$$

$$\beta_0(\epsilon, \lambda) = \begin{cases} 0, & 0 \leq \lambda \leq \frac{3\epsilon}{2}, \\ \sqrt{\frac{2\lambda - 3\epsilon}{2\lambda + 3\epsilon}}, & \lambda \geq \frac{3\epsilon}{2}. \end{cases} \quad (59)$$

In Figures 2, 3, 4 and 5 we plotted (in magenta color) the stationary-point curve  $(\alpha_0(\lambda), \beta_0(\lambda))$  on top of level, one- and two-qutrit entanglement entropies, and squeezing parameter, noting that  $(\alpha_0(\lambda), \beta_0(\lambda)) \rightarrow (1, 1)$  for high  $\lambda \rightarrow \infty$  interactions. We will come to this later in Section VI. Inserting (59) into (57) gives the ground state energy density at the thermodynamic limit

$$E_0(\epsilon, \lambda) = \begin{cases} -\epsilon, & 0 \leq \lambda \leq \frac{\epsilon}{2}, & \text{(I)} \\ -\frac{(2\lambda + \epsilon)^2}{8\lambda}, & \frac{\epsilon}{2} \leq \lambda \leq \frac{3\epsilon}{2}, & \text{(II)} \\ -\frac{4\lambda^2 + 3\epsilon^2}{6\lambda}, & \lambda \geq \frac{3\epsilon}{2}. & \text{(III)} \end{cases} \quad (60)$$

Here we clearly distinguish three different phases: I, II and III, and two second-order QPTs at  $\lambda_{\text{I} \leftrightarrow \text{II}}^{(0)} = \epsilon/2$  and  $\lambda_{\text{II} \leftrightarrow \text{III}}^{(0)} = 3\epsilon/2$ , respectively, where  $\frac{\partial^2 E_0(\epsilon, \lambda)}{\partial \lambda^2}$  are discontinuous. In the stationary (magenta) curve  $(\alpha_0(\lambda), \beta_0(\lambda))$ , the phase I corresponds to the origin  $(\alpha_0, \beta_0) = (0, 0)$  (squared point), phase II corresponds to the horizontal part  $\beta_0 = 0$  up to the star point, and phase III corresponds to  $\beta_0 \neq 0$ .

Note that the ground state is fourfold degenerated in the thermodynamic limit since the four  $U(3)$  SCSs  $|\mathbf{z}_0^{\pm\pm}\rangle = |1, \pm\alpha_0, \pm\beta_0\rangle$  have the same energy density  $E_0$ . These four  $U(3)$  SCSs are related by parity transformations  $\Pi_j$  in (17) and, therefore, parity symmetry is spontaneously broken in the thermodynamic limit. In order to have good variational states for finite  $N$ , to compare with numerical calculations, we have two possibilities: 1) either we use the 3CAT (23) as an ansatz for the ground state, minimizing  $\langle 3\text{CAT} | H | 3\text{CAT} \rangle$ , or 2) we restore the parity symmetry of the  $U(3)$  SCS  $|1, \alpha_0, \beta_0\rangle$  for finite  $N$  by projecting on the even parity sector. Although the first possibility offers a more accurate variational approximation to the ground state, it entails a more tedious numerical minimization than the one already obtained in (58) for  $N \rightarrow \infty$ . Therefore, we shall use the second possibility which, despite being less accurate, it is straightforward and good enough for our purposes. That is, we shall use the 3CAT (23), evaluated at  $\alpha = \alpha_0$  and  $\beta = \beta_0$  and conveniently normalized (24), as a variational approximation  $|3\text{CAT}_0\rangle$  to the numerical (exact) ground state  $|\psi_0\rangle$  for finite  $N$ .

## VI. ENTANGLEMENT AND SQUEEZING AS SIGNATURES OF QPTS

The objective in this Section is to use level and particle entanglement and squeezing measures as signatures of QPTs in these LMG models, playing the role of order parameters that characterize the different phases or markers of the corresponding critical points. We restrict ourselves to linear entropy which, as already shown, gives qualitative information similar to von Neumann entropy for this study, with the advantage that it requires less computational resources. As already commented, Refs. [44, 45] contain more general information about the relation between both

entropies. Linear entropies of one- and two-qutrit RDMs turn also to provide similar qualitative information, although pairwise entanglement shows a more direct relation to spin squeezing.

We have numerically diagonalized the Hamiltonian (56) for  $N = 50$  3-level atoms, and several values of  $\lambda$  (in  $\epsilon$  units), and we have calculated level, one- and two-qutrit entanglement linear entropies for the ground state  $|\psi_0\rangle = \sum_{\vec{n}} c_{\vec{n}} |\vec{n}\rangle$ , plugging the coefficients  $c_{\vec{n}}$  into (8,33,48). We have also calculated level and atom entanglement linear entropies for the variational approximation  $|\mathfrak{3CAT}_0\rangle$  to the ground state  $|\psi_0\rangle$  discussed in the previous Section for  $N = 50$ . In Figure 7 we compare numerical with variational ground state entanglement measures between levels  $i = 1, 2, 3$ . According to Figure 7, we see that, in phase I,  $0 \leq \lambda \leq 1/2$ , variational results indicate that there is no entanglement between levels, whereas numerical results show a small (but non-zero) entanglement for  $N = 50$ . In phase II,  $1/2 \leq \lambda \leq 3/2$ , levels  $i = 1$  and  $i = 2$  get entangled, but level  $i = 3$  remains almost disconnected. In phase III,  $\lambda \geq 3/2$ , level  $i = 3$  gets entangled too. Interlevel entanglement grows with  $\lambda$  attaining the maximum value of 0.84 at the limiting point  $(\alpha_0(\infty), \beta_0(\infty)) = (1, 1)$  for  $N = 50$ . This behavior of the interlevel entropy for the  $\mathfrak{3CAT}$  variational state can be also appreciated by looking at the stationary (magenta) curve in Figure 2 with relation to the isentropic curves.

Concerning atom entanglement, Figure 8 shows a better agreement between variational and numerical results, showing a rise of entanglement when the coupling strength  $\lambda$  grows across the three phases, attaining values close to the large  $N$  maximum values  $\mathcal{L}_1^a = 1$  and  $\mathcal{L}_2^a = 5/6$  at the limiting point  $(\alpha_0(\infty), \beta_0(\infty)) \rightarrow (1, 1)$ . The entanglement growth is more abrupt between phases I and II than between phases II and III. We see that both, level and atom entanglement measures capture differences between the three phases, even for finite  $N$ , and therefore they can be considered as precursors of the corresponding QPT. The main features of the inter-atom entanglement entropy for the  $\mathfrak{3CAT}$  variational state are also captured by the trajectory of the stationary (magenta) curve in Figures 3 and 4 through the isentropic curves.

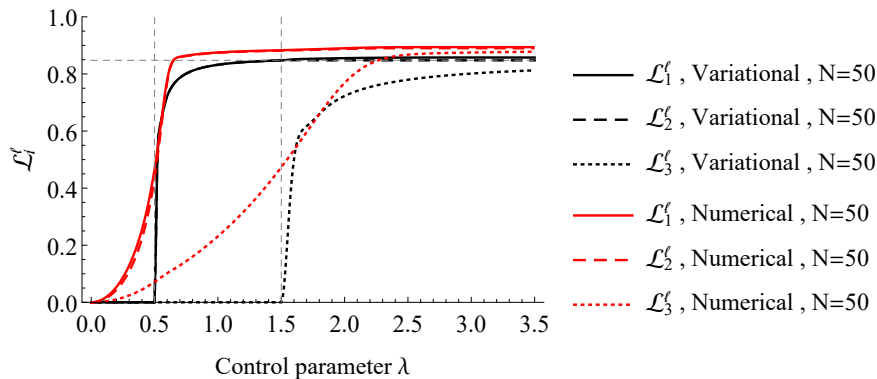


FIG. 7. Level entanglement linear entropies  $\mathcal{L}_i^l$  (for levels  $i = 1, 2$  and  $3$ ) of the ground state of the three-level atom LMG model Hamiltonian (56), for  $N = 50$  atoms, as a function of the control parameter  $\lambda$  (in  $\epsilon$  units). Critical points, at which a QPT takes place, are marked with vertical grid lines, whereas the horizontal grid line labels the asymptotic value  $\mathcal{L}_i^l \rightarrow 1 - 2/\sqrt{\pi N} \simeq 0.84$  of the entropies. We compare exact results, obtained from numerical diagonalization of the Hamiltonian, with variational (analytical) results obtained from a parity symmetry restoration (in terms of Schrödinger cats) of mean field results.

In Figure 9 we represent the  $D = 3$  spin total squeezing parameter  $\xi_D^2$  (55) of the variational and numerical ground states for  $N = 50$  atoms, as a function of the control parameter  $\lambda$  (in  $\epsilon$  units). The results reveal a clear growth of squeezing at the critical points, the change being more abrupt at these points for the variational (parity adapted mean field) than for the numerical ground state. Note that the variational ground state only shows squeezing ( $\xi_D^2 < 1$ ) at the critical points, whereas the numerical ground state exhibits squeezing for any  $\lambda \neq 0$ . Looking at the stationary (magenta) curve of Figure 5 we appreciate that it practically lies in regions of no squeezing (in red color) except near the critical points, where squeezing suddenly increases (yellow color regions).

## VII. CONCLUSIONS AND OUTLOOK

We have extended the concept of pairwise entanglement and spin squeezing for symmetric multi-qubits (namely, identical two-level atoms) to general symmetric multi-quDits (namely, identical  $D$ -level atoms). For it, we have firstly computed expectation values of  $U(D)$  spin operators  $S_{ij}$  in general symmetric multi-quDit states like:  $U(D)$ -spin coherent states, their adaptation to parity (Schrödinger  $\mathfrak{DCAT}$  states), and an extension of NOON states to  $D$

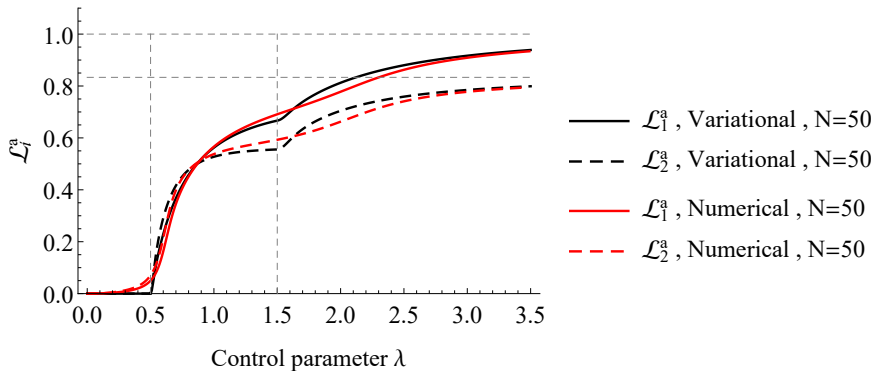


FIG. 8. One-qutrit  $\mathcal{L}_1^a$  and two-qutrit  $\mathcal{L}_2^a$  entanglement linear entropies of the ground state of the three-level atom LMG model Hamiltonian (56) as a function of the control parameter  $\lambda$  (in  $\epsilon$  units). Critical points, at which a QPT takes place, are marked with vertical grid lines, whereas horizontal grid lines label the asymptotic values  $\mathcal{L}_1^a \rightarrow 1$  and  $\mathcal{L}_2^a \rightarrow 5/6$  of the entropies. We compare numerical with variational results for  $N = 50$  atoms.

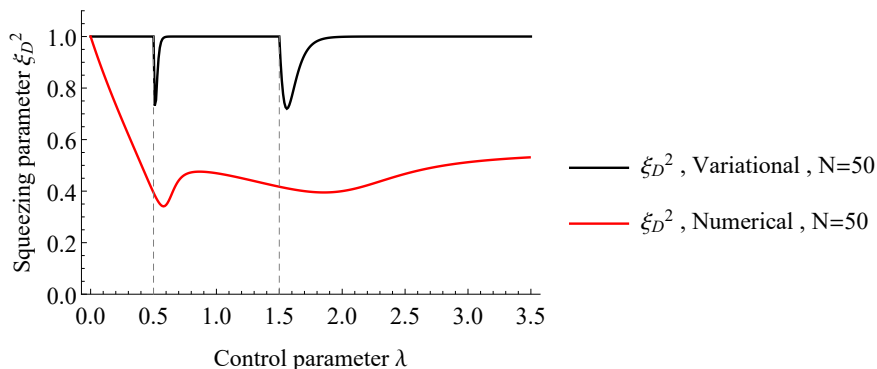


FIG. 9.  $D$ -spin total squeezing parameter  $\xi_{D^2}^2$  (55) of the ground state of the three-level atom LMG model Hamiltonian (56) as a function of the control parameter  $\lambda$  (in  $\epsilon$  units). Critical points, at which a QPT takes place, are marked with vertical grid lines. We compare numerical with variational results for  $N = 50$  atoms.

levels (NODON states). The reduced density matrices to one- and two-quDits extracted at random from a symmetric multi-quDit state exhibit atom entanglement for DCAT states, but not for  $U(D)$ -spin coherent states. We have used entanglement to characterize quantum phase transitions of LMG  $D$ -level atom models (we have restricted to  $D = 3$  for simplicity), where DCAT states (as an adaptation to parity of mean-field spin coherent states) turn out to be a reasonable good variational approximation to the exact (numerical) ground state. We have also proposed an extension of standard  $SU(2)$ -spin squeezing to  $SU(D)$ -spin operators, which recovers  $D = 2$  as a particular case. We have evaluated  $SU(3)$ -spin squeezing of the ground state of the LMG 3-level atom model, as a function of the control parameter  $\lambda$ , and we have seen that squeezing grows in the neighborhood of critical points  $\lambda_c$ , therefore serving as a marker of the corresponding quantum phase transition. A deeper study and discussion of squeezing in these models requires a phase space approach in terms of a coherent (Bargmann) representation of states, such as the Husimi and Wigner functions, and it will be the subject of future work.

#### ACKNOWLEDGMENTS

We thank the support of the Spanish MICINN through the project PGC2018-097831-B-I00 and Junta de Andalucía through the projects SOMM17/6105/UGR, UHU-1262561 and FQM-381. JG also thanks MICINN for financial support from FIS2017-84440-C2-2-P. AM thanks the Spanish MIU for the FPU19/06376 predoctoral fellowship. We

all thank Octavio Castaños for his valuable collaboration in the early stages of this work.

- 
- [1] L. Amico, R. Fazio, A. Osterloh, and V. Vedral, Entanglement in many-body systems, *Rev. Mod. Phys.* **80**, 517–576 (2008).
- [2] L. Pezzè, A. Smerzi, M. K. Oberthaler, R. Schmied, and P. Treutlein, Quantum metrology with nonclassical states of atomic ensembles, *Rev. Mod. Phys.* **90**, 035005 (2018).
- [3] R. Horodecki, P. Horodecki, M. Horodecki, and K. Horodecki, Quantum entanglement, *Rev. Mod. Phys.* **81**, 865–942 (2009).
- [4] J. Ma, X. Wang, C. Sun, and F. Nori, Quantum spin squeezing, *Physics Reports* **509**, 89–165 (2011).
- [5] F. Benatti, R. Floreanini, F. Franchini, and U. Marzolino, Entanglement in indistinguishable particle systems, *Physics Reports* **878**, 1–27 (2020).
- [6] B. Morris, B. Yadin, M. Fadel, T. Zibold, P. Treutlein, and G. Adesso, Entanglement between identical particles is a useful and consistent resource, *Phys. Rev. X* **10**, 041012 (2020).
- [7] N. Killoran, M. Cramer, and M. B. Plenio, Extracting entanglement from identical particles, *Phys. Rev. Lett.* **112**, 150501 (2014).
- [8] B. J. Dalton, J. Goold, B. M. Garraway, and M. D. Reid, Quantum entanglement for systems of identical bosons: I. general features, *Physica Scripta* **92**, 023004 (2017).
- [9] B. J. Dalton, J. Goold, B. M. Garraway, and M. D. Reid, Quantum entanglement for systems of identical bosons: II. spin squeezing and other entanglement tests, *Physica Scripta* **92**, 023005 (2017).
- [10] W. Dür, G. Vidal, and J. I. Cirac, Three qubits can be entangled in two inequivalent ways, *Phys. Rev. A* **62**, 062314 (2000).
- [11] X. Wang and K. Mølmer, Pairwise entanglement in symmetric multi-qubit systems, *The European Physical Journal D* **18**, 385–391 (2002).
- [12] W. K. Wootters, Entanglement of formation of an arbitrary state of two qubits, *Phys. Rev. Lett.* **80**, 2245–2248 (1998).
- [13] J. M. Radcliffe, Some properties of coherent spin states, *Journal of Physics A: General Physics* **4**, 313–323 (1971).
- [14] F. T. Arecchi, E. Courtens, R. Gilmore, and H. Thomas, Atomic coherent states in quantum optics, *Phys. Rev. A* **6**, 2211–2237 (1972).
- [15] M. Kitagawa and M. Ueda, Squeezed spin states, *Phys. Rev. A* **47**, 5138–5143 (1993).
- [16] V. Dodonov, I. Malkin, and V. Man’ko, Even and odd coherent states and excitations of a singular oscillator, *Physica* **72**, 597–615 (1974).
- [17] O. Castaños, R. López-Peña, and V. I. Man’ko, Crystallized schrödinger cat states, *Journal of Russian Laser Research* **16**, 477–525 (1995).
- [18] M. M. Nieto and D. R. Truax, Squeezed states for general systems, *Phys. Rev. Lett.* **71**, 2843–2846 (1993).
- [19] V. Bužek, A. Vidiella-Barranco, and P. L. Knight, Superpositions of coherent states: Squeezing and dissipation, *Phys. Rev. A* **45**, 6570–6585 (1992).
- [20] M. Hillery, Amplitude-squared squeezing of the electromagnetic field, *Phys. Rev. A* **36**, 3796–3802 (1987).
- [21] M. Calixto, A. Mayorgas, and J. Guerrero, Role of mixed permutation symmetry sectors in the thermodynamic limit of critical three-level Lipkin-Meshkov-Glick atom models, *Phys. Rev. E* **103**, 012116 (2021).
- [22] X. Wang and B. C. Sanders, Spin squeezing and pairwise entanglement for symmetric multiqubit states, *Phys. Rev. A* **68**, 012101 (2003).
- [23] A. Sørensen, L. M. Duan, J. I. Cirac, and P. Zoller, Many-particle entanglement with Bose-Einstein condensates, *Nature* **409**, 63–66 (2001).
- [24] A. S. Sørensen and K. Mølmer, Entanglement and extreme spin squeezing, *Phys. Rev. Lett.* **86**, 4431–4434 (2001).
- [25] K. Mølmer and A. Sørensen, Multiparticle entanglement of hot trapped ions, *Phys. Rev. Lett.* **82**, 1835–1838 (1999).
- [26] C. A. Sackett, D. Kielpinski, B. E. King, C. Langer, V. Meyer, C. J. Myatt, M. Rowe, Q. A. Turchette, W. M. Itano, D. J. Wineland, and C. Monroe, Experimental entanglement of four particles, *Nature* **404**, 256–259 (2000).
- [27] O. Castaños, E. Nahmad-Achar, R. López-Peña, and J. G. Hirsch, Superradiant phase in field-matter interactions, *Phys. Rev. A* **84**, 013819 (2011).
- [28] E. Romera, R. del Real, and M. Calixto, Husimi distribution and phase-space analysis of a dicke-model quantum phase transition, *Phys. Rev. A* **85**, 053831 (2012).
- [29] S. Cordero, E. Nahmad-Achar, R. López-Peña, and O. Castaños, Polychromatic phase diagram for  $n$ -level atoms interacting with  $l$  modes of an electromagnetic field, *Phys. Rev. A* **92**, 053843 (2015).
- [30] R. López-Peña, S. Cordero, E. Nahmad-Achar, and O. Castaños, Symmetry adapted coherent states for three-level atoms interacting with one-mode radiation, *Physica Scripta* **90**, 068016 (2015).
- [31] C. Pérez-Campos, J. R. González-Alonso, O. Castaños, and R. López-Peña, Entanglement and localization of a two-mode Bose-Einstein condensate, *Annals of Physics* **325**, 325–344 (2010).
- [32] M. Calixto, E. Romera, and R. del Real, Parity-symmetry-adapted coherent states and entanglement in quantum phase transitions of vibron models, *Journal of Physics A: Mathematical and Theoretical* **45**, 365301 (2012).
- [33] M. Calixto and F. Pérez-Bernal, Entanglement in shape phase transitions of coupled molecular bendings, *Phys. Rev. A* **89**, 032126 (2014).

- [34] M. Calixto and C. Peón-Nieto, Husimi function and phase-space analysis of bilayer quantum hall systems at  $\nu = 2$ , *Journal of Statistical Mechanics: Theory and Experiment* **2018**, 053112 (2018).
- [35] O. Castaños, R. López-Peña, J. G. Hirsch, and E. López-Moreno, Classical and quantum phase transitions in the Lipkin-Meshkov-Glick model, *Phys. Rev. B* **74**, 104118 (2006).
- [36] E. Romera, M. Calixto, and O. Castaños, Phase space analysis of first-, second- and third-order quantum phase transitions in the Lipkin-Meshkov-Glick model, *Physica Scripta* **89**, 095103 (2014).
- [37] M. Calixto, O. Castaños, and E. Romera, Entanglement and quantum phase diagrams of symmetric multi-qubit systems, *Journal of Statistical Mechanics: Theory and Experiment* **2017**, 103103 (2017).
- [38] S. Gnutzmann and M. Kuś, Coherent states and the classical limit on irreducible  $su_3$  representations, *Journal of Physics A: Mathematical and General* **31**, 9871 (1999).
- [39] S. Gnutzmann, F. Haake, and M. Kuś, Quantum chaos of  $su_3$  observables, *Journal of Physics A: Mathematical and General* **33**, 143 (1999).
- [40] D. C. Meredith, S. E. Koonin, and M. R. Zirnbauer, Quantum chaos in a schematic shell model, *Phys. Rev. A* **37**, 3499–3513 (1988).
- [41] W.-G. Wang, F. M. Izrailev, and G. Casati, Structure of eigenstates and local spectral density of states: A three-orbital schematic shell model, *Phys. Rev. E* **57**, 323–339 (1998).
- [42] P. Leboeuf and M. Saraceno, Eigenfunctions of non-integrable systems in generalised phase spaces, *Journal of Physics A: Mathematical and General* **23**, 1745 (1999).
- [43] F. Iachello and A. Arima, *The Interacting Boson Model*, Cambridge Monographs on Mathematical Physics (Cambridge University Press, 1987).
- [44] D. Berry and B. Sanders, Bounds on general entropy measures, *J. Phys. A: Math. Gen.* **36**, 12255 (2003).
- [45] T.-C. Wei, K. Nemoto, P. M. Goldbart, P. G. Kwiat, W. J. Munro, and F. Verstraete, Maximal entanglement versus entropy for mixed quantum states, *Phys. Rev. A* **67**, 022110 (2003).
- [46] M. Moshinsky, The harmonic oscillator and supermultiplet theory: (i) the single shell picture, *Nuclear Physics* **31**, 384–405 (1962).
- [47] M. Moshinsky and J. Nagel, Complete classification of states of supermultiplet theory, *Physics Letters* **5**, 173–174 (1963).
- [48] L. C. Biedenharn and J. Louck, *Angular Momentum in Quantum Physics: Theory and Application*, Encyclopedia of Mathematics and its Applications (Cambridge University Press, 1984).
- [49] P. C. Humphreys, M. Barbieri, A. Datta, and I. A. Walmsley, Quantum enhanced multiple phase estimation, *Phys. Rev. Lett.* **111**, 070403 (2013).
- [50] L. Zhang and K. W. C. Chan, Scalable generation of multi-mode noon states for quantum multiple-phase estimation, *Scientific Reports* **8**, 11440 (2018).
- [51] F. Iachello and R. Levine, *Algebraic Theory of Molecules* (Oxford University Press, 1995).
- [52] A. Frank and P. Van Isacker, *Algebraic methods in molecular and nuclear structure physics* (Wiley, New York, 1994).
- [53] F. Pérez-Bernal and F. Iachello, Algebraic approach to two-dimensional systems: Shape phase transitions, monodromy, and thermodynamic quantities, *Phys. Rev. A* **77**, 032115 (2008).
- [54] P. Pérez-Fernández, J. M. Arias, J. E. García-Ramos, and F. Pérez-Bernal, Finite-size corrections in the bosonic algebraic approach to two-dimensional systems, *Phys. Rev. A* **83**, 062125 (2011).
- [55] W.-M. Zhang, D. H. Feng, and R. Gilmore, Coherent states: Theory and some applications, *Rev. Mod. Phys.* **62**, 867–927 (1990).

### 2.2.1 Information measures in the study of entanglement

- <sup>3</sup> J. Guerrero, A. Mayorgas, and M. Calixto, “Information diagrams in the study of entanglement in symmetric multi-qudit systems and applications to quantum phase transitions in Lipkin–Meshkov–Glick D-level atom models”, *Quant. Inf. Process.* 21, 223 (2022).

#### Quality metrics JCR

- Year: 2022
- Category: PHYSICS, MATHEMATICAL
- Journal Impact Factor (JIF): 2.5
- JIF Rank: 10/56 (Q1)

**Publication citations in Google Scholar (March 2024): 4**

# Information diagrams in the study of entanglement in symmetric multi-quDit systems and applications to quantum phase transitions in Lipkin-Meshkov-Glick $D$ -level atom models

Julio Guerrero\*

*Department of Mathematics, University of Jaén,  
Campus Las Lagunillas s/n, 23071 Jaén, Spain and  
Institute Carlos I of Theoretical and Computational Physics (iC1),  
University of Granada, Fuentenueva s/n, 18071 Granada, Spain*

Alberto Mayorgas†

*Department of Applied Mathematics, University of Granada, Fuentenueva s/n, 18071 Granada, Spain*

Manuel Calixto‡

*Department of Applied Mathematics, University of Granada, Fuentenueva s/n, 18071 Granada, Spain and  
Institute Carlos I of Theoretical and Computational Physics (iC1),  
University of Granada, Fuentenueva s/n, 18071 Granada, Spain*

(Dated: April 23, 2022)

## ABSTRACT

In this paper we pursue the use of information measures (in particular, information diagrams) for the study of entanglement in symmetric multi-quDit systems. We use generalizations to  $U(D)$  of spin  $U(2)$  coherent states and their adaptation to parity (multicomponent Schrödinger cats) and we analyse one- and two-quDit reduced density matrices. We use these correlation measures to characterize quantum phase transitions occurring in Lipkin-Meshkov-Glick models of  $D = 3$ -level identical atoms and we propose the rank of the corresponding reduced density matrix as a discrete order parameter.

Keywords: Information diagrams, entanglement entropies, symmetric quDits, parity adapted coherent states, quantum phase transitions, many-body systems, parity adapted states

## I. INTRODUCTION

Information diagrams were introduced to discuss the relation between two different information measures, like von Neumann entropy and error probability [1], or von Neumann and linear entropies [2]. In the particular case of linear ( $\mathcal{L}$ ) and von Neumann ( $\mathcal{S}$ ) entropies, pairs  $(\mathcal{L}(\rho), \mathcal{S}(\rho))$  are usually plotted for any valid probability distribution  $\rho$ . Here  $\rho$  can also represent the density matrix of a quantum system (or rather a vector with its eigenvalues), and this is our main interest in this paper. Special attention is paid to the boundaries of the resulting information diagram region, where the associated probability distributions (or density matrices) will be denoted as “extremal”. In Ref. [3], a comparison is made between both entropies in the case of two qubits (see also [4] for the case of the ion-laser interaction). In [5], a detailed study of information diagrams is carried out for arbitrary pairs of entropies. There it is proved that, for certain conditions (satisfied by linear, von Neumann and Rényi entropies), the extremal density matrices are always the same. Counterexamples are given but, in general, the deviation will be very small and we can safely assume that these extremal density matrices have universal character.

In this paper we shall use information diagrams to obtain global qualitative information of particle entanglement in symmetric multi-quDit systems described by generalized “Schrödinger cat” (multicomponent  $\text{DCAT}$ ) states (first introduced in [6] as two-component, even and odd, states for an oscillator). These  $\text{DCAT}$  states turn out to be a  $\mathbb{Z}_2^{D-1}$  parity adaptation of  $U(D)$ -spin coherent (quasi-classical) states and they have the structure of a quantum superposition of weakly-overlapping (macroscopically distinguishable) coherent wave packets with interesting quantum properties. For that purpose we make use of one- and two-quDit reduced density matrices (RDM), obtained by extracting one or two particles/atoms from a composite system of  $N$  identical quDits described by a cat state, and tracing out the remaining system. It is well known (see [3] and references therein) that the entropy of these RDMs provides information

---

\* jguerrer@ujaen.es: corresponding author

† albmayer97@ugr.es

‡ calixto@ugr.es

about the entanglement of the system. We shall plot the information diagrams associated to these RDMs and extract qualitative information about one- and two-quDit entanglement, and also about the rank of the corresponding RDM, which also provides information on the entanglement of the original system [7].

We shall apply these results to the characterization of quantum phase transitions (QPT) occurring in Lipkin-Meshkov-Glick models of 3-level identical atoms, complementing the results of [8]. In particular, we have seen that the rank of the one- and two-quDit RDMs can be considered as a discrete order parameter precursor detecting the existence of QPTs.

The paper is organized as follows. Section II reviews the notion of information diagram, describing its main properties, particularly with respect to the rank. Section III reviews the concept of  $U(D)$ -spin coherent states and their  $\mathbb{Z}_2^{D-1}$  parity adapted version, the DCAT. In Section IV we compute one- and two-quDit RDMs for the 2CAT and the 3CAT, their Linear and von Neumann entropies, plotting them and constructing the associated information diagrams. In Section V we use information diagrams to provide qualitative information about QPTs in Lipkin-Meshkov-Glick (LMG) models. Section VI is devoted to conclusions.

## II. INFORMATION DIAGRAMS

To determine the boundaries in information diagrams [2] we need to show that, for two different measures of entropy (or information)  $E_1$  and  $E_2$ , there are maximum and minimum possible values of  $E_1$  (resp.  $E_2$ ) for a given value of  $E_2$  (resp.  $E_1$ ) [5]. That is, the region  $\Delta$  given by the image of the map  $\rho \mapsto (E_1(\rho), E_2(\rho))$  is a bounded set in the plane, where  $\rho$  denotes all possible probability distributions (or density matrices) for a given dimension  $d$ .

Since usual measures of entropy for density matrices are based on the trace, they are invariant under changes of basis. Hence, the only relevant information of a density matrix is contained in its eigenvalues, thus in this paper we shall identify density matrices  $\rho$  with their eigenvalues  $(\lambda_1, \lambda_2, \dots, \lambda_d)$ , the order being irrelevant. Therefore, for our purposes, we can identify probability distributions and density matrices using a vector notation in terms of eigenvalues, referring to both of them as density matrices for short. Notwithstanding, we shall continue to treat density matrices as matrices in some situations.

In [5] it was proved that, under rather general assumptions on the convexity/concavity of the entropy measures, the maximum and minimum values are always attained in two standard forms of density matrices

$$\rho_{\max}(\lambda) = (\lambda, \bar{\lambda}, \overset{(d-1)}{\dots}, \bar{\lambda}), \quad \bar{\lambda} = \frac{1-\lambda}{d-1} \leq \lambda, \quad \lambda \in \left[\frac{1}{d}, 1\right), \quad (1)$$

$$\rho_{\min}^{(k)}(\lambda) = (\lambda, \overset{(k)}{\dots}, \lambda, \bar{\lambda}, 0, \dots, 0), \quad \bar{\lambda} = 1 - k\lambda < \lambda, \quad \lambda \in \left[\frac{1}{k+1}, \frac{1}{k}\right) \quad (2)$$

respectively, where  $k = 1, \dots, d-1$ . Let us write the previous equations as (convex) sums of density matrices, that in turn can be seen as lower dimensional density matrices. For that purpose denote by  $\rho_k$  the maximally mixed density matrix (or equal probabilities distribution) in dimension  $k$ ,  $\rho_k = (\frac{1}{k}, \overset{(k)}{\dots}, \frac{1}{k}) = \frac{1}{k} I_k$ , where  $I_k$  is the identity matrix in dimension  $k$ . Then we have:

$$\rho_{\max}(\epsilon) = (1-\epsilon) \rho_d + \epsilon \rho_1 \oplus 0_{d-1}, \quad \epsilon \in [0, 1) \quad (3)$$

$$\rho_{\min}^{(k)}(\epsilon) = (1-\epsilon) \rho_k \oplus 0_{d-k} + \epsilon 0_k \oplus \rho_1 \oplus 0_{d-1-k}, \quad \epsilon \in \left(0, \frac{1}{1+k}\right] \quad (4)$$

where  $0_k$  is the null matrix (or vector) in dimension  $k$  and  $k = 1, \dots, d-1$ . The relation between  $\epsilon$  and  $\lambda$  is  $\lambda = \frac{1}{d} - (1 - \frac{1}{d}) \epsilon$  for eqns. (1,3) and  $\lambda = \frac{1-\epsilon}{k}$  for eqns. (2,4).

In most cases, the pair of entropies  $(\mathcal{L}, \mathcal{S})$  is considered, where  $\mathcal{L}$  and  $\mathcal{S}$  denote linear and von Neumann entropies, respectively. We shall consider here normalized linear and von Neumann entropies, i.e:

$$\mathcal{L}(\rho) = \frac{d}{d-1} (1 - \text{Tr}(\rho^2)), \quad \mathcal{S}(\rho) = -\text{Tr}(\rho \log_d \rho), \quad (5)$$

in such a way that both entropies range from 0 (pure states) to 1 (maximally mixed states). The values of both entropies for each family of curves are:

$$\begin{aligned} \mathcal{L}(\rho_{\max}(\epsilon)) &= 1 - \epsilon^2, \\ \mathcal{S}(\rho_{\max}(\epsilon)) &= -(d-1) \frac{1-\epsilon}{d} \log_d \left( \frac{1-\epsilon}{d} \right) - \left( \frac{1+(d-1)\epsilon}{d} \right) \log_d \left( \frac{1+(d-1)\epsilon}{d} \right), \end{aligned} \quad (6)$$

and

$$\begin{aligned}\mathcal{L}(\rho_{\min}^{(k)}(\epsilon)) &= \frac{d}{d-1} \left( 1 - \epsilon^2 - \frac{(1-\epsilon)^2}{k} \right), \\ \mathcal{S}(\rho_{\min}^{(k)}(\epsilon)) &= -(1-\epsilon) \log_d(1-\epsilon) - \epsilon \log_d(\epsilon) + (1-\epsilon) \log_d(k).\end{aligned}\quad (7)$$

In Figure 1a the curves  $\rho \mapsto (\mathcal{L}(\rho), \mathcal{S}(\rho))$  are shown for  $\rho$  equal to  $\rho_{\max}(\epsilon)$  and  $\rho_{\min}^{(k)}(\epsilon)$ , delimiting the corresponding region  $\Delta$  (we are setting  $d = 5$ ).

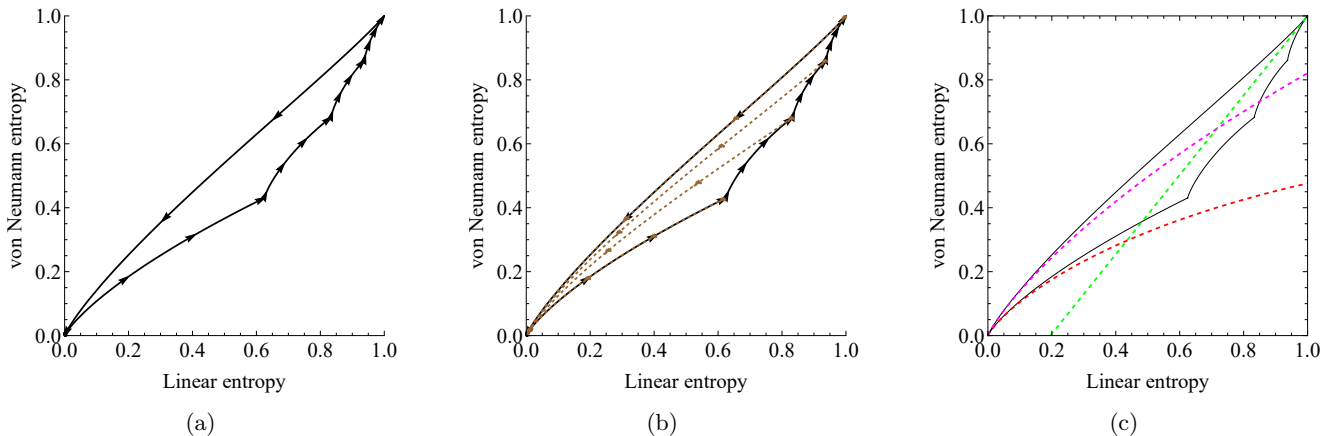


FIG. 1: (a) Information diagram for linear and von Neumann entropies in dimension  $d = 5$ , where the region  $\Delta$  is bounded by the curves associated with the density matrices given by eqns. (3) (above) and (4) (below). All curves except  $\rho_{\max}$  are traced from left to right when  $\epsilon$  increases. (b) Curves associated with density matrices  $\bar{\rho}_{\min}^{(k)}(\epsilon)$  for  $k = 1, \dots, d - 1$ , which are traced from right to left. Note that in the case  $k = 1$  the associated curve is the same as in (a), but traced backwards. Also, for  $k = d - 1$  the associated curve coincides with that of  $\rho_{\max}$ . (c) Plot of the asymptotic curves (8,9) for density matrices near a pure state (bottom-left, red and pink, respectively) and the asymptotic curve (10) near the maximally mixed state (upper-right, green)

Note that the density matrices (3) can be seen (for small  $\epsilon$ ) as the maximally mixed density matrix  $\rho_d$  perturbed by a rank-1 density matrix, while those of (4) can be seen as maximally mixed density matrix of dimension  $k$ ,  $\rho_k$ , perturbed by a (orthogonal) rank-1 density matrix, for  $k = 1, \dots, d - 1$ .

It should be stressed that the range of the parameter  $\epsilon$  in the curves  $\rho_{\min}^{(k)}(\epsilon)$  can be extended to the interval  $[0, 1]$ . Let us denote by  $\bar{\rho}_{\min}^{(k)}(\epsilon)$  the family of density matrices (4) for the range  $\epsilon \in (\frac{1}{1+k}, 1]$ . Their corresponding curves in the information diagram are shown in Figure 1b.

### A. Information diagrams and rank of density matrices

As it can be seen in Figure 1b, there are only  $d - 3$  distinct  $\bar{\rho}_{\min}^{(k)}$  curves, for  $k = 2, \dots, d - 2$ . These curves divide the region  $\Delta$  into  $d - 2$  subregions,  $\Delta_k$ ,  $k = 2, \dots, d - 1$ , bounded by the curves  $\rho_{\min}^{(k)}$ ,  $\bar{\rho}_{\min}^{(k)}$  and  $\bar{\rho}_{\min}^{(k-1)}$ . Each subregion  $\Delta_k$  contains density matrices of rank greater than  $k$ . Density matrices of rank 1 (pure states) lie on the origin, while density matrices of rank 2 lie on the curve  $\rho_{\min}^{(1)} = \bar{\rho}_{\min}^{(1)}$ . See Figure 2 for a plot of a sample of 20000 density matrices of dimension  $d = 5$  randomly generated following a  $\chi^2$  distribution for the eigenvalues where the color of the corresponding point in the information diagram is associated to its rank (warmer colors correspond to higher rank).

From the expression of the extremal density matrices (1,2), or their alternative expressions (3,4), and the expression of the inner curves  $\bar{\rho}_{\min}^{(k)}(\epsilon)$ , it is clear that, for a given value of the linear entropy and a fixed rank  $k + 1$ , the extreme values of the von Neumann entropy are reached for  $k$  identical eigenvalues. If the remaining eigenvalue is larger than the rest (i.e. we are in  $\bar{\rho}_{\min}^{(k)}$ ) then there is a maximum, and if it is smaller than the rest (in  $\rho_{\min}^{(k)}$ ) then it is a minimum of von Neumann entropy.

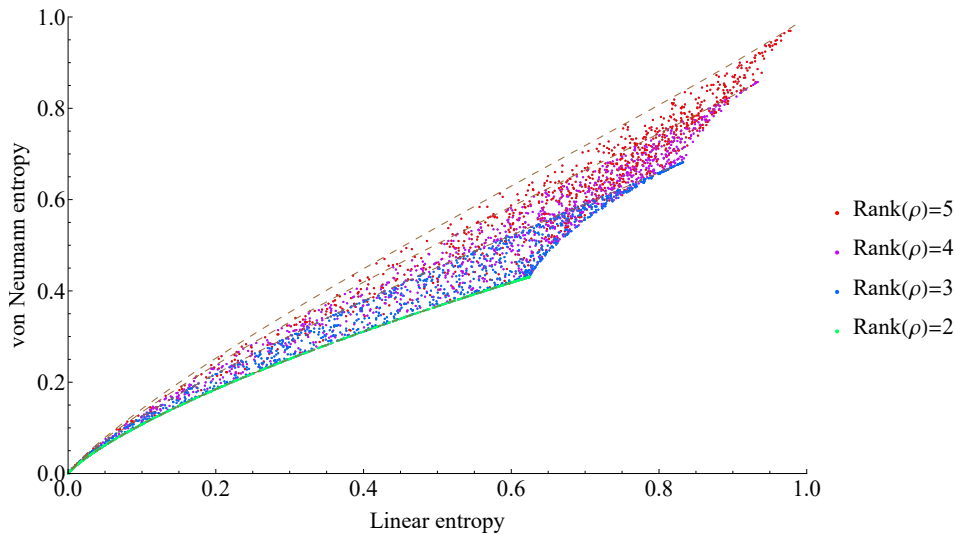


FIG. 2: Colored plot of a sample of 20000 density matrices of dimension  $d = 5$  randomly generated following a  $\chi^2$  distribution for the eigenvalues in an information diagram where the different colors represent the rank of the density matrix (warmer colors represent higher ranks)

### B. Asymptotic curves

It is interesting to obtain approximate expressions for the function  $\mathcal{S}(\mathcal{L})$  in some regions of the information diagram. Near a pure state (bottom left of the information diagram), we have the following asymptotic expressions for the curves  $\rho_{\max}$  and  $\rho_{\min}^{(1)}$ :

$$\mathcal{S}(\mathcal{L}) = \frac{d-1}{2d \log(d)} [(1 + \log(2d)) \mathcal{L} - \mathcal{L} \log(\mathcal{L})], \quad (8)$$

$$\mathcal{S}(\mathcal{L}) = \frac{d-1}{2d \log(d)} [(1 + \log(2d) - \log(d-1)) \mathcal{L} - \mathcal{L} \log(\mathcal{L})], \quad (9)$$

respectively. Near the maximally mixed density matrix (upper right of the information diagram), both  $\rho_{\max}$  and  $\rho_{\min}^{(d-1)}$  collapse into the same curve, with asymptotic expression:

$$\mathcal{S}(\mathcal{L}) = 1 - \frac{d-1}{2 \log(d)} (1 - \mathcal{L}). \quad (10)$$

See Figure 1c for a plot of these asymptotic curves in an information diagram with  $d = 5$ .

Once we have explained what the information diagrams are, and their main features, we shall use them in the study of one- and two-quDit entanglement of generalized Schrödinger cat states, which arise as a parity adaptation of  $U(D)$ -spin (symmetric multi-quDit) coherent states.

### III. $U(D)$ -SPIN COHERENT STATES AND THEIR ADAPTATION TO PARITY IN SYMMETRIC MULTI-QUDIT SYSTEMS

In this section we introduce the main ingredients and notation required to define parity adapted  $U(D)$ -spin coherent states in symmetric multi-quDit systems. These kind of states were introduced long ago in [6] as nonclassical (even and odd) states of light. We shall particularize to  $D = 2$  and  $D = 3$  for practical cases. See [8] for a more detailed study of the general case.

We consider a system of  $N$  identical (indistinguishable) quDits, namely,  $D$ -level identical atoms. Denoting by  $a_i^\dagger$  (resp.  $a_i$ ) the creation (resp. annihilation) operator of an atom in the  $i$ -th level (namely,  $i = 1, 2$  for ground and excited –or spin up and down– in the case  $D = 2$ , or  $i = 1, 2, 3$  for a 3-level atom in the case of  $D = 3$ ), the collective

$U(D)$ -spin operators can be expressed (in the fully symmetric representation) as bilinear products of creation and annihilation operators as (Schwinger representation)

$$S_{ij} = a_i^\dagger a_j, \quad i, j = 1, \dots, D, \quad (11)$$

which generate the unitary symmetry  $U(D)$ . The operator  $S_{ii}$  represents the number of quDits in the level  $i$ , whereas  $S_{ij}, i \neq j$  are raising and lowering (tunneling) operators. The fully symmetric representation space of  $U(D)$  is embedded into Fock space, with Bose-Einstein-Fock basis ( $|\vec{0}\rangle$  denotes the Fock vacuum)

$$|\vec{n}\rangle = |n_1, \dots, n_D\rangle = \frac{(a_1^\dagger)^{n_1} \dots (a_D^\dagger)^{n_D}}{\sqrt{n_1! \dots n_D!}} |\vec{0}\rangle, \quad (12)$$

when fixing  $n_1 + \dots + n_D = N$  (the linear Casimir  $C_1 = S_{11} + \dots + S_{DD}$ ) to the total number  $N$  of quDits. Collective  $U(D)$ -spin operator (11) matrix elements are given by

$$\begin{aligned} \langle \vec{m} | S_{ii} | \vec{n} \rangle &= n_i \delta_{\vec{m}, \vec{n}}, \\ \langle \vec{m} | S_{ij} | \vec{n} \rangle &= \sqrt{(n_i + 1) n_j} \delta_{m_i, n_i + 1} \delta_{m_j, n_j - 1} \prod_{k \neq i, j} \delta_{m_k, n_k}, \quad \forall i \neq j. \end{aligned} \quad (13)$$

The expansion of a general symmetric  $N$ -particle state  $\psi$  in the Fock basis will be written as

$$|\psi\rangle = \sum_{\vec{n}}' c_{\vec{n}} |\vec{n}\rangle = \sum_{n_1 + \dots + n_D = N} c_{n_1, \dots, n_D} |n_1, \dots, n_D\rangle, \quad (14)$$

where  $\sum'$  is a shorthand for the restricted sum. Among all symmetric multi-quDit states, we shall pay special attention to  $U(D)$ -spin coherent states (DSCSs for short), which adopt the multinomial form<sup>1</sup>

$$|\mathbf{z}\rangle = |z_2, \dots, z_D\rangle = \frac{1}{\sqrt{N!}} \left( \frac{a_1^\dagger + z_2 a_2^\dagger + \dots + z_D a_D^\dagger}{\sqrt{1 + |z_2|^2 + \dots + |z_D|^2}} \right)^N |\vec{0}\rangle, \quad (15)$$

and are labeled by complex points  $\mathbf{z} = (z_2, \dots, z_D) \in \mathbb{C}^{D-1}$ . These DSCSs can be seen as Bose-Einstein condensates (BECs) of  $D$  modes, generalizing the spin  $U(2)$  (binomial) coherent states of two modes introduced by [9] and [10] long ago. If we order levels  $i = 1, \dots, D$  from lower to higher energies, the state  $|\mathbf{z} = 0\rangle$  would be the ground state, whereas general  $|\mathbf{z}\rangle$  could be seen as coherent excitations. Coherent states are sometimes called ‘‘quasi-classical’’ states and we shall see in Section V that  $|\mathbf{z}\rangle$  turns out to be a good variational state that reproduces the energy and wave function of the ground state of multilevel LMG atom models in the thermodynamic (classical) limit  $N \rightarrow \infty$ .

Expanding the multinomial (15), we identify the coefficients  $c_{\vec{n}}$  of the expansion (14) of the DSCS  $|\mathbf{z}\rangle$  in the Fock basis as

$$c_{\vec{n}}(\mathbf{z}) = \sqrt{\frac{N!}{\prod_{i=1}^D n_i!}} \frac{\prod_{i=2}^D z_i^{n_i}}{|\mathbf{z}|^N}, \quad (16)$$

where we have written  $|\mathbf{z}| \equiv (\mathbf{z} \cdot \mathbf{z})^{1/2} = (1 + \sum_{i=2}^D |z_i|^2)^{1/2}$  for the ‘‘length’’ of  $\mathbf{z}$ . Note that DSCS are not orthogonal (in general) since

$$\langle \mathbf{z}' | \mathbf{z} \rangle = \frac{(\mathbf{z}' \cdot \mathbf{z})^N}{(\mathbf{z}' \cdot \mathbf{z}')^{N/2} (\mathbf{z} \cdot \mathbf{z})^{N/2}}, \quad \mathbf{z}' \cdot \mathbf{z} \equiv 1 + \bar{z}'_2 z_2 + \dots + \bar{z}'_D z_D, \quad (17)$$

is not zero, in general. However, contrary to the standard (canonical, harmonic oscillator) CSs, they can be orthogonal when  $\mathbf{z}' \cdot \mathbf{z} = 0$ .

In [8] we have shown that DSCSs are separable and exhibit no quDit entanglement (although they do exhibit interlevel entanglement). In fact they can be written as a tensor product of 1-quDit coherent states:

$$|\mathbf{z}\rangle^{(N)} = |\mathbf{z}\rangle_1 \otimes |\mathbf{z}\rangle_2 \otimes \dots \otimes |\mathbf{z}\rangle_N, \quad (18)$$

<sup>1</sup> In eq. (15) and the following ones we have put  $z_1 = 1$ , where  $z_1$  is the parameter multiplying  $a_1^\dagger$ , see [8]. Consequently, it has been removed from the expression of  $|\mathbf{z}\rangle$ .

where we added the superscript ( $N$ ) to the  $N$ -particle coherent state (15), and  $|\mathbf{z}\rangle_i$  denotes the one-particle coherent state for the  $i$ -th quDit. Note that this state is explicitly symmetric under the interchange of quDits and therefore there is no need to symmetrize it.

The situation changes when we deal with parity adapted DSCSs, sometimes called ‘‘Schrödinger cat states’’, since they are a quantum superposition of weakly-overlapping (macroscopically distinguishable) quasi-classical coherent wave packets. These kind of cat states arise in several physical situations and display interesting nonclassical properties. The case of even parity cat states is particularly important since they turn out to be good variational states [10], reproducing the energy of the ground state of quantum critical models in the thermodynamic limit  $N \rightarrow \infty$ . In [8], the even parity multi-quDit cat state  $\text{DCAT}$  have been constructed for general  $D$ , and here we shall reproduce the construction to fix notation.

The parity operators are defined as

$$\Pi_j = \exp(i\pi S_{jj}), \quad j = 1, \dots, D. \quad (19)$$

Note that  $\Pi_i^{-1} = \Pi_i$  and  $\Pi_1 \dots \Pi_D = (-1)^N$ , a constraint that says that the parity group for symmetric quDits is not  $\mathbb{Z}_2 \times \dots \times \mathbb{Z}_2$  but  $\mathbb{Z}_2 \times \dots \times \mathbb{Z}_2 = \mathbb{Z}_2^{D-1}$  instead. Therefore, we can discard in our discussion one of the parity operators, and we select  $\Pi_1$  (since we will use level 1 as reference level in Sec. V).

Parity operators are conserved when the Hamiltonian scatters pairs of particles conserving the parity of the population  $n_j$  in each level  $j = 1, \dots, D$ , like in the  $D$ -level LMG model considered in Sec. V. Using the multinomial expansion (15), it is easy to see that the effect of parity operators on symmetric DSCSs  $|\mathbf{z}\rangle$  is then

$$\Pi_i |\mathbf{z}\rangle = \Pi_i |z_2, \dots, z_i, \dots, z_D\rangle = |z_2, \dots, -z_i, \dots, z_D\rangle, \quad i = 2, \dots, D. \quad (20)$$

The projector onto the even parity subspace is given by:

$$\Pi_{\text{even}} = 2^{1-D} \sum_{\mathbb{b} \in \{0,1\}^{D-1}} \Pi_2^{b_2} \Pi_3^{b_3} \dots \Pi_D^{b_D}, \quad (21)$$

where the binary string  $\mathbb{b} = (b_2, \dots, b_D) \in \{0,1\}^{D-1}$  labels the elements of the parity group  $\mathbb{Z}_2^{D-1}$ . We shall also denote the symbol  $\mathbb{0}$  for the string  $(0, \dots, 0)$ .

Let us define the even parity generalized Schrödinger cat state

$$|\text{DCAT}\rangle = \frac{1}{\mathcal{N}(\text{DCAT})} \Pi_{\text{even}} |\mathbf{z}\rangle = \frac{2^{1-D}}{\mathcal{N}(\text{DCAT})} \sum_{\mathbb{b}} |\mathbf{z}^{\mathbb{b}}\rangle, \quad (22)$$

where  $|\mathbf{z}^{\mathbb{b}}\rangle \equiv |(-1)^{b_2} z_2, \dots, (-1)^{b_D} z_D\rangle$  and we are using  $\sum_{\mathbb{b}}$  as a shorthand for  $\sum_{\mathbb{b} \in \{0,1\}^{D-1}}$ . The  $\text{DCAT}$  is just the projection of a DSCS onto the even parity subspace. The normalization factor is given by

$$\mathcal{N}(\text{DCAT})^2 = 2^{1-D} \frac{\sum_{\mathbb{b}} L_{\mathbb{b}}}{L_{\mathbb{0}}} \quad (23)$$

where  $L_{\mathbb{b}} = 1 + (-1)^{b_2} |z_2|^2 + \dots + (-1)^{b_D} |z_D|^2$ . We shall also use the alternative notation  $L_{\sigma} \equiv L_{\mathbb{b}}$  for  $\sigma = (-1)^{\mathbb{b}} = ((-1)^{b_2}, \dots, (-1)^{b_D})$  for convenience.

As an illustration, let us provide the particular expressions of  $|\text{DCAT}\rangle$  for  $D = 2$  and  $D = 3$ . Denoting by  $|\mathbf{z}\rangle = |z_2\rangle = |\alpha\rangle$  the coherent state (15) for  $D = 2$ , the corresponding even parity  $2\text{CAT}$  state is given by

$$|2\text{CAT}\rangle = \frac{1}{2\mathcal{N}(2\text{CAT})} (|\alpha\rangle + |-\alpha\rangle), \quad (24)$$

with normalization factor

$$\mathcal{N}(2\text{CAT})^2 = \frac{1}{2} \left[ 1 + \left( \frac{1 - |\alpha|^2}{1 + |\alpha|^2} \right)^N \right] = \frac{1}{2} \frac{L_+^N + L_-^N}{L_+^N}, \quad (25)$$

with  $L_{\pm} = 1 \pm |\alpha|^2$ . Note that the overlap  $\langle \alpha | -\alpha \rangle = (L_-/L_+)^N \xrightarrow{N \rightarrow \infty} 0$  for  $\alpha \neq 0$ , which means that  $|\alpha\rangle$  and  $|-\alpha\rangle$  are macroscopically distinguishable wave packets for any  $\alpha \neq 0$  (they are orthogonal for  $|\alpha| = 1$ ).

Likewise, denoting by  $|\mathbf{z}\rangle = |z_2, z_3\rangle = |\alpha, \beta\rangle$  the coherent state (15) for  $D = 3$ , the corresponding even parity  $3\text{CAT}$  state is explicitly given by

$$|3\text{CAT}\rangle = \frac{1}{4\mathcal{N}(3\text{CAT})} (|\alpha, \beta\rangle + |-\alpha, \beta\rangle + |\alpha, -\beta\rangle + |-\alpha, -\beta\rangle), \quad (26)$$

where

$$\begin{aligned}\mathcal{N}(\text{3CAT})^2 &= \frac{1}{4} \left[ 1 + \frac{(1 - |\alpha|^2 + |\beta|^2)^N + (1 + |\alpha|^2 - |\beta|^2)^N + (1 - |\alpha|^2 - |\beta|^2)^N}{(1 + |\alpha|^2 + |\beta|^2)^N} \right] \\ &= \frac{1}{4} \frac{L_{++}^N + L_{-+}^N + L_{+-}^N + L_{--}^N}{L_{++}^N},\end{aligned}\quad (27)$$

with  $L_{\sigma_1\sigma_2} = 1 + \sigma_1|\alpha|^2 + \sigma_2|\beta|^2$ , for  $\sigma_1, \sigma_2 = \pm$ . We shall use (26) and (27) in Section V, when discussing a LMG model of atoms with  $D = 3$  levels. The 3CAT state has also been used in U(3) vibron models of molecules [11, 12] and Dicke models of 3-level atoms interacting with a polychromatic radiation field [13, 14].

#### IV. ENTROPIC MEASURES ON REDUCED DENSITY MATRICES TO QUANTIFY ENTANGLEMENT

One of the most important applications of entropy measures is to quantify the entanglement of the state of a system. For that purpose we define several types of bipartition of the whole system, computing the corresponding RDMs and entanglement measures for symmetric multi-quDit states  $\psi$  in terms of linear  $\mathcal{L}$  and von Neumann  $\mathcal{S}$  entropies. We shall focus on one- and two-quDit entanglement, computing the one- and two-particle RDMs ( $\rho_1$  and  $\rho_2$ ) for a single and a pair of particles extracted at random from a symmetric  $N$ -quDit state  $\psi$ . The procedure is straightforwardly extended to  $\rho_M$  for an arbitrary number  $M \leq N/2$  of quDits. However, as we shall see, it is not necessary to go beyond two particles since the two-particle RDM provides enough information for small values of  $D$ . Actually, in the particular case of  $D = 2$ , the one-particle RDM contains all necessary information about the entanglement of the system.

In [8] we gave the general expression of the one-quDit RDM of any normalized symmetric  $N$ -quDit state  $\psi$  like (14), expressed in terms of expectation values of U( $D$ )-spin operators  $S_{ij}$  as

$$\rho_1^N(\psi) = \frac{1}{N} \sum_{i,j=1}^D \langle \psi | S_{ji} | \psi \rangle E_{ij}, \quad (28)$$

where  $E_{ij}$  represent  $D^2$ ,  $D \times D$ -matrices with entries  $(E_{ij})_{lk} = \delta_{il}\delta_{jk}$  (1 in row  $i$ , column  $j$ , and 0 elsewhere). Likewise, the two-particle RDM of a symmetric state  $\psi$  of  $N > 2$  quDits is written as [8]

$$\rho_2^N(\psi) = \frac{1}{N(N-1)} \sum_{i,j,k,l=1}^D (\langle \psi | S_{ji} S_{lk} | \psi \rangle - \delta_{il} \langle \psi | S_{jk} | \psi \rangle) E_{ij} \otimes E_{kl}. \quad (29)$$

The matrices  $E_{ij}$  are the generalization to arbitrary  $D$  of standard Pauli matrices for qubits ( $D = 2$ ), namely  $E_{12} = \sigma_+$ ,  $E_{21} = \sigma_-$ ,  $E_{11} - E_{22} = \sigma_3$  and  $E_{11} + E_{22} = \sigma_0$  (the  $2 \times 2$  identity matrix). Actually, the one- and two-qubit RDMs for  $D = 2$  were already considered time ago by Wang and Mølmer in [15]. Here we shall consider both cases,  $D = 2$  (qubits) and  $D = 3$  (qutrits), in order to discuss the similitudes and differences.

##### A. One-quDit reduced density matrices

For the case of a DSCS  $|\mathbf{z}\rangle$ , the linear and von Neumann entropies of  $\rho_1(\mathbf{z})$  are zero, i.e. there is no entanglement between quDits in a DSCS. This is because a DSCS is eventually obtained by rotating each quDit individually. The situation changes when we deal with parity adapted DSCSs or ‘‘Schrödinger cat states’’ like (25)-(26). Indeed, the one-quDit RDM  $\rho_1(\text{DCAT})$  does not correspond now to a pure state since it has the expression (we provide its eigenvalues)

$$\rho_1^N(\text{2CAT}) = \frac{1}{2L_{++}^N \mathcal{N}(\text{2CAT})^2} (L_+^{N-1} + L_-^{N-1}, |\alpha|^2 (L_+^{N-1} - L_-^{N-1})), \quad (30)$$

for an  $N$ -qubit system and

$$\begin{aligned}\rho_1^N(\text{3CAT}) &= \frac{1}{4L_{++}^N \mathcal{N}(\text{3CAT})^2} (L_{++}^{N-1} + L_{-+}^{N-1} + L_{+-}^{N-1} + L_{--}^{N-1}, \\ &\quad |\alpha|^2 (L_{++}^{N-1} - L_{-+}^{N-1} + L_{+-}^{N-1} - L_{--}^{N-1}), \\ &\quad |\beta|^2 (L_{++}^{N-1} + L_{-+}^{N-1} - L_{+-}^{N-1} - L_{--}^{N-1})),\end{aligned}\quad (31)$$

for an  $N$ -qutrit system. Note that, for  $\alpha \neq 0$  in the case of  $\rho_1^N(2\text{CAT})$ , and  $\alpha \neq 0$  or  $\beta \neq 0$  in the case  $\rho_1^N(3\text{CAT})$ , the corresponding one-quDit RDM has rank greater than 1. That is, unlike  $|\mathbf{z}\rangle$ , the Schrödinger cat  $|\text{DCAT}\rangle$  is not separable in the tensor product Hilbert space  $[\mathbb{C}^D]^{\otimes N}$ . In addition,  $\rho_1^N(3\text{CAT})$  has rank 2 if  $\alpha \neq 0$  or  $\beta \neq 0$  and has rank 3 if both are different from zero. See below for a more detailed discussion on this point.

Since the main features of these density matrices are captured in the  $N \rightarrow \infty$  (thermodynamic) limit (infinite number of quDits), we shall restrict ourselves to this limit, where the expression of the (diagonalized) density matrices are simpler:

$$\rho_1^\infty(2\text{CAT}) = \frac{1}{1 + |\alpha|^2} (1, |\alpha|^2), \quad (32)$$

$$\rho_1^\infty(3\text{CAT}) = \frac{1}{1 + |\alpha|^2 + |\beta|^2} (1, |\alpha|^2, |\beta|^2). \quad (33)$$

It will be interesting to discuss also the case  $|\alpha| = 1$ , for qubits, and  $(|\alpha|, |\beta|) = (1, 1)$ , for qutrits, since these values will appear as limiting points of the stationary curve  $(\alpha_0(\lambda), \beta_0(\lambda))$  in Eq. (49) for high  $\lambda$ , i.e.  $(\alpha_0(\lambda), \beta_0(\lambda)) \xrightarrow{\lambda \rightarrow \infty} (1, 1)$ , where  $\lambda$  is the strength of two-body (two-quDit) interactions in a  $D$ -level atom LMG model (see later in Section V for more information). Therefore, we are also interested in the “high coupling limit”

$$\lim_{|\alpha| \rightarrow 1} \rho_1^\infty(2\text{CAT}) = \left(\frac{1}{2}, \frac{1}{2}\right), \quad (34)$$

$$\lim_{(|\alpha|, |\beta|) \rightarrow (1, 1)} \rho_1^\infty(3\text{CAT}) = \left(\frac{1}{3}, \frac{1}{3}, \frac{1}{3}\right). \quad (35)$$

Hence, in this high coupling limit, the 1-quDit RDM is maximally mixed and therefore the entanglement is maximum.

For  $D = 2$ , the asymptotic behavior of  $\rho_1^\infty$  for large  $|\alpha|$  is:

$$\rho_1^\infty(2\text{CAT}) = (0, 1) + O\left(\frac{1}{|\alpha|^2}\right)(1, 1), \quad |\alpha|^2 \gg 1, \quad (36)$$

while for  $D = 3$  the limit  $(|\alpha|, |\beta|) \rightarrow (\infty, \infty)$  does not exist. Actually, the asymptotic behavior of  $\rho_1^\infty(3\text{CAT})$  along the lines  $|\alpha| = r \cos \theta, |\beta| = r \sin \theta$ , for large  $r$ , is:

$$\rho_1^\infty(3\text{CAT}) = (0, \sin^2 \theta, \cos^2 \theta) + O\left(\frac{1}{r^2}\right)(1, 1, 1), \quad r \gg 1, \quad (37)$$

implying that, in this limit, the 1-quDit RDMs have in general lower ranks, exhibiting no entanglement for  $D = 2$  and  $D = 3$  for vertical ( $\theta = \pi/2$ ) and horizontal ( $\theta = 0$ ) directional limits.

In Figures 3a and 3b we represent contour plots of linear and von Neumann

$$\mathcal{L}_1^\infty = \frac{D}{D-1} (1 - \text{tr}((\rho_1^\infty)^2)), \quad \mathcal{S}_1^\infty = -\text{tr}(\rho_1^\infty \log_D \rho_1^\infty) \quad (38)$$

entanglement entropies in the limit  $N \rightarrow \infty$  of the one-qutrit RDM,  $\rho_1^\infty(3\text{CAT})$ , of the 3CAT in Eq. (26), as a function of the phase-space  $\mathbb{C}P^2$  coordinates  $(\alpha, \beta)$  [actually, they just depend on the moduli]. Both entropies are again normalized to 1. They attain their maximum value of 1 at the phase-space point  $(\alpha, \beta) = (1, 1)$  corresponding to a maximally mixed RDM. This behavior of the entropies, and therefore of entanglement (together with squeezing, see [8]) parallels that of the standard harmonic oscillator cat states where the maximum entanglement and squeezing takes place for relatively small values of the coherent state parameter [16]. The difference here in the  $D = 3$  case is that for large values of the parameter there can still be entanglement (and squeezing), dependent on the angle of the directional limit (see eq. (37)). These Figures also show (in magenta color) the values of the entropies along the stationary curve  $(\alpha(\lambda), \beta(\lambda))$  in Eq. (49), that we already mentioned before the Eq. (34). For high interactions  $\lambda \rightarrow \infty$  we have  $(\alpha(\lambda), \beta(\lambda)) \rightarrow (1, 1)$ , which means that highly coupled quDits are maximally entangled in a cat-like ground state (we shall come back again to this discussion later in Section V). In Figures 3c and 3d the asymptotic behavior for large  $|\alpha|$  and  $|\beta|$  is shown, where contours of linear and von Neumann entropies coincide with the (isentropic) lines  $\theta = \text{constant}$ , according to the asymptotic behavior of  $\rho_1^\infty(3\text{CAT})$  in (37).

In Figure 4a we plot the information diagram for the family of 1-qutrit RDMs for a 3CAT (31) in the limit  $N \rightarrow \infty$ , for all values of  $|\alpha|$  and  $|\beta|$ . It can be seen that they fill completely the region  $\Delta$ . Also, the stationary curve (49) is shown, starting at the origin (zero entropy and therefore no entanglement), moving on the curve  $\rho_{\min}^{(1)}$  and through the region  $\Delta_2$ , to finish at the maximally mixed state, indicating that this state is maximally entangled.

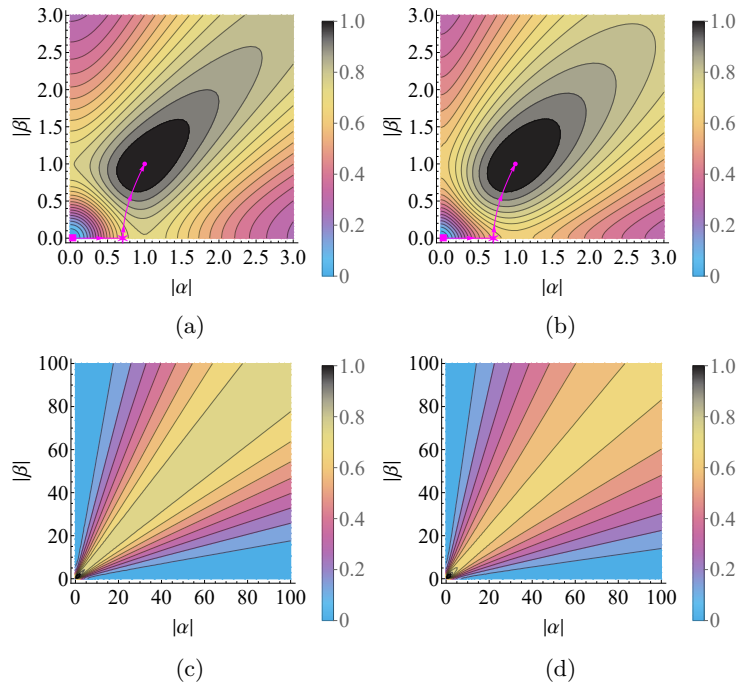


FIG. 3: Contour plots of (a) linear  $\mathcal{L}_1^\infty$  and (b) von Neumann  $\mathcal{S}_1^\infty$  entanglement entropies of the one-qutrit RDM  $\rho_1^\infty(3\text{CAT})$  of a  $U(3)$  Schrödinger cat (26) in the limit of an infinite number of qutrits, as a function of the phase-space coordinates  $\alpha, \beta$  (they just depend on moduli). The asymptotic behaviour of (c)  $\mathcal{L}_1^\infty$  and (d)  $\mathcal{S}_1^\infty$  for large values of  $|\alpha|$  and  $|\beta|$  displays isentropic curves  $\theta = \text{constant}$ , according to the expression of  $\rho_2^\infty(3\text{CAT})$  in Eq. (37).

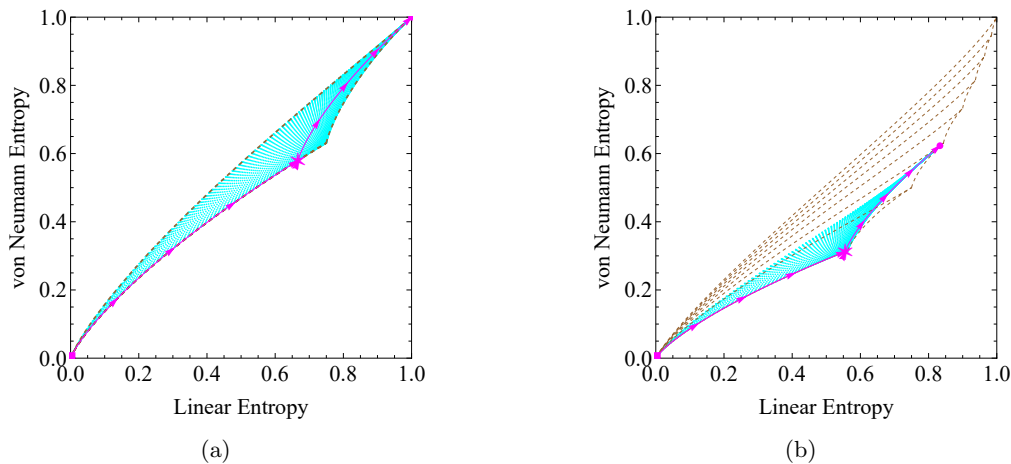


FIG. 4: Information diagram for the family of (a) 1-qutrit RDMs and (b) 2-qutrit RDMs for 3CAT in the limit  $N \rightarrow \infty$ , for all values of  $|\alpha|$  and  $|\beta|$ . See the main text for explanation.

### B. Two-quDit reduced density matrices

As for the one-quDit RDM, the linear and von Neumann entropies for a two-quDit RDM of a DSCS  $|\mathbf{z}\rangle$  are zero, i.e. there is no pairwise quDit entanglement in a DSCS. The situation changes for parity adapted DSCSs or “Schrödinger cat states”  $|\text{DCAT}\rangle$  like the ones in (25)-(26), where the two-quDit RDM  $\rho_2(\text{DCAT})$  in (29) has the expression (once diagonalized) for  $D = 2$  and  $D = 3$  and  $N$  particles:

$$\begin{aligned}
\rho_2^N(2\text{CAT}) &= \frac{1}{2L_{++}^N \mathcal{N}(2\text{CAT})^2} \left( (1 + |\alpha|^4) (L_+^{N-2} + L_-^{N-2}), 2|\alpha|^2 (L_+^{N-2} - L_-^{N-2}), 0, 0 \right), \\
\rho_2^N(3\text{CAT}) &= \frac{1}{4L_{++}^N \mathcal{N}(3\text{CAT})^2} \left( (1 + |\alpha|^4 + |\beta|^4) (L_{++}^{N-2} + L_{-+}^{N-2} + L_{+-}^{N-2} + L_{--}^{N-2}), \right. \\
&\quad 2|\alpha|^2 (L_{++}^{N-2} - L_{-+}^{N-2} + L_{+-}^{N-2} - L_{--}^{N-2}), \\
&\quad 2|\beta|^2 (L_{++}^{N-2} + L_{-+}^{N-2} - L_{+-}^{N-2} - L_{--}^{N-2}), \\
&\quad \left. 2|\alpha|^2 |\beta|^2 (L_{++}^{N-2} - L_{-+}^{N-2} - L_{+-}^{N-2} + L_{--}^{N-2}), 0, 0, 0, 0, 0 \right)
\end{aligned} \tag{39}$$

As it is deduced from the previous expressions, the 2-qudit RDM has rank 1 for  $\alpha = 0$  in the case of the 2CAT, or  $\alpha = \beta = 0$  for the case of the 3CAT. For  $\alpha \neq 0$  (or  $\beta \neq 0$  for the 3CAT) the rank is two, and for  $\alpha \neq 0$  and  $\beta \neq 0$  the rank of  $\rho_2(3\text{CAT})$  is 4.

As for the one-quDit RDM case, it is convenient to consider the thermodynamic limit  $N \rightarrow \infty$  to obtain simpler expressions without losing important qualitative information:

$$\begin{aligned}
\rho_2^\infty(2\text{CAT}) &= \frac{1}{(1 + |\alpha|^2)^2} (1 + |\alpha|^4, 2|\alpha|^2, 0, 0), \\
\rho_2^\infty(3\text{CAT}) &= \frac{1}{(1 + |\alpha|^2 + |\beta|^2)^2} (1 + |\alpha|^4 + |\beta|^4, 2|\alpha|^2, 2|\beta|^2, 2|\alpha|^2 |\beta|^2, 0, 0, 0, 0, 0).
\end{aligned} \tag{40}$$

The high coupling limit,  $|\alpha| \rightarrow 1$  or  $(|\alpha|, |\beta|) \rightarrow (1, 1)$ , discussed before (34) for 1-quDit RDMS, looks like this now for 2-quDit RDMS:

$$\lim_{|\alpha| \rightarrow 1} \rho_2^\infty(2\text{CAT}) = \left( \frac{1}{2}, \frac{1}{2}, 0, 0 \right), \tag{41}$$

$$\lim_{(|\alpha|, |\beta|) \rightarrow (1, 1)} \rho_2^\infty(3\text{CAT}) = \left( \frac{1}{3}, \frac{2}{9}, \frac{2}{9}, \frac{2}{9}, 0, 0, 0, 0, 0 \right), \tag{42}$$

thus implying that, in the high coupling limit, the 2-qubit ( $D = 2$ ) RDM is maximally mixed of rank 2, but it doesn't attain the maximum value of the entropies. For  $D = 3$ , the 2-qutrit RDM is not even maximally mixed of rank 4 (in fact it lies on the curve  $\bar{\rho}_{\min}^{(3)}$ ), although the value of the entropies is very similar to that of  $\rho_4$  (see Figure 1).

For  $D = 2$  the asymptotic behaviour of  $\rho_2^\infty$  for large  $|\alpha|$  is:

$$\rho_2^\infty(2\text{CAT}) = (0, 1, 0, 0) + O\left(\frac{1}{|\alpha|^2}\right)(1, 1, 0, 0), \quad |\alpha| \gg 1, \tag{43}$$

while for  $D = 3$  the limit  $(|\alpha|, |\beta|) \rightarrow (\infty, \infty)$  does not exist. The asymptotic behavior, for large  $r$ , along the lines  $|\alpha| = r \cos \theta$ ,  $|\beta| = r \sin \theta$ , is:

$$\begin{aligned}
\rho_2^\infty(3\text{CAT}) &= \left( \frac{1}{4}(\cos(4\theta) + 3), 0, 0, 2 \cos^2(\theta) \sin^2(\theta), 0, 0, 0, 0, 0 \right) \\
&\quad + O\left(\frac{1}{r^2}\right)(1, 1, 1, 1, 0, 0, 0, 0, 0), \quad r \gg 1,
\end{aligned} \tag{44}$$

implying that, in this limit, the 2-quDit RDMS have in general lower ranks, exhibiting no pairwise entanglement for  $D = 2$  and  $D = 3$  for vertical ( $\theta = \pi/2$ ) and horizontal ( $\theta = 0$ ) directional limits.

In Figure 5a-5b, we represent contour plots of normalized linear and von Neumann

$$\mathcal{L}_2^\infty = \frac{D^2}{D^2 - 1} (1 - \text{tr}((\rho_2^\infty)^2)), \quad \mathcal{S}_2^\infty = -\text{tr}(\rho_2^\infty \log_{D^2} \rho_2^\infty), \tag{45}$$

pairwise entanglement entropies in the thermodynamic limit  $N \rightarrow \infty$  for the two-qutrit RDM,  $\rho_2^\infty(3\text{CAT})$ , of a U(3) Schrödinger cat (26), as a function of the phase-space  $\mathbb{C}P^2$  complex coordinates  $(\alpha, \beta)$  [they just depend on the moduli]. As for the one-qutrit case, they attain their maximum value at the phase-space point  $(\alpha, \beta) = (1, 1)$  ("high coupling limit"); however, unlike the one-qutrit case, pairwise entanglement entropies do not attain the maximum value of 1 at this point, but  $\mathcal{L}_2 = 5/6 \simeq 0.833$  and  $\mathcal{S}_2 \simeq 0.623$  for large  $N$ . As already commented, variational (parity adapted spin coherent) approximations to the ground state of the LMG 3-level atom model [discussed later

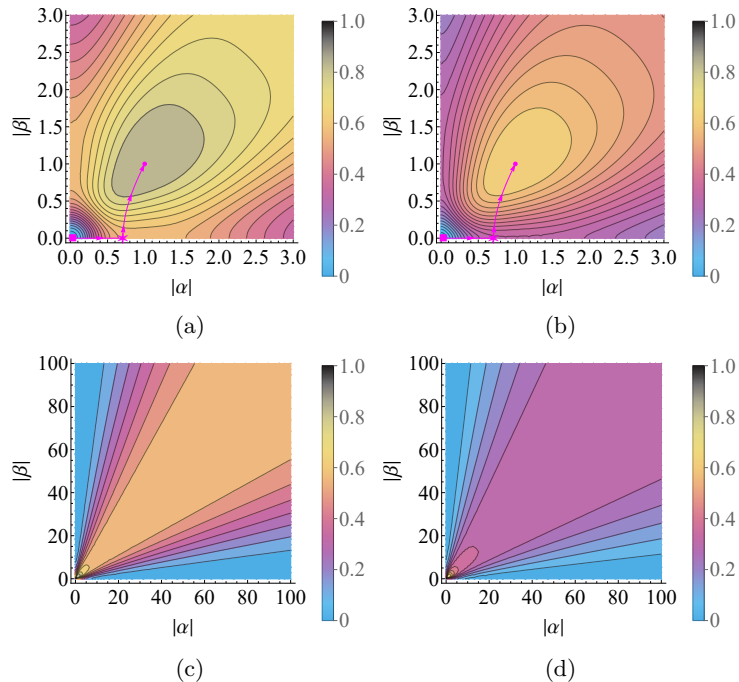


FIG. 5: Contour plots of (a) linear  $\mathcal{L}_2^\infty$  and (b) von Neumann  $\mathcal{S}_2^\infty$  entanglement entropies of the two-qutrit RDM  $\rho_{2(3\text{CAT})}$  of a U(3) Schrödinger cat (26) for  $N \rightarrow \infty$ , as a function of the phase-space coordinates  $\alpha, \beta$  (they just depend on moduli). The meaning of the magenta curve is the same as in the Figure 3. The asymptotic behaviour of (c)  $\mathcal{L}_2^\infty$  and (d)  $\mathcal{S}_2^\infty$  for large values of  $|\alpha|$  and  $|\beta|$  displays isentropic curves  $\theta = \text{constant}$ , according to the expression of  $\rho_{2(3\text{CAT})}^\infty$  in Eq. (44).

in Section V] recover this maximum entanglement point  $(\alpha, \beta) = (1, 1)$  at high interactions  $\lambda \rightarrow \infty$ , as can be seen in the already discussed stationary curve (49). In Figures 5c and 5d, the asymptotic behavior for large  $|\alpha|$  and  $|\beta|$  is shown, where contours of linear and von Neumann entropies coincide with the lines  $\theta = \text{constant}$ , according to the asymptotic behavior of  $\rho_{2(3\text{CAT})}^\infty$  in (44).

We also plot in Figure 4b the information diagram for the 2-qutrit RDM of the 3CAT in the thermodynamic limit  $N \rightarrow \infty$ . It is clear that the  $\Delta$  region is not completely filled; only the subregions  $\Delta_2$  and  $\Delta_3$  are partially filled, the reason being that  $\rho_{2(3\text{CAT})}$  has rank 1, 2 or 4. The stationary curve  $(\alpha_0(\lambda), \beta_0(\lambda))$  in Eq. (49) is also shown, with a behaviour similar to the case of the 1-qutrit RDM, with the difference that it ends near the maximally mixed RDM of rank 4, more precisely, at the point  $(\frac{1}{3}, \frac{2}{9}, \frac{2}{9}, \frac{2}{9}, 0, 0, 0, 0)$ . It is important to notice that the stationary curve is most of the time at the inferior boundary of the set of 2-qutrit RDMs. This means that, from all 2-qutrit RDMs of the 3CAT with a given linear entropy, it has the minimum allowed value of von Neumann entropy. We conjecture that this is due to the variational character of the ground state and the universality of the extremal states lying at the boundaries of the region  $\Delta$ .

## V. INFORMATION DIAGRAMS AND QUANTUM PHASE TRANSITIONS IN LIPKIN-MESHKOV-GLICK MODELS OF 3-LEVEL IDENTICAL ATOMS

Now we apply the previous results to the study of QPTs of  $D$ -level Lipkin-Meshkov-Glick atom models. The standard case of  $D = 2$  level atoms has already been studied in the literature (see e.g. [17]). We shall restrict ourselves to  $D = 3$  level atoms for practical calculations, although the procedure can be easily extended to general  $D$ . In particular, we propose the following LMG-type Hamiltonian

$$H = \frac{\epsilon}{N}(S_{33} - S_{11}) - \frac{\lambda}{N(N-1)} \sum_{i \neq j=1}^3 S_{ij}^2, \quad (46)$$

written in terms of collective U(3)-spin operators  $S_{ij}$ . Hamiltonians of this kind have already been proposed in the literature [18–22] [see also [23] for the role of mixed symmetry sectors in QPTs of multi-quDit LMG systems]. We place levels symmetrically about  $i = 2$ , with intensive energy splitting per particle  $\epsilon/N$ . For simplicity, we consider equal interactions, with coupling constant  $\lambda$ , for atoms in different levels, and vanishing interactions for atoms in the same level (i.e., we discard interactions of the form  $S_{ij}S_{ji}$ ). Therefore,  $H$  is invariant under parity transformations  $\Pi_j$  in (19), since the interaction term scatters pairs of particles conserving the parity of the population  $n_j$  in each level  $j = 1, \dots, D$ . Energy levels have good parity, the ground state being an even state. We divide the two-body interaction in (46) by the number of atom pairs  $N(N-1)$  to make  $H$  an intensive quantity, since we are interested in the thermodynamic limit  $N \rightarrow \infty$ . We shall see that parity symmetry is spontaneously broken in this limit.

As already pointed long ago by Gilmore and coworkers [10, 24], coherent states constitute in general a powerful tool for rigorously studying the ground state and critical properties of some physical systems in the thermodynamic limit. The energy surface associated to a Hamiltonian density  $H$  is defined in general as the coherent state expectation value of the Hamiltonian density in the thermodynamic limit. In our case, the energy surface acquires the following form

$$E_{(\alpha,\beta)}(\epsilon, \lambda) = \lim_{N \rightarrow \infty} \langle \mathbf{z} | H | \mathbf{z} \rangle = \epsilon \frac{\beta \bar{\beta} - 1}{\alpha \bar{\alpha} + \beta \bar{\beta} + 1} - \lambda \frac{\alpha^2 (\bar{\beta}^2 + 1) + (\beta^2 + 1) \bar{\alpha}^2 + \bar{\beta}^2 + \beta^2}{(\alpha \bar{\alpha} + \beta \bar{\beta} + 1)^2}, \quad (47)$$

where we have used the parametrization  $\mathbf{z} = (\alpha, \beta)$ , as in eq. (26), for U(3)-spin coherent states  $|\mathbf{z}\rangle$ . Note that this energy surface is invariant under  $\alpha \rightarrow -\alpha$  and  $\beta \rightarrow -\beta$ , which is a consequence of the inherent parity symmetry of the Hamiltonian (46) and the transformation (20) of  $|\mathbf{z}\rangle$  under parity.

The minimum energy

$$E_0(\epsilon, \lambda) = \min_{\alpha, \beta \in \mathbb{C}} E_{(\alpha, \beta)}(\epsilon, \lambda) \quad (48)$$

is attained at the stationary (real) phase-space values  $\alpha_0^\pm = \pm \alpha_0$  and  $\beta_0^\pm = \pm \beta_0$  with

$$\alpha_0(\epsilon, \lambda) = \begin{cases} 0, & 0 \leq \lambda \leq \frac{\epsilon}{2}, \\ \sqrt{\frac{2\lambda - \epsilon}{2\lambda + \epsilon}}, & \frac{\epsilon}{2} \leq \lambda \leq \frac{3\epsilon}{2}, \\ \sqrt{\frac{2\lambda}{2\lambda + 3\epsilon}}, & \lambda \geq \frac{3\epsilon}{2}, \end{cases} \quad \beta_0(\epsilon, \lambda) = \begin{cases} 0, & 0 \leq \lambda \leq \frac{3\epsilon}{2}, \\ \sqrt{\frac{2\lambda - 3\epsilon}{2\lambda + 3\epsilon}}, & \lambda \geq \frac{3\epsilon}{2}. \end{cases} \quad (49)$$

In Figures 3 and 5 we plotted (in magenta color) the stationary-point curve  $(\alpha_0(\lambda), \beta_0(\lambda))$  on top of one- and two-qutrit entanglement entropies, noting that  $(\alpha_0(\lambda), \beta_0(\lambda)) \rightarrow (1, 1)$  for  $\lambda \rightarrow \infty$  (high interactions). Inserting (49) into (47) gives the ground state energy density at the thermodynamic limit

$$E_0(\epsilon, \lambda) = \begin{cases} -\epsilon, & 0 \leq \lambda \leq \frac{\epsilon}{2}, & \text{(I)} \\ -\frac{(2\lambda + \epsilon)^2}{8\lambda}, & \frac{\epsilon}{2} \leq \lambda \leq \frac{3\epsilon}{2}, & \text{(II)} \\ -\frac{4\lambda^2 + 3\epsilon^2}{6\lambda}, & \lambda \geq \frac{3\epsilon}{2}. & \text{(III)} \end{cases} \quad (50)$$

Here we clearly distinguish three different phases: I, II and III, and two second-order QPTs at  $\lambda_{\text{I} \leftrightarrow \text{II}}^{(0)} = \epsilon/2$  and  $\lambda_{\text{II} \leftrightarrow \text{III}}^{(0)} = 3\epsilon/2$ , respectively, where  $\frac{\partial^2 E_0(\epsilon, \lambda)}{\partial \lambda^2}$  are discontinuous. In the stationary (magenta) curve  $(\alpha_0(\lambda), \beta_0(\lambda))$  shown in Figures 3a, 3b, 4, 5a, 5b, and 6, the phase I corresponds to the origin  $(\alpha_0, \beta_0) = (0, 0)$  (square point), phase II corresponds to the horizontal part  $\beta_0 = 0$  up to the star point, and phase III corresponds to  $\beta_0 \neq 0$ .

Note that the ground state is fourfold degenerated in the thermodynamic limit since the four U(3)-spin coherent states  $|\mathbf{z}_0^{\pm\pm}\rangle = |\pm \alpha_0, \pm \beta_0\rangle$  have the same energy density  $E_0$ . These four coherent states are related by parity transformations and, therefore, parity symmetry is spontaneously broken in the thermodynamic limit. In order to have good variational states for finite  $N$ , to compare with numerical calculations, we have two possibilities: 1) either we use the 3CAT (26) as an ansatz for the ground state, minimizing  $\langle 3\text{CAT} | H | 3\text{CAT} \rangle$ , or 2) we restore the parity symmetry of the coherent state  $|\alpha_0, \beta_0\rangle$  for finite  $N$  by projecting on the even parity sector. Although the first possibility offers a more accurate variational approximation to the ground state, it entails a more tedious numerical minimization than the one already obtained in (48) for  $N \rightarrow \infty$ . Therefore, we shall use the second possibility which, despite being less accurate, it is straightforward and good enough for our purposes. That is, we shall use the 3CAT (26), evaluated at  $\alpha = \alpha_0$  and  $\beta = \beta_0$ , as a variational approximation  $|3\text{CAT}_0\rangle$  to the numerical (exact) ground state  $|\psi_0\rangle$  for finite  $N$ .

Let us apply the tools developed in previous sections to this model and draw the main conclusions. Firstly, in Figure 6a and 6b, we have added to the information diagrams for 1 and 2 qutrits RDMS already shown in Figure 4, the

curves (as a function of  $\lambda$ ) of the numerically computed ground states of the 3-level LMG model for different values on  $N$  (in green colors), together with the already shown analytical variational curve (in magenta)  $(\alpha_0(\lambda), \beta_0(\lambda))$  for  $N \rightarrow \infty$ . We can conclude that they do not lie in the inferior part of the region  $\Delta$ , as the variational one, but as  $N$  grows the numerical curves approach the analytical one.

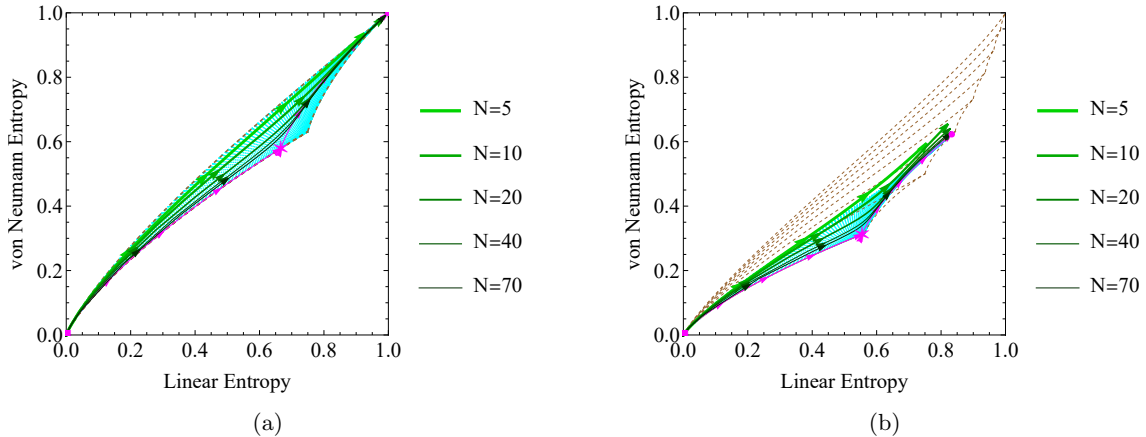


FIG. 6: Information diagram for the family of (a) 1-qutrit RDMs and (b) 2-qutrit RDMs for 3CAT in the limit  $N \rightarrow \infty$ , for all values of  $|\alpha|$  and  $|\beta|$ , where the curves of numerical RDMs, as a function of  $\lambda$  for different values of  $N$ , has been added, as well as the analytical stationary curve for  $N \rightarrow \infty$  (in magenta). Observe that, as  $N$  grows, the numerical (green) curves approach the (magenta) analytical one.

Secondly, suggested by the results about the rank of 1 and 2 quDits RDMs of Section IV, we plot in Figure 7 the rank of the RDMs as a function of  $\lambda$  for both variational ( $N \rightarrow \infty$ ) and numerical ( $N = 50$ ) solutions for the ground state of Hamiltonian (46). The QPT critical points  $\lambda_{\text{I} \leftrightarrow \text{II}}^{(0)} = \epsilon/2$  and  $\lambda_{\text{II} \leftrightarrow \text{III}}^{(0)} = 3\epsilon/2$ , are clearly marked in the case of the variational curve, with a jump from rank 1 to rank 2 at  $\lambda = \epsilon/2$  and another jump from rank 2 to rank 4 (3 in the case of 1 qutrit RDMs) at  $\lambda = 3\epsilon/2$ . In the case of the numerical curve, where a small threshold has been applied to the eigenvalues to suppress spurious oscillations, the first jump continues to be at  $\lambda \simeq 0.5$ , whereas the second jump takes place at slightly larger values of  $\lambda = 1.5$  (in  $\epsilon = 1$  units). This behaviour is the same as with other precursors of QPTs, like susceptibility of fidelity in the 3-level LMG model [23].

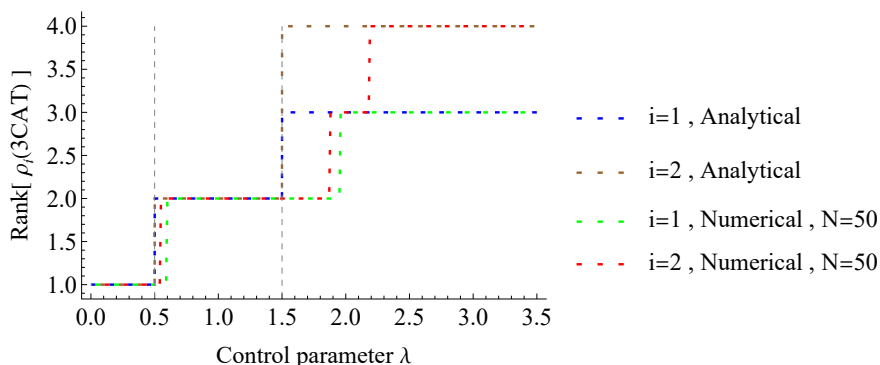


FIG. 7: Plot of rank of 1-quDit and 2-quDit RDMs along the stationary curve both for analytical (variational,  $N \rightarrow \infty$ ) and numerical ( $N = 50$ ) solution of the 3-level LMG model as a function of  $\lambda$  (in  $\epsilon = 1$  units).

From this, it is clear that the rank of the RDMs is a good precursor of a QPT, with the advantage of being a discrete parameter.

## VI. CONCLUSIONS

In this paper we have used an information-theoretic tool like the information diagrams to extract qualitative information about the quDit entanglement (and rank) of parity adapted  $U(D)$ -spin coherent states (DCATS) using one- and two-quDit reduced density matrices, and we have applied it to the study of atom entanglement in the ground state (both variational, in the  $N \rightarrow \infty$ , and numerical, with finite  $N$ ) of the 3-level atom LMG model.

We have shown how the allowed region  $\Delta$  of information diagrams is completely filled in the case of one-qutrit RDMs, while only the lower part of it is partially filled in the case of two-qutrits RDMs. This indicates that the maximum pairwise (2-qutrit) entanglement attained in a 3CAT state is smaller than the maximum one corresponding to a maximally mixed RDM or order  $3^2$ . We have already seen that this maximally entangled 3CAT is attained for the values  $(\alpha, \beta) = (1, 1)$  (or  $\alpha = 1$  for  $D = 2$ ), and these are precisely the values obtained for the variational analytical approximation to the ground state of a 3-level LMG model in the high coupling regime.

In addition, we have shown that the variational curve  $(\alpha_0(\lambda), \beta_0(\lambda))$  practically all the time lies in the inferior part of the information diagram subregion filled by all 3CAT states. We conjecture that this is due to the variational character of these states (minimum of the energy surface (47)) and the universality character of the extremal states lying at the boundary of the region  $\Delta$ .

Information diagrams also provide qualitative information about the rank of the RDMs. This has motivated us to study with detail their rank for different values of the parameters  $\alpha$  and  $\beta$  of 3CAT states (see Section IV), indicating that the one- and two-quDit RDMs have in general lower ranks than the maximal rank allowed by the corresponding dimension. Focusing on the variational analytic curve  $(\alpha_0(\lambda), \beta_0(\lambda))$ , and in the numerical solution for the ground state for finite  $N$ , Figure 7 shows that the rank of one- and two-qutrit RDMs has jumps precisely at the points where QPTs occurs (or near these values in the numerical finite  $N$  case). Therefore the rank can be used as a discrete precursor of a QPT in the LMG model, but this conclusion can be probably extended to other critical models.

All these results motivate us to further study the application of information diagrams and rank of RDMs to other parity adapted  $U(D)$ -spin coherent states, but with different parity character. Here we have restricted ourselves to the even case, but remember that there are  $2^{D-1}$  different parity adapted  $U(D)$ -spin coherent states, the even one just being a particular case. For example, odd parity cat states (for  $D = 2$ ) are known to be well suited as variational states to approximate excited states in, for example, the Dicke model of superradiance [25].

Since the rank of a RDM is equal to the Schmidt number, by the Schmidt decomposition theorem (see, for instance [26]), it would be interesting to study with detail the Schmidt decomposition of parity adapted  $U(D)$ -spin coherent states (not only of the even one, but for all  $2^{D-1}$  parity invariant states) when we extract 1, 2, or in general  $M$  quDits, and find the basis realizing the Schmidt decomposition in the larger factor.

## ACKNOWLEDGMENTS

We thank the support of the Spanish MICINN through the project PGC2018-097831-B-I00 and Junta de Andalucía through the projects SOMM17/6105/UGR, UHU-1262561, FQM-381 and FEDER/UJA-1381026. AM thanks the Spanish MIU for the FPU19/06376 predoctoral fellowship.

## REFERENCES

- [1] M. Feder and N. Merhav, Relations between entropy and error probability, *IEEE Transactions on Information Theory* **40**, 259 (1994).
- [2] P. Harremoës and F. Topsøe, Inequalities between entropy and index of coincidence derived from information diagrams, *IEEE Transactions on Information Theory* **47**, 2944 (2001).
- [3] T.-C. Wei, K. Nemoto, P. M. Goldbart, P. G. Kwiat, W. J. Munro, and F. Verstraete, Maximal entanglement versus entropy for mixed quantum states, *Phys. Rev. A* **67**, 022110 (2003).
- [4] R. Juárez-Amaro, L. M. Rosales, J. A. Anaya-Contreras, A. Zúñiga-Segundo, and H. M. Moya-Cessa, Relation between the entropy and the linear entropy in the ion-laser interaction, *Journal of Modern Optics* **67**, 805 (2020), <https://doi.org/10.1080/09500340.2020.1772393>.
- [5] D. Berry and B. Sanders, Bounds on general entropy measures, *J. Phys. A: Math. Gen.* **36**, 12255 (2003).
- [6] V. Dodonov, I. Malkin, and V. Man'ko, Even and odd coherent states and excitations of a singular oscillator, *Physica* **72**, 597 (1974).
- [7] B. M. Terhal and P. Horodecki, Schmidt number for density matrices, *Phys. Rev. A* **61**, 040301 (2000).
- [8] M. Calixto, A. Mayorgas, and J. Guerrero, Entanglement and  $U(D)$ -spin squeezing in symmetric multi-qudit systems and applications to quantum phase transitions in Lipkin–Meshkov–Glick  $D$ -level atom models, *Quantum Information Processing* **20**, 304 (2021).

- [9] J. M. Radcliffe, Some properties of coherent spin states, *Journal of Physics A: General Physics* **4**, 313 (1971).
- [10] F. T. Arecchi, E. Courtens, R. Gilmore, and H. Thomas, Atomic coherent states in quantum optics, *Phys. Rev. A* **6**, 2211 (1972).
- [11] M. Calixto, E. Romera, and R. del Real, Parity-symmetry-adapted coherent states and entanglement in quantum phase transitions of vibron models, *Journal of Physics A: Mathematical and Theoretical* **45**, 365301 (2012).
- [12] M. Calixto and F. Pérez-Bernal, Entanglement in shape phase transitions of coupled molecular bendings, *Phys. Rev. A* **89**, 032126 (2014).
- [13] S. Cordero, E. Nahmad-Achar, R. López-Peña, and O. Castaños, Polychromatic phase diagram for  $n$ -level atoms interacting with  $\ell$  modes of an electromagnetic field, *Phys. Rev. A* **92**, 053843 (2015).
- [14] R. López-Peña, S. Cordero, E. Nahmad-Achar, and O. Castaños, Symmetry adapted coherent states for three-level atoms interacting with one-mode radiation, *Physica Scripta* **90**, 068016 (2015).
- [15] X. Wang and K. Mølmer, Pairwise entanglement in symmetric multi-qubit systems, *The European Physical Journal D* **18**, 385 (2002).
- [16] V. Bužek, A. Vidiella-Barranco, and P. L. Knight, Superpositions of coherent states: Squeezing and dissipation, *Phys. Rev. A* **45**, 6570 (1992).
- [17] M. Calixto, O. Castaños, and E. Romera, Entanglement and quantum phase diagrams of symmetric multi-qubit systems, *Journal of Statistical Mechanics: Theory and Experiment* **2017**, 103103 (2017).
- [18] S. Gnutzmann and M. Kuś, Coherent states and the classical limit on irreducible  $su_3$  representations, *Journal of Physics A: Mathematical and General* **31**, 9871 (1999).
- [19] S. Gnutzmann, F. Haake, and M. Kuś, Quantum chaos of  $su_3$  observables, *Journal of Physics A: Mathematical and General* **33**, 143 (1999).
- [20] D. C. Meredith, S. E. Koonin, and M. R. Zirnbauer, Quantum chaos in a schematic shell model, *Phys. Rev. A* **37**, 3499 (1988).
- [21] W.-G. Wang, F. M. Izrailev, and G. Casati, Structure of eigenstates and local spectral density of states: A three-orbital schematic shell model, *Phys. Rev. E* **57**, 323 (1998).
- [22] P. Leboeuf and M. Saraceno, Eigenfunctions of non-integrable systems in generalised phase spaces, *Journal of Physics A: Mathematical and General* **23**, 1745 (1999).
- [23] M. Calixto, A. Mayorgas, and J. Guerrero, Role of mixed permutation symmetry sectors in the thermodynamic limit of critical three-level Lipkin-Meshkov-Glick atom models, *Phys. Rev. E* **103**, 012116 (2021).
- [24] W.-M. Zhang, D. H. Feng, and R. Gilmore, Coherent states: Theory and some applications, *Rev. Mod. Phys.* **62**, 867 (1990).
- [25] O. Castaños, E. Nahmad-Achar, R. López-Peña, and J. G. Hirsch, Superradiant phase in field-matter interactions, *Phys. Rev. A* **84**, 013819 (2011).
- [26] M. Huber and J. I. de Vicente, Structure of multidimensional entanglement in multipartite systems, *Phys. Rev. Lett.* **110**, 030501 (2013).

## 2.3 Phase space and parity adapted DSCS in symmetric multi-quDit systems

<sup>4</sup> A. Mayorgas, J. Guerrero, and M. Calixto, “Localization measures of parity adapted  $U(D)$ -spin coherent states applied to the phase space analysis of the  $D$ -level lipkin-meshkov-glick model”, Phys. Rev. E 108, 024107 (2023).

### Quality metrics JCR

- Year: 2022
- Category: PHYSICS, MATHEMATICAL
- Journal Impact Factor (JIF): 2.4
- JIF Rank: 11/56 (Q1)

Publication citations in Google Scholar (March 2024): 0

# Localization measures of parity adapted $U(D)$ -spin coherent states applied to the phase space analysis of the $D$ -level Lipkin-Meshkov-Glick model

Alberto Mayorgas\*

*Department of Applied Mathematics, University of Granada, Fuentenueva s/n, 18071 Granada, Spain*

Julio Guerrero†

*Department of Mathematics, University of Jaen,  
Campus Las Lagunillas s/n, 23071 Jaen, Spain and  
Institute Carlos I of Theoretical and Computational Physics (iC1),  
University of Granada, Fuentenueva s/n, 18071 Granada, Spain*

Manuel Calixto‡

*Department of Applied Mathematics, University of Granada, Fuentenueva s/n, 18071 Granada, Spain and  
Institute Carlos I of Theoretical and Computational Physics (iC1),  
University of Granada, Fuentenueva s/n, 18071 Granada, Spain*

(Dated: May 22, 2023)

## ABSTRACT

We study phase-space properties of critical, parity symmetric,  $N$ -quDit systems undergoing a quantum phase transition (QPT) in the thermodynamic  $N \rightarrow \infty$  limit. The  $D = 3$  level (qutrit) Lipkin-Meshkov-Glick (LMG) model is eventually examined as a particular example. For this purpose, we consider  $U(D)$ -spin coherent states (DSCS), generalizing the standard  $D = 2$  atomic coherent states, to define the coherent state representation  $Q_\psi$  (Husimi function) of a symmetric  $N$ -quDit state  $|\psi\rangle$  in the phase space  $\mathbb{C}P^{D-1}$  (complex projective manifold). DSCS are good variational approximations to the ground state of a  $N$ -quDit system, specially in the  $N \rightarrow \infty$  limit, where the discrete parity symmetry  $\mathbb{Z}_2^{D-1}$  is spontaneously broken. For finite  $N$ , parity can be restored by projecting DSCS onto  $2^{D-1}$  different parity invariant subspaces, which define generalized “Schrödinger cat states” reproducing quite faithfully low-lying Hamiltonian eigenstates obtained by numerical diagonalization. Precursors of the QPT are then visualized for finite  $N$  by plotting the Husimi function of these parity projected DSCS in phase space, together with their Husimi moments and Wehrl entropy, in the neighborhood of the critical points. These are good localization measures and markers of the QPT.

## I. INTRODUCTION

Information theoretic and statistical measures together with phase space methods have proved to be useful in the description and characterization of quantum phase transitions (QPTs). For example, in the traditional Anderson metal-insulator transition [1–3], where Hamiltonian eigenfunctions underlie strong fluctuations. Phase space methods are a fundamental tool in quantum optics [4], providing connections between quantum mechanics (in the so-called Wigner/Weyl/Moyal scheme [5]) and classical statistical mechanics. This connection is often established through (quasi-classical, minimum uncertainty) coherent states (CSs). The best known CSs are the canonical (harmonic oscillator) CSs introduced long time ago by Schrödinger [6] and later used by Glauber to

study the radiation field [7]. Canonical CSs are linked to the Heisenberg-Weyl group (with the typical Lie algebra canonical commutation relations  $[q, p] = i\hbar$ ) and can be seen as a group action/displacement on the vacuum. Replacing the Heisenberg-Weyl group by the rotation group  $SU(2)$  (with angular momentum commutation relations  $[J_x, J_y] = i\hbar J_z$  and cyclic permutations), we get the so called spin- $j$ , atomic or Bloch CSs [8, 9]. From this perspective, generalizations to arbitrary (finite-dimensional) Lie groups  $G$  provide further families of CSs (we address the reader to the standard reference [10]). In particular, this article is involved with the generalization from  $U(2)$  to  $U(D)$ , which is in the heart of the generalization from qubits (physically represented by two-level/component atom/particle quantum systems) to quDits ( $D$ -level quantum systems).

Canonical CSs provide complex analytic (Bargmann, phase space) representations of quantum states and operators in quantum mechanics [11]. Among all phase-space quasi-probability distribution functions (playing a role similar to genuine probability distributions of statistical

---

\* albmayer97@ugr.es

† jguerrer@ujaen.es

‡ calixto@ugr.es

mechanics), the more popular are Wigner  $W$ , Husimi  $Q$  and Glauber-Sudarshan  $P$  (also called Berezin's covariant and contravariant symbols, respectively) functions, usually associated with the symmetric, antinormal and normal ordering of position and momentum operators, respectively [4, 12, 13]. Although Wigner function is perhaps more popular, Husimi function can be more easily extended to general phase spaces associated to coset spaces  $X = G/H$  of a symmetry Lie group  $G$  for an isotropy subgroup  $H \subset G$ . This will be our case, with  $G = U(D)$  the unitary group of degree  $D$ , and phase space  $X = U(D)/U(D-1) = \mathbb{C}P^{D-1}$  the complex projective space generalizing the Bloch sphere  $S^2 = \mathbb{C}P^1$  for  $D = 2$ . This case is linked to the totally symmetric (bosonic) representation of  $U(D)$ , to which we are going to restrict ourselves here (see [14] for other phase spaces like the flag manifold  $U(D)/U(1)^D$  linked to more general fermion mixtures and Young tableaux).

Given a CS system  $\{|z\rangle, z \in X\}$ , the Husimi function of a density matrix  $\rho$  is the phase space  $X$  valued function  $Q_\rho(z) = \langle z|\rho|z\rangle$ . In an attempt to build bridges between classical and quantum entropies, and even though  $Q_\rho(z)$  is only a semiclassical quasi-probability distribution function, a semiclassical Shannon-like entropy was defined by Wehrl [15] as  $S_W(\rho) = -\int Q_\rho(z) \log Q_\rho(z) d\mu_X(z)$ , with  $d\mu_X(z)$  a  $G$ -invariant measure on the phase space  $X$ . Wehrl's entropy measures the area occupied by the quantum state  $\rho$  in phase space; actually, moments  $M_\nu$  of  $Q_\rho$  (and their associated Rényi-Wehrl entropies [16–18]), like the so called inverse participation ratio  $M_2$ , also measure the localization of  $\rho$  in phase space and are easier to compute. Some early works where these measures were studied are [19, 20]. They have also been employed recently in other systems [21–25]

For a critical quantum system described by a Hamiltonian  $H(\lambda)$  depending on a control parameter  $\lambda$ , abrupt changes in the Wehrl entropy of the ground state (as a function of  $\lambda$ ) usually provide good indicators of the existence of a quantum phase transition (QPT) around a critical point  $\lambda_c$ , even for a finite number  $N$  of particles. Moreover, Wehrl entropy can be also used to identify the order of a QPT [26], as an alternative definition to the standard Ehrenfest classification based on discontinuities of the derivatives of the ground state energy density with respect to  $\lambda$  in the thermodynamic limit  $N \rightarrow \infty$ . Husimi function and its Wehrl entropy have already given a good phase space description of interesting quantum critical systems like Bose-Einstein condensates [27], the Dicke model of superradiance for two-level [28, 29] and three-level [30] atoms, the  $U(3)$  vibron model of molecular benders [31], the  $U(4)$  bilayer quantum Hall system [32], the  $U(2)$  (two-level) ubiquitous Lipkin-Meshkov-Glick (LMG) model [33–35], etc. Here we want to extend the scope of applicability of these phase space methods to symmetric multi-quDit systems (like  $D$ -level atom models) described by a  $U(D)$  invariant LMG model. In addition to the obvious technical complication,  $U(D)$  provides some novelties and a much

richer structure that is not possible to grasp starting from  $U(2)$ . In particular, the standard discrete parity symmetry group  $\mathbb{Z}_2 = \{0, 1\}$ , which is spontaneously broken in the thermodynamic limit for second order QPTs of  $D = 2$  level systems, now becomes  $\mathbb{Z}_2^{D-1}$  and provides more case studies of Schrödinger cat states than the standard even and odd ones of the literature [36–39], in the sense of quantum superpositions of weakly overlapping quasiclassical (coherent) states, the most symmetric one mimicking the structure of the ground state in the highly interacting quantum phase (see later in Section V and [40] for previous studies on Dicke models of three-level atoms interacting with one-mode radiation field).

The organization of the article is as follows. In Sec. II we introduce the  $D$ -level LMG model and particularize it for the cases  $D = 2$  (qubits) and  $D = 3$  (qutrits). A brief discussion about the Fock basis and the discrete parity symmetry  $\mathbb{Z}_2^{D-1}$  is also included. In Sec. III we define  $U(D)$ -spin coherent states  $|\mathbf{z}\rangle$  (DSCSs for brevity) labelled by points  $\mathbf{z} \in \mathbb{C}P^{D-1}$  in phase space; we also compute the DSCS matrix elements  $\langle \mathbf{z}|S_{ij}|\mathbf{z}'\rangle$  of  $U(D)$ -spin operators  $S_{ij}$ ,  $i, j = 1, \dots, D$ , and we project DSCSs  $|\mathbf{z}\rangle$  into the  $2^{D-1}$  invariant subspaces  $\mathfrak{c}$  of the parity symmetry group  $\mathbb{Z}_2^{D-1}$ , introducing the notion of “ $\mathfrak{c}$ -parity  $U(D)$  Schrödinger cat states”  $|\mathbf{z}\rangle_{\mathfrak{c}}$  (called  $\mathfrak{c}$ -DCAT states, for short). Then, in Sec. IV, the traditional Husimi function  $Q_\psi(z) = |\langle z|\psi\rangle|^2$  of a quantum state  $|\psi\rangle$  in the standard phase space  $\mathbb{C} \ni z$  (for canonical, harmonic oscillator or Heisenberg-Weyl coherent states) is extended to the phase space  $\mathbb{C}P^{D-1} \ni \mathbf{z}$  using DSCSs  $|\mathbf{z}\rangle$  and a convenient Haar integration measure, which allows to define  $\nu$ -moments of the Husimi function and the Wehrl entropy as useful localization measures in phase space. These measures are computed in the case of DSCS and  $\mathfrak{c}$ -DCAT states, including their thermodynamic limit  $N \rightarrow \infty$ . The Appendices B and C show in more detail some of the long calculations of this section. In Sec. V we focus on the  $D = 3$  level LMG Hamiltonian for symmetric qutrits and the minimization of its energy surface in the limit  $N \rightarrow \infty$  using DSCSs as variational states. The degeneration of the ground state in the thermodynamic limit and the QPTs make their apparition here, but are not discussed in depth until the next two sections. In Sec. VI, the variational ground state obtained in the previous section is projected on parity  $\mathfrak{c}$  subspaces and the corresponding  $\mathfrak{c}$ -DCATs are compared to the low-lying Hamiltonian eigenstates of the LMG model obtained by numerical diagonalization for finite  $N$ . This procedure (projection after energy minimization) provides a fairly good variational approximation to the ground state in terms of the completely even,  $\mathfrak{c} = 0$ , DCAT state, but not so precise for first excited states in terms of DCAT states of other parities  $\mathfrak{c}$ , for which we try a proper overlap maximization (fidelity) procedure. In Sec. VII, the Husimi function and the localization measures of the Sec. IV are employed to visualize how the variational and the numerical eigenstates split into Gaussian-like wave packets throughout the three different quantum phases of the

$D = 3$  level LMG model. The Inverse Participation Ratio (Husimi second moment) and the Wehrl entropy are also used to quantify the overlap of these packets, and hence the localization/spread of the low-lying Hamiltonian eigenstates in phase space is compared to that of DSCS and c-DCAT variational states. Finally, in Sec. VIII we present the main conclusions of this work.

## II. $D$ -LEVEL LMG MODEL HAMILTONIAN AND PARITY SYMMETRY

The original ( $D = 2$  levels/modes) LMG schematic shell model appeared in nuclear physics [41–43] to describe the quantum phase transition from spherical to deformed shapes in nuclei. Since then, it is an ubiquitous model that appears in a multitude of physical contexts. For example, the Hamiltonian of an anisotropic XY Ising model, with  $\mu = 1, \dots, N$  lattice sites, in an external transverse magnetic field  $\varepsilon$  with infinite-range constant interactions

$$H_{XY} = \varepsilon \sum_{\mu=1}^N \sigma_z^{(\mu)} + \sum_{\mu < \nu} \lambda_x \sigma_x^{(\mu)} \sigma_x^{(\nu)} + \sum_{\mu < \nu} \lambda_y \sigma_y^{(\mu)} \sigma_y^{(\nu)}, \quad (1)$$

[ $\sigma_{x,y,z}^{(\mu)}$  denote the Pauli matrices at site  $\mu$ ] adopts the form of the two-level LMG schematic shell model Hamiltonian [41, 42]

$$H_2 = \varepsilon J_z + \frac{\lambda_1}{2} (J_+^2 + J_-^2) + \frac{\lambda_2}{2} (J_+ J_- + J_- J_+) \quad (2)$$

when written in terms of the SU(2) angular momentum collective operators

$$\vec{J} = (J_x, J_y, J_z) = \sum_{\mu=1}^N (\sigma_x^{(\mu)}, \sigma_y^{(\mu)}, \sigma_z^{(\mu)}), \quad (3)$$

and  $J_{\pm} = (J_x \pm iJ_y)/2$ , as usual. We could also think of a model describing a system of  $N$  interacting two-level identical atoms (symmetric “qubits”). Long-range constant interactions make this Hamiltonian translation invariant, that is, it is symmetric under permutation of lattice sites  $\mu \leftrightarrow \nu$  (or permutation of atoms/qubits). Therefore, the Hamiltonian does not couple different angular momentum sectors  $j = N/2, N/2 - 1, \dots, 1/2$  or 0 (for odd or even  $N$ , respectively) and it is a common practice to restrict oneself to the largest (fully symmetric) sector  $j = N/2$  to which the ground state of the system belongs. This restriction reduces the size of the Hamiltonian matrix to be diagonalized from  $2^N$  to  $N + 1 = 2j + 1$  and assumes that  $D = 2$ -level atoms/qubits are indistinguishable. For this case, it is convenient to use a Jordan-Schwinger realization of angular momentum operators in terms of bilinear products of bosonic creation  $a_i^\dagger$  and annihilation  $a_j$  operators as

$$S_{ij} = a_i^\dagger a_j, \quad i, j = 0, \dots, D - 1, \quad (4)$$

where we are already extending to arbitrary  $D$ -level atom systems with U( $D$ ) symmetry. For example, for  $D = 2$  we recover  $J_+ = S_{10}, J_- = S_{01}, J_z = \frac{1}{2}(S_{11} - S_{00})$  and the conserved total number  $N$  of particles  $C_1 = S_{00} + S_{11}$  [the linear Casimir operator of U(2)]. U( $D$ )-spin operators  $S_{ij}$  fulfill the commutation relations

$$[S_{ij}, S_{kl}] = \delta_{jk} S_{il} - \delta_{il} S_{kj}. \quad (5)$$

The LMG Hamiltonian  $H_2$  in (2) for  $D = 2$  level systems is generalized to arbitrary  $D$  levels as

$$H_D = \sum_{i=0}^{D-1} \varepsilon_i (S_{i+1, i+1} - S_{ii}) + \sum_{i \neq j=0}^{D-1} (\lambda_1 S_{ij}^2 + \lambda_2 S_{ij} S_{ji}), \quad (6)$$

where  $\varepsilon_i$  now denotes the energy gap between levels  $i$  and  $i + 1$ . The  $\lambda_1$  interaction term annihilates pairs of particles in one level and creates pairs in other level, whereas the  $\lambda_2$  term scatters one particle from  $i \rightarrow j$  while another is scattered back from  $j \rightarrow i$ . The total number of particles  $N = \sum_{i=0}^{D-1} S_{ii}$  (the linear Casimir operator of U( $D$ )) is conserved. For the sake of simplicity, we shall consider  $\lambda_2 = 0$  and  $\varepsilon_i = \varepsilon$  (same energy spacing between levels). Since we are interested in the thermodynamic limit  $N \rightarrow \infty$ , we shall also renormalize one-body interactions  $\varepsilon \rightarrow \varepsilon/N$  by the total number  $N$  of particles, and two-body interactions  $\lambda_2 \rightarrow -\lambda/[N(N-1)]$  by the total number  $N(N-1)$  of pairs, so that the final Hamiltonian density for us becomes

$$H = \frac{\varepsilon}{N} (S_{D-1, D-1} - S_{00}) - \frac{\lambda}{N(N-1)} \sum_{i \neq j=0}^{D-1} S_{ij}^2. \quad (7)$$

We shall measure energy in  $\varepsilon > 0$  units, and discuss the energy spectrum and the phase diagram in terms of the control parameter  $\lambda$  (see later in Section V). There are already some studies in the literature of this Hamiltonian for  $D = 3$  level atoms and its chaotic behavior (see e.g. [14, 44–49]).

We shall consider indistinguishable atoms, so that the Hilbert space dimension reduces from  $D^N$  to  $\binom{N+D-1}{D-1}$ , the dimension of the fully symmetric irreducible representation of U( $D$ ) (which coincides with the total number of compositions of  $N$  into  $D$  non-negative integers when order does not matter). This restriction considerably reduces the computational complexity for large number of particles  $N$  (see [14] for the role played by other mixed permutation symmetry sectors in the thermodynamic limit  $N \rightarrow \infty$ ). Therefore, the Hilbert space is spanned by the Bose-Einstein-Fock basis states ( $|\vec{0}\rangle$  denotes the Fock vacuum)

$$|\vec{n}\rangle = |n_0, \dots, n_{D-1}\rangle = \frac{(a_0^\dagger)^{n_0} \dots (a_{D-1}^\dagger)^{n_{D-1}}}{\sqrt{n_0! \dots n_{D-1}!}} |\vec{0}\rangle, \quad (8)$$

where  $n_i$  denotes the occupancy number of level  $i$  (the eigenvalue of  $S_{ii}$ ), with the restriction  $n_0 + \dots + n_{D-1} =$

$N$  (the total number of atoms/quDits). In the low-interaction regime  $\lambda \ll 1$ , the ground state of (7) is a Bose-Einstein condensate  $\frac{1}{\sqrt{N!}}(a_0^\dagger)^N|\vec{0}\rangle$  of  $N$  atoms in the  $i = 0$  level, which we shall take as a reference level from now on.

These Fock states are the natural generalization of angular momentum  $j = N/2$  Dicke states  $|j, m\rangle$  with angular momentum third component  $m = -j, \dots, j$ ; more explicitly

$$|j, m\rangle = |n_0 = j + m, n_1 = j - m\rangle, \quad (9)$$

so that  $m = (n_0 - n_1)/2$  (the eigenvalue of  $J_z = \frac{1}{2}(S_{11} - S_{00})$ ) represents the population imbalance between levels  $i = 0$  and  $i = 1$ . The expansion of a general symmetric  $N$ -quDit state  $\psi$  in the Fock basis will be written as

$$|\psi\rangle = \sum_{\|\vec{n}\|_1=N} c_{\vec{n}}|\vec{n}\rangle, \quad (10)$$

where the sum is restricted to  $\|\vec{n}\|_1 = n_0 + \dots + n_{D-1} = N$ . Collective  $U(D)$ -spin operators (4) matrix elements in the Fock basis are easily computed as

$$\langle \vec{m} | S_{ii} | \vec{n} \rangle = n_i \delta_{\vec{m}, \vec{n}}, \quad (11)$$

$$\langle \vec{m} | S_{ij} | \vec{n} \rangle = \sqrt{(n_i + 1)n_j} \delta_{m_i, n_i+1} \delta_{m_j, n_j-1} \prod_{k \neq i \neq j} \delta_{m_k, n_k}.$$

At this point, we would like to highlight the existence of an interesting parity symmetry. Indeed, this symmetry of the Hamiltonian has to do with the fact that the interaction only scatters pairs of particles, thus conserving the parity  $\Pi_j = \exp(i\pi S_{jj})$ , even (+) or odd (-), of the population  $S_{jj}$  in each level  $j = 0, \dots, D-1$ . Note that  $\Pi_j|\vec{n}\rangle = (-1)^{n_j}|\vec{n}\rangle$ , and therefore we have the constraint  $\Pi_0 \dots \Pi_{D-1}|\vec{n}\rangle = (-1)^N|\vec{n}\rangle$  which allows to write for example  $\Pi_0 = (-1)^N \Pi_1 \dots \Pi_{D-1}$ . Hence, this discrete parity symmetry corresponds to the finite group  $\mathbb{Z}_2^{D-1} = \mathbb{Z}_2 \times \dots \times \mathbb{Z}_2$ , with  $\mathbb{Z}_2 = \{0, 1\}$  the usual parity group (the cyclic group of order 2). Consequently, energy eigenstates have well defined parity under  $\mathbb{Z}_2^{D-1}$ . We will see later in Sec. V that low-lying Hamiltonian eigenstates with different parities collapse in the thermodynamic  $N \rightarrow \infty$  limit, giving rise to a degenerate ground state as a consequence of a spontaneous breakdown of the parity symmetry  $\mathbb{Z}_2^{D-1}$ .

Let us denote by the binary string  $\mathfrak{b} = [b_1, \dots, b_{D-1}] \in \{0, 1\}^{D-1}$  one of the  $2^{D-1}$  elements of the parity group  $\mathbb{Z}_2^{D-1}$ . There are  $2^{D-1}$  parity invariant subspaces labeled by the inequivalent group characters  $\mathfrak{c} = [c_1, \dots, c_{D-1}] \in \{0, 1\}^{D-1}$  of the Pontryagin dual group  $\widehat{\mathbb{Z}_2^{D-1}} \sim \mathbb{Z}_2^{D-1}$ . The projectors onto these invariant subspaces of definite parity  $\mathfrak{c}$  are given by

$$\Pi_{\mathfrak{c}} = 2^{1-D} \sum_{\mathfrak{b} \in \{0, 1\}^{D-1}} (-1)^{\mathfrak{c} \cdot \mathfrak{b}} \Pi^{\mathfrak{b}}, \quad (12)$$

with  $\mathfrak{c} \cdot \mathfrak{b} = c_1 b_1 + \dots + c_{D-1} b_{D-1}$  and

$$\Pi^{\mathfrak{b}} \equiv \Pi_1^{b_1} \dots \Pi_{D-1}^{b_{D-1}}. \quad (13)$$

Note that

$$\sum_{\mathfrak{c} \in \{0, 1\}^{D-1}} \Pi_{\mathfrak{c}} = I, \quad (14)$$

the identity  $I$  in the representation space. For example, for  $D = 2$  we have just  $\Pi_0 = \Pi_{\text{even}}$  and  $\Pi_1 = \Pi_{\text{odd}}$  the standard projectors on even and odd parities, with  $I = \Pi_{\text{even}} + \Pi_{\text{odd}}$ . For general  $D$ , we sometimes shall single out the totally even  $0 = [0, \dots, 0]$  and totally odd  $1 = [1, \dots, 1]$  parity representations.

### III. $U(D)$ -SPIN COHERENT STATES AND ADAPTATION TO PARITY

#### A. $U(D)$ -spin coherent states

$U(D)$ -spin coherent states (DSCSs for brevity) are defined as a generalization of standard binomial (two-mode)  $U(2)$ -spin coherent states to the multinomial ( $D$ -mode) case as

$$|\mathbf{z}\rangle^{(N)} = \frac{1}{\sqrt{N!}} \left( \frac{a_0^\dagger + z_1 a_1^\dagger + \dots + z_{D-1} a_{D-1}^\dagger}{\sqrt{1 + |z_1|^2 + \dots + |z_{D-1}|^2}} \right)^N |\vec{0}\rangle, \quad (15)$$

so that they are labeled by  $D-1$  complex numbers  $z_j \in \mathbb{C}$  arranged in the column vector  $\mathbf{z} = (z_1, z_2, \dots, z_{D-1})^t \in \mathbb{C}^{D-1}$ . Properly speaking, this really corresponds to a certain patch of the complex projective manifold  $\mathbb{C}P^{D-1}$ , which results when choosing  $i = 0$  as a reference level; see e.g. [50] for more information about other choices and patches. DSCSs are also labeled by the total number of particles  $N$  [also labelling a specific symmetric representation of  $U(D)$ ], which will be omitted as superscript in eq.(15) to simplify the notation, i.e.  $|\mathbf{z}\rangle \equiv |\mathbf{z}\rangle^{(N)}$ .

DSCSs  $|\mathbf{z}\rangle$  have the form of a Bose-Einstein condensate of  $D$  modes, generalizing the spin  $U(2)$  (binomial) coherent states of two modes introduced by [51] and [9] long time ago. If we take  $i = 0$  as a reference energy level, then the state  $|\mathbf{z} = \mathbf{0}\rangle$  would be the ground state, whereas general  $|\mathbf{z}\rangle$  could be seen as coherent excitations. The coefficients  $c_{\vec{n}}(\mathbf{z})$  of the expansion (10) of  $|\psi\rangle = |\mathbf{z}\rangle$  in the Fock basis are simply

$$c_{\vec{n}}(\mathbf{z}) = \sqrt{\frac{N!}{\prod_{i=0}^{D-1} n_i!}} \frac{\prod_{i=1}^{D-1} z_i^{n_i}}{(1 + \mathbf{z}^\dagger \mathbf{z})^{N/2}}, \quad (16)$$

where  $\mathbf{z}^\dagger \mathbf{z} = |z_1|^2 + \dots + |z_{D-1}|^2$  denotes the standard scalar product in  $\mathbb{C}^{D-1}$ .

In general, DSCSs are not orthogonal since the scalar product

$$\langle \mathbf{z} | \mathbf{z}' \rangle = \frac{(1 + \mathbf{z}^\dagger \mathbf{z}')^N}{(1 + \mathbf{z}^\dagger \mathbf{z})^{N/2} (1 + \mathbf{z}'^\dagger \mathbf{z}')^{N/2}} \quad (17)$$

is not necessarily zero. However, they are a overcomplete

set of states closing a resolution of the identity

$$1 = \int_{\mathbb{C}^{D-1}} |\mathbf{z}\rangle\langle\mathbf{z}| d\mu(\mathbf{z}), \quad (18)$$

$$d\mu(\mathbf{z}) = \frac{(D-1)!}{\pi^{D-1}} \binom{N+D-1}{N} \frac{d^2 z_1 \dots d^2 z_{D-1}}{(1+\mathbf{z}^\dagger \mathbf{z})^D},$$

with  $d^2 z_i = d\Re(z_i) d\Im(z_i)$  the Lebesgue measure on  $\mathbb{C}$  and  $d\mu(\mathbf{z})$  the Fubini-Study measure [16, 52] in the corresponding complex projective space. This closure relation of DSCSs will be important when discussing phase space constructions.

### B. Coherent state operator matrix elements

DSCS matrix elements of  $D$ -spin operators  $S_{ij}$  are easily computed from (11) and (16) and they are simply

$$\langle \mathbf{z}' | S_{ij} | \mathbf{z} \rangle = N z'_i z_j \frac{(1+\mathbf{z}'^\dagger \mathbf{z})^{N-1}}{(1+\mathbf{z}'^\dagger \mathbf{z}')^{N/2} (1+\mathbf{z}^\dagger \mathbf{z})^{N/2}}, \quad (19)$$

where we understand  $z_0 = 1 = z'_0$ . From here, DSCS matrix elements of quadratic powers of  $D$ -spin operators can be concisely written as

$$\langle \mathbf{z}' | S_{ij} S_{kl} | \mathbf{z} \rangle = \delta_{jk} \langle \mathbf{z}' | S_{il} | \mathbf{z} \rangle + \frac{N-1}{N} \frac{\langle \mathbf{z}' | S_{ij} | \mathbf{z} \rangle \langle \mathbf{z}' | S_{kl} | \mathbf{z} \rangle}{\langle \mathbf{z}' | \mathbf{z} \rangle}. \quad (20)$$

Note that

$$\lim_{N \rightarrow \infty} \frac{\langle \mathbf{z} | S_{ij} S_{kl} | \mathbf{z} \rangle}{\langle \mathbf{z} | S_{ij} | \mathbf{z} \rangle \langle \mathbf{z} | S_{kl} | \mathbf{z} \rangle} = 1, \quad (21)$$

which means that quantum fluctuations are negligible in the thermodynamic (classical) limit  $N \rightarrow \infty$ . We shall use these ingredients when computing energy surfaces in Section V.

### C. Parity adapted $U(D)$ -spin coherent states

DSCSs are sometimes called “quasi-classical” states. As we shall see in Section V,  $|\mathbf{z}\rangle$  turns out to be a good variational state, which reproduces the energy and wave function of the ground state of multilevel LMG atom models in the thermodynamic (classical) limit  $N \rightarrow \infty$ . However, DSCSs do not display the parity symmetry  $\mathbb{Z}_2^{D-1}$  of the LMG Hamiltonian, which is commented at the end of Section II. This parity symmetry is spontaneously broken in the thermodynamic limit  $N \rightarrow \infty$  due to the degeneration of the different parity states, but it should be restored for finite  $N$  to properly reproduce the ground (and excited) state wave function properties. A parity adaptation of DSCSs can be done by applying projectors  $\Pi_{\mathfrak{c}}$  in (12) on invariant subspaces of definite parity  $\mathfrak{c}$ . The effect of level  $i$  population parity operations

$\Pi_i = \exp(i\pi S_{ii})$  on DSCSs reduces to

$$\Pi_i |\mathbf{z}\rangle = |(z_1, \dots, -z_i, \dots, z_{D-1})\rangle. \quad (22)$$

That is,  $\Pi_i$  just changes the sign of  $z_i$  in  $|\mathbf{z}\rangle$ . Let us denote by

$$|\mathbf{z}\rangle^{\mathfrak{b}} = \Pi^{\mathfrak{b}} |\mathbf{z}\rangle = |((-1)^{b_1} z_1, \dots, (-1)^{b_{D-1}} z_{D-1})\rangle \equiv |\mathbf{z}^{\mathfrak{b}}\rangle, \quad (23)$$

with  $\Pi^{\mathfrak{b}}$  in (13), and by

$$|\mathbf{z}\rangle_{\mathfrak{c}} \equiv \frac{\Pi_{\mathfrak{c}} |\mathbf{z}\rangle}{\mathcal{N}(\mathbf{z})_{\mathfrak{c}}} = \frac{2^{1-D}}{\mathcal{N}(\mathbf{z})_{\mathfrak{c}}} \sum_{\mathfrak{b} \in \{0,1\}^{D-1}} (-1)^{\mathfrak{c} \cdot \mathfrak{b}} |\mathbf{z}^{\mathfrak{b}}\rangle, \quad (24)$$

with  $\Pi_{\mathfrak{c}}$  in (12), the normalized projection of  $|\mathbf{z}\rangle$  onto the parity  $\mathfrak{c}$  invariant subspace, with squared normalization factor

$$\mathcal{N}(\mathbf{z})_{\mathfrak{c}}^2 = 2^{1-D} \frac{\sum_{\mathfrak{b}} (-1)^{\mathfrak{c} \cdot \mathfrak{b}} (1+\mathbf{z}^\dagger \mathbf{z}^{\mathfrak{b}})^N}{(1+\mathbf{z}^\dagger \mathbf{z})^N}. \quad (25)$$

We will write  $|\mathbf{z}\rangle^{\mathfrak{b}} = |\mathbf{z}^{\mathfrak{b}}\rangle$  indistinctly, with  $\mathbf{z}^{\mathfrak{b}} = ((-1)^{b_1} z_1, \dots, (-1)^{b_{D-1}} z_{D-1})$  as defined in the eq.(23). The same as  $\Pi^{\mathfrak{b}}$  and  $\Pi_{\mathfrak{c}}$  denote different operators, do not confuse  $|\mathbf{z}\rangle^{\mathfrak{b}}$  with  $|\mathbf{z}\rangle_{\mathfrak{c}}$ , which can be seen as the dual Fourier (Walsh-Hadamard) transformed version of  $|\mathbf{z}\rangle^{\mathfrak{b}}$  with

$$\chi_{\mathfrak{c}}(\mathfrak{b}) = (-1)^{\mathfrak{c} \cdot \mathfrak{b}} = (-1)^{c_1 b_1 + \dots + c_{D-1} b_{D-1}} \quad (26)$$

the characters of the parity group  $\mathbb{Z}_2^{D-1}$ . The factors  $(-1)^{c_i b_i}$  are the analogue of the traditional discrete Fourier transform characters  $\chi_{\omega}(t) = e^{i\omega t}$ ,  $\omega, t = 0, \dots, M-1$  but for the additive group  $\mathbb{Z}_M$  of integers modulo  $M$  (or the multiplicative group of  $M$ -th roots of unity), with  $M = 2$  in our case. The characters (26) have some useful properties such as

$$\sum_{\mathfrak{c} \in \{0,1\}^{D-1}} \chi_{\mathfrak{c}}(\mathfrak{b}) = 2^{D-1} \delta_{\mathfrak{c},0}, \quad (27)$$

$$\chi_{\mathfrak{c}}(\mathfrak{b}) = \chi_{\mathfrak{b}}(\mathfrak{c}), \quad (28)$$

$$\chi_{\mathfrak{c}}(0) = 1, \quad (29)$$

$$\chi_{\mathfrak{c}}(\mathfrak{b}) \chi_{\mathfrak{c}'}(\mathfrak{b}) = \chi_{\mathfrak{c}+\mathfrak{c}'}(\mathfrak{b}). \quad (30)$$

The coefficients  $c_{\vec{n}}(\mathbf{z})_{\mathfrak{c}}$  of the expansion (10) of  $|\psi\rangle = |\mathbf{z}\rangle_{\mathfrak{c}}$  in the Fock basis can be derived from (24) and (16),

$$c_{\vec{n}}(\mathbf{z})_{\mathfrak{c}} = \frac{2^{1-D}}{\mathcal{N}(\mathbf{z})_{\mathfrak{c}}} \sum_{\mathfrak{b} \in \{0,1\}^{D-1}} (-1)^{(\mathfrak{c}+\mathfrak{n}) \cdot \mathfrak{b}} c_{\vec{n}}(\mathbf{z})$$

$$= \frac{1}{\mathcal{N}(\mathbf{z})_{\mathfrak{c}}} c_{\vec{n}}(\mathbf{z}) \delta_{\mathfrak{n},\mathfrak{c}}, \quad (31)$$

where  $\mathfrak{n} = [\text{mod}(n_1, 2), \dots, \text{mod}(n_{D-1}, 2)]$  is retrieved from  $\vec{n}$  removing  $n_0$  and expressing it in modulo 2, and  $\delta_{\mathfrak{n},\mathfrak{c}} = \delta_{\text{mod}(n_1,2),c_1} \dots \delta_{\text{mod}(n_{D-1},2),c_{D-1}}$  is the product of Kronecker deltas.

For  $D = 2$ , the parity adaptations  $|\mathbf{z}\rangle_{[0]} = |\mathbf{z}\rangle_+$  and  $|\mathbf{z}\rangle_{[1]} = |\mathbf{z}\rangle_-$  of a  $U(2)$ -spin coherent state  $|\mathbf{z}\rangle$  (for  $\mathbf{z} = (z_1) = z$ ) adopt the form

$$|\mathbf{z}\rangle_{\pm} = \frac{|z\rangle \pm |-z\rangle}{\sqrt{2 \pm 2 \left( \frac{1-|z|^2}{1+|z|^2} \right)^N}}, \quad (32)$$

and are sometimes called even (+) and odd (−) “Schrödinger cat states”, since they are a quantum superposition of weakly-overlapping (or distinguishable, i.e.  $\langle z| - z \rangle \xrightarrow{N \rightarrow \infty} 0$  for  $z \neq 0$ ) quasi-classical (minimal uncertainty) coherent wave packets. Hence, we shall name  $\mathfrak{c}$ -DCATs the  $\mathfrak{c}$ -parity adapted DSCSs  $|\mathbf{z}\rangle_{\mathfrak{c}}$  in (24) from now on.

Likewise, for  $D = 3$  we have  $2^{D-1} = 4$  parity sectors,

$$\mathfrak{c} = [c_1, c_2] \in \{[0, 0], [0, 1], [1, 0], [1, 1]\}, \quad (33)$$

and therefore four Schrödinger cat states associated to the DSCS  $|\mathbf{z}\rangle = |(z_1, z_2)\rangle$  adopting the explicit form

$$|\mathbf{z}\rangle_{\mathfrak{c}} = \frac{1}{4\mathcal{N}(\mathbf{z})_{\mathfrak{c}}} \left[ |(z_1, z_2)\rangle + (-1)^{c_1} |(-z_1, z_2)\rangle + (-1)^{c_2} |(z_1, -z_2)\rangle + (-1)^{c_1+c_2} |(-z_1, -z_2)\rangle \right], \quad (34)$$

with squared norm

$$\mathcal{N}(\mathbf{z})_{\mathfrak{c}}^2 = \frac{1}{4(1 + |z_1|^2 + |z_2|^2)^N} \left[ (1 + |z_1|^2 + |z_2|^2)^N + (-1)^{c_1} (1 - |z_1|^2 + |z_2|^2)^N + (-1)^{c_2} (1 + |z_1|^2 - |z_2|^2)^N + (-1)^{c_1+c_2} (1 - |z_1|^2 - |z_2|^2)^N \right]. \quad (35)$$

Note that there are at most  $2^{D-1}$  Schrödinger cat states  $|\mathbf{z}\rangle_{\mathfrak{c}}$  associated to a DSCS  $|\mathbf{z}\rangle$  for arbitrary  $\mathbf{z}$ . However, we can have  $\Pi_{\mathfrak{c}}|\mathbf{z}\rangle = 0$  and  $\mathcal{N}(\mathbf{z})_{\mathfrak{c}} = 0$  when  $c_i = 1$  and  $z_i = 0$ , so that the  $\mathfrak{c}$ -DCAT in (24) contains an indeterminate form of type “0/0”. For instance, in the previous example with  $D = 2$ , the odd 2CAT state becomes

$$\begin{aligned} \lim_{z \rightarrow 0} |\mathbf{z}\rangle_- &= \lim_{z \rightarrow 0} \frac{|z\rangle - |-z\rangle}{\sqrt{2 - 2 \left( \frac{1-|z|^2}{1+|z|^2} \right)^N}} \\ &= \lim_{z \rightarrow 0} \frac{\left( \frac{2\sqrt{N}}{\sqrt{(N-1)!}} z (a_0^\dagger)^{N-1} a_1^\dagger + O(z^2) \right) |\vec{0}\rangle}{2\sqrt{N}z + O(z^2)} \\ &= |n_0=N-1, n_1=1\rangle. \end{aligned} \quad (36)$$

The result is then a Fock basis state (8), which codifies the antisymmetry of the odd 2CAT  $|\mathbf{z}\rangle_-$  by filling the level  $i = 1$  with  $n_1 = 1$  particle. This “transmutation” of  $\mathfrak{c}$ -DCATs into Fock states for some zero components of

$\mathbf{z}$  will be visualized when plotting the Husimi function of the  $\mathfrak{c}$ -DCATs in the next section. On the other hand, the even 2CAT also transmutes to another Fock basis state in the limit  $\lim_{z \rightarrow 0} |\mathbf{z}\rangle_+ = |n_0=N, n_1=0\rangle$ .

It is also relevant to calculate the  $z_i \rightarrow 0$  limits in the particular case of the  $\mathfrak{c}$ -3CATs, as they will be used to study the variational approach to the Hamiltonian eigenstates of the LMG  $U(3)$  model in the different quantum phases in Sec. VI. For  $D = 3$ , the 3CAT state (34) has the following limits

$$\begin{aligned} \lim_{z_1 \rightarrow 0} |\mathbf{z}\rangle_{\mathfrak{c}}^{(N)} &= (a_1^\dagger)^{c_1} |(0, z_2)\rangle_{[c_2]}^{(N-c_1)}, \\ \lim_{z_2 \rightarrow 0} |\mathbf{z}\rangle_{\mathfrak{c}}^{(N)} &= (a_2^\dagger)^{c_2} |(z_1, 0)\rangle_{[c_1]}^{(N-c_2)}, \\ \lim_{z_1, z_2 \rightarrow 0} |\mathbf{z}\rangle_{\mathfrak{c}}^{(N)} &= |n_0=N-c_1-c_2, n_1=c_1, n_2=c_2\rangle, \end{aligned} \quad (37)$$

where  $a_i^\dagger$  are the bosonic creation operators (4), and

$$\begin{aligned} |(0, z_2)\rangle_{[c_2]} &\propto \Pi_{[c_2]} |(0, z_2)\rangle \\ &= 2^{-1} \sum_{b_2 \in \{0, 1\}} (-1)^{c_2 b_2} |(0, (-1)^{b_2} z_2)\rangle, \\ |(z_1, 0)\rangle_{[c_1]} &\propto \Pi_{[c_1]} |(z_1, 0)\rangle \\ &= 2^{-1} \sum_{b_1 \in \{0, 1\}} (-1)^{c_1 b_1} |((-1)^{b_1} z_1, 0)\rangle, \end{aligned} \quad (38)$$

are reduced-parity projected  $U(3)$  CSs, according to (12) and (22). In the expression (37), we have also recovered the superscript  $|\mathbf{z}\rangle^{(N)}$  notation of the DSCSs (15) to highlight that, the  $\mathfrak{c}$ -3CAT  $|\mathbf{z}\rangle_{\mathfrak{c}}^{(N)} = |(z_1, z_2)\rangle_{[c_1, c_2]}^{(N)}$  of  $N$  particles, becomes a reduced  $[c_2]$ -3CAT  $|(0, z_2)\rangle_{[c_2]}^{(N-c_1)}$  (resp.  $[c_1]$ -3CAT  $|(z_1, 0)\rangle_{[c_1]}^{(N-c_2)}$ ) with  $N - c_1$  (resp.  $N - c_2$ ) particles after the limit  $z_1 \rightarrow 0$  (resp.  $z_2 \rightarrow 0$ ). The new  $[c_i]$ -3CATs after the limits have a smaller parity symmetry group, as  $[c_1]$  and  $[c_2]$  belong to  $\mathbb{Z}_2^1 \neq \mathbb{Z}_2^2$ , the original 3CAT parity group  $\mathbb{Z}_2^{D-1}$  for  $D = 3$ . Despite the states in eq.(38) have a similar structure to the 2CATs in (32), they are actually  $\mathbb{Z}_2^1$ -parity adapted  $U(3)$ -spin CSs, as they belong to a 3-level Fock space. Furthermore, they have a similar structure to the photon-added CSs, which are defined as a creation operator acting on a canonical CS [53], but for the  $U(3)$ -spin CSs in our case. The photon-added CSs has also been extended to  $SU(2)$  [54] and  $SU(1,1)$  [55]. As these states have only been studied for the Heisenberg-Weyl group, and for  $SU(2)$  [54] and  $SU(1,1)$  [55], the generalization to  $SU(D)$  presents a novel research topic [56].

The  $z_i \rightarrow 0$  limits in the general  $\mathfrak{c}$  and  $D$  cases of a  $\mathfrak{c}$ -DCAT are not straightforward to compute analytically (see [56]), thus, the Appendix A is devoted to show in detail these calculations. However, it is necessary to introduce the following limit and notation to progress in our discussion. The zero limit  $z_i \rightarrow 0$  can be used repeatedly for a set of  $l = D - 1 - k$  different coordinates  $\mathbf{z}_L = \{z_{i_1}, \dots, z_{i_l}\}$ , whose indexes are taken from

a set of non-repeated indexes  $L = \{i_1, \dots, i_l\}$ . Equivalently, we can define the set of the  $k$  non-zero coordinates  $\mathbf{z}_K = \{z_{j_1}, \dots, z_{j_k}\}$  which are not used in the limits, where the indexes  $K = \{j_1, \dots, j_k\}$  are not duplicated neither. Note that  $\mathbf{z} = (\mathbf{z}_K, \mathbf{z}_L) = (z_1, \dots, z_{D-1})$  include all the projective coordinates as  $k + l = D - 1$  by definition. After the limits, the  $\mathfrak{c}$ -DCAT is transformed into

$$\lim_{z_L \rightarrow \mathbf{0}_L} |\mathbf{z}\rangle_{\mathfrak{c}}^{(N)} = (a_{i_1}^\dagger)^{c_{i_1}} \dots (a_{i_l}^\dagger)^{c_{i_l}} |(\mathbf{z}_K, \mathbf{z}_L = \mathbf{0}_L)\rangle_{\mathfrak{c}_K}^{(N - \|\mathfrak{c}_L\|_0)}, \quad (39)$$

obtaining a reduced  $\mathfrak{c}_K$ -DCAT  $|(\mathbf{z}_K, \mathbf{z}_L = \mathbf{0}_L)\rangle_{\mathfrak{c}_K}$ , with  $N - \|\mathfrak{c}_L\|_0$  particles,  $\mathfrak{c}_K = [c_{j_1}, \dots, c_{j_k}] \in \mathbb{Z}_2^k$  parity, and to which it is added a series of  $\|\mathfrak{c}_L\|_0$  particles occupying the levels  $n_{i_1} = c_{i_1}, \dots, n_{i_l} = c_{i_l}$ . The expression  $\|\mathfrak{c}_L\|_0$  means the 0-norm (number of non-zero components) of  $\mathfrak{c}_L = [c_{i_1}, \dots, c_{i_l}]$ . The rest of the notation in (39) is similar to the one used in the eq.(A3). The eq.(39) generalizes the results for  $D = 2$  in (36) and for  $D = 3$  in (37).

We will use the equations (34, 35, 37) in Section (V) to restore the parity  $\mathfrak{c} = 0 = [0, 0]$  of the variational DSCS of a  $N$  atoms LMG model with  $D = 3$  levels, since the true ground state of this model exhibits a Schrödinger cat structure with totally even parity  $0$ . We will also see that the other parities in (37) can model some of the first excited states in the LMG  $U(3)$  model. But before that, we shall introduce the Husimi function and some localization measures in phase space to characterize the different quantum phases that appear in the LMG model.

#### IV. HUSIMI FUNCTION AND LOCALIZATION MEASURES IN PHASE SPACE

Coherent states provide phase space representations (also known as Bargmann/holomorphic representation) of wave functions in quantum physics. Here we shall concentrate on the Husimi or  $Q$ -function [57] of a pure state  $|\psi\rangle$ , defined as  $Q_\psi(\mathbf{z}) = |\langle \mathbf{z} | \psi \rangle|^2$  for a given overcomplete set of coherent states  $|\mathbf{z}\rangle$ . The most popular case is in quantum optical systems, for which  $|\mathbf{z}\rangle$  makes reference to a Glauber [7] or canonical (harmonic oscillator) coherent state associated to the Heisenberg-Weyl group. This definition can be extended to other coherent state systems like those associated to more general symmetry groups [10] (see also [58] for some generalizations). In our case, the Husimi function of the quantum state (10) is defined in terms of the DSCS coefficients (16) as

$$Q_\psi(\mathbf{z}) = |\langle \mathbf{z} | \psi \rangle|^2 = \left| \sum_{\|\vec{n}\|_1 = N} \overline{c_{\vec{n}}(\mathbf{z})} c_{\vec{n}}(\psi) \right|^2, \quad (40)$$

and it is normalized

$$\int_{\mathbb{C}^{D-1}} Q_\psi(\mathbf{z}) d\mu(\mathbf{z}) = 1, \quad (41)$$

according to the measure (18). This definition is straightforwardly extended to non pure states defined by a density matrix  $\rho$  as  $Q_\rho(\mathbf{z}) = \langle \mathbf{z} | \rho | \mathbf{z} \rangle$  (see e.g., [16, 58]).

The Husimi function of a DSCS  $|\mathbf{z}\rangle$  is simply  $Q_{|\mathbf{z}\rangle}(\mathbf{z}') = |\langle \mathbf{z}' | \mathbf{z} \rangle|^2$ , where the coherent state overlap  $\langle \mathbf{z}' | \mathbf{z} \rangle$  is given in (17). A more interesting example is the Husimi function of a  $\mathfrak{c}$ -DCAT state  $|\mathbf{z}\rangle_{\mathfrak{c}}$  (24), which adopts the form

$$Q_{|\mathbf{z}\rangle_{\mathfrak{c}}}(\mathbf{z}') = |\langle \mathbf{z}' | \mathbf{z} \rangle_{\mathfrak{c}}|^2 = \frac{4^{1-D}}{\mathcal{N}(\mathbf{z})_{\mathfrak{c}}^2} \left| \sum_{\mathfrak{b}} (-1)^{\mathfrak{c} \cdot \mathfrak{b}} \langle \mathbf{z}' | \mathbf{z}^{\mathfrak{b}} \rangle \right|^2 \\ = \frac{2^{1-D} \left| \sum_{\mathfrak{b}} (-1)^{\mathfrak{c} \cdot \mathfrak{b}} (1 + \mathbf{z}^\dagger \mathbf{z}'^{\mathfrak{b}})^N \right|^2}{(1 + \mathbf{z}'^\dagger \mathbf{z}')^N \sum_{\mathfrak{b}} (-1)^{\mathfrak{c} \cdot \mathfrak{b}} (1 + \mathbf{z}^\dagger \mathbf{z}^{\mathfrak{b}})^N}, \quad (42)$$

where we have used the coherent state overlap  $\langle \mathbf{z}' | \mathbf{z}^{\mathfrak{b}} \rangle$  in (17) and the normalization constant  $\mathcal{N}(\mathbf{z})_{\mathfrak{c}}$  in (25). There are studies in the literature relating the distribution of zeros in phase space of the Husimi function of the ground state of a critical quantum system and the onset of quantum chaos (see e.g. [59, 60]) and also studies on the critical behavior of excited states and its relation to order and chaos [61]. Note that, for  $\mathfrak{c}$ -DCAT states  $|\mathbf{z}\rangle_{\mathfrak{c}}$ , the structure of zeros of their Husimi function (42) depends on the parity  $\mathfrak{c}$ . Moreover, the case  $D > 2$  is much richer and opens new possibilities since  $Q$  is multivariate and its zeros are not necessarily isolated points but form curves, surfaces, etc.

In order to visualize the QPT in the critical LMG model across the phase diagram, we shall use the  $\nu$ -th moments of the Husimi quasi-distribution function

$$M_\nu(\psi) = \int_{\mathbb{C}^{D-1}} [Q_\psi(\mathbf{z})]^\nu d\mu(\mathbf{z}), \quad \nu > 1. \quad (43)$$

Among all Husimi moments, we shall single out  $\nu = 2$ , which corresponds with the so called ‘‘Inverse Participation Ratio’’ (IPR) [2, 32], that measures the localization of (inverse area occupied by)  $Q_\psi$  in phase space and can be generalized to any probability density function [62, 63]. The  $\nu$ -th moments of the Husimi function supposedly reach their maximum value when  $\psi$  itself is a coherent (highly localized) state, that is, when  $\psi$  only participates of a single coherent state. These conjecture has been proved in the cases of families of coherent states of compact semisimple Lie groups [58], including the symmetric and antisymmetric representations of  $SU(D)$  as particular cases [64]. This affirmation is widely known as part of the Lieb conjecture, which is mentioned at the end of this subsection. For example, for the particular case of  $|\psi\rangle = |\mathbf{z} = \mathbf{0}\rangle = \frac{1}{\sqrt{N!}} (a_0^\dagger)^N |\mathbf{0}\rangle$  (a boson condensate of  $N$  atoms in their ground state  $i = 0$ ) and a generic number of levels  $D$ , a quite straightforward calculations gives

$$M_\nu(|\mathbf{0}\rangle) = \frac{(N\nu)! (N + D - 1)!}{N! (N\nu + D - 1)!} \quad (44) \\ = \frac{(N + D - 1)_{D-1}}{(N\nu + D - 1)_{D-1}} \xrightarrow{N \rightarrow \infty} 1/\nu^{D-1},$$

where  $(x)_n = x(x-1)\dots(x-n+1)$  denotes the descending factorial or Pochhammer symbol. The last result (44) can be straightforwardly extended to any DSCS, that is

$$M_\nu(|\mathbf{z}\rangle) = M_\nu(|\mathbf{0}\rangle), \quad \forall \mathbf{z} \in \mathbb{C}^{D-1}, \quad (45)$$

and, in fact, to any boson condensate of  $N$  atoms in any level  $i = 0, \dots, D-1$  (see Appendix B for a proof). This in particular means that all coherent states occupy the same area in phase space. Indeed, any DSCS  $|\mathbf{z}\rangle$  can be obtained by translating/rotating  $|\mathbf{z} = \mathbf{0}\rangle \rightarrow U(\mathbf{z})|\mathbf{0}\rangle$  by a unitary transformation  $U(\mathbf{z}) \in U(D)$  (that is,  $|\mathbf{z}\rangle$  can be seen as a “displaced ground state”), which means that  $Q_{|\mathbf{z}\rangle}(\mathbf{z}') = Q_{|\mathbf{0}\rangle}(\mathbf{z}' * \mathbf{z}^{-1})$  with  $U(\mathbf{z}' * \mathbf{z}^{-1}) = U^\dagger(\mathbf{z})U(\mathbf{z}')$  the composition of two  $U(D)$  transformations; the fact that the Fubini-Study measure  $d\mu(\mathbf{z})$  in (18) is  $U(D)$ -invariant completes the proof. Therefore, the  $\nu$ -moments of the Husimi function of a DSCS  $|\mathbf{z}\rangle$  do not depend on the phase space points  $\mathbf{z} \in \mathbb{C}^{D-1}$ , but just on  $\nu$ , the number of particles/atoms  $N$ , and the number of atom levels  $D$ . The equations (44, 45) agree with those of Refs. [18, 31] in the particular cases of  $D = 2$  and  $D = 3$  respectively, and with [64] in the general  $D$  case.

The  $\mathfrak{c}$ -DCAT states  $|\mathbf{z}\rangle_{\mathfrak{c}}$  in (24) participate on several coherent states  $|\mathbf{z}^{\mathfrak{b}}\rangle$  and therefore have a lower IPR value (i.e., they occupy a bigger area in phase space), usually a fraction of  $M_\nu(|\mathbf{0}\rangle)$ . More concretely, the  $\nu$ -moment of  $Q_{|\mathbf{z}\rangle_{\mathfrak{c}}}$  can be explicitly calculated as in the reference [64],

$$M_\nu(|\mathbf{z}\rangle_{\mathfrak{c}}) = M_\nu(|\mathbf{z}\rangle) \sum_{|\vec{k}|=N\nu} |B_{\vec{k}}^2|, \quad (46)$$

with

$$B_{\vec{k}} = \sqrt{\frac{(N!)^\nu}{(N\nu)!}} \sum_{|\vec{n}_1|=\dots=|\vec{n}_\nu|=N} \binom{\vec{k}}{\vec{n}_1, \vec{n}_2, \dots, \vec{n}_\nu}^{1/2} \times c_{\vec{n}_1}(\mathbf{z})_{\mathfrak{c}} c_{\vec{n}_2}(\mathbf{z})_{\mathfrak{c}} \dots c_{\vec{n}_\nu}(\mathbf{z})_{\mathfrak{c}}, \quad (47)$$

where  $c_{\vec{n}_i}(\mathbf{z})_{\mathfrak{c}}$  are the  $\mathfrak{c}$ -DCAT coefficients in the Fock basis (31). The last sum is restricted to  $\vec{n}_1 + \vec{n}_2 + \dots + \vec{n}_\nu = \vec{k}$ , and we are denoting

$$\binom{\vec{k}}{\vec{n}_1, \vec{n}_2, \dots, \vec{n}_\nu} \equiv \frac{\vec{k}!}{\vec{n}_1! \dots \vec{n}_\nu!}, \quad (48)$$

where all the vectors  $\vec{n}_1, \vec{n}_2, \dots, \vec{n}_\nu$  correspond to different Fock vectors according to (8), i.e.  $|\vec{n}_i\rangle = |n_{i,0}, n_{i,1}, \dots, n_{i,D-1}\rangle$ , so that we mean by  $\vec{n}_i! \equiv \prod_{j=0}^{D-1} (n_{i,j})!$  and by  $|\vec{n}_i| \equiv \sum_{j=0}^{D-1} n_{i,j}$ .

In the thermodynamic  $N \rightarrow \infty$  limit, the bulky expression (46) reduces to the more compact one (see Appendix C for a proof)

$$\lim_{N \rightarrow \infty} M_\nu(|\mathbf{z}\rangle_{\mathfrak{c}}) = (2^{D-1})^{1-\nu} \lim_{N \rightarrow \infty} M_\nu(|\mathbf{z}\rangle) = \frac{(2^{D-1})^{1-\nu}}{\nu^{D-1}}, \quad (49)$$

which proves that  $\mathfrak{c}$ -DCATs have lower IPR value than DSCSs, since  $(2^{D-1})^{1-\nu} < 1$  for all  $\nu \geq 2$ . Hence, DCATs

are less localized (occupy a greater area) than DSCSs in phase space. In addition, the limit is independent of the DCAT parity  $\mathfrak{c}$ . To be more precise, the equation above is only valid when all the coordinates  $z_i$  are non-zero, i.e.  $z_i \neq 0 \forall i = 1, \dots, D-1$ . Nevertheless, for a totally even  $\mathfrak{0}$ -DCAT which has only  $k < D-1$  non-zero vector components in  $\mathbf{z}$ , we can apply the equation (A3) for all the  $z_i$  that tend to 0, transforming the  $\mathfrak{0}$ -DCAT into a reduced  $\mathfrak{0}_K$ -DCAT with a parity symmetry described by  $\mathbb{Z}_2^k$ . This leads to a expression similar to (49),

$$\lim_{N \rightarrow \infty} \lim_{\mathbf{z}_L \rightarrow \mathbf{0}_L} M_\nu(|\mathbf{z}\rangle_{\mathfrak{0}}) = (2^k)^{1-\nu} \lim_{N \rightarrow \infty} \lim_{\mathbf{z}_L \rightarrow \mathbf{0}_L} M_\nu(|\mathbf{z}\rangle) = \frac{(2^k)^{1-\nu}}{\nu^{D-1}}, \quad (50)$$

where the notation is the same as in the eq.(39). Note that the denominator  $\nu^{D-1}$  is the same as in the equation (49), as we calculate the  $N \rightarrow \infty$  limit of a  $U(D)$  CS, not a  $U(k)$  one (this result is proven in the Appendix C). For a general parity  $\mathfrak{c}$ -DCAT, the expression above transforms into

$$\lim_{N \rightarrow \infty} \lim_{\mathbf{z}_L \rightarrow \mathbf{0}_L} M_\nu(|\mathbf{z}\rangle_{\mathfrak{c}}) = \frac{(2^{k+\|\mathfrak{c}_L\|_0})^{1-\nu}}{\nu^{D-1}}, \quad (51)$$

where  $\|\mathfrak{c}_L\|_0$  and  $k = \|\mathbf{z}\|_0$  are the number of non-zero components in  $\mathfrak{c}_L$  and  $\mathbf{z}$  respectively. The sum  $k + \|\mathfrak{c}_L\|_0$  coincides with the number of humps displayed by the Husimi function  $Q_{|\mathbf{z}\rangle_{\mathfrak{c}}}(\mathbf{z}')$  in the phase space coordinates  $\mathbf{z}'$ , as we will see in Section VII. The equation (51) includes the eq.(50) as a particular case, since  $\|\mathfrak{c}_L\|_0 = 0$  for the  $\mathfrak{0}$ -DCAT.

Instead of  $M_\nu(\psi)$ , it is sometimes preferred to express delocalization (as a measure of area in phase space) in terms of Rényi-Wehrl entropy, which is defined as [16–18] as

$$\mathcal{S}_{W,\nu}(\psi) = \frac{1}{1-\nu} \ln[M_\nu(\psi)], \quad \nu \neq 1. \quad (52)$$

Taking the limit  $\nu \rightarrow 1$  in the Rényi-Wehrl entropy (52), one obtains the Wehrl entropy [65] given by

$$\mathcal{S}_W(\psi) = - \int_{\mathbb{C}^{D-1}} Q_\psi(\mathbf{z}) \ln[Q_\psi(\mathbf{z})] d\mu(\mathbf{z}). \quad (53)$$

Since the definition of the Husimi function is related to a specific classical phase space (the  $\mathbb{C}P^{D-1}$  complex projective space defined by DSCSs in our case), the Wehrl entropy is also called (semi)classical entropy [65, 66]. It is the Gibbs entropy continuous form of the Husimi probability function  $Q_\rho$  for the state described by a density matrix  $\rho$  [16, 65]. This picture contrast with other common entropies such as the von Neumann entropy  $\mathcal{S}_N = -\text{tr}(\rho \ln \rho)$ , which we have previously used to study entanglement (quantum nonlocality) in symmetric multiqubit systems [50], and has no immediate relation to classical mechanics. The last one measures how much a state is mixed (non pure), rather than its localization

in phase-space. According to the Lieb conjecture [67], the minimum Wehrl entropy (53) is attained when  $\psi$  is a DSCS. It was proved for  $SU(2)$  spin- $j$  CSs in [66, 68], for symmetric  $SU(D)$  spin CSs (DSCSs for us) in [69], and for any compact semisimple Lie group in [58]. The minimum Wehrl entropy value can be easily obtained from the Husimi  $\nu$ -moment of the highest-weight vector  $|\mathbf{z}\rangle = |\mathbf{0}\rangle$  in (44), once we realize that  $\mathcal{S}_W = \lim_{\nu \rightarrow 1} \mathcal{S}_{W,\nu}$  in (52), and that

$$\min_{\psi} \mathcal{S}_W(\psi) = \mathcal{S}_W(|\mathbf{z}\rangle) = \mathcal{S}_W(|\mathbf{0}\rangle) \quad (54)$$

according to (45). Therefore, taking the limit  $\nu \rightarrow 1$  in (44) we arrive to

$$\begin{aligned} \mathcal{S}_W(|\mathbf{0}\rangle) &= N(\psi^{(0)}(N+D) - \psi^{(0)}(N+1)) \quad (55) \\ &= N \sum_{k=1}^{D-1} \frac{1}{N+k} \xrightarrow{N \rightarrow \infty} D-1, \end{aligned}$$

for a generic number  $D$  of levels, where  $\psi^{(0)}(x) = \Gamma'(x)/\Gamma(x)$  is the digamma function. There is a particular version of this result for a  $U(3)$  vibron model in [31]. As a particular case, in the thermodynamic limit  $N \rightarrow \infty$ , the minimum Wehrl entropy is  $D-1 = 1$  for  $D=2$ , which is the minimum value of the Wehrl entropy predicted by Lieb in [67] for the harmonic oscillator coherent states (Heisenberg-Weyl group). This is so because Bloch  $SU(2)$  spin- $j$  coherent states  $|z\rangle$  tend to the Heisenberg-Weyl (harmonic oscillator) coherent states  $|\alpha\rangle$  in the large spin limit  $j = N/2 \gg 1$  with the rescaling  $z = \alpha/\sqrt{N}$  [10, 70]. Unlike for DSCSs, we do not have closed analytical formulas for the Wehrl entropy of  $\mathfrak{c}$ -DCAT states, except in the thermodynamic limit when, in general,

$$\begin{aligned} \lim_{N \rightarrow \infty} \mathcal{S}_W(|z\rangle_{\mathfrak{c}}) &= \lim_{N \rightarrow \infty} \mathcal{S}_W(|z\rangle) + \log(2^{D-1}) \\ &= (D-1)(1 + \log(2)), \quad (56) \end{aligned}$$

being the same for all different parities  $\mathfrak{c}$ . As we already commented in the equation (50), when there are only  $k$  non-zero components in  $\mathbf{z}$  for the fully even  $\mathfrak{0}$ -DCAT, the expression above (56) has to be replaced by

$$\lim_{N \rightarrow \infty} \lim_{z_L \rightarrow \mathbf{0}_L} \mathcal{S}_W(|z\rangle_{\mathfrak{0}}) = (D-1) + k \log(2). \quad (57)$$

Therefore, the totally even parity adaptation of a DSCS entails a Wehrl entropy (area in phase space) excess of

$$\mathcal{S}_W(|z\rangle_{\mathfrak{0}}) - \mathcal{S}_W(|z\rangle) \xrightarrow{N \rightarrow \infty} k \log(2) \quad (58)$$

in the thermodynamic limit. This is a particular case of the result proposed by Mintert and Zyczkowski in [16]. Also, the limits (50,57) for the  $\mathfrak{0}$ -DCAT generalize the results obtained in [31] for  $D=3$  and  $\mathbf{z} = (z_1, -\bar{z}_1)$ , which is equivalent to have only one non-zero component in  $\mathbf{z}$ , i.e.,  $k=1$ . For the general  $\mathfrak{c}$ -parity case, we use the eq.(51) to obtain

$$\lim_{N \rightarrow \infty} \lim_{z_L \rightarrow \mathbf{0}_K} \mathcal{S}_W(|z\rangle_{\mathfrak{c}}) = (D-1) + (k + \|\mathfrak{c}_L\|_0) \log(2). \quad (59)$$

All the expressions in the thermodynamic limit presented in this section are examined in more detail in the Appendix C.

In Section VII, we propose Husimi second moments and Rényi-Wehrl entropies of the ground state of a 3-level atom LMG model (7) as localization measures in phase space, in order to characterize the three quantum phases appearing in this model. But previously we are going to study the phase diagram of the critical  $D=3$  level LMG model in the next section.

## V. LMG MODEL FOR THREE-LEVEL ATOMS AND ITS QUANTUM PHASE DIAGRAM

We particularize the Hamiltonian (7) for  $D=3$  (3-level atoms or qutrits). Therefore, our Hamiltonian density will be

$$H = \frac{\epsilon}{N} (S_{33} - S_{11}) - \frac{\lambda}{N(N-1)} \sum_{i \neq j=1}^3 S_{ij}^2. \quad (60)$$

We shall measure energy in  $\epsilon$  units and discuss the energy spectrum and the phase diagram in terms of the only control parameter  $\lambda$ . In [14] we have proved that this model displays three different quantum phases for the completely symmetric unitary irreducible representation of  $U(3)$  labelled by the total number of particles  $N$ ; Ref. [14] also studies other permutation symmetry sectors (fermionic mixtures from two-row Young diagrams) which will not be discussed here. Let us summarize the essential points. Coherent (semiclassical) states are in general good variational states which faithfully reproduce the ground state energy of Hamiltonian models in the semiclassical/thermodynamic limit  $N \rightarrow \infty$ . Therefore, we define the energy surface associated to the Hamiltonian density  $H$  in (60) as the DSCS expectation value of the Hamiltonian density in the thermodynamic limit

$$\begin{aligned} E_{|z\rangle}(\epsilon, \lambda) &= \lim_{N \rightarrow \infty} \langle z | H | z \rangle \quad (61) \\ &= \lim_{N \rightarrow \infty} \left( \epsilon \frac{\langle z | S_{33} | z \rangle - \langle z | S_{11} | z \rangle}{N} - \lambda \frac{\sum_{i \neq j=1}^3 \langle z | S_{ij} | z \rangle^2}{N(N-1)} \right), \end{aligned}$$

with  $\langle z | S_{ij} | z \rangle$  in (19). Note that we have used that there are no spin fluctuations in the thermodynamic limit (21). Denoting  $\mathbf{z} = (z_1, z_2)$  the phase space coordinates for  $U(3)$ -spin coherent states (15), the energy surface has the explicit form

$$E_{|z\rangle}(\epsilon, \lambda) = \epsilon \frac{|z_2|^2 - 1}{|z_1| + |z_2|^2 + 1} - \lambda \frac{z_1^2 (\bar{z}_2^2 + 1) + z_2^2 + \text{c.c.}}{(|z_1| + |z_2|^2 + 1)^2}. \quad (62)$$

This energy surface is invariant under parity transformations  $z_1 \rightarrow -z_1$ ,  $z_2 \rightarrow -z_2$ , a symmetry which is inherited from the discrete parity symmetry of the Hamiltonian (60). In fact, the energy surface  $E_{|z\rangle}(\epsilon, \lambda)$  coincides with all  $\mathfrak{c}$ -DCAT Hamiltonian expectation values in the

thermodynamic limit, that is

$$E_{|\mathbf{z}\rangle_{\mathfrak{c}}}(\epsilon, \lambda) = E_{|\mathbf{z}\rangle}(\epsilon, \lambda) \quad \forall \mathfrak{c} \in \mathbb{Z}_2^{D-1}. \quad (63)$$

This can be seen by using the linear and quadratic  $U(D)$ -spin operator expectation values in a  $\mathfrak{c}$ -parity DCAT defined in [50], and realizing that

$$\lim_{N \rightarrow \infty} \langle \mathfrak{c} | \mathbf{z} | S_{ij} | \mathbf{z} \rangle_{\mathfrak{c}} = \lim_{N \rightarrow \infty} \langle \mathbf{z} | S_{ij} | \mathbf{z} \rangle, \quad (64)$$

which can also be extended to quadratic (two-body)  $U(D)$ -spin operator expectation values because of the absence of quantum fluctuations in the thermodynamic limit (21). This fact has important consequences in the spontaneous breakdown of the parity symmetry in the thermodynamic limit and the quantum phase transition, as we are going to see in the following.

The variational minimum (ground state) energy

$$E^{(0)}(\epsilon, \lambda) = \min_{z_1, z_2 \in \mathbb{C}} E_{|(z_1, z_2)\rangle}(\epsilon, \lambda) \quad (65)$$

is attained at the critical (real) coherent state parameters

$$z_{1\pm}^{(0)}(\epsilon, \lambda) = \pm \begin{cases} 0, & 0 \leq \lambda \leq \frac{\epsilon}{2}, \\ \sqrt{\frac{2\lambda - \epsilon}{2\lambda + \epsilon}}, & \frac{\epsilon}{2} \leq \lambda \leq \frac{3\epsilon}{2}, \\ \sqrt{\frac{2\lambda}{2\lambda + 3\epsilon}}, & \lambda \geq \frac{3\epsilon}{2}, \end{cases} \\ z_{2\pm}^{(0)}(\epsilon, \lambda) = \pm \begin{cases} 0, & 0 \leq \lambda \leq \frac{3\epsilon}{2}, \\ \sqrt{\frac{2\lambda - 3\epsilon}{2\lambda + 3\epsilon}}, & \lambda \geq \frac{3\epsilon}{2}. \end{cases} \quad (66)$$

Inserting (66) into (62) gives the ground state energy density in the thermodynamic limit

$$E^{(0)}(\epsilon, \lambda) = \begin{cases} -\epsilon, & 0 \leq \lambda \leq \frac{\epsilon}{2}, & \text{(I)} \\ -\frac{(2\lambda + \epsilon)^2}{8\lambda}, & \frac{\epsilon}{2} \leq \lambda \leq \frac{3\epsilon}{2}, & \text{(II)} \\ -\frac{4\lambda^2 + 3\epsilon^2}{6\lambda}, & \lambda \geq \frac{3\epsilon}{2}. & \text{(III)} \end{cases} \quad (67)$$

Here we clearly distinguish three different phases: I, II and III, and two second-order QPTs (according to Ehrenfest's classification) occurring at critical points  $\lambda_{\text{I} \leftrightarrow \text{II}}^{(0)} = \epsilon/2$  and  $\lambda_{\text{II} \leftrightarrow \text{III}}^{(0)} = 3\epsilon/2$ , respectively, at which the second derivative of  $E_0(\epsilon, \lambda)$  is discontinuous. As we have already anticipated, the ground state is degenerated, since there are four different DSCs  $|z_{1\pm}^{(0)}, z_{2\pm}^{(0)}\rangle$  (or equivalently, four 3CAT states  $|\mathbf{z}\rangle_{\mathfrak{c}}$  with parities  $\mathfrak{c} = [0, 0], [1, 0], [0, 1],$  and  $[1, 1]$ ) with the same energy (67) in the thermodynamic limit  $N \rightarrow \infty$ . This is a consequence of the spontaneous breakdown of the discrete parity symmetry  $\mathbb{Z}_2^2$  of the Hamiltonian (60), as was already pointed out in [14]. For general  $D$ , the ground state degeneracy would go as  $2^k$ , with  $k$  the number of nonzero components of  $\mathbf{z}^{(0)}$ , with a maximum degeneracy of  $2^{D-1}$  (the number of elements of the parity group  $\mathbb{Z}_2^{D-1}$ ).

## VI. FIDELITY BETWEEN VARIATIONAL CATS AND NUMERICAL LOW-LYING HAMILTONIAN EIGENSTATES WITH DEFINITE PARITY

For a finite number  $N$  of atoms, coherent states  $|\mathbf{z}\rangle$  still provide a fairly good approximation to the ground state when properly adapted to the (not yet broken) parity. There are two possible variational approaches for finite  $N$ :

1. Project  $|\mathbf{z}\rangle$  onto parity  $\mathfrak{c} = 0 = [0, 0]$  (the ground state is always totally even), use this 0-3CAT state  $|\mathbf{z}\rangle_0$  as a variational state, and determine the critical coherent state parameters  $\mathbf{z}^{(0, N)}$  that minimize the energy expectation value  ${}_0\langle \mathbf{z} | H | \mathbf{z} \rangle_0$  for finite  $N$  (the matrix elements  ${}_0\langle \mathbf{z} | S_{ij} | \mathbf{z} \rangle_0$  can be found in [50]), or
2. Use one of the four critical coherent state parameters combinations  $\mathbf{z}^{(0)} = (z_{1+}^{(0)}, z_{2+}^{(0)})$  obtained for  $N \rightarrow \infty$  in (66), substitute them into  $|\mathbf{z}\rangle$  for finite  $N$  creating  $|\mathbf{z}^{(0)}\rangle$ , then restore parity by projecting onto fully even parity

$$\Pi_0 |\mathbf{z}^{(0)}\rangle = \frac{1}{4} \left[ |z_{1+}^{(0)}, z_{2+}^{(0)}\rangle + |z_{1+}^{(0)}, z_{2-}^{(0)}\rangle + |z_{1-}^{(0)}, z_{2+}^{(0)}\rangle + |z_{1-}^{(0)}, z_{2-}^{(0)}\rangle \right] \quad (68)$$

and normalize

$$|\mathbf{z}^{(0)}\rangle_0 = \frac{\Pi_0 |\mathbf{z}^{(0)}\rangle}{\mathcal{N}(\mathbf{z}^{(0)})_0}. \quad (69)$$

The second procedure is less accurate but much easier. We shall adopt it in the following to obtain variational approximations  $|\mathbf{z}^{(0)}\rangle_0$  (the properly normalized projection of  $\Pi_0 |\mathbf{z}^{(0)}\rangle$ ) to the ground state  $|\psi_0\rangle$ , and to evaluate how faithful (in the sense of [71]) they are to numerical solutions obtained by direct Hamiltonian diagonalization. Moreover, we shall naively extend this procedure to evaluate the fidelity between other  $\mathfrak{c}$ -3CATs  $|\mathbf{z}^{(0)}\rangle_{\mathfrak{c}} \propto \Pi_{\mathfrak{c}} |\mathbf{z}^{(0)}\rangle$  and the first excited states  $|\psi_i\rangle, i = 1, 2, 3, 4, 5$  (in increasing order of energy), which have definite parity  $\mathfrak{c}$  and are obtained by numerical diagonalization of the Hamiltonian (60) for different values of the control parameter  $\lambda$ . In this case, the  $\mathfrak{c}$ -3CATs are reduced to a smaller parity group 3CATs when some of the coordinates in  $\mathbf{z}^{(0)} = (z_{1+}^{(0)}, z_{2+}^{(0)})$  tend to 0 (see equation (37) and the discussion below it). Therefore, it would be more precise to define the variational excited states (ES for short) as

$$|\mathbf{z}^{(0)}\rangle_{\mathfrak{c}} = \lim_{\mathbf{z} \rightarrow \mathbf{z}^{(0)}} |\mathbf{z}\rangle_{\mathfrak{c}}, \quad \forall \mathfrak{c} \neq 0 \quad (70)$$

rather than directly using the equation (69), in order to avoid a null projection (see the discussion above the eq.(36) for more details). This will become important when plotting Figures 2, 6 and 9.

The condition for a Hamiltonian eigenstate  $|\psi_i\rangle$  to have a definite parity  $\mathfrak{c}$  is  $\langle\psi_i|\Pi_{\mathfrak{c}}|\psi_i\rangle = 1$ . In particular, for  $N = 20$  and  $\lambda \in (0, 3)$ , we have obtained the following parities for the first low-lying Hamiltonian eigenstates (in increasing order of energy)

$$\begin{aligned} \langle\psi_0|\Pi_{[0,0]}|\psi_0\rangle = 1, & \quad \langle\psi_1|\Pi_{[1,0]}|\psi_1\rangle = 1, & (71) \\ \langle\psi_2|\Pi_{[0,0]}|\psi_2\rangle = 1, & \quad \langle\psi_3|\Pi_{[0,1]}|\psi_3\rangle = 1, \\ \langle\psi_4|\Pi_{[1,0]}|\psi_4\rangle = 1, & \quad \langle\psi_5|\Pi_{[1,1]}|\psi_5\rangle = 1. \end{aligned}$$

In Figure 1 we represent the low-lying spectrum of the LMG Hamiltonian (60) as a function of the control parameter  $\lambda$  for  $N = 20$  particles. The four colored lines represent the states  $\psi_i$ ,  $i = 0, 1, 3, 5$  which have the same  $\mathfrak{c}$ -parity of specific  $\mathfrak{c}$ -DCATs. After the first phase transition around  $\lambda_{\text{I} \leftrightarrow \text{II}}^{(0)} = \epsilon/2$ , the states  $i = 0, 1$  (red and blue) start getting closer until they finally merge for large  $\lambda$ . This degeneracy in the ground state for finite  $N$  can be considered as a "precursor" of the first QPT at  $\lambda = \epsilon/2$ . The degeneracy is also present in the excited states  $i = 3, 5$  (green and orange) around  $\lambda_{\text{I} \leftrightarrow \text{II}}^{(0)}$ . Furthermore, as we move towards the next critical point  $\lambda_{\text{II} \leftrightarrow \text{III}}^{(0)} = 3\epsilon/2$ , the states  $i = 0, 1, 3, 5$  start to merge in a 4-fold degenerate ground state, providing another "precursor" but for the second QPT at  $\lambda = 3\epsilon/2$ . This degeneracy phenomenon is more and more evident as we approach the thermodynamic limit, where the ground state is completely 4-fold degenerate.

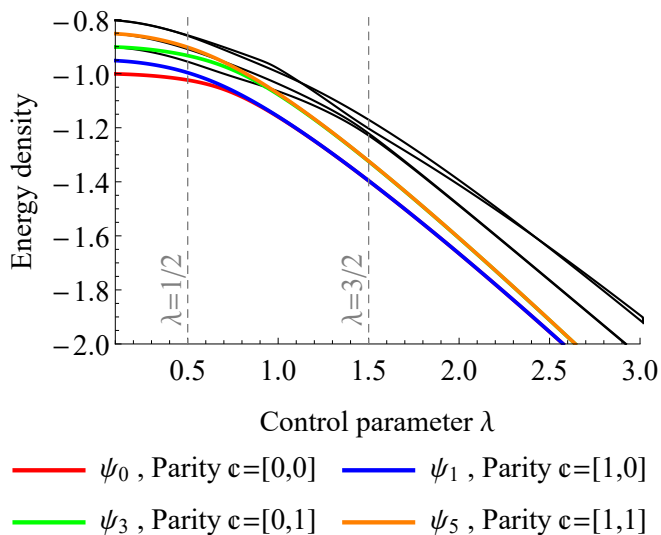


FIG. 1. Energy density spectrum of the first excited states of the LMG U(3) model, obtained by numerical diagonalization of the LMG U(3) Hamiltonian (60) for  $N = 20$  particles, as a function of the control parameter  $\lambda$ . The colored lines represent states with well defined parity, which is indicated in the legend. The black lines represent the rest of the eigenstates energy densities. The quantum critical points  $\lambda_{\text{I} \leftrightarrow \text{II}}^{(0)} = \epsilon/2$  and  $\lambda_{\text{II} \leftrightarrow \text{III}}^{(0)} = 3\epsilon/2$  are indicated by vertical dashed grid lines. Energies and  $\lambda$  are given in  $\epsilon$  units.

Figure 2 shows the fidelity

$$F(|\mathbf{z}^{(0)}\rangle_{\mathfrak{c}}, |\psi_i\rangle) = |\langle\mathbf{z}^{(0)}|\psi_i\rangle|^2, \quad (72)$$

between variational excited states (70) and numerical low-lying Hamiltonian eigenstates  $\psi_i$  with the same parity  $\mathfrak{c}$  (states with different parities are orthogonal). As expected, the 3CAT state  $|\mathbf{z}^{(0)}\rangle_0$  gives a fairly good approximation to the ground state  $|\psi_0\rangle$ , with a high fidelity  $F \gtrsim 0.8$  (specially in phase I), except near the critical points  $\lambda_{\text{I} \leftrightarrow \text{II}}^{(0)} = \epsilon/2$  and  $\lambda_{\text{II} \leftrightarrow \text{III}}^{(0)} = 3\epsilon/2$ , where fidelity always drops. Figure 2 also shows the fidelity between the variational approximations  $|\mathbf{z}^{(0)}\rangle_{\mathfrak{c}}$ , with parities  $\mathfrak{c} = [1, 0], [0, 1], [1, 1]$ , and the excited states  $|\psi_i\rangle$ ,  $i = 1, 3, 5$ , respectively. The excited states  $|\psi_2\rangle$  and  $|\psi_4\rangle$  are not considered in this discussion because they already share parity with  $|\psi_0\rangle$  and  $|\psi_1\rangle$ , respectively, and therefore they can not be faithful to  $|\mathbf{z}^{(0)}\rangle_{[0,0]}$  and  $|\mathbf{z}^{(0)}\rangle_{[1,0]}$  since  $\langle\psi_2|\psi_0\rangle = 0$  and  $\langle\psi_4|\psi_1\rangle = 0$ , i.e., they are mutually orthogonal as Hamiltonian eigenstates with different eigenvalues. Let us continue discussing Figure 2. The fidelity  $|\langle_{[1,0]} \mathbf{z}^{(0)} | \psi_1 \rangle|$  is also fairly high, although not as much as for the ground state. Note that, according to Eq. (66), the first component  $z_1^{(0)}$  of  $\mathbf{z}^{(0)}$  is zero in phase I and  $z_2^{(0)} = 0$  in phases I and II. Therefore, according to the equations (37) and (38), in the phases I and II, the fidelity must be calculated using reduced-parity 3CATs. For instance, in the phase I, the 3CAT  $|\mathbf{z}^{(0)}\rangle_{[1,0]}$  becomes a Fock basis state  $|n_0=N-1, n_1=1, n_2=0\rangle$  because  $\mathbf{z}^{(0)}(\lambda) = (0, 0)$  at  $\lambda < \epsilon/2$ ; and in the phase II, it “transmutes” to a  $\mathbb{Z}_2$ -parity 3CAT  $|(z_{1+}^{(0)}, 0)\rangle_{[1]}$ . The same happens with the fidelities  $|\langle_{[0,1]} \mathbf{z}^{(0)} | \psi_3 \rangle|$  and  $|\langle_{[1,1]} \mathbf{z}^{(0)} | \psi_5 \rangle|$ , which are fairly high far from the critical points. All the fidelities presented in Figure 2 tend to 1 when  $\lambda \rightarrow 0$ , which corresponds to the coordinates  $\mathbf{z}^{(0)}(\lambda) = (0, 0)$ . This is possible because the numerical diagonalization in the noninteracting case ( $\lambda = 0$ ) reproduces very accurately the Fock basis states at the bottom of the eq. (37). The spectrum classification of the non-interacting LMG U(3) model was already studied analytically in [14], giving Fock basis states as eigenstates of the Hamiltonian. Additionally, the 4-fold degeneracy of the eigenstates  $i = 0, 1, 3, 5$  is present in Figure 2 at high  $\lambda \gg 1$ , where all the colored lines merge.

The failure of the variational state  $|\mathbf{z}^{(0)}\rangle_{\mathfrak{c}}$  to properly represent the numerical Hamiltonian eigenstate  $|\psi_i\rangle$  (for the corresponding parity  $\mathfrak{c}$ ) near the quantum critical points  $\lambda = \epsilon/2$  and  $\lambda = 3\epsilon/2$ , can be fixed by simply maximizing the overlap

$$|\langle\mathbf{z}|\psi_i(\lambda)\rangle|^2 = \mathcal{N}(\mathbf{z})_{\mathfrak{c}}^2 Q_{\psi_i(\lambda)}(\mathbf{z}) \quad (73)$$

in the phase space coordinates  $\mathbf{z} = (z_1, z_2)$  for each value of  $\lambda$ . This procedure, of course, results in fitting values  $\mathbf{z}_i^{\max} = (z_{1,i}^{\max}, z_{2,i}^{\max})$ , which are different from the critical values  $\mathbf{z}^{(0)} = (z_{1\pm}^{(0)}, z_{2\pm}^{(0)})$  in (66) at the thermodynamic limit. Indeed, in Figure 3 we plot the (real) values of  $\mathbf{z}_i^{\max}$ , to be compared to  $\mathbf{z}^{(0)}$ , as a function of  $\lambda$ . Both

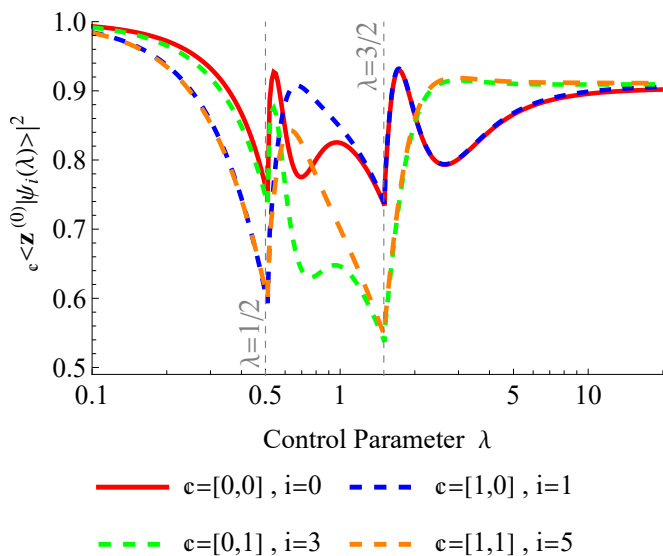


FIG. 2. Fidelity  $|\epsilon \langle \mathbf{z}^{(0)} | \psi_i(\lambda) \rangle|^2$  between the variational  $c$ -3CATs (70) and the numerical LMG Hamiltonian eigenstates  $\psi_i$  as a function of  $\lambda$  ( $\epsilon$  units and log-scale in abscissa axis) for  $N = 20$ . Vertical grid lines denote the quantum critical points.

values meet at  $\lambda = 0$  and  $\lambda \gg 1$ , i.e. when the two-body interaction is not present and when it predominates, respectively. Then, in Figure 4, we represent the overlap  $|\epsilon \langle \mathbf{z}_i^{\max} | \psi_i(\lambda) \rangle|^2$ , which now attains values above 0.8 for all values of  $\lambda$ , thus improving the results of (72).

## VII. LOCALIZATION MEASURES OF THE GROUND STATE IN PHASE SPACE THROUGHOUT THE PHASE DIAGRAM

Now we are interested in analyzing the QPT of the three-level atom LMG model by using the localization measures (area in phase space) introduced in Section IV.

Let us start by analyzing the structure of the Husimi function  $Q_{|\mathbf{z}^{(0)}\rangle_0}(\mathbf{z}')$  of the variational ground state  $|\mathbf{z}^{(0)}\rangle_0$  (see eq.(69)). The variational Husimi function  $Q_{|\mathbf{z}^{(0)}\rangle_0}(\mathbf{z}')$  depends on the complex phase space coordinates  $\mathbf{z}' = (z'_1, z'_2) \in \mathbb{C}^2$ . It also depends on the control parameter  $\lambda$  through the critical point  $\mathbf{z}^{(0)} = (z_{1+}^{(0)}, z_{2+}^{(0)})$  (we take  $\epsilon$  energy units for simplicity, see eq.(66)). In order to plot  $Q_{|\mathbf{z}^{(0)}\rangle_0}(\mathbf{z}')$  in phases I, II and III, we shall separate “position”  $x_{1,2} = \text{Re}(z'_{1,2})$  and “momentum”  $p_{1,2} = \text{Im}(z'_{1,2})$  coordinates (see e.g. [72, 73] for phase-space approaches to quantum mechanics and [29, 31] for a justification in other models, like quadratures of the electromagnetic field).

In Figure 5 we make contour plots of the variational Husimi function in position (left panel) and momentum (right panel) spaces for three different characteristic val-

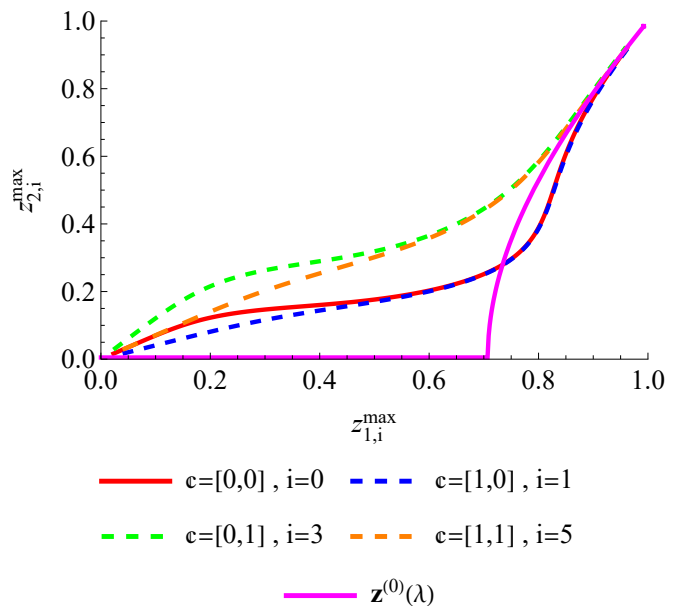


FIG. 3. Parametric plot of the fitting points  $\mathbf{z}_i^{\max} = (z_{1,i}^{\max}, z_{2,i}^{\max})$  maximizing the overlap or fidelity  $|\epsilon \langle \mathbf{z} | \psi_i(\lambda) \rangle|^2$ , as a function of  $\lambda \in (0, 20)$  ( $\epsilon$  units and log-scale) for  $N = 20$  particles. The fitting points are compared to the critical values  $\mathbf{z}^{(0)} = (z_{1\pm}^{(0)}, z_{2\pm}^{(0)})$  in (66), represented by the solid magenta line.

ues  $\lambda_1, \lambda_2, \lambda_3$ ,

$$\lambda_1 = 0 < \lambda_{\text{I} \leftrightarrow \text{II}}^{(0)} < \lambda_2 = 1 < \lambda_{\text{II} \leftrightarrow \text{III}}^{(0)} < \lambda_3 = 2.5, \quad (74)$$

of the control parameter  $\lambda$  inside each phase for  $N = 20$  particles. Contour plots of  $Q_{|\mathbf{z}^{(0)}\rangle_0}(\mathbf{z})$  in position space give a clear visual explanation of the delocalization of the ground state in phase space as we move from phase I to phases II and III. Indeed, the Husimi function is composed of a single lump/hump/packet in phase I, which coincides with  $2^k = 1$  for  $k = 0$ , the number of non-zero components of  $\mathbf{z}^{(0)} = (z_{1+}^{(0)}, z_{2+}^{(0)})$  according to (66); similarly, we have  $2^k = 2$  and  $2^k = 4$  lumps in phases II and III for  $k = 1$  and  $k = 2$  non-zero components of  $\mathbf{z}^{(0)}$ , respectively. The behavior of the Husimi function in momentum space is a little bit more subtle, as it entails some modulations which, in the large  $N$  limit, correspond to a (Gaussian-like) packet modulated by a cosine function which oscillates rapidly for high  $N$  mainly in phase III (see [28] for a similar behavior in the Dicke model in the superradiant phase).

Additionally, in Figure 6 we study the Husimi function  $Q_{|\mathbf{z}^{(0)}\rangle_e}(\mathbf{z}')$  of variational excited states  $i = 1, 3, 5$  of the LMG  $U(3)$  model (already defined in eqs.(66,70) and classified in Figure 1). We shall restrict the plot and discussion to position coordinates  $x_{1,2} = \text{Re}(z'_{1,2})$  for convenience. It is interesting that, in the phase I at  $\lambda = 0$  (left column in Figure 6), the variational ES Husimi functions have more than a single hump, which

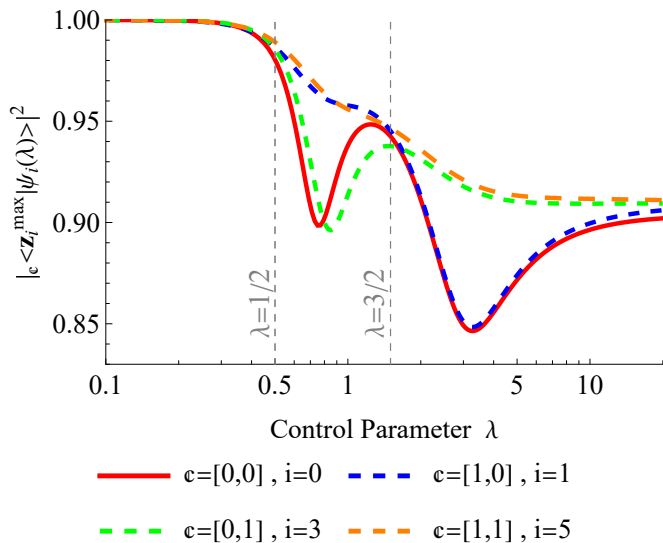


FIG. 4. Maximum overlap or fidelity  $|\langle \mathbf{z}_i^{\max} | \psi_i(\lambda) \rangle|^2$  between the  $\mathfrak{c}$ -DCATs  $|\mathbf{z}\rangle_{\mathfrak{c}}$  and the LMG numerical eigenvectors  $|\psi_i(\lambda)\rangle$  of different parity as a function of  $\lambda$  ( $\epsilon$  units and log-scale) for  $N = 20$  particles.

was not the case of the GS in Figure 5. This is because the variational ES  $|\mathbf{z}^{(0)}\rangle_{\mathfrak{c}}$  preserve their parity  $\mathfrak{c} \neq 0$  even when  $\mathbf{z}^{(0)} \xrightarrow{\lambda \rightarrow 0} (0, 0)$ . Actually, this limit was already given in the eq. (37). For instance, the variational first ES  $\mathfrak{c} = [1, 0]$  (top row in Figure 6) transforms into a Fock state  $|\mathbf{z}^{(0)}\rangle_{[1,0]}^{(N)} \xrightarrow{\lambda \rightarrow 0} |n_0=N-1, n_1=1, n_2=0\rangle$ . Having only one particle in level 1,  $n_1 = 1$ , implies odd-parity in  $x_1 = \text{Re}(z'_1)$  when plotting  $Q_{\mathbf{z}^{(0)}}(\mathbf{z}')$  (check the eqs. (16) and (40)). Therefore, the variational first ES cannot be 0 at  $x_1 = x_2 = 0$  and has two humps along the  $x_1$ -axis direction (top left panel in Figure 6). The variational third ES  $\mathfrak{c} = [1, 0]$  (middle row) has a similar behavior at  $\lambda = 0$  but along the  $x_2$ -axis,  $|\mathbf{z}^{(0)}\rangle_{[1,0]}^{(N)} \xrightarrow{\lambda \rightarrow 0} |n_0=N-1, n_1=0, n_2=1\rangle$ . The fifth ES  $\mathfrak{c} = [1, 1]$  (bottom row) has double odd-parity in the axis  $x_1$  and  $x_2$  and presents four humps,  $|\mathbf{z}^{(0)}\rangle_{[1,1]}^{(N)} \xrightarrow{\lambda \rightarrow 0} |n_0=N-2, n_1=1, n_2=1\rangle$ . In the phase II at  $\lambda = 1$  (middle column in Figure 6), all the Husimi functions of the variational ES have symmetric humps along the  $x_1$ -axis as the GS did in Figure 5. However, the third and fifth ES also display symmetric humps along the  $x_2$ -axis, as both have  $c_2 = 1$  in  $\mathfrak{c}$ . Finally, in the phase III at  $\lambda = 2.5$  (right column in Figure 6), the ESs have four humps as the GS, demonstrating the degeneration already showed in Figure 1 at  $\lambda \gg 1$ . This result agrees with the eq.(C6) in Appendix C (number of terms in the sum  $\sum_{\mathfrak{b} \in \{0,1\}^2}$ ), but for relatively large finite ( $N = 20$ ) number of particles.

As a general rule, we propose that the number of humps (in the phase space coordinates  $\mathbf{z}'$ ) of a  $\mathfrak{c}$ -DCAT

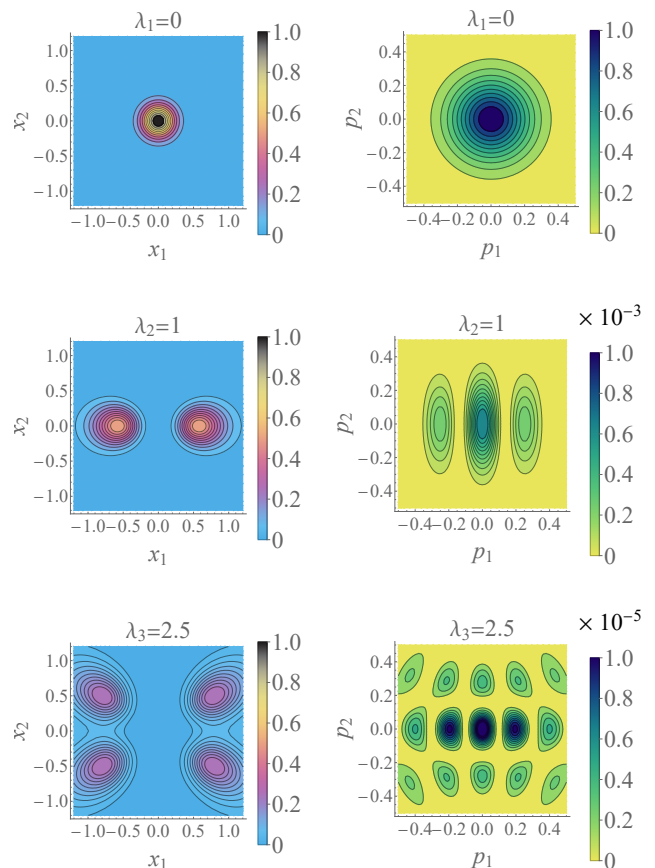


FIG. 5. Contour plots in phase space coordinates of the Husimi function  $Q_{|\mathbf{z}^{(0)}_0}(\mathbf{z}')$  of the variational ground state  $|\mathbf{z}^{(0)}_0\rangle$  of the LMG  $U(3)$  model (66,69), for  $N = 20$  particles and three different values of the control parameter  $\lambda$  ( $\epsilon$  units) inside the three phases I, II and III. The left and right columns correspond to “position”  $x_{1,2} = \text{Re}(z'_{1,2})$  and “momentum”  $p_{1,2} = \text{Im}(z'_{1,2})$  coordinates, respectively.

Husimi function is

$$\#\text{humps}(Q_{|\mathbf{z}\rangle_{\mathfrak{c}}}(\mathbf{z}')) = 2^{\|\mathbf{z}\|_0 + \|\mathfrak{c}_L\|_0} \quad \forall N \gg 1, \quad (75)$$

where  $K = \{j_1, \dots, j_k\}$  and  $L = \{i_1, \dots, i_l\}$  are the set of indexes of the non-zero and zero coordinates in  $\mathbf{z}$  respectively, and  $k = \|\mathbf{z}\|_0$  and  $\|\mathfrak{c}_L\|_0$  are the number of non-zero components in  $\mathbf{z}$  and  $\mathfrak{c}_L$  respectively (see the eqs.(A3,39,51) to revisit the notation). The proof of this proposition is based on the thermodynamic limit of  $Q_{|\mathbf{z}\rangle_{\mathfrak{c}}}(\mathbf{z}')$  and its  $\nu$ -moments (51). The number of humps in the expression above cannot be greater than  $2^{D-1}$ , as  $\|\mathbf{z}\|_0 + \|\mathfrak{c}_L\|_0 \leq D - 1$ , where  $\|\mathbf{z}\|_0 = k \leq D - 1$  and  $\|\mathfrak{c}_L\|_0 \leq l = D - 1 - k$  by construction. For instance, in the case  $D = 3$ , we have a maximum of  $2^2 = 4$  humps, like in Figures 5 and 6. If we focus on the eq.(39), we realize that  $2^{\|\mathbf{z}\|_0}$  is the number of humps of the reduced  $\mathfrak{c}_K$ -DCAT  $|\langle \mathbf{z}_K, \mathbf{z}_L = \mathbf{0}_L \rangle\rangle_{\mathfrak{c}_K}^{(N - \|\mathfrak{c}_L\|_0)}$  in the thermodynamic limit, while the Fock state  $|\tilde{n}_K = \vec{0}_K, \tilde{n}_L = \mathfrak{c}_L\rangle$  has

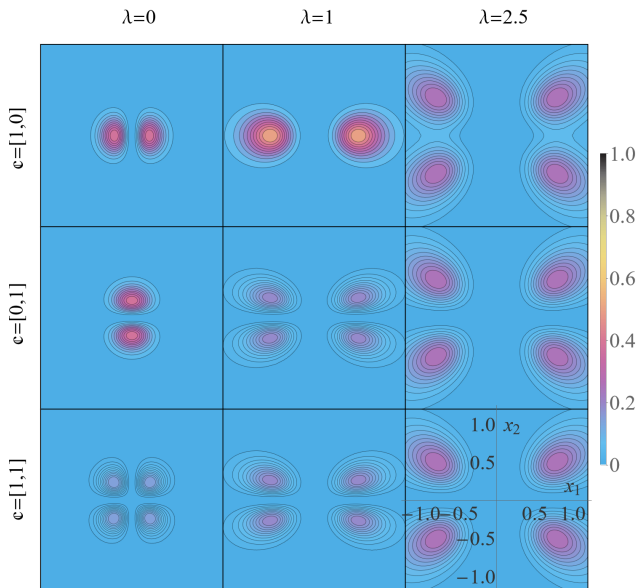


FIG. 6. Contour plots in phase space position coordinates  $x_{1,2} = \text{Re}(z'_{1,2})$  of the Husimi function  $Q_{|z^{(0)}_c\rangle}(z')$ , where  $|z^{(0)}_c\rangle$  are the variational excited states (70) of the LMG U(3) model (66). We have chosen  $N = 20$  particles and three different values of the control parameter  $\lambda$  ( $\epsilon$  units) inside the three phases I, II and III (columns from left to right). Each row in the plot represents a variational excited state of definite  $c$ -parity.

$2^{\|c_L\|_0}$  humps by construction. The reduced  $c_K$ -DCAT coordinates  $z_K$  are non-zero by definition, so  $\|z\|_0 = k$  and we obtain the maximum number of humps  $2^k$  allowed in a reduced phase space with  $k$  coordinates. In the case of the fully even DCAT,  $c = 0$  and  $\|c_L\|_0 = 0$ , we recover the results of Figure 5 and the equation (C16). We shall also highlight that  $2^{\|z\|_0 + \|c_L\|_0}$  is also the rank of the  $M$ -particle reduced density matrix of a  $c$ -DCAT, as it is shown in [56]. The connection of the two concepts is subject to further investigation.

The delocalization (area) of the Husimi function in phase space, which is perceived in Figures 5 and 6 across the different phase transitions, can be quantified by using the Wehrl entropy (53). In Figure 7, we present the Wehrl entropy of the variational (black curves) and numerical (red curves) ground state (GS) of the LMG U(3) model, as a function of the control parameter  $\lambda$  for different values of  $N$ . The entropy suddenly grows around the quantum critical points  $\lambda_{\text{I} \leftrightarrow \text{II}}^{(0)} = 1/2$  and  $\lambda_{\text{II} \leftrightarrow \text{III}}^{(0)} = 3/2$ , which are represented with vertical dashed lines. This effect is more abrupt with increasing  $N$ . In addition, the values of the entropy in each phase tend to the thermodynamic limit of the 3CAT entropy (57), with different number  $k$  of non-zero components in  $z$ . In particular for  $D = 3$ , this limit is  $2 + k \log(2)$  with  $k = 0, 1, \text{ and } 2$  in the phases I, II, and III respectively, which corresponds to

the gray dashed horizontal lines in Figure 7. When there is a QPT in the LMG U(3) model, the GS Husimi function in the position space (left column in Figure 5) splits into two identical subpackets with negligible overlap, so the Wehrl entropy experiences an increment of  $\ln(2)$  (see [29] for a similar result in the case of the Dicke model of superradiance). This delocalization effect happens twice from the phase I to the III, hence the  $2^2$  subpackets of the Husimi function in the phase III and the total growth of  $2 \log(2)$  in the Wehrl entropy.

The ‘‘Numerical’’ red curves in Figure 7 refer to the ground state obtained by numerical diagonalization of the Hamiltonian (60). The eigenvectors are calculated in the Fock basis (10), introduced in the Husimi function equation (40), and then, the Wehrl function (53) is numerically integrated. The change of entropy in the numerical (exact) case (red curves) is less abrupt than in the variational one (black curves) around the quantum critical points for a given number of particles  $N$ , although it becomes steeper and steeper as  $N$  increases.

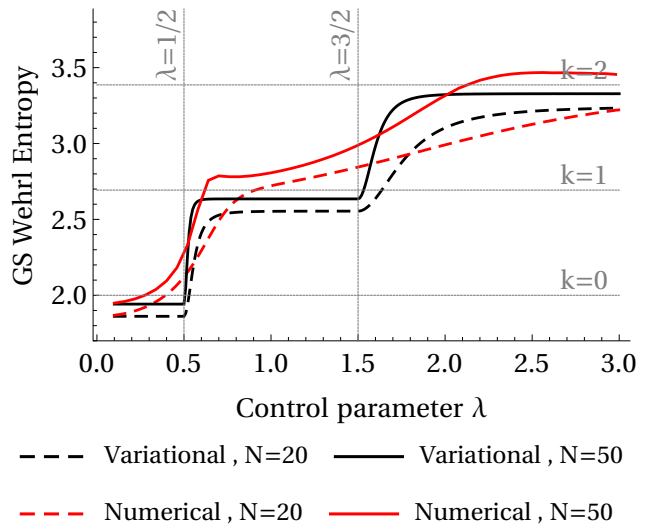


FIG. 7. Wehrl entropy of the variational  $|z^{(0)}_0\rangle$  and numerical  $|\psi_0\rangle$  ground state of the LMG U(3) model for  $N = 20$  and 50 particles. The gray dashed vertical lines represent the quantum critical points at  $\lambda_{\text{I} \leftrightarrow \text{II}}^{(0)} = 1/2$  and  $\lambda_{\text{II} \leftrightarrow \text{III}}^{(0)} = 3/2$  (in  $\epsilon$  units). The gray dashed horizontal lines are the  $N \rightarrow \infty$  limits of the Wehrl entropy of the 0-3CAT  $|z^{(0)}_0\rangle$  (57), with  $k$  humps (the number of non-zero coordinates in  $z^{(0)}(\lambda)$ ).

Equivalently, one can also measure the localization of the ground state in phase space with the IPR or the Husimi second moment (43). This quantity is usually easier (and faster) to calculate than the Wehrl entropy. That is why it is more common to focus on the IPR when studying localization [74–76]. The IPR of the ground state attains the thermodynamic limit value presented in the equation (50) for  $\nu = 2$  and  $k = 0, 1, 2$ . Variational calculations provide sharper results than the numerical

ones. For large values of the control parameter  $\lambda$ , the ground state behaves as a 3CAT which is less localized than the DSCS in phase space (check out Husimi function in Figure 5), and therefore, Figure 8 shows a decrease of the IPR when increasing  $\lambda$ .

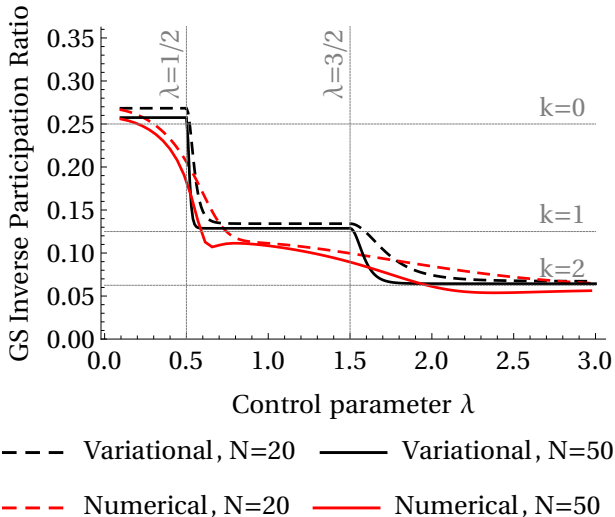


FIG. 8. Inverse Participation Ratio (IPR) of the variational  $|\mathbf{z}^{(0)}\rangle_0$  and numerical  $|\psi_0\rangle$  ground state of the LMG U(3) model for  $N = 20$  and  $50$  particles. The gray dashed vertical lines represent the critical points at  $\lambda_{\text{I} \leftrightarrow \text{II}}^{(0)} = 1/2$  and  $\lambda_{\text{II} \leftrightarrow \text{III}}^{(0)} = 3/2$  (in  $\epsilon$  units). The gray dashed horizontal lines are the  $N \rightarrow \infty$  limit of the IPR of the 0-3CAT according to (50) for  $\nu = 2$  and  $D = 3$ , that is,  $\lim_{N \rightarrow \infty} M_2(|\mathbf{z}^{(0)}\rangle_0) = 2^{-k-2} = \{\frac{1}{4}, \frac{1}{8}, \frac{1}{16}\}$ , for  $k = 0, 1, 2$  the number of non-zero components in  $\mathbf{z}^{(0)}(\lambda)$ .

As the IPR numerical computation is faster than the Wehrl entropy one, it is also feasible to reproduce Figure 8 but for the ESs of the LMG U(3) model. In particular, Figure 9 shows the IPR of the numerical ESs  $|\psi_i\rangle$ ,  $i = 0, 1, 3, 5$ , and its associated variational ESs  $|\mathbf{z}^{(0)}\rangle_{\mathbf{c}}$  regarding the equation (70), where we have used  $N = 20$  particles and the color code is the same as in the energy spectrum in Figure 1. In the top panel, the variational ESs approximate faster to the gray dashed horizontal lines (eq.(51) for  $\nu = 2$  and  $k + \|\mathbf{c}_L\|_0 = 0, 1, 2$ ) than the numerical ones in the bottom panel, as it happened in Figure 8 for the GS. The three different phases of Figure 9 are delimited by the gray dashed vertical lines, so that in the phases I, II and III there are  $k = \|\mathbf{z}^{(0)}(\lambda)\|_0 = 0, 1, 2$  non-zero coordinates in  $\mathbf{z}^{(0)}(\lambda)$  (see eq.(66)). Therefore, the IPR of the ESs reaches the gray dashed horizontal lines according the number of humps displayed in Figures 5 and 6, which depends on  $k$  and  $\|\mathbf{c}_L\|_0$  as  $2^{k+\|\mathbf{c}_L\|_0}$  (see eq.(75)). That is, for example, for  $\mathbf{c} = [1, 0]$  or  $i = 1$  (blue line), the ES has two ( $k = 0$ ,  $\|\mathbf{c}_L\|_0 = 1$ ), two ( $k = 1$ ,  $\|\mathbf{c}_L\|_0 = 0$ ), and four ( $k = 2$ ,  $\|\mathbf{c}_L\|_0 = 0$ ) humps in the three respective phases of Figure 6 (top row); hence, it attains the values  $k + \|\mathbf{c}_L\|_0 = 1, 1, 2$  marked by gray

dashed horizontal lines in each phase of Figure 9, respectively. This result is in agreement with the general expression in eq. (51) for the thermodynamic limit of the  $\mathbf{c}$ -DCAT Husimi moments for  $\nu = 2$  and  $D = 3$ .

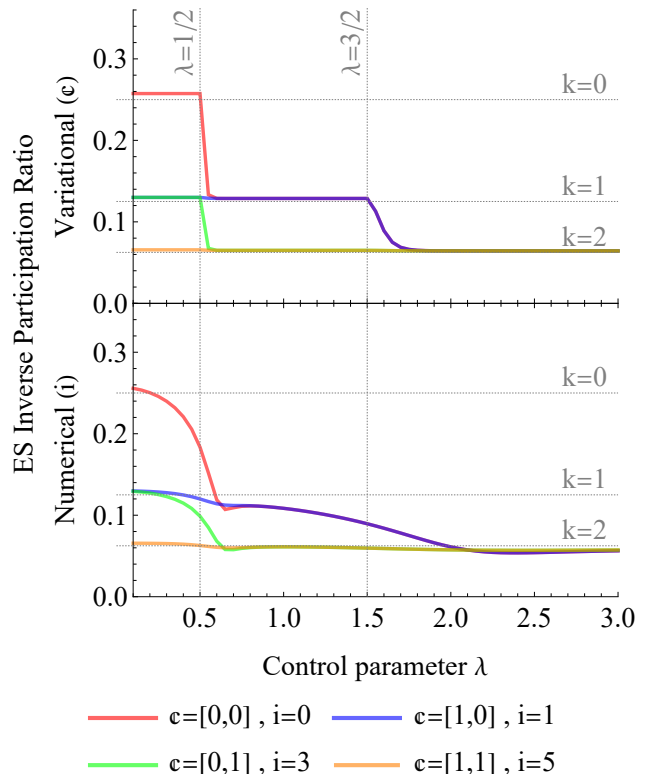


FIG. 9. Inverse Participation Ratio (IPR) of the variational  $|\mathbf{z}^{(0)}\rangle_{\mathbf{c}}$  (top panel) and numerical  $|\psi_i\rangle$  (bottom panel) excited states of the LMG U(3) model for  $N = 50$  particles. The gray dashed vertical lines represent the critical points at  $\lambda_{\text{I} \leftrightarrow \text{II}}^{(0)} = 1/2$  and  $\lambda_{\text{II} \leftrightarrow \text{III}}^{(0)} = 3/2$  (in  $\epsilon$  units). The gray dashed horizontal lines are the  $N \rightarrow \infty$  limit of the IPR of the  $\mathbf{c}$ -3CAT according to (51) for  $\nu = 2$  and  $D = 3$ , that is,  $\lim_{N \rightarrow \infty} M_2(|\mathbf{z}^{(0)}\rangle_{\mathbf{c}}) = 2^{-k-\|\mathbf{c}_L\|_0-2} = \{\frac{1}{4}, \frac{1}{8}, \frac{1}{16}\}$ , for  $k + \|\mathbf{c}_L\|_0 = 0, 1, 2$  the possible number of humps of  $Q_{|\mathbf{z}^{(0)}\rangle_{\mathbf{c}}}(\mathbf{z}')$  for  $N \gg 1$  (75).

## VIII. CONCLUSIONS

The concept of Husimi function in the canonical phase space is extended to the complex projective space  $\mathbb{C}P^{D-1} = \text{U}(D)/[\text{U}(1) \times \text{U}(D-1)]$  using  $\text{U}(D)$ -spin coherent states (DSCSs for short) for symmetric multi-quDit systems. The  $\nu$ -moments of the Husimi function and some localization measures in phase space such as the Inverse Participation Ratio and the Wehrl entropy are accordingly extended with a proper integration (Haar) measure. We prove that the Lieb conjecture is fulfilled for the DSCSs in the eq.(44) and the Appendix B. The parity  $\mathbb{Z}_2^{D-1} \ni \mathbf{c}$  adaptations of DSCSs (called  $\mathbf{c}$ -DCAT

states) turn out to be less localized than the DSCSs, which exhibit maximum localization (minimum area in phase space) according to Lieb’s conjecture. This becomes clear when we calculate the thermodynamic limit of the Husimi function  $\nu$ -th moments and Wehrl entropy for DSCSs and  $\mathfrak{c}$ -DCAT states.

The previous study of the LMG U(3) ground state [14] is then extended to the first excited states, which turn out to be modeled by  $\mathfrak{c}$ -3CATs of different parities, as Figures 1 and 2 show. In particular, we compare the numerical eigenstates of the LMG U(3) model (for finite  $N$ ) to different variational  $\mathfrak{c}$ -3CATs states via fidelity (72), where the variational states are evaluated at the critical points  $\mathbf{z}^{(0)} = (z_{1\pm}^{(0)}, z_{2\pm}^{(0)})$  which minimize the LMG U(3) energy surface in the thermodynamic limit (66). The variational  $\mathfrak{c}$ -3CAT states turn out to be fairly faithful to the low-lying excited Hamiltonian eigenstates except in the vicinity of the critical points  $\lambda_{\text{I}\leftrightarrow\text{II}}^{(0)} = \epsilon/2$  and  $\lambda_{\text{II}\leftrightarrow\text{III}}^{(0)} = 3\epsilon/2$  separating quantum phases I, II and III. We believe this is a consequence of the growth of quantum fluctuations at the critical points. However, this fidelity can be improved by maximizing the corresponding overlap in the complex projective phase space  $\mathbb{C}P^2 \ni \mathbf{z}$ , as we display in Figures 3 and 4.

The fact that the minimization of the energy surface in the thermodynamic limit provides critical vectors  $\mathbf{z}^{(0)}$  with some zero components in certain phases, makes it necessary to revise the  $\mathbb{Z}_2^{D-1}$ -parity adaptation  $|\mathbf{z}^{(0)}\rangle_{\mathfrak{c}}$  of  $|\mathbf{z}^{(0)}\rangle_{\mathfrak{c}}$  and to resolve some “0/0” indeterminacies. In the case when  $\mathbf{z}$  has  $l = D - 1 - k$  null coordinates, the corresponding  $\mathfrak{c}$ -DCAT  $|\mathbf{z}^{(0)}\rangle_{\mathfrak{c}}$  reduces to  $\mathfrak{c}_K$ -DCATs with lower  $\mathbb{Z}_2^k$ -parity times a Fock state with  $\mathbb{Z}_2^{\|\mathfrak{c}_L\|_0}$ -parity (39). This result permeates in the majority of magnitudes (Husimi function, its moments, etc.) calculated in this work.

The QPTs of the LMG U(3) model are visualized in the phase space  $\mathbb{C}P^2 \ni \mathbf{z}'$  across the phase diagram via the Husimi function  $Q_0(\mathbf{z}')$  of the variational ground state  $|\mathbf{z}^{(0)}\rangle_0$ . We draw contour plots of the Husimi function in “position space”  $(x_1, x_2) = \text{Re}(\mathbf{z}')$  and in “momentum space”  $(p_1, p_2) = \text{Im}(\mathbf{z}')$  in Figure 5). In position space, the variational GS Husimi function  $Q_0(\mathbf{z}')$  displays several humps depending on the number of non-zero coordinates of  $\mathbf{z}^{(0)}(\lambda)$ , which changes in the different quantum phases I, II and III. A similar reasoning is followed in Figure 6 with the Husimi function of the other variational  $\mathfrak{c}$ -3CAT states  $|\mathbf{z}^{(0)}\rangle_{\mathfrak{c}}$  mimicking low-lying Hamiltonian eigenstates with parity  $\mathfrak{c}$ . We propose a general expression (75) for the number of humps (in position phase) of the Husimi function of general  $\mathfrak{c}$ -3CATs  $|\mathbf{z}\rangle_{\mathfrak{c}}$ , depending on the number of zero components of  $\mathbf{z}$  and the parity  $\mathfrak{c}$ . This number also appears in the thermodynamic limit of the  $\mathfrak{c}$ -DCAT Husimi moments (51) and in the rank of the  $M$ -particle reduced density matrix of a  $\mathfrak{c}$ -DCAT [56].

Finally, we also characterize the QPTs via localization measures in phase space, since the Husimi function  $Q_0$  of the ground state of the LMG model suddenly suffers de-

localization when passing through the quantum critical  $\lambda^{(0)}$  points, as shown in Figures of Wehrl entropy 7 and IPR 8 of  $Q_0$  as a function of the control parameter  $\lambda$ . More localization implies less Wehrl entropy (less area) and more IPR. This effect is more abrupt for the variational ground state than for the numerical one, and gets sharper and sharper when increasing  $N$ , approaching to the limits proposed in Section IV and proved in the Appendix C. The same analysis is extended to the numerical excited states and variational  $\mathfrak{c}$ -3CATs in Figure 9, which also experience delocalization, but only when its Husimi function number of humps changes according to Figure 6.

## ACKNOWLEDGMENTS

We thank the support of the Spanish MICINN through the project PGC2018-097831-B-I00 and Junta de Andalucía through the projects UHU-1262561 and FQM-381. JG also thanks MICINN for financial support from FIS2017-84440-C2-2-P. AM thanks the Spanish MIU for the FPU19/06376 predoctoral fellowship. We all thank Octavio Castaños for his valuable comments in the early stages of this work.

### Appendix A: Reduced parity adapted U( $D$ )-spin coherent states

We generalize the  $z_i \rightarrow 0$  limits in (36) and (37) for a general  $\mathfrak{c}$ -DCAT. Firstly, in the fully even case  $\mathfrak{c} = 0$ , it is easy to check that the  $0$ -DCAT in the equation (24) turns into a reduced  $0_i$ -DCAT,

$$\lim_{z_i \rightarrow 0} |\mathbf{z}\rangle_0^{(N)} = |\mathbf{z}_i\rangle_{0_i}^{(N)} = \frac{\Pi_{0_i}}{\mathcal{N}(\mathbf{z}_i)_{0_i}} |\mathbf{z}_i\rangle^{(N)}, \quad (\text{A1})$$

whose projective coordinates include  $z_i = 0$ ,  $\mathbf{z}_i = (z_1, \dots, z_{i-1}, 0, z_{i+1}, \dots, z_{D-1})$ , but its parity string  $\mathfrak{c}$  does not contain  $c_i = 0$ , i.e.  $0_i = [0, \binom{D-2}{\cdot}, 0] \in \mathbb{Z}_2^{D-2}$ . That is,  $\Pi_{0_i}$  only acts onto the non-zero coordinates of  $|\mathbf{z}_i\rangle$ . Note that the reduced  $0_i$ -DCAT is not a  $(D-1)$ CAT, as it is the  $\mathbb{Z}_2^{D-2}$ -parity adapted version of a DSCS with  $z_i = 0$ , i.e.  $|\mathbf{z}_i\rangle^{(N)} = \lim_{z_i \rightarrow 0} |\mathbf{z}\rangle^{(N)}$ . The normalization constant  $\mathcal{N}(\mathbf{z}_i)_{0_i}$  is calculated as in (25) but using a reduced sum in  $b_i \in \{0, 1\}^{D-2}$ , and with the new coordinates  $\mathbf{z}_i$ ,

$$\mathcal{N}(\mathbf{z}_i)_{0_i}^2 = 2^{2-D} \frac{\sum_{b_i \in \{0, 1\}^{D-2}} (1 + \mathbf{z}_i^\dagger \mathbf{z}_i^{b_i})^N}{(1 + \mathbf{z}_i^\dagger \mathbf{z}_i)^N}. \quad (\text{A2})$$

The zero limit (A1) can be used repeatedly for a set of  $l = D - 1 - k$  different coordinates  $\mathbf{z}_L = \{z_{i_1}, \dots, z_{i_l}\}$ , whose indexes are taken from the set  $L = \{i_1, \dots, i_l\}$ , transforming the totally even  $0$ -DCAT into a reduced  $0_K$ -DCAT with a parity symmetry given by  $\mathbb{Z}_2^k$ ,

$$\lim_{z_L \rightarrow \mathbf{0}_L} |\mathbf{z}\rangle_0^{(N)} = |(\mathbf{z}_K, \mathbf{z}_L = \mathbf{0}_L)\rangle_{0_K}^{(N)}, \quad (\text{A3})$$

where  $(\mathbf{z}_K, \mathbf{z}_L = \mathbf{0}_L) = \lim_{z_L \rightarrow \mathbf{0}_L} \mathbf{z}$  has only  $k$  non-zero coordinates  $\mathbf{z}_K = \{z_{j_1}, \dots, z_{j_k}\}$ , whose associated parity components are  $\mathbb{0}_K = [0, \binom{k}{2}, 0] \in \mathbb{Z}_2^k$ . That is,  $K = \{j_1, \dots, j_k\}$  is the set including all the  $k$  non-zero coordinates of  $\mathbf{z}$ .  $\mathbf{0}_L$  denotes the  $l$  coordinates  $(0, \dots, 0)$ . The existence and uniqueness of the multiple limit (A3) can be derived using hyperspherical coordinates with the moduli of  $|z_i|$ . The norm of the reduced  $\mathbb{0}_K$ -DCAT in (A3) is calculated using an equivalent expression of the eq.(A2).

In the case where all coordinates  $z_i$  tend to 0 ( $k = 0$ ), the  $\mathbb{0}$ -DCAT collapses to a Fock state,

$$\lim_{\mathbf{z} \rightarrow \mathbf{0}} |\mathbf{z}\rangle_0^{(N)} = |n_0=N, n_1=0, \dots, n_{D-1}=0\rangle, \quad (\text{A4})$$

which is the highest weight vector of the  $N$ -particle symmetric irreducible representation of  $U(D)$  that we are considering. This highest weight vector deserves our attention because it is the ground state of the free ( $\lambda = 0$ ) LMG  $U(D)$  Hamiltonian (see in Section V for a detailed discussion). The limit (A4) has previously been calculated in [56] for a general  $\mathfrak{c}$ -DCAT, giving the so called *Fock-cat states*.

### Appendix B: Analytical calculation of the $\nu$ -moments of the Husimi function of a DSCS

Here we show in detail the calculations that lead to the expressions of the  $\nu$ -th moments of the DSCSs (44,45), the DCATs (46) and its thermodynamic limit (44,49,50).

Firstly, the moments of the DSCSs are computed by previously using the highest-weight state  $|\psi\rangle = |\mathbf{z} = \mathbf{0}\rangle = (a_0^\dagger)^N / \sqrt{N!} |\bar{0}\rangle$  (a boson condensate of  $N$  atoms in their lower level  $i = 0$ ) according to the equation(15). Using the scalar product of the DSCSs (17), we calculate the Husimi function (40) of this state as

$$Q_{|\mathbf{0}\rangle}(z) = |\langle \mathbf{z} | \mathbf{0} \rangle|^2 = \frac{1}{(1 + \mathbf{z}^\dagger \mathbf{z})^N}. \quad (\text{B1})$$

It is straightforward to perform the integration in the  $\nu$ -moments formula (43) for the Husimi function  $Q_{|\mathbf{0}\rangle}(z)$  and arbitrary  $\nu$ . The integral in  $\mathbb{C}^{D-1}$  is mapped to  $(\mathbb{R}^+ \times [0, 2\pi])^{D-1}$  using polar coordinates  $z_j = \rho_j e^{i\theta_j}$ ,  $d^2 z_j = \rho_j d\rho_j d\theta_j$  for all  $j = 1, \dots, D-1$ . Then, we integrate recursively for all  $\rho_j$  from  $j = 1$  to  $j = D-1$ , and the equation (44) for  $M_\nu(|\mathbf{0}\rangle)$  is achieved. The extension (45) from  $|\mathbf{z} = \mathbf{0}\rangle$  to an arbitrary DSCS  $|\mathbf{z}\rangle$  is direct using the  $U(D)$  invariance of the Fubini-Study measure  $d\mu(\mathbf{z})$  in  $\mathbb{C}P^{D-1}$ .

### Appendix C: Thermodynamic limit of the $\nu$ -moments of the Husimi function of a $\mathfrak{c}$ -DCAT

In Eq. (46) we have given the  $\nu$ -moments of the Husimi function  $Q_{|\mathbf{z}_\mathfrak{c}\rangle}$  of a  $\mathfrak{c}$ -DCAT. This bulky expression ac-

quires a simpler form (50) in the thermodynamic limit. Let us prove it.

We shall initially give some auxiliary results and calculate their Husimi function. First of all, the scalar product of the DSCSs (17) has a Kronecker delta-like thermodynamic limit,

$$\lim_{N \rightarrow \infty} \langle \mathbf{z}' | \mathbf{z} \rangle = \begin{cases} 1 & \text{if } \mathbf{z}' = \mathbf{z}, \\ 0 & \text{if } \mathbf{z}' \neq \mathbf{z}, \end{cases} \quad (\text{C1})$$

which leads to

$$\lim_{N \rightarrow \infty} \langle \mathbf{z}' | \mathbf{z}^{\mathfrak{b}} \rangle \langle \mathbf{z}^{\mathfrak{b}'} | \mathbf{z}' \rangle = \begin{cases} 1 & \text{if } \mathbf{z}' = \mathbf{z}^{\mathfrak{b}} \text{ and } \mathbf{z}' = \mathbf{z}^{\mathfrak{b}'}, \\ 0 & \text{elsewhere,} \end{cases} \quad (\text{C2})$$

as  $(1 + \mathbf{z}^\dagger \mathbf{z}^{\mathfrak{b}}) < (1 + \mathbf{z}^\dagger \mathbf{z})$  for all  $\mathfrak{b} \neq \mathbf{0}$  and  $\mathbf{z}$  with non-zero components. The non-null condition of the last equation implies that  $\mathbf{z}^{\mathfrak{b}} = \mathbf{z}^{\mathfrak{b}'}$ , what leads to  $\mathfrak{b} = \mathfrak{b}'$  provided that  $z_i \neq 0$  for all  $i = 1, \dots, D-1$ . Therefore, we begin studying the case where  $\mathbf{z}$  does not have any null component.

The Husimi function of the  $\mathfrak{c}$ -DCAT (42) can also be written using the Husimi function (40) and the  $\mathfrak{c}$ -DCAT (24) definitions,

$$\begin{aligned} Q_{|\mathbf{z}\rangle_\mathfrak{c}}(\mathbf{z}') &= |\langle \mathbf{z}' | \mathbf{z} \rangle_\mathfrak{c}|^2 \\ &= \left( \frac{2^{1-D}}{\mathcal{N}(\mathbf{z})_\mathfrak{c}} \right)^2 \sum_{\mathfrak{b}, \mathfrak{b}'} (-1)^{\mathfrak{c} \cdot (\mathfrak{b} + \mathfrak{b}')} \langle \mathbf{z}' | \mathbf{z}^{\mathfrak{b}} \rangle \langle \mathbf{z}^{\mathfrak{b}'} | \mathbf{z}' \rangle. \end{aligned} \quad (\text{C3})$$

Since the  $\mathfrak{c}$ -DCAT normalization  $\mathcal{N}(\mathbf{z})_\mathfrak{c}$  is non-zero for all  $\mathbf{z}$  (without any null component) and  $\mathfrak{c}$ , we take the limit of the numerator and denominator of  $Q_{|\mathbf{z}\rangle_\mathfrak{c}}(\mathbf{z}')$  separately. The denominator is, according to the equation (25),

$$\begin{aligned} \lim_{N \rightarrow \infty} \mathcal{N}(\mathbf{z})_\mathfrak{c}^2 &= \lim_{N \rightarrow \infty} 2^{1-D} \frac{\sum_{\mathfrak{b}} (-1)^{\mathfrak{c} \cdot \mathfrak{b}} (1 + \mathbf{z}^\dagger \mathbf{z}^{\mathfrak{b}})^N}{(1 + \mathbf{z}^\dagger \mathbf{z})^N} \\ &= 2^{1-D} \sum_{\mathfrak{b}} (-1)^{\mathfrak{c} \cdot \mathfrak{b}} \lim_{N \rightarrow \infty} \frac{(1 + \mathbf{z}^\dagger \mathbf{z}^{\mathfrak{b}})^N}{(1 + \mathbf{z}^\dagger \mathbf{z})^N} \\ &= 2^{1-D}. \end{aligned} \quad (\text{C4})$$

The numerator limit is performed using the equation (C2) and its derived condition  $\mathfrak{b} = \mathfrak{b}'$ ,

$$\begin{aligned} &\lim_{N \rightarrow \infty} \sum_{\mathfrak{b}, \mathfrak{b}'} (-1)^{\mathfrak{c} \cdot (\mathfrak{b} + \mathfrak{b}')} \langle \mathbf{z}' | \mathbf{z}^{\mathfrak{b}} \rangle \langle \mathbf{z}^{\mathfrak{b}'} | \mathbf{z}' \rangle \\ &= \lim_{N \rightarrow \infty} \sum_{\mathfrak{b}} (-1)^{\mathfrak{c} \cdot (\mathfrak{b} + \mathfrak{b})} \langle \mathbf{z}' | \mathbf{z}^{\mathfrak{b}} \rangle \langle \mathbf{z}^{\mathfrak{b}} | \mathbf{z}' \rangle \\ &= \lim_{N \rightarrow \infty} \sum_{\mathfrak{b}} Q_{|\mathbf{z}^{\mathfrak{b}}\rangle}(\mathbf{z}'), \end{aligned} \quad (\text{C5})$$

as  $(-1)^{\mathfrak{c} \cdot (\mathfrak{b} + \mathfrak{b})} = 1$ . Therefore, the limit of the  $\mathfrak{c}$ -DCAT Husimi function is

$$\lim_{N \rightarrow \infty} Q_{|\mathbf{z}\rangle_\mathfrak{c}}(\mathbf{z}') = 2^{1-D} \lim_{N \rightarrow \infty} \sum_{\mathfrak{b}} Q_{|\mathbf{z}^{\mathfrak{b}}\rangle}(\mathbf{z}'). \quad (\text{C6})$$

The number of humps of  $\lim_{N \rightarrow \infty} Q_{|\mathbf{z}\rangle_c}(\mathbf{z}')$  in the phase space  $\mathbf{z}'$  will be the number of terms in the sum  $\sum_{\mathbf{b}}$  (right term in eq.(C6)), that is  $2^{D-1}$ , as showed in Figures 5 and 6 for  $D = 3$  and  $\lambda = 2.5$ .

The next step is calculate the limit of the  $\nu$ -th power of the Husimi function of the  $\mathfrak{c}$ -DCAT,  $[Q_{|\mathbf{z}\rangle_c}(\mathbf{z}')]^\nu$  for all  $\nu \geq 2$ . We split again the limit in numerator and denominator, where the last one is trivial using the same procedure as in (C4), that is  $\lim_{N \rightarrow \infty} \mathcal{N}(\mathbf{z})_{\mathfrak{c}}^{2\nu} = (2^{1-D})^\nu$ . The numerator limit is

$$\begin{aligned} & \lim_{N \rightarrow \infty} \left( \sum_{\mathbf{b}, \mathbf{b}'} (-1)^{\mathfrak{c} \cdot (\mathbf{b} + \mathbf{b}')} \langle \mathbf{z}' | \mathbf{z}^{\mathbf{b}} \rangle \langle \mathbf{z}^{\mathbf{b}'} | \mathbf{z}' \rangle \right)^\nu \quad (C7) \\ &= \lim_{N \rightarrow \infty} \sum_{\mathbf{b}_1, \dots, \mathbf{b}_\nu} \sum_{\mathbf{b}'_1, \dots, \mathbf{b}'_\nu} (-1)^{\mathfrak{c} \cdot \sum_{i=1}^\nu (\mathbf{b}_i + \mathbf{b}'_i)} \\ & \quad \times \prod_{i=1}^\nu \langle \mathbf{z}' | \mathbf{z}^{\mathbf{b}_i} \rangle \langle \mathbf{z}^{\mathbf{b}'_i} | \mathbf{z}' \rangle, \end{aligned}$$

which reduces, with the auxiliary equation (C2), to

$$\begin{aligned} & \lim_{N \rightarrow \infty} \sum_{\mathbf{b}} (-1)^{\mathfrak{c} \cdot 2\nu \mathbf{b}} \prod_{i=1}^\nu \langle \mathbf{z}' | \mathbf{z}^{\mathbf{b}} \rangle \langle \mathbf{z}^{\mathbf{b}} | \mathbf{z}' \rangle \\ &= \lim_{N \rightarrow \infty} \sum_{\mathbf{b}} [Q_{|\mathbf{z}^{\mathbf{b}}\rangle}(\mathbf{z}')]^\nu. \quad (C8) \end{aligned}$$

So we have

$$\lim_{N \rightarrow \infty} [Q_{|\mathbf{z}\rangle_c}(\mathbf{z}')]^\nu = (2^{1-D})^\nu \lim_{N \rightarrow \infty} \sum_{\mathbf{b}} [Q_{|\mathbf{z}^{\mathbf{b}}\rangle}(\mathbf{z}')]^\nu. \quad (C9)$$

Eventually, we can calculate the  $\nu$ -moments of the  $\mathfrak{c}$ -DCAT Husimi function, that is

$$\lim_{N \rightarrow \infty} M_\nu(|\mathbf{z}\rangle_c) = \lim_{N \rightarrow \infty} \int_{\mathbb{C}^{D-1}} [Q_{|\mathbf{z}\rangle_c}(\mathbf{z}')]^\nu d\mu(\mathbf{z}'). \quad (C10)$$

Employing the equation (C9), and commuting the integral and the limit, the last expression turns into

$$\begin{aligned} \lim_{N \rightarrow \infty} M_\nu(|\mathbf{z}\rangle_c) &= (2^{1-D})^\nu \int \lim_{N \rightarrow \infty} \sum_{\mathbf{b}} [Q_{|\mathbf{z}^{\mathbf{b}}\rangle}(\mathbf{z}')]^\nu d\mu(\mathbf{z}') \\ &= (2^{1-D})^\nu \lim_{N \rightarrow \infty} \sum_{\mathbf{b}} \int [Q_{|\mathbf{z}^{\mathbf{b}}\rangle}(\mathbf{z}')]^\nu d\mu(\mathbf{z}'). \quad (C11) \end{aligned}$$

The new integral is equal to the moment  $M_\nu(|\mathbf{z}^{\mathbf{b}}\rangle)$  of the DSCS  $|\mathbf{z}^{\mathbf{b}}\rangle$ , which fulfills  $M_\nu(|\mathbf{z}^{\mathbf{b}}\rangle) = M_\nu(|\mathbf{z}\rangle) = M_\nu(|\mathbf{0}\rangle)$  according to the equation (45) and the Fubini-Study measure invariance. In the end, the equation (49) of the moments of the  $\mathfrak{c}$ -DCAT in the thermodynamic limit is reached,

$$\begin{aligned} \lim_{N \rightarrow \infty} M_\nu(|\mathbf{z}\rangle_c) &= (2^{1-D})^\nu \lim_{N \rightarrow \infty} \sum_{\mathbf{b}} M_\nu(|\mathbf{z}\rangle) \\ &= (2^{D-1})^{1-\nu} \lim_{N \rightarrow \infty} M_\nu(|\mathbf{z}\rangle). \quad (C12) \end{aligned}$$

When there are only  $k$  non-zero components in  $\mathbf{z}$ , the even  $\mathfrak{0}$ -DCAT (with  $\mathfrak{0} \in \mathbb{Z}_2^{D-1}$ ) reduces to a  $\mathfrak{0}_K$ -DCAT with a smaller parity symmetry  $\mathfrak{0}_K = [0, \binom{k}{\cdot}, 0] \in \mathbb{Z}_2^k$  (see the notation of the eq.(A3)). Therefore, the equation (C3) turns into

$$\begin{aligned} \lim_{z_L \rightarrow \mathbf{0}_L} Q_{|\mathbf{z}\rangle_{\mathfrak{0}}}(\mathbf{z}') &= Q_{|\mathbf{z}_K\rangle_{\mathfrak{0}_K}}(\mathbf{z}') = |\langle \mathbf{z}' | \mathbf{z}_K \rangle_{\mathfrak{0}_K}|^2 \\ &= \left( \frac{2^{-k}}{\mathcal{N}(\mathbf{z}_K)_{\mathfrak{0}_K}} \right)^2 \sum_{\mathbf{b}_K, \mathbf{b}'_K} (-1)^{\mathfrak{0}_K \cdot (\mathbf{b}_K + \mathbf{b}'_K)} \langle \mathbf{z}' | \mathbf{z}_K^{\mathbf{b}_K} \rangle \langle \mathbf{z}_K^{\mathbf{b}'_K} | \mathbf{z}' \rangle, \quad (C13) \end{aligned}$$

where  $\mathbf{z}_K = \lim_{z_L \rightarrow \mathbf{0}_L} \mathbf{z}$  (it would be more correct to write it as  $(\mathbf{z}_K, \mathbf{z}_L = \mathbf{0}_L)$ ) and  $\mathfrak{0}_K, \mathbf{b}_K, \mathbf{b}'_K \in \mathbb{Z}_2^k$ . As previously done in the non-zero case (C4), the reduced normalization constant of the denominator tends to  $\lim_{N \rightarrow \infty} \mathcal{N}(\mathbf{z}_K)_{\mathfrak{0}_K} = 2^{-k}$ , where we have used a generalization of the expression (A2). The equation (C2) can be adapted to

$$\lim_{N \rightarrow \infty} \langle \mathbf{z}' | \mathbf{z}_K^{\mathbf{b}_K} \rangle \langle \mathbf{z}_K^{\mathbf{b}'_K} | \mathbf{z}' \rangle = \begin{cases} 1 & \text{if } \mathbf{z}' = \mathbf{z}_K^{\mathbf{b}_K} \text{ and } \mathbf{z}' = \mathbf{z}_K^{\mathbf{b}'_K}, \\ 0 & \text{elsewhere,} \end{cases} \quad (C14)$$

where the non-null value is achieved when  $\mathbf{z}_K^{\mathbf{b}_K} = \mathbf{z}_K^{\mathbf{b}'_K}$ , which implies  $\mathbf{b}_K = \mathbf{b}'_K$ . This is true because all the coordinates in  $\mathbf{z}_K$  ( $(\mathbf{z}_K, \mathbf{z}_L = \mathbf{0}_L)$  in fact) associated to  $\mathbf{b}_K$  are non-zero by construction. Consequently, the numerator in (C13) transforms into

$$\begin{aligned} & \lim_{N \rightarrow \infty} \sum_{\mathbf{b}_K, \mathbf{b}'_K} (-1)^{\mathfrak{0}_K \cdot (\mathbf{b}_K + \mathbf{b}'_K)} \langle \mathbf{z}' | \mathbf{z}_K^{\mathbf{b}_K} \rangle \langle \mathbf{z}_K^{\mathbf{b}'_K} | \mathbf{z}' \rangle \\ &= \lim_{N \rightarrow \infty} \sum_{\mathbf{b}_K} \langle \mathbf{z}' | \mathbf{z}_K^{\mathbf{b}_K} \rangle \langle \mathbf{z}_K^{\mathbf{b}_K} | \mathbf{z}' \rangle \\ &= \lim_{N \rightarrow \infty} \sum_{\mathbf{b}_K} Q_{|\mathbf{z}_K^{\mathbf{b}_K}\rangle}(\mathbf{z}'), \quad (C15) \end{aligned}$$

using in the second line the property (29) of the parity group characters. The thermodynamic limit of the  $\mathfrak{0}$ -DCAT Husimi function is finally

$$\lim_{N \rightarrow \infty} Q_{|\mathbf{z}_K\rangle_{\mathfrak{0}_K}}(\mathbf{z}') = 2^{-k} \lim_{N \rightarrow \infty} \sum_{\mathbf{b}_K} Q_{|\mathbf{z}_K^{\mathbf{b}_K}\rangle}(\mathbf{z}'). \quad (C16)$$

From this moment on, it is straightforward to adapt the procedure followed at the beginning for the moments of the  $\mathfrak{c}$ -DCAT to the  $\mathfrak{0}_K$ -DCAT, arriving to the expression

$$\begin{aligned} & \lim_{N \rightarrow \infty} M_\nu(|\mathbf{z}_K\rangle_{\mathfrak{0}_K}) \quad (C17) \\ &= (2^{-k})^\nu \lim_{N \rightarrow \infty} \sum_{\mathbf{b}_K} \int_{\mathbb{C}^{D-1}} [Q_{|\mathbf{z}_K^{\mathbf{b}_K}\rangle}(\mathbf{z}')]^\nu d\mu(\mathbf{z}') \\ &= (2^{-k})^\nu \lim_{N \rightarrow \infty} \sum_{\mathbf{b}_K} M_\nu(|\mathbf{z}_K^{\mathbf{b}_K}\rangle) = (2^k)^{(1-\nu)} \lim_{N \rightarrow \infty} M_\nu(|\mathbf{z}\rangle), \end{aligned}$$

since  $M_\nu(|\mathbf{z}_K^{\mathbf{b}_K}\rangle) = M_\nu(|\mathbf{z}\rangle)$  (45), and using the parity characters property (27) for the reduced parity group

$\mathbb{Z}_2^k$ . The last equation ends the calculations to prove the eq.(50) for the 0-DCAT. The general case of zero coordinates in the c-DCAT (see eq.(51)) has been computed with a symbolic calculation software, so the analytical calculations are devoted to future research.

## REFERENCES

- [1] P. W. Anderson, Absence of diffusion in certain random lattices, *Phys. Rev.* **109**, 1492–1505 (1958).
- [2] C. Aulbach, A. Wobst, G.-L. Ingold, P. Hänggi, and I. Varga, Phase-space visualization of a metal–insulator transition, *New Journal of Physics* **6**, 70–70 (2004).
- [3] F. Evers and A. D. Mirlin, Anderson transitions, *Rev. Mod. Phys.* **80**, 1355–1417 (2008).
- [4] W. P. Schleich, *Quantum Optics in Phase Space* (Wiley-VCH Verlag Berlin GmbH, 2001).
- [5] F. E. and J. Schroeck, *Quantum Mechanics on Phase Space* (Springer Netherlands, 1996).
- [6] E. Schrödinger, Der stetige Übergang von der mikrozur makromechanik, *Naturwissenschaften* **14**, 664–666 (1926).
- [7] R. J. Glauber, Coherent and incoherent states of the radiation field, *Phys. Rev.* **131**, 2766–2788 (1963).
- [8] W.-M. Zhang, D. H. Feng, and R. Gilmore, Coherent states: Theory and some applications, *Rev. Mod. Phys.* **62**, 867–927 (1990).
- [9] F. T. Arecchi, E. Courtens, R. Gilmore, and H. Thomas, Atomic coherent states in quantum optics, *Phys. Rev. A* **6**, 2211–2237 (1972).
- [10] A. Perelomov, *Generalized Coherent States and Their Applications* (Springer-Verlag Berlin Heidelberg, 1986).
- [11] A. Vourdas, Analytic representations in quantum mechanics, *Journal of Physics A: Mathematical and General* **39**, R65–R141 (2006).
- [12] U. Leonhardt, *Measuring the quantum state of light*, Cambridge studies in modern optics (Cambridge University Press, 1997).
- [13] T. L. Curtright, D. B. Fairlie, and C. K. Zachos, *A concise treatise on quantum mechanics in phase space* (World Scientific Publishing, 2014).
- [14] M. Calixto, A. Mayorgas, and J. Guerrero, Role of mixed permutation symmetry sectors in the thermodynamic limit of critical three-level Lipkin-Meshkov-Glick atom models, *Phys. Rev. E* **103**, 012116 (2021).
- [15] A. Wehrl, On the relation between classical and quantum-mechanical entropy, *Reports on Mathematical Physics* **16**, 353–358 (1979).
- [16] F. Mintert and K. Życzkowski, Wehrl entropy, lieb conjecture, and entanglement monotones, *Phys. Rev. A* **69**, 022317 (2004).
- [17] S. Gnutzmann and K. Życzkowski, Rényi-wehrl entropies as measures of localization in phase space, *Journal of Physics A: Mathematical and General* **34**, 10123–10139 (2001).
- [18] V. Giovannetti, S. Lloyd, L. Maccone, J. H. Shapiro, and B. J. Yen, Minimum rényi and wehrl entropies at the output of bosonic channels, *Phys. Rev. A* **70**, 022328 (2004).
- [19] B. Mirbach and H. J. Korsch, Phase space entropy and global phase space structures of (chaotic) quantum systems, *Phys. Rev. Lett.* **75**, 362 (1995).
- [20] T. Gorin, H. Korsch, and B. Mirbach, Phase-space localization and level spacing distributions for a driven rotor with mixed regular/chaotic dynamics, *Chemical Physics* **217**, 145 (1997), dynamics of Driven Quantum Systems.
- [21] B. Batistić, i. c. v. Lozej, and M. Robnik, Statistical properties of the localization measure of chaotic eigenstates and the spectral statistics in a mixed-type billiard, *Phys. Rev. E* **100**, 062208 (2019).
- [22] I. Saideh, D. Finkelstein-Shapiro, T. o. Pullerits, and A. Keller, Projection-based adiabatic elimination of bipartite open quantum systems, *Phys. Rev. A* **102**, 032212 (2020).
- [23] D. Villaseñor, S. Pilatowsky-Cameo, M. A. Bastarrachea-Magnani, S. Lerma-Hernández, and J. G. Hirsch, Quantum localization measures in phase space, *Phys. Rev. E* **103**, 052214 (2021).
- [24] D. J. Nader, C. A. González-Rodríguez, and S. Lerma-Hernández, Avoided crossings and dynamical tunneling close to excited-state quantum phase transitions, *Phys. Rev. E* **104**, 064116 (2021).
- [25] i. c. v. Lozej, G. Casati, and T. c. v. Prosen, Quantum chaos in triangular billiards, *Phys. Rev. Res.* **4**, 013138 (2022).
- [26] O. Castaños, M. Calixto, F. Pérez-Bernal, and E. Romera, Identifying the order of a quantum phase transition by means of Wehrl entropy in phase space, *Phys. Rev. E* **92**, 052106 (2015).
- [27] C. Pérez-Campos, J. R. González-Alonso, O. Castaños, and R. López-Peña, Entanglement and localization of a two-mode Bose-Einstein condensate, *Annals of Physics* **325**, 325–344 (2010).
- [28] E. Romera, R. del Real, and M. Calixto, Husimi distribution and phase-space analysis of a dicke-model quantum phase transition, *Phys. Rev. A* **85**, 053831 (2012).
- [29] R. del Real, M. Calixto, and E. Romera, The husimi distribution, the Wehrl entropy and the superradiant phase in spin–boson interactions, *Physica Scripta* **T153**, 014016 (2013).
- [30] O. Castaños, S. Cordero, R. López-Peña, and E. Nahmad-Achar, Phase space properties of light within the generalised dicke model, *Physica Scripta* **93**, 085102 (2018).
- [31] M. Calixto, R. del Real, and E. Romera, Husimi distribution and phase-space analysis of a vibron-model quantum phase transition, *Phys. Rev. A* **86**, 032508 (2012).
- [32] M. Calixto and C. Peón-Nieto, Husimi function and phase-space analysis of bilayer quantum hall systems at  $\nu = 2$ , *Journal of Statistical Mechanics: Theory and Experiment* **2018**, 053112 (2018).
- [33] E. Romera, M. Calixto, and O. Castaños, Phase space analysis of first-, second- and third-order quantum phase transitions in the Lipkin-Meshkov-Glick model, *Physica Scripta* **89**, 095103 (2014).
- [34] E. Romera, O. Castaños, M. Calixto, and F. Pérez-Bernal, Delocalization properties at isolated avoided crossings in Lipkin-Meshkov-Glick type hamiltonian models, *Journal of Statistical Mechanics: Theory and Experiment* **2017**, 013101 (2017).
- [35] O. Castaños, R. López-Peña, J. G. Hirsch, and E. López-Moreno, Classical and quantum phase transitions in the lipkin-meshkov-glick model, *Phys. Rev. B* **74**, 104118 (2006).
- [36] V. Dodonov, I. Malkin, and V. Man’ko, Even and odd coherent states and excitations of a singular oscillator, *Physica* **72**, 597–615 (1974).

- [37] V. Dodonov, I. Malkin, and V. Man'ko, Even and odd coherent states and excitations of a singular oscillator, *Physica* **72**, 597 (1974).
- [38] V. V. Dodonov, V. I. Man'ko, and D. E. Nikonov, Even and odd coherent states for multimode parametric systems, *Phys. Rev. A* **51**, 3328 (1995).
- [39] C. C. Gerry and R. Grobe, Two-mode  $su(2)$  and  $su(1,1)$  schrödinger cat states, *Journal of Modern Optics* **44**, 41–53 (1997), <https://doi.org/10.1080/09500349708232898>.
- [40] R. López-Peña, S. Cordero, E. Nahmad-Achar, and O. Castaños, Symmetry adapted coherent states for three-level atoms interacting with one-mode radiation, *Physica Scripta* **90**, 068016 (2015).
- [41] H. J. Lipkin, N. Meshkov, and A. J. Glick, Validity of many-body approximation methods for a solvable model. (i). exact solutions and perturbation theory, *Nuclear Physics* **62**, 188–198 (1965).
- [42] H. J. Lipkin, N. Meshkov, and A. J. Glick, Validity of many-body approximation methods for a solvable model: (iii). diagram summations, *Nuclear Physics* **62**, 211–224 (1965).
- [43] P. Ring and P. Schuch, *The Nuclear Many-Body Problem* (Springer, Berlin, 1980).
- [44] D. C. Meredith, S. E. Koonin, and M. R. Zirnbauer, Quantum chaos in a schematic shell model, *Phys. Rev. A* **37**, 3499–3513 (1988).
- [45] M. T. Lopez-Arias and V. R. Manfredi, Wave function behaviours of the three-level lipkin, meshkov, glick model, *Zeitschrift für Physik A Atomic Nuclei* **334**, 255 (1989).
- [46] S. Gnutzmann and M. Kuś, Coherent states and the classical limit on irreducible  $su(3)$  representations, *Journal of Physics A: Mathematical and General* **31**, 9871 (1999).
- [47] S. Gnutzmann, F. Haake, and M. Kuś, Quantum chaos of  $su(3)$  observables, *Journal of Physics A: Mathematical and General* **33**, 143 (1999).
- [48] W.-G. Wang, F. M. Izrailev, and G. Casati, Structure of eigenstates and local spectral density of states: A three-orbital schematic shell model, *Phys. Rev. E* **57**, 323–339 (1998).
- [49] P. Leboeuf and M. Saraceno, Eigenfunctions of non-integrable systems in generalised phase spaces, *Journal of Physics A: Mathematical and General* **23**, 1745 (1999).
- [50] M. Calixto, A. Mayorgas, and J. Guerrero, Entanglement and  $U(D)$ -spin squeezing in symmetric multi-qudit systems and applications to quantum phase transitions in Lipkin–Meshkov–Glick  $D$ -level atom models, *Quantum Information Processing* **20**, 304 (2021).
- [51] J. M. Radcliffe, Some properties of coherent spin states, *Journal of Physics A: General Physics* **4**, 313–323 (1971).
- [52] I. Bengtsson and K. Życzkowski, *Geometry of Quantum States: An Introduction to Quantum Entanglement* (Cambridge University Press, 2006).
- [53] G. S. Agarwal and K. Tara, Nonclassical properties of states generated by the excitations on a coherent state, *Phys. Rev. A* **43**, 492 (1991).
- [54] K. Berrada, Construction of photon-added spin coherent states and their statistical properties, *Journal of Mathematical Physics* **56**, 072104 (2015), <https://doi.org/10.1063/1.4926355>.
- [55] H. B. Monir, N. Amir, and S. Iqbal, Photon-added  $su(1, 1)$  coherent states and their non-classical properties, *International Journal of Theoretical Physics* **58**, 1776 (2019).
- [56] J. Guerrero, A. Sojo, A. Mayorgas, and M. Calixto, Schmidt decomposition of parity adapted coherent states for symmetric multi-qudits (2023).
- [57] K. Husimi, Some formal properties of the density matrix, *Proceedings of the Physico-Mathematical Society of Japan. 3rd Series* **22**, 264–314 (1940).
- [58] A. Sugita, Proof of the generalized lieb-wehrl conjecture for integer indices larger than one, *Journal of Physics A: Mathematical and General* **35**, L621–L626 (2002).
- [59] P. Leboeuf and A. Voros, Chaos-revealing multiplicative representation of quantum eigenstates, *Journal of Physics A: Mathematical and General* **23**, 1765–1774 (1990).
- [60] F. J. Arranz, L. Seidel, C. G. Giralda, R. M. Benito, and F. Borondo, *Phys. Rev. E* **87**, 062901 (2013).
- [61] P. Pérez-Fernández, A. Relaño, J. M. Arias, P. Cejnar, J. Dukelsky, and J. E. García-Ramos, Excited-state phase transition and onset of chaos in quantum optical models, *Phys. Rev. E* **83**, 046208 (2011).
- [62] F. Wegner, Inverse participation ratio in  $2+\epsilon$  dimensions, *Zeitschrift für Physik B Condensed Matter* **36**, 209–214 (1980).
- [63] B. Kramer and A. MacKinnon, Localization: theory and experiment, *Reports on Progress in Physics* **56**, 1469–1564 (1993).
- [64] A. Sugita, Moments of generalized husimi distributions and complexity of many-body quantum states, *Journal of Physics A: Mathematical and General* **36**, 9081–9103 (2003).
- [65] A. Wehrl, General properties of entropy, *Rev. Mod. Phys.* **50**, 221–260 (1978).
- [66] E. H. Lieb and J. P. Solovej, Proof of an entropy conjecture for bloch coherent spin states and its generalizations, *Acta Math.* **212**, 379–398 (2014).
- [67] E. H. Lieb, Proof of an entropy conjecture of wehrl, *Communications in Mathematical Physics* **62**, 35–41 (1978).
- [68] A. Baecklund, *Maximization of the Wehrl Entropy in Finite Dimensions*, Master's thesis, KTH Royal Institute of Technology, Stockholm (2013).
- [69] E. H. Lieb and J. P. Solovej, Proof of the wehrl-type entropy conjecture for symmetric  $SU(N)$  coherent states, *Communications in Mathematical Physics* **348**, 567–578 (2016).
- [70] E. H. Lieb, The classical limit of quantum spin systems, *Communications in Mathematical Physics* **31**, 327–340 (1973).
- [71] R. Jozsa, Fidelity for mixed quantum states, *Journal of Modern Optics* **41**, 2315–2323 (1994), <https://doi.org/10.1080/09500349414552171>.
- [72] B. Hall, The segal-bargmann "coherent state" transform for compact lie groups, *Journal of Functional Analysis* **122**, 103–151 (1994).
- [73] B. C. Hall, The inverse segal–bargmann transform for compact lie groups, *Journal of Functional Analysis* **143**, 98–116 (1997).
- [74] C. Berke, E. Varvelis, S. Trebst, A. Altland, and D. P. DiVincenzo, Transmon platform for quantum computing challenged by chaotic fluctuations, *Nature Communications* **13**, 2495 (2022).
- [75] S. Giannini, A. Carof, M. Ellis, H. Yang, O. G. Ziogos, S. Ghosh, and J. Blumberger, Quantum localization and delocalization of charge carriers in organic semiconducting crystals, *Nature Communications* **10**, 3843 (2019).
- [76] S. Giannini, W.-T. Peng, L. Cupellini, D. Padula,

A. Carof, and J. Blumberger, Exciton transport in molecular organic semiconductors boosted by transient quan-

tum delocalization, *Nature Communications* **13**, 2755 (2022).

### 2.3.1 Schmidt decomposition of parity adapted coherent states

- <sup>5</sup> J. Guerrero, A. Sojo, A. Mayorgas, and M. Calixto, “Schmidt decomposition of parity adapted coherent states for symmetric multi-qudits”, *Journal of Physics A: Mathematical and Theoretical* 56, 355304 (2023).

Supplemental material link

#### Quality metrics JCR

- Year: 2022
- Category: PHYSICS, MATHEMATICAL
- Journal Impact Factor (JIF): 2.1
- JIF Rank: 14/56 (Q1)

Publication citations in Google Scholar (March 2024): 3

# Schmidt decomposition of parity adapted coherent states for symmetric multi-quDits

Julio Guerrero\*

*Department of Mathematics, University of Jaén,  
Campus Las Lagunillas s/n, 23071 Jaén, Spain and  
Institute Carlos I of Theoretical and Computational Physics (iC1),  
University of Granada, Fuentenueva s/n, 18071 Granada, Spain*

Antonio Sojo†

*Department of Mathematics, University of Jaén, Campus Las Lagunillas s/n, 23071 Jaén, Spain*

Alberto Mayorgas‡

*Department of Applied Mathematics, University of Granada, Fuentenueva s/n, 18071 Granada, Spain*

Manuel Calixto§

*Department of Applied Mathematics, University of Granada, Fuentenueva s/n, 18071 Granada, Spain and  
Institute Carlos I of Theoretical and Computational Physics (iC1),  
University of Granada, Fuentenueva s/n, 18071 Granada, Spain*

(Dated: January 22, 2023)

In this paper we study the entanglement in symmetric  $N$ -quDit systems. In particular we use generalizations to  $U(D)$  of spin  $U(2)$  coherent states and their projections on definite parity  $\mathfrak{c} \in \mathbb{Z}_2^{D-1}$  (multicomponent Schrödinger cat) states and we analyse their reduced density matrices when tracing out  $M < N$  quDits. The eigenvalues (or Schmidt coefficients) of these reduced density matrices are completely characterized, allowing to prove a theorem for the decomposition of a  $N$ -quDit Schrödinger cat state with a given parity  $\mathfrak{c}$  into a sum over all possible parities of tensor products of Schrödinger cat states of  $N - M$  and  $M$  particles. Diverse asymptotic properties of the Schmidt eigenvalues are studied and, in particular, for the (rescaled) double thermodynamic limit ( $N, M \rightarrow \infty, M/N$  fixed), we reproduce and generalize to quDits known results for photon loss of parity adapted coherent states of the harmonic oscillator, thus providing an unified Schmidt decomposition for both multi-quDits and (multi-mode) photons. These results allow to determine the entanglement properties of these states and also their decoherence properties under quDit loss, where we demonstrate the robustness of these states.

Keywords: Symmetric multi-quDits, coherent states, parity adapted states, entanglement entropy, Schmidt decomposition

---

\* jguerrer@ujaen.es: corresponding author

† asojo@ujaen.es

‡ albmayer97@ugr.es

§ calixto@ugr.es

## I. INTRODUCTION

Coherent states (CS), either of the harmonic oscillator (HO) or for a spin system, have many applications in Quantum Mechanics and Quantum Optics (among many other fields), and in particular parity adapted CS (a particular instance of a Schrödinger cat state) for the HO or for  $U(2)$ <sup>1</sup> are interesting since they are used in many protocols in Quantum Information Processing or appear as the lower energy states in some nuclear or molecular models like the Dicke [1] or Lipkin-Meshkov-Glick (LMG) models [2].

We shall consider in this paper “spin” CS for  $U(D)$  in its symmetric representation (i.e. made of a fixed number  $N$  of indistinguishable quDits) and we shall construct from them parity adapted CS, i.e states which are invariant under the parity group. The parity group in the case of  $U(D)$  is  $\mathbb{Z}_2^{D-1}$ , generalizing the case of  $SU(2)$ , where the parity group is simply  $\mathbb{Z}_2 = \{-1, +1\}$ .

For applications, it is important to characterize the entanglement properties of these states, therefore we shall consider entropic entanglement measures in terms of the entropy of  $M$ -particle reduced density matrices (RDM), i.e. in terms of a bipartition of the  $N$  quDits in  $N - M$  and  $M$  quDits and tracing out the  $N - M$  subsystem.

There is an intense debate in the literature concerning the notion of entanglement in systems of identical and indistinguishable particles (like the case of symmetric multi-quDits). Some authors [3, 4] consider that particle entanglement, obtained through RDM by tracing out a number of particles [5–7], cannot be used as a quantum resource in quantum information tasks for indistinguishable particles. Other authors consider that the entanglement due to exchange symmetry can indeed be useful in those tasks, providing some examples of it [8, 9]. The authors of [3, 4] propose mode entanglement as the only meaningful way of defining entanglement for indistinguishable particles.

In this paper we shall consider the notion of particle entanglement in symmetric multi-quDit systems since it is mathematically consistent and physically justified in the case of parity adapted coherent states. The case of mode entanglement will be considered in a future work.

To characterize the entanglement of parity adapted  $U(D)$  CS, we need to compute the Schmidt decomposition of these states when a bipartition in  $N - M$  and  $M$  particles is considered. The main result of this paper is that, under this decomposition, parity adapted CS decompose as the convolution over all possible parities, of tensor products of parity adapted CS of  $N - M$  and  $M$  particles. The coefficients of this decomposition (Schmidt coefficients) and their squares (Schmidt eigenvalues) are determined for all  $N$  and  $M$ , and the main features of them and their behaviour under various limits are studied. For a detailed account of these features, a variety of graphical tools are used, like contour plots, angular plots, etc., but, in the case of a large  $D$ , information diagrams (see [10] and references therein) prove to be a valuable tool when appropriate colormaps are used (see the Supplementary Material).

The content of the paper is the following. In Sec. II the symmetric representation of  $U(D)$  is reviewed in order to fix notation (second quantization approach), and parity transformations and parity projectors are introduced. In Sec. III CS for the symmetric representation of  $U(D)$  are reviewed, and some results for their relation with identical tensor product states are given. In Sec. IV parity adapted CS are defined and some of their properties are given, in particular their behaviour under certain limits. In Sec. V we specify the entanglement measure used in this paper to study the entanglement properties of parity adapted CS. In Sec. VI the main result of this paper is proved, namely the Schmidt decomposition of parity adapted CS of  $N$  particles into  $N - M$  and  $M$  particle subsystems, with the determination of the Schmidt coefficients and eigenvalues. In Sec. VII some limits for the Schmidt eigenvalues are studied. In Sec. VIII some physical applications and possible methods to generate these states are given, in particular the interesting subject of quDit loss, where the Schmidt decomposition here provided can be of crucial importance. The paper ends with a concluding section X. In the Supplementary Material, a reminder of the subject of information diagrams is included, and an exhaustive set of figures showing the entanglement properties of parity adapted CS for  $D > 2$  is provided.

## II. SYMMETRIC REPRESENTATION OF $U(D)$

The fully symmetric representation of dimension  $\binom{N+D-1}{N}$  of  $U(D)$  can be realized as a system of  $N$  identical and indistinguishable particles (atoms) with  $D$  levels (internal states), that will be referred to as quDits, with levels labelled by  $|0\rangle, |1\rangle, \dots, |D-1\rangle$  (for  $D = 2$  we have the standard qubit usually labelled by  $|0\rangle, |1\rangle$  or  $|\uparrow\rangle, |\downarrow\rangle$ ).

Introducing the boson operators  $a_i, a_i^\dagger$  ( $a_i^\dagger$  creates a quDit in the  $i$ -th level and  $a_i$  annihilates it), the Lie algebra of  $U(D)$  can be realized (in the Schwinger representation [11]) as:

$$S_{ij} = a_i^\dagger a_j, \quad i, j = 0, \dots, D-1. \quad (1)$$

<sup>1</sup> We shall consider in this paper unitary groups  $U(D)$  instead of special unitary groups  $SU(D)$  since the difference between them is an irrelevant global phase and it is easier to write down a basis of the Lie algebra in the case of unitary groups.

The operator  $S_{ii}$  is the number operator for the population of the  $i$ -th level, and  $S_{ij}$  ( $i \neq j$ ) creates a quDit in the level  $i$  and annihilates another one in the level  $j$ . Therefore  $S_{ij}$  preserves the total number  $N$  of quDits.

It is important to note that the  $U(D)$  operators  $S_{ij}$  are collective operators, in the sense that they do not act on the individual states of the particles (which can be an ill-defined concept due to symmetrization). They have in fact been built up using the second quantization formalism [12, 13]. They fulfill the commutation relations:

$$[S_{ij}, S_{kl}] = \delta_{jk} S_{il} - \delta_{il} S_{kj}. \quad (2)$$

The carrier Hilbert space  $\mathcal{H}_N$  of our symmetric  $N$ -quDit system is spanned by the Bose-Einstein-Fock basis states ( $|\vec{0}\rangle$  denotes the Fock vacuum):

$$|\vec{n}\rangle = |n_0, \dots, n_{D-1}\rangle = \frac{(a_0^\dagger)^{n_0} \dots (a_{D-1}^\dagger)^{n_{D-1}} |\vec{0}\rangle}{\sqrt{n_0! \dots n_{D-1}!}}, \quad n_0 + \dots + n_{D-1} = N, \quad (3)$$

where  $n_i \geq 0$  denotes the occupancy number of the  $i$ th-level (the eigenvalue of  $S_{ii}$ ), with the restriction given by the linear Casimir of  $U(D)$ ,  $C_1 = \sum_{i=0}^{D-1} S_{ii}$ , the total number of quDits. The expansion of a general symmetric  $N$ -quDit state  $\psi$  in the Fock basis will be written as

$$|\psi\rangle = \sum_{\|\vec{n}\|_1=N} c_{\vec{n}} |\vec{n}\rangle, \quad (4)$$

where the sum is restricted to those  $\vec{n}$  such that  $\|\vec{n}\|_1 = n_0 + \dots + n_{D-1} = N$ .

In order to define the notion of entanglement, we shall consider in  $\mathcal{H}_N$  various families of states. The simplest states that one usually introduces, in order to define separable (non-entangled) states, are Tensor Product States (TPS)  $|\vec{\psi}\rangle^{(N)} = |\psi_1\rangle \otimes \dots \otimes |\psi_N\rangle$ . However, due to the exchange symmetry, in  $\mathcal{H}_N$  the only TPS are the subset of *identical* tensor product states (ITPS):

$$\mathcal{A}_N^{ITPS} = \{|\psi\rangle^{\otimes N} \in \mathcal{H}_N : |\psi\rangle^{\otimes N} = |\psi\rangle \otimes \dots \otimes |\psi\rangle\} \subset \mathcal{H}_N. \quad (5)$$

with  $|\psi\rangle \in \mathcal{H}_1$ . If the one-quDit state  $|\psi\rangle \in \mathcal{H}_1$  is expressed as:

$$|\psi\rangle = w_0|0\rangle + w_1|1\rangle + \dots + w_{D-1}|D-1\rangle \equiv |w_0, w_1, \dots, w_{D-1}\rangle \equiv |\mathbf{w}\rangle, \quad |w_0|^2 + |w_1|^2 \dots + |w_{D-1}|^2 = 1, \quad (6)$$

then it can be shown (see [14]) that the expression of the  $N$ -quDit state  $|\psi\rangle^{\otimes N}$  in the Fock basis is:

$$|\psi\rangle^{\otimes N} \equiv |\mathbf{w}\rangle^{\otimes N} = \sum_{\|\vec{n}\|_1=N} \sqrt{\binom{N}{\vec{n}}} \left( \prod_{j=0}^{D-1} w_j^{n_j} \right) |\vec{n}\rangle, \quad (7)$$

where  $\binom{N}{\vec{n}} = \frac{N!}{\vec{n}!}$  is a multinomial and  $\vec{n}!$  stands for  $\prod_{i=0}^{D-1} n_i!$ .

As an important example of ITPS we have the coherent states discussed below.

In place of TPS, in  $\mathcal{H}_N$  we can consider the subset of Symmetrized TPS (STPS), obtained from a TPS under symmetrization:

$$\mathcal{A}_N^{STPS} = \left\{ |\vec{\psi}\rangle^{(\Sigma N)} \in \mathcal{H}_N : |\vec{\psi}\rangle^{(\Sigma N)} = \frac{1}{\mathcal{N}(\vec{\psi})^{(\Sigma N)}} \Sigma |\vec{\psi}\rangle = \frac{1}{\mathcal{N}(\vec{\psi})^{(\Sigma N)}} \frac{1}{N!} \sum_{\sigma \in S_N} |\psi_{\sigma(1)}\rangle \otimes \dots \otimes |\psi_{\sigma(N)}\rangle \right\} \subset \mathcal{H}_N, \quad (8)$$

with  $\left( \mathcal{N}(\vec{\psi})^{(\Sigma N)} \right)^2 = \binom{N}{\vec{\psi}} \langle \vec{\psi} | \Sigma | \vec{\psi} \rangle^{(N)}$ ,  $S_N$  is the symmetric group of permutations of  $N$  elements, and where  $\Sigma$  is the symmetrization operator, i.e. the projector operator onto the symmetric subspace under  $S_N$ .

Another important family of states is the Hilbert subspace spanned by  $\mathcal{A}_N^{ITPS}$ , i.e.  $\mathcal{H}_N^{ITPS} = \text{span}(\mathcal{A}_N^{ITPS})$ , containing all possible finite linear combinations of ITPS. We shall focus on this paper on states obtained as finite linear combinations of coherent states (see Sec. III), which belong to  $\mathcal{H}_N^{ITPS}$ .

### A. Parity operators for $U(D)$

Parity operators play an important role in the representation theory of the group  $U(D)$ , and also in its physical applications. They are given by (Roman  $i$  denotes the imaginary unit):

$$\Pi_j = \exp(i\pi S_{jj}) \quad , \quad j = 0, 1, \dots, D-1, \quad (9)$$

with the action on Fock states:

$$\Pi_j |\vec{n}\rangle = (-1)^{n_j} |\vec{n}\rangle, \quad (10)$$

indicating the even (+) or odd (−) character of the population  $n_j$  of each level  $j = 0, \dots, D-1$ . Note that parity operators, like the  $U(D)$  generators  $S_{ij}$ , are collective operators, in the sense that they only depend on the populations of each level, and do not depend on the individual particle states (which could be ill-defined due to symmetrization).

The action of parity operators on ITPS states is given by:

$$\Pi_j |\mathbf{w}\rangle^{\otimes N} = \sum_{\|\vec{n}\|_1=N} \sqrt{\binom{N}{\vec{n}}} \left( \prod_{i=0}^{D-1} w_i^{n_i} \right) (-1)^{n_j} |\vec{n}\rangle = |w_0, \dots, -w_j, \dots, w_{D-1}\rangle^{\otimes N}. \quad (11)$$

Due to the constraint of the fixed number of particles equating to  $N$ , we have the relation  $\Pi_0 \dots \Pi_{D-1} |\vec{n}\rangle = (-1)^N |\vec{n}\rangle$ . Hence, discarding for instance  $\Pi_0$ , the true discrete parity symmetry group corresponds to the finite Abelian group  $\mathbb{Z}_2^{D-1} = \mathbb{Z}_2 \times \overset{D-1}{\dots} \times \mathbb{Z}_2$ .

Taking this into account, let us denote by  $\Pi^{\mathbf{b}} = \Pi_1^{b_1} \dots \Pi_{D-1}^{b_{D-1}}$ , where  $\Pi_i^{b_i} = (\Pi_i)^{b_i}$  and the binary string  $\mathbf{b} = [b_1, \dots, b_{D-1}] \in \{0, 1\}^{D-1}$  denotes one of the  $2^{D-1}$  elements of the parity group  $\mathbb{Z}_2^{D-1}$ . There are  $2^{D-1}$  parity invariant subspaces labelled by the inequivalent group characters  $\chi_{\mathbf{c}}$ , with  $\mathbf{c} = [c_1, \dots, c_{D-1}] \in \{0, 1\}^{D-1}$  denoting elements of the Pontryagin dual group  $\widehat{\mathbb{Z}_2^{D-1}} \sim \mathbb{Z}_2^{D-1}$ .

The projectors onto these invariant subspaces of definite parity  $\mathbf{c}$  are given by the Fourier Transform (FT) between  $\mathbb{Z}_2^{D-1}$  and its dual  $\widehat{\mathbb{Z}_2^{D-1}}$  (which in this case is a multidimensional Discrete Fourier Transform of dimension  $2 \times \overset{D-1}{\dots} \times 2$ , whose matrix realization is the Walsh-Hadamard transform [15]):

$$\Pi_{\mathbf{c}} = 2^{1-D} \sum_{\mathbf{b}} \chi_{\mathbf{c}}(\mathbf{b}) \Pi^{\mathbf{b}}, \quad (12)$$

with group characters  $\chi_{\mathbf{c}}(\mathbf{b}) = (-1)^{\mathbf{c} \cdot \mathbf{b}} = (-1)^{c_1 b_1 + \dots + c_{D-1} b_{D-1}}$ . The sum in  $\mathbf{b}$  is on the whole parity group  $\mathbb{Z}_2^{D-1}$ , but we shall omit it for notational convenience (the same applies to the sums in  $\mathbf{c}$  that run on the dual group, which is isomorphic to  $\mathbb{Z}_2^{D-1}$ ).

Using the properties of the characters  $\chi_{\mathbf{c}}$  of the parity group  $\mathbb{Z}_2^{D-1}$ , the projectors satisfy:

$$\Pi_{\mathbf{c}} \Pi_{\mathbf{c}'} = \delta_{\mathbf{c}, \mathbf{c}'} \Pi_{\mathbf{c}} \quad (13)$$

and since they are self-adjoint, they are orthogonal projectors.

By the Fourier inversion formula between  $\widehat{\mathbb{Z}_2^{D-1}}$  and  $\mathbb{Z}_2^{D-1}$ , the parity operators can be recovered from the parity projectors through the inverse FT:

$$\Pi^{\mathbf{b}} = \sum_{\mathbf{c}} \chi_{\mathbf{c}}(\mathbf{b}) \Pi_{\mathbf{c}}, \quad (14)$$

where we have used that, in this case, the characters are real and therefore  $\overline{\chi_{\mathbf{c}}(\mathbf{b})} = \chi_{\mathbf{c}}(\mathbf{b})$ . Denoting by  $\mathbb{0}$  and  $\mathbb{1}$  the binary strings  $[0, 0, \dots, 0]$  and  $[1, 1, \dots, 1]$ , respectively, we obtain:

$$\Pi^{\mathbb{0}} = \sum_{\mathbf{c}} \Pi_{\mathbf{c}} = I, \quad (15)$$

$$\Pi^{\mathbb{1}} = \sum_{\mathbf{c}} (-1)^{\mathbf{c} \cdot \mathbb{1}} \Pi_{\mathbf{c}}, \quad (16)$$

with  $I$  the identity operator on  $\mathcal{H}_N$ . Note that  $\Pi^{\mathbb{1}} = \Pi_1 \dots \Pi_{D-1}$  represents the total parity of all the states  $1, 2, \dots, D-1$ , and that  $\Pi^{\mathbb{0}} = I$  and  $\Pi^{\mathbb{1}}$  generate a  $\mathbb{Z}_2$  subgroup (the “total parity” subgroup) of the parity group.

By Eq. (15) and the orthogonality of the projectors, the Hilbert space  $\mathcal{H}_N$  decomposes into a direct sum of parity adapted (or projected) subspaces:

$$\mathcal{H}_N = \bigoplus_{\mathfrak{c}} \mathcal{H}_N^{(\mathfrak{c})}. \quad (17)$$

In order to clarify the meaning of the different objects appearing in the remaining sections, we shall make explicit the number of particles (say  $M$ ) of the involved representations in the notation of  $U(D)$  generators, parity, projection and identity operators:

$$S_{ij} \longrightarrow S_{ij}^{(M)}, \quad \Pi^{\mathfrak{b}} \longrightarrow \Pi^{\mathfrak{b}(M)}, \quad \Pi_{\mathfrak{c}} \longrightarrow \Pi_{\mathfrak{c}}^{(M)}, \quad I \longrightarrow I^{(M)}. \quad (18)$$

Let us state the following Lemma, which will be helpful in the proof of the rest of results of this paper.

*Lemma 1.*  $M$ -particle parity operators  $\Pi_i^{(M)}$  can be factorized into one-particle parity operators:

$$\Pi_i^{(M)} = \prod_{k=1}^M I^{(k-1)} \otimes \Pi_i^{(1)} \otimes I^{(M-k)}. \quad (19)$$

*Proof:* The proof is a consequence of the fact that  $M$ -particle collective  $U(D)$  generators  $S_{ij}^{(M)}$  can be decomposed as a sum of one-particle  $U(D)$  generators  $S_{ij}^{(1)}$  (see [14]):

$$S_{ij}^{(M)} = \sum_{k=1}^M I^{(k-1)} \otimes S_{ij}^{(1)} \otimes I^{(M-k)}. \quad (20)$$

Then eq. (19) follows from the definition of parity operators (9) and the commutativity of the diagonal operators  $S_{ii}^{(M)}$ . ■

According to this Lemma the parity operators are *identical tensor product operators* (ITPO). These operators preserve the subset  $\mathcal{A}_N^{ITPS}$  and therefore leave invariant the Hilbert subspace  $\mathcal{H}_N^{ITPS}$ . They also commute with the symmetrization operator  $\Sigma$ , as  $\Pi^{\mathfrak{b}}$  and  $\Pi_{\mathfrak{c}}$  also do.

### III. COHERENT STATES FOR THE SYMMETRIC REPRESENTATION OF $U(D)$

$U(D)$ -spin coherent states are defined as [16]:

$$|\mathbf{z}\rangle = \frac{1}{\sqrt{N!}} \left( \frac{a_0^\dagger + z_1 a_1^\dagger + \cdots + z_{D-1} a_{D-1}^\dagger}{\sqrt{1 + |z_1|^2 + \cdots + |z_{D-1}|^2}} \right)^N |\vec{0}\rangle. \quad (21)$$

They are labeled by  $D-1$  complex numbers  $z_j \in \mathbb{C}$  arranged in the column vector  $\mathbf{z} = (z_1, z_2, \dots, z_{D-1})^t \in \mathbb{C}^{D-1}$ . They are in fact labelled by the points in the complex projective space  $\mathbb{C}\mathbb{P}^{D-1}$ , but for simplicity we have considered the chart in  $\mathbb{C}\mathbb{P}^{D-1}$  where  $z_0 \neq 0$  and divided all coefficients by  $z_0$  (see, for instance, [17]).

Note that the state for  $\mathbf{z} = \mathbf{0}$ ,  $|\mathbf{0}\rangle = \frac{a_0^\dagger{}^N}{\sqrt{N!}} |\vec{0}\rangle$  (usually denoted as highest-weight state), should not be confused with the Fock vacuum  $|\vec{0}\rangle$ .

The coefficients  $c_{\vec{n}}(\mathbf{z})$  of  $|\psi\rangle = |\mathbf{z}\rangle$  in the Fock basis are (see eq. (4))

$$c_{\vec{n}}(\mathbf{z}) = \sqrt{\frac{N!}{\vec{n}!}} \frac{\prod_{i=1}^{D-1} z_i^{n_i}}{(1 + \mathbf{z}^\dagger \mathbf{z})^{N/2}}, \quad (22)$$

where  $\mathbf{z}^\dagger \mathbf{z} = |z_1|^2 + \cdots + |z_{D-1}|^2$  denotes the standard scalar product in  $\mathbb{C}^{D-1}$  and  $\vec{n}!$  stands for  $\prod_{i=0}^{D-1} n_i!$ .

From the previous expression, and comparing with eq. (7), it is clear that coherent states are ITPS, cf. eq. (6), with coefficients  $w_j = \frac{z_j}{\sqrt{1 + \mathbf{z}^\dagger \mathbf{z}}}$ ,  $j = 0, 1, \dots, D-1$  (where  $z_0 = 1$ ).

In general, these CS are non-orthogonal since the scalar product

$$\langle \mathbf{z} | \mathbf{z}' \rangle = \frac{(1 + \mathbf{z}^\dagger \mathbf{z}')^N}{(1 + \mathbf{z}^\dagger \mathbf{z})^{N/2} (1 + \mathbf{z}'^\dagger \mathbf{z}')^{N/2}} \quad (23)$$

is not necessarily zero. However, they constitute an overcomplete set of states closing a resolution of the identity [16]

$$I = \int_{\mathbb{C}^{D-1}} |\mathbf{z}\rangle\langle\mathbf{z}| d\mu(\mathbf{z}), \quad (24)$$

$$d\mu(\mathbf{z}) = \frac{(D-1)!}{\pi^{D-1}} \binom{N+D-1}{N} \frac{d^2 z_1 \dots d^2 z_{D-1}}{(1+\mathbf{z}^\dagger \mathbf{z})^D},$$

with  $d^2 z_i = d\text{Re}(z_i) d\text{Im}(z_i)$  the usual (Lebesgue) measure on  $\mathbb{C} \sim \mathbb{R}^2$ .

It turns out that a CS for a representation with  $N$  particles is the tensor product of  $N$  copies of one-particle CS states, all of them with the same value of  $\mathbf{z}$  (see, for instance, [14]). Therefore coherent states belong to the subset  $\mathcal{A}_N^{ITPS}$ , and will be denoted as  $|\mathbf{z}\rangle^{\otimes N}$  when we need to specify the number of quDits in the representation.

In fact, the only ITPS are coherent states, as it is proven in the following Lemma and Proposition.

*Lemma 2.* There is a bijective map between  $\mathcal{H}_1$  and the set of one-particle coherent states.

*Proof:* An arbitrary state in  $\mathcal{H}_1$  is given by eq. (6), with  $|w_0|^2 + |w_1|^2 + \dots + |w_{D-1}|^2 = 1$ . By the projective character of  $\mathcal{H}_1$  (invariance under a global phase), the topology of this space is that of the product of the first hyperoctant of  $\mathbb{S}^{D-1}$  times the hypertorus  $\mathbb{T}^{D-1}$  (the relative phases), see [18]. Note that for  $U(2)$  this reduces to  $\mathbb{S}^2 \equiv \mathbb{C}\mathbb{P}^1$ , usually referred to as the Bloch sphere (for pure states). In general, it corresponds to the projective space  $\mathbb{C}\mathbb{P}^{D-1}$ , which we shall call the *Bloch projective space*.

To construct the bijection with one-particle coherent states, let us consider a particular chart and suppose  $w_0 \neq 0$ , then invariance under a global phase allows to choose  $w_0 > 0$ .

One-particle coherent states are of the form

$$|\mathbf{z}\rangle = \frac{|0\rangle + z_1|1\rangle + z_2|2\rangle + \dots + z_{D-1}|D-1\rangle}{\sqrt{1 + |z_1|^2 + \dots + |z_{D-1}|^2}}, \quad (25)$$

and the geometry is also that of the projective space  $\mathbb{C}\mathbb{P}^{D-1}$ , where again we have used the chart where  $z_0 \neq 0$  (see, for instance, [19]).

Thus, to a one-particle coherent state we can associate a unique element of the Bloch projective space given by:

$$w_0 = \frac{1}{\sqrt{1 + |z_1|^2 + \dots + |z_{D-1}|^2}} > 0, \quad w_i = \frac{z_i}{\sqrt{1 + |z_1|^2 + \dots + |z_{D-1}|^2}}, \quad (26)$$

for  $i = 1, \dots, D-1$ . Conversely, to an element of the Bloch projective space (with  $w_0 > 0$ ) we can associate the coherent state with parameters:

$$z_i = \frac{w_i}{w_0}. \quad (27)$$

The case  $w_0 = 0$  is handled considering a different chart in the projective space of coherent states and in the Bloch projective space. ■

*Proposition 1.* There is a bijection between  $\mathcal{A}_N^{ITPS}$  and the set of  $N$ -particle coherent states.

*Proof:* Consider tensor products of the same one-particle state and apply the previous Lemma for each particle. ■

As a corollary of this result, it turns out that  $\mathcal{H}_N^{ITPS}$  coincides with  $\text{span}(\{|\mathbf{z}\rangle^{\otimes N} : \mathbf{z} \in \mathbb{C}^{D-1}\})$ .

From Eq. (27) it is clear that the parameterization  $\mathbf{z}$  for coherent states is the projective version of the parametrization  $\mathbf{w}$  for the Bloch projective space. Thus, we can identify the general one-particle state (6) and its corresponding  $N$ -particle ITPS as:

$$|\psi\rangle = |\mathbf{w}\rangle = |\mathbf{z}\rangle^{\otimes N}, \quad |\psi\rangle^{\otimes N} = |\mathbf{w}\rangle^{\otimes N} = |\mathbf{z}\rangle^{\otimes N}. \quad (28)$$

However, the parametrization  $\mathbf{z}$  has important properties from the analytical and geometrical point of view, making them more suitable in the applications. According to these results, the family of coherent states, due to their useful geometric and analytic properties, is a convenient way of parametrizing  $\mathcal{H}_N^{ITPS}$ .

We can go one step further and write any state in  $\mathcal{H}_N$  as a finite linear combination of coherent states (or ITPS, as you like).

*Theorem 1.* Any state in  $\mathcal{H}_N$  can be written as a finite linear combination of ITPS, i.e.  $\mathcal{H}_N^{ITPS} = \mathcal{H}_N$ .

*Proof:* We provide here an sketch of the proof, leaving a detailed proof for a future publication [20]. Although coherent states are not orthogonal, they generate the whole space  $\mathcal{H}_N$  since they are overcomplete by eq. (24). Since  $\mathcal{H}_N$  is finite-dimensional, it is possible to find a finite subset of coherent states generating the whole  $\mathcal{H}_N$  (see for instance [21] for the case of  $SU(2)$ ), and therefore  $\mathcal{H}_N^{ITPS} = \mathcal{H}_N$ . ■

Note that this theorem does not hold in the case of non-compact groups, where the irreducible unitary representations are realized in an infinite dimensional Hilbert space  $\mathcal{H}_\infty$ , and therefore finite linear combinations of coherent states are only dense in the Hilbert space, i.e.  $\mathcal{H}_N^{ITPS} \neq \mathcal{H}_\infty$  but  $\overline{\mathcal{H}_N^{ITPS}} = \mathcal{H}_\infty$  (see [22] for the case of  $SU(1,1)$ ).

For the case of  $SU(2)$  an stronger result can be given:  $\mathcal{H}_N$  is made of symmetrized tensor product states.

*Theorem 2.* For  $D = 2$ ,  $\mathcal{H}_N = \mathcal{A}_N^{STPS}$ .

*Proof:* The usual proof is given in terms of the Majorana representation and Majorana constellation [23, 24]. The Majorana representation for the  $SU(2)$  state  $|\psi\rangle$  of spin  $s$ , with  $N = 2s$ , is given in terms of the Husimi amplitude  $M(z) = \langle z|\psi\rangle$ . Ignoring a global factor depending on  $|z|$ , the Majorana function  $M(z)$  is a polynomial in  $\bar{z}$  which is characterized by its zeros, having up to  $2s$  zeros. Completing this zeros with the zeros at infinity of  $M(z)$ , the Majorana representation of the state  $|\psi\rangle$  is characterized by  $2s$  points on the sphere (once the complex zeros are mapped to the sphere by inverse stereographic projection and the zeros at infinity are associated with the North pole of the sphere), denoted as Majorana constellation.

On the other hand, the Majorana representation of a STPS  $|\vec{\psi}\rangle$  is given by:

$$\begin{aligned} M_{\vec{\psi}}(z) &= \frac{1}{\mathcal{N}(\vec{\psi})^{(\Sigma N)}} \frac{1}{N!} \sum_{\sigma \in S_N} \langle z|\psi_{\sigma(1)}\rangle \otimes \cdots \otimes \langle z|\psi_{\sigma(N)}\rangle \\ &= \frac{1}{\mathcal{N}(\vec{\psi})^{(\Sigma N)}} \langle z|\psi_1\rangle \cdots \langle z|\psi_N\rangle, \end{aligned} \quad (29)$$

which coincides, up to a global normalization factor independent of  $z$ , with the Majorana representation of a (non-symmetrical) TPS state. By Lemma 2 every  $|\psi_i\rangle$  coincides with a coherent state  $|z_i\rangle$ , thus

$$M_{\vec{\psi}}(z) = \frac{1}{\mathcal{N}(\vec{\psi})^{(\Sigma N)}} \langle z|z_1\rangle \cdots \langle z|z_N\rangle. \quad (30)$$

The zeros of  $M_{\vec{\psi}}(z)$  are clearly those values of  $z$  that make zero any of the overlaps  $\langle z|z_i\rangle$ , for some  $i = 1, \dots, N$ , and, for  $SU(2)$  coherent states, the unique zero values of the overlaps are the antipodal points  $-\frac{1}{\bar{z}_i}$ . By the unicity of the representation of the Majorana function in terms of its zeros, we conclude that any state of spin  $s$  corresponds to a STPS. ■

Unfortunately, although we can define a Majorana representation for  $D \geq 3$  in terms of the Husimi amplitudes  $M(\mathbf{z}) = \langle \mathbf{z}|\Psi\rangle$ , defined on the projective spaces  $\mathbb{C}\mathbb{P}^{D-1}$ , they cannot be characterized in terms of their zeros (which are no longer isolated points), and a result like Theorem 2 is not available. However, Theorem 1 is still valid and it can be used to compute the Schmidt decomposition of arbitrary parity adapted multi-quDit states [20].

#### IV. PARITY ADAPTED U(D)-SPIN COHERENT STATES

Parity operators  $\Pi_j = \exp(i\pi S_{jj})$  act on CS as

$$\Pi_j|\mathbf{z}\rangle = |z_1, \dots, -z_j, \dots, z_{D-1}\rangle, \quad j = 0, 1, \dots, D-1, \quad (31)$$

thus  $\Pi_j$  just changes the sign of  $z_j$  in  $|\mathbf{z}\rangle$ . Let us denote  $\mathbf{z}^b \equiv ((-1)^{b_1} z_1, \dots, (-1)^{b_{D-1}} z_{D-1})^t$ , then

$$|\mathbf{z}^b\rangle \equiv \Pi^b|\mathbf{z}\rangle = \prod_{i=1}^{D-1} \Pi_i^{b_i} |\mathbf{z}\rangle. \quad (32)$$

Define also parity  $\mathfrak{c}$  adapted  $U(D)$ -spin CS as

$$|\mathbf{z}\rangle_{\mathfrak{c}} \equiv \frac{\Pi_{\mathfrak{c}}|\mathbf{z}\rangle}{\mathcal{N}_{\mathfrak{c}}(\mathbf{z})} = \frac{2^{1-D}}{\mathcal{N}_{\mathfrak{c}}(\mathbf{z})} \sum_{\mathfrak{b}} \chi_{\mathfrak{c}}(\mathfrak{b}) |\mathbf{z}^b\rangle, \quad (33)$$

as the normalized projection of  $|\mathbf{z}\rangle$  onto the invariant subspace of parity  $\mathfrak{c}$  (or normalized FT of  $|\mathbf{z}^{\mathfrak{b}}\rangle$ ), where the normalization factor is given by:

$$\mathcal{N}_{\mathfrak{c}}(\mathbf{z})^2 = 2^{1-D} \sum_{\mathfrak{b}} \chi_{\mathfrak{c}}(\mathfrak{b}) \langle \mathbf{z} | \mathbf{z}^{\mathfrak{b}} \rangle = 2^{1-D} \frac{\sum_{\mathfrak{b}} \chi_{\mathfrak{c}}(\mathfrak{b}) (1 + \mathbf{z}^{\dagger} \mathbf{z}^{\mathfrak{b}})^N}{(1 + \mathbf{z}^{\dagger} \mathbf{z})^N}, \quad (34)$$

i.e.,  $\mathcal{N}_{\mathfrak{c}}(\mathbf{z})^2$  is the FT of the overlap between a coherent state and its parity transformed versions. Note that  $\mathcal{N}_{\mathfrak{c}}(\mathbf{z})$  is a function only of the absolute values  $|z_i|$ ,  $i = 1, \dots, D-1$ , and does not depend on the relative phases.

Note that  $\mathcal{N}_{\mathfrak{c}}(\mathbf{z})$  can be zero (as well as  $\Pi_{\mathfrak{c}}|\mathbf{z}\rangle$ ) for some particular values of  $\mathbf{z}$  and  $\mathfrak{c}$ . We shall discuss these cases in the next subsections.

The rest of the paper will be devoted to study the entanglement properties of these parity adapted CS, which can be seen as particular instances of Entangled CS [25] (see also the review [26]).

### A. Limit values for normalization factors

It is worth showing some particular values of the normalization factor, that will be useful in computing some limit values of the Schmidt eigenvalues in Sec. VII.

At  $\mathbf{z} = \mathbf{0}$  we have

$$\mathcal{N}_{\mathfrak{c}}(\mathbf{0})^2 = \delta_{\mathfrak{c},0}, \quad (35)$$

implying that the normalization at  $\mathbf{z} = \mathbf{0}$  is zero except for the completely even unnormalized parity adapted CS state (see Sec. IV C for a detailed study of the limit  $\mathbf{z} \rightarrow \mathbf{0}$  of these states).

The  $\|\mathbf{z}\| \rightarrow \infty$  limit does not exist (except for the case  $D = 2$ , see below), since its value depends on the direction. Using hyper-spherical coordinates in the first hyper-octant,  $|z_i| = r y_i(\vec{\theta})$ ,  $\vec{\theta} \in [0, \frac{\pi}{2}]^{D-2}$ ,  $i = 1, 2, \dots, D-1$ , we can compute the directional limits:

$$\lim_{r \rightarrow \infty} \mathcal{N}_{\mathfrak{c}}(\mathbf{z})^2 = 2^{1-D} \sum_{\mathfrak{b}} \chi_{\mathfrak{c}}(\mathfrak{b}) Y_{\mathfrak{b}}(\vec{\theta})^N, \quad (36)$$

with  $Y_{\mathfrak{b}}(\vec{\theta}) = \sum_{i=1}^{D-1} (-1)^{b_i} y_i(\vec{\theta})^2$ . For instance, for  $D = 3$  we have polar coordinates, and in this case  $Y_{\mathfrak{b}}(\theta) = (-1)^{b_1} \cos^2 \theta + (-1)^{b_2} \sin^2 \theta$ .

For  $D = 2$  the limit  $|z| \rightarrow \infty$  exists, and it is given by:

$$\lim_{|z| \rightarrow \infty} \mathcal{N}_{\mathfrak{c}}(z)^2 = \delta_{N_{\mathfrak{c}},0}. \quad (37)$$

with  $N_{\mathfrak{c}} = (N - c) \bmod 2$ .

Another interesting limit is the thermodynamic limit, i.e. when the number of particles  $N$  grows to infinity:

$$\lim_{N \rightarrow \infty} \mathcal{N}_{\mathfrak{c}}(\mathbf{z})^2 = 2^{-k} \delta_{\mathfrak{c}_0,0_0}, \quad (38)$$

where  $k = \|\mathbf{z}\|_0$ , with the 0-norm being the number of nonzero components of the vector  $\mathbf{z}$ , and  $\mathfrak{c}_0$  indicates the subset of components of  $\mathfrak{c}$  whose indices coincide with the indices of the zero components of  $\mathbf{z}$ .

Finally, let us consider the rescaled thermodynamic limit, when  $N$  grows to infinity but at the same time  $\mathbf{z}$  approach  $\mathbf{0}$  such that  $\sqrt{N}\mathbf{z} = \boldsymbol{\alpha}$  is finite. This process is equivalent to the group contraction from  $U(D)$  to the harmonic oscillator (HO) group in  $D-1$  dimensions<sup>2</sup>,  $\text{HO}_{D-1}$ :

$$\lim_{N \rightarrow \infty} \mathcal{N}_{\mathfrak{c}} \left( \frac{\boldsymbol{\alpha}}{\sqrt{N}} \right)^2 = \prod_{i=1}^{D-1} (\mathcal{N}_{c_i}^{\text{HO}}(\alpha_i))^2, \quad (39)$$

where  $\mathcal{N}_{c_i}^{\text{HO}}(\alpha)$  are the normalization factors of the even ( $c = 0$ ) and odd ( $c = 1$ ) Schrödinger cat states of the one-dimensional harmonic oscillator:

$$(\mathcal{N}_{c_i}^{\text{HO}}(\alpha))^2 = \frac{1}{2} \sum_{b=0,1} (-1)^{bc} \langle \alpha | (-1)^b \alpha \rangle = \frac{1}{2} \sum_{b=0,1} (-1)^{bc} e^{((-1)^{b-1})|\alpha|^2} = e^{-|\alpha|^2} \exp_c(|\alpha|^2), \quad (40)$$

<sup>2</sup> The harmonic oscillator group in  $D-1$  dimensions is the Lie group generated by the Lie algebra of the canonical annihilation and creation operators in  $D-1$  dimensions, including the corresponding number operators and the rotations. Alternatively, this contraction procedure can be seen as the large  $N$  limit of the generalized Holstein-Primakoff realization of  $SU(D)$ , see [27, 28].

with  $|\alpha\rangle$  the coherent states of the harmonic oscillator, and where:

$$\exp_c(x) = \begin{cases} \cosh(x) & , c = 0 \text{ (even)}, \\ \sinh(x) & , c = 1 \text{ (odd)}. \end{cases} \quad (41)$$

The behaviour of the normalization factors  $\mathcal{N}_c(\mathbf{z})^2$  is summarized in Fig. 1 for the case  $D = 2$ .

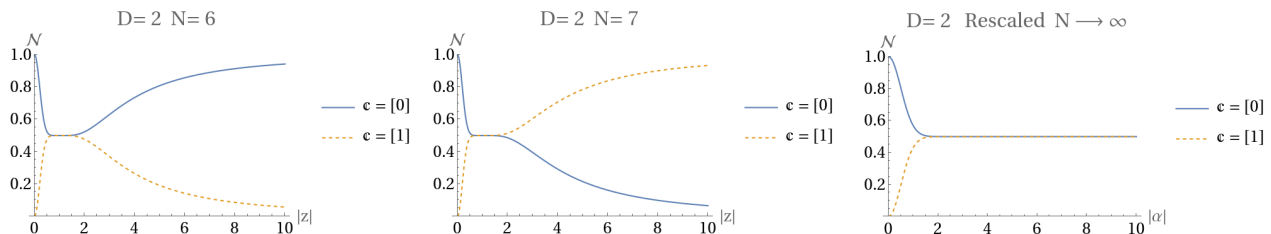


FIG. 1. Plots of the normalization factor  $\mathcal{N}_c(\mathbf{z})^2$  for  $D = 2$ ,  $N = 6$  (left),  $N = 7$  (center) and in the rescaled thermodynamic limit (right), for  $|z|, |\alpha| \in [0, 10]$ .

## B. Fock coefficients

The coefficients  $c_{\vec{n}}(\mathbf{z})_c$  of  $|\mathbf{z}\rangle_c$  in the Fock basis are:

$$c_{\vec{n}}(\mathbf{z})_c = \frac{2^{1-D}}{\mathcal{N}_c(\mathbf{z})} \sum_{\mathbf{b}} \chi_{\mathbf{c}+\mathbf{n}}(\mathbf{b}) c_{\vec{n}}(\mathbf{z}) = \frac{c_{\vec{n}}(\mathbf{z})}{\mathcal{N}_c(\mathbf{z})} \delta_{\vec{n}_0 \bmod 2, c}, \quad (42)$$

where  $\vec{n}_0 = (n_1, \dots, n_{D-1})$  is retrieved from  $\vec{n}$  by removing  $n_0$ . With this expression of the Fock coefficients for  $|\mathbf{z}\rangle_c$ , the squared norm can be rewritten as

$$\mathcal{N}_c(\mathbf{z})^2 = \sum_{\|\vec{n}\|_1=N} \delta_{\vec{n}_0 \bmod 2, c} |c_{\vec{n}}(\mathbf{z})|^2 \quad (43)$$

Thus, parity adapted  $U(D)$ -spin CS  $|\mathbf{z}\rangle_c$  in Eq. (33) contain only basis Fock states  $|\vec{n}\rangle$  with the same parity as  $c$  (in the indices  $i = 1, \dots, D-1$ ).

Due to these properties, parity adapted CS can be considered multicomponent Schrödinger cat states, being an extension to  $D$  levels and parity  $c \in \mathbb{Z}_2^{D-1}$  of  $SU(2)$  Schrödinger cat states [29], which in turn are the  $SU(2)$  version of the traditional even and odd Schrödinger cat states for one-mode harmonic oscillator [30]. They are also the  $U(D)$  version (extended to all possible parities) of Schrödinger cat states of the multimode harmonic oscillator [31]. The  $SU(2)$  version of these states are related to spin cat states [32–35], with interesting metrological properties. We shall call them “ $c$ -DCATS”, or “DCATS” for short when the parity  $c$  is not relevant.

It is interesting to note that if we consider parity adapted CS but restricted to the total parity subgroup, i.e. the one generated by  $\Pi^0 = I$  and  $\Pi^1$ , the resulting states are the  $U(D)$  version of the *even* and *odd* multimode (or polychromatic) Schrödinger cat states introduced in [31]. In this case, the even or odd parity refers to the total parity, i.e. that of the sum  $n_1 + n_2 + \dots + n_{D-1} = N - n_0$ .

Finally, note that due to the equivalence between the set of coherent states and the Bloch projective space, given by Lemma 2 and Proposition 1, we can extend the definitions in this section to the states parametrized by the Bloch projective space and the ITPS obtained from them, i.e. we can define in the obvious way the ( $N$ -particle states):

$$|\mathbf{w}^{\mathbf{b}}\rangle, \quad |\mathbf{w}\rangle_c, \quad |\psi^{\mathbf{b}}\rangle, \quad |\psi\rangle_c, \quad (44)$$

where  $|\psi\rangle$  here stands for  $N$  identical copies of the state given in Eq. (6). Note that the parity transformed states  $|\mathbf{w}^{\mathbf{b}}\rangle$  and  $|\psi^{\mathbf{b}}\rangle$  are  $N$ -particle ITPS, whereas the parity adapted states  $|\mathbf{w}\rangle_c$  and  $|\psi\rangle_c$  are finite sums of ITPS.

Also, by Theorem 1, any state  $|\Psi\rangle \in \mathcal{H}_N$  (not necessarily an ITPS) can be written as a finite sum of coherent states. Therefore we can define  $|\Psi\rangle^{\mathbf{b}}$  and  $|\Psi\rangle_c$  as the corresponding finite sums of parity transformed or parity adapted coherent states. Although parity transformations are well defined for any state through its action on Fock states, see eq. (10), for the purpose of the Schmidt decomposition the expansion in terms of coherent states will be useful in order to use the factorization property of parity transformations given in Lemma 1.

### C. Limit values for DCATS at $\mathbf{z} = \mathbf{0}$ : *Fock-cat* states

It could seem that  $\mathbb{C}$ -DCATS for parities  $\mathbb{C} \neq \mathbb{0}$  do not exist at  $\mathbf{z} = \mathbf{0}$ , in view of the zero value of the norm of the unnormalized parity adapted states  $\Pi_{\mathbb{C}}|\mathbf{z}\rangle$  (see Eq. (35) and Fig. 1 for  $D = 2$ ). However, if we consider the normalized  $\mathbb{C}$ -DCATS states  $|\mathbf{z}\rangle_{\mathbb{C}}$  in Eq. (33), they are well-behaved at  $\mathbf{z} = \mathbf{0}$ , and their Fock coefficients have the expression:

$$\lim_{\mathbf{z} \rightarrow \mathbf{0}} c_{\vec{n}}(\mathbf{z})_{\mathbb{C}} = \delta_{\vec{n}_0, \mathbb{C}}. \quad (45)$$

This means that  $\mathbb{C}$ -DCATS are Fock states at  $\mathbf{z} = \mathbf{0}$ , in particular the ones given by:

$$\lim_{\mathbf{z} \rightarrow \mathbf{0}} |\mathbf{z}\rangle_{\mathbb{C}} = |n_0 = N - k, \vec{n}_0 = \mathbb{C}\rangle = |N - k, c_1, \dots, c_{D-1}\rangle, \quad (46)$$

with  $k = \|\mathbb{C}\|_0$  the number of non-zero components of  $\mathbb{C}$ . We shall call these states *Fock-cat* states, since they are Fock states but sharing many properties with DCATS, since they are limits of DCATS when  $\mathbf{z} \rightarrow \mathbf{0}$ .

In the thermodynamic limit ( $N \rightarrow \infty$ ), the same result still applies, but now  $n_0 \rightarrow \infty$  in all cases.

In the rescaled thermodynamic limit (the contraction to  $D - 1$  harmonic oscillators), the result is also similar, but in this case the  $\mathbf{z} \rightarrow \mathbf{0}$  limit is the  $(D - 1)$ -dimensional harmonic oscillator Fock state:

$$\lim_{\mathbf{z} \rightarrow \mathbf{0}} |\mathbf{z}\rangle_{\mathbb{C}}^{\text{HO}} = |\mathbb{C}\rangle = |c_1, \dots, c_{D-1}\rangle. \quad (47)$$

### D. Limit values for DCATS when $\|\mathbf{z}\| \rightarrow \infty$

As it can be seen for the case  $D = 2$  at Fig. 1 (the two leftmost graphics), the norm approaches either zero or one when  $\|\mathbf{z}\| \rightarrow \infty$ . A similar behaviour can be observed for higher values of  $D$  at the coordinate axes. This suggests that we should study with detail these limits in order to properly identify these states.

Define the vector  $\mathbf{z} \in \{0, 1\}^{D-1}$  such that  $\|\mathbf{z}\|_0 = 1$ , i.e.  $\mathbf{z}$  is a unitary vector pointing in the positive direction of one of the coordinate axes in  $\mathbb{R}^{D-1}$  (that is,  $\mathbf{z}$  is a particular element of the canonical basis of  $\mathbb{R}^{D-1}$ ). Then the Fock coefficients of the  $\mathbb{C}$ -DCATS in the limit along the coordinate axes are given by:

$$\lim_{r \rightarrow \infty} c_{\vec{n}}(r\mathbf{z})_{\mathbb{C}} = \delta_{\vec{n}_0, \mathbb{C} + (N - \|\mathbb{C}\|_0 - N_{\mathbb{C}})\mathbf{z}}, \quad (48)$$

with  $N_{\mathbb{C}} = (N - \|\mathbb{C}\|_0) \bmod 2$ . This means again that  $\mathbb{C}$ -DCATS approach Fock states in these limits, in particular the ones given by:

$$\lim_{r \rightarrow \infty} |r\mathbf{z}\rangle_{\mathbb{C}} = |N_{\mathbb{C}}, \mathbb{C} + (N - \|\mathbb{C}\|_0 - N_{\mathbb{C}})\mathbf{z}\rangle, \quad (49)$$

and thus they are also *Fock-cat* states.

In some particular cases, depending on the parity of  $N$  and on  $\mathbb{C}$  and  $\mathbf{z}$ , the resulting Fock state has all the particles in the same level (i.e. they are ITPS, with no entanglement). For instance, for  $D = 2$  the resulting Fock state in the limit  $|\mathbf{z}| \rightarrow \infty$  is  $|0, N\rangle$  if  $N$  and  $\mathbb{C}$  have the same parity. For  $D = 3$ ,  $\mathbb{C} = [0, 0]$ , and even  $N$ , in the limit  $\mathbf{z} \rightarrow (\infty, 0)$  the resulting state is  $|0, N, 0\rangle$  and in the limit  $\mathbf{z} \rightarrow (0, \infty)$  the resulting state is  $|0, 0, N\rangle$ . For  $\mathbb{C} = [1, 0]$  and odd  $N$ , in the limit  $\mathbf{z} \rightarrow (\infty, 0)$  the resulting state is  $|0, N, 0\rangle$ . For  $\mathbb{C} = [0, 1]$  and odd  $N$ , in the limit  $\mathbf{z} \rightarrow (0, \infty)$  the resulting state is  $|0, 0, N\rangle$ . For  $\mathbb{C} = [1, 1]$ , in none of the cases we obtain a Fock state with all the particles in the same level.

It should be noted that  $z_i \rightarrow \infty$  for some  $i = 1, \dots, D - 1$  means that the chosen chart (the one for which  $z_0 \neq 0$ ) is no longer valid since  $z_0$  turns out to be zero. In this case the chart for which  $z_i \neq 0$  should be used instead.

Taking into account this fact, the cases  $\|\mathbf{z}\| \rightarrow 0$  and  $z_i \rightarrow \infty$  for some  $i = 1, \dots, D - 1$  should stand on the same foot. For instance, the Fock state  $|0, \dots, 0, N, 0, \dots, 0\rangle$ , with the  $N$  particles at level  $i$ , corresponds (in the notation used in Eq. (6)) to  $w_i = 1, w_j = 0$  for  $j \neq i$  and  $\mathbb{C} = \mathbb{0}$  if  $N$  is even and  $\mathbb{C} = [0, \dots, 0, 1, 0, \dots, 0]$  (with a one at position  $i$ ) if  $N$  is odd. The other cases can be treated in a similar fashion.

## V. ENTANGLEMENT MEASURES

Entanglement implies quantum correlations among the different parts of a multipartite system. We shall restrict to bipartite entanglement of pure states, where different measures of entanglement exist, depending on how non-entangled (separable) states are defined. In [3] some definitions of entanglement are introduced, and in the most basic one (Entanglement-I) separable states are identical TPS states (ITPS), thus the only separable states are coherent

states, as shown in Prop. 1. In particular, symmetrized TPS are entangled according to this definition, due to the exchange symmetry.

For other definitions of entanglement, like (Entanglement-V) in [3], also known as mode entanglement, separable states are obtained, in the second quantization formalism, by acting on the Fock vacuum with a product of creation operators which act on a different set of modes (or levels). An example of separable states are basis Fock states  $|\vec{n}\rangle$ , which however are not separable (except in the case when all the particles are in the same level) with respect to Entanglement-I. Also, with respect to Entanglement-V, coherent states are not separable (see, for instance, [19] for  $U(3)$  coherent states).

There is an intense debate in the literature about which of the different notions of entanglement is the correct one for indistinguishable particles, in the sense that entanglement could be used as a resource in quantum information, computation, communication or metrology tasks, see [3, 4, 9] and references therein.

Without entering in this debate, we shall stick in this paper to the notion of Entanglement-I, which is very common in the literature, and which provides a mathematically consistent notion of entanglement in terms of  $M$ -particle RDMs (when  $N - M$  quDits are traced out) and their corresponding Schmidt coefficients (see [36] and references therein). We shall use entropic measures on the RDMs to quantify the entanglement (see [5] for the case of qubits). From the physical (and also the mathematical) point of view, this is justified since we shall work only with CS and finite sums of them. Also, in certain situations, like quDit loss (see Sec. VIII B), the process of losing one or more quDits is modelled by tracing out by these quDits, and our decomposition fits in perfectly in this scheme.

Since the computation of many entropies (like von Neumann entropy) requires the knowledge of the eigenvalues of the RDM, we shall mainly focus on computing the eigenvalues of these  $M$ -particle RDMs.

By the Schmidt decomposition theorem (see [36]) the nonzero eigenvalues (the squares of the so called Schmidt coefficients) of the  $M$ -particle RDM coincide with those of the  $(N - M)$ -particle RDM, thus we shall restrict to  $1 \leq M \leq \lfloor \frac{N}{2} \rfloor$ . Only in the study of robustness (see Sec. VIII B) we will be interested in the  $(N - M)$ -particle RDM.

Starting with a pure state  $|\psi\rangle^{(N)}$  in the symmetric irreducible representation of  $U(D)$  with  $N$  particles/quDits, we define the  $M$ -particle RDM as:

$$\rho^{(M)} = \text{Tr}_{N-M} |\psi\rangle\langle\psi|^{(N)}. \quad (50)$$

Due to the symmetry of the original state  $|\psi\rangle^{(N)}$ , the resulting density matrix  $\rho^{(M)}$  lies in the symmetric irreducible representation of  $U(D)$  with  $M$  particles.

## VI. SCHMIDT DECOMPOSITION OF DCATS

In this section we provide the main results of the paper on Schmidt decomposition of DCATS under the bipartition in  $M$  and  $N - M$  particles, with  $1 \leq M \leq \lfloor \frac{N}{2} \rfloor$ .

### A. Decomposition of definite parity projection operators

The following Lemma will be of extreme importance in the following results about Schmidt coefficients of reduced density matrices for states with definite parity, stating that projectors  $\Pi_{\mathfrak{c}}$  onto subspaces of definite parity  $\mathfrak{c}$  for a given number of particles can be decomposed as a sum over all possible parities of tensor products of projectors on subspaces of definite parity with smaller number of particles.

*Lemma 3.* Let  $N, M$  integers with  $N > 1$  and  $1 \leq M \leq \lfloor \frac{N}{2} \rfloor$ . Then:

$$\Pi_{\mathfrak{c}}^{(N)} = \sum_{\mathfrak{c}'} \Pi_{\mathfrak{c}-\mathfrak{c}'}^{(N-M)} \otimes \Pi_{\mathfrak{c}'}^{(M)} = \sum_{\mathfrak{c}'} \Pi_{\mathfrak{c}-\mathfrak{c}'}^{(M)} \otimes \Pi_{\mathfrak{c}'}^{(N-M)} = \sum_{\mathfrak{c}'} \Pi_{\mathfrak{c}'}^{(N-M)} \otimes \Pi_{\mathfrak{c}-\mathfrak{c}'}^{(M)}. \quad (51)$$

*Proof:* The proof is obvious using Convolution Theorem for  $\mathbb{Z}_2^{D-1}$ :

$$\begin{aligned} \Pi_{\mathfrak{c}}^{(N)} &= 2^{1-D} \sum_{\mathfrak{b}} \chi_{\mathfrak{c}}(\mathfrak{b}) \Pi^{\mathfrak{b}(N)} = 2^{1-D} \sum_{\mathfrak{b}} \chi_{\mathfrak{c}}(\mathfrak{b}) \left( \Pi^{\mathfrak{b}(N-M)} \otimes I^{(M)} \right) \left( I^{(N-M)} \otimes \Pi^{\mathfrak{b}(M)} \right) \\ &= \sum_{\mathfrak{c}'} \left( \Pi_{\mathfrak{c}-\mathfrak{c}'}^{(N-M)} \otimes I^{(M)} \right) \left( I^{(N-M)} \otimes \Pi_{\mathfrak{c}'}^{(M)} \right) = \sum_{\mathfrak{c}'} \Pi_{\mathfrak{c}-\mathfrak{c}'}^{(N-M)} \otimes \Pi_{\mathfrak{c}'}^{(M)}, \end{aligned} \quad (52)$$

where we have used Lemma 1 to factorize  $\Pi^{\mathfrak{b}(N)}$ :

$$\begin{aligned}\Pi^{\mathfrak{b}(N)} &= \Pi_1^{b_1} \dots \Pi_{D-1}^{b_{D-1}} = \exp(i\pi \sum_{j=1}^{D-1} b_j S_{jj}^{(N)}) = \exp(i\pi \sum_{j=1}^{D-1} b_j (S_{jj}^{(N-M)} \otimes I^{(M)} + I^{(N-M)} \otimes S_{jj}^{(M)})) \\ &= \exp(i\pi \sum_{j=1}^{D-1} b_j S_{jj}^{(N-M)} \otimes I^{(M)}) \exp(i\pi \sum_{j=1}^{D-1} b_j I^{(N-M)} \otimes S_{jj}^{(M)}) = \left( \Pi^{\mathfrak{b}(N-M)} \otimes I^{(M)} \right) \left( I^{(N-M)} \otimes \Pi^{\mathfrak{b}(M)} \right),\end{aligned}\quad (53)$$

together with the fact that the number operators  $S_{jj}$  commute among them for all values of  $j$ . ■

Note the symmetry under the interchange  $(N-M) \leftrightarrow M$ , due to the Schmidt Theorem, and the symmetry under the interchange  $(\mathfrak{c} - \mathfrak{c}') \leftrightarrow \mathfrak{c}'$ , due to the Convolution Theorem.

## B. Decomposition of parity adapted CS

Using the previous result applied to a coherent state we obtain the main result of this paper:

*Theorem 3.* Let  $N, M$  integers with  $N > 1$  and  $1 \leq M \leq \lfloor \frac{N}{2} \rfloor$ . Then the  $\mathfrak{c}$ -DCAT of  $N$  particles can be decomposed in terms of superpositions of tensor products of DCATS of  $M$  and  $N - M$  particles as:

$$|\mathbf{z}\rangle_{\mathfrak{c}}^{(N)} = \sum_{\mathfrak{c}'} l_{\mathfrak{c}, \mathfrak{c}'}^{N, M}(\mathbf{z}) |\mathbf{z}\rangle_{\mathfrak{c} - \mathfrak{c}'}^{(N-M)} \otimes |\mathbf{z}\rangle_{\mathfrak{c}'}^{(M)}, \quad (54)$$

with Schmidt coefficients

$$l_{\mathfrak{c}, \mathfrak{c}'}^{N, M}(\mathbf{z}) = \frac{\mathcal{N}_{\mathfrak{c} - \mathfrak{c}'}^{(N-M)}(\mathbf{z}) \mathcal{N}_{\mathfrak{c}'}^{(M)}(\mathbf{z})}{\mathcal{N}_{\mathfrak{c}}^{(N)}(\mathbf{z})}. \quad (55)$$

*Proof:* The proof is obvious by applying the previous Lemma and restoring the normalization of the diverse DCATS appearing in the equation. ■

The Schmidt eigenvalues of the RDM obtained after tracing out  $N - M$  particles are given by the squares of the Schmidt coefficients:

$$\lambda_{\mathfrak{c}, \mathfrak{c}'}^{N, M}(\mathbf{z}) = \left( l_{\mathfrak{c}, \mathfrak{c}'}^{N, M}(\mathbf{z}) \right)^2. \quad (56)$$

Note that the Schmidt eigenvalues depend only on the absolute values  $|z_i|$ ,  $i = 1, \dots, D - 1$ , and do not depend on the relative phases. They are also invariant under the simultaneous interchange of  $(N - M) \leftrightarrow M$  and  $(\mathfrak{c} - \mathfrak{c}') \leftrightarrow \mathfrak{c}'$ .

The  $M$ -particle RDMs are well-defined density matrices, since the eigenvalues are positive and their sum is one.

*Proposition 2.* The trace of the  $M$ -particle RDM  $\rho_{\mathfrak{c}}^{(M)}(\mathbf{z})$  of a  $\mathfrak{c}$ -DCAT is:

$$\text{Tr} \rho_{\mathfrak{c}}^{(M)}(\mathbf{z}) = \text{Tr} \left( \text{Tr}_{N-M}^{(N)} |\mathbf{z}\rangle_{\mathfrak{c}} \langle \mathbf{z}|^{(N)} \right) = \sum_{\mathfrak{c}'} \lambda_{\mathfrak{c}, \mathfrak{c}'}^{N, M}(\mathbf{z}) = 1. \quad (57)$$

*Proof:* Using the definition of the Schmidt numbers, it is easily proven that

$$\begin{aligned}\sum_{\mathfrak{c}'} \lambda_{\mathfrak{c}, \mathfrak{c}'}^{N, M}(\mathbf{z}) &= \frac{1}{\left( \mathcal{N}_{\mathfrak{c}}^{(N)}(\mathbf{z}) \right)^2} \sum_{\mathfrak{c}'} \left( \mathcal{N}_{\mathfrak{c} - \mathfrak{c}'}^{(N-M)}(\mathbf{z}) \mathcal{N}_{\mathfrak{c}'}^{(M)}(\mathbf{z}) \right)^2 = \frac{1}{\left( \mathcal{N}_{\mathfrak{c}}^{(N)}(\mathbf{z}) \right)^2} 2^{1-D} \sum_{\mathfrak{b}} \chi_{\mathfrak{c}}(\mathfrak{b}) \langle \mathbf{z} | \mathbf{z}^{\mathfrak{b}} \rangle^{(N-M)} \langle \mathbf{z} | \mathbf{z}^{\mathfrak{b}} \rangle^{(M)} \\ &= \frac{1}{\left( \mathcal{N}_{\mathfrak{c}}^{(N)}(\mathbf{z}) \right)^2} 2^{1-D} \sum_{\mathfrak{b}} \chi_{\mathfrak{c}}(\mathfrak{b}) \langle \mathbf{z} | \mathbf{z}^{\mathfrak{b}} \rangle^{(N)} = 1,\end{aligned}\quad (58)$$

where Convolution Theorem for  $\mathbb{Z}_2^{D-1}$  has been used again in the second line. ■

It could seem that the Schmidt decomposition provided by Eq. (54) is ill-defined since the right-hand side of the equation is not invariant under particle permutations. However, it is easy to show that, due to the group-theoretical properties of parity adapted CS, it is in fact symmetric, guaranteeing that the standard Schmidt decomposition for distinguishable bipartite systems works in our case without the need of modification (see for instance the modification suggested in [7] for the case of two indistinguishable qubits).

### C. Schmidt rank of DCATs

Although there are  $2^{D-1}$  terms in the decomposition of a parity adapted CS, not all the eigenvalues  $\lambda_{\mathfrak{c}, \mathfrak{c}'}^{N, M}$  are in general different from zero. There are some general bounds on the rank that we should take into account:

- If some  $z_i = 0$  in eq. (21)  $\Rightarrow$  the number of eigenvalues is reduced in a factor 2 if  $c_i = 0$  (see Sec. VII C). Thus, the minimum Schmidt number (attained when  $\mathbf{z} \rightarrow \mathbf{0}$ ) is  $2^k$ , with  $k = \|\mathfrak{c}\|_0$  the number of non-zero components of the vector  $\mathfrak{c}$ .
- For a given  $M$ , the dimension of the symmetric representation with  $M$  particles is  $\binom{M+D-1}{M}$ .

From this considerations, the next Corollary follows.

*Corollary 1.* The Schmidt number of the  $M$ -particle RDM, defined as the rank of  $\rho_{\mathfrak{c}}^{(M)}(\mathbf{z})$ , for a  $\mathfrak{c}$ -DCAT satisfy the bounds:

$$\text{rank}(\rho_{\mathfrak{c}}^{(M)}(\mathbf{z})) = \min\{2^{\|\mathbf{z}\|_0 + \|\mathfrak{c}_0\|_0}, \binom{M+D-1}{M}\}, \quad (59)$$

with  $\|\mathbf{z}\|_0 \leq D-1$  the number of non-zero entries of the vector  $\mathbf{z}$ , and where  $\|\mathfrak{c}_0\|_0$  is the number of nonzero entries of the vector  $\mathfrak{c}_0$ , defined as the subset of components of  $\mathfrak{c}$  whose indices coincide with the indices of the zero components of  $\mathbf{z}$ .

In Table I some examples for the different dimensions are shown, indicating in red the cases where the dimension of the symmetric representation with  $M$  particles is smaller than the maximum number of DCATs.

	Full tensor product $D^M$	Symmetric irrep $\binom{M+D-1}{M}$	Maximum number of DCATs $2^{D-1}$
$D = 2, M = 1$	2	2	2
$D = 3, M = 1$	3	3	4
$D = 3, M = 2$	9	6	4
$D = 4, M = 1$	4	4	8
$D = 4, M = 2$	16	10	8
$D = 5, M = 1$	5	5	16
$D = 5, M = 2$	25	15	16
$D = 5, M = 3$	125	35	16

TABLE I. Dimensions of the full tensor product space  $\mathcal{H}_1^{\otimes M}$  and the symmetric representation space  $\mathcal{H}_M$  compared with the maximum number of DCATs, for different values of  $D$  and  $M$ . Red colors refer to cases where the maximum number of DCATs exceeds the dimension of  $\mathcal{H}_M$ .

As it can be seen, in general, for  $D = 2$  (qubits) it is enough to consider 1-particle RDMs to account for the two possible 2CATs (even and odd). For  $D = 3$  (qutrits) we need 2-particle RDMs to have enough room to accommodate the four 3CATs, and for  $D = 5$  it is necessary to use 3-particle RDMs to have room for the sixteen 5CATs. Since  $2^{D-1}$  grows exponentially with  $D$ , whereas the binomial coefficient  $\binom{M+D-1}{M}$  grows as a polynomial of degree  $M$  in  $D$ , if we fix  $M$ , clearly the number of DCATs will exceed the maximum rank of the RDMs as  $D$  grows. We need to increase also  $M$  to have enough room for all possible DCATs in the RDMs.

From the previous discussion, we can compute the Schmidt rank, i.e. the maximum Schmidt number for all possible  $M$ -RDM.

*Corollary 2.* The Schmidt rank of a  $\mathfrak{c}$ -DCAT is:

$$\text{Schmidt rank of } |\mathbf{z}\rangle_{\mathfrak{c}} = \max_{1 \leq M \leq \lfloor \frac{N}{2} \rfloor} \text{rank}(\rho_{\mathfrak{c}}^{(M)}(\mathbf{z})) = 2^{\|\mathbf{z}\|_0 + \|\mathfrak{c}_0\|_0} \leq 2^{D-1}. \quad (60)$$

### D. $M$ -wise Entanglement entropy of parity adapted $U(D)$ -spin coherent states

The knowledge of the Schmidt coefficients and eigenvalues allows to easily compute the Linear and von Neumann entropies

$$\mathcal{L}(\rho) = \frac{d}{d-1}(1 - \text{Tr}(\rho^2)), \quad \mathcal{S}(\rho) = -\text{Tr}(\rho \log_d \rho) \quad (61)$$

of the  $M$ -wise RDM matrices, with  $d$  a suitable dimension to normalize the entropies between 0 and 1.

In our case the chosen dimensions (according to the dimension of the symmetric representation for  $M$  particles, when  $M$  is finite, and to the maximum rank of the RDM for parity adapted CS) are:

$$d = \begin{cases} \binom{M+D-1}{M} , & \text{finite } M , \\ 2^{D-1} & , \text{ infinite } M . \end{cases} \quad (62)$$

In Sec. IX (and in the Supplementary Material) we shall show different plots of von Neumann entropy (line plots for  $D = 2$ , contour plots for  $D = 3$ , angular plots with  $\|\mathbf{z}\|_2 = R$  for  $D = 4$  and information diagrams for arbitrary values of  $D$ ). In these plots we shall observe the main features of the entropy of the  $M$ -wise RDM of parity adapted CS, and therefore of the entanglement of these states.

## VII. SOME INTERESTING LIMITS OF THE SCHMIDT EIGENVALUES

In this section we shall analyse with detail the behaviour of the Schmidt eigenvalues under certain limits ( $N \rightarrow \infty$ ,  $M \rightarrow \infty$ ,  $\|\mathbf{z}\| \rightarrow 0$ ,  $z_i \rightarrow 1$ ,  $\|\mathbf{z}\| \rightarrow \infty$ , etc.). We shall make use of the limit values of the normalization factors  $\mathcal{N}_{\mathfrak{c}}(\mathbf{z})$  computed in Sec. IV.

### A. Single thermodynamic limit

In many-body systems, the thermodynamic limit is the limit where the number of particles  $N$  grows to infinity. The limit  $N \rightarrow \infty$  of the Schmidt eigenvalues has the expression:

$$\lim_{N \rightarrow \infty} \lambda_{\mathfrak{c}, \mathfrak{c}'}^{N, M}(\mathbf{z}) = \left( \mathcal{N}_{\mathfrak{c}'}^{(M)}(\mathbf{z}) \right)^2 . \quad (63)$$

It turns out that, in this limit, the Schmidt eigenvalues do not depend on the original parity  $\mathfrak{c}$ , therefore all  $\mathfrak{c}$ -DCATS have the same Schmidt decomposition in the thermodynamic limit. Thus, looking at the RDMs, we cannot infer the parity of the original state in this limit. This confers an universal character to the thermodynamic limit of the Schmidt decomposition, erasing all information about the parity  $\mathfrak{c}$  of the original state.

### B. Double thermodynamic limit

Another interesting limit is the double thermodynamic limit, when both  $N$  and  $M$  go to infinity independently. However, this limit is not well-defined. In fact only one of the iterated limits makes sense (since  $M \leq N$ ). The only possible iterated double thermodynamic limit is:

$$\lim_{M \rightarrow \infty} \lim_{N \rightarrow \infty} \lambda_{\mathfrak{c}, \mathfrak{c}'}^{N, M}(\mathbf{z}) = 2^{-k} \delta_{\mathfrak{c}_0, \mathfrak{c}'_0} , \quad (64)$$

where  $k = \|\mathbf{z}\|_0$  is the number of nonzero components of the vector  $\mathbf{z}$ , and  $\mathfrak{c}_0$  indicates the subset of components of  $\mathfrak{c}$  whose indices coincide with the indices of the zero components of  $\mathbf{z}$ .

This shows that the  $\infty$ -RDM of an infinite number of quDits corresponds to a maximally mixed state of dimension  $2^k$ .

We can also consider the rescaled directional double thermodynamic limit, where both  $N$  and  $M$  go to infinity but with  $M/N = 1 - \eta$  fixed, and simultaneously the variable  $\mathbf{z}$  is rescaled by  $\sqrt{N}$ :

$$\lim_{\substack{N \rightarrow \infty \\ M=(1-\eta)N}} \lambda_{\mathfrak{c}, \mathfrak{c}'}^{N, M}(\boldsymbol{\alpha}/\sqrt{N}) = \prod_{i=1}^{D-1} \lambda_{c_i, c'_i}^{HO, \eta}(\alpha_i) \quad (65)$$

with

$$\lambda_{c, c'}^{HO, \eta}(\alpha) = \left( \frac{\mathcal{N}_{c-c'}^{HO}(\sqrt{\eta}\alpha) \mathcal{N}_{c'}^{HO}(\sqrt{1-\eta}\alpha)}{\mathcal{N}_c^{HO}(\alpha)} \right)^2 \quad (66)$$

with  $\eta \in [\frac{1}{2}, 1)$ . Using the expression of  $\mathcal{N}_c^{HO}(\alpha)$  given in Sec. IV, we arrive at:

$$\lambda_{c,c'}^{HO,\eta}(\alpha) = \frac{\exp_{c-c'}(\eta|\alpha|^2)\exp_{c'}((1-\eta)|\alpha|^2)}{\exp_c(|\alpha|^2)} = \frac{1}{2} + (-1)^{c-c'} \frac{\exp_c((1-2\eta)|\alpha|^2)}{2\exp_c(|\alpha|^2)}. \quad (67)$$

Note that for  $\eta = \frac{1}{2}$  we have  $\lambda_{1,c'}^{HO,\frac{1}{2}}(\alpha) = \frac{1}{2}$  (the odd cat state is maximally entangled for all non-zero values of  $\alpha$ ), and for  $\eta \rightarrow 1$  we have

$$\lim_{\eta \rightarrow 1} \lambda_{c,c'}^{HO,\eta}(\alpha) = \delta_{c',0}, \quad (68)$$

indicating that the fidelity with respect to the original state approaches 1 as  $\eta \rightarrow 1$  (see Sec. VIII B).

This represents a generalization to higher dimensions of the results of [37] (see also [38] for the case  $\eta = \frac{1}{2}$ ), for decoherence of a Schrödinger cat state of the harmonic oscillator (realized with a laser beam) by photon absorption modelled by the passage through a beam splitter of transmissivity  $\eta$ .

This suggests that in the case of DCATS, the Schmidt decomposition we have obtained can be physically interpreted as a decoherence process under the loss of  $M$ -quDits. In this sense, our results can help in designing quantum systems robust under quDit loss, for instance in quantum error correction protocols (see [39, 40] for the case of qubit loss). We shall further discuss this point in Section VIII B.

### C. Limits when $\|\mathbf{z}\| \rightarrow 0$ , $|z_i| \rightarrow 1$ , $\|\mathbf{z}\| \rightarrow \infty$

In this subsection we shall consider diverse limits of the Schmidt eigenvalues in the variable  $\mathbf{z}$ .

The limit at  $\mathbf{z} = \mathbf{0} = (0, 0, \dots, 0)$  is important since it will provide the minimum rank of the RDM. Its general expression is cumbersome and we will only give the cases  $D = 2$  and  $D = 3$ .

For  $D = 2$  we have:

$$\lim_{z \rightarrow 0} \lambda_{c,c'}^{N,M}(z) = \frac{M}{N} \delta_{c,c'} + \frac{N-M}{N} \delta_{c',0}. \quad (69)$$

Thus at  $z = 0$  the Schmidt rank is 1 (pure state) for the completely even ( $c = 0$ ) 2CAT and 2 for the even case ( $c = 1$ ) 2CAT. Note that this last statement should be understood in the limit sense since for  $c \neq 0$  the action of the parity projector onto the highest state (which lies in the completely even subspace) is zero,  $\Pi_c|\mathbf{0}\rangle = 0$ .

For  $D = 3$  we have:

$$\begin{aligned} \lim_{(z_1, z_2) \rightarrow (0,0)} \lambda_{[0,0],c'}^{N,M}(z_1, z_2) &= (1, 0, 0, 0) \\ \lim_{(z_1, z_2) \rightarrow (0,0)} \lambda_{[0,1],c'}^{N,M}(z_1, z_2) &= \left( \frac{M}{N}, \frac{N-M}{N}, 0, 0 \right) \\ \lim_{(z_1, z_2) \rightarrow (0,0)} \lambda_{[1,0],c'}^{N,M}(z_1, z_2) &= \left( \frac{M}{N}, 0, \frac{N-M}{N}, 0 \right) \\ \lim_{(z_1, z_2) \rightarrow (0,0)} \lambda_{[1,1],c'}^{N,M}(z_1, z_2) &= \left( \frac{M(M-1)}{N(N-1)}, \frac{M(N-M)}{N(N-1)}, \frac{M(N-M)}{N(N-1)}, \frac{(N-M)(N-M-1)}{N(N-1)} \right), \end{aligned} \quad (70)$$

where at the right-hand side the vector of Schmidt eigenvalues is shown, ordered according to the decimal expression of  $c'$ . From this expression the rank of the RDM at  $\mathbf{z} = \mathbf{0}$  is easily obtained and generalized to arbitrary  $D$ , resulting in a rank equal to  $2^{\|\mathbf{c}'\|_0}$ . Note that if some  $c_i = 0$ , in the limit  $\mathbf{z} \rightarrow \mathbf{0}$  the DCATS with  $c'_i = 1$  are absent in the Schmidt decomposition.

The expression we have obtained for the Schmidt eigenvalues in the limit  $\mathbf{z} \rightarrow \mathbf{0}$  provide the Schmidt decomposition of Fock-cat states appearing in Secs. IV C and IV D.

The limit when  $|z_i| \rightarrow 1$ ,  $i = 1, \dots, D-1$  also deserves attention, since at this point the entropy of the RDM takes its maximum value, as can be checked in the graphs shown in the Supplementary Material. However, the general analytic expression of the limit is cumbersome, therefore we shall consider only some special cases.

For  $D = 2$  we have:

$$\lim_{|z| \rightarrow 1} \lambda_{c,c'}^{N,M}(z) = \frac{1}{2}, \quad \forall c, c', \forall N, M, \quad 1 \leq M \leq \lfloor \frac{N}{2} \rfloor. \quad (71)$$

Then we conclude that for  $D = 2$  the RDM is maximally mixed at  $|z| = 1$ .

For  $D = 3$  we have:

$$\lim_{(|z_1|, |z_2|) \rightarrow (1, 1)} \lambda_{\mathfrak{c}, \mathfrak{c}'}^{N, M}(\mathbf{z}) = \frac{(3^{N-M} + (-1)^{c_1 - c'_1} + (-1)^{c_2 - c'_2} + (-1)^{c_1 + c_2 - c'_1 - c'_2 + N - M})(3^M + (-1)^{c'_1} + (-1)^{c'_2} + (-1)^{c'_1 + c'_2 + M})}{4(3^N + (-1)^{c_1} + (-1)^{c_2} + (-1)^{c_1 + c_2 + N})}, \quad (72)$$

$\forall \mathfrak{c}, \mathfrak{c}', \forall N, M \quad 1 \leq M \leq \lfloor \frac{N}{2} \rfloor$ . In particular we have for  $M = 1$ :

$$\lim_{(|z_1|, |z_2|) \rightarrow (1, 1)} \lambda_{\mathfrak{c}, [1, 1]}^{N, 1}(\mathbf{z}) = 0, \quad \forall \mathfrak{c}, \forall N > 1, \quad (73)$$

which is due to the fact that  $\mathcal{N}_{[1, 1]}(\mathbf{z})^{(1)} = 0, \forall \mathbf{z} \in \mathbb{C}^2$ . Also, in this case for the other values of  $\mathfrak{c}' \neq [1, 1]$  and  $k > 1$ :

$$\lim_{(|z_1|, |z_2|) \rightarrow (1, 1)} \lambda_{[0, 0], \mathfrak{c}'}^{2k, 1}(\mathbf{z}) = \frac{1}{3}, \quad (74)$$

$$\lim_{(|z_1|, |z_2|) \rightarrow (1, 1)} \lambda_{[1, 1], \mathfrak{c}'}^{2k+1, 1}(\mathbf{z}) = \frac{1}{3}. \quad (75)$$

In all other cases the nonzero eigenvalues are practically  $\frac{1}{3}$ , approaching  $\frac{1}{3}$  for large odd  $N$ . Then we conclude that for  $M = 1$  the RDM is (approximately) maximally mixed when  $(|z_1|, |z_2|) = (1, 1)$ .

Similar conclusions can be obtained for larger values of  $D$ , although the expressions are cumbersome. Then we can conclude that at the point  $|z_i| = 1, i = 1, \dots, D - 1$ , the rank of the  $M$ -wise RDM is  $\min\{\binom{M+D-1}{M}, 2^{D-1}\}$ .

The  $\|z\| \rightarrow \infty$  limit does not exist (except for the case  $D = 2$ , see below), since its value depends on the direction. Using hyper-spherical coordinates in the first hyper-octant,  $|z_i| = r y_i(\vec{\theta}), \vec{\theta} \in [0, \frac{\pi}{2}]^{D-2}, i = 1, 2, \dots, D - 1$ , we can compute the directional limits:

$$\lim_{r \rightarrow \infty} \lambda_{\mathfrak{c}, \mathfrak{c}'}^{N, M}(r, \vec{\theta}) = 2^{1-D} \frac{\sum_{\mathfrak{b}} \chi_{\mathfrak{c} - \mathfrak{c}'}(\mathfrak{b}) Y_{\mathfrak{b}}(\vec{\theta})^{N-M} \sum_{\mathfrak{b}} \chi_{\mathfrak{c}'}(\mathfrak{b}) Y_{\mathfrak{b}}(\vec{\theta})^M}{\sum_{\mathfrak{b}} \chi_{\mathfrak{c}}(\mathfrak{b}) Y_{\mathfrak{b}}(\vec{\theta})^N}, \quad (76)$$

with  $Y_{\mathfrak{b}}(\vec{\theta}) = \sum_{i=1}^{D-1} (-1)^{b_i} y_i(\vec{\theta})^2$ .

For instance, for  $D = 3$  we have polar coordinates  $Y_{\mathfrak{b}}(\vec{\theta}) = (-1)^{b_1} \cos^2 \theta + (-1)^{b_2} \sin^2 \theta$ .

The case  $D = 2$  deserves special attention, since the limit exists, but care should be taken since in some particular cases undetermined limits can appear. The result is:

$$\lim_{|z| \rightarrow \infty} \lambda_{\mathfrak{c}, \mathfrak{c}'}^{N, M}(z) = \frac{1}{2} \left[ 1 + \frac{N-M}{N} (-1)^{c'+M} + \frac{M}{N} (-1)^{c-c'+N-M} \right]. \quad (77)$$

## VIII. PHYSICAL APPLICATIONS

Quantum superpositions of macroscopically distinct quasi-classical states (the so-called Schrödinger cat states) are an important resource for quantum metrology, quantum communication and quantum computation. In particular, superpositions  $\frac{1}{2N(\alpha)} (|\alpha\rangle \pm |e^{i\phi}\alpha\rangle)$  of harmonic oscillator CS  $|\alpha\rangle$  with the same  $|\alpha|$  but with different phases (like the even  $\phi = 0$  and odd  $\phi = \pi$  parity adapted CS discussed here) are a common resource in a large variety of experiments (see for instance the encode of a logical qubit in the subspace generated by this kind of superpositions, which is protected against phase-flip errors [41, 42]).

In this section we shall discuss how the DCATS introduced in this paper can be generated using different Hamiltonians, and how the Schmidt decomposition found here can be useful to study the interesting problem of quDit loss.

### A. DCATS generation

In [37] different methods of producing optical Schrödinger cats for the harmonic oscillator were discussed, and some of them have been realized experimentally [43]. The experimental creation of optical Schrödinger cat states in cavity

QED is discussed in [44]. A Schrödinger cat state of an ion in a trap has been generated experimentally [45], and a Schrödinger cat state formed by two interacting Bose condensates of atoms in different internal states (two-well) has been proposed [46]. Another proposal is the generation of optomechanical Schrödinger cat states in a cavity Bose-Einstein condensate [47], with a considerable enhancement in the size of the mechanical Schrödinger cat state.

An important technique to produce Schrödinger cat states is the use of Kerr or Kerr-like media, like in [41, 42], which allows to create, control and measure a qubit in the subspace generated by various Schrödinger cat states, which is protected against phase-flip errors.

Another Hamiltonian where Schrödinger cat states appear is the Lipkin-Meshkov-Glick (LMG) nuclear model [2]. In this case they appear as the ground state solution in the thermodynamic limit, or as approximate solutions for the lowest eigenstates of the Hamiltonian for finite  $N$ . The LMG model has been also realized in circuit QED scheme [48], and proposed for optimal state preparation with collective spins [49].

### 1. LMG $D$ -Level model

It is surprising that in the literature, when multimode (with  $D > 2$  modes) systems are considered, the only studied cat states are the ones associated to the total parity subgroup  $\mathbb{Z}_2 \subset \mathbb{Z}_2^{D-1}$  (the one formed by the parity transformations in Eqns. (15)-(16), see for instance [50, 51]). However, there are models, like the  $D$ -level LMG model, where the Hamiltonian is invariant under parity transformations, where the lowest energy eigenstate and some of the first excited states are parity adapted CS. More precisely in the limit where the interaction parameter  $\lambda \rightarrow \infty$  in the LMG  $D$ -level model for a finite number of particles, the lowest energy state is approximately (with a high fidelity) a completely even DCAT with  $\mathbf{z} = (1, 1, \dots, 1)$  [17], which corresponds to a maximally entangled state among all parity adapted CS, as was shown in Eqns. (72)-(75). Also, some of the lower excited energy eigenstates are also  $\mathbb{C}$ -DCATS with different parities  $\mathfrak{c}$ .

### 2. Generation by Kerr-like effect

The optical Kerr effect is a universal technique to generate non-classical states in quantum optics. In [52] multi-component Schrödinger cat states were generated in a circuit QED where an intense artificial Kerr effect is created, allowing for single-photon Kerr regime.

In [53], a logical qubit is encoded in two or four harmonic oscillator Schrödinger cat states of a microwave cavity, of the form  $\frac{1}{2\mathcal{N}(\alpha)}(|\alpha\rangle \pm |-\alpha\rangle)$  and  $\frac{1}{2\mathcal{N}(\alpha)}(|i\alpha\rangle \pm |-i\alpha\rangle)$ , realizing the  $\pi/2$  rotation around the  $z$ -axis by means of Kerr effect, and exploiting multi-photon driven dissipative processes. A two-photon driven dissipative process is used to stabilize a logical qubit basis of two-component Schrödinger cat states against photon dephasing errors, while a four-photon driven dissipative process stabilizes a logical qubit in four-component Schrödinger cat states, which is protected against single-photon loss.

In [41] a logical qubit is created in the subspace of four Schrödinger cat states,  $\frac{1}{2\mathcal{N}(\alpha)}(|\alpha\rangle \pm |-\alpha\rangle)$  and  $\frac{1}{2\mathcal{N}(\alpha)}(|\alpha\rangle \pm i|-\alpha\rangle)$ , using a Hamiltonian that encompasses both Kerr effect and squeezing in a superconducting microwave resonator. The created qubit is protected under phase-flip errors.

Kerr-like effect in  $U(2)$  and  $U(D)$  can also be exploited to create Schrödinger cat states, using Hamiltonians of the type  $H_{\text{kerr}} = \chi J_z^2$  ( $J_z = \frac{1}{2}(S_{22} - S_{11})$  is the third component of the angular momentum operator) for  $SU(2)$  or

$$H_{\text{kerr}} = \chi \sum_{j=1}^{D-1} S_{jj}^2 \quad (78)$$

for the case of  $U(D)$ . Note that this Hamiltonian is a particular case of the interacting term of the LMG Hamiltonian for general  $D$  [17], which, in the rescaled double thermodynamic limit, approaches the (multimode) Kerr Hamiltonian plus a squeezing term (see [28]).

Denoting the revival time as  $T_{\text{rev}} = \frac{2\pi}{\chi}$ , for times  $t = T_{\text{rev}}/q$ , with  $q = 2, 3, \dots$ , this kind of Hamiltonians produce multicomponent Schrödinger cat states, where the number of components is  $q$  for odd  $q$  and  $\frac{q}{2}$  for even  $q$  (see [54] for the case of  $SU(2)$  and the harmonic oscillator).

## B. QuDit loss

As commented in Sec. VIIA, when the rescaled directional double thermodynamic limit was discussed and the results in the literature for the study of photon loss were recovered (and generalized to a larger number or harmonic

oscillators, or polychromatic lasers), we can infer that the Schmidt decomposition of parity adapted CS in terms of a sum for all parities of tensor products of parity adapted CS with smaller number of particles, really corresponds to the physical process of quDit loss, when some quDits of a symmetric multi-quDit state are lost by some irreversible process (like decoherence by interaction with the environment or other similar process), and that this process is mathematically described by the partial trace (see, for instance [55]).

This suggests that in the case of  $\mathfrak{c}$ -DCATS, the Schmidt decomposition we have obtained can be used to describe a decoherence process under the loss of  $M$ -quDits. In this sense, our results can help in designing quantum error correction protocols (see [39, 40] for the case of qubit loss).

Our Schmidt decomposition can also be useful in the generalization to quDits of the study of *robustness of entanglement under qubit loss* [55]. In this context, robustness is defined as the survival of entanglement after the loss of  $M$  qubits, i.e. the RDM after tracing out  $M$  qubits,  $\rho_{\mathfrak{c}}^{(N-M)}(\mathbf{z})$  (which describes in general a mixed state), is entangled.

In our case, as it can be checked in the limit values discussed in Sec. VII and in the Figures in Sec. IX (and in the Supplementary Material), the rank of the RDM is larger than one except possibly in the cases  $\|\mathbf{z}\| \rightarrow 0$  and  $|z_i| \rightarrow \infty$  (i.e. along some of the axes), and the entropy of the RDM is lower than the NEMs (Not Entangled Mixed States) limit except in the cases marked in red in Table I (changing  $M$  by  $N - M$ ), when maximally mixed (not entangled) RDM can appear.

The limits of the DCATS when  $\|\mathbf{z}\| \rightarrow 0$  and  $|z_i| \rightarrow \infty$  were studied in Secs. IV C and IV D, and they turn to be Fock states and in some particular cases they are ITPS. Thus, except for the cases where the original state is an ITPS (and therefore it is not entangled), the rank of the resulting RDM is larger than one and  $\rho_{\mathfrak{c}}^{(N-M)}(\mathbf{z})$  is entangled (except in the cases marked in red in Table I).

Therefore, we can guarantee that, except in the mentioned cases, the entanglement of the original DCAT is robust under quDit loss. This should be compared with the case of GHZ or NOON states, which are maximally entangled but they are fragile under qubit loss [55]. In fact, spin cat states [32] with moderate entanglement can reach the standard quantum limit even in the presence of a relative large amount of qubit loss, whereas GHZ states lose this capability with an small fraction of qubit loss.

Motivated by the example discussed in [37, 38], where in the case of photon loss when  $\eta \rightarrow 1$  the fidelity with the original state approaches one, we would like to introduce the concept of fidelity also in our case. Strictly speaking, the fidelity

$$F_{\mathfrak{c}}^{N,M}(\mathbf{z}) \equiv \langle \rho_{\mathfrak{c}}^{(N-M)}(\mathbf{z}) | \rho_{\mathfrak{c}}^{(N)}(\mathbf{z}) \rangle_{\mathfrak{c}}, \quad (79)$$

makes sense only in the case  $N \rightarrow \infty$ , since otherwise the number of particles do not match and the expectation value makes no sense. Alternatively, we can define the fidelity for finite  $N$  as:

$$F_{\mathfrak{c}}^{N,M}(\mathbf{z}) \equiv \lambda_{\mathfrak{c},0}^{N,M}(\mathbf{z}), \quad (80)$$

i.e., as the component in the Schmidt decomposition where the  $(N - M)$  subsystem has the same parity as the original system, and this, according to our definition, corresponds to  $\mathfrak{c}' = 0$  in Eqn. (54).

This definition of fidelity (and its maximization with respect to  $\mathbf{z}$ ) could be interesting in some protocols where it is important that the parity  $\mathfrak{c}$  of the state should be robust under quDit loss. In other situations, however, it could be interesting the fact that the state has a (quasi) definite parity under quDit loss, without worrying about its value. In this case,  $\lambda_{\mathfrak{c},\mathfrak{c}'}^{N,M}(\mathbf{z})$  should be maximized for all possible values of  $\mathfrak{c}'$ , too. And in other situations, it could be interesting to maximize a balanced combination of robustness + fidelity.

## IX. FIGURES FOR $D = 2$ ATOM LEVELS (QUBITS)

### A. Finite number $N$ of qubits

In this section, in Figures 2 ( $N = 6$ ) and 3 ( $N = 7$ ) we show plots of the normalized von Neumann entropy (see Eq. (61)) of  $M$ -wise RDMs of the even ( $\mathfrak{c} = [0]$ ) and odd ( $\mathfrak{c} = [1]$ )  $\mathfrak{c}$ -2CAT as a function of  $|z|$ , for values in the range  $[0, 10]$ . We can observe that all normalized entropies reach the maximum for  $|z| = 1$ , with a value 1, i.e. the 2CAT is maximally entangled, for  $M = 1$ .

In the case of an even number of particles  $N$ , for the even parity ( $\mathfrak{c} = [0]$ ) 2CAT the entropy is zero (i.e. the 2CAT is a separable pure state) at  $z = 0$  and for large  $|z|$ , whereas for the odd ( $\mathfrak{c} = [1]$ ) 2CAT both at  $z = 0$  and for large  $|z|$  the entropy takes the same non-zero value, approaching  $\frac{1}{2}$  when  $\frac{M}{N}$  approaches  $\frac{1}{2}$ .

For  $N$  odd, the behaviour is similar but the even and odd  $\mathfrak{c}$  cases get interchanged for large  $|z|$ .

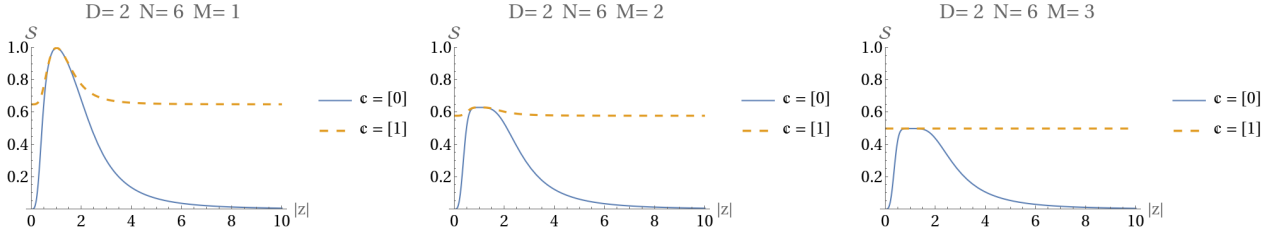


FIG. 2. Plots of von Neumann entropy for  $D = 2$ ,  $N = 6$  and  $M = 1, 2, 3$ , for  $|z| \in [0, 10]$ .

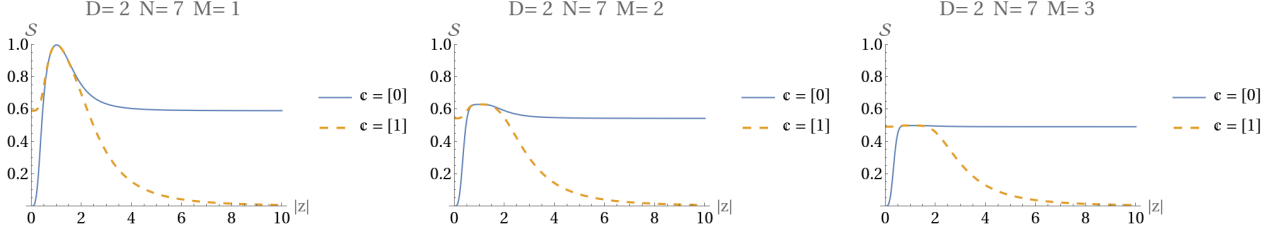


FIG. 3. Plots of von Neumann entropy for  $D = 2$ ,  $N = 7$  and  $M = 1, 2, 3$ , for  $|z| \in [0, 10]$ .

### B. Single thermodynamic limit

In this section, in Figure 4 we show plots of the normalized von Neumann entropy of RDMs of the even ( $\mathfrak{c} = [0]$ ) and odd ( $\mathfrak{c} = [1]$ )  $\mathfrak{c}$ -2CAT as a function of  $|z|$ , for values in the range  $[0, 10]$ , in the case  $N \rightarrow \infty$ . We can observe that all normalized entropies reach the maximum for  $|z| = 1$ , with a value of 1 (i.e. the 2cats are maximally entangled) for  $M = 1$ , and approach zero when  $|z|$  approach zero or grows to infinity. In this case the entropies coincide for both parities, agreeing with Eq. (63).

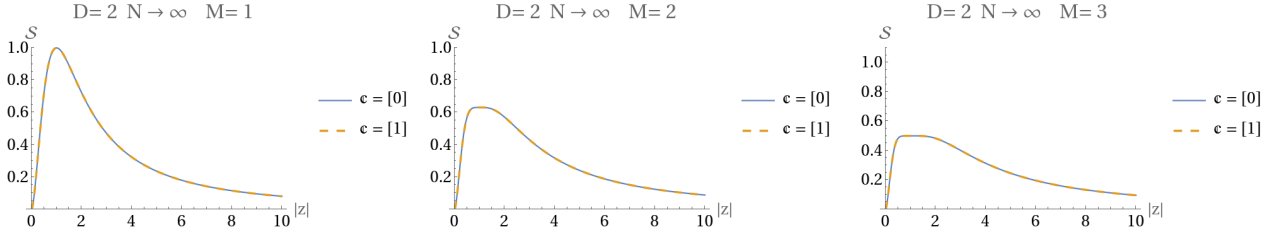


FIG. 4. Plots of von Neumann entropy for  $D = 2$ ,  $N = 6$  and  $M = 1, 2, 3$ , for  $|z| \in [0, 10]$ .

### C. Rescaled double thermodynamic limit

Finally, in Figure 5 we show plots of the normalized von Neumann entropy of RDM of the even ( $\mathfrak{c} = [0]$ ) and odd ( $\mathfrak{c} = [1]$ )  $\mathfrak{c}$ -2CAT as a function of  $|z|$ , for values in the range  $[0, 10]$ , in the case  $N, M \rightarrow \infty$  with  $M = (1 - \eta)N$ . We can observe that for the even 2CAT the normalized entropy reach the maximum of 1 when  $|z|$  grows to infinity, and approach zero when  $z$  approach zero. For the odd 2CAT, the normalized entropy reach the maximum of 1 when  $|z|$  grows to infinity, but approach a non-zero value when  $|z| \rightarrow 0$ , and this value approach 1 when  $\eta$  approach  $\frac{1}{2}$ , agreeing with the results of Sec. VII B.

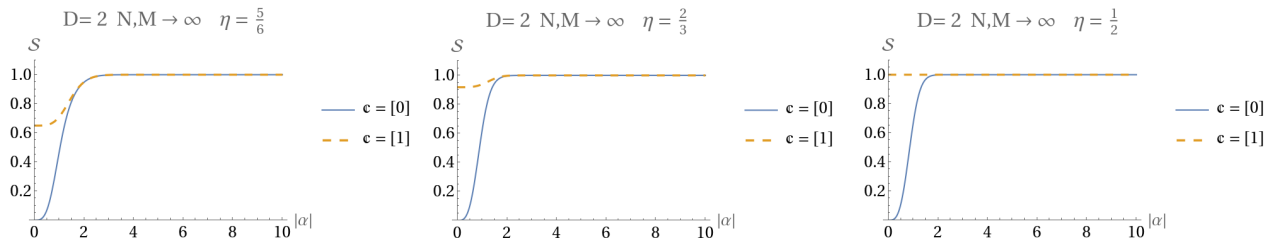


FIG. 5. Plots of von Neumann entropy for  $D = 2$ ,  $N = 6$  and  $M = 1, 2, 3$ , for  $|z| \in [0, 10]$ .

## X. CONCLUSIONS

In this paper we provide a thorough discussion of the entanglement properties of symmetric  $N$ -quDit systems described by parity adapted CS for  $U(D)$  ( $c$ -DCATS), in terms of the entropy of the  $M$ -wise RDM and proving a Schmidt decomposition theorem under a bipartition of the system in terms of  $M < N$  and  $N - M$  particles (quDits).

We show that the Schmidt decomposition turns out to be a sum over all possible parities of tensor products of parity adapted CS with smaller number of particles. This Schmidt decomposition is well-defined even though we are treating with indistinguishable particles, the reason being the constraints imposed by the group-theoretical properties of the parity adapted states.

The properties of the Schmidt eigenvalues have been studied for different limit values and different thermodynamic limits, reproducing, in the case of the rescaled double thermodynamic limit, known results in the literature for photon loss. This suggests that the obtained Schmidt decomposition and entanglement properties could be useful in designing quantum information and computation protocols with parity adapted CS for quDits of arbitrary  $D$ , and studying their decoherence properties under quDit loss.

Possible generalizations of this work in different directions are under study. One of them is considering different transformation groups generalizing the parity group  $\mathbb{Z}_2^{D-1}$ , for instance  $\mathbb{Z}_n^{D-1}$  with  $n > 2$  (an anisotropic version  $\mathbb{Z}_{n_1} \times \dots \times \mathbb{Z}_{n_{D-1}}$  could also be considered). See [56] for a the particular case of the one-mode harmonic oscillator.

Another possible generalization is to consider mode entanglement instead of particle entanglement, i.e. considering a bipartition of different modes or levels, for instance  $D - K$  and  $K$ , with  $0 < K < \lfloor \frac{D}{2} \rfloor$ . In this case, it is expected that a similar result for the Schmidt decomposition should hold but the decomposition involving parity adapted CS of  $U(D - K)$  and  $U(K)$ . Interlevel entanglement for the case  $K = 1$  has already been discussed in [19] for  $K = 1$ .

## ACKNOWLEDGMENTS

We thank the support of the Spanish MICINN through the project PGC2018-097831-B-I00 and Junta de Andalucía through the projects UHU-1262561, FEDER-UJA-1381026 and FQM-381. AM thanks the Spanish MIU for the FPU19/06376 predoctoral fellowship and AS thanks Junta de Andalucía for a contract under the project FEDER-UJA-1381026.

- 
- [1] R. H. Dicke, “Coherence in spontaneous radiation processes,” *Phys. Rev.* **93**, 99–110 (1954).
  - [2] H. J. Lipkin, N. Meshkov, and A. J. Glick, “Validity of many-body approximation methods for a solvable model. (i). exact solutions and perturbation theory,” *Nuclear Physics* **62**, 188–198 (1965).
  - [3] F. Benatti, R. Floreanini, F. Franchini, and U. Marzolino, “Entanglement in indistinguishable particle systems,” *Physics Reports* **878**, 1–27 (2020).
  - [4] Fabio Benatti, Roberto Floreanini, and Ugo Marzolino, “Entanglement and non-locality in quantum protocols with identical particles,” *Entropy* **23** (2021), 10.3390/e23040479.
  - [5] X. Wang and K. Mølmer, “Pairwise entanglement in symmetric multi-qubit systems,” *The European Physical Journal D* **18**, 385–391 (2002).
  - [6] Rosario Lo Franco and Giuseppe Compagno, “Quantum entanglement of identical particles by standard information-theoretic notions,” *Scientific Reports* **6**, 20603 (2016).
  - [7] Stefania Sciara, Rosario Lo Franco, and Giuseppe Compagno, “Universality of schmidt decomposition and particle identity,” *Scientific Reports* **7**, 44675 (2017).

- [8] N. Killoran, M. Cramer, and M. B. Plenio, “Extracting entanglement from identical particles,” *Phys. Rev. Lett.* **112**, 150501 (2014).
- [9] Benjamin Morris, Benjamin Yadin, Matteo Fadel, Tilman Zibold, Philipp Treutlein, and Gerardo Adesso, “Entanglement between identical particles is a useful and consistent resource,” *Phys. Rev. X* **10**, 041012 (2020).
- [10] J. Guerrero, A. Mayorgas, and M. Calixto, “Information diagrams in the study of entanglement in symmetric multi-qudit systems and applications to quantum phase transitions in lipkin–meshkov–glick d-level atom models,” *Quant. Inf. Process.* **21**, 223 (2022).
- [11] J Schwinger, “On angular momentum,” (1952), 10.2172/4389568.
- [12] Paul Adrien Maurice Dirac, “The quantum theory of the emission and absorption of radiation,” *Proc. R. Soc. Lond. A*, 243–265 (1927).
- [13] V. Fock, “Konfigurationsraum und zweite quantelung,” *Zeitschrift für Physik* **75**, 622–647 (1932).
- [14] Ayumu Sugita, “Moments of generalized husimi distributions and complexity of many-body quantum states,” *Journal of Physics A: Mathematical and General* **36**, 9081–9103 (2003).
- [15] Kunz, “On the equivalence between one-dimensional discrete walsh-hadamard and multidimensional discrete fourier transforms,” *IEEE Transactions on Computers* **C-28**, 267–268 (1979).
- [16] Askold Perelomov, *Generalized Coherent States and Their Applications* (Springer-Verlag Berlin Heidelberg, 1986).
- [17] Manuel Calixto, Alberto Mayorgas, and Julio Guerrero, “Role of mixed permutation symmetry sectors in the thermodynamic limit of critical three-level Lipkin-Meshkov-Glick atom models,” *Phys. Rev. E* **103**, 012116 (2021).
- [18] Ingemar Bengtsson and Karol Życzkowski, *Geometry of Quantum States: An Introduction to Quantum Entanglement* (Cambridge University Press, 2006).
- [19] Manuel Calixto, Alberto Mayorgas, and Julio Guerrero, “Entanglement and U(D)-spin squeezing in symmetric multi-qudit systems and applications to quantum phase transitions in Lipkin–Meshkov–Glick D-level atom models,” *Quantum Information Processing* **20**, 304 (2021).
- [20] A. Mayorgas J. Guerrero, A. Sojo and M. Calixto, in preparation.
- [21] M. Calixto, J. Guerrero, and J. C. Sánchez-Monreal, “Sampling theorem and discrete Fourier transform on the Riemann sphere,” *J. Fourier Anal. Appl.* **14**, 538–567 (2008).
- [22] M. Calixto, J. Guerrero, and J. C. Sánchez-Monreal, “Sampling theorem and discrete fourier transform on the hyperboloid,” *J. Fourier Anal. Appl.* **17**, 240–264 (2011).
- [23] Ettore Majorana, “Atomi orientati in campo magnetico variabile,” *Il Nuovo Cimento* (1924-1942) **9**, 43–50 (1932).
- [24] A. R. Usha Devi, Sudha, and A. K. Rajagopal, “Majorana representation of symmetric multiqubit states,” *Quantum Information Processing* **11**, 685–710 (2012).
- [25] Barry C. Sanders, “Entangled coherent states,” *Phys. Rev. A* **45**, 6811–6815 (1992).
- [26] Barry C Sanders, “Review of entangled coherent states,” *Journal of Physics A: Mathematical and Theoretical* **45**, 244002 (2012).
- [27] C. Providencia, J. da Providencia, Y. Tsue, and M. Yamamura, “Boson realization of the su(3)-algebra. II: – holstein-primakoff representation for the lipkin model –,” **115**, 155–164.
- [28] S. Randjbar-Daemi, Abdus Salam, and J. Strathdee, “Generalized spin systems and  $\sigma$  models,” *Phys. Rev. B* **48**, 3190–3205 (1993).
- [29] Christopher C. Gerry and Rainer Grobe, “Two-mode su(2) and su(1,1) schrödinger cat states,” *Journal of Modern Optics* **44**, 41–53 (1997), <https://doi.org/10.1080/09500349708232898>.
- [30] V.V. Dodonov, I.A. Malkin, and V.I. Man’ko, “Even and odd coherent states and excitations of a singular oscillator,” *Physica* **72**, 597–615 (1974).
- [31] N. A. Ansari and V.I. Man’ko, “Photon statistics of multimode even and odd coherent light,” *Phys. Rev. A* **50**, 1942 (1994).
- [32] Jiahao Huang, Xizhou Qin, Honghua Zhong, Yongguan Ke, and Chaohong Lee, “Quantum metrology with spin cat states under dissipation,” *Scientific Reports* **5**, 17894 (2015).
- [33] Jiahao Huang, Hongtao Huo, Min Zhuang, and Chaohong Lee, “Efficient generation of spin cat states with twist-and-turn dynamics via machine optimization,” *Phys. Rev. A* **105**, 062456 (2022).
- [34] Caspar Groiseau, Stuart J. Masson, and Scott Parkins, “Generation of spin cat states in an engineered dicke model,” *Phys. Rev. A* **104**, 053721 (2021).
- [35] Yusef Maleki and Aleksei M. Zheltikov, “Spin cat-state family for heisenberg-limit metrology,” *J. Opt. Soc. Am. B* **37**, 1021–1026 (2020).
- [36] Ryszard Horodecki, Paweł Horodecki, Michał Horodecki, and Karol Horodecki, “Quantum entanglement,” *Rev. Mod. Phys.* **81**, 865–942 (2009).
- [37] Scott Glancy and Hilma Macedo de Vasconcelos, “Methods for producing optical coherent state superpositions,” *J. Opt. Soc. Am. B* **25**, 712–733 (2008).
- [38] Steven J. van Enk and Osamu Hirota, “Entangled coherent states: Teleportation and decoherence,” *Physical Review A* **64**, 022313 (2000).
- [39] Roman Stricker, Davide Vodola, Alexander Erhard, Lukas Postler, Michael Meth, Philipp Schindler, Thomas Monz, Markus Müller, and Rainer Blatt, “Experimental deterministic correction of qubit loss,” *Nature* **585**, 207–210 (2020).
- [40] S.M. Zangi and Cong-Feng Qiao, “Robustness of  $2xN \times M$  entangled states against qubit loss,” *Physics Letters A* **400**, 127322 (2021).
- [41] A. Grimm, N. E. Frattini, S. Puri, S. O. Mundhada, S. Touzard, M. Mirrahimi, S. M. Girvin, S. Shankar, and M. H. Devoret, “Stabilization and operation of a kerr-cat qubit,” *Nature* **584**, 205–209 (2020).

- [42] Shruti Puri, Alexander Grimm, Philippe Campagne-Ibarcq, Alec Eickbusch, Kyungjoo Noh, Gabrielle Roberts, Liang Jiang, Mazyar Mirrahimi, Michel H. Devoret, and S. M. Girvin, “Stabilized cat in a driven nonlinear cavity: A fault-tolerant error syndrome detector,” *Phys. Rev. X* **9**, 041009 (2019).
- [43] Alexei Ourjoumtsev, Rosa Tualle-Brouri, Julien Laurat, and Philippe Grangier, “Generating optical schrödinger kittens for quantum information processing,” *Science* **312**, 83–86 (2006), <https://www.science.org/doi/pdf/10.1126/science.1122858>.
- [44] S. Haroche, “Mesoscopic coherences in cavity qed,” *Il Nuovo Cimento B* (1971-1996) **110**, 545–556 (1995).
- [45] C. Monroe, D. M. Meekhof, B. E. King, and D. J. Wineland, “A ”schrödinger cat” superposition state of an atom,” *Science* **272**, 1131–1136 (1996), <https://www.science.org/doi/pdf/10.1126/science.272.5265.1131>.
- [46] J. I. Cirac, M. Lewenstein, K. Mølmer, and P. Zoller, “Quantum superposition states of bose-einstein condensates,” *Phys. Rev. A* **57**, 1208–1218 (1998).
- [47] Baijun Li, Wei Qin, Ya-Feng Jiao, Cui-Lu Zhai, Xun-Wei Xu, Le-Man Kuang, and Hui Jing, “Optomechanical schrödinger cat states in a cavity bose-einstein condensate,” *Fundamental Research* (2022), <https://doi.org/10.1016/j.fmre.2022.07.001>.
- [48] J. Larson, “Circuit qed scheme for the realization of the lipkin-meshkov-glick model,” *Europhysics Letters* **90**, 54001 (2010).
- [49] Manuel H. Muñoz-Arias, Ivan H. Deutsch, and Pablo M. Poggi, “Phase space geometry and optimal state preparation in quantum metrology with collective spins,” (2022).
- [50] V. V. Dodonov, V. I. Man’ko, and D. E. Nikonov, “Even and odd coherent states for multimode parametric systems,” *Phys. Rev. A* **51**, 3328–3336 (1995).
- [51] D. V. Fastovets, Yu. I. Bogdanov, N. A. Bogdanova, and V. F. Lukichev, “Schmidt decomposition and coherence of interfering alternatives,” *Russian Microelectronics* **50**, 287–296 (2021).
- [52] Gerhard Kirchmair, Brian Vlastakis, Zaki Leghtas, Simon E. Nigg, Hanhee Paik, Eran Ginossar, Mazyar Mirrahimi, Luigi Frunzio, S. M. Girvin, and R. J. Schoelkopf, “Observation of quantum state collapse and revival due to the single-photon Kerr effect,” *Nature* **495**, 205–209 (2013).
- [53] Mazyar Mirrahimi, Zaki Leghtas, Victor V Albert, Steven Touzard, Robert J Schoelkopf, Liang Jiang, and Michel H Devoret, “Dynamically protected cat-qubits: a new paradigm for universal quantum computation,” *New Journal of Physics* **16**, 045014 (2014).
- [54] S. Arjika, M. Calixto, and J. Guerrero, “Quantum statistical properties of multiphoton hypergeometric coherent states and the discrete circle representation,” *Journal of Mathematical Physics* **60**, 103506 (2019), <https://doi.org/10.1063/1.5099683>.
- [55] A. Neven, J. Martin, and T. Bastin, “Entanglement robustness against particle loss in multiqubit systems,” *Phys. Rev. A* **98**, 062335 (2018).
- [56] D. B. Horoshko, S. De Bièvre, M. I. Kolobov, and G. Patera, “Entanglement of quantum circular states of light,” *Phys. Rev. A* **93**, 062323 (2016).

*The art of doing mathematics consists in finding that special case which contains all the germs of generality.*

— David Hilbert

# 3

## Hilbert space structure of the low energy sector of $U(D)$ quantum Hall ferromagnets

<sup>6</sup> M. Calixto, A. Mayorgas, and J. Guerrero, “Hilbert space structure of the low energy sector of  $U(N)$  quantum Hall ferromagnets and their classical limit”, *Symmetry* 14 (2022).

### Quality metrics (2022)

- Year: 2022
- Category: MULTIDISCIPLINARY SCIENCES
- Journal Impact Factor (JIF): 2.7
- JIF Rank: 36/73 (Q2)

Publication citations in Google Scholar (March 2024): 2

# Hilbert space structure of the low energy sector of $U(N)$ quantum Hall ferromagnets and their classical limit

Manuel Calixto\*

*Department of Applied Mathematics, University of Granada, Fuentenueva s/n, 18071 Granada, Spain and  
Institute Carlos I of Theoretical and Computational Physics (iC1),  
University of Granada, Fuentenueva s/n, 18071 Granada, Spain*

Alberto Mayorgas†

*Department of Applied Mathematics, University of Granada, Fuentenueva s/n, 18071 Granada, Spain*

Julio Guerrero‡

*Department of Mathematics, University of Jaen, Campus Las Lagunillas s/n, 23071 Jaen, Spain and  
Institute Carlos I of Theoretical and Computational Physics (iC1),  
University of Granada, Fuentenueva s/n, 18071 Granada, Spain*

(Dated: April 25, 2022)

Using the Lieb-Mattis ordering theorem of electronic energy levels, we identify the Hilbert space of the low energy sector of  $U(N)$  quantum Hall/Heisenberg ferromagnets at filling factor  $M$  for  $L$  Landau/lattice sites with the carrier space of irreducible representations of  $U(N)$  described by rectangular Young tableaux of  $M$  rows and  $L$  columns, and associated to Grassmannian phase spaces  $U(N)/U(M) \times U(N - M)$ . We embed this  $N$ -component fermion mixture in Fock space through a Schwinger-Jordan (boson and fermion) representation of  $U(N)$ -spin operators. We provide different realizations of basis vectors using Young diagrams, Gelfand-Tsetlin patterns and Fock states (for an electron/flux occupation number in the fermionic/bosonic representation).  $U(N)$ -spin operator matrix elements in the Gelfand-Tsetlin basis are explicitly given. Coherent state excitations above the ground state are computed and labeled by complex  $(N - M) \times M$  matrix points  $Z$  on the Grassmannian phase space. They adopt the form of a  $U(N)$  displaced/rotated highest-weight vector, or a multinomial Bose-Einstein condensate in the flux occupation number representation. Replacing  $U(N)$ -spin operators by their expectation values in a Grassmannian coherent state allows for a semi-classical treatment of the low energy (long wavelength)  $U(N)$ -spin-wave coherent excitations (skyrmions) of  $U(N)$  quantum Hall ferromagnets in terms of Grassmannian nonlinear sigma models.

PACS numbers: 75.10.Jm Heisenberg model, Quantized spin models – 71.10.Fd Lattice fermion models – 03.65.Fd Algebraic methods

MSC numbers: 81V70 Many-body theory; quantum Hall effect – 81R30 Coherent states – 81Rxx Groups and algebras in quantum theory – 14M15 Grassmannians, Schubert varieties, flag manifolds

Keywords:  $N$ -component fermion mixtures, quantum Hall ferromagnets, unitary group representations, boson Schwinger-Jordan realizations, Young tableaux, Lieb-Mattis theorem, Grassmannian sigma models.

---

\* Corresponding author: calixto@ugr.es

† albmayer97@ugr.es

‡ jguerrer@ujaen.es

## I. INTRODUCTION

The breakthrough in the development of new quantum technologies requires mathematical modeling and an adequate theoretical framework for the study of the underlying nuclear, atomic, molecular, optical and condensed matter systems. Algebraic, numerical, analytical and topological mathematical tools for dealing with complex many-body quantum systems are necessary to analyze their properties. In particular, for the understanding of new and exotic topological quantum phases of matter [characterized by topological numbers like Chern, Pontryagin, Skyrmin (64), etc. and other winding numbers] and their exploitation for technological applications. Indeed, the discovery of new quantum phases of matter (mainly of a topological nature), their classification, analysis and understanding, is a very hot/topical subject. High-temperature superconductors and an emergent category two-dimensional materials provide new types of topological phases, sometimes characterized by exotic electronic (edge) states and currents remarkably robust to impurities and thermal fluctuations. Quantum Hall effect provides the paradigmatic example of a topological phase, but dispersion-less edge currents also appear in the absence of magnetic field, for example, in some graphene analogues (silicene, germanene, etc) with a strong spin-orbit coupling. Two-dimensional topological insulators (see [1] for a text book, [2, 3] for reviews and [4] for progress and prospects) were predicted theoretically by Kane and Mele [5] using a two-dimensional graphene-like material model with spin-orbit interaction. They were first proposed [6] and observed experimentally [7] in mercury cadmium telluride (HgTe/CdTe) semiconductor quantum wells and later in other materials. Another rapidly developing field has to do with topological quantum computation; see [8] for Kitaev's original proposal, [9] for a text book and [10] for a current perspective on Majorana zero modes. Topological quantum computation is an approach to fault-tolerant quantum computation in which the unitary quantum gates result from the braiding of certain topological quantum objects called “anyons”. Topological degrees of freedom promise to encode decoherence-resistant and scalable quantum information. For example, magnetic skyrmions are promising for technological applications, including spintronics and neuromorphic computing. They might be used as information carriers in future advanced memories, logic gates and computing devices (see [11, 12] and [13] for bilayer systems). The creation and transmission of an isolated magnetic skyrmion in thin films is a key for future skyrmionics, which utilizes skyrmions as information carriers in advanced memories, logic gates and computing devices [11, 12]. Therefore, a deeper fundamental/theoretical study of models related to this subject is justified by its future use in quantum technologies.

In this article we concentrate on the study of systems of interacting  $N$ -component fermions. Traditionally, the paradigmatic case for electrons is  $N = 2$  (spin  $1/2$ ), extensible to  $N = 3$  (flavor, color) components for leptons and quarks (see [14] for high energy consequences of topological quantum effects),  $N = 4$  (spin-isospin) components in nuclear physics, etc. The subject of  $SU(N)$  fermions has been recently further fueled in condensed matter physics by the fact that  $SU(N)$  symmetries can be extended to larger  $N$  in ultracold atomic gases (see e.g. the text books [15, 16] and [17] for a review). For example, fermionic alkaline-earth atomic gases trapped in optical lattices realize the  $SU(N)$  generalization of the Hubbard model [18, 19]. Exciting recent advances in cooling, trapping and manipulating more and more complex systems of this kind, make Feynman's original ideas about the simulation of quantum systems and quantum information processing increasingly possible.

Here we want to revisit and deepen the particular subject of  $U(N)$  quantum Hall (Heisenberg-like) ferromagnets (QHF). As it is briefly reviewed in Appendix A, the exchange interaction for  $N$ -component planar electrons in a perpendicular magnetic field adopts the form of a  $U(N)$  QHF Hamiltonian

$$H = -\mathcal{J} \sum_{\langle \alpha, \beta \rangle} \sum_{i, j=1}^N S_{ij}(\alpha) S_{ji}(\beta), \quad (1)$$

on a square lattice when written in terms of  $U(N)$ -spin operators  $S_{ij}(\alpha) = c_i^\dagger(\alpha) c_j(\alpha)$  realized in terms of creation  $c_i^\dagger(\alpha)$  and annihilation  $c_i(\alpha)$  operators of an electron with component  $i, j = 1, \dots, N$  in a given Landau/lattice site  $\alpha$  of a given Landau level (namely, the lowest one). The sum over  $\langle \alpha, \beta \rangle$  extends over all near-neighbor Landau/lattice sites, and  $\mathcal{J}$  is the exchange coupling constant (the spin stiffness for the XY model). Electrons become multicomponent when, for example, in addition to the usual spin components  $\uparrow$  and  $\downarrow$ , they acquire extra “pseudospin” internal components associated: (a) with layer (for a multilayer arrangement), (b) with valley (like in graphene and other 2D Dirac materials), (c) with sub-lattice, etc. In addition, multilayer arrays introduce extra components (“flavors”) to the electron and much richness, so that the unitary group  $U(N)$  also plays a fundamental role here. For example, twisted bilayer (and trilayer) graphene for “magic” angles exhibit interesting superconducting properties [20, 21]. In the case of a bilayer quantum Hall system in the lowest Landau level, one Landau site can accommodate  $N = 4$  internal states  $|i\rangle, i = 1, 2, 3, 4$  (let us call them fermion “flavors/components”, in general); more schematically

$$|1\rangle = |\uparrow t\rangle, \quad |2\rangle = |\uparrow b\rangle, \quad |3\rangle = |\downarrow t\rangle, \quad |4\rangle = |\downarrow b\rangle, \quad (2)$$

where  $t$  and  $b$  make reference to the “top” and “bottom” layers, respectively. Since the electron field has  $N = 4$  degenerate components, the bilayer system possesses an underlying  $U(4)$  symmetry. Likewise, the  $\ell$ -layer case carries a  $U(2\ell)$  symmetry (see next Section II for more details).

For  $N$ -component electrons, the Pauli exclusion principle allows  $M \leq N$  electrons per Landau/lattice site (the filling factor). Selecting a ground state  $|\Phi_0\rangle$  ( $|0\rangle_F$  denotes the Fock vacuum)

$$|\Phi_0\rangle = \prod_{\alpha=1}^L \prod_{i=1}^M c_i^\dagger(\alpha) |0\rangle_F, \quad (3)$$

which fills all  $L$  Landau sites with the first  $M$  internal levels  $i = 1, \dots, M \leq N$  [i.e., for integer filling factor  $M$ ], spontaneously breaks the  $U(N)$  symmetry since a general unitary transformation mixes the first  $M$  “spontaneously chosen” occupied internal levels with the  $N - M$  unoccupied ones. The ground state  $|\Phi_0\rangle$  is still invariant under the stability subgroup  $U(M) \times U(N - M)$  of transformations among the  $M$  occupied levels and the  $N - M$  unoccupied levels, respectively. Therefore, the transformations that do not leave  $|\Phi_0\rangle$  invariant are parametrized by the Grassmannian coset  $\mathbb{G}_M^N = U(N)/U(M) \times U(N - M)$ , which reduces to the well known sphere  $S^2 = U(2)/U(1) \times U(1)$  for  $N = 2$  spin components and  $M = 1$  electron per Landau site. The kind of irreducible representations (IRs) of  $U(N)$  related to Grassmann phase spaces  $\mathbb{G}_M^N$  are those described by rectangular Young tableaux of  $M$  rows and  $L$  columns, where  $L$  labels the corresponding IR, just as spin  $s$  does for  $SU(2)$ .

The objective of this article is to describe the carrier Hilbert space associated with these  $U(N)$  representations, their coherent states (see e.g. the standard text books [22, 23]), and the classical limit. In the classical limit  $L \rightarrow \infty$  (large  $U(N)$ -spin representations), the collective operators  $S_{ij}$  become c-numbers (their coherent state expectation values, to be more precise), and the low energy (long wavelength)  $U(N)$ -spin-wave coherent excitations are named “skyrmions” (see e.g. some recent books and thesis [24–27]). These coherent excitations turn out to be described by a ferromagnetic order parameter associated to this spontaneous symmetry breaking and labeled by  $(N - M) \times M$  complex matrices  $Z$  parametrizing the complex Grassmannian manifold  $\mathbb{G}_M^N$  (see later on Section V for more information about its structure). Actually, the classical dynamics associated to these  $SU(N)$  quantum spin chains can be described by a Grassmannian nonlinear sigma model (NL $\sigma$ M) [28–33], generalizing the  $SU(2)$  NL $\sigma$ M for the continuum dynamics of Heisenberg (anti)ferromagnets [34–36]. In references like [30, 31],  $N$  represents the number of fermion “flavors”, whereas  $L$  is referred to as the number of “colours”  $n_c$ .

The organization of the paper is the following. In Section II we motivate the description of low energy sectors of  $U(N)$  QHF by representations linked rectangular Young tableaux, using the Lieb-Mattis ordering of electronic energy levels based on the pouring principle for Young tableaux. In Section III we develop this idea and construct the Hilbert space of  $ML$   $N$ -component fermions occupying  $L$  Landau sites (integer filling factor  $M$ ) making use of a bosonic realization of the  $U(N)$ -spin collective operators  $S_{ij}$  acting on Fock space states. The whole construction relies on the definition of a highest-weight (ground) state in Sec. III A, a “boson condensate” version of the ground state (3). We provide a representation of basis vectors in terms of Young tableaux, Gelfand-Tsetlin vectors and Fock (boson and fermion) states III B. The monolayer  $N = 2$  case at filling factor  $M = 1$ , the bilayer  $N = 4$  case at filling factor  $M = 2$  and the trilayer  $N = 6$  case at  $M = 3$  are worked out as particular examples. General Hilbert-space dimension formulas are provided in Sec. III C. Matrix elements of the  $U(N)$  physical operators are provided in Sec. IV, together with the spectrum of Casimir operators, paying special attention to the quadratic Casimir operator since it is related with the exchange interaction Hamiltonian at low energies. Section V is devoted to the discussion of Grassmannian coherent states and the expectation values of  $U(N)$ -spin collective operators.  $U(N)$  coherent states can be seen as coherent excitations above the highest weight (ground) state in the form of Bose-Einstein condensates. Coherent states are essential to discuss the classical limit of large  $L$  representations of  $U(N)$  QHF in terms of NL $\sigma$ Ms on Grassmannian manifolds  $\mathbb{G}_M^N$ , of which we also comment in the second half of Section V. The last Section VI is devoted to conclusions and outlook. For completeness, and to be as self-contained as possible, we include in Appendix A a brief remind on the derivation of  $U(N)$  QHF models from first principle (two-body exchange) interactions. The proof of propositions II.1 and III.1 is given in Appendices B and C, respectively. A more detailed relation between Gelfand-Tsetlin and Fock states is left for the Appendix D. The spin-pseudospin structure of basis states for bilayer  $U(4)$  QHF at filling factor  $M = 2$  is made explicit in the Appendix E. Explicit particular expressions of  $U(N)$ -spin matrices for  $N = 4, M = 1, L = 1, 2$  and  $N = 4, M = 2, L = 1$  are given in Appendix F. Finally, general considerations about the highest weight state for Young tableaux of arbitrary shape are given in Appendix G.

## II. $U(N)$ FERROMAGNETISM AND LIEB-MATTIS ORDERING OF ELECTRONIC ENERGY LEVELS

Let us denote by  $\mathcal{H}_N^\alpha[1^M]$  the  $\binom{N}{M}$ -dimensional carrier Hilbert space at site  $\alpha$  of the fully antisymmetric IR of  $U(N)$  described by the Young frames/diagrams of shape  $[1^M]$ , that is, with  $M$  boxes on a single column. This is a convenient way of graphically representing  $U(N)$  (and symmetric group  $\mathfrak{S}_P$ ) invariant subspaces, i.e., by Young diagrams of  $P$

boxes/particles

$$\begin{array}{|c|c|c|c|c|c|} \hline \overbrace{\dots\dots\dots}^{h_1} \\ \hline \dots \\ \hline \vdots \\ \hline \dots \\ \hline \end{array} \quad (4)$$

of shape  $h = [h_1, \dots, h_N]$ , with  $h_1 \geq \dots \geq h_N$ ,  $h_i$  the number of boxes in row  $i = 1, \dots, N$  and  $h_1 + \dots + h_N = P$  the total number of particles. This is why  $h$  is also called a partition of  $P$ . We sometimes use the shorthand  $[h, \overset{M}{\cdot}, h, 0, \dots, 0] = [h^M]$ , obviating zero-box rows. Basis vectors of  $\mathcal{H}_N^\alpha[1^M]$  are the  $M$ -particle Slater determinants (in Fock and Young tableau notation)

$$\prod_{\mu=1}^M c_{i_\mu}^\dagger(\alpha)|0\rangle_F = \begin{array}{|c|} \hline i_1 \\ \hline \vdots \\ \hline i_M \\ \hline \end{array} \quad (5)$$

obtained by filling out columns of the corresponding Young diagram with components  $i_\mu \in \{1, \dots, N\}$  in strictly increasing order  $i_1 < \dots < i_M$ . The ground state (“highest weight”) vector (3) is just one example. One can see that there are exactly  $\binom{N}{M}$  different arrangements of this kind (the dimension of  $\mathcal{H}_N^\alpha[1^M]$ ).

The Hilbert space of a  $U(N)$  QHF with  $L$  Landau/lattice sites at integer filling factor  $M$  is the  $\binom{N}{M}^L$ -dimensional  $L$ -fold tensor product space  $\mathcal{H}_N^{\otimes L}[1^M] = \bigotimes_{\alpha=1}^L \mathcal{H}_N^\alpha[1^M]$ . In Young tableau notation

$$M \left\{ \begin{array}{|c|} \hline \square \\ \hline \vdots \\ \hline \square \\ \hline \end{array} \right\} \otimes \overset{L \text{ times}}{\dots} \otimes \begin{array}{|c|} \hline \square \\ \hline \vdots \\ \hline \square \\ \hline \end{array} \leftrightarrow [1^M]^{\otimes L} = [1^M] \otimes \dots \otimes [1^M]. \quad (6)$$

This tensor product representation of  $U(N)$  is reducible and it decomposes into a direct sum of irreducible representations of different shapes. For example, the Clebsch-Gordan decomposition of a tensor product of  $L = 2$  IRs of  $U(N)$  of shape  $[1^M]$ , with filling factor  $M = 2 \leq N \geq 4$ , is represented by the following Young diagrams

$$\begin{array}{|c|} \hline \square \\ \hline \square \\ \hline \end{array} \otimes \begin{array}{|c|} \hline \square \\ \hline \square \\ \hline \end{array} = \begin{array}{|c|c|} \hline \square & \square \\ \hline \square & \square \\ \hline \end{array} \oplus \begin{array}{|c|c|} \hline \square & \square \\ \hline \square & \\ \hline \end{array} \oplus \begin{array}{|c|} \hline \square \\ \hline \square \\ \hline \square \\ \hline \end{array} \leftrightarrow [1^2] \otimes [1^2] = [2^2] \oplus [2, 1^2] \oplus [1^4]. \quad (7)$$

The  $P(= ML)$ -particle ground state (3) is a vector of  $\mathcal{H}_N^{\otimes L}[1^M]$ . In particular, for filling factor  $M = 2$  and  $L = 2$  lattice sites,  $|\Phi_0\rangle$  is represented by the rectangular Young tableau

$$\prod_{\alpha=1}^2 \prod_{i=1}^2 c_i^\dagger(\alpha)|0\rangle_F = \begin{array}{|c|c|} \hline 1 & 1 \\ \hline 2 & 2 \\ \hline \end{array}, \quad (8)$$

where rows are filled in a non-decreasing order. One can see that, for  $N = 4$  electron components, there are 20 different Young tableau arrangements of this kind, which is the dimension of the IR of  $U(4)$  given by the rectangular Young diagram of shape  $[2^2]$  (see later on Section III C for general dimension formulas). In fact, the corresponding dimensions for the tensor product decomposition (7) for  $N = 4$  is  $6 \times 6 = 20 + 15 + 1$ . Note that the ground state (3) is invariant under permutation of lattice sites  $\alpha$  (look at the equations (A4, A5)); therefore, it will always belong to IRs of  $U(N)$  of rectangular shape

$$[L^M] = M \left\{ \begin{array}{|c|c|c|} \hline \overbrace{\dots\dots\dots}^L \\ \hline \vdots \\ \hline \dots \\ \hline \end{array} \right\} \quad (9)$$

arising in the Clebsch-Gordan decomposition of the tensor product (6). The rectangular Young tableaux of shape  $[L^M]$  are antisymmetric under the interchange of rows (electron components or “flavors”) and symmetric under the interchange of columns (lattice sites or “colors”).

Let us show how Lieb-Mattis’ theorem [37], and some generalizations [38], also confer “dominance” to the rectangular Young diagrams  $[L^M]$  [like  $[2^2]$  in (7)] over the rest of diagrams arising in the Clebsch-Gordan decomposition of (6).

The set of Young diagrams is partially ordered (not all  $P$ -particle diagrams can be compared for  $P > 5$ ) by the so called “dominance order”  $\succeq$ , such that

$$[h_1, \dots, h_N] \succeq [h'_1, \dots, h'_N] \leftrightarrow h_1 + \dots + h_k \geq h'_1 + \dots + h'_k \quad \forall k \in [1, N]. \quad (10)$$

It is said that  $h$  dominates  $h'$  or that  $h'$  precedes  $h$  ( $h' \preceq h$ ). Intuitively, it means that one can go from  $h$  to  $h'$  by moving a certain number of boxes from upper rows to lower rows, so that  $h$  is “more symmetric”. Lieb-Mattis’ theorem [37] talks about the “pouring principle”, saying that  $h'$  can be “poured into”  $h$ . The theorem states that, under general conditions on the symmetric Hamiltonian of the system, if  $h' \preceq h$  then  $E(h) < E(h')$  [ $E(h) \leq E(h')$  for “pathologic” potentials], with  $E(h)$  the ground state energy inside each IR  $h$  of  $U(N)$ . From this, the following proposition can be demonstrated

**Proposition II.1.** *All Young diagrams arising in the Clebsch-Gordan direct sum decomposition of the  $L$ -fold tensor product (6) can be pored into the rectangular Young tableaux of shape  $[L^M]$ . That is, the ground state for a  $U(N)$  QHF at filling factor  $M$  belongs to the carrier Hilbert space  $\mathcal{H}_N[L^M]$  of the rectangular IR  $[L^M]$  of  $U(N)$  inside the total Hilbert space  $\mathcal{H}_N^{\otimes L}[1^M]$ .*

The proof is made in the Appendix B. Note that states in  $[L^M]$  are invariant under the permutation of lattice sites  $\alpha = 1, \dots, L$ , thus becoming indistinguishable (“bosonized”). Another way of interpreting it is the following. Given the Fourier transform  $\mathcal{S}_{ij}(q) = \sum_{\alpha=1}^L e^{iq\alpha} S_{ij}(\alpha)$  of  $U(N)$ -spin operators, the long-wavelength (low momentum/energy  $q \simeq 0$ ) ground state excitations are described by the collective operators  $\mathcal{S}_{ij}(0) = \sum_{\alpha=1}^L S_{ij}(\alpha)$ , which are invariant under site permutations  $\alpha \leftrightarrow \alpha'$ . Moreover, the low-energy long-wavelength semi-classical ( $L \rightarrow \infty$ ) dynamics of  $U(N)$  QHF is described by a NL $\sigma$ M which target space is the Grassmannian (the phase space associated to  $U(N)$  IRs with rectangular Young diagrams).

Once we have motivated/highlighted the dominant role of rectangular Young diagrams of shape  $[L^M]$  at low energies, let us explicitly construct these representations in a boson realization of  $U(N)$  generators, together with their associated coherent states labeled by matrix points  $Z$  on the Grassmann phase space  $U(N)/U(M) \times U(N-M)$ . These kind of representations have been studied in (mainly mathematically oriented) text books like [39], but rarely associated with the low energy sector of spin systems like the ones pursued in this article. This is why we think this discussion deserves attention.

### III. LOW ENERGY SECTOR OF $U(N)$ QUANTUM HALL FERROMAGNETS AT FILLING FACTOR $M$

#### A. Boson realization of $U(N)$ -spin operators, Fock space, highest-weight state and ladder operators

In the quantum Hall approach, each electron occupies on average a surface area of  $2\pi\ell_B^2$  (a Landau site, with  $\ell_B$  the magnetic length) that is pierced by one magnetic flux quantum  $\phi_0 = 2\pi\hbar/e$  (see Appendix A for more information about this picture). This image allows a dual bosonic Schwinger realization of  $U(N)$ -spin operators

$$S_{ij} = \sum_{\mu=1}^M a_{i\mu}^\dagger a_{j\mu}, \quad i, j = 1, \dots, N, \quad (11)$$

this time in terms of creation  $a_{i\mu}^\dagger$  and annihilation  $a_{j\mu}$  boson operators of magnetic flux quanta attached to the electron  $\mu = 1, \dots, M$  with component  $i = 1, \dots, N$  [we use Greek indices  $\mu, \nu$  for electron labels to avoid confusion]. From the usual bosonic commutation relations  $[a_{i\mu}, a_{j\nu}^\dagger] = \delta_{ij}\delta_{\mu\nu}$  we derive the  $U(N)$ -spin commutation relations

$$[S_{ij}, S_{kl}] = \delta_{jk}S_{il} - \delta_{il}S_{kj}, \quad (12)$$

where  $\delta_{jk}$  is the usual Kronecker delta. This bosonic picture is quite common in algebraic approaches to nuclear and molecular structure [40–42], for example in the interacting boson model (IBM) [43]. Therefore, we have a representation of  $U(N)$  in Fock space made of Fock states

$$|n\rangle = \frac{\prod_{i=1}^N \prod_{\mu=1}^M (a_{i\mu}^\dagger)^{n_{\mu i}}}{(\prod_{i=1}^N \prod_{\mu=1}^M n_{\mu i}!)^{1/2}} |0\rangle_{\text{F}}. \quad (13)$$

The exponent  $n_{\mu i}$  of  $a_{i\mu}^\dagger$  indicates the number of Landau/lattice sites (flux quanta) available to the electron  $\mu$  of flavor  $i$  (that is, the occupancy number  $a_{i\mu}^\dagger a_{i\mu}$ ). We write  $n_{\mu i}$  and not  $n_{i\mu}$  because  $\mu$  will later make reference to a row index

of a Young diagram. Since  $U(N)$  IRs are finite-dimensional, we know that the representation of  $U(N)$  in Fock space must be reducible. In particular,  $U(N)$ -spin operators conserve the total number of particles  $C_1 = \sum_{i=1}^N S_{ii} \sim ML$  [the linear Casimir operator of  $U(N)$ ]. According to Schur's lemma, for a  $U(N)$  IR, every operator acting on the representation space and commuting with all  $S_{ij}$  must be trivial (a multiple of the identity). Note that the operators

$$\Lambda_{\mu\nu} = \sum_{i=1}^N a_{i\mu}^\dagger a_{i\nu}, \quad \mu, \nu = 1, \dots, M, \quad (14)$$

close a  $U_\Lambda(M)$  Lie algebra, where we are writing the subscript  $\Lambda$  to emphasize that this is different from all the other appearances of  $U(M)$  that are related to the "first"  $S_{ij}$  generators ( $i, j \leq M$ ) of  $U(M)$  as a subgroup of  $U(N)$ . In fact, the operators  $\Lambda_{\mu\nu}$  are in general independent of  $S_{ij}$ , that is,  $\Lambda_{\mu\nu}$  can not be written in terms of  $S_{ij}$  (except for  $M = 1$ , when  $\Lambda_{11} = C_1$ ) since they realize an independent Lie algebra. The operators  $\Lambda_{\mu\nu}$  preserve the IR space and they commute with all the  $U(N)$ -spin operators, i.e.

$$[S_{ij}, \Lambda_{\mu\nu}] = \sum_{\mu'=1}^M \sum_{i'=1}^N [a_{i'\mu'}^\dagger a_{j\mu'}, a_{i'\mu}^\dagger a_{i'\nu}] = 0.$$

Therefore, the operators  $\Lambda_{\mu\nu}$  can be consistently imposed as constraints on Fock state vectors to reduce the representation of  $S_{ij}$  in a consistent manner. Actually, since each electron has  $L$  Landau/lattice sites at its disposal (i.e., a total number of  $L$  flux quanta), then the constraint  $\Lambda_{\mu\mu}|\psi_{\text{phys.}}\rangle = L|\psi_{\text{phys.}}\rangle$  has to be imposed on physical states  $|\psi_{\text{phys.}}\rangle$ . This constraint is extended to  $\Lambda_{\mu\nu}|\psi_{\text{phys.}}\rangle = L\delta_{\mu\nu}|\psi_{\text{phys.}}\rangle$  for non-diagonal  $\mu \neq \nu$  operators [see below in eq. (18) for the case of the highest weight vector]. For the basis Fock states (13), the constraint  $\Lambda_{\mu\mu}|n\rangle = L|n\rangle$  in particular means that  $\sum_{i=1}^N n_{\mu i} = L$ , the total number of Landau/lattice sites available to electron  $\mu$ .

Our aim is to construct a state basis of the Hilbert space  $\mathcal{H}_N[L^M] \subset \mathcal{H}_{N,M}^{\otimes L}$ , carrying the IR  $[L^M]$  of  $U(N)$ , given in terms of linear combinations of Fock states (13). The Hilbert space  $\mathcal{H}_N[L^M]$  can be constructed from the so called "highest weight" HW (resp. lowest-weight) vector  $|\mathfrak{m}_{\text{hw}}\rangle$  by applying lowering  $S_{ij}, i > j$  (resp. raising  $S_{ij}, i < j$ ) operators (see below for a more detailed explanation). This procedure reminds the standard construction of  $SU(2)$  spin- $j$  (Dicke) states  $\{|j, m\rangle, m = -j, \dots, j\}$  from the highest (resp. lowest) weight state  $|j, j\rangle$  (resp.  $|j, -j\rangle$ ) by applying ladder angular momentum operators  $J_-$  (resp.  $J_+$ ). Given a common eigenvector  $|\psi_w\rangle$  of  $S_{ii}, i = 1, \dots, N$ , its weight  $w = [w_1, \dots, w_N]$  is made of the corresponding eigenvalues  $w_i, i = 1, \dots, N$ , which count the number of electrons with flavor/component  $i$ ; therefore,  $w_1 + \dots + w_N = P = ML$ , the total number of particles, which is the value of the linear Casimir operator  $C_1 = S_{11} + \dots + S_{NN}$  of  $U(N)$ . Any other state  $|\psi_{w'}\rangle$  has lower weight  $w'$  than  $|\psi_w\rangle$  if the first non-vanishing coefficient of  $w - w'$  is positive. It is clear that the highest weight must be  $W = [L, \overset{M}{\cdot}, L, 0, \overset{N-M}{\cdot}, 0]$ , which can also be read from the shape of the Young diagram  $[L^M]$  (remember that we are discarding zeros). Let us state this in a more formal way. Before, for the sake of compact notation, we shall denote by

$$A = \begin{pmatrix} a_{11} & \dots & a_{1M} \\ \vdots & & \vdots \\ a_{N1} & \dots & a_{NM} \end{pmatrix}, \quad A^\dagger = \begin{pmatrix} a_{11}^\dagger & \dots & a_{N1}^\dagger \\ \vdots & & \vdots \\ a_{1M}^\dagger & \dots & a_{NM}^\dagger \end{pmatrix}, \quad (15)$$

the  $N \times M$  and  $M \times N$  annihilation and creation operator matrices, respectively.

**Proposition III.1.** *Let  $A_{\text{hw}}^\dagger$  be the  $M \times M$  submatrix*

$$A_{\text{hw}}^\dagger = \begin{pmatrix} a_{11}^\dagger & \dots & a_{M1}^\dagger \\ \vdots & & \vdots \\ a_{1M}^\dagger & \dots & a_{MM}^\dagger \end{pmatrix} \quad (16)$$

of  $A^\dagger$  in (15), given by its first  $M$  columns (the leading principal submatrix of order  $M$ ). Then the state

$$|\mathfrak{m}_{\text{hw}}\rangle = \frac{\det(A_{\text{hw}}^\dagger)^L}{\left(\prod_{p=1}^M (p)_L\right)^{1/2}} |0\rangle_{\text{F}}, \quad (p)_L = p(p+1)\dots(p+L-1) \quad (17)$$

satisfies the highest weight (HW) conditions:

$$\Lambda_{\mu\nu}|\mathfrak{m}_{\text{hw}}\rangle = L\delta_{\mu\nu}|\mathfrak{m}_{\text{hw}}\rangle, \quad \mu, \nu = 1, \dots, M, \quad (18)$$

$$S_{ij}|\mathfrak{m}_{\text{hw}}\rangle = \begin{cases} L\delta_{ij}|\mathfrak{m}_{\text{hw}}\rangle, & i, j \leq M \\ 0, & j > M. \end{cases} \quad (19)$$

It is also normalized [ $(p)_L$  denotes the Pochhammer symbol] and invariant under  $U(M) \times U(N - M) \subset U(N)$  transformations.

The proof is left for the Appendix C. The vector  $|\mathfrak{m}_{\text{hw}}\rangle$  is the boson analogue of the fermion state  $|\Phi_0\rangle$  in (3). The determinant structure of  $|\mathfrak{m}_{\text{hw}}\rangle$  guarantees that this state is *antisymmetric* under electron exchange (i.e. under row exchange of  $A_{\text{hw}}^\dagger$ ) as long as  $L$  is odd. Otherwise, a statistical transmutation occurs for the fermion mixture.

Let us identify the ladder operators. It can be seen that any other state  $S_{jk}|\mathfrak{m}_{\text{hw}}\rangle$  is either zero or has lower weight than  $W = [L, \overset{M}{\cdot}, L, 0, \overset{N-M}{\cdot}, 0]$ . Indeed, using the commutation relations (12),

$$[S_{ii}, S_{jk}] = \delta_{ij}S_{ik} - \delta_{ik}S_{ji} \Rightarrow S_{ii}S_{jk}|\mathfrak{m}_{\text{hw}}\rangle = (W_i + \delta_{ij} - \delta_{ik})S_{jk}|\mathfrak{m}_{\text{hw}}\rangle. \quad (20)$$

Actually, from property (19),  $S_{jk}|\mathfrak{m}_{\text{hw}}\rangle$  gives a non-zero vector of weight  $w \neq W$  only when  $k \leq M < j$ . The resulting vector  $S_{jk}|\mathfrak{m}_{\text{hw}}\rangle$  has the same structure as  $|\mathfrak{m}_{\text{hw}}\rangle$  but replacing column  $k$ ,  $(a_{k1}^\dagger, \dots, a_{kM}^\dagger)^t$ , of  $A_{\text{hw}}^\dagger$  in  $|\mathfrak{m}_{\text{hw}}\rangle$  by column  $j$ ,  $(a_{j1}^\dagger, \dots, a_{jM}^\dagger)^t$  of  $A^\dagger$  in (15). When  $i \leq M$ , the weight component  $w_i$  of  $S_{jk}|\mathfrak{m}_{\text{hw}}\rangle$  is  $w_i = W_i - \delta_{ik} = L - \delta_{ik}$ . When  $i > M$  the weight component  $w_i$  of  $S_{jk}|\mathfrak{m}_{\text{hw}}\rangle$  is  $w_i = 0 + \delta_{ij}$ . Only the weight components  $W_j$  and  $W_k$  are shifted:  $W_j$  increases by 1 and  $W_k$  decreases by 1. Therefore,  $S_{jk}|\mathfrak{m}_{\text{hw}}\rangle$  becomes of lower weight since the first non-vanishing coefficient of  $W - w$  is  $(W - w)_k = 1 > 0$ . In this sense,  $S_{jk}$ , with  $j > k$  acts as a *lowering* ladder operator; It transfers one electron from component  $k$  into component  $j > k$ . Of special interest are the step 1 lowering operators  $S_{i,i-1}$ , from which we can obtain the action of any other lowering operator making use of the recursion formulas

$$S_{i,i-k} = [S_{i,i-1}, S_{i-1,i-k}], \quad k > 0. \quad (21)$$

The same argument can be applied to raising ladder operators  $S_{kj}$  with  $j > k$ . We shall provide an explicit expression for the matrix elements of step 1 lowering  $S_{i,i-1}$  and raising  $S_{i-1,i}$  operators for any IR of  $U(N)$  of a given HW in Section IV.

Let us see how to label and graphically represent basis states of any IR of shape  $h$  of  $U(N)$  in Young tableau and Gelfand notation. We shall pay special attention to the Hilbert space  $\mathcal{H}_N[L^M]$ ,

## B. Young tableaux, Gelfand and Fock basis states

Young tableaux are constructed by filling out rows (resp. columns) of the corresponding Young diagram with components  $i = 1, \dots, N$  in non-decreasing (resp. strictly increasing) order from left to right (resp. from top to bottom). For example, for filling factor  $M = 2$ ,  $L = 7$  Landau sites and  $N = 4$  fermion components/flavors, the following Young tableau

$$\begin{array}{|c|c|c|c|c|c|c|} \hline 1 & 1 & 1 & 2 & 2 & 2 & 3 \\ \hline 2 & 3 & 3 & 3 & 4 & 4 & 4 \\ \hline \end{array} \quad (22)$$

is in the standard form. The occupancy number  $n_{\mu i}$  described after (13) can be calculated as the number of times that the state  $i$  appears in the row  $\mu$  (counting downwards) of the tableau. In the previous example we have

$$n_{11} = 3, n_{12} = 3, n_{13} = 1; n_{22} = 1, n_{23} = 3, n_{24} = 3,$$

and zero the rest. It is clear that  $\sum_{i=1}^N n_{\mu i} = L, \mu = 1, \dots, M$ , that is, each electron  $\mu = 1, \dots, M$  has  $L$  Landau sites available ("it carries  $L$  flux quanta"). The highest weight vector  $|\mathfrak{m}_{\text{hw}}\rangle$  in (17) is written in Young tableau notation as

$$|\mathfrak{m}_{\text{hw}}\rangle = \begin{array}{|c|c|c|} \hline 1 & \dots & 1 \\ \hline \vdots & \vdots & \vdots \\ \hline M & \dots & M \\ \hline \end{array}. \quad (23)$$

To subsequently write matrix elements of  $U(N)$ -spin operators  $S_{ij}$  in a compact form (see Section IV), it is convenient to introduce the Gelfand-Tsetlin notation for vectors as triangular patterns of non-negative integer numbers  $m_{i,j}$  of the form

$$|\mathfrak{m}\rangle = \left\langle \begin{array}{cccccccc} m_{1,N} & & m_{2,N} & & \dots & & m_{N-1,N} & & m_{N,N} \\ & m_{1,N-1} & & m_{2,N-1} & & \dots & & m_{N-1,N-1} & \\ & & \dots & & \dots & & \dots & & \\ & & & \dots & & \dots & & & \\ & & & & m_{1,1} & & & & \end{array} \right\rangle \quad (24)$$

obeying the betweenness conditions

$$m_{i,j} \geq m_{i,j-1} \geq m_{i+1,j} \geq 0. \quad (25)$$

That is, each number in the pattern  $\mathfrak{m}$  is constrained to vary between its two closest upper neighbors. Sometimes we shall denote a Gelfand pattern by its  $N$  rows  $\mathfrak{m} = \{m_N, \dots, m_1\}$ . The relation between a Young tableau and the corresponding Gelfand pattern  $\mathfrak{m} = \{m_N, \dots, m_1\}$  is built as follows (the prescription applies to a Young tableau of general shape, not only rectangular  $[L^M]$ ):

- The top row  $m_N$  is read off the shape of the tableau, and it coincides with the highest weight. In terms of the occupancy numbers  $n_{\mu i}$ , we have

$$m_N = \left[ \sum_{i=1}^N n_{1,i}, \dots, \sum_{i=1}^N n_{N,i} \right]. \quad (26)$$

- The second row  $m_{N-1}$  is read off the shape of the tableau that remains after all boxes containing the component/flavor  $i = N$  are removed, that is,  $m_{i,N-1} = m_{i,N} - n_{i,N}$ .
- ...
- $m_{N-k}$  is read off the shape of the tableau that remains after all boxes containing the flavors  $i = N, N-1, \dots, N-k+1$  are removed, that is,  $m_{i,N-k} = m_{i,N-k+1} - n_{i,N-k+1}$ .
- ...
- $m_2$  is read off the shape of the tableau that remains after all remaining boxes containing  $i = 3$  are removed.
- Finally,  $m_1$  is read off the shape of the tableau that remains after all remaining boxes containing  $i = 2$  are removed.

For example, for the Young tableau (22) we have

$$\begin{array}{|c|c|c|c|c|c|c|} \hline 1 & 1 & 1 & 2 & 2 & 2 & 3 \\ \hline 2 & 3 & 3 & 3 & 4 & 4 & 4 \\ \hline \end{array} = \left\langle \begin{array}{cccccc} 7 & 7 & 0 & 0 & & \\ 7 & 4 & 0 & & & \\ & 6 & 1 & & & \\ & & 3 & & & \end{array} \right\rangle. \quad (27)$$

Let us work out some particular examples, for the sake of clarity, before stating more general formulas.

### 1. $U(2)$ quantum Hall ferromagnet at filling factor $M = 1$

Let us describe the simplest example of a QHF where each Landau site accommodates  $M = 1$  electron with  $N = 2$  flavors, for example, a spin 1/2 electron

$$\boxed{1} = |\uparrow\rangle, \quad \boxed{2} = |\downarrow\rangle. \quad (28)$$

For  $L$  Landau sites, the Hilbert space  $\mathcal{H}_2[L^1]$  basis vectors can be labeled by the number  $L_1$  of spin-up (flavor  $i = 1$ ) electrons in Young tableau, Gelfand and Fock (boson and fermion) forms as

$$\overbrace{\boxed{1 \dots 1} \boxed{2 \dots 2}}^{L_1+L_2=L} = \left| \begin{array}{c} L \\ L_1 \end{array} \right\rangle = \frac{(a_{11}^\dagger)^{L_1} (a_{21}^\dagger)^{L_2}}{\sqrt{L_1! L_2!}} |0\rangle_{\text{F}} = \frac{1}{\sqrt{L!}} \sum_{\sigma \in \mathfrak{S}_L} \prod_{\alpha=1}^{L_1} c_1^\dagger(\sigma(\alpha)) \prod_{\beta=L_1+1}^{L_2} c_2^\dagger(\sigma(\beta)) |0\rangle_{\text{F}}, \quad (29)$$

where  $\mathfrak{S}_L$  is the symmetric group of degree  $L$  and  $\sigma$  a permutation. Moreover, for this case, a Dicke state representation  $\{|j, m\rangle, m = -j, \dots, j\}$  is also possible, with total angular momentum  $j = L/2$  and spin third component  $m = (2L_1 - L)/2$ . The highest ( $L_1 = L$ ) and lowest ( $L_2 = L$ ) weight states correspond to angular momentum third components  $m = L/2 = j$  and  $m = -L/2 = -j$ , respectively. The Hilbert space dimension is clearly  $D[L^1] = L + 1 = 2j + 1$ .

This is time for a clarification. Even though we are using the equality sign “=” in (29), to be precise, each of the vectors in those equalities belong to different vector spaces. That is, they are different mathematical ways of representing the same physical state. However, we will keep this little abuse of notation in the hope that no confusion arises.

### 2. $U(4)$ quantum Hall ferromagnet at filling factor $M = 2$

Let us consider now a bilayer system (with top  $t$  and bottom  $b$  layers) where each Landau site accommodates  $M = 2$  electrons with  $N = 4$  flavors

$$\boxed{1} = |\uparrow t\rangle, \quad \boxed{2} = |\uparrow b\rangle, \quad \boxed{3} = |\downarrow t\rangle, \quad \boxed{4} = |\downarrow b\rangle. \quad (30)$$

The basis states of  $[L^2]$  are given by the Gelfand vectors and their betweenness conditions

$$|m\rangle = \left| \begin{array}{cccccc} L & & & & & \\ & L & & & & \\ & & L & & & \\ & & & m_{23} & & \\ & & & & m_{22} & \\ & & & & & m_{11} \end{array} \right\rangle, \quad \begin{cases} L \geq m_{23} \geq 0, \\ L \geq m_{12} \geq m_{23}, \\ m_{23} \geq m_{22} \geq 0, \\ m_{12} \geq m_{11} \geq m_{22}. \end{cases} \quad (31)$$

In this case, the basis vectors are indexed by four labels  $(m_{11}, m_{12}, m_{22}, m_{23})$ . Particular examples are the highest- $|m_{\text{hw}}\rangle$  and the lowest- $|m_{\text{lw}}\rangle$  weight states

$$|m_{\text{hw}}\rangle = \begin{array}{|c|c|c|} \hline 1 & \dots & 1 \\ \hline 2 & \dots & 2 \\ \hline \end{array} = \left| \begin{array}{cccccc} L & & & & & \\ & L & & & & \\ & & L & & & \\ & & & L & & \\ & & & & L & \\ & & & & & 0 \end{array} \right\rangle = [(1)_L(2)_L]^{-\frac{1}{2}} \left| \begin{array}{cc} a_{11}^\dagger & a_{21}^\dagger \\ a_{12}^\dagger & a_{22}^\dagger \end{array} \right|^L |0\rangle_{\text{F}} = \prod_{\alpha=1}^L c_1^\dagger(\alpha) c_2^\dagger(\alpha) |0\rangle_{\text{F}}, \quad (32)$$

$$|m_{\text{lw}}\rangle = \begin{array}{|c|c|c|} \hline 3 & \dots & 3 \\ \hline 4 & \dots & 4 \\ \hline \end{array} = \left| \begin{array}{cccccc} L & & & & & \\ & L & & & & \\ & & L & & & \\ & & & L & & \\ & & & & L & \\ & & & & & 0 \end{array} \right\rangle = [(1)_L(2)_L]^{-\frac{1}{2}} \left| \begin{array}{cc} a_{31}^\dagger & a_{41}^\dagger \\ a_{32}^\dagger & a_{42}^\dagger \end{array} \right|^L |0\rangle_{\text{F}} = \prod_{\alpha=1}^L c_3^\dagger(\alpha) c_4^\dagger(\alpha) |0\rangle_{\text{F}}, \quad (33)$$

in Young tableau, Gelfand and Fock (boson and fermion) notation, respectively. The relation between Gelfand and Fock states for general  $L$  is a bit more involved for states other than the highest and lowest weight; therefore, we leave the general prescriptions for the Appendix D. An alternative basis for this case was, noted by

$$|j, m\rangle_{q_t, q_b}, \quad q_t, q_b = -j, \dots, j, \quad 0 \leq 2j + m \leq L, \quad (34)$$

has been given in [44], where  $j$  (half-integer) represents an angular momentum and  $m$  (integer) is related to a population imbalance between layers  $t$  and  $b$  (both non-negative).

From the betweenness conditions (31), one can easily compute the dimension of the IR  $[L^2]$  of  $U(4)$  as

$$D[L^2] = \sum_{m_{23}=0}^L \sum_{m_{12}=m_{23}}^L \sum_{m_{22}=0}^{m_{23}} \sum_{m_{11}=m_{22}}^{m_{12}} 1 = \frac{1}{12}(L+1)(L+2)^2(L+3). \quad (35)$$

Note that  $D[L^2]$  grows as  $L^4/12$  for large  $L$ . We shall recover in Section III C the expression (35) as a particular case of the so called ‘‘hook-length’’ general formula, which is a special case of the Weyl’s character formula (see e.g. [39]).

In Appendix E we explicitly work out the case  $L = 1$ , for which  $D[1^2] = 6$ , thus recovering the dimension  $\binom{N}{M}$  of the totally antisymmetric IR  $[1, 1]$  of  $U(4)$ . The corresponding basis vectors for this case can be divided into two spin/pseudospin (layer) sectors, and we shall make use of them when writing Grassmannian  $\mathbb{G}_2^4$  coherent states later in equation (60).

### 3. $U(6)$ quantum Hall ferromagnet at filling factor $M = 3$

Let us consider now a trilayer system (with top  $t$ , central  $c$ , and bottom  $b$  layers) where each Landau site accommodates  $M = 3$  electrons with  $N = 6$  flavors

$$\boxed{1} = |\uparrow t\rangle, \quad \boxed{2} = |\uparrow c\rangle, \quad \boxed{3} = |\uparrow b\rangle, \quad \boxed{4} = |\downarrow t\rangle, \quad \boxed{5} = |\downarrow c\rangle, \quad \boxed{6} = |\downarrow b\rangle. \quad (36)$$

The basis states of  $[L^3]$  are given by the Gelfand vectors indexed by 9 labels

$$(m_{11}; m_{12}, m_{22}; m_{13}, m_{23}, m_{33}; m_{24}, m_{34}; m_{35}).$$

In particular, the HW state

$$|m_{\text{hw}}\rangle = \begin{array}{|c|c|c|} \hline 1 & \dots & 1 \\ \hline 2 & \dots & 2 \\ \hline 3 & \dots & 3 \\ \hline \end{array} = [(1)_L(2)_L(3)_L]^{-1/2} \left| \begin{array}{ccc} a_{11}^\dagger & a_{21}^\dagger & a_{31}^\dagger \\ a_{12}^\dagger & a_{22}^\dagger & a_{32}^\dagger \\ a_{13}^\dagger & a_{23}^\dagger & a_{33}^\dagger \end{array} \right|^L |0\rangle_{\text{F}} = \prod_{\alpha=1}^L c_1^\dagger(\alpha) c_2^\dagger(\alpha) c_3^\dagger(\alpha) |0\rangle_{\text{F}} \quad (37)$$

corresponds to the Gelfand vector with all 9 labels  $m_{ij} = L$ . As we did in (35), from the betweenness conditions (25) of these labels, one can compute the dimension

$$D[L^3] = \frac{(L+1)(L+2)^2(L+3)^3(L+4)^2(L+5)}{8640}. \quad (38)$$

For  $L = 1$  we have  $D[1^3] = 20$ , thus recovering the dimension  $\binom{N}{M}$  of the totally antisymmetric IR  $[1^3]$  of  $U(6)$ . Note that  $D[L^3]$  grows like  $L^9/8640$  for large  $L$ .

### C. General dimension formulas

The dimension of the carrier Hilbert space of a IR of  $U(N)$  with general HW  $m_N = [m_{1N}, \dots, m_{NN}]$  (a partition of  $P$ ) is given by the Weyl dimension formula (see e.g. [39])

$$D[m_N] = \frac{\prod_{i < j} (m_{iN} - m_{jN} + j - i)}{\prod_{i=1}^{N-1} i!}. \quad (39)$$

It can also be written with the so called ‘‘hook formula’’

$$D[m_N] = \prod_{i,j} \frac{N + j - i}{|h_{m_N}(i, j)|}, \quad (40)$$

where  $|h_{m_N}(i, j)|$  is the length of the hook located at the box/cell position  $(i, j)$  (row, column) of the corresponding Young diagram of shape  $m_N$ . The hook  $h_{m_N}(i, j)$  is the set of cells/boxes  $(k, l)$  such that  $k = i$  and  $l \geq j$  or  $k \geq i$  and  $l = j$ . The hook length  $|h_{m_N}(i, j)|$  is the number of cells/boxes in  $h_{m_N}(i, j)$ .

These formulas correspond to the number of independent Gelfand patterns  $\mathfrak{m}$  fulfilling the betweenness conditions (25), and also to the number of different Young tableau arrangements.

For rectangular Young diagrams  $m_N = [L^M, 0^{N-M}]$  the dimension formula (39) acquires the form

$$D[L^M] = \frac{\prod_{i=N-M+1}^N \binom{i+L-1}{i-1}}{\prod_{i=2}^M \binom{i+L-1}{i-1}}, \quad (41)$$

This formula reproduces the previous particular examples. Note that  $D[L^M] = D[L^{N-M}]$  (conjugated representation).

## IV. MATRIX ELEMENTS OF $U(N)$ -SPIN COLLECTIVE OPERATORS

In this Section we shall provide explicit expressions for matrix elements  $\langle \mathfrak{m}' | S_{ij} | \mathfrak{m} \rangle$  of  $U(N)$ -spin operators  $S_{ij}$  (11) in the Gelfand-Tsetlin basis  $\{|\mathfrak{m}\rangle\}$ . We have already given some indications in Section III B. In fact, recursion formulas

$$S_{i,i-l} = [S_{i,i-1}, S_{i-1,i-l}], \quad S_{i-l,i} = [S_{i-l,i-1}, S_{i-1,i}], \quad l > 1, \quad (42)$$

allow us to obtain any non diagonal operator  $S_{ij}$  matrix element from the matrix elements of step 1 lowering  $S_{i,i-1}$  and raising  $S_{i-1,i}$  operators. Let us consider an arbitrary IR of  $U(N)$  of HW  $m_N$ . Denoting by  $\bar{m}_k = \sum_{i=1}^k m_{ik}$ ,  $k = 1, \dots, N$  the sum of  $k$ -th row of a pattern  $\mathfrak{m}$ , and setting  $\bar{m}_0 \equiv 0$ , the action of diagonal operators  $S_{kk}$  on an arbitrary Gelfand state  $|\mathfrak{m}\rangle$  is

$$S_{kk}|\mathfrak{m}\rangle = (\bar{m}_k - \bar{m}_{k-1})|\mathfrak{m}\rangle, \quad (43)$$

which reproduces the expressions (19) for the highest-weight vector  $|\mathfrak{m}_{\text{hw}}\rangle$  with rows  $m_{N-k} = [L^M, 0^{N-M-k}]$  for  $0 \leq k < N - M$  and  $m_k = [L^k]$  for  $1 \leq k \leq M$ . The linear Casimir  $C_1 = \sum_{k=1}^N S_{kk}$  fulfills  $C_1|\mathfrak{m}\rangle = ML|\mathfrak{m}\rangle$ , the eigenvalue  $P = ML$  being the total number of particles.

Let us denote by  $e_{jk}$  the ‘‘auxiliary pattern’’ with 1 at place  $(j, k)$  and zeros elsewhere [we call it ‘‘pattern’’ because it has the triangular shape, although it does not necessarily fulfill the betweenness conditions (25)]. The action of step 1 lowering  $S_{-k} \equiv S_{k,k-1}$  and rising operators  $S_{+k} \equiv S_{k-1,k}$  is given by [39]

$$S_{\pm k}|\mathfrak{m}\rangle = \sum_{j=1}^{k-1} c_{j,k-1}^{\pm}(\mathfrak{m})|\mathfrak{m} \pm e_{j,k-1}\rangle, \quad (44)$$

with coefficients

$$c_{j,k-1}^{\pm}(\mathfrak{m}) = \left( -\frac{\prod_{i=1}^N (m'_{ik} - m'_{j,k-1} + \frac{1 \mp 1}{2}) \prod_{i=1}^{k-2} (m'_{i,k-2} - m'_{j,k-1} - \frac{1 \pm 1}{2})}{\prod_{i \neq j} (m'_{i,k-1} - m'_{j,k-1}) (m'_{i,k-1} - m'_{j,k-1} \mp 1)} \right)^{1/2}, \quad (45)$$

where  $m'_{ik} = m_{ik} - i$  and  $c_{j,k-1}^{\pm}(\mathfrak{m}) \equiv 0$  whenever any indeterminacy arises. In fact, from the commutation relations (20), the weight  $w'$  of  $S_{-k}|\mathfrak{m}\rangle$  is given by

$$S_{ii}S_{-k}|\mathfrak{m}\rangle = (w_i + \delta_{i,k} - \delta_{i,k-1})S_{-k}|\mathfrak{m}\rangle = w'_i S_{-k}|\mathfrak{m}\rangle, \quad (46)$$

and therefore,  $S_{-k}|\mathfrak{m}\rangle$  becomes of lower weight than  $|\mathfrak{m}\rangle$  since the first non-vanishing coefficient of  $w - w'$  is  $(w - w')_{k-1} = 1 > 0$ . From the definition (45) one can prove that

$$c_{j,k-1}^{\pm}(\mathfrak{m}) = c_{j,k-1}^{\mp}(\mathfrak{m} \pm \mathbf{e}_{j,k-1}), \quad (47)$$

which means that  $S_{+k}^{\dagger} = S_{-k}$ . Also, applying induction and the recurrence formulas (42), we obtain  $S_{k,k-l}^{\dagger} = S_{k-l,k}$ . Therefore, we can construct proper hermitian  $U(N)$ -spin operators as:  $\mathcal{S}_{ii} = S_{ii}$ ,  $\mathcal{S}_{ij} = S_{ij} + S_{ji}$  and  $\tilde{\mathcal{S}}_{ij} = i(S_{ij} - S_{ji})$ ,  $i < j \leq N$ , with  $i$  the imaginary unit. In Appendix F we provide explicit expressions of these  $U(N)$ -spin matrix elements for particularly interesting cases.

For completeness, we shall provide the eigenvalues of the  $N$  invariant (Casimir)  $U(N)$  operators  $C_p$  belonging to the enveloping algebra, whose expression is given by  $p$  powers of the operators  $S_{ij}$  as

$$C_p = S_{i_1, i_2} S_{i_2, i_3} \cdots S_{i_{p-1}, i_p} S_{i_p, i_1}, \quad p = 1, \dots, N, \quad (48)$$

where sum on repeated indices is understood. That is,  $C_p$  is of degree  $p$ . We have already argued that  $C_1|\mathfrak{m}\rangle = \bar{m}_N|\mathfrak{m}\rangle$  with  $\bar{m}_N = \sum_{i=1}^N m_{iN}$ . For  $m_N = [L^M, 0^{N-M}]$ , the  $C_1$  eigenvalue is  $\bar{m}_N = ML = P$  the total number of particles. The eigenvalues of  $C_p$  on the carrier Hilbert space of  $m_N$  are given in [39] and they are constructed as follows. Let  $B$  a  $N \times N$  square matrix with entries

$$b_{ij} = (m_{iN} + N - i)\delta_{ij} - u_{ij}, \quad u_{ij} = \begin{cases} 1 & \text{for } i < j \\ 0 & \text{for } i \geq j, \end{cases}$$

and let  $J$  be the  $N \times N$  all-ones matrix (that is,  $J_{ij} = 1$ ). Then the spectrum of the Casimir operators is given by

$$C_p(m_N) = \text{tr}(B^p J), \quad (49)$$

where  $B^p$  is the  $p$ -th power of  $B$ . The quadratic Casimir operator  $C_2$  plays a fundamental role as the  $U(N)$  invariant part of the QHF Hamiltonian and we shall pay special attention to it. In particular, the eigenvalue of the quadratic Casimir operator is simply given in general by  $C_2(m_N) = \sum_{i=1}^N m_{iN}(m_{iN} + N + 1 - 2i)$  and, for the case of  $m_N = [L^M, 0^{N-M}]$ , the expression reduces to  $C_2(m_N) = ML(L + N - M)$ .

## V. GRASSMANNIAN COHERENT STATES AND NONLINEAR SIGMA MODELS

### A. Grassmannian coherent states

We have seen in Proposition III.1 that the HW (ground) state  $|\mathfrak{m}_{\text{hw}}\rangle$  is invariant under the subgroup  $U(M) \times U(N - M)$  of  $U(N)$ . Therefore  $|\mathfrak{m}_{\text{hw}}\rangle$  breaks the  $U(N)$  symmetry since a general  $U(N)$  rotation mixes the first  $M$  (“spontaneously chosen”) occupied internal orbitals with the remainder  $(N - M)$  unoccupied ones. This structure is also very relevant for systems with particle-hole symmetry, like in nuclear and molecular models [40–43].  $U(N)$ -spin-wave excitations occur in  $U(N)$  QHF. These coherent excitations (named “skyrmions”) turn out to be described by a ferromagnetic order parameter associated to this spontaneous symmetry breaking and labeled by  $(N - M) \times M$  complex matrices  $Z$  parametrizing the complex Grassmannian coset  $\mathbb{G}_M^N = U(N)/[U(M) \times U(N - M)]$ . This parametrization is related to the Bruhat-Iwasawa block matrix decomposition (see e.g. Chapter 3 of Ref. [39]) of the complexification  $GL(N, \mathbb{C})$  of  $U(N)$ . For the fundamental  $N$ -dimensional representation, this block matrix decomposition reads

$$U = \left( \begin{array}{c|c} A & B \\ \hline C & D \end{array} \right) = \underbrace{\left( \begin{array}{c|c} \Delta_1 & -Z^{\dagger} \Delta_2 \\ \hline Z \Delta_1 & \Delta_2 \end{array} \right)}_{Q(Z)} \underbrace{\left( \begin{array}{c|c} V_1 & 0 \\ \hline 0 & V_2 \end{array} \right)}_V \quad (50)$$

where  $A$  and  $D$  are invertible square complex matrices of orders  $M$  and  $N - M$ , respectively, with

$$Z = CA^{-1}, \quad \Delta_1 = (AA^\dagger)^{1/2} = (\mathbb{1}_M + Z^\dagger Z)^{-1/2}, \quad \Delta_2 = (DD^\dagger)^{1/2} = (\mathbb{1}_{N-M} + ZZ^\dagger)^{-1/2} \quad (51)$$

and  $V_1 = \Delta_1^{-1}A \in U(M)$ ,  $V_2 = \Delta_2^{-1}D \in U(N - M)$  are unitary matrices. The normalization matrix factors  $\Delta_{1,2}$  are related by the Woodbury matrix identity  $\Delta_1^2 = \mathbb{1}_M - Z^\dagger \Delta_2^2 Z$ . Complex  $(N - M) \times M$  matrix points  $Z$  on the Grassmann manifold  $\mathbb{G}_M^N$  are associated to quotient representatives  $Q(Z) \in U(N)$ .

Let us firstly discuss the simplest  $N = 2$  case. The decomposition (50) for  $U \in U(2)$  adopts the form

$$U = \begin{pmatrix} a & b \\ c & d \end{pmatrix} = \underbrace{\begin{pmatrix} \delta & -\bar{z}\delta \\ z\delta & \delta \end{pmatrix}}_{Q(z)} \begin{pmatrix} a/\delta & 0 \\ 0 & d/\delta \end{pmatrix}, \quad \delta = (1 + |z|^2)^{-1/2}, \quad (52)$$

which is adapted to the quotient  $\mathbb{G}_1^2 = U(2)/[U(1) \times U(1)] = \mathbb{S}^2$  (the two-sphere), with  $z = c/a = \tan(\theta/2)e^{i\phi}$  the stereographic projection of a point  $(\theta, \phi)$  (polar and azimuthal angles) of the sphere  $\mathbb{S}^2$  onto the complex plane  $\mathbb{C} \ni z$ . Let us consider filling factor  $M = 1$ . The  $M \times N$  creation operator matrix  $A^\dagger$  in (15) reduces to  $A^\dagger = (a_{11}^\dagger, a_{21}^\dagger)$ . Denote by  $Q_{\text{hw}}(z) = (\delta, z\delta)^\dagger$  the first column of  $Q(z)$  in (52). Coherent excitations above the HW vector  $|\mathfrak{m}_{\text{hw}}\rangle = \frac{(a_{11}^\dagger)^L}{\sqrt{L!}}|0\rangle_{\text{F}}$  for filling factor  $M = 1$  can be written as a two-mode Bose-Einstein condensate of the form

$$\begin{aligned} |z\rangle^L &= \frac{A^\dagger Q_{\text{hw}}(z)|0\rangle_{\text{F}}}{\sqrt{L!}} = \frac{1}{\sqrt{L!}} \left( \frac{a_{11}^\dagger + za_{21}^\dagger}{\sqrt{1 + |z|^2}} \right)^L |0\rangle_{\text{F}} \\ &= \underbrace{[\cos(\theta/2)|\uparrow\rangle + \sin(\theta/2)e^{i\phi}|\downarrow\rangle]}_{|z\rangle}^{\otimes L} = |z\rangle^{\otimes L}, \end{aligned} \quad (53)$$

where we are using the notation (28) for spin up and down states at a Landau site, respectively. That is, the spin  $j = L/2$  coherent state  $|z\rangle^L$  adopts the form of a symmetric  $L$ -qubit state. The direct product structure (not entanglement between lattice sites) ensures the underlying translational invariance. For example, for the particular case of  $L = 2$  (spin  $j = 1$ ) we have

$$|z\rangle^2 = \frac{(|\uparrow\rangle + z|\downarrow\rangle)^{\otimes 2}}{1 + |z|^2} = \frac{|\uparrow\uparrow\rangle + z(|\uparrow\downarrow\rangle + |\downarrow\uparrow\rangle) + z^2|\downarrow\downarrow\rangle}{1 + |z|^2}, \quad (54)$$

where we identify the spin triplet

$$\{|1, 1\rangle = |\uparrow\uparrow\rangle, \quad |1, 0\rangle = \frac{|\uparrow\downarrow\rangle + |\downarrow\uparrow\rangle}{\sqrt{2}}, \quad |1, -1\rangle = |\downarrow\downarrow\rangle\}$$

basis written in terms of the usual Dicke (total angular momentum) states  $|j, m\rangle$  (with  $m = -j, \dots, j$ , the magnetic quantum number) already discussed after (29). In general, spin  $j = L/2$  coherent states can be written in the Dicke basis as (see e.g. [22, 23] for standard references)

$$|z\rangle^{2j} = (1 + |z|^2)^j \sum_{m=-j}^j \sqrt{\binom{2j}{j-m}} z^{j-m} |j, m\rangle. \quad (55)$$

Even further, coherent states  $|z\rangle^L$  can also be created by applying a  $U(2)$  transformation/rotation on the HW vector

$$|z\rangle^L = e^{yS_{21} - \bar{y}S_{12}} |\mathfrak{m}_{\text{hw}}\rangle = \frac{e^{zS_{21}} |\mathfrak{m}_{\text{hw}}\rangle}{\sqrt{1 + |z|^2}}, \quad z = \frac{y}{|y|} \tan |y|, \quad y = \frac{\theta}{2} e^{i\phi}, \quad (56)$$

where  $S_{21}$  is the spin lowering operator, and the relation between the complex coordinate  $y$  and the stereographic projection coordinate  $z$  arises from the application of the Baker-Campbell-Hausdorff-Zassenhaus factorization formula to the group  $U(2)$  [22, 23]. Note that, in the tensor product representation of  $U(2)$ , all qubits/spins are rotated ‘‘in unison’’ to account for translation/permutation symmetry. Other non-symmetric definitions of spin coherent states are possible for the group product  $U(2) \times \dots \times U(2)$ , in which every qubit/spin is rotated independently of each other (see e.g. [45]). Here we restrict ourselves to spin  $j = L/2$  (Bloch/atomic) symmetric coherent states introduced a long time ago by [46] and [47]. Haldane used them to study the semi-classical approximation of 1-D Heisenberg anti-ferromagnetic spin chains, whose continuum dynamics is described by  $SU(2)$  NL $\sigma$ Ms [34–36].

All these construction can be extended to  $U(N)$  QHF at filling factor  $M$  as follows. Define  $Q_{\text{hw}}(Z) = \begin{pmatrix} \mathbb{1}_M \\ Z \end{pmatrix} \Delta_1$  as the first  $M$  columns of  $Q(Z)$  in (50) and split the  $M \times N$  creation operator matrix  $A^\dagger$  in (15) into a 2-block matrix  $A^\dagger = (A_{\text{hw}}^\dagger | A_{\text{lw}}^\dagger)$ , where  $A_{\text{hw}}^\dagger$  makes reference to the first  $M$  columns (HW components) and  $A_{\text{lw}}^\dagger$  to the last  $N - M$  columns (LW components). Grassmannian  $\mathbb{G}_M^N$  coherent states (see [23] for related fermionic coherent states) are then labeled by the  $(N - M) \times M$  complex matrices  $Z$  and have the form of a Bose-Einstein condensate

$$|Z\rangle^L = \frac{\det(A^\dagger Q_{\text{hw}}(Z))^L |0\rangle_{\text{F}}}{\prod_{p=1}^M (p)^{\frac{1}{2}L}} = \frac{1}{\prod_{p=1}^M (p)^{\frac{1}{2}L}} \left( \frac{\det(A_{\text{hw}}^\dagger + A_{\text{lw}}^\dagger Z)}{\sqrt{\det(\mathbb{1}_M + Z^\dagger Z)}} \right)^L |0\rangle_{\text{F}}. \quad (57)$$

Note that  $|Z = 0\rangle^L$  corresponds to the HW state (17). As for spin coherent states in (56), Grassmannian coherent states can also be written as a  $U(N)$  transformation/rotation of the HW vector as

$$\begin{aligned} |Z\rangle^L &= \exp \left[ \sum_{1 \leq j \leq M, M+1 \leq i \leq N+M} (Y_{ij} S_{ij} - \bar{Y}_{ij} S_{ji}) \right] |\mathfrak{m}_{\text{hw}}\rangle \\ &= \frac{\exp \left[ \sum_{1 \leq j \leq M, M+1 \leq i \leq N+M} Z_{ij} S_{ij} \right] |\mathfrak{m}_{\text{hw}}\rangle}{\sqrt{\det(\mathbb{1}_M + Z^\dagger Z)}}, \quad Z = Y(Y^\dagger Y)^{-\frac{1}{2}} \tan(Y^\dagger Y)^{\frac{1}{2}}, \end{aligned} \quad (58)$$

where the relation between the  $(N - M) \times M$  complex matrices  $Y$  and  $Z$  [similar to the relation between  $y$  and  $z$  in (56)] now arises from the application of the Baker-Campbell-Hausdorff-Zassenhaus factorization formula to the group  $U(N)$  (see e.g. [23] for related fermionic coherent states). Note that Grassmannian coherent states  $|Z\rangle^L$  can be seen as a matrix version/extension of spin coherent states  $|z\rangle^L$ .

Let us explicitly work out a couple of examples related to the bilayer system ( $N = 4$ ) of Section III B 2. We shall denote the states like in (30) and talk about spin  $\uparrow, \downarrow$  and pseudo-spin or layer  $t, b$ . For filling factor  $M = 1$  we have

$$|Z\rangle^L = \frac{[|1\rangle + z_2|2\rangle + z_3|3\rangle + z_4|4\rangle]^{\otimes L}}{(1 + |z_2|^2 + |z_3|^2 + |z_4|^2)^{L/2}}, \quad (59)$$

where  $Z = (1, z_2, z_3, z_4)^t$  denotes a point on the complex projective space  $\mathbb{C}P^3 = U(4)/U(1) \times U(3)$ . For filling factor  $M = 2$ , the Hilbert space  $\mathcal{H}_4^\alpha[1^2]$  at each Landau/lattice site  $\alpha$  has dimension  $\binom{4}{2} = 6$ . In Appendix E we provide a basis (made of spin triplet  $|\mathfrak{S}_{\pm 1, 0}\rangle$  and pseudo-spin triplet  $|\mathfrak{P}_{\pm 1, 0}\rangle$  states) for  $\mathcal{H}_4^\alpha[1^2]$  adapted to the spin-layer intrinsic structure of this case. Coherent states here adopt the form

$$\begin{aligned} |Z\rangle^L &= \frac{1}{\sqrt{2}} \frac{\left| \begin{pmatrix} a_{11}^\dagger & a_{21}^\dagger \\ a_{12}^\dagger & a_{22}^\dagger \end{pmatrix} + \begin{pmatrix} a_{31}^\dagger & a_{41}^\dagger \\ a_{32}^\dagger & a_{42}^\dagger \end{pmatrix} \begin{pmatrix} z_{11} & z_{12} \\ z_{21} & z_{22} \end{pmatrix} \right|^L |0\rangle_{\text{F}}}{\det(\mathbb{1}_2 + Z^\dagger Z)^{L/2}} \\ &= \frac{\left[ \sqrt{2}|\mathfrak{S}_1\rangle + (z_{11} + z_{22})|\mathfrak{S}_0\rangle + \begin{vmatrix} z_{11} & z_{12} \\ z_{21} & z_{22} \end{vmatrix} |\mathfrak{S}_{-1}\rangle + \sqrt{2}z_{12}|\mathfrak{P}_1\rangle + (z_{22} - z_{11})|\mathfrak{P}_0\rangle - \sqrt{2}z_{21}|\mathfrak{P}_{-1}\rangle \right]^{\otimes L}}{\det(\mathbb{1}_2 + Z^\dagger Z)^{L/2}}, \quad (60) \end{aligned}$$

with  $Z = \begin{pmatrix} z_{11} & z_{12} \\ z_{21} & z_{22} \end{pmatrix}$  a matrix point on the Grassmannian  $\mathbb{G}_2^4 = U(4)/U(2)^2$ .  $|Z\rangle^L$  can also be written in terms of Gelfand vectors  $|\mathfrak{m}\rangle$  as the  $U(N)$  rotation (58) with  $U(N)$ -spin operators  $S_{ij}$  given by their matrix elements (45) (see e.g. Appendix F for some particular cases).

Coherent states are sometimes called “semi-classical” (they exhibit minimal uncertainty, etc.) and they are used as variational states to study the semiclassical and thermodynamic limit, specially in quantum phase transitions [48]. We have used  $U(4)$  coherent states, introduced by us in [44, 49], to study their entanglement properties [50] and the phase diagram of bilayer quantum Hall systems at filling factor  $M = 2$  in [51, 52], which turn out to reproduce previous results of Ezawa and collaborators [53, 54]. Let’s take a closer look to the role of Grassmannian coherent states to construct semi-classical models of  $U(N)$  QHF in terms of  $NL\sigma\text{M}$ .

## B. Grassmannian nonlinear sigma models

In order to study the semi-classical/thermodynamical limit  $L \rightarrow \infty$  of  $U(N)$  QHF, one has to replace  $U(N)$ -spin operators  $S_{ij}$  by their coherent state expectation values  $\langle Z | S_{ij} | Z \rangle$ . Let us adopt a compact notation and denote by  $S$

the operator matrix with operator matrix entries  $S_{ij}$ . The corresponding coherent state expectation value matrix is

$$\mathcal{S}(Z) \equiv \frac{2}{L} \langle Z | S - \frac{L}{2} \mathbb{1}_N | Z \rangle^L = Q(Z)^\dagger E_M Q(Z), \quad E_M = \text{diag}(1, \overset{M}{\cdot}, 1, -1, \overset{N-M}{\cdot}, -1), \quad (61)$$

where  $Q(Z)$  is defined in (50). We have renormalized the matrix operator  $S$  by  $L$  to define the matrix expectation value  $\mathcal{S}$  as a density (intensive quantity), with a good thermodynamical limit  $L \rightarrow \infty$ . Moreover, we have shifted Cartan  $U(N)$ -spin operators  $S_{ii}$  by  $L/2$  for convenience. The complex  $N \times N$  matrix  $\mathcal{S}(Z)$  plays the role of a ferromagnetic order parameter associated to the symmetry-breaking ground state. Let us take the continuum limit, that is, small lattice constant  $\ell \rightarrow 0$  and large number of lattice sites  $L \rightarrow \infty$ , so that  $\alpha\ell \rightarrow x = (x_1, x_2)$  are coordinates on the plane and the finite difference  $(\mathcal{S}(\alpha + 1) - \mathcal{S}(\alpha))/\ell \rightarrow \partial_x \mathcal{S}(x)$  becomes the derivative; that is, the order parameter  $\mathcal{S}$  becomes a matrix field at every point  $x$  of the plane. The low energy physics of the  $U(N)$  QH ferromagnet [when considering only nearest-neighbor interactions  $\mathcal{J}_{\alpha\beta} = \mathcal{J}\delta_{\alpha,\beta\pm 1}$  in the exchange energy (A9)] is then described by a  $NL\sigma M$  field theory with action

$$A[Z] = \int dx_0 dx_1 dx_2 \left[ \text{tr}(E_M Q^\dagger \partial_{x_0} Q) + \mathcal{J} \text{tr}(\vec{\nabla} \mathcal{S} \cdot \vec{\nabla} \mathcal{S}) \right], \quad (62)$$

where  $\partial_{x_0} \equiv \partial_0$  means partial derivative with respect to time  $t = x_0$ ,  $\vec{\nabla} = (\partial_{x_1}, \partial_{x_2}) \equiv (\partial_1, \partial_2)$  is the gradient and  $\vec{\nabla} \mathcal{S} \cdot \vec{\nabla} \mathcal{S}$  is the scalar product. The first (kinetic) term of the action (62) is the Berry term (provided by the coherent state representation of the path integral quantization (see e.g. [31, 33] for more information about the origin of the Berry term, and [55] for the application of path-integral quantization to indistinguishable particle systems topologically confined by a magnetic field). The second term describes the energy cost when the order parameter is not uniform. The topological current

$$J^\mu = \frac{i}{16\pi} \varepsilon^{\mu\nu\lambda} \text{tr}(\mathcal{S} \partial_\nu \mathcal{S} \partial_\lambda \mathcal{S}) \quad (63)$$

( $\varepsilon$  is the Levi-Civita antisymmetric symbol in 1+2 dimensions) leads to the topological (Pontryagin) charge or Skyrmion number

$$\mathcal{C} = \int dx_1 dx_2 J^0. \quad (64)$$

See e.g. Ref. [33] for more information.

Note that we do not have  $N^2$  real field components for  $\mathcal{S}$  but only  $2M(N - M)$  corresponding to the  $(N - M) \times M$  complex matrix  $Z$ . This is due to the constraints given by the  $N$  values (49) of the  $N$  Casimir operators (48). For example, the linear and quadratic Casimir values say that

$$C_1 = \sum_{i=1}^N \langle Z | S_{ii} | Z \rangle = ML, \quad C_2 = \sum_{i,j=1}^N \langle Z | S_{ij} S_{ji} | Z \rangle = ML(L + N - M). \quad (65)$$

For large  $L$ , the leading term for the expectation values of quadratic spin powers is  $\langle Z | S_{ij} S_{ji} | Z \rangle \simeq \langle Z | S_{ij} | Z \rangle \langle Z | S_{ji} | Z \rangle$  (spin fluctuations are negligible in the classical  $L \rightarrow \infty$  limit). For  $N = 2$ ,  $M = 1$  and  $L = 2j$ , the linear  $C_1 = 2j$  and quadratic  $C_2 = 2j(2j + 1)$  Casimir constraints reproduce the well known sphere equation  $\vec{J}^2 = j(j + 1)$  for  $J_x = (S_{12} + S_{21})/2$ ,  $J_y = (S_{12} - S_{21})/(2i)$  and  $J_z = (S_{11} - S_{22})/2$ .

Since the kinetic (Berry) term involves a single time derivative, half of the Grassmannian fields  $Z$  are conjugate momenta of the other half (that is, The Grassmannian  $\mathbb{G}_M^N$  target space is a phase space), thus expecting  $M(N - M)$  independent spin-wave modes. Given the relation (61) between the order parameter  $\mathcal{S}$  and the Grassmann matrix  $Z$ , after a little bit of algebra, the spatial part (potential energy) of the Lagrangian (62) can be written in terms of minimal matrix fields  $Z$  as [56, 57]

$$\mathcal{J} \text{tr}(\vec{\nabla} \mathcal{S} \cdot \vec{\nabla} \mathcal{S}) = \mathcal{J} \text{tr} \left( \Delta_2^2 \vec{\nabla} Z \cdot \Delta_1^2 \vec{\nabla} Z^\dagger \right), \quad (66)$$

where we have used the expression (61) of  $\mathcal{S}(Z)$  in terms of  $Q(Z)$  in (50), together with the Woodbury matrix identity  $\Delta_2^2 Z = Z \Delta_1^2$ . It would be worth revising the classical limit of  $U(N)$  quantum Hall ferromagnets for large  $L \rightarrow \infty$  representations, considered long time ago by [28–33] for anti-ferromagnets, in boson/fermion mixture picture exposed in this article. This is work in progress.

## VI. CONCLUSIONS AND OUTLOOK

In this article we have presented several group-theoretical tools to study interacting  $N$ -component fermions on a lattice, like  $U(N)$  quantum Hall ferromagnets arising from two-body exchange interactions. We have restricted ourselves to the lower energy permutation symmetry sector (according to the Lieb-Mattis theorem [37]) corresponding to fermion mixtures described by rectangular Young diagrams with  $M$  rows (the filling factor) and  $L$  columns (Landau/lattice sites). We have provided orthonormal basis vectors of the corresponding Hilbert space in terms of Young tableaux, Gelfand-Tsetlin patterns  $|\mathfrak{m}\rangle$  and boson/fermion Fock states. We have written general matrix elements of  $U(N)$ -spin collective operators  $S_{ij}$  in the Gelfand-Tsetlin basis. Several particular examples have been explicitly worked out to better understand the general expressions, specially the case of bilayer  $U(4)$  quantum Hall systems at filling factor  $M = 2$  appearing in the literature [53, 54, 58–65]. Dimension formulas for these irreducible representations of  $U(N)$  have also been provided. Special attention has been paid to the highest weight state, which can be associated to the ground state of the system. From this perspective, the “spontaneously chosen” ground state breaks the original  $U(N)$  symmetry and the associated  $U(N)$  ferromagnetic order parameter  $\mathcal{S}$  [the expectation value of collective  $U(N)$ -spin operators  $S$  in a Grassmannian coherent state  $|Z\rangle$ ] describes coherent state excitations in the classical limit, whose dynamics is governed by a Grassmannian nonlinear sigma model.

Restricting to the dominant permutation symmetry sector is a common practice to reduce the computational complexity when dealing with quantum many-body systems. For example, critical and chaotic quantum systems of  $P$ ,  $N$ -level/component, identical particles (“quNits”, a higher dimensional generalization of qubits for  $N > 2$ ) undergoing a quantum phase transition in the thermodynamic (classical) limit  $P \rightarrow \infty$ , are usually studied by restricting to the  $\binom{P+N-1}{P}$ -dimensional (the number of ways of exciting  $P$  particles with  $N$  levels when order does not matter) totally symmetric sector  $[P]$  in the  $N^P$ -dimensional  $P$ -fold tensor product  $[1]^{\otimes P} = [P] \oplus [P-1, 1] \oplus \dots$  of  $N$ -dimensional (fundamental) irreducible representations  $[1]$  of  $U(N)$ . Replacing  $[1]^{\otimes P}$  by  $[P]$  then reduces the size of the Hilbert space from  $N^P$  to  $\binom{P+N-1}{P}$ , which is a great simplification when  $N > 1$  and  $P$  is large. The justification of this restriction is that the ground state of the many-body system always belongs to totally symmetric representation, in accordance with the Lieb-Mattis ordering problem. In more physical terms, and for the particular example of the Dicke model of super-radiance [66], the assumption that the  $P$  atoms of  $N = 2$ -levels are indistinguishable (bosons) is admissible when the emitters are confined to a cavity volume  $V \ll \ell^3$  much smaller than the scale of the wavelength  $\ell$  of the optical transition. However, the role of mixed permutation symmetry sectors in many body quantum systems should not be disregarded at higher energies, and we have already made some steps in [67] for the case of critical  $N$ -level Lipkin-Meshkov-Glick atom models. Entanglement characterization of quantum phases in these systems have also been studied [68]. This is also our next step for  $U(N)$  quantum Hall ferromagnets.

Finally, concerning physical applications and quantum technological implementations, as we have already mentioned in the introduction, the subject of  $SU(N)$  fermions and  $SU(N)$  magnetism has been recently further fueled in condensed matter physics with exciting advances in cooling, trapping and manipulating fermionic alkaline-earth atoms trapped in optical lattices. Also, magnetic Skyrmion materials display a robust topological magnetic structure, being a candidate for the next generation of spintronic memory devices. Multilayer quantum Hall arrangements, bearing larger  $U(N)$  symmetries, also display interesting new physics. Such is the case of superconducting properties of twisted bilayer (and trilayer) graphene predicted by [20] and observed by [21]. Therefore, this is a highly topical subject, in which we believe this article makes a novel (not standard) contribution of a fundamental nature. Further perspectives worth exploring have to do with the interplay between quantum information and quantum topological phases of matter. Namely, the identification of topological order by entanglement entropy (see e.g. [69, 70]). Indeed, quantum information concepts can be used to reformulate and characterize topological order. Some of us have already applied quantum information techniques to the characterization of topological insulator phases of graphene analogues [71–75] and fosforene [76, 77]. Also, Schur basis, like the ones discussed here in terms of Young tableaux, have proved to be useful for efficient quNit circuits [78].

## ACKNOWLEDGEMENTS

We thank the support of the Spanish MICINN through the project PGC2018-097831-B-I00 and Junta de Andalucía through the projects SOMM17/6105/UGR, UHU-1262561, FQM-381 and FEDER/UJA-1381026. AM thanks the Spanish MIU for the FPU19/06376 predoctoral fellowship. We all thank E. Pérez-Romero for his collaboration in the early stages of this work.

### Appendix A: Quantum Hall ferromagnets from exchange interactions

Let us briefly remind how the Hamiltonian of a  $U(N)$  quantum Hall ferromagnet can be derived from fundamental microscopic two-body (let us say Coulomb) interactions between  $N$ -component electrons (see also [54]). The field theoretical expression of the Hamiltonian for two-body interactions between  $N$ -component electrons in 2-dimensional space is

$$H_C = \frac{1}{2} \sum_{i,j=1}^N \int d^2x d^2x' \Psi_i^\dagger(x) \Psi_j^\dagger(x') V(|x-x'|) \Psi_j(x') \Psi_i(x), \quad (\text{A1})$$

where  $V(|x-x'|)$  is the two-body potential and  $\Psi_i(x)$  is the electron field, which can be expanded in terms of a set of one-body wave (Wannier) functions  $\{\psi_\alpha(x)\}$ , localized around the lattice/Landau sites  $\alpha = 1, \dots, L$ , with  $L$  the total number of lattice/landau sites as

$$\Psi_i(x) = \sum_{\alpha=1}^L c_i(\alpha) \psi_\alpha(x). \quad (\text{A2})$$

In the case of quantum Hall systems in the Landau gauge  $\vec{A}(x) = (Bx_2, 0, 0)$  ( $B$  is the constant perpendicular magnetic field and  $\vec{A}$  is the vector potential), the one-body functions are canonical (harmonic oscillator) coherent states

$$\psi_k(x) = \frac{1}{\sqrt{\pi^{1/2} \ell_B}} \exp(ikx_1) \exp\left(-\frac{1}{2\ell_B^2}(x_2 + k\ell_B^2)^2\right), \quad (\text{A3})$$

describing a plane wave propagating in the  $x_1$  direction with momentum  $\hbar k$  ( $\ell_B = \sqrt{\hbar/(eB)}$  denotes the magnetic length). The probability of finding the electron at  $x_2$  has a sharp peak at  $x_2 = -k\ell_B^2$  and a width  $\Delta x_2 = \ell_B^2 \Delta k$ , where  $\Delta k = 2\pi/\lambda_1$  (here  $\lambda_1$  denotes the  $x_1$ -size of the system), because the wave number is quantized as  $k_n = 2\pi n/\lambda_1$ , with  $n$  an integer. Thus, these states are represented by strips on a rectangular geometry occupying an area of  $\Delta\mathcal{A} = \lambda_1 \Delta x_2 = 2\pi\ell_B^2$  and defining a *von Neumann lattice* (see e.g.[54]). Therefore, the number of Landau/lattice sites enclosed by the system of area  $\mathcal{A} = \lambda_1 \lambda_2$  is  $L = \mathcal{A}/\Delta\mathcal{A} = \mathcal{A}/(2\pi\ell_B^2)$ , which coincides with the number of magnetic flux quanta penetrating the sample, that is, the ratio of the total magnetic flux  $B\mathcal{A}$  to the magnetic flux quantum  $\phi_0 = 2\pi\hbar/e$ . In the symmetric gauge  $\vec{A}(x) = (Bx_2, -Bx_1, 0)/2$ , the ‘‘strips in a rectangular geometry’’ image is replaced by ‘‘rings in a disk geometry’’, where the linear momentum  $k$  is replaced by the angular momentum  $m$  (see [54] for more information).

The coefficients  $c_i(\alpha)$  ( $c_i^\dagger(\alpha)$ ) denote annihilation (creation) operators of electrons of component  $i = 1, \dots, N$  at site  $\alpha$ , fulfilling the usual anticommutation rules

$$\{c_i(\alpha), c_j^\dagger(\alpha)\} = \delta_{ij} \quad , \quad \{c_i(\alpha), c_j(\alpha)\} = \{c_i^\dagger(\alpha), c_j^\dagger(\alpha)\} = 0 \quad \forall i, j = 1, \dots, N. \quad (\text{A4})$$

It is also important to emphasize that these operators commute among different Landau/lattice sites, that is,

$$[c_i(\alpha), c_j^\dagger(\beta)] = [c_i(\alpha), c_j(\beta)] = [c_i^\dagger(\alpha), c_j^\dagger(\beta)] = 0, \quad i, j = 1, \dots, N, \quad \alpha \neq \beta. \quad (\text{A5})$$

Let us denote by

$$V_{\beta\alpha\beta'\alpha'} = \frac{1}{2} \int d^2x d^2x' \bar{\psi}_\beta(x) \psi_\alpha(x) V(|x-x'|) \bar{\psi}_{\beta'}(x') \psi_{\alpha'}(x'). \quad (\text{A6})$$

The terms that effectively contribute to the energy are  $\mathcal{U}_{\beta\beta'} = V_{\beta\beta\beta'\beta'}$  and  $\mathcal{J}_{\beta\alpha} = V_{\beta\alpha\alpha\beta}$ , corresponding to the *direct* (D) and *exchange* (E) energies

$$H_C = H_C^D + H_C^E = \sum_{\beta, \beta'=1}^L \mathcal{U}_{\beta\beta'} \rho(\beta) \rho(\beta') + \sum_{\beta, \alpha=1}^L \sum_{i, j=1}^N \mathcal{J}_{\beta\alpha} c_i^\dagger(\beta) c_j^\dagger(\alpha) c_j(\beta) c_i(\alpha), \quad (\text{A7})$$

where  $\rho(\beta) = \sum_{i=1}^N c_i^\dagger(\beta) c_i(\beta)$  is the electron number operator at site  $\beta$ . In the case of Coulomb interaction, the direct term  $H_C^D$  represents the usual Coulomb energy between two charge distributions  $|\psi_\beta(x)|^2$  and  $|\psi_{\beta'}(x')|^2$  localized around the Landau/lattice sites  $\beta$  and  $\beta'$ , respectively. The exchange term  $H_C^E$  has no classical counterpart and owes

its origin to the Pauli exclusion principle. Note that  $\mathcal{J}_{\beta\alpha}$  vanishes when there is no overlap between the wave functions  $\psi_\beta$  and  $\psi_\alpha$  at sites  $\beta$  and  $\alpha$  (for example, for distant sites). One can define the  $U(N)$ -spin operators at site  $\alpha$  by

$$S_{ij}(\alpha) = c_i^\dagger(\alpha)c_j(\alpha). \quad (\text{A8})$$

They allow one to write the exchange energy as a generalized Heisenberg spin-spin interaction

$$H_C^E = - \sum_{\alpha,\beta=1}^L \mathcal{J}_{\alpha\beta} \sum_{i,j=1}^N S_{ij}(\alpha)S_{ji}(\beta) + N \sum_{\alpha=1}^L \mathcal{J}_{\alpha\alpha}\rho(\alpha). \quad (\text{A9})$$

which depends on the relative  $U(N)$ -spin orientation at neighboring sites  $\alpha$  and  $\beta$ . From here the name of ‘‘ $U(N)$  quantum Hall ferromagnet’’, where all  $U(N)$ -spins tend to be equally polarized (for  $\mathcal{J}_{\alpha\beta} > 0$ ) to lower the exchange energy  $H_C^E$ . This Hamiltonian is  $U(N)$ -invariant and therefore the  $U(N)$ -spin ‘‘direction’’ is spontaneously chosen. This invariance can be explicitly broken by adding Zeeman, pseudo-Zeeman, layer bias, etc. external couplings [54].

### Appendix B: Proof of Proposition II.1

We shall proceed by induction in  $L$ . The  $L = 2$ -fold tensor product representation of  $U(N)$  decomposes as

$$\begin{array}{|c|} \hline \square \\ \hline \vdots \\ \hline \end{array} \otimes \begin{array}{|c|} \hline \square \\ \hline \vdots \\ \hline \end{array} = [1^M] \otimes [1^M] = \bigoplus_{k=0}^{k^*} [2^{M-k}, 1^{2k}] \quad , \quad k^* = \begin{cases} N - M & \forall M > \lfloor \frac{N}{2} \rfloor \\ M & \forall M \leq \lfloor \frac{N}{2} \rfloor \end{cases}, \quad (\text{B1})$$

where we understand  $[a^0] = [0]$  for all  $a \in \mathbb{N}$ . It is clear that  $[2^M] \succeq [2^{M-k}, 1^{2k}]$  for all  $k = 0, \dots, k^*$ , in accordance with the dominance order definition (10). Now suppose that  $[L^M]$  dominates over all Young diagrams arising in  $[1^M]^{\otimes L}$ . Then, we have to prove by induction that  $[(L+1)^M]$  dominates over all Young diagrams arising in  $[1^M]^{\otimes L+1}$ . Firstly, we shall state an auxiliary lemma.

**Lemma B.1.** *Let  $[h] = [h_1, h_2, \dots, h_N]$  be any Young diagram of  $U(N)$ . The tensor product  $[h] \otimes [1^M]$  between  $[h]$  and the totally antisymmetric IR  $[1^M]$  leads to a decomposition into Young diagrams with shape*

$$[\tilde{h}] = [\tilde{h}_1, \tilde{h}_2, \dots, \tilde{h}_N] = [h_1 + n_1, h_2 + n_2, \dots, h_N + n_N], \quad n_i \in \{0, 1\}, \quad \sum_{i=1}^N n_i = M, \quad \tilde{h}_1 \geq \dots \geq \tilde{h}_N. \quad (\text{B2})$$

*Proof.* It is straightforward taking into consideration the multiplication rules of Young diagrams (section 9.5.1 of [79]). Specially the one which states: Reading the resulting diagrams from right to left and starting with the top row, at any point must the number of  $a_i$ 's encountered exceed the number of previously encountered  $a_{i-1}$ 's. If we are multiplying any diagram with the totally antisymmetric (one column), every  $a_i$  will appear only once in the new diagrams. Therefore, the aforementioned rule will limit by one the number of boxes per row that we can add to the original diagram to construct the new ones. For instance, using a  $U(6)$  diagram and the antisymmetric IR  $[1^5]$ ,

$$\begin{array}{|c|c|c|c|} \hline \square & \square & \square & \square \\ \hline \square & \square & \square & \square \\ \hline \square & \square & \square & \square \\ \hline \square & \square & \square & \square \\ \hline \square & \square & \square & \square \\ \hline \end{array} \otimes \begin{array}{|c|} \hline a_1 \\ \hline a_2 \\ \hline a_3 \\ \hline a_4 \\ \hline a_5 \\ \hline \end{array} \cong \begin{array}{|c|c|c|c|} \hline \square & \square & \square & a_1 \\ \hline \square & \square & \square & a_2 \\ \hline \square & \square & \square & a_3 \\ \hline \square & \square & \square & a_4 \\ \hline \square & \square & \square & a_5 \\ \hline \end{array} \oplus \begin{array}{|c|c|c|c|} \hline \square & \square & \square & a_1 \\ \hline \square & \square & \square & a_2 \\ \hline \square & \square & \square & a_3 \\ \hline \square & \square & \square & a_4 \\ \hline \square & \square & \square & a_5 \\ \hline \end{array} \oplus \begin{array}{|c|c|c|c|} \hline \square & \square & \square & a_1 \\ \hline \square & \square & \square & a_2 \\ \hline \square & \square & \square & a_3 \\ \hline \square & \square & \square & a_4 \\ \hline \square & \square & \square & a_5 \\ \hline \end{array} \oplus \dots \quad (\text{B3})$$

□

It is convenient to name the rectangular diagram as  $[h] = [h_1, h_2, \dots, h_N] = [L^M] = [L, \overset{M}{\cdot}, L, 0, \overset{N-M}{\cdot}, 0]$ , and all Young diagrams arising from  $[1^M]^{\otimes L}$  as  $[h'] = [h'_1, h'_2, \dots, h'_N]$ , including the rectangular one ( $h' = h$ ). Therefore, the dominance of  $[L^M]$  is written as  $[h] \succeq [h']$ , or equivalently (10),

$$kL = h_1 + \dots + h_k \geq h'_1 + \dots + h'_k \quad \forall k \in [1, N]. \quad (\text{B4})$$

According to the lemma B.1, the tensor product  $[1^M]^{\otimes(L+1)} = [1^M]^{\otimes L} \otimes [1^M]$  generates the diagrams  $[\tilde{h}] = [\tilde{h}'_1, \tilde{h}'_2, \dots, \tilde{h}'_N] = [h'_1 + n_1, h'_2 + n_2, \dots, h'_N + n_N]$  with  $n_i \in \{0, 1\}$  and  $\sum_{i=1}^N n_i = M$ . Among them, there is a new

rectangular diagram  $[\tilde{h}] = [\tilde{h}_1, \dots, \tilde{h}_N] = [(L+1)^M] = [h_1 + 1, \dots, h_M + 1, h_{M+1}, \dots, h_N]$ , with  $h_{M+1}, \dots, h_N = 0$ . The restriction  $\sum_{i=1}^N n_i = M$  implies  $\sum_{i=1}^k n_i \leq k$ , which leads to

$$\tilde{h}_1 + \dots + \tilde{h}_k = h_1 + \dots + h_k + k \geq h_1 + \dots + h_k + n_1 + \dots + n_k \quad \forall k \in [1, N], \quad (\text{B5})$$

and using the equation (B4),

$$\tilde{h}_1 + \dots + \tilde{h}_k \geq h_1 + \dots + h_k + n_1 + \dots + n_k \geq h'_1 + \dots + h'_k + n_1 + \dots + n_k = \tilde{h}'_1 + \dots + \tilde{h}'_k \quad \forall k \in [1, N]. \quad (\text{B6})$$

Therefore, considering the dominance order definition, we arrive to  $[\tilde{h}] \succeq [\tilde{h}']$ , eventually proving that the rectangular Young diagram  $[\tilde{h}] = [(L+1)^M]$  dominates the other diagrams arising from  $[1^M]^{\otimes(L+1)}$  and concluding the proof by induction. ■

### Appendix C: Proof of Proposition III.1

Looking at the structure of

$$\det(A_{\text{hw}}^\dagger) = \sum_{\sigma \in \mathfrak{S}_M} \text{sgn}(\sigma) \prod_{i=1}^M a_{i, \sigma_i}^\dagger = \sum_{\mu_1, \dots, \mu_M=1}^M \varepsilon_{\mu_1, \dots, \mu_M} \prod_{i=1}^M a_{i, \mu_i}^\dagger,$$

[where  $\mathfrak{S}_M$  is the symmetric group of degree  $M$  and  $\varepsilon$  is the Levi-Civita symbol] it is clear that  $\det(A_{\text{hw}}^\dagger)^L |0\rangle_{\text{F}}$  is made of  $P = ML$  particles, as desired. The basic boson commutation relations  $[a, a^\dagger] = 1$  imply that  $[a, \psi(a^\dagger)] = \psi'(a^\dagger)$  or  $a\psi(a^\dagger)|0\rangle_{\text{F}} = \psi'(a^\dagger)|0\rangle_{\text{F}}$ , where  $\psi$  is a function and  $\psi'$  denotes the formal derivative with respect to the argument. Therefore, let us simply write  $a_{i\mu} = \partial/\partial a_{i\mu}^\dagger$ . In order to prove (18), we have that

$$\Lambda_{\mu\nu} \det(A_{\text{hw}}^\dagger)^L |0\rangle_{\text{F}} = \sum_{i=1}^N a_{i\mu}^\dagger \frac{\partial}{\partial a_{i\nu}^\dagger} \det(A_{\text{hw}}^\dagger)^L |0\rangle_{\text{F}} = L \det(A_{\text{hw}}^\dagger)^{L-1} \sum_{i=1}^M a_{i\mu}^\dagger \frac{\partial}{\partial a_{i\nu}^\dagger} \det(A_{\text{hw}}^\dagger) |0\rangle_{\text{F}}.$$

The last summation consists of replacing row  $\nu$  by row  $\mu$  inside the determinant  $\det(A_{\text{hw}}^\dagger)$ , and therefore we have

$$\sum_{i=1}^M a_{i\mu}^\dagger \frac{\partial}{\partial a_{i\nu}^\dagger} \det(A_{\text{hw}}^\dagger) = \delta_{\mu\nu} \det(A_{\text{hw}}^\dagger),$$

which proves the constraint (18). To prove (19), we follow the same steps as for (18), that is

$$S_{ij} \det(A_{\text{hw}}^\dagger)^L |0\rangle_{\text{F}} = \sum_{\mu=1}^M a_{i\mu}^\dagger \frac{\partial}{\partial a_{j\mu}^\dagger} \det(A_{\text{hw}}^\dagger)^L |0\rangle_{\text{F}} = L \det(A_{\text{hw}}^\dagger)^{L-1} \sum_{\mu=1}^M a_{i\mu}^\dagger \frac{\partial}{\partial a_{j\mu}^\dagger} \det(A_{\text{hw}}^\dagger) |0\rangle_{\text{F}}.$$

If  $i, j \leq M$ , the last summation consists of replacing column  $j$  by column  $i$  inside the determinant  $\det(A_{\text{hw}}^\dagger)$ , and therefore  $S_{ij} |\mathfrak{m}_{\text{hw}}\rangle = L \delta_{ij} |\mathfrak{m}_{\text{hw}}\rangle$ , which means that  $|\mathfrak{m}_{\text{hw}}\rangle$  is invariant under the subgroup  $U(M) \subset U(N)$ . If  $j > M$ , then column  $j$  is absent from  $\det(A_{\text{hw}}^\dagger)$  and  $S_{ij} |\mathfrak{m}_{\text{hw}}\rangle = 0$ , which means that  $|\mathfrak{m}_{\text{hw}}\rangle$  is in fact invariant under the subgroup  $U(M) \times U(N-M) \subset U(N)$ . Note the similarities with invariance properties of the ground state  $|\Phi_0\rangle$  of Eq. (3). This will be an important fact when discussing the Grassmannian structure associated to  $U(N)$  quantum Hall ferromagnets at filling factor  $M$  later in Section V. The other possibilities for  $S_{ij}$  correspond to rising and lowering operators and will be discussed later.

It remains to prove that the squared norm of  $\det(A_{\text{hw}}^\dagger)^L |0\rangle_{\text{F}}$  is given by  $\mathcal{N}_L = \prod_{p=1}^M (p)_L$  in (17), where  $(p)_L$  is the usual Pochhammer symbol. We proceed by mathematical induction. Firstly we prove that  $\mathcal{N}_1 = M!$ . Indeed,

$$\langle 0 | \det(A_{\text{hw}}) \det(A_{\text{hw}}^\dagger) | 0 \rangle_{\text{F}} = \sum_{\sigma \in \mathfrak{S}_M} 1 = M!.$$

Now we assume that  $\langle 0 | \det(A_{\text{hw}})^L \det(A_{\text{hw}}^\dagger)^L | 0 \rangle_{\text{F}} = \mathcal{N}_L$  and we shall prove that

$$\langle 0 | \det(A_{\text{hw}})^{L+1} \det(A_{\text{hw}}^\dagger)^{L+1} | 0 \rangle_{\text{F}} = \mathcal{N}_{L+1}.$$

Indeed, it can be shown that

$$\langle 0 | \det(A_{\text{hw}})^{L+1} \det(A_{\text{hw}}^\dagger)^{L+1} | 0 \rangle_{\text{F}} = (L+1)_M \langle 0 | \det(A_{\text{hw}})^L \det(A_{\text{hw}}^\dagger)^L | 0 \rangle_{\text{F}}.$$

The proof is cumbersome in general and we shall restrict ourselves to the more maneuverable  $M = 2$  case, which grasps the essence of the general case. In fact,

$$\begin{aligned} \det(A_{\text{hw}}) \det(A_{\text{hw}}^\dagger)^{L+1} | 0 \rangle_{\text{F}} &= \left( \frac{\partial}{\partial a_{11}^\dagger} \frac{\partial}{\partial a_{22}^\dagger} - \frac{\partial}{\partial a_{12}^\dagger} \frac{\partial}{\partial a_{21}^\dagger} \right) (a_{11}^\dagger a_{22}^\dagger - a_{12}^\dagger a_{21}^\dagger)^{L+1} | 0 \rangle_{\text{F}} \\ &= (L+1)L \det(A_{\text{hw}}^\dagger)^L | 0 \rangle_{\text{F}} + 2(L+1) \det(A_{\text{hw}}^\dagger)^L | 0 \rangle_{\text{F}} \\ &= (L+1)_2 \det(A_{\text{hw}}^\dagger)^L | 0 \rangle_{\text{F}}. \end{aligned}$$

In general

$$\det(A_{\text{hw}}) \det(A_{\text{hw}}^\dagger)^{L+1} | 0 \rangle_{\text{F}} = (L+1)_M \det(A_{\text{hw}}^\dagger)^L | 0 \rangle_{\text{F}}.$$

To finish, we realize that  $(L+1)_M \mathcal{N}_L = \mathcal{N}_{L+1}$ , which concludes the proof by induction. ■

#### Appendix D: Relation between Gelfand-Tsetlin and Fock states

We already know the general expression of the HW state  $|m_{\text{hw}}\rangle$  in Fock space, given by (17). In this expression, the leading principal minor  $\det(A_{\text{hw}}^\dagger)$  of order  $M$  of  $A^\dagger$  plays a fundamental role. Remember that the  $M \times M$  square submatrix  $A_{\text{hw}}^\dagger$  was obtained from  $A^\dagger$  in (15) by deleting the last  $N - M$  columns. In the proof of Proposition III.1, in the Appendix C, we argued that ladder operators  $S_{ij}, i \neq j$  replace column  $j$  by column  $i$  inside the minor  $\det(A_{\text{hw}}^\dagger)$ . In general, we can obtain  $\binom{N}{M}$  different minors of size  $M \times M$ , corresponding to the different ways one can choose  $M$  columns from the  $N$  columns of  $A^\dagger$ . Let  $I = \{i_1, \dots, i_M\}$ , with  $i_\mu < i_{\mu+1}$  (increasing order), denote one of these  $\binom{N}{M}$  column choices and

$$A_I^\dagger = \begin{pmatrix} a_{i_1 1}^\dagger & \dots & a_{i_M 1}^\dagger \\ \vdots & & \vdots \\ a_{i_1 M}^\dagger & \dots & a_{i_M M}^\dagger \end{pmatrix} \quad (\text{D1})$$

the corresponding  $M \times M$  submatrix of  $A^\dagger$ . The cases  $I = \{1, \dots, M\}$  (first  $M$  columns) and  $I' = \{N - M, \dots, N\}$  (last  $M$  columns) are special, since they are related to the highest- and lowest-weight states, respectively; actually, we are denoting  $A_{\{1, \dots, M\}}^\dagger$  simply by  $A_{\text{hw}}^\dagger$ . There are several ways of attaching  $n_{\mu, i}$  flux quanta to the electron  $\mu \leq M$  with flavor  $i \leq N$ . For a given  $I = \{i_1, \dots, i_M\}$  containing  $i$ , let us denote  $\{l_I \geq 0\}$  a composition (a partition where order matters) of  $n_{\mu, i}$  in the sense that

$$n_{\mu, i} = \sum_{i_1 < \dots < i_\mu < \dots < i_M} l_{\{i_1, \dots, i_M\}}, \quad 0 \leq i_k \leq N. \quad (\text{D2})$$

[ $i_\mu$  means that we put  $i$  in the  $\mu$ -th place]. Namely, for the example (22), we have  $M = 2$  ( $\mu = 1, 2$ ) and we can arrange these compositions into planar tables, where sum on column  $i$  gives  $n_{1i}$  and sum on row  $i$  gives  $n_{2i}$ , as follows

$$\begin{array}{c|ccc} & n_{11} = 3 & n_{12} = 3 & n_{13} = 1 \\ \hline n_{24} = 3 & l_{14} & l_{24} & l_{34} \\ n_{23} = 3 & l_{13} & l_{23} & \\ n_{22} = 1 & l_{12} & & \end{array} = \begin{array}{ccc} 1 & 1 & 1 \\ 1 & 2 & \\ 1 & & \end{array} + \begin{array}{ccc} 0 & 2 & 1 \\ 2 & 1 & \\ & & \end{array} + \begin{array}{ccc} 2 & 0 & 1 \\ 0 & 3 & \\ & & \end{array}. \quad (\text{D3})$$

Denoting  $\Delta_I = \det\left(A_I^\dagger\right)$  a minor of size  $M \times M$  of  $A^\dagger$ , a Gelfand state  $|\mathfrak{m}\rangle$  corresponds to the following (un-normalized) Fock state

$$|\mathfrak{m}\rangle \propto \sum_{l(\mathfrak{m})} \prod_{I=1}^{\binom{N}{M}} \Delta_I^{l_I} |0\rangle_{\text{F}}, \quad (\text{D4})$$

where the sum is extended to all components  $l(\mathfrak{m})$  associated to  $\mathfrak{m}$  (or equivalently, to the occupancy numbers  $n_{\mu i}$ ). Note that  $\prod_I \Delta_I^{l_I}$  is a homogeneous polynomial of degree  $ML$  in the creation operators  $a_{i\mu}^\dagger$ . For example, taking into account the three components (D3) of the Gelfand state (27) for filling factor  $M = 2$  and  $N = 4$  flavors, the corresponding Fock state can be written as

$$\left(\Delta_{12}^1 \Delta_{13}^1 \Delta_{14}^1 \Delta_{23}^2 \Delta_{24}^1 \Delta_{34}^1 + \Delta_{12}^1 \Delta_{13}^2 \Delta_{14}^0 \Delta_{23}^1 \Delta_{24}^2 \Delta_{34}^1 + \Delta_{12}^1 \Delta_{13}^0 \Delta_{14}^2 \Delta_{23}^3 \Delta_{24}^0 \Delta_{34}^1\right) |0\rangle_{\text{F}}. \quad (\text{D5})$$

This expression gets simpler for highest and lowest weight states. For example, in (32) and (37) we have seen that the corresponding HW states for  $M = 2$  and  $M = 3$  are just given in terms of  $\Delta_{12}$  and  $\Delta_{123}$  (just one single component), respectively. In the same way, the lowest-weight state  $|\mathfrak{m}_{1w}\rangle$  for  $N = 4$  and  $M = 2$  is given in terms of only  $\Delta_{34}$  in (33). The computation of compositions (D2) of the occupancy numbers  $n_{\mu i}$  for  $M > 2$  gets more and more involved since the planar picture (D3) becomes a higher-dimensional arrangement.

#### Appendix E: Single Landau site Hilbert space basis for a bilayer $U(4)$ QHF at $M = 2$

Let us explicitly work out the case  $N = 4$ ,  $M = 2$  and  $L = 1$ , for which the Hilbert space  $\mathcal{H}_4[1^2]$  has dimension  $\binom{N}{M} = 6$ . The corresponding basis vectors for this case can be divided into two sectors: the spin-triplet pseudospin-singlet sector

$$\begin{aligned} |\mathfrak{S}_1\rangle &= c_{\uparrow t}^\dagger c_{\uparrow b}^\dagger |0\rangle_{\text{F}} = \frac{1}{2} = \begin{vmatrix} 1 & 1 & 0 & 0 \\ 1 & 1 & 0 \\ 1 & 1 & 1 \\ 1 & & & \end{vmatrix} = \frac{1}{\sqrt{2}} \begin{vmatrix} a_{11}^\dagger & a_{21}^\dagger \\ a_{12}^\dagger & a_{22}^\dagger \end{vmatrix} |0\rangle_{\text{F}}, \\ |\mathfrak{S}_{-1}\rangle &= c_{\downarrow t}^\dagger c_{\downarrow b}^\dagger |0\rangle_{\text{F}} = \frac{3}{4} = \begin{vmatrix} 1 & 1 & 0 & 0 \\ 1 & 0 & 0 \\ 0 & 0 & 0 \\ 0 & & & \end{vmatrix} = \frac{1}{\sqrt{2}} \begin{vmatrix} a_{31}^\dagger & a_{41}^\dagger \\ a_{32}^\dagger & a_{42}^\dagger \end{vmatrix} |0\rangle_{\text{F}}, \\ |\mathfrak{S}_0\rangle &= \frac{c_{\uparrow t}^\dagger c_{\downarrow b}^\dagger + c_{\downarrow t}^\dagger c_{\uparrow b}^\dagger}{\sqrt{2}} |0\rangle_{\text{F}} = \frac{1}{\sqrt{2}} \left( \frac{1}{4} - \frac{2}{3} \right) = \frac{1}{\sqrt{2}} \left( \begin{vmatrix} 1 & 1 & 0 & 0 \\ 1 & 0 & 0 \\ 1 & 0 & 0 \\ 1 & & & \end{vmatrix} - \begin{vmatrix} 1 & 1 & 0 & 0 \\ 1 & 1 & 0 \\ 1 & 0 & 0 \\ 0 & & & \end{vmatrix} \right) \\ &= \frac{1}{\sqrt{2}} \left( \begin{vmatrix} a_{11}^\dagger & a_{41}^\dagger \\ a_{12}^\dagger & a_{42}^\dagger \end{vmatrix} - \begin{vmatrix} a_{21}^\dagger & a_{31}^\dagger \\ a_{22}^\dagger & a_{32}^\dagger \end{vmatrix} \right) |0\rangle_{\text{F}}. \end{aligned} \quad (\text{E1})$$

and the pseudospin-triplet spin-singlet sector

$$\begin{aligned}
|\mathfrak{P}_1\rangle &= c_{\uparrow t}^\dagger c_{\downarrow t}^\dagger |0\rangle_F = \frac{1}{3} = \left| \begin{array}{cccc} 1 & 1 & 0 & 0 \\ & 1 & 1 & 0 \\ & & 1 & 0 \\ & & & 1 \end{array} \right\rangle = \frac{1}{\sqrt{2}} \left| \begin{array}{cc} a_{11}^\dagger & a_{31}^\dagger \\ a_{12}^\dagger & a_{32}^\dagger \end{array} \right| |0\rangle_F, \\
|\mathfrak{P}_{-1}\rangle &= c_{\uparrow b}^\dagger c_{\downarrow b}^\dagger |0\rangle_F = \frac{2}{4} = \left| \begin{array}{cccc} 1 & 1 & 0 & 0 \\ & 1 & 0 & 0 \\ & & 1 & 0 \\ & & & 0 \end{array} \right\rangle = \frac{1}{\sqrt{2}} \left| \begin{array}{cc} a_{21}^\dagger & a_{41}^\dagger \\ a_{22}^\dagger & a_{42}^\dagger \end{array} \right| |0\rangle_F, \\
|\mathfrak{P}_0\rangle &= \frac{c_{\uparrow t}^\dagger c_{\downarrow b}^\dagger - c_{\downarrow t}^\dagger c_{\uparrow b}^\dagger}{\sqrt{2}} |0\rangle_F = \frac{1}{\sqrt{2}} \left( \frac{1}{4} + \frac{2}{3} \right) = \frac{1}{\sqrt{2}} \left( \left| \begin{array}{cccc} 1 & 1 & 0 & 0 \\ & 1 & 0 & 0 \\ & & 1 & 0 \\ & & & 1 \end{array} \right\rangle + \left| \begin{array}{cccc} 1 & 1 & 0 & 0 \\ & 1 & 1 & 0 \\ & & 1 & 0 \\ & & & 0 \end{array} \right\rangle \right) \\
&= \frac{1}{\sqrt{2}} \left( \left| \begin{array}{cc} a_{11}^\dagger & a_{41}^\dagger \\ a_{12}^\dagger & a_{42}^\dagger \end{array} \right| + \left| \begin{array}{cc} a_{21}^\dagger & a_{31}^\dagger \\ a_{22}^\dagger & a_{32}^\dagger \end{array} \right| \right) |0\rangle_F.
\end{aligned} \tag{E2}$$

### Appendix F: Explicit particular expressions of $U(N)$ -spin matrix elements

In Section IV we have given general formulas (45) for the matrix coefficients  $\langle m' | S_{ij} | m \rangle$  of the  $U(N)$ -spin operators  $S_{ij}$  in the Gelfand basis  $\{|m\rangle\}$  for a given IR of  $U(N)$  characterized by the highest-weight  $h = m_N = [m_{1,N}, \dots, m_{N,N}]$  [top row of the Gelfand vector  $|m\rangle$  in (24)]. In this Appendix we provide particular examples to explain the underlying algorithm. Firstly, we need to order the Gelfand basis  $\{|m\rangle\}$ . For it, we choose an increasing order of the components  $m_{ij}, j < N$  of the Gelfand vector array (24) from top to bottom and from left to right, fulfilling the betweenness conditions (25). Schematically, the vectors of the basis are ordered within a list generated by nested indexes

$$\{ \{ \dots \{ \{ \dots \{ |m\rangle \}^{m_{12}} \}_{m_{11}=m_{22}} \dots \}^{m_{1,N-1}} \}_{m_{1,N-2}=m_{2,N-1}} \}^{m_{N,N}} \}_{m_{N-1,N-1}=m_{N-1,N}} \dots \}^{m_{2,N}} \}_{m_{2,N-1}=m_{3,N}} \}^{m_{1,N}} \}_{m_{1,N-1}=m_{2,N}}. \tag{F1}$$

For example, this ordering convention coincides with the order in which we add in equation (35) the basis vectors of the representation  $m_4 = [L^2]$  of  $U(4)$  to compute its dimension. Note that the first basis vector is the lowest weight vector  $|m_{lw}\rangle$ , whereas the last basis vector is the highest weight vector  $|m_{hw}\rangle$ . Let us see some particular simple examples.

#### 1. $U(2)$ -spin matrices for $M = 1$ and $L = 1$

The general formulas (45) for the Gelfand-Tsetlin basis vectors

$$|1\rangle = \left| \begin{array}{ccc} 1 & & 0 \\ & 1 & \\ & & 0 \end{array} \right\rangle, \quad |2\rangle = \left| \begin{array}{ccc} 1 & & 0 \\ & 1 & \\ & & 1 \end{array} \right\rangle, \tag{F2}$$

give the  $U(2)$ -spin operator matrices

$$S_{11} = \begin{pmatrix} 0 & 0 \\ 0 & 1 \end{pmatrix}, \quad S_{12} = \begin{pmatrix} 0 & 0 \\ 1 & 0 \end{pmatrix}, \quad S_{21} = \begin{pmatrix} 0 & 1 \\ 0 & 0 \end{pmatrix}, \quad S_{22} = \begin{pmatrix} 1 & 0 \\ 0 & 0 \end{pmatrix}. \tag{F3}$$

These matrices are in one-to-one correspondence to the  $SU(2)$  Pauli matrices ( $j = 1/2$ ),  $\sigma_z = S_{22} - S_{11}$ ,  $\sigma_+ = S_{21}$ ,  $\sigma_- = S_{12}$  plus identity.

#### 2. $U(2)$ -spin matrices for $M = 1$ and $L = 2$

$$|1\rangle = \left| \begin{array}{ccc} 2 & & 0 \\ & 2 & \\ & & 0 \end{array} \right\rangle, \quad |2\rangle = \left| \begin{array}{ccc} 2 & & 0 \\ & 2 & \\ & & 1 \end{array} \right\rangle, \quad |3\rangle = \left| \begin{array}{ccc} 2 & & 0 \\ & 2 & \\ & & 2 \end{array} \right\rangle. \tag{F4}$$

$$S_{11} = \begin{pmatrix} 0 & 0 & 0 \\ 0 & 1 & 0 \\ 0 & 0 & 2 \end{pmatrix}, \quad S_{12} = \begin{pmatrix} 0 & 0 & 0 \\ \sqrt{2} & 0 & 0 \\ 0 & \sqrt{2} & 0 \end{pmatrix}, \quad S_{21} = \begin{pmatrix} 0 & \sqrt{2} & 0 \\ 0 & 0 & \sqrt{2} \\ 0 & 0 & 0 \end{pmatrix}, \quad S_{22} = \begin{pmatrix} 2 & 0 & 0 \\ 0 & 1 & 0 \\ 0 & 0 & 0 \end{pmatrix}. \quad (\text{F5})$$

These matrices are related to the SU(2) spin  $j = 1$  matrices,  $J_z = \frac{1}{2}(S_{22} - S_{11})$ ,  $J_+ = S_{21}$ ,  $J_- = S_{12}$ .

### 3. U(4)-spin matrices for $M = 2$ and $L = 1$

$$\begin{aligned} |1\rangle &= \begin{vmatrix} 1 & 1 & 0 & 0 \\ & 1 & 0 & 0 \\ & & 0 & 0 \\ & & & 0 \end{vmatrix}, & |2\rangle &= \begin{vmatrix} 1 & 1 & 0 & 0 \\ & 1 & 0 & 0 \\ & & 1 & 0 \\ & & & 0 \end{vmatrix}, & |3\rangle &= \begin{vmatrix} 1 & 1 & 0 & 0 \\ & 1 & 0 & 0 \\ & & 1 & 0 \\ & & & 1 \end{vmatrix}, \\ |4\rangle &= \begin{vmatrix} 1 & 1 & 0 & 0 \\ & 1 & 1 & 0 \\ & & 1 & 0 \\ & & & 0 \end{vmatrix}, & |5\rangle &= \begin{vmatrix} 1 & 1 & 0 & 0 \\ & 1 & 1 & 0 \\ & & 1 & 0 \\ & & & 1 \end{vmatrix}, & |6\rangle &= \begin{vmatrix} 1 & 1 & 0 & 0 \\ & 1 & 1 & 0 \\ & & 1 & 1 \\ & & & 1 \end{vmatrix}. \end{aligned} \quad (\text{F6})$$

$$S_{11} = \begin{pmatrix} 0 & 0 & 0 & 0 & 0 & 0 \\ 0 & 0 & 0 & 0 & 0 & 0 \\ 0 & 0 & 1 & 0 & 0 & 0 \\ 0 & 0 & 0 & 0 & 0 & 0 \\ 0 & 0 & 0 & 0 & 1 & 0 \\ 0 & 0 & 0 & 0 & 0 & 1 \end{pmatrix}, \quad S_{22} = \begin{pmatrix} 0 & 0 & 0 & 0 & 0 & 0 \\ 0 & 1 & 0 & 0 & 0 & 0 \\ 0 & 0 & 0 & 0 & 0 & 0 \\ 0 & 0 & 0 & 1 & 0 & 0 \\ 0 & 0 & 0 & 0 & 0 & 0 \\ 0 & 0 & 0 & 0 & 0 & 1 \end{pmatrix}, \quad S_{33} = \begin{pmatrix} 1 & 0 & 0 & 0 & 0 & 0 \\ 0 & 0 & 0 & 0 & 0 & 0 \\ 0 & 0 & 0 & 0 & 0 & 0 \\ 0 & 0 & 0 & 1 & 0 & 0 \\ 0 & 0 & 0 & 0 & 1 & 0 \\ 0 & 0 & 0 & 0 & 0 & 0 \end{pmatrix}, \quad S_{44} = \begin{pmatrix} 1 & 0 & 0 & 0 & 0 & 0 \\ 0 & 1 & 0 & 0 & 0 & 0 \\ 0 & 0 & 1 & 0 & 0 & 0 \\ 0 & 0 & 0 & 0 & 0 & 0 \\ 0 & 0 & 0 & 0 & 0 & 0 \\ 0 & 0 & 0 & 0 & 0 & 0 \end{pmatrix},$$

$$S_{12} = \begin{pmatrix} 0 & 0 & 0 & 0 & 0 & 0 \\ 0 & 0 & 0 & 0 & 0 & 0 \\ 0 & 1 & 0 & 0 & 0 & 0 \\ 0 & 0 & 0 & 0 & 0 & 0 \\ 0 & 0 & 0 & 1 & 0 & 0 \\ 0 & 0 & 0 & 0 & 0 & 0 \end{pmatrix}, \quad S_{23} = \begin{pmatrix} 0 & 0 & 0 & 0 & 0 & 0 \\ 1 & 0 & 0 & 0 & 0 & 0 \\ 0 & 0 & 0 & 0 & 0 & 0 \\ 0 & 0 & 0 & 0 & 0 & 0 \\ 0 & 0 & 0 & 0 & 0 & 0 \\ 0 & 0 & 0 & 0 & 1 & 0 \end{pmatrix}, \quad S_{34} = \begin{pmatrix} 0 & 0 & 0 & 0 & 0 & 0 \\ 0 & 0 & 0 & 0 & 0 & 0 \\ 0 & 0 & 0 & 0 & 0 & 0 \\ 0 & 1 & 0 & 0 & 0 & 0 \\ 0 & 0 & 1 & 0 & 0 & 0 \\ 0 & 0 & 0 & 0 & 0 & 0 \end{pmatrix}. \quad (\text{F7})$$

The rest of the  $S_{ij}$  matrices can be obtained using the commutation relations in the equation (42).

### Appendix G: The case of non-rectangular Young tableaux

For a Young tableau of general shape  $m_N = [m_{1N}, \dots, m_{NN}]$ , the HW state (17) is generalized to

$$|\mathfrak{m}_{\text{hw}}\rangle = \mathcal{N}(m_N) \Delta_1^{m_{1N} - m_{2N}} \Delta_{12}^{m_{2N} - m_{3N}} \dots \Delta_{1, \dots, N-1}^{m_{N-1, N} - m_{NN}} \Delta_{1, \dots, N}^{m_{NN}} |0\rangle_{\text{F}}, \quad (\text{G1})$$

where  $\Delta_{1, \dots, n} = \det(A_{\{1, \dots, n\}}^\dagger)$  are leading (corner) principal minors of order  $n$  of  $A^\dagger$  (for  $M = N$ , in general), like in (D4);  $\mathcal{N}(m_N)$  denotes a normalizing factor. This HW state satisfies the HW conditions:

$$\Lambda_{\mu\nu} |\mathfrak{m}_{\text{hw}}\rangle = m_{\mu N} \delta_{\mu\nu} |\mathfrak{m}_{\text{hw}}\rangle, \quad \mu \leq \nu, \quad (\text{G2})$$

$$S_{ij} |\mathfrak{m}_{\text{hw}}\rangle = m_{iN} \delta_{ij} |\mathfrak{m}_{\text{hw}}\rangle, \quad i \leq j. \quad (\text{G3})$$

If all components of  $m_N$  are different, that is,  $m_{1N} > m_{2N} > \dots > m_{NN}$ , then all leading principal minors  $\Delta_I$  of  $A^\dagger$  are present in the product (G1) and the HW state  $|\mathfrak{m}_{\text{hw}}\rangle$  is only invariant under  $U(1)^N \subset U(N)$  (all internal/flavor states  $i = 1, \dots, N$  are occupied). In this case, the ferromagnetic order parameter associated to the symmetry breaking

is labeled by  $\dim_{\mathbb{C}}[U(N)/U(1)^N] = N(N-1)/2$  complex parameters  $z_{ij} \in \mathbb{C}, i > j = 1, \dots, N-1$ , parameterizing the coset (*flag manifold*)  $\mathbb{F}_{N-1} = U(N)/U(1)^N$ . See e.g. [57] for the Bruhat-Iwasawa decomposition in this case.

- 
- [1] B. A. Bernevig, *Topological Insulators and Topological Superconductors* (Princeton University Press, 2013).
- [2] M. Z. Hasan and C. L. Kane, *Rev. Mod. Phys.* **82**, 3045 (2010).
- [3] X.-L. Qi and S.-C. Zhang, *Rev. Mod. Phys.* **83**, 1057 (2011).
- [4] L. Kou, Y. Ma, Z. Sun, T. Heine, and C. Chen, *The Journal of Physical Chemistry Letters* **8**, 1905 (2017).
- [5] C. L. Kane and E. J. Mele, *Phys. Rev. Lett.* **95**, 226801 (2005).
- [6] B. A. Bernevig, T. L. Hughes, and S.-C. Zhang, *Science* **314**, 1757 (2006).
- [7] M. König, S. Wiedmann, C. Brune, A. Roth, H. Buhmann, L. W. Molenkamp, X.-L. Qi, and S.-C. Zhang, *Science* **318**, 766 (2007).
- [8] A. Kitaev, *Annals of Physics* **303**, 2 (2003).
- [9] J. K. Pachos, *Introduction to Topological Quantum Computation* (Cambridge University Press, 2012).
- [10] S. D. Sarma, M. Freedman, and C. Nayak, *npj Quantum Information* **1**, 15001 (2015).
- [11] X. Zhang, M. Ezawa, and Y. Zhou, *Scientific Reports* **5**, 9400 (2015).
- [12] X. Zhang, Y. Zhou, M. Ezawa, G. P. Zhao, and W. Zhao, *Scientific Reports* **5**, 11369 (2015).
- [13] X. Zhang, Y. Zhou, and M. Ezawa, *Nature Communications* **7**, 10293 (2016).
- [14] J. E. Jacak, *Journal of High Energy Physics* **2022**, 2 (2022).
- [15] C. J. Pethick and H. Smith, *Bose-Einstein Condensation in Dilute Gases*, 2nd ed. (Cambridge University Press, 2008).
- [16] M. Lewenstein, A. Sanpera, and V. Ahufinger, *Ultracold Atoms in Optical Lattices: Simulating quantum many-body systems*, 1st ed. (Oxford University Press, 2012).
- [17] M. A. Cazalilla and A. M. Rey, *Reports on Progress in Physics* **77**, 124401 (2014).
- [18] C. Honerkamp and W. Hofstetter, *Phys. Rev. Lett.* **92**, 170403 (2004).
- [19] M. A. Cazalilla, A. F. Ho, and M. Ueda, *New Journal of Physics* **11**, 103033 (2009).
- [20] R. Bistritzer and A. H. MacDonald, *Proceedings of the National Academy of Sciences* **108**, 12233 (2011).
- [21] Y. Cao, V. Fatemi, A. Demir, S. Fang, S. L. Tomarken, J. Y. Luo, J. D. Sanchez-Yamagishi, K. Watanabe, T. Taniguchi, E. Kaxiras, R. C. Ashoori, and P. Jarillo-Herrero, *Nature* **556**, 80 (2018).
- [22] A. Perelomov, *Generalized Coherent States and Their Applications* (Springer-Verlag Berlin Heidelberg, 1986).
- [23] J. Gazeau, *Coherent States in Quantum Physics* (John Wiley & Sons, Ltd, 2009).
- [24] S. Seki and M. Mochizuki, *Skyrmions in Magnetic Materials* (Springer, Cham, 2016).
- [25] J. H. Han, *Skyrmions in Condensed Matter* (Springer, Cham, 2017).
- [26] G. Finocchio and C. Panagopoulos, eds., *Magnetic Skyrmions and Their Applications* (Woodhead Publishing, 2021).
- [27] S. Zhang, *Chiral and Topological Nature of Magnetic Skyrmions* (Springer, Cham, 2018).
- [28] I. Affleck, *Nuclear Physics B* **257**, 397 (1985).
- [29] I. Affleck, *Nuclear Physics B* **265**, 409 (1986).
- [30] I. Affleck, *Nuclear Physics B* **305**, 582 (1988).
- [31] N. Read and S. Sachdev, *Nuclear Physics B* **316**, 609 (1989).
- [32] N. Read and S. Sachdev, *Phys. Rev. B* **42**, 4568 (1990).
- [33] D. P. Arovas, A. Karlhede, and D. Lilliehöök, *Phys. Rev. B* **59**, 13147 (1999).
- [34] F. Haldane, *Physics Letters A* **93**, 464 (1983).
- [35] F. D. M. Haldane, *Phys. Rev. Lett.* **50**, 1153 (1983).
- [36] F. D. M. Haldane, *Phys. Rev. Lett.* **61**, 1029 (1988).
- [37] E. Lieb and D. Mattis, *Phys. Rev.* **125**, 164 (1962).
- [38] J. Decamp, J. Gong, H. Loh, and C. Miniatura, *Phys. Rev. Research* **2**, 023059 (2020).
- [39] A. Barut and R. Raczka, *Theory of Group Representations and Applications* (Polish Scientific Publishers, Warszawa, 1980).
- [40] R. Casten, P. Lipas, D. Warner, T. Otsuka, K. Heyde, and J. Draayer, *Algebraic Approaches to Nuclear Structure: Interacting Boson and Fermion Models (1st ed.)*, edited by R. Casten (CRC Press, 1993).
- [41] A. Frank and P. Van Isacker, *Algebraic methods in molecular and nuclear structure physics* (Wiley, New York, 1994).
- [42] F. Iachello and R. Levine, *Algebraic Theory of Molecules* (Oxford University Press, 1995).
- [43] F. Iachello and A. Arima, *The Interacting Boson Model*, Cambridge Monographs on Mathematical Physics (Cambridge University Press, 1987).
- [44] M. Calixto and E. Pérez-Romero, *Journal of Physics A: Mathematical and Theoretical* **47**, 115302 (2014).
- [45] A. Sugita, *Journal of Physics A: Mathematical and General* **36**, 9081 (2003).
- [46] J. M. Radcliffe, *Journal of Physics A: General Physics* **4**, 313 (1971).
- [47] F. T. Arecchi, E. Courtens, R. Gilmore, and H. Thomas, *Phys. Rev. A* **6**, 2211 (1972).
- [48] R. Gilmore, *Catastrophe Theory for Scientists and Engineers* (Wiley, New York, 1981).
- [49] M. Calixto and E. Pérez-Romero, *Journal of Physics A: Mathematical and Theoretical* **48**, 495304 (2015).
- [50] M. Calixto and E. Pérez-Romero, *Journal of Physics: Condensed Matter* **26**, 485005 (2014).
- [51] M. Calixto, C. Peón-Nieto, and E. Pérez-Romero, *Phys. Rev. B* **95**, 235302 (2017).
- [52] M. Calixto and C. Peón-Nieto, *Journal of Statistical Mechanics: Theory and Experiment* **2018**, 053112 (2018).

- [53] K. Hasebe and Z. F. Ezawa, *Phys. Rev. B* **66**, 155318 (2002).
- [54] Z. Ezawa, *Quantum Hall Effects* (World Scientific, 2013).
- [55] J. E. Jacak, *Phys. Rev. A* **97**, 012108 (2018).
- [56] A. MacFarlane, *Physics Letters B* **82**, 239 (1979).
- [57] M. Calixto, C. Peón-Nieto, and E. Pérez-Romero, *Annals of Physics* **373**, 52 (2016).
- [58] Z. F. Ezawa, M. Eliashvili, and G. Tsitsishvili, *Phys. Rev. B* **71**, 125318 (2005).
- [59] A. H. MacDonald, R. Rajaraman, and T. Jungwirth, *Phys. Rev. B* **60**, 8817 (1999).
- [60] J. Schliemann and A. H. MacDonald, *Phys. Rev. Lett.* **84**, 4437 (2000).
- [61] A. Fukuda, A. Sawada, S. Kozumi, D. Terasawa, Y. Shimoda, Z. F. Ezawa, N. Kumada, and Y. Hirayama, *Phys. Rev. B* **73**, 165304 (2006).
- [62] K. Yang, S. Das Sarma, and A. H. MacDonald, *Phys. Rev. B* **74**, 075423 (2006).
- [63] K. Yang, K. Moon, L. Zheng, A. H. MacDonald, S. M. Girvin, D. Yoshioka, and S.-C. Zhang, *Phys. Rev. Lett.* **72**, 732 (1994).
- [64] K. Moon, H. Mori, K. Yang, S. M. Girvin, A. H. MacDonald, L. Zheng, D. Yoshioka, and S.-C. Zhang, *Phys. Rev. B* **51**, 5138 (1995).
- [65] K. Yang, K. Moon, L. Belkhir, H. Mori, S. M. Girvin, A. H. MacDonald, L. Zheng, and D. Yoshioka, *Phys. Rev. B* **54**, 11644 (1996).
- [66] R. H. Dicke, *Phys. Rev.* **93**, 99 (1954).
- [67] M. Calixto, A. Mayorgas, and J. Guerrero, *Phys. Rev. E* **103**, 012116 (2021).
- [68] M. Calixto, A. Mayorgas, and J. Guerrero, *Quantum Information Processing* **20**, 304 (2021).
- [69] H.-C. Jiang, Z. Wang, and L. Balents, *Nature Physics* **8**, 902 (2012).
- [70] B. Zeng, X. Chen, D.-L. Zhou, and X.-G. Wen, *Quantum Information Meets Quantum Matter: From Quantum Entanglement to Topological Phases of Many-Body Systems* (Springer Nature, 2019).
- [71] M. Calixto and E. Romera, *EPL (Europhysics Letters)* **109**, 40003 (2015).
- [72] E. Romera and M. Calixto, *Journal of Physics: Condensed Matter* **27**, 175003 (2015).
- [73] M. Calixto and E. Romera, *Journal of Statistical Mechanics: Theory and Experiment* **2015**, P06029 (2015).
- [74] E. Romera and M. Calixto, *EPL (Europhysics Letters)* **111**, 37006 (2015).
- [75] E. Romera, M. Calixto, and J. Bolivar, *Physica A: Statistical Mechanics and its Applications* **511**, 174 (2018).
- [76] O. Castaños, E. Romera, and M. Calixto, *Materials Research Express* **6**, 106316 (2019).
- [77] M. Calixto, E. Romera, and O. Castaños, *International Journal of Quantum Chemistry* **121**, e26464 (2021).
- [78] D. Bacon, I. L. Chuang, and A. W. Harrow, *Phys. Rev. Lett.* **97**, 170502 (2006).
- [79] P. Cvitanovic, *Group theory: Birdtracks, Lie's and exceptional groups* (Princeton University Press, 2008).



*It is not knowledge, but the act of learning,  
not possession but the act of getting there,  
which grants the greatest enjoyment.*

— Carl Friedrich Gauss

# 4

## Topological phase transitions in 2D materials

<sup>7</sup> M. Calixto, A. Mayorgas, N. A. Cordero, E. Romera, and O. Castaños, “Faraday rotation and transmittance as markers of topological phase transitions in 2D materials”, *SciPost Phys.* 16, 077 (2024).

### **Quality metrics (2022)**

- Year: 2022
- Category: PHYSICS, MULTIDISCIPLINARY
- Journal Impact Factor (JIF): 5.5
- JIF Rank: 17/85 (Q1)

**Publication citations in Google Scholar (March 2024): 0**

# Faraday rotation and transmittance as markers of topological phase transitions in 2D materials

Manuel Calixto\*

*Department of Applied Mathematics, University of Granada, Fuentenueva s/n, 18071 Granada, Spain and  
Institute Carlos I for Theoretical for Theoretical and Computational Physics (iC1), Fuentenueva s/n, 18071 Granada, Spain*

Alberto Mayorgas†

*Department of Applied Mathematics, University of Granada, Fuentenueva s/n, 18071 Granada, Spain*

Nicolás A. Cordero‡

*Department of Physics, University of Burgos, E-09001 Burgos, Spain  
International Research Center in Critical Raw Materials for Advanced Industrial Technologies (ICCRAM),  
University of Burgos, E-09001 Burgos, Spain and  
Institute Carlos I for Theoretical for Theoretical and Computational Physics (iC1), Fuentenueva s/n, 18071 Granada, Spain*

Elvira Romera§

*Department of Atomic, Molecular and Nuclear Physics,  
University of Granada, Fuentenueva s/n, 18071 Granada, Spain and  
Institute Carlos I for Theoretical for Theoretical and Computational Physics (iC1), Fuentenueva s/n, 18071 Granada, Spain*

Octavio Castaños¶

*Institute of Nuclear Sciences, National Autonomous University of Mexico, Apdo. Postal 70-543, 04510, CDMX, Mexico  
(Dated: September 21, 2023)*

We analyze the magneto-optical conductivity (and related magnitudes like transmittance and Faraday rotation of the irradiated polarized light) of some elemental two-dimensional Dirac materials of group IV (graphene analogues, buckled honeycomb lattices, like silicene, germanene, stannane, etc.), group V (phosphorene), and zincblende heterostructures (like HgTe/CdTe quantum wells) near the Dirac and gamma points, under out-of-plane magnetic and electric fields, to characterize topological-band insulator phase transitions and their critical points. We provide plots of the Faraday angle and transmittance as a function of the polarized light frequency, for different external electric and magnetic fields, chemical potential, HgTe layer thickness and temperature, to tune the material magneto-optical properties. We have shown that absorbance/transmittance acquires extremal values at the critical point, where the Faraday angle changes sign, thus providing fine markers of the topological phase transition. In the case of non-topological materials as phosphorene, a minimum of the transmittance is also observed due to the energy gap closing by an external electric field.

## I. INTRODUCTION

Two-dimensional (2D) materials have been extensively studied in recent years (and are expected to be one of the crucial research topics in future years) especially because of their remarkable electronic and magneto-optical properties which make them hopeful candidates for next generation optoelectronic devices. Graphene is the archetype of a 2D nanomaterial with exceptional high tensile strength, electrical conductivity, transparency, etc. In spite of being the thinnest one, it exhibits a giant Faraday rotation ( $\Theta_F \sim 6^\circ$ ) on polarized light in single- and multilayer arrangements [1–6] with experimental confirmation [7]. Faraday rotation is a funda-

mental magneto-optical phenomenon used in various optical control, laser technology and magnetic field sensing techniques.

Magneto-optical properties of other buckled honeycomb lattices, like silicene [8], have been studied in [9–11], together with other monolayer transition metal dichalcogenides [12] and anisotropic versions like phosphorene [13]. Magneto-optical measurements also provide signatures of the topological phase transition (TPT; see [14–16] for standard textbooks on the subject) in inverted HgTe/CdTe quantum wells (QW), distinguishing quantum Hall (QH) from quantum spin Hall (QSH) phases [17], where one can tune the band structure by fabricating QWs with different thicknesses  $\lambda$ . A universal value of the Faraday rotation angle, close to the fine structure constant, has been experimentally observed in thin HgTe QW with critical thickness [18].

To determine experimentally the Faraday rotation effect in Dirac materials it is convenient to consider: (1) A transverse-magnetic-polarized wave incident from the left onto a single topological insulator sandwiched by dielec-

---

\* Corresponding author: calixto@ugr.es

† albmayer97@ugr.es

‡ ncordero@ubu.es

§ eromera@ugr.es

¶ ocasta@nucleares.unam.mx

tric layers, which yields an enhancement of the Faraday rotation with an angle larger than 700 mrad and with a transmission higher than 90% [19]. (2) A graphene sheet sandwiched by one-dimensional topological photonic crystals also an enhancement of the Faraday rotation can be achieved with high transmittance [20]. (3) In thin films of 3D topological insulators [21] or by considering thin films of Floquet topological insulators where giant Faraday and Ker rotations have been observed under the action of a perpendicular magnetic field or in a non-resonant optical field [22]. The inverse Faraday effect (IFE) has been studied in Dirac materials in 2D and 3D, and these studies have concluded that IFE is stronger than in conventional semiconductors. Then the Dirac materials can be potentially useful for the optical control of magnetization in optoelectronic devices [23].

Information theoretic measures also provide signatures of the TPT in silicene [24–28] and HgTe/CdTe QWs [29], as an alternative to the usual topological (Chern) numbers. They also account for semimetallic behavior of phosphorene [30, 31] under perpendicular electric fields.

In this paper we perform a comparative study of the magneto-optical properties of several 2D Dirac materials, looking for TPT signatures when the band structure is tuned by applying external fields or by changing the material characteristics. For this purpose, we focus on transmittance and Faraday rotation near the critical point of the topological phase transition for topological materials such as silicene and HgTe quantum wells. We found that, for these materials, transmittance attains an absolute minimum  $\mathcal{T}_0$  at the critical TPT point for a certain value  $\Omega_0$  of the normal incident polarized light frequency. This minimal behavior does not depend on the chosen values of magnetic field, chemical potential and temperature, although the location of  $\Omega_0$  varies with them. An inflection point of the Faraday angle is observed at each peak of the transmittance, coinciding in frequency. As a novel perspective, we study that non-topological materials, such as phosphorene, also exhibit an extremal value of the transmittance when the energy gap is closed by an external electric field.

The organization of the article is as follows. In Sec. II we discuss the structure of time independent Bloch Hamiltonians for general two-band 2D-Dirac material models, their Chern numbers and their minimal coupling to an external perpendicular magnetic field. We particularize to graphene analogues (silicene, germanene, etc.) in Sec. II A, zincblende heterostructures (HgTe/CdTe quantum wells) in Sec. II B and anisotropic materials like phosphorene in II C, calculating their energy spectrum and Hamiltonian eigenstates (Landau levels) and describing their topological phases (when they exist). In Sec. III we recall the Kubo-Greenwood formula for the magneto-optical conductivity tensor  $\boldsymbol{\sigma}$  of a 2D electron system in a perpendicular magnetic field  $B$  and an oscillating electric field of frequency  $\Omega$ . In particular, we are interested in analyzing the transmittance and Faraday rotation of linearly polarized light of frequency  $\Omega$  for nor-

mal incidence on the 2D material. Magneto-optical properties of graphene analogues, zincblende heterostructures and phosphorene are analyzed in Sections III A, III B and III C, respectively. For topological insulator materials, we find that the critical point is generally characterized by a minimum transmittance  $\mathcal{T}_0$  at a given light frequency  $\Omega_0$ , where the Faraday angle changes sign. The effect of anisotropies is also discussed in phosphorene in Section III C. Finally, Sec. IV is devoted to conclusions.

## II. SOME TWO-BAND 2D-DIRAC MATERIAL MODELS

The time independent Bloch Hamiltonian of a two-band 2D insulator has the general form

$$H(\mathbf{k}) = \epsilon_0(\mathbf{k})\tau_0 + \mathbf{d}(\mathbf{k}) \cdot \boldsymbol{\tau}, \quad (1)$$

where  $\boldsymbol{\tau} = (\tau_x, \tau_y, \tau_z)$  is the Pauli matrix vector,  $\tau_0$  denotes the  $2 \times 2$  identity matrix and  $\mathbf{d}(\mathbf{k})$  parameterizes an effective spin-orbit coupling near the center  $\Gamma$  or the Dirac valleys  $K$  and  $K'$  of the first Brillouin zone (FBZ), with  $\mathbf{k} = (k_x, k_y)$  the two-dimensional wavevector. The energy of the two bands is  $\epsilon_{\pm}(\mathbf{k}) = \epsilon_0(\mathbf{k}) \pm |\mathbf{d}(\mathbf{k})|$ .

To distinguish between band insulator and topological insulator phases, one can use the TKNN (Thouless-Kohmoto-Nightingale-Nijs) formula [32] providing the Chern-Pontryagin number (related to the quantum spin Hall conductance and the Berry phase [33])

$$\mathcal{C} = \frac{1}{2\pi} \int \int_{\text{FBZ}} d^2\mathbf{k} \left( \frac{\partial \hat{\mathbf{d}}(\mathbf{k})}{\partial k_x} \times \frac{\partial \hat{\mathbf{d}}(\mathbf{k})}{\partial k_y} \right) \cdot \hat{\mathbf{d}}(\mathbf{k}), \quad (2)$$

with  $\hat{\mathbf{d}} = \mathbf{d}/|\mathbf{d}|$ , which counts the number of times (winding number) the unit vector  $\hat{\mathbf{d}}(\mathbf{k})$  wraps around the unit sphere as  $\mathbf{k}$  wraps around the entire FBZ. The Chern number  $\mathcal{C}$  usually depends on the sign of some material and (external) control parameters in the Hamiltonian  $H$  (see later for some examples), taking different values in different phases. We shall see that magneto-optical conductivity measures also capture the topological phase transition.

We shall consider the interaction with a perpendicular magnetic field  $\mathbf{B} = (0, 0, B)$ . Promoting the wavevector  $\mathbf{k}$  to the momentum operator  $\mathbf{k} \rightarrow \mathbf{p}/\hbar = -i\nabla$ , this interaction is introduced through the usual minimal coupling,  $\mathbf{p} \rightarrow \mathbf{P} = \mathbf{p} + e\mathbf{A}$  with  $\mathbf{A} = (A_x, A_y) = (-By, 0)$  the electromagnetic potential (in the Landau gauge) and  $e$  the elementary charge (in absolute value). After Peierls' substitution, which results in

$$k_x \rightarrow P_x/\hbar = \frac{a^\dagger + a}{\sqrt{2}\ell_B}, \quad k_y \rightarrow P_y/\hbar = \frac{a^\dagger - a}{i\sqrt{2}\ell_B}, \quad (3)$$

the Hamiltonian (1) can be eventually written in terms of creation  $a^\dagger$  and annihilation

$$a = \frac{\ell_B}{\sqrt{2}\hbar} (P_x - iP_y) = \frac{-1}{\sqrt{2}\ell_B} (y - y_0 + i\ell_B^2 p_y/\hbar), \quad (4)$$

	$\Delta_{\text{so}}$ (meV)	$l$ (Å)	$v$ ( $10^5$ m/s)
Si	4.2	0.22	4.2
Ge	11.8	0.34	8.8
Sn	36.0	0.42	9.7
Pb	207.3	0.44	–

TABLE I. Approximate values of model parameters  $\Delta_{\text{so}}$  (spin-orbit coupling),  $l$  (interlattice distance) and  $v$  (Fermi velocity) for two dimensional Si, Ge, Sn and Pb sheets. These data have been obtained from first-principles computations in [38] ( $\Delta_{\text{so}}$  and  $l$ ) and [39, 40] ( $v$ ).

operators, where  $\ell_B = \sqrt{\hbar/(eB)}$  is the magnetic length and  $y_0 = \ell_B^2 k_x$  is the coordinate of the conserved center of the cyclotron orbit.

Let us review some relevant physical examples.

### A. Graphene analogues: silicene, germanene, etc

Silicene, germanene, and other transition metal dichalcogenides (of the Xene type) exhibit an intrinsic non-zero spin-orbit coupling  $H_{\text{so}} = -\frac{1}{2}s\xi\Delta_{\text{so}}\tau_z$  ( $s = \pm 1$  is the spin of the electron and  $\xi = \pm 1$  refer to the Dirac valleys  $K$  and  $K'$ ) due to second neighbors hopping terms in the tight binding model [34]. Spin-orbit interaction  $H_{\text{so}}$  combined with an external perpendicular electric field coupling  $H_{\Delta_z} = \frac{1}{2}\Delta_z\tau_z$ , gives  $\mathbf{d}(\mathbf{k}) = (v\hbar\xi k_x, v\hbar k_y, \Delta_{s\xi})$ , where  $\Delta_{s\xi} = (\Delta_z - s\xi\Delta_{\text{so}})/2$  results in a tunable (Dirac mass) gap (see e.g. [35–38]). In Table I we show a comparative of spin-orbit coupling and Fermi velocity values for several 2D materials.

The Chern number (2) turns out to be

$$\mathcal{C}_{s\xi} = \xi \text{sgn}(\Delta_{s\xi}), \quad (5)$$

where we have integrated on the whole plane, as corresponds to the FBZ in the continuum limit (zero lattice constant). Therefore, the topological phase is determined by the sign of the Dirac mass at each valley  $\xi$ . More precisely, there is a TPT from a topological insulator (TI,  $|\Delta_z| < \Delta_{\text{so}}$ ) to a band insulator (BI,  $|\Delta_z| > \Delta_{\text{so}}$ ), at a charge neutrality point (CNP)  $\Delta_z^{(0)} = s\xi\Delta_{\text{so}}$ , where there is a gap cancellation between the perpendicular electric field and the spin-orbit coupling.

Using the general prescription (3), the minimal coupling with a perpendicular magnetic field  $B$  then results in a different Hamiltonian  $H_\xi$  for each valley  $\xi = \pm 1$

$$H_1 = \begin{pmatrix} \Delta_{s,1} & \hbar\omega a \\ \hbar\omega a^\dagger & -\Delta_{s,1} \end{pmatrix}, \quad H_{-1} = \begin{pmatrix} \Delta_{s,-1} & -\hbar\omega a^\dagger \\ -\hbar\omega a & -\Delta_{s,-1} \end{pmatrix}, \quad (6)$$

where  $\omega = \sqrt{2}v/\ell_B$  denotes the cyclotron frequency. The eigenvalues of both Hamiltonians are simply:

$$E_n^{s\xi} = \begin{cases} \text{sgn}(n)\sqrt{|n|\hbar^2\omega^2 + \Delta_{s\xi}^2}, & n \neq 0, \\ -\xi\Delta_{s\xi}, & n = 0, \end{cases} \quad (7)$$

and the corresponding eigenstates are written in terms of Fock states  $|n\rangle$ , for Landau level (LL) index  $n = 0, \pm 1, \pm 2, \dots$  [valence ( $-$ ) and conduction ( $+$ ) states], as spinors

$$|n\rangle_{s\xi} = \begin{pmatrix} A_n^{s\xi} |n - \frac{\xi+1}{2}\rangle \\ B_n^{s\xi} |n + \frac{\xi-1}{2}\rangle \end{pmatrix}, \quad (8)$$

with coefficients (see [9, 41–43] for similar results)

$$A_n^{s\xi} = \begin{cases} \frac{\text{sgn}(n)}{\sqrt{2}}\sqrt{1 + \text{sgn}(n)\cos\theta_n^{s\xi}}, & n \neq 0, \\ (1 - \xi)/2, & n = 0, \end{cases} \quad (9)$$

$$B_n^{s\xi} = \begin{cases} \frac{\xi}{\sqrt{2}}\sqrt{1 - \text{sgn}(n)\cos\theta_n^{s\xi}}, & n \neq 0, \\ (1 + \xi)/2, & n = 0, \end{cases}$$

where  $\theta_n^{s\xi} = \arctan(\hbar\omega\sqrt{|n|}/\Delta_{s\xi})$ , that is,  $\cos\theta_n^{s\xi} = \Delta_{s\xi}/|E_n^{s\xi}|$ . Note that  $A_n^{s\xi}$  and  $B_n^{s\xi}$  can eventually be written as  $\cos(\theta_n^{s\xi}/2)$  or  $\sin(\theta_n^{s\xi}/2)$ , depending on  $\text{sgn}(n)$ .

In Figure 1 we plot the low energy spectra of silicene, given by (7), as a function of the external electric field  $\Delta_z$ , together with the charge neutrality (critical) points  $\Delta_z^{(0)} = \pm|\Delta_{\text{so}}|$  (marked by vertical dashed lines) at which the TPT takes place.

### B. HgTe/CdTe quantum wells

In [44–47] it was shown that quantum spin Hall effect can be realized in mercury telluride-cadmium telluride semiconductor quantum wells. Similar effects were also predicted in Type-II semiconductor quantum wells made from InAs/GaSb/AlSb [48]. The surface states in these 3D topological insulators can be described by a 2D modified effective Dirac Hamiltonian

$$H = \begin{pmatrix} H_+ & 0 \\ 0 & H_- \end{pmatrix}, \quad H_s(\mathbf{k}) = \epsilon_0(\mathbf{k})\tau_0 + \mathbf{d}_s(\mathbf{k}) \cdot \boldsymbol{\tau}, \quad (10)$$

where  $s = \pm 1$  is the spin and  $H_-(\mathbf{k}) = H_+^*(-\mathbf{k})$  (temporarily reversed). The expansion of  $H_s(\mathbf{k})$  about the center  $\Gamma$  of the first Brillouin zone gives [45]

$$\epsilon_0(\mathbf{k}) = \gamma - \delta\mathbf{k}^2, \quad \mathbf{d}_s(\mathbf{k}) = (\alpha s k_x, \alpha k_y, \mu - \beta\mathbf{k}^2), \quad (11)$$

where  $\alpha, \beta, \gamma, \delta$  and  $\mu$  are expansion parameters that depend on the heterostructure (the HgTe layer thickness  $\lambda$ ). The most important one is the mass or gap parameter  $\mu$ , which changes sign at a critical HgTe layer thickness  $\lambda_c$  when going from the normal ( $\lambda < \lambda_c$  or  $\mu/\beta < 0$ ) to the inverted ( $\lambda > \lambda_c$  or  $\mu/\beta > 0$ ) regime [49]. Typical values of these parameters for different HgTe layer thickness (below and above  $\lambda_c$ ) can be found in [49] and in Table II ( $\gamma$  can be neglected).

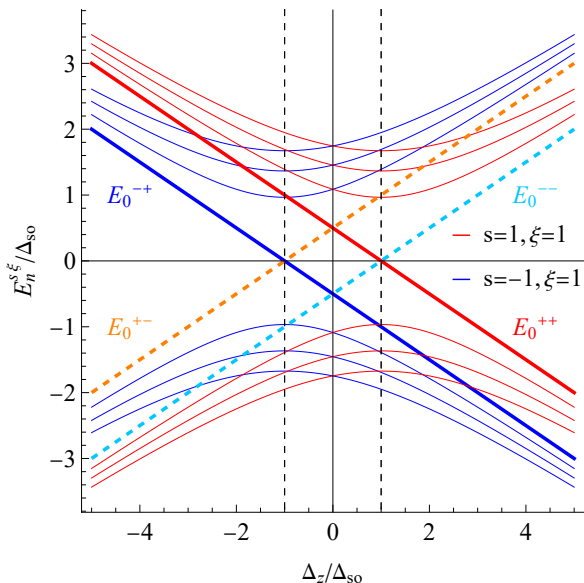


FIG. 1. Low energy spectra of silicene as a function of the external electric potential  $\Delta_z$  (in  $\Delta_{so}$  units) for  $B = 0.05$  T. Landau levels  $n = \pm 1, \pm 2$  and  $\pm 3$  [valence (-) and conduction (+)], at valley  $\xi = 1$ , are represented by thin solid lines, blue for  $s = -1$  and red for  $s = 1$  (for the other valley we simply have  $E_n^{s,-\xi} = E_n^{-s,\xi}$ ). The edge states  $n = 0$  are represented by thick lines at both valleys: solid at  $\xi = 1$  and dashed at  $\xi = -1$ . Vertical dashed gray lines indicate the charge neutrality points separating band insulator ( $|\Delta_z| > \Delta_{so}$ ) from topological insulator ( $|\Delta_z| < \Delta_{so}$ ) phases.

$\lambda$ (nm)	$\alpha$ (meV·nm)	$\beta$ (meV·nm <sup>2</sup> )	$\delta$ (meV·nm <sup>2</sup> )	$\mu$ (meV)
5.5	387	-480	-306	9
6.1	378	-553	-378	-0.15
7.0	365	-686	-512	-10

TABLE II. Material parameters for HgTe/CdTe quantum wells with different HgTe layer thicknesses  $\lambda$  [49].

The energy of the two bands is

$$\epsilon_{\pm}(\mathbf{k}) = \epsilon_0(\mathbf{k}) \pm \sqrt{\alpha^2 \mathbf{k}^2 + (\mu - \beta \mathbf{k}^2)^2}. \quad (12)$$

The TKNN formula (2) for  $\mathbf{d}_s(\mathbf{k})$  provides the Chern number

$$\mathcal{C}_s = s[\text{sign}(\mu) + \text{sign}(\beta)], \quad (13)$$

where we have integrated on the whole plane, as corresponds to the continuum limit. According to Table II,  $\beta$  does not change sign and, therefore, the topological phase transition occurs when  $\mu$  changes sign, as already mentioned. In reference [49], the normal and inverted regimes are equivalently given by the sign of  $\mu/\beta$ .

Using again the general prescription (3), the minimal coupling with a perpendicular magnetic field  $B$  now re-

sults in

$$H_{\pm} = \begin{pmatrix} \gamma + \mu - \frac{(\delta + \beta)(2N + 1)}{\ell_B^2} & \frac{\sqrt{2}\alpha}{\ell_B} a \\ \frac{\sqrt{2}\alpha}{\ell_B} a^\dagger & \gamma - \mu - \frac{(\delta - \beta)(2N + 1)}{\ell_B^2} \end{pmatrix},$$

$$H_{\pm} = \begin{pmatrix} \gamma + \mu - \frac{(\delta + \beta)(2N + 1)}{\ell_B^2} & -\frac{\sqrt{2}\alpha}{\ell_B} a^\dagger \\ -\frac{\sqrt{2}\alpha}{\ell_B} a & \gamma - \mu - \frac{(\delta - \beta)(2N + 1)}{\ell_B^2} \end{pmatrix}, \quad (14)$$

with  $N = a^\dagger a$ . A Zeeman term contribution

$$H_s^Z = -\frac{s}{2} B \mu_B \left( g_e \frac{\tau_0 + \tau_z}{2} + g_h \frac{\tau_0 - \tau_z}{2} \right) \quad (15)$$

can also be added to the Hamiltonian, with  $\mu_B \simeq 0.058$  meV/T the Bohr magneton and  $g_{e,h}$  the effective (out-of-plane)  $g$ -factors for electrons and holes (conduction and valence bands).

Using (Fock state) eigenvectors  $||n\rangle$  of the (Landau level) number operator  $N = a^\dagger a$ , one can analytically obtain the eigenspectrum

$$E_n^s = \gamma - \frac{2\delta|n| - s\beta}{\ell_B^2} - s \frac{g_e + g_h}{4} B \mu_B \quad (16)$$

$$+ \text{sgn}(n) \sqrt{\frac{2\alpha^2|n|}{\ell_B^2} + \left( \mu - \frac{2\beta|n| - s\delta}{\ell_B^2} - s \frac{g_e - g_h}{4} B \mu_B \right)^2},$$

for LL index  $n = \pm 1, \pm 2, \pm 3, \dots$  [valence (-) and conduction (+)], and

$$E_0^s = \gamma - s\mu - \frac{\delta - s\beta}{\ell_B^2} - B \mu_B \left( \frac{s+1}{4} g_h + \frac{s-1}{4} g_e \right), \quad (17)$$

for the edge states  $n = 0$ ,  $s = \pm 1$ . These eigenvalues coincide with those in [17, 50, 51] for the identification  $s = \{-1, 1\} = \{\uparrow, \downarrow\}$ .

The corresponding eigenvectors are

$$|n\rangle_s = \begin{pmatrix} A_n^s | |n| - \frac{s+1}{2} \rangle \\ B_n^s | |n| + \frac{s-1}{2} \rangle \end{pmatrix}, \quad (18)$$

with coefficients

$$A_n^s = \begin{cases} \frac{\text{sgn}(n)}{\sqrt{2}} \sqrt{1 + \text{sgn}(n) \cos \vartheta_n^s}, & n \neq 0, \\ (1-s)/2, & n = 0, \end{cases} \quad (19)$$

$$B_n^s = \begin{cases} \frac{s}{\sqrt{2}} \sqrt{1 - \text{sgn}(n) \cos \vartheta_n^s}, & n \neq 0, \\ (1+s)/2, & n = 0, \end{cases}$$

where

$$\vartheta_n^s = \arctan \left( \frac{\sqrt{2|n|} \alpha / \ell_B}{\mu - \frac{2\beta|n| - s\delta}{\ell_B^2} - s \frac{g_e - g_h}{4} B \mu_B} \right). \quad (20)$$

As for the graphene analogues in (10), the coefficients  $A_n^s$  and  $B_n^s$  can eventually be written as sine and cosine of half angle, depending on  $\text{sgn}(n)$ .

According to (17), the band inversion for edge states occurs when

$$E_0^+ = E_0^- \Rightarrow B_{\text{inv}} = \frac{\mu}{e\beta/\hbar - \mu_B(g_e + g_h)/4}, \quad (21)$$

which gives the critical magnetic field  $B_c$  which separates the QSH and QH regimes [51]. For example, for the material parameters in Table II corresponding to a QW thickness  $\lambda = 7.0$  nm and  $g$ -factors  $g_e = 22.7$ ,  $g_h = -1.21$ , one obtains  $B_{\text{inv}} \simeq 7.4$  T. See also Figure 2 for a graphical representation of this band inversion.

From now on we shall discard Zeeman coupling for the sake of convenience since our main conclusions remain qualitatively equivalent. We address the interested reader to the Supplemental Material [52] where we reproduce some results of Reference [17] for non-zero Zeeman coupling and contrast with the zero Zeeman coupling case.

We shall use a linear fit

$$\begin{aligned} \mu(\lambda) &= 77.31 - 12.53\lambda, \\ \alpha(\lambda) &= 467.49 - 14.65\lambda, \\ \beta(\lambda) &= 283.58 - 138.16\lambda, \\ \delta(\lambda) &= 458.46 - 138.25\lambda, \end{aligned} \quad (22)$$

of the material parameters in Table II as a function of the HgTe layer thickness  $\lambda$  (dimensionless units and  $\lambda$  in nm units). In all cases the coefficient of determination is  $R^2 > 0.99$ . Looking at  $\mu(\lambda)$  in (22), we can obtain an estimation of the critical HgTe thickness at which the topological phase transition occurs as

$$\mu = 0 \Rightarrow \lambda_c = 6.17 \text{ nm}. \quad (23)$$

In Figure 2 we plot the low energy spectra given by (16) and (17) as a function of the HgTe layer thickness  $\lambda$ , where we have extrapolated the linear fit (22) to the interval [4 nm, 8 nm]. When neglecting Zeeman coupling, the band inversion for edge states (21) occurs for  $B = \hbar\mu/(e\beta)$  which, using the linear fit (22), provides a relation

$$\lambda_{\text{inv}}(B) = \frac{368.31 - 2.05B}{59.7 - B} \quad (24)$$

between the applied magnetic field  $B$  (in Tesla) and the HgTe layer thickness  $\lambda_{\text{inv}}(B)$  (in nanometers) at which the band inversion  $E_0^+ = E_0^-$  takes place. Note that  $\lambda_{\text{inv}}(B) \simeq \lambda_c = 6.17$  nm for low  $B \ll 1$  T, and that  $E_0^+ = E_0^- \simeq 0$  meV at this point as shows Figure 2.

### C. Phosphorene as an anisotropic material

The physics of phosphorene has been extensively studied [53–67]. There are several approaches to the low energy Hamiltonian of phosphorene in the literature. Rudenko *et al.* [68] and Ezawa [69] propose a four-band and five-neighbors tight-binding model later simplified to

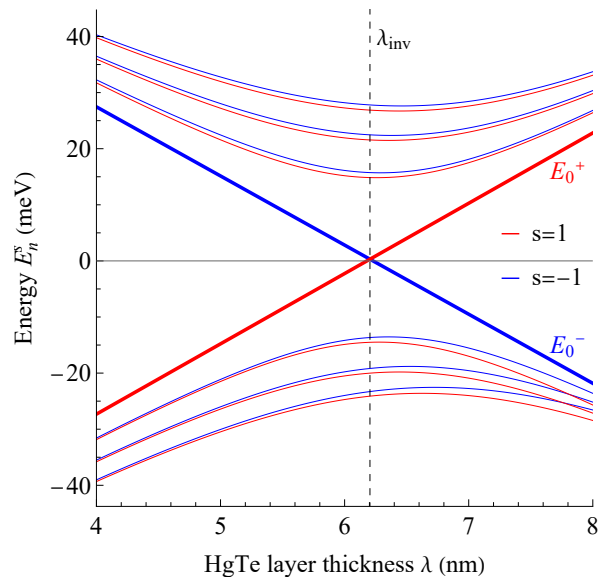


FIG. 2. Low-energy spectra  $E_n^s$  of a HgTe/CdTe quantum well as a function of the HgTe layer thickness  $\lambda$  for  $B = 0.5$  T. Landau levels  $n = \pm 1, \pm 2, \pm 3$  [valence (-) and conduction (+)] are represented by thin solid lines, blue for spin  $s = -1$  and red for  $s = 1$ . Edge states ( $n = 0$ ) are represented by thick lines. A vertical dashed black line indicates the HgTe thickness  $\lambda_{\text{inv}}(0.5) = 6.20$  nm  $\simeq \lambda_c$  where the band inversion for edge states occurs for  $B = 0.5$  T according to (24).

two-bands [69]. Several approximations of this two-band model have been used in [13, 70–72]. We shall choose for our study the Hamiltonian

$$H = \begin{pmatrix} E_c + \alpha_x k_x^2 + \alpha_y k_y^2 & \gamma k_x \\ \gamma k_x & E_v - \beta_x k_x^2 - \beta_y k_y^2 \end{pmatrix}. \quad (25)$$

proposed by Zhou and collaborators [13]. This corresponds to a Bloch Hamiltonian (1) with

$$\begin{aligned} \epsilon_0(\mathbf{k}) &= \frac{E_c + E_v + (\alpha_x - \beta_x)k_x^2 + (\alpha_y - \beta_y)k_y^2}{2}, \\ \mathbf{d}(\mathbf{k}) &= \left( \gamma k_x, 0, \frac{E_c - E_v + (\alpha_x + \beta_x)k_x^2 + (\alpha_y + \beta_y)k_y^2}{2} \right), \end{aligned} \quad (26)$$

The Hamiltonian (25) provides a trivial Chern number (2), even in the presence of a tunable perpendicular constant electric field (see below), which means that monolayer phosphorene does not have a topological phase *per se*. It has been shown that topological transitions can be induced in phosphorene when rapidly driven by in-plane time-periodic laser fields [73]; these are called in general “Floquet topological insulators” (see e.g. [74–76]), but we shall not consider this possibility here. Although phosphorene is not a topological material, we will see in Sec. III C that the critical magneto-optical properties (e.g., minimum transmittance) observed for silicene and HgTe

QWs are still valid in phosphorene when closing the energy gap through an external electric field. Another possibility to modify the energy gap could be by applying strain [60, 70] (see later in Sec. III C).

The material parameters of phosphorene can be written in terms of conduction (c) and valence (v) effective masses as (see [13] for more information)

$$\alpha_{x,y} = \frac{\hbar^2}{2m_{cx,cy}}, \quad \beta_{x,y} = \frac{\hbar^2}{2m_{vx,vy}}, \quad (27)$$

with

$$\begin{aligned} m_{cx} &= 0.793m_e, & m_{cy} &= 0.848m_e, \\ m_{vx} &= 1.363m_e, & m_{vy} &= 1.142m_e, \end{aligned} \quad (28)$$

and  $m_e$  is the free electron mass. Conduction and valence band edge energies are  $E_c = 0.34$  eV and  $E_v = -1.18$  eV, so that the energy gap is  $E_g = E_c - E_v = 1.52$  eV. The interband coupling parameter is  $\gamma = -0.523$  eV·nm.

When coupling to an external perpendicular magnetic field, the anisotropic character of phosphorene slightly modifies Peierls' substitution (3), which now adopts the following form

$$k_x \rightarrow \frac{P_x}{\hbar} = \frac{a^\dagger + a}{\sqrt{2}\alpha_{yx}\ell_B}, \quad k_y \rightarrow \frac{P_y}{\hbar} = \frac{\alpha_{yx}(a^\dagger - a)}{i\sqrt{2}\ell_B}, \quad (29)$$

with  $\alpha_{yx} = \left(\frac{m_{cy}}{m_{cx}}\right)^{1/4}$ . Therefore, applying this prescription to (25), the final Hamiltonian can be written as

$$\begin{aligned} H &= \hbar\omega_\gamma(a + a^\dagger)\tau_x + [E_c + \hbar\omega_c(a^\dagger a + 1/2)] \frac{\tau_0 + \tau_z}{2} \\ &+ [E_v - \hbar\omega_v(a^\dagger a + 1/2) - \hbar\omega'(a^2 + a^{\dagger 2})] \frac{\tau_0 - \tau_z}{2}, \end{aligned} \quad (30)$$

in terms of the annihilation (and creation  $a^\dagger$ ) operator

$$a = \sqrt{\frac{m_{cy}\omega_c}{2\hbar}} \left( y - y_0 + i \frac{\hat{p}_y}{m_{cy}\omega_c} \right), \quad (31)$$

in analogy to (4), where some effective frequencies have been defined as

$$\begin{aligned} \omega_c &= \frac{eB}{\sqrt{m_{cx}m_{cy}}}, & \omega_\gamma &= \frac{\gamma}{\sqrt{2\hbar\alpha_{yx}\ell_B}}, \\ \omega_v &= (r_x + r_y)\omega_c, & \omega' &= (r_x - r_y)\omega_c/2, \end{aligned} \quad (32)$$

with

$$r_x = \frac{m_{cx}}{2m_{vx}}, \quad r_y = \frac{m_{cy}}{2m_{vy}}.$$

As we did for silicene, we shall also consider here the application of a perpendicular electric field to the phosphorene sheet in the usual form [77]  $\hat{H}_\Delta = \Delta_z \tau_z$ , with  $\Delta_z$  the on-site electric potential. Unlike for silicene and HgTe QWs, the diagonalization of the phosphorene Hamiltonian (30) has to be done numerically [30].

Note that the Hamiltonian (30) preserves the parity  $\pi(n, s) = e^{i\pi n_s}$  of the state  $|\mathbf{n}\rangle_s$ , with  $n_s = n + (s + 1)/2$  (see e.g. [30]). This means that the matrix elements  ${}_s\langle \mathbf{n} | H | \mathbf{n}' \rangle_{s'} \propto \delta_{\pi(n,s), \pi(n',s')}$  are zero between states of different parity. Therefore, this parity symmetry helps in the diagonalization process and any (non-degenerate) eigenstate of  $H$  has a definite parity. The Hamiltonian eigenstates can now be written as

$$|\psi_l\rangle = \sum_{n,s} c_{n,s}^{(l)} |\mathbf{n}\rangle_s, \quad (33)$$

where  $l \in \mathbb{Z}$  denotes the LL index ( $l > 0$  for conduction and  $l \leq 0$  for valence band). The sum  $\sum_{n,s}$  is constrained to  $\pi(n, s) = \pm 1$ , depending on the even (+) and odd (−) parity of  $k$ . The coefficients  $c_{n,s}^{(k)}$  are obtained by numerical diagonalization of the Hamiltonian matrix, which is truncated to  $n \leq N$ , with  $N$  large enough to achieve convergent results for given values of the magnetic and electric fields. In particular, we have used Fock states with  $N \leq 1000$  to achieve convergence (with error tolerance  $\leq 10^{-15}$  eV) for  $B = 0.5$  T in the six first Hamiltonian eigenvalues in the range  $-1.55 \leq \Delta_z \leq -1.49$  eV. The resulting spectrum, as a function of the electric field potential  $\Delta_z$ , can be seen in Figure 3 for a magnetic field of  $B = 0.5$  T (higher magnetic fields need less Fock states to achieve convergence). The vertical dashed line gives the point  $\Delta_z = -1.520$  eV at which the electric potential equals minus the energy gap  $E_g = E_c - E_v = 1.52$  eV of phosphorene. This is not really a critical point in the same sense as  $\Delta_z^{(0)} = \Delta_{so} = 4.2$  meV for silicene and  $\lambda_c = 6.17$  nm for HgTe QWs, since phosphorene as such (as already said) does not display a topological phase. However, we will see in Section III C that the phosphorene transmittance still presents a minimum at  $\Delta_z^{(0)} = -1.523$  eV, which closes the energy gap  $E_g = 1.52$  eV at low magnetic fields.

It is also interesting to note that the LLs of phosphorene are degenerated in pairs for an electric potential below  $\Delta_z \simeq -1.53$  eV. Namely, we obtain numerically that  $|E_l^{\text{even}} - E_{l+1}^{\text{odd}}| \leq 10^{-4}$  eV for all  $\Delta_z < -1.53$  eV and  $l = -6, -4, -2, 0, 2, 4$  as it shows the left hand side of Figure 3. This energy degeneracy will influence the conductivity as well.

### III. MAGNETO-OPTICAL CONDUCTIVITY

The magneto-optical conductivity tensor  $\sigma$  of a 2D electron system in a perpendicular magnetic field  $B$  and an oscillating electric field of frequency  $\Omega$ , can be obtained from Kubo-Greenwood formula [32, 78, 79] in the Landau-level representation:

$$\sigma_{ij}(\Omega, B) = \frac{i\hbar}{2\pi\ell_B^2} \sum_{\mathbf{n}, \mathbf{m}} \frac{f_m - f_n}{E_n - E_m} \frac{\langle \mathbf{m} | j_i | \mathbf{n} \rangle \langle \mathbf{n} | j_j | \mathbf{m} \rangle}{\hbar\Omega + E_m - E_n + i\eta}, \quad (34)$$

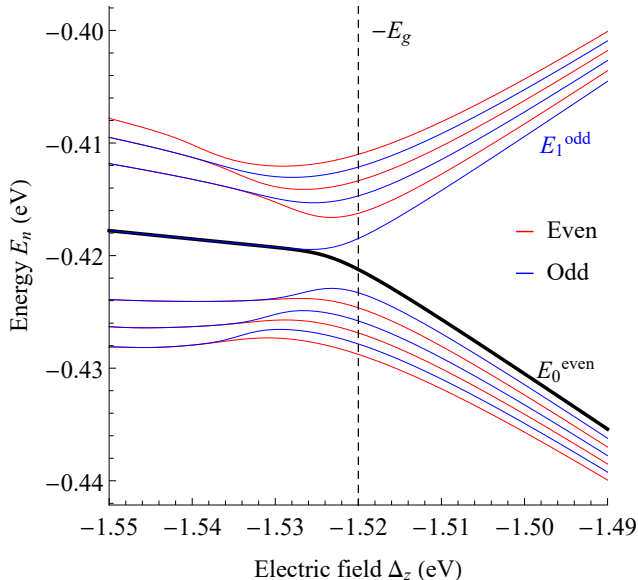


FIG. 3. Low energy spectra  $E_l$  of phosphorene as function of the electric field potential  $\Delta_z$  for thirteen Hamiltonian eigenstates  $l = -6, \dots, 0, \dots, 6$  and a magnetic field  $B = 0.5$  T. Valence and conduction band states of even (odd) parity  $l = \pm 2, \pm 4, \pm 6$  ( $n = \pm 1, \pm 3, \pm 5$ ) are represented in red (blue) color. The edge state  $E_0^{\text{even}}$  is represented by a thick black line. The vertical dashed black line is the point  $\Delta_z = -E_g = -1.520$  eV at which the electric potential equals the energy gap of phosphorene.

where

$$\mathbf{j} = \frac{ie}{\hbar} [H, \mathbf{r}] = \frac{e}{\hbar} \nabla_{\mathbf{k}} H \quad (35)$$

is the current operator, with  $\mathbf{r} = (x, y)$  and  $\nabla_{\mathbf{k}} = (\partial_{k_x}, \partial_{k_y})$  [the minimal coupling prescription (3) is understood under external electromagnetic fields], and  $f_n = 1/(1 + \exp[(E_n - \mu_F)/(k_B T)])$  is the Fermi distribution function at temperature  $T$  and chemical potential  $\mu_F$ . In the zero temperature limit, the Fermi function  $f_n$  is replaced by the Heaviside step function  $\Theta(\mu_F - E_n)$ , which enforces the Pauli exclusion principle for optical transitions (they are allowed between occupied and unoccupied states). The parameter  $\eta$  is a small residual scattering rate of charge carriers and, although the exact shape of  $\sigma_{ij}$  would depend on the details of the scattering mechanisms, using a constant  $\eta$  gives a good, qualitative description of the essential mechanisms relevant for magneto-optical experiments. In  $\sum_{\mathbf{n}}$  of eq. (34) it is also implicit the sum over spin  $s$  and valley  $\xi$ , besides the LL index  $n$  (for graphene, there is a twofold spin and valley degeneracy, so that the extra sum just contributes with a degeneracy factor  $g = 4$ ). We shall measure  $\sigma_{ij}$  in units of the conductance quantum  $\sigma_0 = e^2/h = 38.8 \mu\text{S}$  [78] and renormalize the currents as  $\bar{\mathbf{j}} = \mathbf{j}/(e/\hbar) = \nabla_{\mathbf{k}} H$ ,

so that

$$\frac{\sigma_{ij}(\Omega, B)}{\sigma_0} = \frac{i}{\ell_B^2} \sum_{\mathbf{n}, \mathbf{m}} \frac{f_m - f_n}{E_n - E_m} \frac{\langle \mathbf{m} | \bar{j}_i | \mathbf{n} \rangle \langle \mathbf{n} | \bar{j}_j | \mathbf{m} \rangle}{\hbar\Omega + E_m - E_n + i\eta}, \quad (36)$$

We shall analyze the transmittance and Faraday rotation of linearly polarized light of frequency  $\Omega$  for normal incidence on the 2D material, where the electric fields of incident ( $\mathbf{E}^i$ ) and transmitted ( $\mathbf{E}^t$ ) waves are related through the conductivity tensor  $\boldsymbol{\sigma}$  by the formula [80–82]

$$\mathbf{E}^t = (\mathbf{I} + \frac{1}{2} Z_0 \boldsymbol{\sigma})^{-1} \cdot \mathbf{E}^i, \quad (37)$$

where  $Z_0 = 2\alpha/\sigma_0$  is the vacuum impedance ( $\alpha = 1/137$  is the fine-structure constant) and  $\mathbf{I}$  denotes the  $2 \times 2$  identity matrix. We also assume that the incident field is linearly polarized in the  $x$  axis, that is  $\mathbf{E}^i = (E_x^i, 0)$ . From here, the transmittance  $\mathcal{T}$  and the Faraday rotation angle  $\Theta_F$  (in degrees) are [2, 82]

$$\mathcal{T} = \frac{1}{2} (|t_+|^2 + |t_-|^2) \simeq 1 - Z_0 \text{Re}(\sigma_{xx}), \quad (38)$$

$$\Theta_F = \frac{1}{2} (\arg(t_+) + \arg(t_-)) \simeq \frac{180}{2\pi} Z_0 \text{Re}(\sigma_{xy}), \quad (39)$$

where  $t_{\pm} = E_{\pm}^t/|\mathbf{E}^i|$  are the transmission amplitudes in the circular polarization basis [83, 84] or chiral basis [85],  $\mathbf{E}_{\pm}^t = E_x^t \pm iE_y^t$ .  $\text{Re}(\sigma_{ij})$  means the real part of  $\sigma_{ij}$  and  $\arg(t_{\pm})$  the complex argument. We have also provided the approximate expressions in the limit of weak absorption for isotropic materials. Note that, in this case, according to (39), the absorption peaks of  $\text{Re}[\sigma_{xx}(\Omega)]$  shown in Figure 6, correspond to dips of the transmittance  $\mathcal{T}$ . Silicene and HgTe QWs have both longitudinal conductivities equal  $\sigma_{xx} = \sigma_{yy}$ , but this symmetry is broken for anisotropic materials like phosphorene [10, 85] (see later on Section III C). Therefore, in phosphorene, we cannot apply the approximation in eq.(39) and we have to use the strict equality.

In the circular polarization (right- and left-handed  $\pm$ ) basis, the conductivity is given by  $\sigma_{\pm} = \sigma_{xx} \pm i\sigma_{xy}$ , and the absorptive part is therefore  $\text{Re}(\sigma_{\pm}) = \text{Re}(\sigma_{xx}) \mp \text{Im}(\sigma_{xy})$ . In the Supplemental Material [52] we provide extra plots for the silicene conductivity under circular polarization which reproduce the results of [9].

#### A. Magneto-optical properties of graphene analogues

The current operator (35) for this case is  $\mathbf{j} = (j_x, j_y) = ev(\xi\tau_x, \tau_y)$ . The matrix elements

$$\begin{aligned} \langle \mathbf{m} | \tau_x | \mathbf{n} \rangle_{s\xi} &= A_m^{s\xi} B_n^{s\xi} \delta_{|m|-\xi, |n|} + A_n^{s\xi} B_m^{s\xi} \delta_{|m|+\xi, |n|}, \\ \langle \mathbf{m} | \tau_y | \mathbf{n} \rangle_{s\xi} &= -iA_m^{s\xi} B_n^{s\xi} \delta_{|m|-\xi, |n|} + iA_n^{s\xi} B_m^{s\xi} \delta_{|m|+\xi, |n|}, \end{aligned} \quad (40)$$

provide the familiar selection rules  $|n| = |m| \pm 1$  for LL transitions. Plugging (40) into the general expression (36) we obtain the magneto-optical conductivity for

graphene analogues. In Figure 4 we plot the real and imaginary parts of the conductivity tensor components  $\sigma_{ij}$  (in  $\sigma_0 = e^2/h$  units) of silicene as a function of the polarized light frequency  $\Omega$  at three different electric potentials  $\Delta_z = 0.5\Delta_{so}, \Delta_{so}, 1.5\Delta_{so}$  around the critical point  $\Delta_z^{(0)} = \Delta_{so}$ , for a magnetic field  $B = 0.05$  T and some representative values of the chemical potential  $\mu_F = 2.1$  meV, temperature  $T = 1$  K and scattering rate  $\eta = 0.1$  meV. For  $\hbar\Omega \in [0, 20]$  meV, we achieve convergence with 100 LLs, that is, restricting the sum in (36) as  $\sum_{n=-\infty}^{\infty} \rightarrow \sum_{n=-100}^{100}$ . More explicitly, for the parameters mentioned above,

$$\left| \sum_{n=-100}^{n=100} \sigma_{ij} - \sum_{n=-99}^{n=99} \sigma_{ij} \right| / \sigma_0 \leq \begin{cases} 10^{-5} & \text{if } \sigma_{ij} = \text{Re}(\sigma_{xx}), \\ 10^{-15} & \text{if } \sigma_{ij} = \text{Re}(\sigma_{xy}), \\ 10^{-3} & \text{if } \sigma_{ij} = \text{Im}(\sigma_{xx}), \\ 10^{-14} & \text{if } \sigma_{ij} = \text{Im}(\sigma_{xy}). \end{cases} \quad (41)$$

Each peak on the plot of the conductivity  $\text{Re}(\sigma_{xx})$  against  $\hbar\Omega$  represents an electron transition between two LLs  $n, m$  connected by the selection rules  $|n| = |m| \pm 1$  and generally arranged above and below the Fermi level  $\mu_F$ ; this latter constrain comes from the Fermi functions factor  $(f_m - f_n)$  of the Kubo formula (34), which becomes a step function at low temperatures. For more information, see the Supplemental Material [52] where we illustrate these electron transitions by arrows in the energy spectrum in an animated gif. The value of  $\hbar\Omega$  where a peak of the conductivity occurs coincides with the energy difference  $(E_n - E_m)$  of the LL transition  $n \rightarrow m$ . This is clear by looking at the denominator of the Kubo formula. For example, the two main peaks of  $\text{Re}(\sigma_{xx})$  at low frequencies  $\hbar\Omega \in [2, 6]$  meV in Figure 4 correspond to the transitions  $0 \rightarrow 1$  for spin and valley  $s = \xi = 1$  and  $s = \xi = -1$  (purple and green arrows in the animated gif of [52]). The other conductivity peaks located at higher frequencies correspond to electron transitions between higher LLs and different spin/valley combinations according to (40). When the external electric field  $\Delta_z$  is such that the energy differences of the two main peaks are the same, that is, when  $E_1^{++} - E_0^{++}$  is equal to  $E_1^{--} - E_0^{--}$ , both peaks merge into a bigger one. Using the silicene spectrum energy equation (7), we find that this condition is fulfilled at the critical point  $\Delta_z = \Delta_{so}$  for any value of the magnetic field  $B$ . This result implies that we can extract information of the TPT occurring at  $\Delta_z^{(0)} = \Delta_{so}$  by looking at the conductivity  $\text{Re}(\sigma_{xx})$  plot for different values of  $\Delta_z$ .

To be more specific, in Figure 5 we represent the behavior of the two observables given in (39), that is, the Faraday angle  $\Theta_F$  and the transmittance  $\mathcal{T}$ , as a function of the polarized light frequency  $\Omega$  around the critical point  $\Delta_z^{(0)} = \Delta_{so} = 4.2$  meV. We focus on the frequency interval  $\hbar\Omega \in [2, 6]$  meV where the main peaks (transition  $0 \rightarrow 1$ ) in Figure 4 are located. We find an absolute minimum of the transmittance  $\mathcal{T}_0 = 0.704$  at the critical point  $\Delta_z^{(0)} = \Delta_{so}$  and  $\hbar\Omega = 4.06$  meV. This “mini-

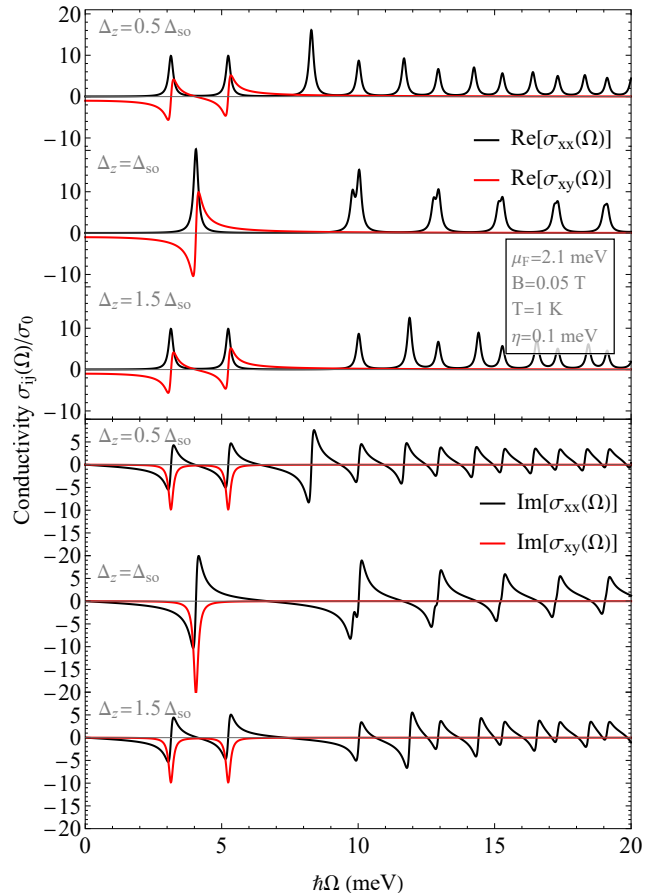


FIG. 4. Real and imaginary parts of the longitudinal  $\sigma_{xx}$  and transverse Hall  $\sigma_{xy}$  magneto-optical conductivities in a silicene monolayer under three different electric potentials  $\Delta_z = 0.5\Delta_{so}, \Delta_{so}, 1.5\Delta_{so}$ , as a function of the polarized light frequency  $\Omega$  and in  $\sigma_0 = e^2/h$  units. We set the conductivity parameters as  $\mu_F = 2.1$  meV,  $B = 0.05$  T,  $T = 1$  K and  $\eta = 0.1$  meV.

mal” behavior does not depend on the particular values of magnetic field, chemical potential and temperature, which only change the actual value of  $\mathcal{T}_0$  and  $\hbar\Omega$  of the peak. Actually, the minimum peaks in the transmittance plot are related to the maximum peaks of the absorbance  $\text{Re}(\sigma_{xx})$ , according to equation (39). The Faraday angle at the critical point (black curve in Figure 5) changes sign at the minimum transmittance point  $\hbar\Omega = 4.06$  meV, a behavior that can also be extrapolated to other 2D materials (see later for HgTe QWs and phosphorene). In fact, each peak of the transmittance in Figure 5 coincides in frequency with an inflection point of the Faraday angle, where it attains a value of 0 degrees.

Changing the chemical potential  $\mu_F$  locks/unlocks other electronic transitions, so we would see different peaks in the conductivity and transmittance plots (see e.g., [10]). Increasing the scattering rate  $\eta$  smoothes the peaks in the transmittance, so it would be more diffi-

cult to distinguish when they overlap. We have chosen values of  $\eta$  approximately an order of magnitude below the frequency of the conductivity peaks, for which the resolution is fine.

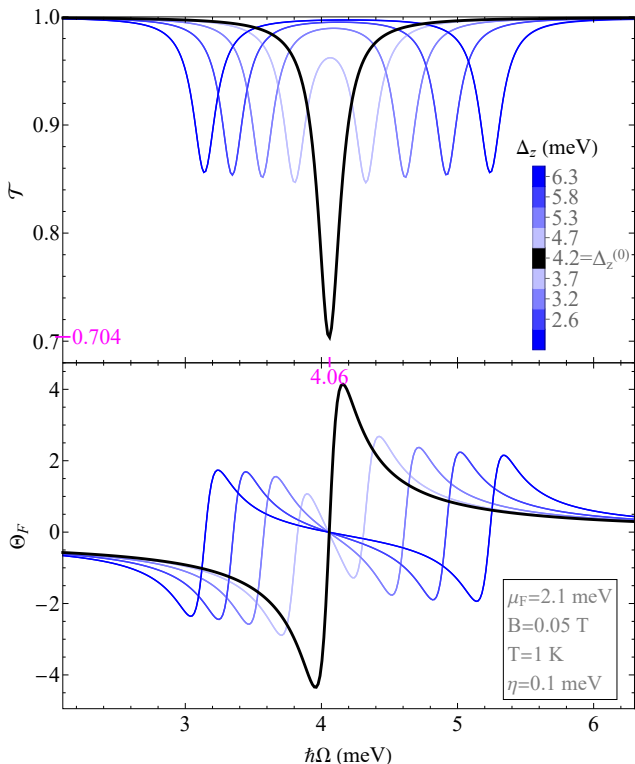


FIG. 5. Transmittance  $\mathcal{T}$  and Faraday angle  $\Theta_F$  (in degrees) in a silicene monolayer as a function of the incident polarized light frequency  $\Omega$ , and for different electric fields below and above the critical frequency  $\Delta_z^{(0)} = \Delta_{so} = 4.2$  meV.  $\mathcal{T}$  and  $\Theta_F$  are symmetric about  $\Delta_z^{(0)}$ . We set the conductivity parameters as  $\mu_F = 2.1$  meV,  $B = 0.05$  T,  $T = 1$  K and  $\eta = 0.1$  meV.

For completeness, in the Supplemental Material [52] we show several contour plots of the Faraday angle using different cross sections in the  $\{\hbar\Omega, \Delta_z, B, T, \mu_F\}$  parameter space.

### B. Magneto-optical properties of zincblende heterostructures

From the Hamiltonian (10), the current operator (35) for zincblende heterostructures is

$$\begin{aligned} j_x^s &= \frac{e}{\hbar} (s\alpha\tau_x - 2k_x(\beta\tau_z + \delta\tau_0)), \\ j_y^s &= \frac{e}{\hbar} (\alpha\tau_y - 2k_y(\beta\tau_z + \delta\tau_0)), \end{aligned} \quad (42)$$

which, after minimal coupling according to the general prescription (3), results in

$$\begin{aligned} j_x^s &= \frac{e}{\hbar} \left( s\alpha\tau_x - \sqrt{2} \frac{a^\dagger + a}{\ell_B} (\beta\tau_z + \delta\tau_0) \right), \\ j_y^s &= \frac{e}{\hbar} \left( \alpha\tau_y + i\sqrt{2} \frac{a^\dagger - a}{\ell_B} (\beta\tau_z + \delta\tau_0) \right). \end{aligned} \quad (43)$$

Note that, in fact,  $j_y^s$  does not depend on  $s$ . The current matrix elements for this case are

$$\begin{aligned} \langle \mathbf{m} | j_x^s | \mathbf{n} \rangle_s &= \frac{es\alpha}{\hbar} \Xi_{m,n}^{s,+} - \frac{\sqrt{2}e}{\hbar\ell_B} \Phi_{m,n}^{s,+}, \\ \langle \mathbf{m} | j_y^s | \mathbf{n} \rangle_s &= -i \frac{e\alpha}{\hbar} \Xi_{m,n}^{s,-} + i \frac{\sqrt{2}e}{\hbar\ell_B} \Phi_{m,n}^{s,-}, \end{aligned} \quad (44)$$

where

$$\begin{aligned} \Xi_{m,n}^{s,\pm} &= (A_m^s B_n^s \delta_{|m|-s,|n|} \pm A_n^s B_m^s \delta_{|m|+s,|n|}), \\ \Phi_{m,n}^{s,\pm} &= ((\delta + \beta) A_m^s A_n^s + (\delta - \beta) B_m^s B_n^s) \\ &\quad \times \left( \sqrt{|n|+1 + \frac{s-1}{2}} \delta_{|m|-1,|n|} \pm \sqrt{|n| - \frac{s+1}{2}} \delta_{|m|+1,|n|} \right). \end{aligned} \quad (45)$$

Despite the more involved structure of the current than for silicene, the corresponding matrix elements maintain the same familiar selection rules  $|n| = |m| \pm 1$  for LL transitions.

Inserting the matrix elements (40) into the general expression (36) we obtain the magneto-optical conductivity for general zincblende heterostructures. In Figure 6 we plot the real and imaginary parts of the conductivity tensor components  $\sigma_{ij}$  (in  $\sigma_0 = e^2/h$  units) of a HgTe QW as a function of the polarized light frequency  $\Omega$  at three different HgTe layer thicknesses  $\lambda = 5.50$  nm  $< \lambda_c$ ,  $\lambda = 6.17$  nm  $= \lambda_c$ , and  $\lambda = 7.00$  nm  $> \lambda_c$ , a magnetic field  $B = 0.5$  T and some representative values of the chemical potential  $\mu_F = 12.5$  meV, temperature  $T = 1$  K and scattering rate  $\eta = 0.5$  meV. For  $\hbar\Omega \in [0, 60]$  meV, we achieve convergence with 100 LLs, that is, restricting the sum in (36) as  $\sum_{n=-\infty}^{\infty} \rightarrow \sum_{n=-100}^{100}$ . More explicitly, for the parameters mentioned above,

$$\left| \sum_{n=-100}^{n=100} \sigma_{ij} - \sum_{n=-99}^{n=99} \sigma_{ij} \right| / \sigma_0 \leq \begin{cases} 10^{-5} & \text{if } \sigma_{ij} = \text{Re}(\sigma_{xx}), \\ 10^{-4} & \text{if } \sigma_{ij} = \text{Re}(\sigma_{xy}), \\ 10^{-3} & \text{if } \sigma_{ij} = \text{Im}(\sigma_{xx}), \\ 10^{-7} & \text{if } \sigma_{ij} = \text{Im}(\sigma_{xy}). \end{cases} \quad (46)$$

Similar to silicene, we can see in Figure 6 that there are multiple peaks in the absorptive components  $\text{Re}(\sigma_{xx})$  and  $\text{Im}(\sigma_{xy})$ , corresponding to transitions between occupied and unoccupied LLs obeying the selection rules  $|n| = |m| \pm 1$ . At lower frequencies  $\hbar\Omega \in [0, 30]$  meV, inside each curve of Figure 6, we find the main peaks corresponding to the transitions  $0 \rightarrow 1$  for spin  $s = 1$  and  $s = -1$ . Both peaks merge approximately at  $\lambda \simeq \lambda_c = 6.17$  nm. This is because the energy differences  $E_1^+ - E_0^+$  and  $E_1^- - E_0^-$  are similar when  $\lambda \simeq \lambda_c$  for low magnetic fields  $B \ll 1$  T,

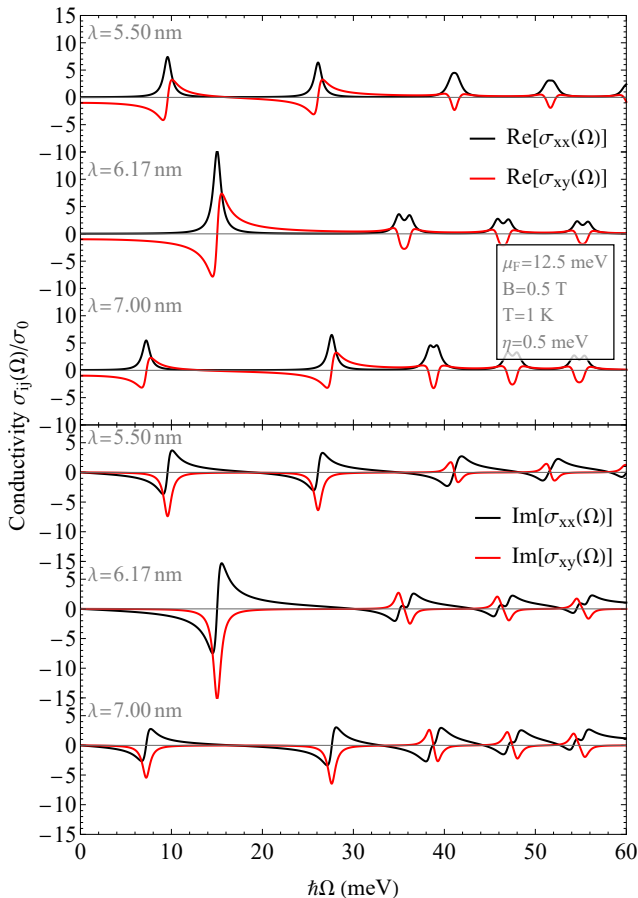


FIG. 6. Real and imaginary parts of the longitudinal  $\sigma_{xx}$  and transverse Hall  $\sigma_{xy}$  magneto-optical conductivities in a bulk HgTe QW of thickness  $\lambda = 5.50, 6.17, 7.00$  nm, as a function of the polarized light frequency  $\Omega$  and in  $\sigma_0 = e^2/h$  units. We set the conductivity parameters as  $\mu_F = 12.5$  meV,  $B = 0.5$  T,  $T = 1$  K and  $\eta = 0.5$  meV.

according to equations (16,17). In order to extend this result to higher values of the magnetic field, we insert the parameter fits (22) into the equation  $E_1^+ - E_0^+ = E_1^- - E_0^-$ , and solve it numerically for  $\lambda^* = \lambda^*(B)$ , obtaining the values represented by blue dots in Figure 7. These values fit the equation

$$\lambda_{\text{fit}}^*(B) = \frac{218.4 - 17.3B}{35.4 - 2.8B}, \quad (47)$$

which is represented as an orange curve in Figure 7. Consequently, only for small magnetic fields, we can infer the critical thickness  $\lambda_c$  where the TPT in HgTe QW occurs from the conductivity  $\text{Re}(\sigma_{xx})$  plot, that is,  $\lambda^* \simeq \lambda_c = 6.17$  nm for  $B \ll 1$  T.

The behavior of the Faraday angle and the transmittance as a function of the polarized light frequency  $\Omega$  around the critical HgTe layer thickness  $\lambda_c = 6.17$  nm (at which the material parameter  $\mu$  changes sign/Chern number) is shown in Figure 8. As for silicene, we focus

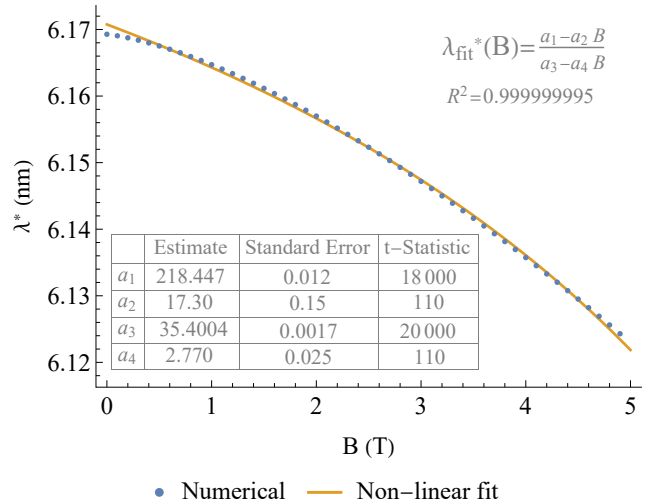


FIG. 7. Numerical solutions  $\lambda^*$  (in nm, blue dots) of the equation  $E_1^+ - E_0^+ = E_1^- - E_0^-$  (energies (16,17) of HgTe QW) for 50 different values of the external magnetic field  $B$ . In orange, non-linear fit (47) of the numerical values.

on the lower frequencies  $\hbar\Omega \in [0, 30]$  meV where the main peaks are located, and find again a minimum of the transmittance, this time  $\mathcal{T}_0 = 0.78$ , at the critical point  $\lambda_c$  and  $\hbar\Omega = 15.0$  meV. For this material, the “minimal” behavior does depend on the particular values of magnetic field, as we saw in equation (47). However, for small magnetic fields like  $B = 0.5$  T in Figure 8, the minimum of the transmittance still takes place at  $\lambda^* \simeq \lambda_c = 6.17$  nm. The Faraday angle at the critical point (black curve in Figure 8) changes sign at the minimum transmittance frequency  $\hbar\Omega = 15.0$  meV, a behavior shared with silicene.

For completeness, in the Supplemental Material [52] we show several contour plots of the Faraday angle using different cross sections in the  $\{\hbar\Omega, \lambda, B, T, \mu_F\}$  parameter space.

### C. Magneto-optical properties of phosphorene and effect of anisotropies

From the phosphorene Hamiltonian (25), the current operator (35) is

$$\begin{aligned} j_x^s &= \frac{e}{\hbar} (\gamma\tau_x + k_x(\tau_0(\alpha_x - \beta_x) + \tau_z(\alpha_x + \beta_x))), \\ j_y^s &= \frac{e}{\hbar} k_y (\tau_0(\alpha_y - \beta_y) + \tau_z(\alpha_y + \beta_y)), \end{aligned} \quad (48)$$

which, after minimal coupling, according to prescription (29), results in

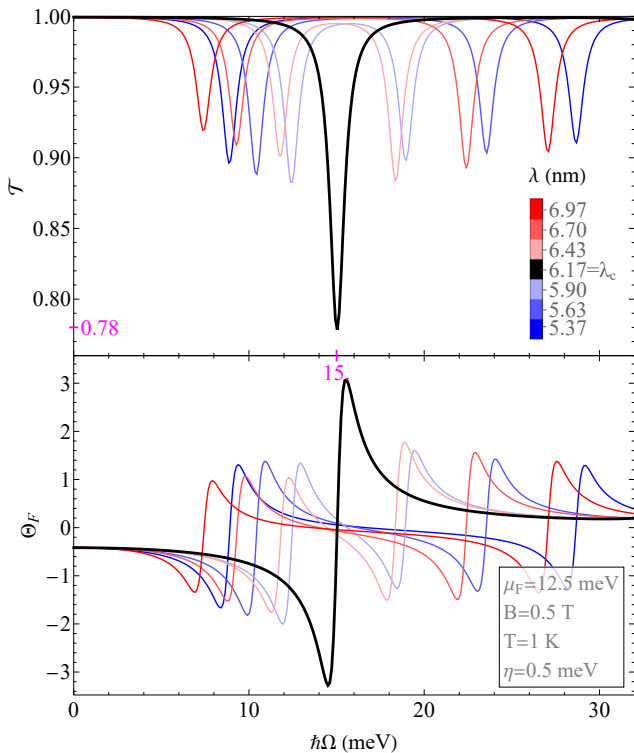


FIG. 8. Transmittance  $\mathcal{T}$  and Faraday angle  $\Theta_F$  (in degrees) in a bulk HgTe QW as a function of the polarized light frequency  $\Omega$ , and for thickness  $\lambda < \lambda_c$ ,  $\lambda = \lambda_c$  and  $\lambda > \lambda_c$ , with  $\lambda_c = 6.17$  nm (black line). We set the conductivity parameters as  $\mu_F = 12.5$  meV,  $B = 0.5$  T,  $T = 1$  K and  $\eta = 0.5$  meV.

$$j_x^s = \frac{e}{\hbar} \left( \gamma \tau_x + \frac{a^\dagger + a}{\sqrt{2} \alpha_{yx} \ell_B} (\tau_0 (\alpha_x - \beta_x) + \tau_z (\alpha_x + \beta_x)) \right),$$

$$j_y^s = \frac{e}{\hbar} \frac{\alpha_{yx} (a^\dagger - a)}{i \sqrt{2} \ell_B} (\tau_0 (\alpha_y - \beta_y) + \tau_z (\alpha_y + \beta_y)). \quad (49)$$

Plugging these matrix elements into the general expression (36) we obtain the magneto-optical conductivity for phosphorene. Note that, unlike silicene and HgTe QW, there is now a large asymmetry between  $\sigma_{xx}$  and  $\sigma_{yy}$  (about one order of magnitude difference), as evidenced by Figure 9. This asymmetry was already highlighted by [71], where tunable optical properties of multilayer black phosphorus thin films were studied for  $B = 0$ . In Figure 9 we plot the real and imaginary parts of the conductivity tensor components  $\sigma_{ij}$  (in  $\sigma_0 = e^2/h$  units) of phosphorene as a function of the polarized light frequency  $\Omega$ , for some values of the electric potential around  $\Delta_z^{(0)} = -E_g = -1.52$  eV (closing the energy gap), a magnetic field of  $B = 0.5$  T, like in Figure 3, and some representative values of the chemical potential  $\mu_F = -0.417$  eV, temperature  $T = 1$  K and scattering rate  $\eta = 0.2$  meV. We are using the same threshold of

$N = 1000$  Fock states that we used to find convergence in the first 6 Hamiltonian eigenstates of the numerical diagonalization in Figure 3. This convergence is ensured for  $\hbar\Omega \in [0, 20]$  meV. The anisotropic character of phosphorene also implies that the current  $j_y^s$  is significantly lower than  $j_x^s$  [the Hamiltonian (25) is of second order in  $k_y$ ]. This makes transversal components of the conductivity significantly lower than longitudinal components. This is why we have disposed Figure 9 in a slightly different manner from Figures 4 for silicene and 6 for HgTe QW, which display a more isotropic structure.

Due to the parity symmetry of the Hamiltonian (30), only the electronic transitions between LLs of different parities are allowed [30]. The main peak (smaller frequency) of the conductivity  $\text{Re}(\sigma_{xx})$  in Figure 9 corresponds to the electronic transitions  $E_0^{\text{even}} \rightarrow E_3^{\text{odd}}$  and  $E_1^{\text{odd}} \rightarrow E_2^{\text{even}}$ , which have approximately the same energy difference for all  $\Delta_z < -1.53$  eV with a tolerance  $\leq 10^{-14}$  eV. That is,  $E_0^{\text{even}}$  and  $E_1^{\text{odd}}$ , and  $E_2^{\text{even}}$  and  $E_3^{\text{odd}}$ , are degenerate for all  $\Delta_z < -1.53$  eV as the spectrum in Figure 3 shows. When the degeneracy is broken around the electric potential  $\Delta_z \simeq -1.53$  eV, the main conductivity  $\text{Re}(\sigma_{xx})$  peak splits into two as we can see in Figure 9.

The anisotropic character of phosphorene also affects the Faraday angle, which attains much lower values (in absolute value) than for silicene or HgTe QWs. Indeed, in Figure 10 we plot Faraday angle and transmittance as a function of the polarized light frequency  $\Omega$  for different electric field potentials  $-1.535 \leq \Delta_z \leq -1.519$  eV. Like for silicene and HgTe QWs, we find a minimal behavior in the transmittance of phosphorene  $\mathcal{T}_0 = 0.50$  for a polarized light frequency  $\hbar\Omega = 2.6$  meV at electric field potential  $\Delta_z^{(0)} = -1.523$  eV, which is close to minus the energy gap  $-E_g = -1.52$  eV. Note that this value of the minimal transmittance of phosphorene is much smaller than for silicene and HgTe QWs; actually, the assumption of low absorbance in formula (39) is no longer valid here and we have used the exact expressions for  $\mathcal{T}$  and  $\Theta_F$  in (39). Moreover, unlike for graphene analogues and HgTe QWs, this minimum of the transmittance does not seem to be related to the union of two conductivity peaks into a bigger one; rather, it is simply related to the energy gap closure. Actually, the critical electric potential  $\Delta_z^{(0)}$  where the transmittance of phosphorene reaches a minimum depends on the magnetic field  $B$  chosen, as Figure 11 shows. We perform a non-linear fit of the numerical values of  $\Delta_z^{(0)}(B)$  and obtain the equation ( $B$  in dimensionless units)

$$\left( \Delta_z^{(0)} \right)_{\text{fit}}(B) = \frac{-77.4 - 3.5B}{50.9 + 2.2B} \text{ eV}, \quad (50)$$

which is represented as a orange curve in Figure 11. For small magnetic fields, we can deduce that the critical electric field potential is similar to minus the energy gap  $-E_g$  of phosphorene, that is  $\Delta_z^{(0)}(B) \simeq -E_g = -1.52$  eV for  $B \ll 1$  T. We have also checked numerically that

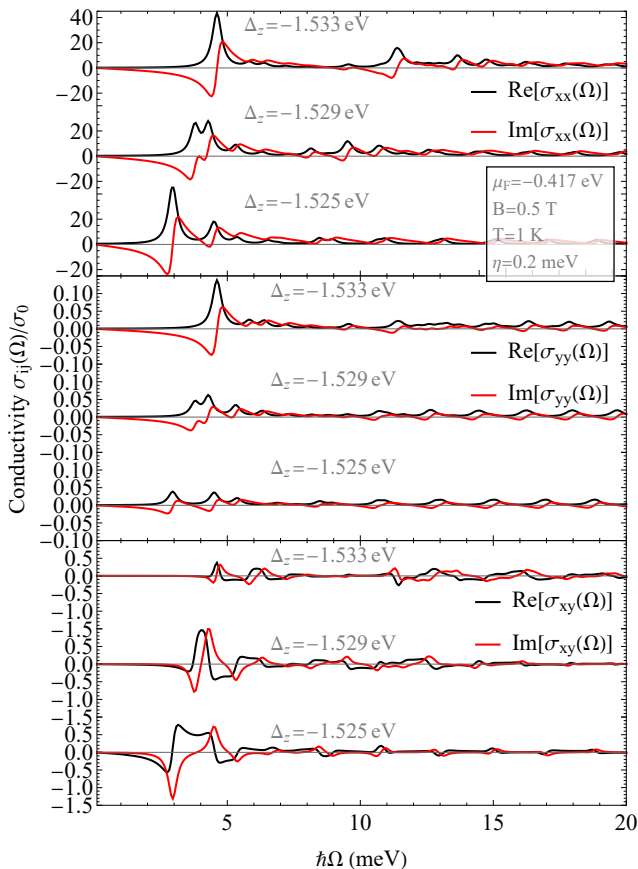


FIG. 9. Real and imaginary parts of the longitudinal  $\sigma_{xx}$ ,  $\sigma_{yy}$  and transverse Hall  $\sigma_{xy}$  magneto-optical conductivities in a phosphorene monolayer, as a function of the polarized light frequency  $\Omega$  and in  $\sigma_0 = e^2/h$  units. Phosphorene is under a perpendicular electric field potential  $\Delta_z^{(0)} = -E_g = -1.52$  eV closing the energy gap in Figure 3. The  $y$ -axis ticks have different values in each subplot as the conductivities  $\sigma_{xy}$  and  $\sigma_{yy}$  attain smaller values than  $\sigma_{xx}$  (phosphorene anisotropy). We set the conductivity parameters as  $\mu_F = -0.417$  meV,  $B = 0.5$  T,  $T = 1$  K and  $\eta = 0.2$  meV.

the critical electric potentials  $\Delta_z^{(0)}(B)$  are independent of the parameters  $\mu_F$  and  $\eta$  for a fixed magnetic field  $B$ . However, we set different values of  $\mu_F$  for small fields  $B \leq 2$  T (see caption of Figure 11), in order to avoid blocking the electric transition  $E_1^{\text{odd}} \rightarrow E_2^{\text{even}}$  of the main peak of the transmittance. We also increment  $N$  as  $B$  decreases in order to achieve convergence in the diagonalization.

Additionally, Figure 10 shows how one peak of the transmittance splits into two around  $\Delta_z \simeq -1.53$  eV (blue lines), since the LL  $E_0^{\text{even}}$  breaks its degeneracy approximately for  $\Delta_z > -1.53$  eV (see Figure 3). For  $\Delta_z = \Delta_z^{(0)} = -1.523$  eV (thick black line), the big peak on the left in Figure 10 corresponds to the electronic transition  $E_1^{\text{odd}} \rightarrow E_2^{\text{even}}$ , and moves toward smaller values of  $\hbar\Omega$  when increasing  $\Delta_z$ . The other small peak in the black line corresponds to the electronic transition

$E_0^{\text{even}} \rightarrow E_3^{\text{odd}}$ , which moves toward bigger values of  $\hbar\Omega$  when increasing  $\Delta_z$ . The Faraday angle also presents inflection points at the frequencies where the peaks of the transmittance are located.

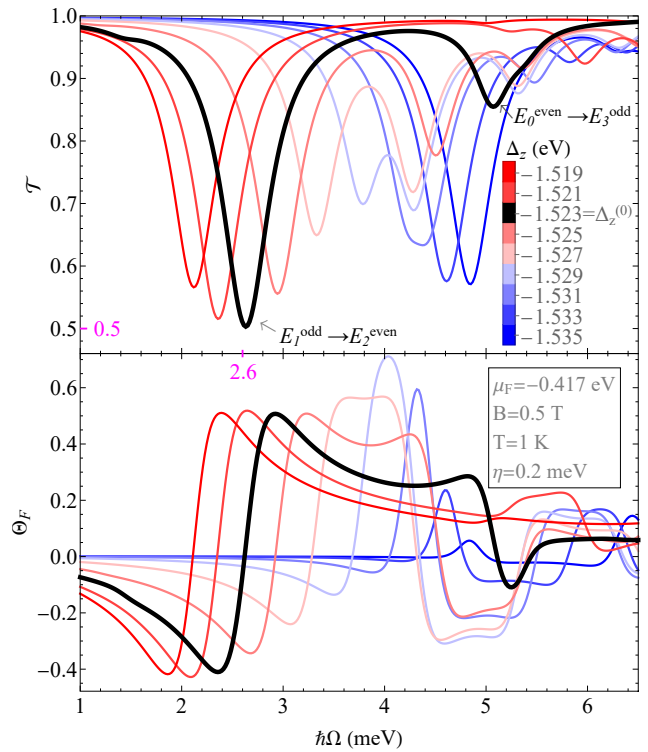


FIG. 10. Transmittance  $\mathcal{T}$  and Faraday angle  $\Theta_F$  (in degrees) in a phosphorene monolayer as a function of the polarized light frequency  $\Omega$ , and for electric fields  $-1.535 < \Delta_z < -1.519$  eV around the minus energy gap  $-E_g = -1.52$  eV. The black line corresponds to the electric potential  $\Delta_z^{(0)} = -1.523$  eV  $\simeq -E_g$  where the transmittance attains a minimum of  $\mathcal{T}_0 = 0.5$  at  $\hbar\Omega = 2.5$  meV. We set the conductivity parameters as  $\mu_F = -0.417$  meV,  $B = 0.5$  T,  $T = 1$  K and  $\eta = 0.2$  meV.

Therefore, we see that anisotropies affect the values of the Faraday angle and transmittance. There are mechanical ways of introducing anisotropies in 2D materials by subjecting them to strain (like for strained [86] or rippled [87] graphene). This kind of anisotropies can be treated by replacing the scalar Fermi velocity  $v$  by a  $2 \times 2$  symmetric tensor  $\mathbf{v}$  (see e.g. [82]). Namely, for graphene, the Hamiltonian (1) vector  $\mathbf{d}$  components  $d_j = \hbar v k_j$  are replaced by  $d_j = \hbar k_i v_{ij}$ ,  $i = 1, 2, d_3 = 0$ . Actually, for uniformly strained graphene with strain tensor  $\boldsymbol{\varepsilon}$ , the Fermi velocity tensor is (up to first order)  $\mathbf{v} = v(\tau_0 - \beta \boldsymbol{\varepsilon})$  (see e.g. [82, 88]), where  $\beta \sim 2$ . The relation between the isotropic  $\boldsymbol{\sigma}^0$  and the anisotropic  $\boldsymbol{\sigma}$  magneto-optical conductivity tensors is simply  $\boldsymbol{\sigma}(\Omega, B) = \mathbf{v} \boldsymbol{\sigma}^0(\Omega, B) \mathbf{v} / \det(\mathbf{v})$ , with  $B = B \det(\mathbf{v}) / v^2$  an effective magnetic field. Interesting discussions on how measurements of dichroism and trans-

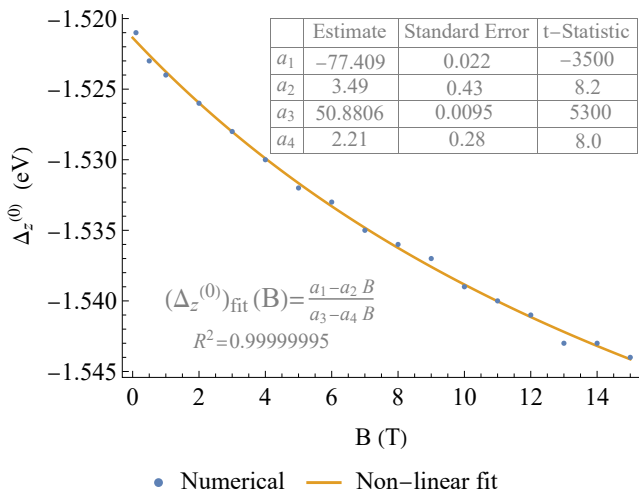


FIG. 11. Electric field potential at which phosphorene transmittance reaches a minimum, as a function of different magnetic fields. In orange, non-linear fit (50) of the numerical values. In general, we set the conductivity parameters  $\mu_F = -0.41$  eV,  $T = 1$  K,  $\eta = 1$  meV, and use  $N = 300$  Fock state in the numerical diagonalization, for all  $B \geq 3$  T. For smaller magnetic fields  $B = 0.1, 0.5, 1, 2$  T, we set  $\mu_F = -0.419, -0.418, -0.416, -0.416$  eV respectively. In the case of  $B = 0.1$  T we also set  $\eta = 1$  meV and  $N = 500$  Fock states to achieve energy diagonalization convergence.

parency for two different light polarization directions can be used to determine the magnitude and direction of strain can be found in [81]. Also, photoelastic effects in graphene [86], strain-modulated anisotropies in silicene [89, 90], etc. The band gap  $E_g = E_v - E_c$  of phosphorene can be furthermore modulated by strain and by the number of layers in a stack [60, 70].

#### IV. CONCLUSIONS

We have studied magneto-optical properties of different 2D materials, focusing on transmittance and Faraday rotation near the critical point of the topological phase transition for topological insulators like silicene and HgTe

quantum wells. We have seen that, in all topological 2D materials analyzed, transmittance attains an absolute minimum  $\mathcal{T}_0$  at the critical TPT point for a certain value  $\Omega_0$  of the normal incident polarized light frequency. This is a universal behavior for graphene analogues, that is, the minimal behavior of the transmittance does not depend on the chosen values of magnetic field, chemical potential and temperature, although the location of  $\Omega_0$  varies with them. In addition, we have found that each peak of the transmittance coincides in frequency with an inflection point of the Faraday angle, for a fixed selection of the electric field, magnetic field, chemical potential and temperature parameters.

This extremal universal behavior is shared with other topological 2D materials like HgTe quantum wells as long as the applied magnetic field remains small enough  $B \ll 1$  T. In HgTe quantum wells we have verified that there is a minimum of the transmittance  $\mathcal{T}_0$  at the critical HgTe layer thickness at a given frequency  $\Omega'_0$  (for this material this minimal behavior depends on the magnetic field) and the Faraday angle at the critical point changes sign at the minimum transmittance frequency  $\Omega'_0$ .

For other non-topological anisotropic materials like phosphorene, this minimal behavior of the transmittance still remains when the energy gap is closed, the Faraday angle being much smaller (in absolute value) than in silicene and HgTe QWs. In this case the critical electric potential where the transmittance reaches a minimum depends on the magnetic field.

Therefore, these extremal properties of transmittance/absorbance and chirality change of Faraday angle at the critical point turn out to provide sharp markers of either the topological phase transition or the energy gap closure.

#### ACKNOWLEDGMENTS

We thank the support of the Spanish MICINN through the project PGC2018-097831-B-I00 and Junta de Andalucía through the projects FEDER/UJA-1381026 and FQM-381. AM thanks the Spanish MIU for the FPU19/06376 predoctoral fellowship. OC is on sabbatical leave at Granada University, Spain, since the 1st of September 2023. OC thanks support from the program PASPA from DGAPA-UNAM.

- 
- [1] I. Crassee, J. Levallois, A. L. Walter, M. Ostler, A. Bostwick, E. Rotenberg, T. Seyller, D. van der Marel, and A. B. Kuzmenko, Giant faraday rotation in single- and multilayer graphene, *Nature Physics* **7**, 48 (2011).
- [2] A. Ferreira, J. Viana-Gomes, Y. V. Bludov, V. Pereira, N. M. R. Peres, and A. H. Castro Neto, Faraday effect in graphene enclosed in an optical cavity and the equation of motion method for the study of magneto-optical transport in solids, *Phys. Rev. B* **84**, 235410 (2011).

- [3] I. Fialkovsky and D. V. Vassilevich, Faraday rotation in graphene, *The European Physical Journal B* **85**, 384 (2012).
- [4] M. Tymchenko, A. Y. Nikitin, and L. Martín-Moreno, Faraday rotation due to excitation of magnetoplasmons in graphene microribbons, *ACS Nano* **7**, 9780 (2013).
- [5] F. Yang, X. Xu, and R.-B. Liu, Giant faraday rotation induced by the berry phase in bilayer graphene under strong terahertz fields, *New Journal of Physics* **16**,

- 043014 (2014).
- [6] C.-Y. Lin, T.-N. Do, Y.-K. Huang, and M.-F. Lin, *Optical Properties of Graphene in Magnetic and Electric Fields*, 2053-2563 (IOP Publishing, 2017).
- [7] R. Shimano, G. Yumoto, J. Y. Yoo, R. Matsunaga, S. Tanabe, H. Hibino, T. Morimoto, and H. Aoki, Quantum faraday and kerr rotations in graphene, *Nature Communications* **4**, 1841 (2013).
- [8] M. J. Spencer and T. M. (Eds.), *Silicene: Structure, Properties and Applications*, (Springer Series in Materials Science vol. 235, 2016).
- [9] C. J. Tabert and E. J. Nicol, Magneto-optical conductivity of silicene and other buckled honeycomb lattices, *Phys. Rev. B* **88**, 085434 (2013).
- [10] M. Shah and M. S. Anwar, Magneto-optical effects in the landau level manifold of 2d lattices with spin-orbit interaction, *Opt. Express* **27**, 23217 (2019).
- [11] P. Nualpijit and B. Soodchomshom, Enhanced faraday rotation and control of pure spin-valley optical conductivity by topological phase in silicene, *Physica E: Low-dimensional Systems and Nanostructures* **137**, 115011 (2022).
- [12] N. D. Hien, C. V. Nguyen, N. N. Hieu, S. S. Kubakaddi, C. A. Duque, M. E. Mora-Ramos, L. Dinh, T. N. Bich, and H. V. Phuc, Magneto-optical transport properties of monolayer transition metal dichalcogenides, *Phys. Rev. B* **101**, 045424 (2020).
- [13] X. Y. Zhou, R. Zhang, J. P. Sun, Y. L. Zou, D. Zhang, W. K. Lou, F. Cheng, G. H. Zhou, F. Zhai, and K. Chang, Landau levels and magneto-transport property of monolayer phosphorene, *Scientific Reports* **5**, 12295 (2015).
- [14] S.-Q. Shen, *Topological Insulators: Dirac Equation in Condensed Matters* (Springer-Verlag Berlin Heidelberg, 2012).
- [15] B. A. Bernevig, *Topological Insulators and Topological Superconductors* (Princeton University Press, 2013).
- [16] L. O. J. K. Asboth and A. S. A. Palyi, *A Short Course on Topological Insulators: Band Structure and Edge States in One and Two Dimensions* (Springer International Publishing Switzerland, 2016).
- [17] B. Scharf, A. Matos-Abiague, I. Žutić, and J. Fabian, Probing topological transitions in HgTe/CdTe quantum wells by magneto-optical measurements, *Phys. Rev. B* **91**, 235433 (2015).
- [18] A. Shuvaev, V. Dziom, Z. D. Kvon, N. N. Mikhailov, and A. Pimenov, Universal faraday rotation in hgte wells with critical thickness, *Phys. Rev. Lett.* **117**, 117401 (2016).
- [19] A. G. Ardakani and Z. Zare, Strong faraday rotation in a topological insulator single layer using dielectric multilayered structures, *J. Opt. Soc. Am. B* **38**, 2562 (2021).
- [20] Y. Liang, Y. Xiang, and X. Dai, Enhancement of graphene faraday rotation in the one-dimensional topological photonic crystals, *Opt. Express* **28**, 24560 (2020).
- [21] Y. Shao, K. W. Post, J.-S. Wu, S. Dai, A. J. Frenzel, A. R. Richardella, J. S. Lee, N. Samarth, M. M. Fogler, A. V. Balatsky, D. E. Kharzeev, and D. N. Basov, Faraday rotation due to surface states in the topological insulator (bi<sub>1-x</sub>sbx)<sub>2</sub>te<sub>3</sub>, *Nano Letters* **17**, 980 (2017).
- [22] M. Shah, M. Q. Mehmood, Y. S. Ang, M. Zubair, and Y. Massoud, Magneto-optical conductivity and giant faraday-kerr rotation in floquet topological insulators, *Phys. Rev. B* **107**, 235115 (2023).
- [23] I. D. Tokman, Q. Chen, I. A. Shereshevsky, V. I. Pozdnyakova, I. Oladyshkin, M. Tokman, and A. Belyanin, Inverse faraday effect in graphene and weyl semimetals, *Phys. Rev. B* **101**, 174429 (2020).
- [24] M. Calixto and E. Romera, Identifying topological-band insulator transitions in silicene and other 2d gapped dirac materials by means of rényi-wehrl entropy, *EPL (Europhysics Letters)* **109**, 40003 (2015).
- [25] E. Romera and M. Calixto, Uncertainty relations and topological-band insulator transitions in 2d gapped dirac materials, *Journal of Physics: Condensed Matter* **27**, 175003 (2015).
- [26] M. Calixto and E. Romera, Inverse participation ratio and localization in topological insulator phase transitions, *Journal of Statistical Mechanics: Theory and Experiment* **2015**, P06029 (2015).
- [27] E. Romera and M. Calixto, Band inversion at critical magnetic fields in a silicene quantum dot, *EPL (Europhysics Letters)* **111**, 37006 (2015).
- [28] E. Romera, M. Calixto, and J. Bolívar, Information measures and topological-band insulator transitions in 2d-dirac materials under external circularly polarized lasers, and static electric and magnetic fields, *Physica A: Statistical Mechanics and its Applications* **511**, 174 (2018).
- [29] M. Calixto, N. A. Cordero, E. Romera, and O. Castaños, Signatures of topological phase transitions in higher landau levels of hgte/cdte quantum wells from an information theory perspective, *Physica A: Statistical Mechanics and its Applications* **605**, 128057 (2022).
- [30] O. Castaños, E. Romera, and M. Calixto, Information theoretic analysis of landau levels in monolayer phosphorene under magnetic and electric fields, *Materials Research Express* **6**, 106316 (2019).
- [31] M. Calixto, E. Romera, and O. Castaños, Analogies between the topological insulator phase of 2d dirac materials and the superradiant phase of atom-field systems, *International Journal of Quantum Chemistry* **121**, e26464 (2021), <https://onlinelibrary.wiley.com/doi/pdf/10.1002/qua.26464>.
- [32] D. J. Thouless, M. Kohmoto, M. P. Nightingale, and M. den Nijs, Quantized hall conductance in a two-dimensional periodic potential, *Phys. Rev. Lett.* **49**, 405 (1982).
- [33] D. Xiao, M.-C. Chang, and Q. Niu, Berry phase effects on electronic properties, *Rev. Mod. Phys.* **82**, 1959 (2010).
- [34] C. L. Kane and E. J. Mele, Quantum spin hall effect in graphene, *Phys. Rev. Lett.* **95**, 226801 (2005).
- [35] N. D. Drummond, V. Zólyomi, and V. I. Fal'ko, Electrically tunable band gap in silicene, *Phys. Rev. B* **85**, 075423 (2012).
- [36] C.-C. Liu, W. Feng, and Y. Yao, Quantum spin hall effect in silicene and two-dimensional germanium, *Phys. Rev. Lett.* **107**, 076802 (2011).
- [37] C.-C. Liu, H. Jiang, and Y. Yao, Low-energy effective hamiltonian involving spin-orbit coupling in silicene and two-dimensional germanium and tin, *Phys. Rev. B* **84**, 195430 (2011).
- [38] W.-F. Tsai, C.-Y. Huang, T.-R. Chang, H. Lin, H.-T. Jeng, and A. Bansil, Gated silicene as a tunable source of nearly 100% spin-polarized electrons, *Nature Communications* **4**, 1500 (2013).
- [39] S. Trivedi, A. Srivastava, and R. Kurchania, Silicene and Germanene: A First Principle Study of Electronic Structure and Effect of Hydrogenation-Passivation, *Journal of Computational and Theoretical Nanoscience* **11**, 781 (2014).

- [40] B. van den Broek, M. Houssa, E. Scalise, G. Pourtois, V. V. Afanas'ev, and A. Stesmans, Two-dimensional hexagonal tin: ab initio geometry, stability, electronic structure and functionalization, *2D Materials* **1**, 021004 (2014).
- [41] L. Stille, C. J. Tabert, and E. J. Nicol, Optical signatures of the tunable band gap and valley-spin coupling in silicene, *Phys. Rev. B* **86**, 195405 (2012).
- [42] C. J. Tabert and E. J. Nicol, Valley-spin polarization in the magneto-optical response of silicene and other similar 2d crystals, *Phys. Rev. Lett.* **110**, 197402 (2013).
- [43] M. Tahir and U. Schwingenschlögl, Valley polarized quantum hall effect and topological insulator phase transitions in silicene, *Scientific Reports* **3**, 1075 (2013).
- [44] E. G. Novik, A. Pfeuffer-Jeschke, T. Jungwirth, V. Latussek, C. R. Becker, G. Landwehr, H. Buhmann, and L. W. Molenkamp, Band structure of semimagnetic  $\text{Hg}_{1-y}\text{Mn}_y\text{Te}$  quantum wells, *Phys. Rev. B* **72**, 035321 (2005).
- [45] B. A. Bernevig, T. L. Hughes, and S.-C. Zhang, Quantum spin hall effect and topological phase transition in HgTe quantum wells, *Science* **314**, 1757 (2006), <https://www.science.org/doi/pdf/10.1126/science.1133734>.
- [46] M. König, S. Wiedmann, C. Brüne, A. Roth, H. Buhmann, L. W. Molenkamp, X.-L. Qi, and S.-C. Zhang, Quantum spin hall insulator state in HgTe quantum wells, *Science* **318**, 766 (2007), <https://www.science.org/doi/pdf/10.1126/science.1148047>.
- [47] M. König, H. Buhmann, L. W. Molenkamp, T. Hughes, C.-X. Liu, X.-L. Qi, and S.-C. Zhang, The quantum spin hall effect: Theory and experiment, *Journal of the Physical Society of Japan* **77**, 031007 (2008), <https://doi.org/10.1143/JPSJ.77.031007>.
- [48] C. Liu, T. L. Hughes, X.-L. Qi, K. Wang, and S.-C. Zhang, Quantum spin hall effect in inverted type-II semiconductors, *Phys. Rev. Lett.* **100**, 236601 (2008).
- [49] X.-L. Qi and S.-C. Zhang, Topological insulators and superconductors, *Rev. Mod. Phys.* **83**, 1057 (2011).
- [50] B. Büttner, C. X. Liu, G. Tkachov, E. G. Novik, C. Brüne, H. Buhmann, E. M. Hankiewicz, P. Recher, B. Trauzettel, S. C. Zhang, and L. W. Molenkamp, Single valley Dirac fermions in zero-gap HgTe quantum wells, *Nature Physics* **7**, 418 (2011).
- [51] B. Scharf, A. Matos-Abiad, and J. Fabian, Magnetic properties of HgTe quantum wells, *Phys. Rev. B* **86**, 075418 (2012).
- [52] For details, see the Supplemental Material at, [URL\\_will\\_be\\_inserted\\_by\\_publisher](https://www.nature.com/articles/s41598-014-01111-1).
- [53] D. Corbridge, *Phosphorus: Chemistry, Biochemistry and Technology 6th edn* (CRC Press, 2013).
- [54] P. W. Bridgman, Two new modifications of phosphorus., *Journal of the American Chemical Society*, *Journal of the American Chemical Society* **36**, 1344 (1914).
- [55] P. W. Bridgman, Further note on black phosphorus., *Journal of the American Chemical Society*, *Journal of the American Chemical Society* **38**, 609 (1916).
- [56] Z. Zhu and D. Tománek, Semiconducting layered blue phosphorus: A computational study, *Phys. Rev. Lett.* **112**, 176802 (2014).
- [57] H. Guo, N. Lu, J. Dai, X. Wu, and X. C. Zeng, Phosphorene nanoribbons, phosphorus nanotubes, and van der Waals multilayers, *The Journal of Physical Chemistry C, The Journal of Physical Chemistry C* **118**, 14051 (2014).
- [58] J. Guan, Z. Zhu, and D. Tománek, Phase coexistence and metal-insulator transition in few-layer phosphorene: A computational study, *Phys. Rev. Lett.* **113**, 046804 (2014).
- [59] H. Liu, A. T. Neal, Z. Zhu, Z. Luo, X. Xu, D. Tománek, and P. D. Ye, Phosphorene: An unexplored 2d semiconductor with a high hole mobility, *ACS Nano*, *ACS Nano* **8**, 4033 (2014).
- [60] A. Carvalho, M. Wang, X. Zhu, A. S. Rodin, H. Su, and A. H. Castro Neto, Phosphorene: from theory to applications, *Nature Reviews Materials* **1**, 16061 (2016).
- [61] R. Wan, X. Cao, and J. Guo, Simulation of phosphorene Schottky-barrier transistors, *Applied Physics Letters* **105**, 163511 (2014), <https://doi.org/10.1063/1.4900410>.
- [62] H. Liu, Y. Du, Y. Deng, and P. D. Ye, Semiconducting black phosphorus: synthesis, transport properties and electronic applications, *Chem. Soc. Rev.* **44**, 2732 (2015).
- [63] M. Akhtar, G. Anderson, R. Zhao, A. Alruqi, J. E. Mroczkowska, G. Sumanasekera, and J. B. Jasinski, Recent advances in synthesis, properties, and applications of phosphorene, *npj 2D Materials and Applications* **1**, 5 (2017).
- [64] L. Li, Y. Yu, G. J. Ye, Q. Ge, X. Ou, H. Wu, D. Feng, X. H. Chen, and Y. Zhang, Black phosphorus field-effect transistors, *Nature Nanotechnology* **9**, 372 (2014).
- [65] P. Chen, N. Li, X. Chen, W.-J. Ong, and X. Zhao, The rising star of 2d black phosphorus beyond graphene: synthesis, properties and electronic applications, *2D Materials* **5**, 014002 (2017).
- [66] X. Ling, H. Wang, S. Huang, F. Xia, and M. S. Dresselhaus, The renaissance of black phosphorus, *Proceedings of the National Academy of Sciences* **112**, 4523 (2015), <https://www.pnas.org/content/112/15/4523.full.pdf>.
- [67] R. Xu, S. Zhang, F. Wang, J. Yang, Z. Wang, J. Pei, Y. W. Myint, B. Xing, Z. Yu, L. Fu, Q. Qin, and Y. Lu, Extraordinarily bound quasi-one-dimensional trions in two-dimensional phosphorene atomic semiconductors, *ACS Nano*, *ACS Nano* **10**, 2046 (2016).
- [68] A. N. Rudenko and M. I. Katsnelson, Quasiparticle band structure and tight-binding model for single- and bilayer black phosphorus, *Phys. Rev. B* **89**, 201408 (2014).
- [69] M. Ezawa, Topological origin of quasi-flat edge band in phosphorene, *New Journal of Physics* **16**, 115004 (2014).
- [70] A. S. Rodin, A. Carvalho, and A. H. Castro Neto, Strain-induced gap modification in black phosphorus, *Phys. Rev. Lett.* **112**, 176801 (2014).
- [71] T. Low, A. S. Rodin, A. Carvalho, Y. Jiang, H. Wang, F. Xia, and A. H. Castro Neto, Tunable optical properties of multilayer black phosphorus thin films, *Phys. Rev. B* **90**, 075434 (2014).
- [72] M. Ezawa, Highly anisotropic physics in phosphorene, *Journal of Physics: Conference Series* **603**, 012006 (2015).
- [73] C. Dutreix, E. A. Stepanov, and M. I. Katsnelson, Laser-induced topological transitions in phosphorene with inversion symmetry, *Phys. Rev. B* **93**, 241404 (2016).
- [74] N. H. Lindner, G. Refael, and V. Galitski, Floquet topological insulator in semiconductor quantum wells, *Nature Physics* **7**, 490 (2011).
- [75] T. Kitagawa, T. Oka, A. Brataas, L. Fu, and E. Demler, Transport properties of nonequilibrium systems under the application of light: Photoinduced quantum hall insulators without Landau levels, *Phys. Rev. B* **84**, 235108 (2011).

- [76] J. Cayssol, B. Dóra, F. Simon, and R. Moessner, Floquet topological insulators, *Physica Status Solidi (RRL) – Rapid Research Letters* **7**, 101 (2013).
- [77] G.-H. Chen, Y.-N. Chen, Y.-W. Zhou, Y.-L. Sun, and E.-J. Ye, Strain and electric field tunable electronic transport in armchair phosphorene nanodevice with normal-metal electrodes, *AIP Advances* **10**, 105012 (2020), <https://doi.org/10.1063/5.0021775>.
- [78] G. D. Mahan, *Many-Particle Physics, 3rd edition* (Kluwer Academic/Plenum Publishers, New York, 2000).
- [79] P. Allen, Chapter 6 electron transport, in *Conceptual Foundations of Materials*, Contemporary Concepts of Condensed Matter Science, Vol. 2, edited by S. G. Louie and M. L. Cohen (Elsevier, 2006) pp. 165–218.
- [80] T. Stauber, N. M. R. Peres, and A. K. Geim, Optical conductivity of graphene in the visible region of the spectrum, *Phys. Rev. B* **78**, 085432 (2008).
- [81] M. Oliva-Leyva and G. G. Naumis, Tunable dichroism and optical absorption of graphene by strain engineering, *2D Materials* **2**, 025001 (2015).
- [82] M. Oliva-Leyva and C. Wang, Magneto-optical conductivity of anisotropic two-dimensional Dirac–Weyl materials, *Annals of Physics* **384**, 61 (2017).
- [83] K. Chiu, T. Lee, and J. Quinn, Infrared magneto-transmittance of a two-dimensional electron gas, *Surface Science* **58**, 182 (1976).
- [84] R. F. O’Connell and G. Wallace, Ellipticity and faraday rotation due to a two-dimensional electron gas in a metal-oxide-semiconductor system, *Phys. Rev. B* **26**, 2231 (1982).
- [85] A. Chakraborty, G. Bian, and G. Vignale, Frequency-dependent faraday and kerr rotation in anisotropic non-symmorphic dirac semimetals in a magnetic field (2023), [arXiv:2302.05385 \[cond-mat.mes-hall\]](https://arxiv.org/abs/2302.05385).
- [86] V. M. Pereira, R. M. Ribeiro, N. M. R. Peres, and A. H. C. Neto, Optical properties of strained graphene, *Europhysics Letters* **92**, 67001 (2011).
- [87] J. Schiefele, L. Martin-Moreno, and F. Guinea, Faraday effect in rippled graphene: Magneto-optics and random gauge fields, *Phys. Rev. B* **94**, 035401 (2016).
- [88] F. M. D. Pellegrino, G. G. N. Angilella, and R. Pucci, Linear response correlation functions in strained graphene, *Phys. Rev. B* **84**, 195407 (2011).
- [89] M. Farokhnezhad, M. Esmailzadeh, and K. Shakouri, Strain-modulated anisotropy of quantum transport properties in single-layer silicene: Spin and valley filtering, *Phys. Rev. B* **96**, 205416 (2017).
- [90] Z. B. Siu and M. B. A. Jalil, Effective hamiltonian for silicene under arbitrary strain from multi-orbital basis, *Scientific Reports* **11**, 7575 (2021).

# Faraday rotation and transmittance as markers of topological phase transitions in 2D materials:

## Supplemental material

Manuel Calixto\*

*Department of Applied Mathematics, University of Granada, Fuentenueva s/n, 18071 Granada, Spain and  
Institute Carlos I for Theoretical for Theoretical and Computational Physics (iC1), Fuentenueva s/n, 18071 Granada, Spain*

Alberto Mayorgas†

*Department of Applied Mathematics, University of Granada, Fuentenueva s/n, 18071 Granada, Spain*

Nicolás A. Cordero‡

*Department of Physics, University of Burgos, E-09001 Burgos, Spain  
International Research Center in Critical Raw Materials for Advanced Industrial Technologies (ICRAM),  
University of Burgos, E-09001 Burgos, Spain and  
Institute Carlos I for Theoretical for Theoretical and Computational Physics (iC1), Fuentenueva s/n, 18071 Granada, Spain*

Elvira Romera§

*Department of Atomic, Molecular and Nuclear Physics,  
University of Granada, Fuentenueva s/n, 18071 Granada, Spain and  
Institute Carlos I for Theoretical for Theoretical and Computational Physics (iC1), Fuentenueva s/n, 18071 Granada, Spain*

Octavio Castaños¶

*Institute of Nuclear Sciences, National Autonomous University of Mexico, Apdo. Postal 70-543, 04510, CDMX, Mexico  
(Dated: September 20, 2023)*

### I. LANDAU LEVELS PLOT VERSUS EXTERNAL MAGNETIC FIELD

We provide an additional plot of the Landau levels of the three different materials as a function of the external magnetic field  $B$ . Critical values of the electric field and layer thickness are selected, that is, in the case of the silicene  $\Delta_z = \Delta_{\text{so}} = 4.2$  meV, for the HgTe QW  $\lambda = \lambda_c = 6.17$  nm, and for the phosphorene  $\Delta_z = -E_g = -1.52$  eV.

### II. SILICENE CONDUCTIVITY IN THE CIRCULARLY POLARIZATION BASIS

We complete the analysis of magneto-optical properties of graphene analogues by discussing the case of circularly polarized light. In this case, the conductivity is  $\sigma_{\pm}(\Omega) = \sigma_{xx}(\Omega) \pm i\sigma_{xy}(\Omega)$  for right-handed (+) and left-handed (-) polarization [1]. Therefore, the absorptive part is  $\text{Re}(\sigma_{\pm}) = \text{Re}(\sigma_{xx}) \mp \text{Im}(\sigma_{xy})$ . In Figure 2, we present both absorptive parts  $\text{Re}(\sigma_{\pm})$  for a silicene monolayer under an electric potential  $\Delta_z = 0.5\Delta_{\text{so}}$  as a function of the frequency of the incident light  $\Omega$ . The conductivity parameters are specifically chosen to reproduce the results in [2], that is,  $\mu_F = 3.0\Delta_{\text{so}}$ ,  $B/\Delta_{\text{so}}^2 = 657$  G/meV<sup>2</sup>,  $T = 0$  K and  $\eta = 0.05\Delta_{\text{so}}$ . Note that we have defined the conductance quantum as  $\sigma_0 = e^2/h = 38.8$   $\mu\text{S}$ , whereas the authors in reference [2] take  $\sigma_0 = e^2/(4\hbar)$ .

### III. HGTE QUANTUM WELL CONDUCTIVITY WITH ZEEMAN EFFECT

We recalculate the conductivity of the HgTe quantum well with and without Zeeman coupling to support the argument that the results are qualitatively equivalent, the quantitative differences being small. A layer thickness of  $\lambda = 7.0$  nm is selected, so the material parameters are  $\alpha = 365$  meV·nm,  $\beta = -686$  meV·nm<sup>2</sup>,  $\delta = -512$  meV·nm<sup>2</sup>, and  $\mu = -10$  meV, as taken from Ref. [3]. In Figure 3, we plot the real and imaginary parts of the longitudinal  $\sigma_{xx}$  and

\* Corresponding author: calixto@ugr.es

† albmayer97@ugr.es

‡ ncordero@ubu.es

§ eromera@ugr.es

¶ ocasta@nucleares.unam.mx

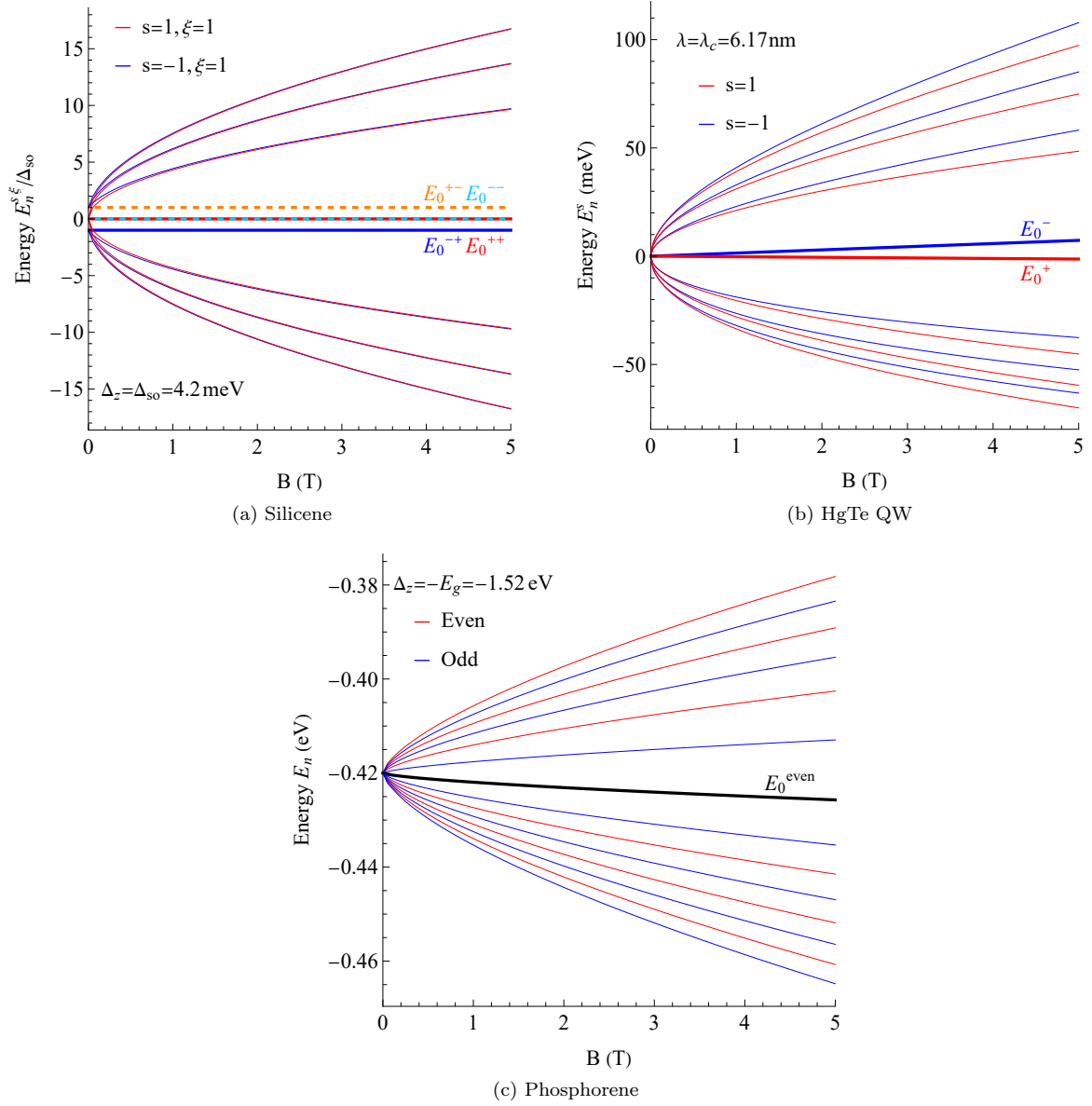


FIG. 1: Energies (Landau levels) of (a) Silicene, (b) HgTe QW, and (c) Phosphorene as a function of the external magnetic field  $B$ . Critical values of the electric field and layer thickness are selected, that is, in the case of the silicene  $\Delta_z = \Delta_{\text{so}} = 4.2$  meV, for the HgTe QW  $\lambda = \lambda_c = 6.17$  nm, and for the phosphorene  $\Delta_z = -E_g = -1.52$  eV.

transverse  $\sigma_{xy}$  conductivities as a function of the polarized light frequency  $\Omega$ . The conductivity parameters are chosen to reproduce the results in [4] with Zeeman coupling, that is,  $\mu_F = 8$  meV,  $B = 5$  T,  $T = 1$  K and  $\eta = 1$  meV. The conductance quantum used here is again  $\sigma_0 = e^2/h = 38.8 \mu\text{S}$ , whereas the authors in reference [4] take  $\sigma_0 = e^2/h$ .

#### IV. ANIMATIONS OF THE ENERGY SPECTRUM AND CONDUCTIVITIES

Attached in the supplementary material is a series of animations called

- Silicene\_Conductivity\_and\_Energy\_VS\_Omega.gif,
- HgTe\_Conductivity\_and\_Energy\_VS\_Omega.gif,
- Phosphorene\_Conductivity\_and\_Energy\_VS\_Omega.gif,

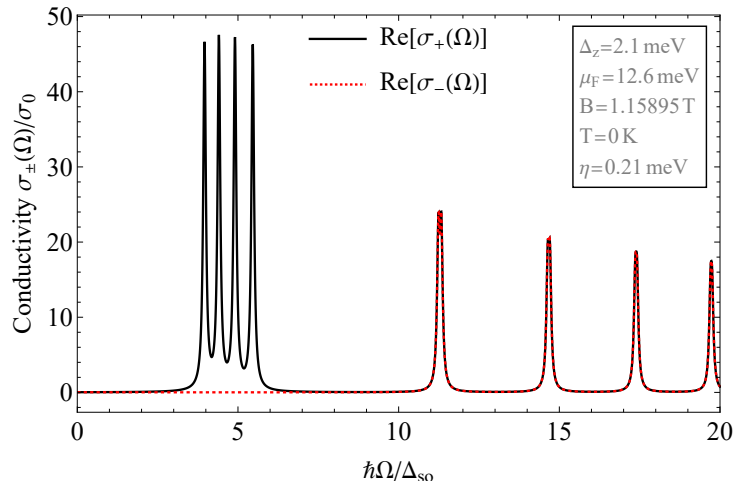


FIG. 2: Conductivity absorptive parts  $\text{Re}(\sigma_{\pm}) = \text{Re}(\sigma_{xx}) \mp \text{Im}(\sigma_{xy})$  for right-handed (+) and left-handed (-) polarization in a silicene monolayer under an electric potential  $\Delta_z = 0.5\Delta_{\text{so}}$ , as a function of the polarized light frequency  $\Omega$  (in  $\sigma_0 = e^2/h$  units). We set the conductivity parameters  $\mu_F = 3.0\Delta_{\text{so}}$ ,  $B/\Delta_{\text{so}}^2 = 657 \text{ G/meV}^2$ ,  $T = 0 \text{ K}$  and  $\eta = 0.05\Delta_{\text{so}}$  as in Ref. [2].

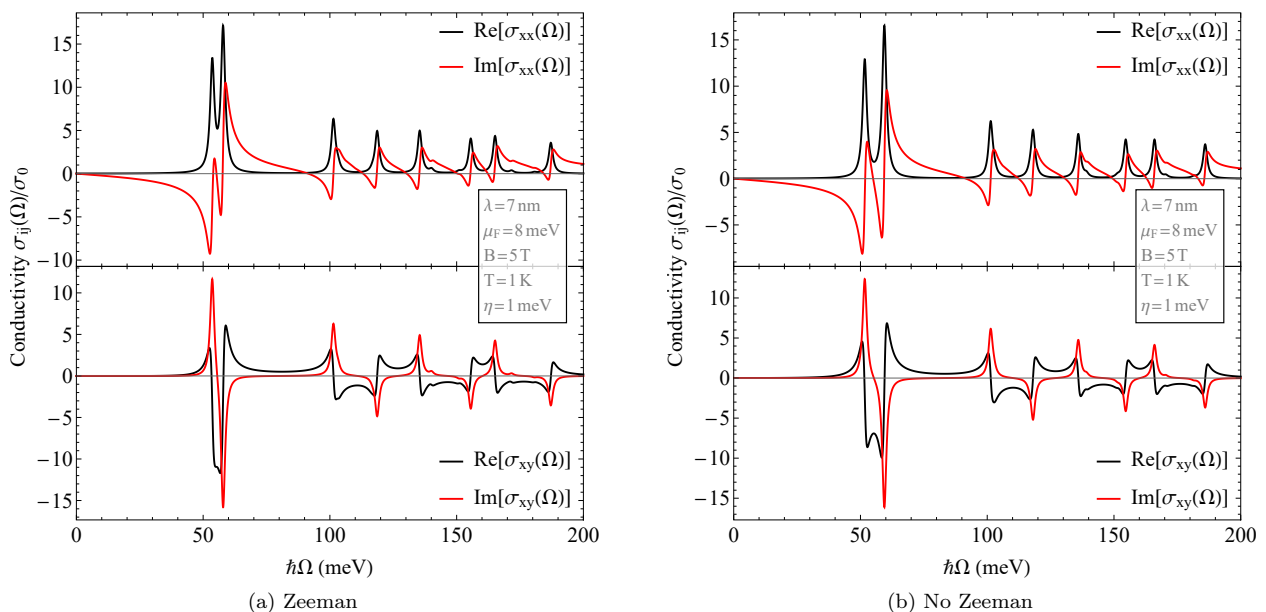


FIG. 3: Real and imaginary parts of the longitudinal  $\sigma_{xx}$  and transverse Hall  $\sigma_{xy}$  (magneto-)optical conductivities in a bulk HgTe QW of a thicknesses  $\lambda = 7.0 \text{ nm}$ , as a function of the polarized light frequency  $\Omega$  (in  $\sigma_0 = e^2/h$  units) with and without Zeeman coupling. We set the conductivity parameters  $\mu_F = 8 \text{ meV}$ ,  $B = 5 \text{ T}$ ,  $T = 1 \text{ K}$  and  $\eta = 1 \text{ meV}$ , as in Ref. [4].

where we plot the energy spectrum at right, and the real part  $\text{Re}[\sigma_{xx}(\Omega)]$  and  $\text{Re}[\sigma_{xy}(\Omega)]$  of the conductivity components at left, for three different materials studied in the main text: silicene, HgTe QW, and phosphorene. The external electric field  $\Delta_z$  in the case of the silicene and phosphorene, and the layer thickness  $\lambda$  of the HgTe QW, are used as “time coordinate” on the animations, so each frame corresponds to one value of these control parameters.

The conductivities are plotted as a function of the polarized light frequency  $\Omega$ , and they change in each frame according to the values of  $\Delta_z$  or  $\lambda$ . Therefore, we can observe how the main peaks of the longitudinal conductivity  $\text{Re}(\sigma_{xx})$  merge for the critical values  $\Delta_z^{(0)} = \Delta_{\text{so}} = 4.12 \text{ meV}$  (silicene) or  $\lambda = \lambda_c = 6.17 \text{ nm}$  (HgTe QW), where the

topological phase transition occurs in these 2D materials.

In the case of the phosphorene, we only observe the degeneration of Landau levels  $n = 0$  and  $n = 1$  in the conductivity around the electric potential  $\Delta_z \simeq -1.53$  eV. That is, the electronic transitions  $E_1^{\text{odd}} \rightarrow E_2^{\text{even}}$  and  $E_0^{\text{even}} \rightarrow E_3^{\text{odd}}$  have a similar energy and share a longitudinal conductivity peak (main peak at left in the gif), until the degeneration breaks for electric fields approximately higher than  $-1.53$  eV, when both electronic transitions will have different energies so the main peak will split into two.

On the other hand, the energy spectrum is static on the animation, as it is plotted as a function of all the values that  $\Delta_z$  or  $\lambda$  take. However, we plot a moving vertical dashed line on it, representing the value of  $\Delta_z$  or  $\lambda$  in the conductivity frame. On top of this vertical line, we also draw arrows representing the electronic transitions allowed between Landau levels (LLs) for the specific value  $\Delta_z$  or  $\lambda$ , where the Fermi energy  $\mu_F$  is represented by an horizontal dashed line. The color of the arrows is the same as the color of the points plotted on the top of the longitudinal conductivity main peaks. The length of the arrows represents the energy difference  $|E_n - E_m|$  between the corresponding Landau levels in this particular electronic transition  $n \leftrightarrow m$ , which also coincides with the frequency  $\hbar\Omega$  of the longitudinal conductivity peak associated with this transition. Therefore, when two arrows have the same length, we can observe two longitudinal conductivity peaks merging at the critical point. We have only drawn the arrows of the main peaks or lower Landau level electronic transitions for the sake of simplicity.

## V. FARADAY ANGLE CONTOUR PLOTS

For completeness, in Figure 4 we show the variability of the Faraday angle for silicene across the parameter space: polarized light frequency  $\hbar\Omega$ , electric field potential  $\Delta_z$ , magnetic field  $B$ , temperature  $T$  and chemical potential  $\mu_F$ , using several contour plots corresponding to different cross sections. Also, in Figure 5 we do the same for the Faraday angle in HgTE quantum wells using different cross sections in the  $\{\hbar\Omega, \lambda, B, T, \mu_F\}$  parameter space, where the critical thickness  $\lambda_c \simeq 6.17$  nm is marked with a vertical magenta grid line. The variability of the Faraday angle with those parameters is shown with a color code (in degrees), going from the most negative value (blue) to the most positive (red).

In the case of the silicene, we have also repeated the contour plot of the parameters  $\{\hbar\Omega, \Delta_z\}$  for different values of the temperature  $T = 1, 10, 100, 200$  K in Figure 6. The shape of the contour lines is almost the same when varying the temperature, but oscillation amplitude in the Faraday angle diminish when increasing  $T$ , as the colors of the plots tend to be more flat and yellow ( $\Theta_F \simeq 0$  according to the legend).

- 
- [1] A. Pound, J. P. Carbotte, and E. J. Nicol, Magneto-optical conductivity in graphene including electron-phonon coupling, *Phys. Rev. B* **85**, 125422 (2012).
  - [2] C. J. Tabert and E. J. Nicol, Magneto-optical conductivity of silicene and other buckled honeycomb lattices, *Phys. Rev. B* **88**, 085434 (2013).
  - [3] X.-L. Qi and S.-C. Zhang, Topological insulators and superconductors, *Rev. Mod. Phys.* **83**, 1057 (2011).
  - [4] B. Scharf, A. Matos-Abiague, I. Žutić, and J. Fabian, Probing topological transitions in HgTe/CdTe quantum wells by magneto-optical measurements, *Phys. Rev. B* **91**, 235433 (2015).

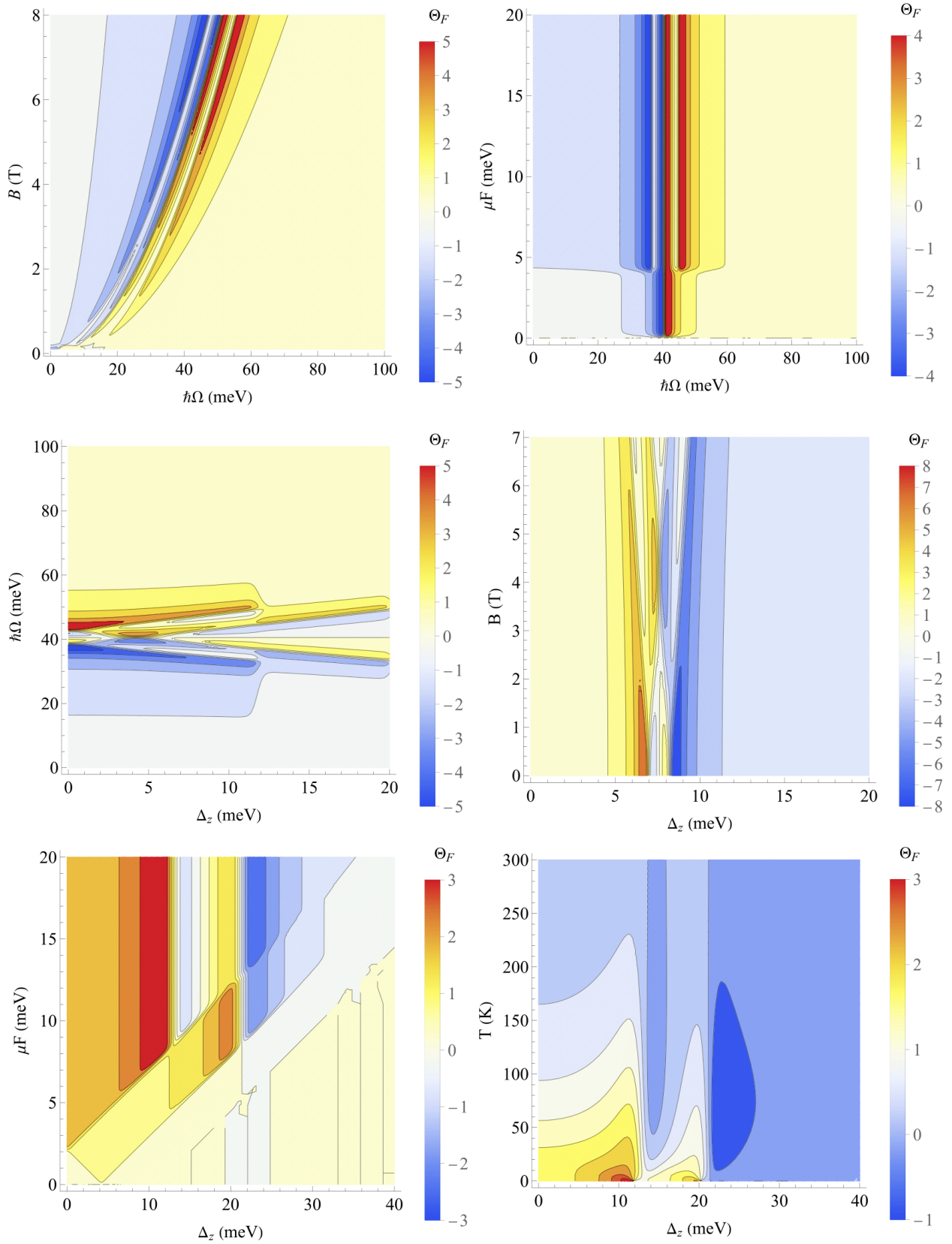


FIG. 4: Faraday rotation angle  $\Theta_F$  (in degrees) in a silicene monolayer for  $\eta = 1$  meV (all) and  $\mu_F = 8$  meV,  $T = 1$  K,  $\hbar\Omega = 50$  meV,  $B = 5$  T and  $\Delta_z = \Delta_{so}$ , when they are not varying.

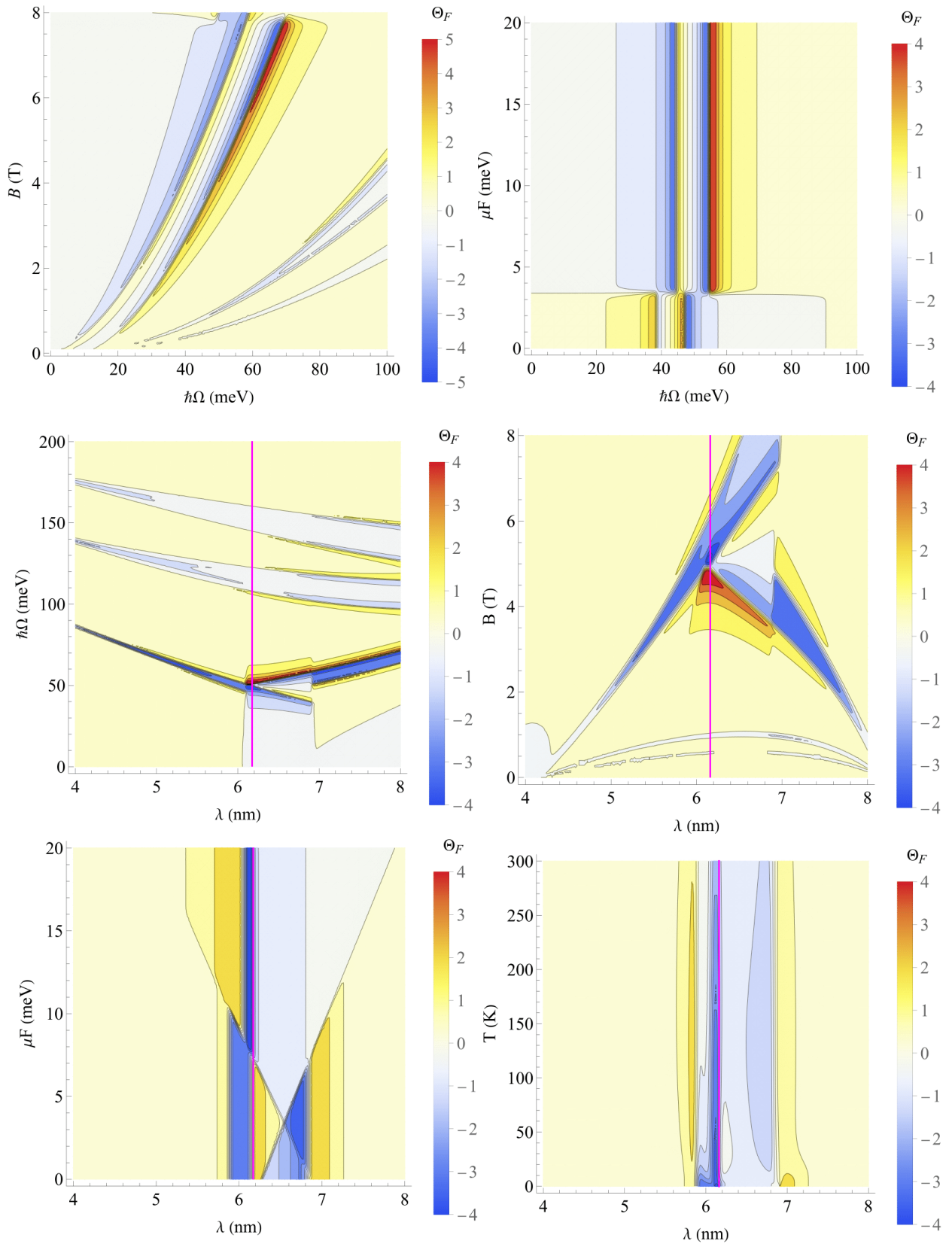


FIG. 5: Faraday rotation angle  $\Theta_F$  (in degrees) in a bulk HgTe QW for  $\eta = 1$  meV (all) and  $\mu_F = 8$  meV,  $T = 1$  K,  $\hbar\Omega = 50$  meV,  $B = 5$  T and  $\lambda = 6.55$  nm, when they are not varying. The critical point  $\lambda_c \simeq 6.17$  nm is marked with a vertical magenta grid line.

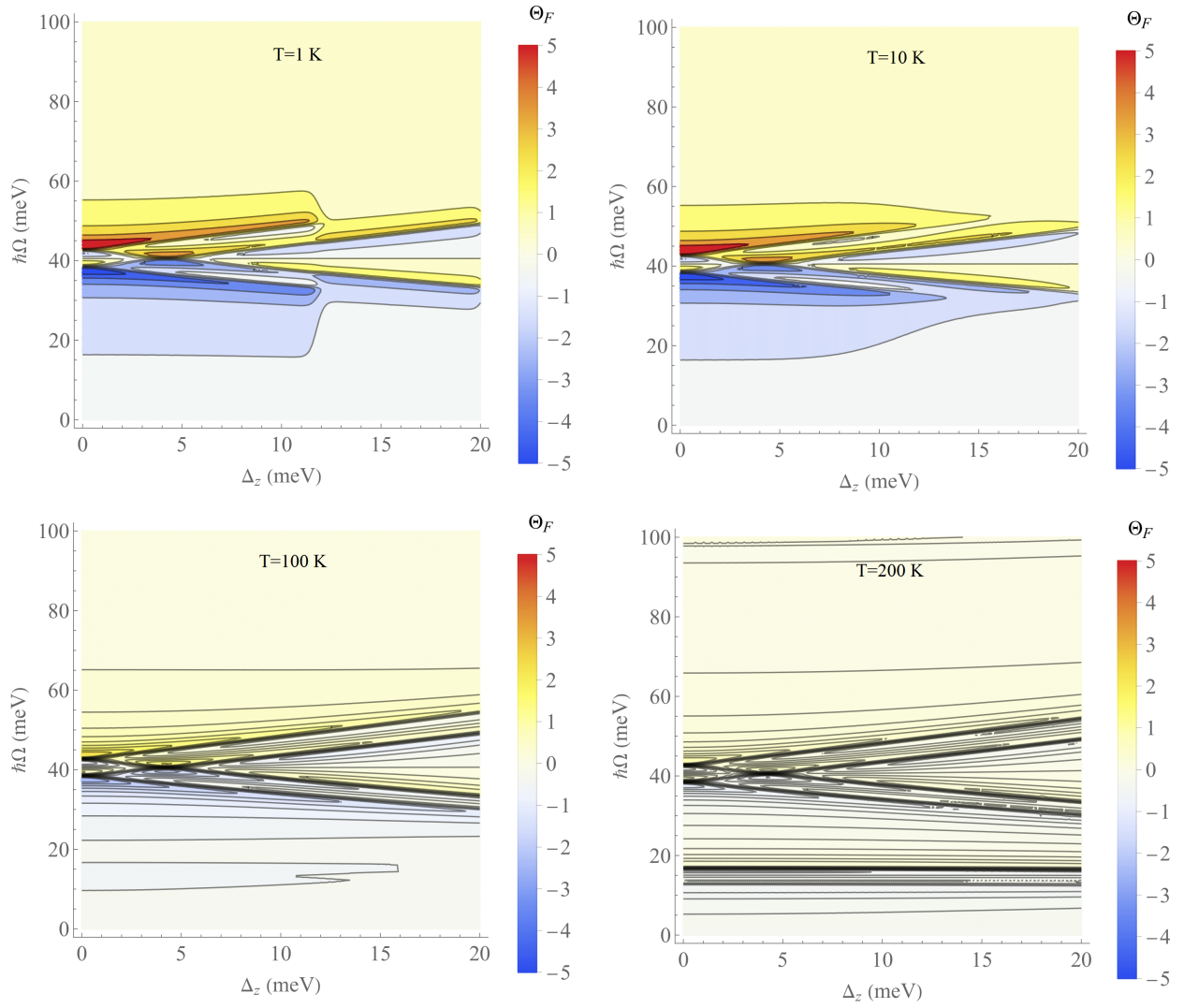


FIG. 6: Faraday rotation angle  $\Theta_F$  (in degrees) in a silicene monolayer in the parameter space  $\{\hbar\Omega, \Delta_z\}$ , and for different values of the temperature  $T = 1, 10, 100, 200$  K. We set the other parameters as  $\eta = 1$  meV,  $\mu_F = 8$  meV, and  $B = 5$  T.

*Fear does not work as long as there is hope*

— President Snow - *The Hunger Games*

# 5

## Conclusions

In the LMG  $U(3)$  model, we propose a more general scheme where the particles belong to a variety of permutation symmetry sectors labeled by  $\mu$  [1]. We prove that the ground state belongs to the totally symmetric sector  $\mu = 1$ , as it is often claimed without justification in the literature [105–109]. We also observe that the QPT can be extended to MSQPT, since every lowest-energy state of a given symmetry sector  $\mu$  displays a QPT at a certain value of the control parameter  $\lambda(\mu)$  as a function of the symmetry sector. We would like to mention that this permutation symmetry can be used in quantum technological applications, such as the thermodynamic advantages of bosonic over fermionic symmetry [110] and in the study of the quantum Gibbs paradox [111, 112].

In Chapter 2, we have also made an extensive study of the totally symmetric sector of the LMG model, containing the ground state that is modeled with parity adapted coherent states or DCATs. Their QPTs can be detected using entanglement measures such as the linear and von Neumann entropies, which give good results in the variational approach (using DSCS) compared to the numerical (matrix representation of the Hamiltonian and diagonalization). In addition, we prove that spin squeezing is connected to pairwise  $D$ -level atom entanglement and is useful in the QPT detection [2]. The information diagrams and the rank of the RDMs also serve as QPT markers in [3]. For further research, we propose to extend these entanglement measures to mixed symmetry sectors of  $U(D)$ , allowing the study of excited states in the LMG model and even in more complex many-body systems.

After an intensive study of the LMG ground state using even parity DCATs, we define the  $\mathfrak{c}$ -DCAT states as DSCS adapted to more general representations of the discrete parity symmetry  $\mathbb{Z}_2^{D-1}$ . They turn out to be variational states modeling the first excited states of the LMG model, capable to detect QPT through the Husimi function, its moments, and the Wehrl entropy of them. The discrete parity symmetry  $\mathbb{Z}_2^{D-1}$  is partially broken in the non trivial (highly interacting) phase due to the GS degeneration, transforming a  $\mathfrak{c}$ -DCAT into a  $\mathfrak{c}_K$ -DCAT with lower  $\mathbb{Z}_2^k$  parity

times a Fock state with  $\mathbb{Z}_2^{D-1-k}$  parity [4]. Furthermore, the Schmidt decomposition theorem applies to the  $\mathfrak{c}$ -DCAT of  $N$  particles, which can be decomposed in terms of superpositions of tensor products of DCATs of  $M$  and  $N - M$  particles [5]. This result makes possible to compute RDM and consequently particle entanglement measures for the  $\mathfrak{c}$ -DCATs. These states could become crucial in the QPT modeling of other many-body systems with a discrete parity symmetry like Dicke [25, 28, 113] or vibron [12, 114, 115] models. A possible generalization of this work is to compute level entanglement instead of particle entanglement, decomposing the  $\mathfrak{c}$ -DCAT into parity adapted CS of  $U(D - K)$  and  $U(K)$ . The Wigner function of these states is also an interesting topic for further research due to a lack of clear definition and its interesting properties as a quasi-distribution function in phase space.

The extension of the coherent state formalism, its adaptation to parity (DCATs), the entanglement measures, and the phase space functions to  $D$ -level systems ( $U(D)$  symmetry) has become a crucial pathway in this thesis, making it possible to study more complex systems than the well known 2- and 3-level [17, 21, 28, 34, 113, 116–119]. Moreover, the formalism studied in Chapter 3 allows us to study any kind of mixed permutation symmetry in a  $D$ -level system, so it is possible to characterize any particle mixture different from bosons and fermions [6].

Connecting with the first paragraph, mixed symmetry sectors are connected to fractionary parastatistics, which are useful to classify quasiparticles and help to understand complex phenomena in condensed matter physics [120]. In particular, we show how particle mixtures in multicomponent quantum Hall systems can be described by rectangular Young diagrams [121–123], a diagrammatic representation of the mixed symmetry sectors. Lieb-Mattis theorem indicates the dominant sector where the ground state lies on, thus we can restrict to it in practice and reduce the computational complexity of the problem, a usual barrier in quantum many-body systems [6]. This could shed light on more complex problems such as multilayer quantum Hall arrangements, which use larger  $U(D)$  symmetries. One example is the case of superconducting properties of twisted bilayer (and trilayer) graphene [124, 125].

Lastly, we have shown that the transmittance and the Faraday angle are universal markers of TPT in different 2D materials, ranging from graphene (and other Dirac materials) to HgTe quantum wells and even anisotropic materials such as the phosphorene [7]. These magneto-optical properties become crucial to characterize 2D materials in condensed matter physics, and to find new topological insulators as hopeful candidates for next generation optoelectronic devices [79, 126]. Furthermore, the path to take in future research is to apply our results to other anisotropic 2D materials, which are promising building blocks for future photonic and optoelectronic devices, as they present low structural symmetry and in-plane optical anisotropy compared to isotropic materials [127, 128].

*If I have seen further than others,  
it is by standing upon the shoulders of giants.*

— Isaac Newton

## References

Disclaimer: The references included in this section are a selection of the bibliography found in the attached articles, and some additional references that have been useful in the candidate’s academic training.

- <sup>1</sup>M. Calixto, A. Mayorgas, and J. Guerrero, “Role of mixed permutation symmetry sectors in the thermodynamic limit of critical three-level Lipkin-Meshkov-Glick atom models”, *Phys. Rev. E* **103**, 012116 (2021).
- <sup>2</sup>M. Calixto, A. Mayorgas, and J. Guerrero, “Entanglement and U(D)-spin squeezing in symmetric multi-qudit systems and applications to quantum phase transitions in Lipkin–Meshkov–Glick D-level atom models”, *Quantum Information Processing* **20**, 304 (2021).
- <sup>3</sup>J. Guerrero, A. Mayorgas, and M. Calixto, “Information diagrams in the study of entanglement in symmetric multi-qudit systems and applications to quantum phase transitions in Lipkin–Meshkov–Glick D-level atom models”, *Quant. Inf. Process.* **21**, 223 (2022).
- <sup>4</sup>A. Mayorgas, J. Guerrero, and M. Calixto, “Localization measures of parity adapted U(D)-spin coherent states applied to the phase space analysis of the D-level lipkin-meshkov-glick model”, *Phys. Rev. E* **108**, 024107 (2023).
- <sup>5</sup>J. Guerrero, A. Sojo, A. Mayorgas, and M. Calixto, “Schmidt decomposition of parity adapted coherent states for symmetric multi-qudits”, *Journal of Physics A: Mathematical and Theoretical* **56**, 355304 (2023).
- <sup>6</sup>M. Calixto, A. Mayorgas, and J. Guerrero, “Hilbert space structure of the low energy sector of U(N) quantum Hall ferromagnets and their classical limit”, *Symmetry* **14** (2022).
- <sup>7</sup>M. Calixto, A. Mayorgas, N. A. Cordero, E. Romera, and O. Castaños, “Faraday rotation and transmittance as markers of topological phase transitions in 2D materials”, *SciPost Phys.* **16**, 077 (2024).
- <sup>8</sup>A. Mayorgas, J. Guerrero, and M. Calixto, “Mixed permutation symmetry quantum phase transitions of critical three-level atom models”, *SciPost Phys. Proc.*, 036 (2023).
- <sup>9</sup>J. Guerrero, A. Sojo, A. Mayorgas, and M. Calixto, “Study of entanglement in symmetric multi-quDits systems through information diagrams”, *SciPost Phys. Proc.*, 029 (2023).
- <sup>10</sup>M. Calixto, A. Mayorgas, and J. Guerrero, “Hilbert space structure and classical limit of the low energy sector of U(N) quantum Hall ferromagnets”, *SciPost Phys. Proc.*, 021 (2023).
- <sup>11</sup>A. Mayorgas, J. Guerrero, and M. Calixto, “Phase space analysis of the 3-level Lipkin-Meshkov-Glick model using parity adapted U(D)-spin coherent states”, *Journal of Physics: Conference Series* **2667**, 012065 (2023).

- <sup>12</sup>F. Iachello and R. Levine, *Algebraic theory of molecules* (Oxford University Press, 1995).
- <sup>13</sup>M. A. Caprio, P. Cejnar, and F. Iachello, “Excited state quantum phase transitions in many-body systems”, *Annals of Physics* **323**, 1106–1135 (2008).
- <sup>14</sup>M. E. Fisher and M. N. Barber, “Scaling theory for finite-size effects in the critical region”, *Phys. Rev. Lett.* **28**, 1516–1519 (1972).
- <sup>15</sup>P. Zanardi and N. Paunković, “Ground state overlap and quantum phase transitions”, *Phys. Rev. E* **74**, 031123 (2006).
- <sup>16</sup>J. Ma, L. Xu, H.-N. Xiong, and X. Wang, “Reduced fidelity susceptibility and its finite-size scaling behaviors in the Lipkin-Meshkov-Glick model”, *Phys. Rev. E* **78**, 051126 (2008).
- <sup>17</sup>E. Romera, M. Calixto, and O. Castaños, “Phase space analysis of first-, second- and third-order quantum phase transitions in the Lipkin-Meshkov-Glick model”, *Physica Scripta* **89**, 095103 (2014).
- <sup>18</sup>H. J. Lipkin, N. Meshkov, and A. J. Glick, “Validity of many-body approximation methods for a solvable model. (i). exact solutions and perturbation theory”, *Nuclear Physics* **62**, 188–198 (1965).
- <sup>19</sup>H. J. Lipkin, N. Meshkov, and A. J. Glick, “Validity of many-body approximation methods for a solvable model: (iii). diagram summations”, *Nuclear Physics* **62**, 211–224 (1965).
- <sup>20</sup>O. Castaños, R. López-Peña, J. G. Hirsch, and E. López-Moreno, “Classical and quantum phase transitions in the Lipkin-Meshkov-Glick model”, *Phys. Rev. B* **74**, 104118 (2006).
- <sup>21</sup>O. Castaños, R. López-Peña, E. Nahmad-Achar, and J. G. Hirsch, “Quantum phase transitions in the LMG model by means of quantum information concepts”, *Journal of Physics: Conference Series* **387**, 012021 (2012).
- <sup>22</sup>F. Iachello and A. Arima, *The interacting boson model*, Cambridge Monographs on Mathematical Physics (Cambridge University Press, 1987).
- <sup>23</sup>R. Gilmore and D. Feng, “Phase transitions in nuclear matter described by pseudospin hamiltonians”, *Nuclear Physics A* **301**, 189–204 (1978).
- <sup>24</sup>D. H. Feng, R. Gilmore, and S. R. Deans, “Phase transitions and the geometric properties of the interacting boson model”, *Phys. Rev. C* **23**, 1254–1258 (1981).
- <sup>25</sup>R. H. Dicke, “Coherence in spontaneous radiation processes”, *Phys. Rev.* **93**, 99–110 (1954).
- <sup>26</sup>E. Romera and Á. Nagy, “Rényi entropy and quantum phase transition in the dicke model”, *Physics Letters A* **375**, 3066–3069 (2011).
- <sup>27</sup>Á. Nagy and E. Romera, “Fisher information, Rényi entropy power and quantum phase transition in the Dicke model”, *Physica A: Statistical Mechanics and its Applications* **391**, 3650–3655 (2012).
- <sup>28</sup>O. Castaños, S. Cordero, R. López-Peña, and E. Nahmad-Achar, “Phase space properties of light within the generalised Dicke model”, *Physica Scripta* **93**, 085102 (2018).

- <sup>29</sup>R. del Real, M. Calixto, and E. Romera, “The husimi distribution, the Wehrl entropy and the superradiant phase in spin–boson interactions”, *Physica Scripta* **T153**, 014016 (2013).
- <sup>30</sup>E. Romera, M. Calixto, and A. Nagy, “Entropic uncertainty and the quantum phase transition in the Dicke model”, *EPL* **97**, 20011 (2012).
- <sup>31</sup>S. Cordero, E. Nahmad-Achar, R. López-Peña, and O. Castaños, “Quantum phase diagrams of matter-field hamiltonians I: fidelity, bures distance, and entanglement”, *Physica Scripta* **96**, 035104 (2021).
- <sup>32</sup>N. Read and S. Sachdev, “Some features of the phase diagram of the square lattice  $su(n)$  antiferromagnet”, *Nuclear Physics B* **316**, 609–640 (1989).
- <sup>33</sup>S. L. Sondhi, S. M. Girvin, J. P. Carini, and D. Shahar, “Continuous quantum phase transitions”, *Rev. Mod. Phys.* **69**, 315–333 (1997).
- <sup>34</sup>C. Pérez-Campos, J. R. González-Alonso, O. Castaños, and R. López-Peña, “Entanglement and localization of a two-mode Bose-Einstein condensate”, *Annals of Physics* **325**, 325–344 (2010).
- <sup>35</sup>M. Vojta, “Quantum phase transitions”, *Reports on Progress in Physics* **66**, 2069 (2003).
- <sup>36</sup>D. Bitko, T. F. Rosenbaum, and G. Aeppli, “Quantum critical behavior for a model magnet”, *Phys. Rev. Lett.* **77**, 940–943 (1996).
- <sup>37</sup>E. Dagotto, “Correlated electrons in high-temperature superconductors”, *Rev. Mod. Phys.* **66**, 763–840 (1994).
- <sup>38</sup>J. Orenstein and A. J. Millis, “Advances in the physics of high-temperature superconductivity”, *Science* **288**, 468–474 (2000).
- <sup>39</sup>S. Sachdev, “Quantum criticality: competing ground states in low dimensions”, *Science* **288**, 475–480 (2000).
- <sup>40</sup>S. V. Kravchenko, W. E. Mason, G. E. Bowker, J. E. Furneaux, V. M. Pudalov, and M. D’Iorio, “Scaling of an anomalous metal-insulator transition in a two-dimensional system in silicon at  $B=0$ ”, *Phys. Rev. B* **51**, 7038–7045 (1995).
- <sup>41</sup>P. Coleman, “Theories of non-Fermi liquid behavior in heavy fermions”, *Physica B: Condensed Matter* **259-261**, 353–358 (1999).
- <sup>42</sup>R. N. Deb, “Quantum entanglement in multiparticle systems of two-level atoms”, *Phys. Rev. A* **84**, 032327 (2011).
- <sup>43</sup>M. Calixto, E. Romera, and O. Castaños, “Analogies between the topological insulator phase of 2D Dirac materials and the superradiant phase of atom-field systems”, *International Journal of Quantum Chemistry* **121**, e26464 (2021).
- <sup>44</sup>B. Hall, *Lie Groups, Lie Algebras, and Representations* (Springer, 2015).
- <sup>45</sup>W. Warner, *Foundations of Differentiable Manifolds and Lie Groups* (Springer, 1983).
- <sup>46</sup>J. Wybourne, *Classical groups for physicists* (Wiley and Sons, 1974).
- <sup>47</sup>P. Jordan, “Der zusammenhang der symmetrischen und linearen gruppen und das mehrkörperproblem”, *Zeitschrift für Physik* **94**, 531–535 (1935).
- <sup>48</sup>J. Schwinger, “On angular momentum”, 10.2172/4389568 (1952).

- <sup>49</sup>L. C. Biedenharn and J. Louck, *Angular momentum in quantum physics: theory and application*, Encyclopedia of Mathematics and its Applications (Cambridge University Press, 1984).
- <sup>50</sup>A. Klein and E. Marshalek, “Boson realizations of Lie algebras with applications to nuclear physics”, *Rev. Mod. Phys.* **63**, 375–558 (1991).
- <sup>51</sup>F. Iachello, *Lie algebras and applications* (Springer, 2015).
- <sup>52</sup>A. Barut and R. Raczka, *Theory of group representations and applications*, eng (Polish Scientific Publishers, 1980).
- <sup>53</sup>W. Greiner and B. Müller, *Quantum mechanics. symmetries* (Springer, 1994).
- <sup>54</sup>W.-K. Tung, *Group theory in physics* (World Scientific, 1985).
- <sup>55</sup>E. Lieb and D. Mattis, “Theory of ferromagnetism and the ordering of electronic energy levels”, *Phys. Rev.* **125**, 164–172 (1962).
- <sup>56</sup>A. Perelomov, *Generalized coherent states and their applications* (Springer, 1986).
- <sup>57</sup>J. Gazeau, *Coherent states in quantum physics* (John Wiley & Sons, Ltd, 2009).
- <sup>58</sup>S. Gnutzmann and M. Kus, “Coherent states and the classical limit on irreducible representations”, *Journal of Physics A: Mathematical and General* **31**, 9871–9896 (1998).
- <sup>59</sup>I. Iachello, “Algebraic models of many-body systems and their dynamic symmetries and supersymmetries”, *Journal of Physics: Conference Series* **1194**, 012048 (2019).
- <sup>60</sup>R. Horodecki, P. Horodecki, M. Horodecki, and K. Horodecki, “Quantum entanglement”, *Rev. Mod. Phys.* **81**, 865–942 (2009).
- <sup>61</sup>I. Bengtsson and K. Życzkowski, *Geometry of quantum states: an introduction to quantum entanglement* (Cambridge University Press, 2006).
- <sup>62</sup>P. A. M. Dirac, “Note on exchange phenomena in the thomas atom”, *Mathematical Proceedings of the Cambridge Philosophical Society* **26**, 376–385 (1930).
- <sup>63</sup>C. Cohen-Tannoudji, B. Diu, and F. Laloë, *Quantum mechanics* (Wiley, 1977).
- <sup>64</sup>M. A. Nielsen and I. L. Chuang, *Quantum computation and quantum information: 10th anniversary edition* (Cambridge University Press, 2010).
- <sup>65</sup>D. Berry and B. Sanders, “Bounds on general entropy measures”, *J. Phys. A: Math. Gen.* **36**, 12255 (2003).
- <sup>66</sup>T.-C. Wei, K. Nemoto, P. M. Goldbart, P. G. Kwiat, W. J. Munro, and F. Verstraete, “Maximal entanglement versus entropy for mixed quantum states”, *Phys. Rev. A* **67**, 022110 (2003).
- <sup>67</sup>P. Harremoës and F. Topsøe, “Inequalities between entropy and index of coincidence derived from information diagrams”, *IEEE Transactions on Information Theory* **47**, 2944–2960 (2001).
- <sup>68</sup>R. Juárez-Amaro, L. M. Rosales, J. A. Anaya-Contreras, A. Zúñiga-Segundo, and H. M. Moya-Cessa, “Relation between the entropy and the linear entropy in the ion-laser interaction”, *Journal of Modern Optics* **67**, 805–810 (2020).
- <sup>69</sup>P. W. Anderson, “Absence of diffusion in certain random lattices”, *Phys. Rev.* **109**, 1492–1505 (1958).

- <sup>70</sup>C. Aulbach, A. Wobst, G.-L. Ingold, P. Hänggi, and I. Varga, “Phase-space visualization of a metal–insulator transition”, *New Journal of Physics* **6**, 70–70 (2004).
- <sup>71</sup>F. Evers and A. D. Mirlin, “Anderson transitions”, *Rev. Mod. Phys.* **80**, 1355–1417 (2008).
- <sup>72</sup>F. E. and J. Schroeck, *Quantum mechanics on phase space* (Springer Netherlands, 1996).
- <sup>73</sup>W. P. Schleich, *Quantum optics in phase space* (Wiley-VCH Verlag Berlin GmbH, 2001).
- <sup>74</sup>J. Gazeau, *Coherent states in quantum physics* (Wiley-VCH, 2009).
- <sup>75</sup>A. Vourdas, “Analytic representations in quantum mechanics”, *Journal of Physics A: Mathematical and General* **39**, R65–R141 (2006).
- <sup>76</sup>T. L. Curtright, D. B. Fairlie, and C. K. Zachos, *A concise treatise on quantum mechanics in phase space* (World Scientific Publishing, 2014).
- <sup>77</sup>U. Leonhardt, *Measuring the quantum state of light* (Cambridge University Press, 1997).
- <sup>78</sup>C. Brif and A. Mann, “A general theory of phase-space quasiprobability distributions”, *Journal of Physics A: Mathematical and General* **31**, L9–L17 (1998).
- <sup>79</sup>B. A. Bernevig, *Topological insulators and topological superconductors* (Princeton University Press, 2013).
- <sup>80</sup>M. Z. Hasan and C. L. Kane, “Colloquium: topological insulators”, *Rev. Mod. Phys.* **82**, 3045–3067 (2010).
- <sup>81</sup>X.-L. Qi and S.-C. Zhang, “Topological insulators and superconductors”, *Rev. Mod. Phys.* **83**, 1057–1110 (2011).
- <sup>82</sup>J. Watson and G. Castro, “A review of high-temperature electronics technology and applications”, *Journal of Materials Science: Materials in Electronics* **26**, 9226–9235 (2015).
- <sup>83</sup>P. Dreike, D. Fleetwood, D. King, D. Sprauer, and T. Zipperian, “An overview of high-temperature electronic device technologies and potential applications”, *IEEE Transactions on Components, Packaging, and Manufacturing Technology: Part A* **17**, 594–609 (1994).
- <sup>84</sup>L. Kou, Y. Ma, Z. Sun, T. Heine, and C. Chen, “Two-dimensional topological insulators: progress and prospects”, *The Journal of Physical Chemistry Letters* **8**, 1905–1919 (2017).
- <sup>85</sup>C. L. Kane and E. J. Mele, “Quantum Spin Hall Effect in Graphene”, *Phys. Rev. Lett.* **95**, 226801 (2005).
- <sup>86</sup>S.-Q. Shen, *Topological Insulators: Dirac Equation in Condensed Matters* (Springer-Verlag Berlin Heidelberg, 2012).
- <sup>87</sup>L. O. J. K. Asboth and A. S. A. Palyi, *A short course on topological insulators: band structure and edge states in one and two dimensions* (Springer International Publishing Switzerland, 2016).
- <sup>88</sup>B. A. Bernevig, T. L. Hughes, and S.-C. Zhang, “Quantum Spin Hall Effect and Topological Phase Transition in HgTe Quantum Wells”, *Science* **314**, 1757–1761 (2006).

- <sup>89</sup>M. König, S. Wiedmann, C. Brune, A. Roth, H. Buhmann, L. W. Molenkamp, X.-L. Qi, and S.-C. Zhang, “Quantum Spin Hall Insulator State in HgTe Quantum Wells”, *Science* **318**, 766–770 (2007).
- <sup>90</sup>A. Carvalho, M. Wang, X. Zhu, A. S. Rodin, H. Su, and A. H. Castro Neto, “Phosphorene: from theory to applications”, *Nature Reviews Materials* **1**, 16061 (2016).
- <sup>91</sup>A. S. Rodin, A. Carvalho, and A. H. Castro Neto, “Strain-induced gap modification in black phosphorus”, *Phys. Rev. Lett.* **112**, 176801 (2014).
- <sup>92</sup>H. Guo, N. Lu, J. Dai, X. Wu, and X. C. Zeng, “Phosphorene Nanoribbons, Phosphorus Nanotubes, and van der Waals Multilayers”, *The Journal of Physical Chemistry C* **118**, 14051–14059 (2014).
- <sup>93</sup>H. Liu, A. T. Neal, Z. Zhu, Z. Luo, X. Xu, D. Tománek, and P. D. Ye, “Phosphorene: an unexplored 2d semiconductor with a high hole mobility”, *ACS Nano* **8**, 4033–4041 (2014).
- <sup>94</sup>T. Low, A. S. Rodin, A. Carvalho, Y. Jiang, H. Wang, F. Xia, and A. H. Castro Neto, “Tunable optical properties of multilayer black phosphorus thin films”, *Phys. Rev. B* **90**, 075434 (2014).
- <sup>95</sup>X. Y. Zhou, R. Zhang, J. P. Sun, Y. L. Zou, D. Zhang, W. K. Lou, F. Cheng, G. H. Zhou, F. Zhai, and K. Chang, “Landau levels and magneto-transport property of monolayer phosphorene”, *Scientific Reports* **5**, 12295 (2015).
- <sup>96</sup>M. J. Spencer and T. M. (Eds.), *Silicene: structure, properties and applications*, (Springer Series in Materials Science vol. 235, 2016).
- <sup>97</sup>C. J. Tabert and E. J. Nicol, “Magneto-optical conductivity of silicene and other buckled honeycomb lattices”, *Phys. Rev. B* **88**, 085434 (2013).
- <sup>98</sup>M. Shah and M. S. Anwar, “Magneto-optical effects in the landau level manifold of 2d lattices with spin-orbit interaction”, *Opt. Express* **27**, 23217–23233 (2019).
- <sup>99</sup>P. Nualpijit and B. Soodchomshom, “Enhanced faraday rotation and control of pure spin-valley optical conductivity by topological phase in silicene”, *Physica E: Low-dimensional Systems and Nanostructures* **137**, 115011 (2022).
- <sup>100</sup>N. D. Hien, C. V. Nguyen, N. N. Hieu, S. S. Kubakaddi, C. A. Duque, M. E. Mora-Ramos, L. Dinh, T. N. Bich, and H. V. Phuc, “Magneto-optical transport properties of monolayer transition metal dichalcogenides”, *Phys. Rev. B* **101**, 045424 (2020).
- <sup>101</sup>D. J. Thouless, M. Kohmoto, M. P. Nightingale, and M. den Nijs, “Quantized hall conductance in a two-dimensional periodic potential”, *Phys. Rev. Lett.* **49**, 405–408 (1982).
- <sup>102</sup>G. D. Mahan, *Many-particle physics, 3rd edition* (Kluwer Academic/Plenum Publishers, New York, 2000).
- <sup>103</sup>P. Allen, “Chapter 6 electron transport”, in *Conceptual foundations of materials*, Vol. 2, edited by S. G. Louie and M. L. Cohen, Contemporary Concepts of Condensed Matter Science (Elsevier, 2006), pp. 165–218.
- <sup>104</sup>J. W. von Goethe, *Wilhelm Meisters Wanderjahre oder die Entsagenden* (Cotta, 1829).
- <sup>105</sup>S. Gnuzmann and M. Kuś, “Coherent states and the classical limit on irreducible su3 representations”, *Journal of Physics A: Mathematical and General* **31**, 9871 (1999).

- <sup>106</sup>S. Gnutzmann, F. Haake, and M. Kuś, “Quantum chaos of su3 observables”, *Journal of Physics A: Mathematical and General* **33**, 143 (1999).
- <sup>107</sup>D. C. Meredith, S. E. Koonin, and M. R. Zirnbauer, “Quantum chaos in a schematic shell model”, *Phys. Rev. A* **37**, 3499–3513 (1988).
- <sup>108</sup>W.-G. Wang, F. M. Izrailev, and G. Casati, “Structure of eigenstates and local spectral density of states: a three-orbital schematic shell model”, *Phys. Rev. E* **57**, 323–339 (1998).
- <sup>109</sup>P. Leboeuf and M. Saraceno, “Eigenfunctions of non-integrable systems in generalised phase spaces”, *Journal of Physics A: Mathematical and General* **23**, 1745 (1999).
- <sup>110</sup>N. M. Myers and S. Deffner, “Bosons outperform fermions: the thermodynamic advantage of symmetry”, *Phys. Rev. E* **101**, 012110 (2020).
- <sup>111</sup>M. A. M. Versteegh and D. Dieks, “The gibbs paradox and the distinguishability of identical particles”, *American Journal of Physics* **79**, 741–746 (2011).
- <sup>112</sup>B. Yadin, B. Morris, and G. Adesso, “Extracting work from mixing indistinguishable systems: A quantum Gibbs paradox”, in (2020).
- <sup>113</sup>M. Calixto, O. Castaños, and E. Romera, “Entanglement and quantum phase diagrams of symmetric multi-qubit systems”, *Journal of Statistical Mechanics: Theory and Experiment* **2017**, 103103 (2017).
- <sup>114</sup>M. Calixto, E. Romera, and R. del Real, “Parity-symmetry-adapted coherent states and entanglement in quantum phase transitions of vibron models”, *Journal of Physics A: Mathematical and Theoretical* **45**, 365301 (2012).
- <sup>115</sup>M. Calixto, E. Romera, and R. del Real, “Parity-symmetry-adapted coherent states and entanglement in quantum phase transitions of vibron models”, *Journal of Physics A: Mathematical and Theoretical* **45**, 365301 (2012).
- <sup>116</sup>E. Romera, R. del Real, and M. Calixto, “Husimi distribution and phase-space analysis of a Dicke-model quantum phase transition”, *Phys. Rev. A* **85**, 053831 (2012).
- <sup>117</sup>M. Calixto, R. del Real, and E. Romera, “Husimi distribution and phase-space analysis of a vibron-model quantum phase transition”, *Phys. Rev. A* **86**, 032508 (2012).
- <sup>118</sup>R. López-Peña, S. Cordero, E. Nahmad-Achar, and O. Castaños, “Symmetry adapted coherent states for three-level atoms interacting with one-mode radiation”, *Physica Scripta* **90**, 068016 (2015).
- <sup>119</sup>O. Castaños, R. López-Peña, E. Nahmad-Achar, and J. G. Hirsch, “Matter-field entanglement within the Dicke model”, *AIP Conference Proceedings* **1488**, 138–149 (2012).
- <sup>120</sup>L. Venema, B. Verberck, I. Georgescu, G. Prando, E. Couderc, S. Milana, M. Maragkou, L. Persechini, G. Pacchioni, and L. Fleet, “The quasiparticle zoo”, *Nature Physics* **12**, 1085–1089 (2016).
- <sup>121</sup>M. Calixto, C. Peón-Nieto, and E. Pérez-Romero, “Coherent states for N-component fractional quantum Hall systems and their nonlinear sigma models”, *Annals of Physics* **373**, 52–66 (2016).
- <sup>122</sup>M. Calixto, C. Peón-Nieto, and E. Pérez-Romero, “Hilbert space and ground-state structure of bilayer quantum Hall systems at  $\nu = 2/\lambda$ ”, *Phys. Rev. B* **95**, 235302 (2017).

- <sup>123</sup>M. Calixto and C. Peón-Nieto, “Husimi function and phase-space analysis of bilayer quantum Hall systems at  $\nu = 2$ ”, *Journal of Statistical Mechanics: Theory and Experiment* **2018**, 053112 (2018).
- <sup>124</sup>R. Bistritzer and A. H. MacDonald, “Moiré bands in twisted double-layer graphene”, *Proceedings of the National Academy of Sciences* **108**, 12233–12237 (2011).
- <sup>125</sup>Y. Cao, V. Fatemi, A. Demir, S. Fang, S. L. Tomarken, J. Y. Luo, J. D. Sanchez-Yamagishi, K. Watanabe, T. Taniguchi, E. Kaxiras, R. C. Ashoori, and P. Jarillo-Herrero, “Correlated insulator behaviour at half-filling in magic-angle graphene superlattices”, *Nature* **556**, 80–84 (2018).
- <sup>126</sup>I. D. Tokman, Q. Chen, I. A. Shereshevsky, V. I. Pozdnyakova, I. Oladyshkin, M. Tokman, and A. Belyanin, “Inverse Faraday effect in graphene and Weyl semimetals”, *Phys. Rev. B* **101**, 174429 (2020).
- <sup>127</sup>J. Zhao, D. Ma, C. Wang, Z. Guo, B. Zhang, J. Li, G. Nie, N. Xie, and H. Zhang, “Recent advances in anisotropic two-dimensional materials and device applications”, *Nano Research* **14**, 897–919 (2021).
- <sup>128</sup>X. Li, H. Liu, C. Ke, W. Tang, M. Liu, F. Huang, Y. Wu, Z. Wu, and J. Kang, “Review of anisotropic 2d materials: controlled growth, optical anisotropy modulation, and photonic applications”, *Laser & Photonics Reviews* **15**, 2100322 (2021).